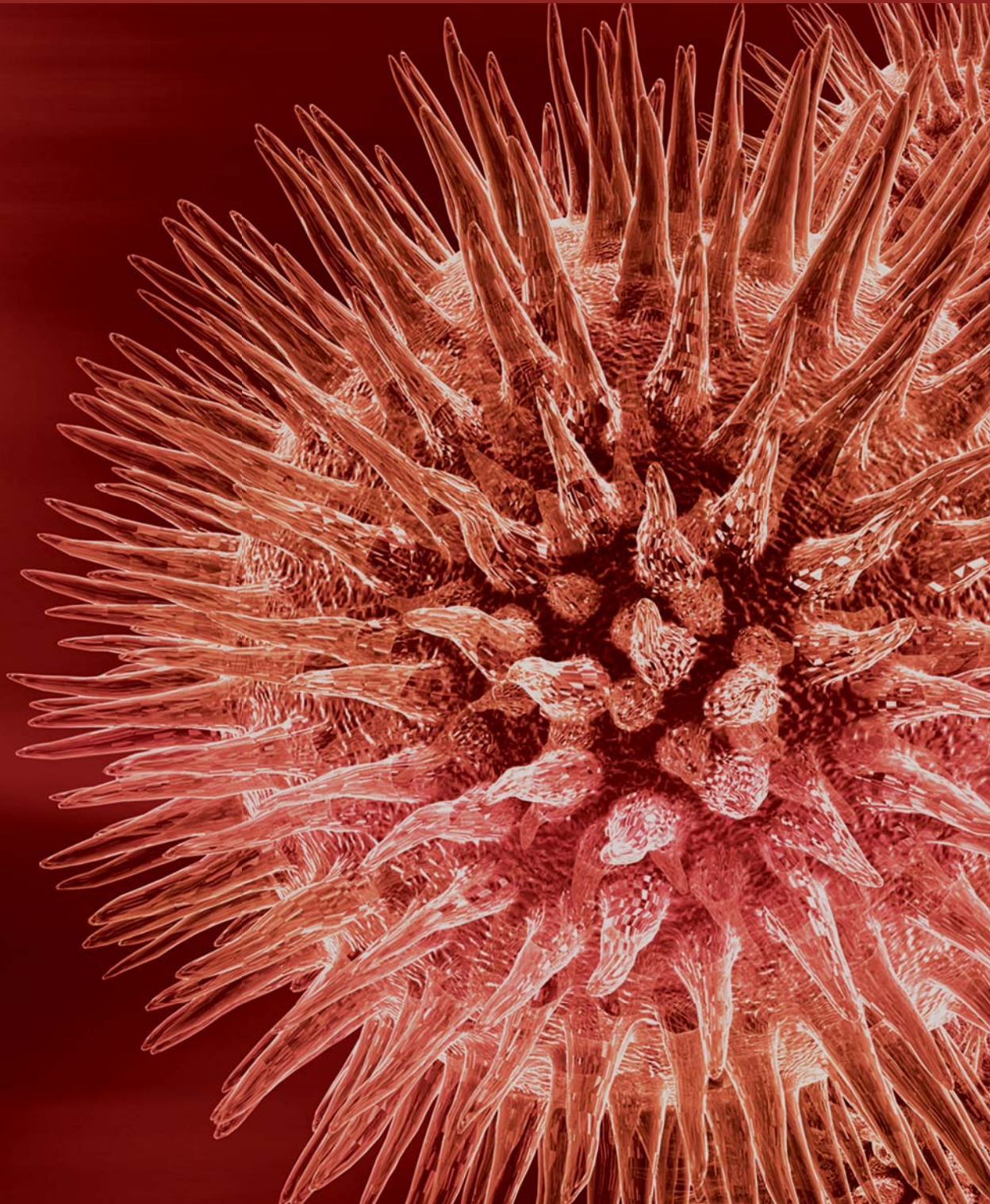


Journal of Biomedicine and Biotechnology

Muscle Contractility and Cell Motility

Guest Editors: J.-P. Jin, Robert J. Bloch, Xupei Huang, and Lars Larsson





Muscle Contractility and Cell Motility

Journal of Biomedicine and Biotechnology

Muscle Contractility and Cell Motility

Guest Editors: J.-P. Jin, Robert J. Bloch, Xupei Huang,
and Lars Larsson



Copyright © 2012 Hindawi Publishing Corporation. All rights reserved.

This is a special issue published in “Journal of Biomedicine and Biotechnology.” All articles are open access articles distributed under the Creative Commons Attribution License, which permits unrestricted use, distribution, and reproduction in any medium, provided the original work is properly cited.

Editorial Board

The editorial board of the journal is organized into sections that correspond to the subject areas covered by the journal.

Agricultural Biotechnology

Guihua H. Bai, USA	Hari B. Krishnan, USA	B. C. Saha, USA
Christopher P. Chanway, Canada	Carol A. Mallory-Smith, USA	Mariam B. Sticklen, USA
Ravindra N. Chibbar, Canada	Dennis P. Murr, Canada	Chiu-Chung Young, Taiwan
Ian Godwin, Australia	Rodomiro Ortiz, Sweden	

Animal Biotechnology

E. S. Chang, USA	Tosso Leeb, Switzerland	Lawrence B. Schook, USA
Bhanu P. Chowdhary, USA	James D. Murray, USA	Mari A. Smits, The Netherlands
Noelle E. Cockett, USA	Anita M. Oberbauer, USA	Leon Spicer, USA
Peter Dovc, Slovenia	Jorge A. Piedrahita, USA	J. Verstegen, USA
Scott C. Fahrenkrug, USA	Daniel Pomp, USA	Matthew B. Wheeler, USA
Dorian J. Garrick, USA	Kent M. Reed, USA	Kenneth L. White, USA
Thomas A. Hoagland, USA	Lawrence Reynolds, USA	

Biochemistry

Robert Blumenthal, USA	Paul W. Doetsch, USA	Wen-Hwa Lee, USA
David Ronald Brown, UK	Hicham Fenniri, Canada	Richard D. Ludescher, USA
Saulius Butenas, USA	Nick V. Grishin, USA	George Makhatadze, USA
Vittorio Calabrese, Italy	J. Guy Guillemette, Canada	Leonid Medved, USA
Miguel Castanho, Portugal	Paul W. Huber, USA	Susan A. Rotenberg, USA
Francis J. Castellino, USA	Chen-Hsiung Hung, Taiwan	Jason Shearer, USA
Roberta Chiaraluce, Italy	Michael Kalafatis, USA	Andrei Surguchov, USA
D. M. Clarke, Canada	B. E. Kemp, Australia	John B. Vincent, USA
Francesca Cutruzzolà, Italy	Phillip E. Klebba, USA	Y. George Zheng, USA

Bioinformatics

T. Akutsu, Japan	Stavros J. Hamodrakas, Greece	Florencio Pazos, Spain
Miguel A. Andrade, Germany	Paul Harrison, USA	Zhirong Sun, China
Mark Y. Borodovsky, USA	George Karypis, USA	Ying Xu, USA
Rita Casadio, Italy	Jack A. Leunissen, The Netherlands	Alexander Zelikovsky, USA
Artem Cherkasov, Canada	Guohui Lin, Canada	Albert Zomaya, Australia
David Corne, UK	Satoru Miyano, Japan	
Sorin Draghici, USA	Zoran Obradovic, USA	

Biophysics

Miguel Castanho, Portugal
P. Bryant Chase, USA
Kuo-Chen Chou, USA
Rizwan Khan, India

Ali A. Khraibi, Saudi Arabia
Rumiana Koynova, USA
Serdar Kuyucak, Australia
Jianjie Ma, USA

S. B. Petersen, Denmark
Peter Schuck, USA
Claudio M. Soares, Portugal

Cell Biology

Omar Benzakour, France
Sanford I. Bernstein, USA
Phillip I. Bird, Australia
Eric Bouhassira, USA
Mohamed Boutjdir, USA
Chung-Liang Chien, Taiwan
Richard Gomer, USA
Paul J. Higgins, USA
Pavel Hozak, Czech Republic

Xudong Huang, USA
Anton M. Jetten, USA
Seamus J. Martin, Ireland
Manuela Martins-Green, USA
Shoichiro Ono, USA
George Perry, USA
M. Piacentini, Italy
George E. Plopper, USA
Lawrence Rothblum, USA

Michael Sheetz, USA
James L. Sherley, USA
G. S. Stein, USA
Richard Tucker, USA
Thomas van Groen, USA
Andre Van Wijnen, USA
Steve Winder, UK
Chuan Yue Wu, USA
Bin-Xian Zhang, USA

Genetics

Adewale Adeyinka, USA
Claude Bagnis, France
J. Birchler, USA
Susan Blanton, USA
Barry J. Byrne, USA
R. Chakraborty, USA
Domenico Coviello, Italy
Sarah H. Elsea, USA
Celina Janion, Poland

J. Spencer Johnston, USA
M. Ilyas Kamboh, USA
Feige Kaplan, Canada
Manfred Kayser, The Netherlands
Brynn Levy, USA
Xiao Jiang Li, USA
Thomas Liehr, Germany
James M. Mason, USA
Mohammed Rachidi, France

Raj S. Ramesar, South Africa
Elliot D. Rosen, USA
Dharambir K. Sanghera, USA
Michael Schmid, Germany
Markus Schuelke, Germany
Wolfgang Arthur Schulz, Germany
Jorge Sequeiros, Portugal
Mouldy Sioud, Norway
Rongjia Zhou, China

Genomics

Vladimir Bajic, Saudi Arabia
Margit Burmeister, USA
Settara Chandrasekharappa, USA
Yataro Daigo, Japan

J. Spencer Johnston, USA
Vladimir Larionov, USA
Thomas Lufkin, Singapore
John L. McGregor, France

John V. Moran, USA
Yasushi Okazaki, Japan
Gopi K. Podila, USA
Momiao Xiong, USA

Immunology

Hassan Alizadeh, USA
Peter Bretscher, Canada
Robert E. Cone, USA
Terry L. Delovitch, Canada
Anthony L. DeVico, USA
Nick Di Girolamo, Australia
Don Mark Estes, USA
Soldano Ferrone, USA
Jeffrey A. Frelinger, USA
John Robert Gordon, Canada

James D. Gorham, USA
Silvia Gregori, Italy
Thomas Griffith, USA
Young S. Hahn, USA
Dorothy E. Lewis, USA
Bradley W. McIntyre, USA
R. Lee Mosley, USA
Marija Mostarica-Stojković, Serbia
Hans Konrad Muller, Australia
Ali Ouaiissi, France

Kanury V. S. Rao, India
Yair Reisner, Israel
Harry W. Schroeder, USA
Wilhelm Schwaeble, UK
Nilabh Shastri, USA
Yufang Shi, China
Piet Stinissen, Belgium
Hannes Stockinger, Austria
J. W. Tervaert, The Netherlands
Graham R. Wallace, UK

Microbial Biotechnology

Jozef Anné, Belgium
Yoav Bashan, Mexico
Marco Bazzicalupo, Italy
Nico Boon, Belgium

Luca Simone Cocolin, Italy
Peter Coloe, Australia
Daniele Daffonchio, Italy
Han de Winde, The Netherlands

Yanhe Ma, China
Bernd H. A. Rehm, New Zealand
Angela Sessitsch, Austria

Microbiology

D. Beighton, UK
Steven R. Blanke, USA
Stanley Brul, The Netherlands
Isaac K. O. Cann, USA
Stephen K. Farrand, USA
Alain Filloux, UK

Gad Frankel, UK
Roy Gross, Germany
Hans-Peter Klenk, Germany
Tanya Parish, UK
Gopi K. Podila, USA
Frederick D. Quinn, USA

Didier A. Raoult, France
Isabel Sá-Correia, Portugal
P. L. C. Small, USA
Michael Thomm, Germany
H. C. van der Mei, The Netherlands
Schwan William, USA

Molecular Biology

Rudi Beyaert, Belgium
Michael Bustin, USA
Douglas Cyr, USA
K. Iatrou, Greece
Lokesh Joshi, Ireland

David W. Litchfield, Canada
Wuyuan Lu, USA
Patrick Matthias, Switzerland
John L. McGregor, France
S. L. Mowbray, Sweden

Elena Orlova, UK
Yeon-Kyun Shin, USA
William S. Trimble, Canada
Lisa Wiesmuller, Germany
Masamitsu Yamaguchi, Japan

Oncology

Colin Cooper, UK	Steve B. Jiang, USA	Allal Ouhtit, Oman
F. M. J. Debruyne, The Netherlands	Daehee Kang, Republic of Korea	Frank Pajonk, USA
Nathan Ames Ellis, USA	Abdul R. Khokhar, USA	Waldemar Priebe, USA
Dominic Fan, USA	Rakesh Kumar, USA	F. C. Schmitt, Portugal
Gary E. Gallick, USA	Macus Tien Kuo, USA	Sonshin Takao, Japan
Daila S. Gridley, USA	Eric W. Lam, UK	Ana Maria Tari, USA
Xin-yuan Guan, Hong Kong	Sue-Hwa Lin, USA	Henk G. Van Der Poel, The Netherlands
Anne Hamburger, USA	Kapil Mehta, USA	Haodong Xu, USA
Manoor Prakash Hande, Singapore	Orhan Nalcioğlu, USA	David J. Yang, USA
Beric Henderson, Australia	P. J. Oefner, Germany	

Pharmacology

Abdel A. Abdel-Rahman, USA	Ayman El-Kadi, Canada	Kennerly S. Patrick, USA
M. Badr, USA	Jeffrey Hughes, USA	Vickram Ramkumar, USA
Stelvio M. Bandiera, Canada	Kazim Husain, USA	Michael J. Spinella, USA
Ronald E. Baynes, USA	Farhad Kamali, UK	Quadiri Timour, France
R. Keith Campbell, USA	Michael Kassiou, Australia	Todd W. Vanderah, USA
Hak-Kim Chan, Australia	Joseph J. McArdle, USA	Val J. Watts, USA
Michael D. Coleman, UK	Mark J. McKeage, New Zealand	David J. Waxman, USA
J. Descotes, France	Daniel T. Monaghan, USA	
Dobromir Dobrev, Germany	T. Narahashi, USA	

Plant Biotechnology

Prem L. Bhalla, Australia	Liwen Jiang, Hong Kong	Ralf Reski, Germany
J. R. Botella, Australia	Pulugurtha B. Kirti, India	Sudhir Sopory, India
Elvira G. De Mejia, USA	Yong Pyo Lim, Republic of Korea	
H. M. Häggman, Finland	Gopi K. Podila, USA	

Toxicology

Michael Aschner, USA	Youmin James Kang, USA	R. S. Tjeerdema, USA
Michael L. Cunningham, USA	M. Firoze Khan, USA	Kenneth Turteltaub, USA
Laurence D. Fechter, USA	Pascal Kintz, France	Brad Upham, USA
Hartmut Jaeschke, USA		

Virology

Nafees Ahmad, USA
Edouard Cantin, USA
Ellen Collisson, USA
Kevin M. Coombs, Canada
Norbert K. Herzog, USA
Tom Hobman, Canada
Shahid Jameel, India

Fred Kibenge, Canada
Fenyong Liu, USA
Éric Rassart, Canada
Gerald G. Schumann, Germany
Y.-C. Sung, Republic of Korea
Gregory Tannock, Australia

Ralf Wagner, Germany
Jianguo Wu, China
Decheng Yang, Canada
Jiing-Kuan Yee, USA
Xueping Zhou, China
Wen-Quan Zou, USA

Contents

Muscle Contractility and Cell Motility, J.-P. Jin, Robert J. Bloch, Xupei Huang, and Lars Larsson
Volume 2012, Article ID 257812, 3 pages

Various Jobs of Proteolytic Enzymes in Skeletal Muscle during Unloading: Facts and Speculations,
E. V. Kachaeva and B. S. Shenkman
Volume 2012, Article ID 493618, 15 pages

Influences of Desmin and Keratin 19 on Passive Biomechanical Properties of Mouse Skeletal Muscle,
Sameer B. Shah, James M. Love, Andrea O'Neill, Richard M. Lovering, and Robert J. Bloch
Volume 2012, Article ID 704061, 12 pages

Physiology and Pathophysiology of CLC-1: Mechanisms of a Chloride Channel Disease, Myotonia,
Chih-Yung Tang and Tsung-Yu Chen
Volume 2011, Article ID 685328, 10 pages

Obscurin Depletion Impairs Organization of Skeletal Muscle in Developing Zebrafish Embryos,
Maide Ö. Raeker and Mark W. Russell
Volume 2011, Article ID 479135, 15 pages

Diffusion Tensor MRI to Assess Damage in Healthy and Dystrophic Skeletal Muscle after Lengthening Contractions,
Alan B. McMillan, Da Shi, Stephen J. P. Pratt, and Richard M. Lovering
Volume 2011, Article ID 970726, 10 pages

Tissue Expression and Actin Binding of a Novel N-Terminal Utrophin Isoform, Richard A. Zuellig,
Beat C. Bornhauser, Ralf Amstutz, Bruno Constantin, and Marcus C. Schaub
Volume 2011, Article ID 904547, 18 pages

A High-Throughput Solid-Phase Microplate Protein-Binding Assay to Investigate Interactions between Myofilament Proteins,
Brandon J. Biesiadecki and J.-P. Jin
Volume 2011, Article ID 421701, 8 pages

Dynamic Changes in Sarcoplasmic Reticulum Structure in Ventricular Myocytes, Amanda L. Vega,
Can Yuan, V. Scott Votaw, and Luis F. Santana
Volume 2011, Article ID 382586, 14 pages

Planar Cell Polarity Signaling Pathway in Congenital Heart Diseases, Gang Wu, Jiao Ge, Xupei Huang,
Yimin Hua, and Dezhi Mu
Volume 2011, Article ID 589414, 8 pages

Effects of Theophylline on Anesthetized Malignant Hyperthermia-Susceptible Pigs, Marko Fiege,
Ralf Weisshorn, Kerstin Kolodzie, Frank Wappler, and Mark U. Gerbershagen
Volume 2011, Article ID 937479, 4 pages

Myosin Binding Protein-C: A Regulator of Actomyosin Interaction in Striated Muscle,
Maegen A. Ackermann and Aikaterini Kontrogianni-Konstantopoulos
Volume 2011, Article ID 636403, 9 pages

The Combined Effect of Electrical Stimulation and High-Load Isometric Contraction on Protein Degradation Pathways in Muscle Atrophy Induced by Hindlimb Unloading, Naoto Fujita, Shinichiro Murakami, and Hidemi Fujino
Volume 2011, Article ID 401493, 8 pages

The Dystrophin-Glycoprotein Complex in the Prevention of Muscle Damage, Jessica D. Gumerson and Daniel E. Michele
Volume 2011, Article ID 210797, 13 pages

Use of BODIPY (493/503) to Visualize Intramuscular Lipid Droplets in Skeletal Muscle, Espen E. Spangenburg, Stephen J. P. Pratt, Lindsay M. Wohlers, and Richard M. Lovering
Volume 2011, Article ID 598358, 8 pages

Transversal Stiffness and Beta-Actin and Alpha-Actinin-4 Content of the M. Soleus Fibers in the Conditions of a 3-Day Reloading after 14-Day Gravitational Unloading, I. V. Ogneva
Volume 2011, Article ID 393405, 7 pages

On Benzofuroindole Analogues as Smooth Muscle Relaxants, Ike dela Peña and Jae Hoon Cheong
Volume 2011, Article ID 389056, 7 pages

Equal Force Recovery in Dysferlin-Deficient and Wild-Type Muscles Following Saponin Exposure, Piming Zhao, Li Xu, Younss Ait-Mou, Pieter P. de Tombe, and Renzhi Han
Volume 2011, Article ID 235216, 9 pages

Differential Effect of Calsequestrin Ablation on Structure and Function of Fast and Slow Skeletal Muscle Fibers, Cecilia Paolini, Marco Quarta, Laura D'Onofrio, Carlo Reggiani, and Feliciano Protasi
Volume 2011, Article ID 634075, 10 pages

Synergistic Effects between Phosphorylation of Phospholamban and Troponin I Promote Relaxation at Higher Heart Rate, Lin Zhang, Yuan Yu, Zhen Song, Yun-Ying Wang, and Zhi-Bin Yu
Volume 2011, Article ID 651627, 10 pages

Adherent Primary Cultures of Mouse Intercostal Muscle Fibers for Isolated Fiber Studies, Patrick Robison, Erick O. Hernández-Ochoa, and Martin F. Schneider
Volume 2011, Article ID 393740, 11 pages

Editorial

Muscle Contractility and Cell Motility

J.-P. Jin,¹ Robert J. Bloch,² Xupei Huang,³ and Lars Larsson⁴

¹ Department of Physiology, Wayne State University School of Medicine, Detroit, MI 48201, USA

² Department of Physiology, University of Maryland School of Medicine, Baltimore, MD 21201, USA

³ Department of Biomedical Sciences, Florida Atlantic University Charles E. Schmidt College of Medicine, Boca Raton, FL 33431, USA

⁴ Department of Neuroscience, Clinical Neurophysiology, Uppsala University, 751 85 Uppsala, Sweden

Correspondence should be addressed to J.-P. Jin, jjin@med.wayne.edu

Received 30 November 2011; Accepted 30 November 2011

Copyright © 2012 J.-P. Jin et al. This is an open access article distributed under the Creative Commons Attribution License, which permits unrestricted use, distribution, and reproduction in any medium, provided the original work is properly cited.

Muscle contractility and cell motility play a vital role in various physiological and pathological processes, ranging from animal locomotion to cardiovascular function to myopathies and heart failure. Actin-activated myosin II motors power muscle contraction and non-muscle-cell motility. Actin-myosin-derived contractility has been most extensively studied in striated muscle (skeletal and cardiac muscles), but it is also the foundation for smooth muscle contraction and non-muscle-cell motility. Recent advances in biology and medicine have significantly enriched our understanding of the molecular mechanisms underlying muscle contractility and cell motility.

The generation and regulation of contractility present a natural topic for a special issue of this Journal. Three centuries of scientific investigation since Leeuwenhoek and Croone has led to a detailed understanding of muscle function and the broader field of cell motility, which allows us to understand biological movements, their biochemical and mechanical underpinnings, and their effects on the integrity of muscle tissue in health and disease. Therefore, a challenge of the seemingly straightforward task of editing this special issue is the coverage of the vast areas of research on biological movement. With the enthusiasm of our outstanding contributing authors, this special issue comes with a nice collection of six review articles, 13 original research papers, and one methodology report, covering a broad range of topics in the current research of contractility and muscle function.

Among the six review articles, C.-Y. Tang and T.-Y. Chen discussed the CLC-1 chloride channel, a member of the CLC channel/transporter family, for its roles in the

physiological function and diseases of skeletal muscle. The observation that mutations scattered throughout the entire CLC-1 protein result in myotonia congenita, with no clear relationship to the inheritance pattern or channel function, suggests that the pathophysiology of myotonia mutations may involve multiple molecular and cellular mechanisms including channel function or protein synthesis and membrane trafficking mechanisms.

G. Wu and colleagues presented a summary of the planar cell polarity signaling pathway in congenital heart diseases. This pathway, responsible for tissue polarity in *Drosophila* and gastrulation movements and cardiogenesis in vertebrates, plays multiple roles during cardiac differentiation. Knowledge gained in studies of planar cell polarity signaling has helped investigators understand the pathogenesis of congenital heart diseases.

The review by I. dela Pena and J. H. Cheong, on benzofuroindole analogues as smooth muscle relaxants, focused on the potential therapeutic implications of benzofuroindole compounds in disease states linked to smooth muscle hyperactivity caused by the potentiation of large conductance Ca²⁺-activated K⁺ channels. The authors also discussed the value of benzofuroindole compounds and the challenges that need to be overcome if they are to be considered as smooth muscle relaxant drugs.

J. Gumerson and D. Michele reviewed the role of the dystrophin-glycoprotein complex in the prevention of muscle damage. Although normally benign in healthy muscle, contractions in dystrophic muscle may contribute to a higher degree of muscle damage, which eventually overwhelms

the capacity of muscle to regenerate. The dystrophin-glycoprotein complex plays an important function in preventing muscle damage and, when impaired, may contribute to the pathogenesis of muscular dystrophy. It also plays potentially significant roles in signaling pathways that are essential to muscle health.

The review by M. Ackermann and A. Kontogianni-Konstantopoulos on myosin-binding protein-C focuses on its role as a regulator of actomyosin interaction in striated muscle. The cardiac, slow skeletal, and fast skeletal muscle isoforms of myosin-binding protein-C contribute to the assembly and stabilization of thick filaments and regulate the formation of actomyosin cross-bridges via direct interactions with both thick myosin and thin actin filaments. Studies on the mutations in cardiac myosin-binding protein-C associated with familial hypertrophic cardiomyopathy are summarized.

E. Kachaeva and B. S. Shenkman present a review on the functions of proteolytic enzymes in skeletal muscle during unloading. A shift of protein synthesis/proteolysis balance towards increased protein degradation is associated with disuse muscle atrophy. Disuse atrophy of postural muscles caused by unloading differs from that induced by denervation or other conditions. Maintaining of the balance, in which approaches lead to muscle adaptation to disuse rather than muscle degeneration, is discussed with recent data on the activity of related signaling systems.

The thirteen research papers collected in this special issue also covered a broad range of topics. For example, A. McMillan and colleagues studied diffusion tensor magnetic resonance imaging to assess damage in healthy and dystrophic skeletal muscle after injuries caused by lengthening contractions. The aim was to determine if diffusion tensor imaging would serve as a reliable marker of damage after a muscle strain injury in dystrophic and control mice. The study found greater increases in apparent diffusion coefficient and axial and radial diffusivity in injured *mdx* muscles versus controls. These changes were paralleled by decreases in fractional anisotropy. The data suggest that diffusion tensor magnetic resonance imaging is an accurate and early indicator of muscle injury.

The paper by P. Robison et al. presents a study of adherent primary cultures of mouse intercostal muscle fibers for physiological studies. They described a system that allows for monitoring functional properties of living muscle fibers in culture, with or without electrical-field-stimulated fiber contraction, at physiological or pathological respiratory firing patterns. They also report initial characterization of these fibers, demonstrating several common techniques in this new model system in the context of the established flexor digitorum brevis muscle primary culture model.

I. Ogneva present a study on the transversal stiffness and beta-actin and alpha-actinin-4 content of rat soleus muscle fibers in 3-day reloading after 14-day gravitational unloading by hindlimb suspension. Analyzing the structural changes in different parts of the sarcolemma and contractile apparatus of muscle fibers by measuring their transversal stiffness by atomic force microscopy, the author showed that 14 days of disuse reduced the transverse stiffness of all points of

the sarcolemma and contractile apparatus. Readaptation for 3 days led to complete or partial recovery of the values of the transverse stiffness of the sarcolemma and contractile apparatus, respectively.

P. Zhao and colleagues studied the equal force recovery in dysferlin-deficient and wild-type mouse muscles following saponin exposure. Their study found that dysferlin-deficient muscles recovered tetanic force production to the same extent as wild-type controls following a 5-min saponin exposure. The slow soleus muscle recovered significantly better than the fast extensor digitorum longus muscle. The results suggest that it is unlikely that dysferlin is involved in repairing saponin-induced membrane damage and that slow muscle is more efficient than fast muscle in repairing such damage.

A. L. Vega et al. report the dynamic changes in sarcoplasmic reticulum structure in ventricular cardiomyocytes. They tested the hypothesis that the sarcoplasmic reticulum is a structurally inert organelle in ventricular myocytes. The results suggest that, rather than being static, the sarcoplasmic reticulum undergoes frequent dynamic structural changes, which occurred in the absence of changes in $[Ca^{2+}]_i$. Microtubules and the molecular motors, dynein and kinesin 1 (Kif5b), were important regulators of the sarcoplasmic reticulum motility.

E. Spangenburg and colleagues studied the use of BOD-IPY (493/503) dye to visualize intramuscular lipid droplets in skeletal muscle. They found that this dye was a convenient and simple reagent to visualize lipid droplets in both sectioned skeletal muscle and cultured adult single fibers. The dye was effective in both fixed and unfixed cells and was unaffected by permeabilization and thus provides a simple method for visualizing lipid droplets in skeletal muscle.

M. Fiege et al. investigated the *in vivo* effects of theophylline on anesthetized malignant hyperthermia-susceptible pigs. The results showed that theophylline induced comparable clinical alterations in the anesthetized malignant hyperthermia-susceptible and control swine. No pig developed hypermetabolism and/or malignant hyperthermia. Even at cumulative doses much higher than the doses used therapeutically in humans, theophylline was thus not a trigger of malignant hyperthermia in genetically determined swine.

C. Paolini and coworkers studied the differential effect of calsequestrin ablation on the structure and function of fast and slow skeletal muscle fibers. They found that, in extensor digitorum longus and soleus muscles of adult mice lacking calsequestrin, the main sarcoplasmic reticulum Ca^{2+} -binding proteins induced ultrastructural alterations in ~30% of soleus fibers but not in extensor digitorum longus fibers. Twitch time parameters were prolonged in both muscles, although tension was not reduced. Calsequestrin is essential in extensor digitorum longus muscle to provide large amount of Ca^{2+} released from the sarcoplasmic reticulum during tetanic stimulation, whereas soleus muscle tolerated better in the absence of calsequestrin.

L. Zhang and colleagues present a study of the synergistic effects between phosphorylation of phospholamban and cardiac troponin I on promoting cardiac muscle relaxation.

In isolated working rat hearts, less increases in cardiac output and relaxation rate were found in rapid pacing than that in isoproterenol treatment at the same increments of heart rates. Rapid pacing induced phosphorylation of phospholamban at Thr₁₇, whereas isoproterenol induced phosphorylation of cardiac troponin I and phospholamban at Ser₁₆ and Thr₁₇. The results suggest synergistic effects of phospholamban and cardiac troponin I on diastolic cardiac function to facilitate filling at high heart rate.

The study presented by R. A. Zuellig et al. investigated the tissue expression and actin binding of a novel N-terminal utrophin isoform. Utrophin and dystrophin are two large proteins that link the intracellular actin cytoskeleton to the extracellular matrix via the C-terminal-associated protein complex. The authors report a novel short N-terminal isoform of utrophin and its expression in various rat tissues. The short N-terminal utrophin bound actin with pronounced negative cooperativity and was Ca²⁺ insensitive. Recombinant short N-terminal utrophin associated to cell membranes, suggesting that it may be responsible for the anchoring of the cortical actin cytoskeleton to the membranes in muscle and other tissues.

S. B. Shah and colleagues present a paper on the influences of desmin and keratin 19 on passive biomechanical properties of mouse skeletal muscle. The authors examined the passive load-bearing response of single fibers from the extensor digitorum longus muscle of 3- and 10-month wild-type, desmin-null, K19-null, and desmin/K19 double-null mice. Though fibers are more compliant in all mutant genotypes compared to wildtype, the structural response of each genotype is distinct, suggesting multiple mechanisms by which desmin and keratin influence the biomechanical properties of myofibers and providing insights into the influences of intermediate filaments on the structure and function of skeletal muscle.

M. Raeker and M. Russell report that obscurin depletion impairs organization of skeletal muscle in developing zebrafish embryos. Using the developing zebrafish embryo as a model, they examined the relationship between new myofibril assembly and the organization of the membrane domains involved in cell-extracellular matrix interactions. The results showed that depletion of obscurin, a giant muscle protein, resulted in irregular cell morphology and disturbed extracellular matrix organization during skeletal muscle development. The impairment suggests that obscurin participates in organizing the internal structure of the myocyte and in regulating the ability of muscle cells to organize the surrounding matrix.

N. Fujita et al. studied the combined effect of electrical stimulation and high-load isometric contraction on protein degradation pathways in muscle atrophy induced by hindlimb unloading. Electrical stimulation alone resulted in slight attenuation of muscle atrophy. Combining electrical stimulation with high-load isometric contraction enhanced this effect. Electrical stimulation alone inhibited the overexpression of calpain 1, calpain 2, and MuRF-1 mRNA. Electrical stimulation with high-load isometric contraction further inhibited the overexpression of cathepsin L and atrogin-1. These findings suggest that the combination of electrical

stimulation and high-load isometric contraction may be effective as a countermeasure against muscle atrophy.

To conclude this special issue, the methodology report by B. Biesiadecki and J.-P. Jin describes a high-throughput solid-phase microplate protein-binding assay with examples investigating interactions between myofilament proteins. This novel method assesses protein-protein interactions at physiological conditions, utilizes relatively small amounts of protein, is free of protein modification, and does not require specialized instrumentation. Detailed methodology is presented for quantitative studies. Optimization of the assay conditions and its broader application in studies of other protein-protein interactions are also presented.

Acknowledgments

On behalf of all contributing authors, we would like to thank the JBB Editorial Office for the opportunity of producing this special issue. Our sincerest thanks also go to the outstanding external reviewers for their expert assistance.

*J.-P. Jin
Robert J. Bloch
Xupei Huang
Lars Larsson*

Review Article

Various Jobs of Proteolytic Enzymes in Skeletal Muscle during Unloading: Facts and Speculations

E. V. Kachaeva and B. S. Shenkman

SSC RF Institute for Biomedical Problems, RAS, Moscow, Russia

Correspondence should be addressed to E. V. Kachaeva, e_kachaeva@mail.ru

Received 12 May 2011; Revised 11 October 2011; Accepted 3 November 2011

Academic Editor: Lars Larsson

Copyright © 2012 E. V. Kachaeva and B. S. Shenkman. This is an open access article distributed under the Creative Commons Attribution License, which permits unrestricted use, distribution, and reproduction in any medium, provided the original work is properly cited.

Skeletal muscles, namely, postural muscles, as soleus, suffer from atrophy under disuse. Muscle atrophy development caused by unloading differs from that induced by denervation or other stimuli. Disuse atrophy is supposed to be the result of shift of protein synthesis/proteolysis balance towards protein degradation increase. Maintaining of the balance involves many systems of synthesis and proteolysis, whose activation leads to muscle adaptation to disuse rather than muscle degeneration. Here, we review recent data on activity of signaling systems involved in muscle atrophy development under unloading and muscle adaptation to the lack of support.

1. Introduction

Functional unloading caused by prolonged weightlessness or bed rest (after trauma, etc.) leads to sufficient physiological alterations of skeletal muscles, mainly postural, as soleus. Studies on animals [1] and volunteers [2] showed that unloading leads to changes at the molecular level, which manifest in muscle mass loss and deterioration of its function.

In this paper, we paid attention mainly to the atrophy caused by hindlimb suspension, since this is the most correct experimental disuse mode, while muscle denervation, for instance, leads not only to disuse, but also to impaired trophic regulation of the muscle, which complicates atrophy data interpretation.

To study molecular processes during disuse, special models are used for animals (hindlimb unloading) [3] and volunteers (bed rest, dry immersion). Each of the models leads to development of a complex of structural and functional changes, as decrease of cross-sectional area and contractile activity of muscle itself and its single fibers [4–7]. There are also changes in myosin phenotype observed [8, 9] as well as enzyme activity [1]. Such hypogravitational syndrome [10] is supposed to be caused by changes in concentration and activity of factors circulating in blood (glucocorticoids and anabolic steroids) [11]. At the same time, cortisol was

shown to affect muscle under disuse indirectly [12]; while in muscle cytosol, quite high concentration of glucocorticoid receptors was observed [13]. Consequently, there are other mechanisms involved in muscle atrophy stimulation and development during unloading.

Muscle atrophy development under hypokinesia/hypogravity involves different signaling systems directed towards proteolysis activation and protein balance maintaining. Thus, an increase in content of components of the TGF- β /Smads (transforming growth factor- β) signaling pathway [14] and decrease of activity of phosphatidylinositol-3-kinase (PI3K/Akt) cascade were shown. These changes reflect activation of both proteolytic and synthetic signaling pathways in skeletal muscle [15]. Therefore, we aimed at the analysis of the known pathways of proteolysis in postural muscles during functional unloading.

2. Main Systems of Proteolysis in Skeletal Muscles

Three catabolic pathways are known to be involved in the atrophy process during hypokinesia/hypogravity: Ca²⁺-dependent, lysosomal, and ATP-ubiquitin-dependent proteolytic pathways. However, these systems participate differ-

ently in muscle atrophy development caused by denervation and disuse. Thus, under disuse, activity of lysosomal proteases does not increase significantly [16].

Animals hindlimb suspension (HS) and human head-down bed-rest lead to an increase in mRNA of 14 kDa ubiquitin-binding enzyme, and 20S proteasome subunits [17, 18] and to an increment of ubiquitinated proteins [19], which proves significant contribution of ubiquitin proteasome system (UPS) in muscle atrophy under unloading.

Besides, Ca^{2+} -dependent proteases (calpains) also play an important role in skeletal muscle atrophy under disuse [17, 20, 21], being a system of primary protein degradation, since they do not degrade proteins to amino acids or small peptides [22].

Complex effect of activation of different proteolytic systems results in loss of muscle structural proteins and, thus, in decrease of muscle functional properties. A number of results obtained showed that atrophic changes during a space flight or under head-down bed-rest are accompanied by decrease of total muscle protein [23] and myofibril proteins degradation [24].

We suppose that first stage of muscle protein degradation can be Ca^{2+} -dependent proteases, since Ca^{2+} overloading is the first event observed in unloaded muscles, and it is calcium ions which stimulate primary myofibrils degradation. Stimuli inducing Ca^{2+} accumulation are not studied well. Thus, we start our review of proteolytic systems from calcium-dependent system.

Further, we will discuss proteolytic systems in details.

3. Calcium-Dependent Pathways of Proteolysis

Looking for a trigger of proteolysis researchers paid attention to Ca^{2+} -dependent proteases. Calcium redistribution between cytoplasm and sarcoplasmic reticulum (SR) during muscle atrophy caused by different diseases was first demonstrated about 30 years ago [25, 26]. Later, it was shown that 14 days of rat HS significantly increased induced by caffeine Ca^{2+} efflux from soleus SR [27]. However, myoplasm overloading with calcium was demonstrated only in 2001 by Ingalls et al. [28] who registered Ca^{2+} quantity increase at the 3rd day of rats functional unloading. Dihydropyridine-sensitive channels (DHPCs) and ryanodine receptors (RYRs) are main Ca^{2+} channels. DHPCs are the L-type Ca^{2+} channels, m.w. 165 kDa, specifically blocked by dihydropyridine [29]. They are localized predominantly in T-tubes of muscle fibers and are activated by depolarization of fiber membrane. At that, Ca^{2+} enters myoplasm without consumption of ATP hydrolysis energy.

We demonstrated that DHPCs specific inhibitor, nifedipin, caused significant decrease of Ca^{2+} in soleus fibers during unloading [30]. Since DHPCs are the voltage-dependent structures, they should be activated by changes of electrochemical potential at the myofiber membrane under disuse. Some authors showed membrane potential decrease in disused rat soleus [31, 32]. Six percent of decrease of membrane potential was observed at the 3rd day of animal hind limb suspension (HS) [32]. However, potential alteration was not

significant, and there were no direct evidences of membrane potential influence to Ca^{2+} accumulation, so the question of possible trigger of Ca^{2+} accumulation remains unclear.

RYR is another source of Ca^{2+} , localized in terminal cisternae membrane near DHPCs. These channels efficacy significantly exceeds that of DHPCs. RYR main function is fast Ca^{2+} influx to cytosol, where calcium ions interact with troponin C stimulating mechanism of fiber contraction. RYR and DHPC are known to be connected with each other structurally and functionally in fiber T-system. RYRs are activated when interact with Ca^{2+} -activated DHPC [29].

Ca^{2+} accumulation in myoplasm stimulates Ca^{2+} -dependent proteolytic processes. Experiments with activators of Ca^{2+} transport demonstrated the increase in protein degradation [33], while dantrolene (specific blocker of Ca^{2+} exit from SR) decreased proteolysis rate [34].

However, Ca^{2+} -dependent proteolysis localization is not clear, since there are a number of data supporting [35] and contradicting [33] its lysosomal localization. Though, calcium can affect indirectly lysosomal proteases like cathepsin B [35], and nonlysosomal ones localized in cytosol of myofibers [33].

In myoplasm, Ca^{2+} activates cystein proteases, calpains, which are divided into two groups according to their sensitivity to Ca^{2+} : μ - and m-calpains (calpain 1 and calpain 2); they are activated by micromolar and millimolar calcium concentrations, correspondingly. Skeletal muscles contain also calpain 3 (p94), which has common structure with calpains 1 and 2. Ca^{2+} dependence of p94 was proved only in 2006 [36]. At the early stages of functional unloading, calpains are activated and redistributed from cytoplasm fraction to the membrane in slow and fast muscles [37].

The fact that activity of soluble and membrane fractions significantly increased after 12 hours of animal hindlimb suspension and remains high till 9th day of disuse proves that calpains take part in muscle atrophy development under hypokinesia/hypogravity [37]. Moreover, we found twofold increase in soluble calpain fraction activity and fivefold increment of membrane fraction activity after 3 days of animal disuse [38] and were first to show directly that increase in $[\text{Ca}^{2+}]$ stimulates μ -calpain activity, which in its turn activates m-calpains [20, 36]. Local application of Ca^{2+} chelator 1,2-bis(2-aminophenoxy)ethan-N,N,N',N'-tetraacetate (BAPTA-AM) to soleus during unloading allowed us to demonstrate directly dependence of calpain activity on $[\text{Ca}^{2+}]$ in vivo [38]. Importantly, techniques for determination of calpain activity used in the works [37] and [38] registered the enzymes activity at high millimolar concentration of calcium in the incubation medium, where higher activity of all calpain molecules was observed. Increase in calpains activity under disuse can be caused by their expression intensification or by other Ca^{2+} -independent regulators, as calpastatin. Thus, hindlimb suspension leads to pronounced decrement of calpastatin expression in soleus, while calpain 1 expression increases slightly [39]. Activity of calpains decreased in unloaded muscle under local application of calcium chelator [38] can be evidence of Ca^{2+} -dependence of regulation of calpastatin expression.

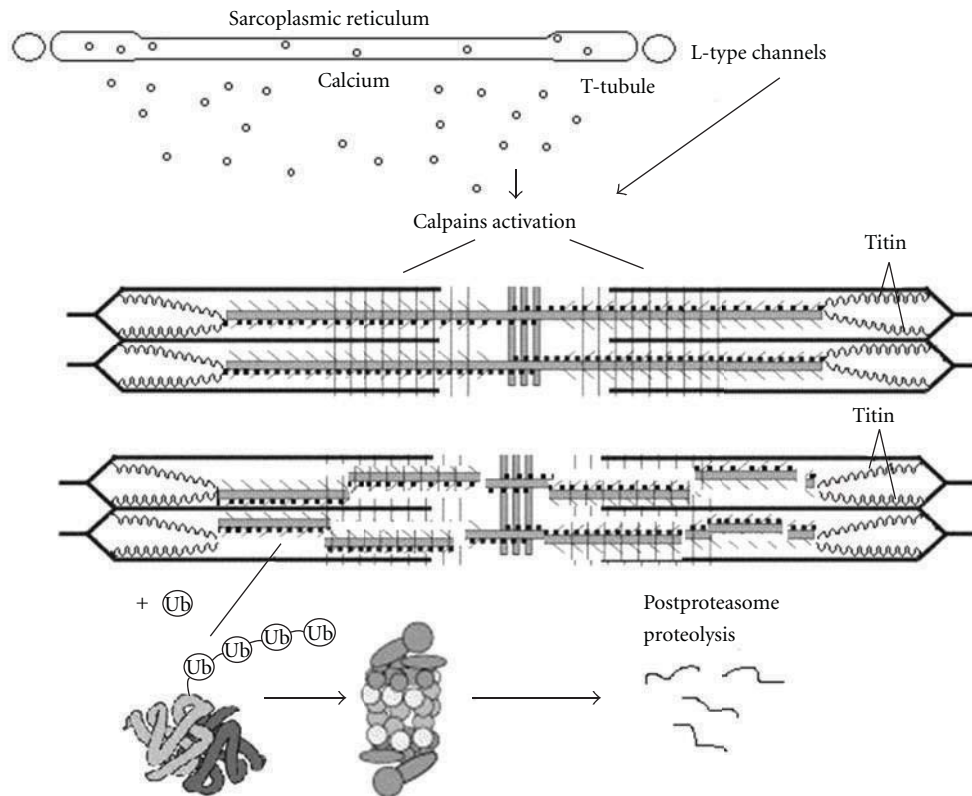


FIGURE 1: Interaction between proteolytic systems in mammals skeletal muscles under disuse atrophy. Preliminary disorganization of myofibrils by calpains helps to degrade myofibril proteins by UPS. Ca^{2+} accumulation can activate calpains localized near Z-disk. Main calpains target is titin, whose cleavage leads to E3-ubiquitin ligases activation.

Calpains contribute about 10% to disuse muscle atrophy. Their key role was demonstrated in HS experiments with mice overexpressing calpastatin, in which no reduction of muscle fiber size was observed [21]. These results are in agreement with recent data on calpastatin expression decrement under HS [39]. Interestingly, hypokinesia/hypogravity caused decrease of NO content leading to calpains inhibition [40]. At that, content of neuronal NO-synthase in soleus fibers under functional unloading decreased [41, 42].

Calpains cannot degrade proteins to small peptides or amino acids and cause only withdrawal of proteins from myofibrils, making them accessible to ubiquitination. Recently, titin was found to bind calpain-3 (p94) through a p94-specific region, suggesting that titin can regulate calpain-3 activity [43]. Calpain-3 was shown to activate expression of components of ubiquitin-proteasome system (UPS) [44–46]. P94 blocked binding of ankyrin repeats with titin molecule [47]. Ankyrin repeats normally are translocated to the nucleus, where they activate NF κ B binding with DNA, hence stimulating ubiquitin ligase expression [47].

Thus, calpains and UPS work jointly (Figure 1) [23]. At that UPS, most probably, realizes final protein degradation. Close interrelation between Ca^{2+} -dependent proteases and UPS complicates studies of their individual contribution into atrophy development under disuse.

Intracellular localization of calpains in association with titin molecule makes possible the interrelation between UPS and calpains. Calcium accumulation under disuse activates calpains, which partly degrade titin molecule or change its conformation [41, 48]. Titin not only is involved in fiber contractility, but also realizes its signaling function through phosphorylation of ubiquitin ligases (MuRF-1 and MuRF-2) localized near titin kinase domain (in M-line), which can affect the titin molecule itself [49, 50]. 14-day HS is known to significantly decrease relative content of titin in rat soleus (Table 1) [51–53]. The same decrease of titin content was observed in human soleus after 7 days of dry immersion experiment [10], interestingly, that titin molecule remains intact at the 3rd day of animal HS [7, 51]. These results prove that, at the early stage of disuse, titin remains intact in spite of myoplasm overloading with calcium [7, 28] and increase in calpain activity. Consequently, phosphorylation of titin bound UPS components and their low activity is maintained. Meanwhile, calpastatin overexpression in mice under disuse was shown to prevent slow-to-fast shift in myosin heavy chains (MHCs) [21]. Probably, degradation of one of the calpain targets under disuse impairs regulation of slow MHC expression, which determines MHC phenotype transformation. Moreover, calpain 2 under HS translocates into the nucleus, where it initiates apoptosis [54]. Thus,

TABLE 1: Changes of titin and nebulin quantity in rat soleus under disuse [7].

Group	Titin 1/MHC	Titin 2/MHC	Titin 2/titin 1	Nebulin/MHC
Control	0.162 ± 0.022	0.033 ± 0.011	0.190 ± 0.048	0.040 ± 0.008
7 days of HS	0.090 ± 0.027	0.158 ± 0.037	1.890 ± 1.200	0.019 ± 0.005
14 days of HS	0.081 ± 0.014	0.084 ± 0.010	1.020 ± 0.035	0.020 ± 0.004

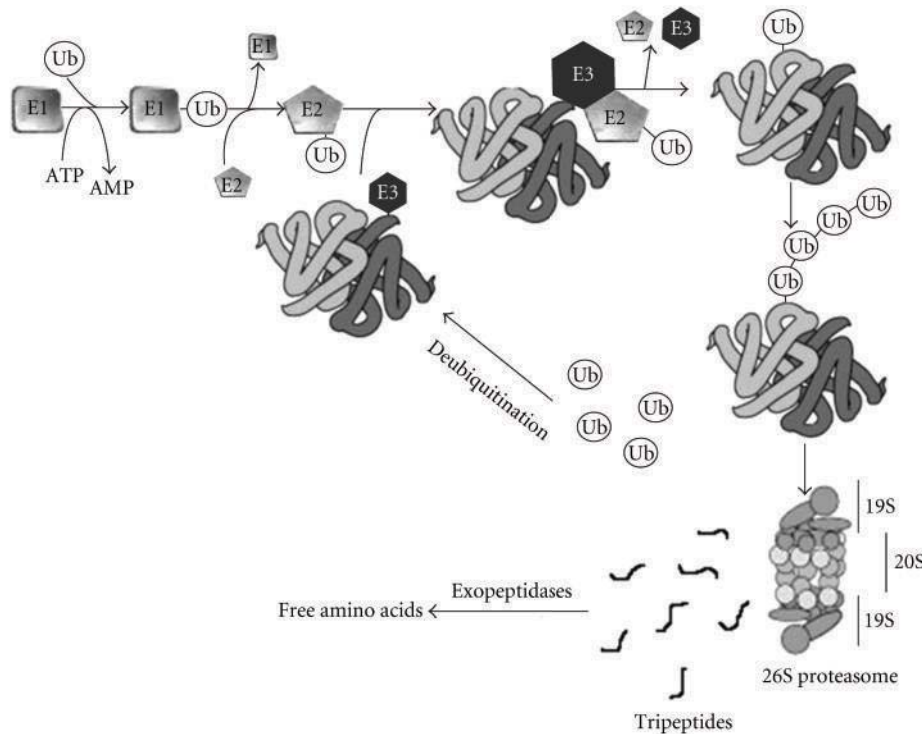


FIGURE 2: Scheme of UPS activity.

calpains in skeletal muscles besides their direct proteolytic activity possess also signaling properties, which are realized partly through the E3-ubiquitin ligases [50].

4. Ubiquitin Proteasome System

Components of ubiquitin proteasome system (UPS) [19, 55, 56] were shown to be actively synthesized under disuse [15, 17, 19, 57] and under muscle atrophy of other nature [55, 58]. Intensification of proteolytic activity is caused by increase in quantity of mRNA encoding main UPS members (polyubiquitin, ubiquitin binding enzymes, ubiquitin ligases, 20S proteasome subunits) and following synthesis of corresponding proteins [59]. The scheme of UPS-dependent degradation of proteins is shown at the Figure 2. Ubiquitination process needs activation of three UPS enzymes: ubiquitin-activating enzyme (E1), ubiquitin-binding enzyme (E2), and ubiquitin ligases (E3). At first ubiquitin binds to E1 (ATP-dependent process) and then translocates to E2. E3 ligases covalently bind protein substrate and then interact with E2, which carries activated ubiquitin. Ubiquitin in its turn translocates from E2 to the target protein. The process repeats till target protein binds

a chain of 4-5 ubiquitin molecules. Then, the ubiquitinated protein degrades into peptides inside proteasome [60]. E3 ligases play an important role in recognition of proteins to be degraded. E2 enzyme and E3 ligase are tissue specific, individual E2 interacts with particular E3 ligase. Usually two main markers of UPS activity are studied, atrogin-1 or muscle atrophy F-box (MAFbx) and MuRF1 (muscle RING finger protein 1) [60]. MAFbx participates in formation of functional ligase complex. MuRF-1 binds conservative domain of titin molecule localized between titin kinase domain and titin C-terminal (in M-line) [48, 61]. This interaction is supposed to regulate metabolism of myofibrils, their trophic state, and maintains entirety of M-line region [62].

MAFbx is supposed to ubiquitinate and degrade MyoD [63] and eukaryotic factor of translation initiation 3 (eIF3) [64], thus playing role in muscle protein synthesis inhibition rather than in proteolysis activation in wasting muscle. MuRF-1 ubiquitinates and degrades troponin I [65] and myosin heavy chains [66].

4.1. E3 Ubiquitin Ligases under Functional Unloading. Expression rate of E3 ubiquitin ligases genes increased after denervation, immobilization, hindlimb suspension, and

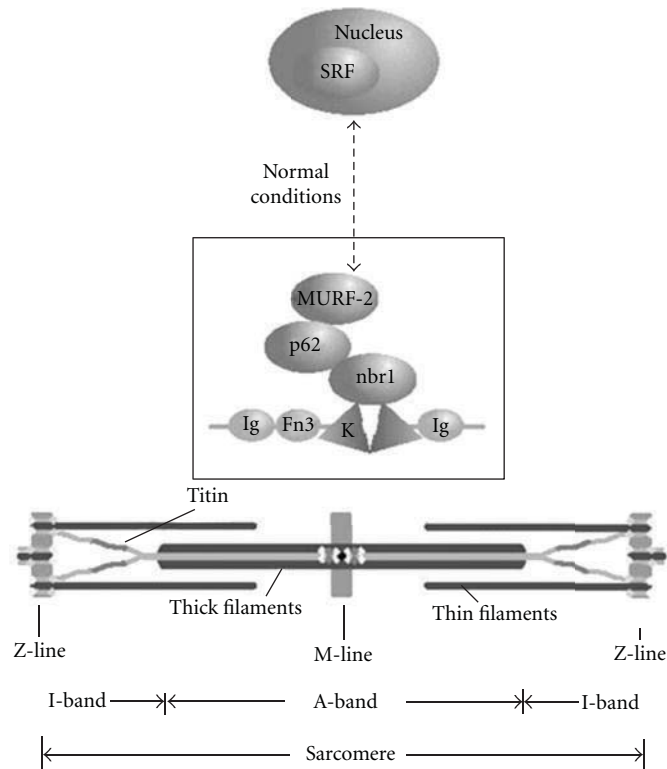


FIGURE 3: MuRF-2 localization on titin molecule [73].

after 11 days of animal space flight, which demonstrated MAFbx- and MuRF-1-dependent proteolysis under disuse [15, 58, 67]. Generally, MAFbx and MuRF-1 are universal proteases participating in skeletal muscle atrophy of different kinds [15].

Results of studies on volunteers using biopsy of vastus lateralis revealed difference between muscle atrophy development in animal and in human, because, in human biopsy significant decrement of protein synthesis and lack of proteolysis increase were observed [68]. At the same time, studies on volunteers during antiorthostatic head-down bed-rest showed increased MuRF-1 quantity in soleus (slow muscle), rather than in vastus lateralis (containing predominantly fast fibers) [69]. Later, expression intensification of MAFbx and ubiquitin ligase cbl-b was found in vastus lateralis after 20 days of disuse [70]. After 48 hours of unilateral lower limb suspension of volunteers, complete genomic analysis revealed increase in expression rate of mRNA of E3 ubiquitin ligases [71], also accumulation of 3-methylhistidine, product of degradation of myofibril proteins (actin and some myosin) was observed [72]. Ten days of immobilization caused threefold increase in MuRF-1 mRNA content in quadriceps femoris, which, however, was diminished to the control level to the 21st day of unloading [73]. We also observed changes in expression rate of ubiquitin ligases under HS of animals. Thus, we found that expression rate of MuRF-1 and MAFbx mRNA in rat soleus increased 3.3 and 2.1 times, correspondingly, at the 3rd day of disuse. To the 7th day of HS, this parameter decreased but was 1.27 and 1.52 times higher than in control (Figure 3) [74]. The 37% increase in

total level of protein ubiquitination at the 4th day of functional unloading [75] confirms our data.

4.2. MuRF-2 and Signaling Role of E3 Ubiquitin Ligases.

Recently, information appeared about functions of another E3 ubiquitin ligase, MuRF-2, which is splice variant of MuRF-1. MuRF-2 is usually found in embryonic muscle, while, in adult animals, its quantity decreased. In spite of its predominant localization in cytoplasm, partly MuRF-2 is bound to nbr1 and p62 proteins, which localize at titin molecule near M-line (Figure 4) [49, 76]. Normally, one of the main functions of this protein is stabilization of microtubules population and several proteins of sarcomeric cytoskeleton (desmin, vimentin) during myofibrillogenesis [62]. Besides, along with MuRF-1, MuRF-2 participates in ubiquitination of myofibril proteins [77]. It should be noticed that MuRF-2 is regulated, at least partly, by titin-dependent mechanism [62]. Changes in spatial arrangement of titin kinase domain after denervation can cause loss of its main function. Consequently, dephosphorylated MuRF-2 dissociates from titin and translocates into the nucleus, where it forces out serum response factor protein (SRF), which is responded for c-fos-mediated stimulation of protein synthesis, cytoskeletal molecules expression, and expression of several growth factors. Our preliminary data showed MuRF-2 translocation to the nucleus and its increased expression under disuse. Thus, 7 days of HS caused increase in MuRF-2 concentration as in myoplasm (from 32.2+5.2 r.u. to 291.9 + 58.5 r.u., according to western blot densitometry

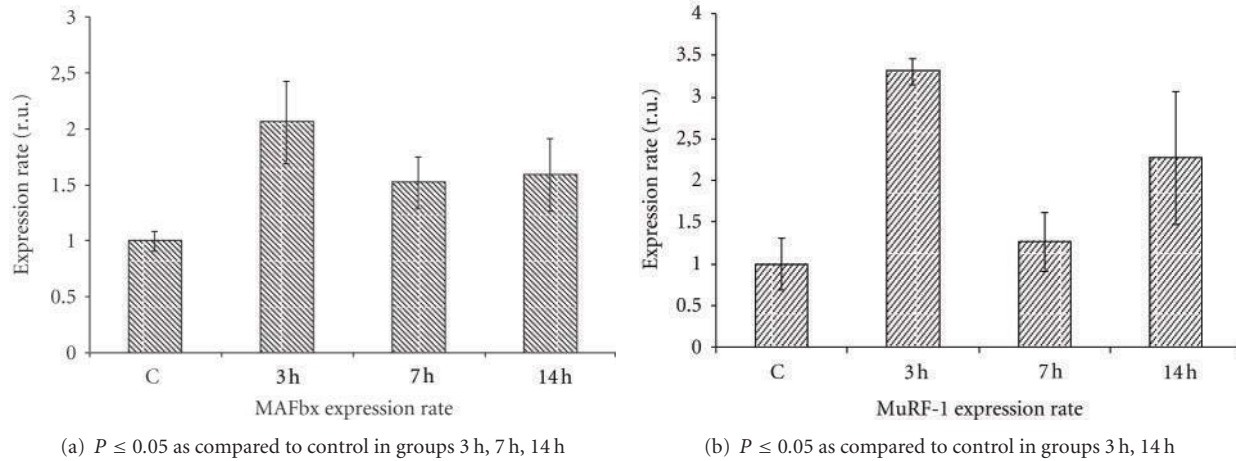


FIGURE 4: Changes in expression rate of MuRF-1 and MAFbx after different periods of unloading. HS3, HS7, HS14-hindlimb suspension for 3, 7, and 14 days, respectively. GAPDH and beta-actin were used as reference genes.

data), so in nucleus (from $56.1 + 6.1$ to $769.4 + 62.2$ r.u.) (unpublished data). Increment of MuRF-2 protein quantity increased further being almost twice as higher at the 14th day of disuse in myoplasm and nucleus. Thus, disuse induces synthesis and translocation of MuRF-2 into the nucleus. According to the data of Lange et al. [49], it seems that titin conformational changes under unloading should cause degradation of signaling complex, associated with titin kinase domain, and allow MuRF-2 migration to the nucleus. Such change in protein conformation was observed after 2 days of unloading [53], while data of other authors did not reveal any changes in titin content at the 3rd day of disuse [7, 53]. MuRF-2 concentration in nucleus fraction of rat soleus did not change, as compared to control, at the 3rd day of HS. However, data exist, which demonstrate titin stability at the 3rd day of HS; only after 7 days of HS, titin was degraded noticeably (Table 1). These data confirm that at the early stage of unloading myoplasm overloading with calcium [7, 28] and calpains activation cannot stimulate titin proteolysis and, thus, ubiquitin ligases dephosphorylation. Therefore, two triggers of MuRF-1 and MuRF-2 dephosphorylation can exist: Ca^{2+} -dependent calpain activation, which initiates myofibril proteins disorganization, and titin conformational changes caused by titin sensitivity to mechanical strain. Further studies are necessary to answer the question.

Normally, MuRF-1 and MuRF-2 expression is more pronounced in fast fibers (II type), while, in mice MuRF-1 and MuRF-2 knockouts, and especially in double knockouts (MuRF-1 and MuRF-2), number of fast soleus fibers is significantly decreased. At that, lack of MuRF-1 noticeably prevented atrophy of II type fibers of tibialis anterior [79]. In double knockouts expression of myozenin-1 (calsarcin-1), an endogenous inhibitor of calcineurin/NFAT signaling pathway was blocked. Obviously, nucleus localization of MuRF-1 and MuRF-2 stimulates calsarcin expression leading to stabilization of fast phenotype of muscle fiber. Mice MuRF-1 knockouts did not show significant atrophy of soleus after 10 days of HS, while fatigue characteristics were more pronounced, posttetanic potentiation was not as

increased as in mice of wild type [80]. The authors suppose possible MuRF-1 influence on intensified processes of phosphorylation of regulatory myosin light chains [81, 82].

Signaling roles of E3 ligases and some of their targets are known now. Thus, MAFbx ubiquitinates MyoD and eIF3 [63, 64]. Taking part in eIF3 ubiquitination MAFbx plays important role in regulation of reciprocal interaction between anabolic and catabolic signaling pathways. Troponin I [65] and myosin heavy chains [66] are the targets of MuRF-1, playing an important role in deterioration of muscle contractility.

Interestingly, ubiquitination of histone deacetylase of II type is supposed to be one of the mechanisms of fast-to-slow transformation of myosin phenotype, which is supported by decrease of slow myosin expression under application of proteasome inhibitor MG132 [83]. At that, exact E3 ubiquitin ligase participating in this phenomenon remains unknown.

Data discussed above showed that direct ubiquitination and indirect participation of E3 ubiquitin ligases in signaling processes makes them important components of central signaling mechanisms in muscle fiber. Unfortunately, today, there is not enough information to understand completely role of E3 ligases in processes of transformation or stabilization of myosin phenotype and concomitant events.

4.3. Regulation of Ubiquitin Ligases Expression. In spite of some progress in understanding of activation and possible functions of ubiquitin proteasome system, trigger mechanism stimulating its activity, particularly activity of E3 ubiquitin ligases, remains to be determined.

5. NFkB

Transcription regulation factor NFkB, which is a mediator of cytokine $TNF\alpha$ (tumor necrosis factor α) during cachexia and inflammation, plays important role in skeletal muscle atrophy. $TNF\alpha$, in its turn, induces muscle fibers apoptosis

and specific transcription mechanism, which blocks IGF-1-induced anabolic process [84]. Inactivated NF κ B forms complex with I κ B in myoplasm. TNF α stimulates I κ B kinase, which phosphorylates I κ B leading to ubiquitination and degradation of proteins of this family. NF κ B then moves to the nucleus and binds to sense sequence of DNA, thus regulating transcription of NF κ B-dependent genes. TNF α -induced NF κ B activation is known to suppress regulatory muscle factor MyoD at posttranscriptional level [85]. In 2004, Cai and colleagues demonstrated at least partial relation of muscle atrophy caused by cachexia, with activation of MuRF-1, but not with MAFbx [86]. This discovery stimulated study of action mechanism of NF κ B system in muscles under disuse.

It was found that atrophy caused by functional unloading in rodents can be partly explained by TNF α -independent activation of NF κ B. Seven days of HS in soleus stimulated DNA-binding activity of NF κ B and led to an increase of reporter proteins p-50, c-Rel, and nuclear I κ B protein Bcl-3 [86, 87]. Akt activation and TNF α expression did not increase as it happened during cachexia. These facts proved mechanism of atypical activation of NF κ B during atrophy caused by functional unloading. This mechanism was called *trans*-regulation [87]. Importantly, NF κ B pathway was not activated under disuse in fast muscles [87]. Possible targets of *trans*-activation of NF κ B under hypokinesia were found recently [88]. Disuse was shown to induce NF κ B-dependent increase in expression rate of ubiquitin ligases MAFbx and Nedd4. Analysis of 5'-flanking sites of genes of these ligases allowed finding numerous potential binding sites of NF κ B. Moreover, 4EBP1, FoxO3a, and cathepsin L (lysosomal enzyme, which degrades membrane proteins) are also possible targets of NF κ B; their expression was increased under disuse atrophy [88]. At the same time, in mice overexpressing IKK β , specific component of muscle signaling pathway, 15-fold increase in NF κ B activity was shown to stimulate MuRF-1 activity. In the experiments with C2C12 culture of myotubes, 4.6-fold rise of MuRF-1 promoter activity was found, which was blocked by I κ B α -SR transfection. Thus, as opposed to disuse-stimulated atrophy, during TNF α -dependent atrophy, induction of MuRF-1 transcription was observed [87]. These data reveal predominant NF κ B-mediated activation of MAFbx under disuse, while MuRF-1 is stimulated by NF κ B during other kinds of atrophy. Since MuRF-1 is known to be activated under muscle wasting, there must be other mechanisms which activate MuRF-1 expression. Thus, transcription regulators FoxO1 and FoxO3 were shown to activate MuRF-1 expression [89, 90].

6. FoxO and Myostatin

Fox factors of transcription regulation have got their name according to their structure (forkhead box) [91], and, in mammals, they are called FoxO (other), because of different structure of their DNA-binding domains; among them FoxO1, FoxO3 a, FoxO4, and FoxO6 [92].

FoxO factors participate in a number of physiological and pathological processes, aging and cancer, for instance [92].

Proteins of this family being phosphorylated by Akt can bind chaperone 14-3-3 in cytoplasm, which leads to loss of their capacity for expression regulation [92]. Model of atrophy on myotube culture revealed decrease of activity of IGF-1/insulin/phosphatidylinositol-3-kinase (PI3 K/Akt) signaling pathway, which caused initiation of FoxO transcription factors and MAFbx induction (Figure 5) [93]. Importantly, FoxO3 directly interacts with MAFbx promoter stimulating expression of the proteases genes, which leads to atrophy of myotubes in culture and animal muscle fibers [93]. Since PI3 K/Akt is known to suppress MuRF-1 expression, so FoxO participates also in regulation of MuRF-1 activity [90]. Recently, FoxO1 was shown to negatively affect expression of myosin heavy chain of type I [94], which confirms important role of FoxO factors in skeletal muscle atrophy.

Balance between protein synthesis and proteolysis involves not only Akt signaling pathway, but also FoxO-dependent cascade, which includes activation of 4EBP1 (protein binding eukaryotic factors 4E) and inhibition of mTOR. At that, FoxO is regulated by different posttranslational modifications, as phosphorylation, acetylation, mono- and polyubiquitination [94]. Some of these modifications are independent on Akt; hence, they also can be involved into muscle atrophy development under stress.

Akt-FoxO signaling pathway is known to interact with IKK-NF κ B system during muscle atrophy development. Thus, inflammatory cytokine TNF α activating NF κ B pathway blocks sensitivity to insulin and inhibits IGF-1 pathway [95–97]. Moreover, interaction between these two signaling systems was confirmed by the results of the study on IKK β knockout mice, whose were insensitive to muscle atrophy induced by denervation, while demonstrated excessive Akt phosphorylation [98].

Search for triggering mechanism initiating dephosphorylation of Akt and FoxO and stimulating ubiquitin ligases expression under disuse allowed to find process of degradation of IRS-I (insulin receptor-I), which is intermediate in IGF-1/PI3 K/Akt signaling cascade. IRS-I content and its phosphorylation level in Ser_{636–639} and Ser₇₈₉ sites decreased significantly after 14 days of HS [99]. Later, it was found that IRS-I is degraded by ubiquitin ligase cbl-b, which expression is increased noticeably under disuse [100]. Cbl-b expression is regulated during membrane process of lipid peroxidation.

As was shown previously, FoxO factors mediate ubiquitin ligases activation also through myostatin [101]. The latter blocks IGF-1/PI3 K/Akt pathway, which activates FoxO1, thus stimulating MAFbx expression [101]. Data on regulation of myostatin expression by FoxO1 showed that myostatin signaling pathway is related to Akt-FoxO cascade [102]. Mature myostatin protein forms active dimers, which bind activin receptors on the cell surface stimulating phosphorylation of Smad2 and Smad3 and their interaction with Smad4. Such complex is a transcription regulation factor, which can penetrate the cell and induce expression of any gene flanked with corresponding sequence. In other words, myostatin blocks myoblasts growth in the cell, inhibiting thus the expression of myogenic factors as MyoD and p21 [102]. Myostatin negatively regulates activation and self-renewal of cells and, probably, participates in process of the satellite

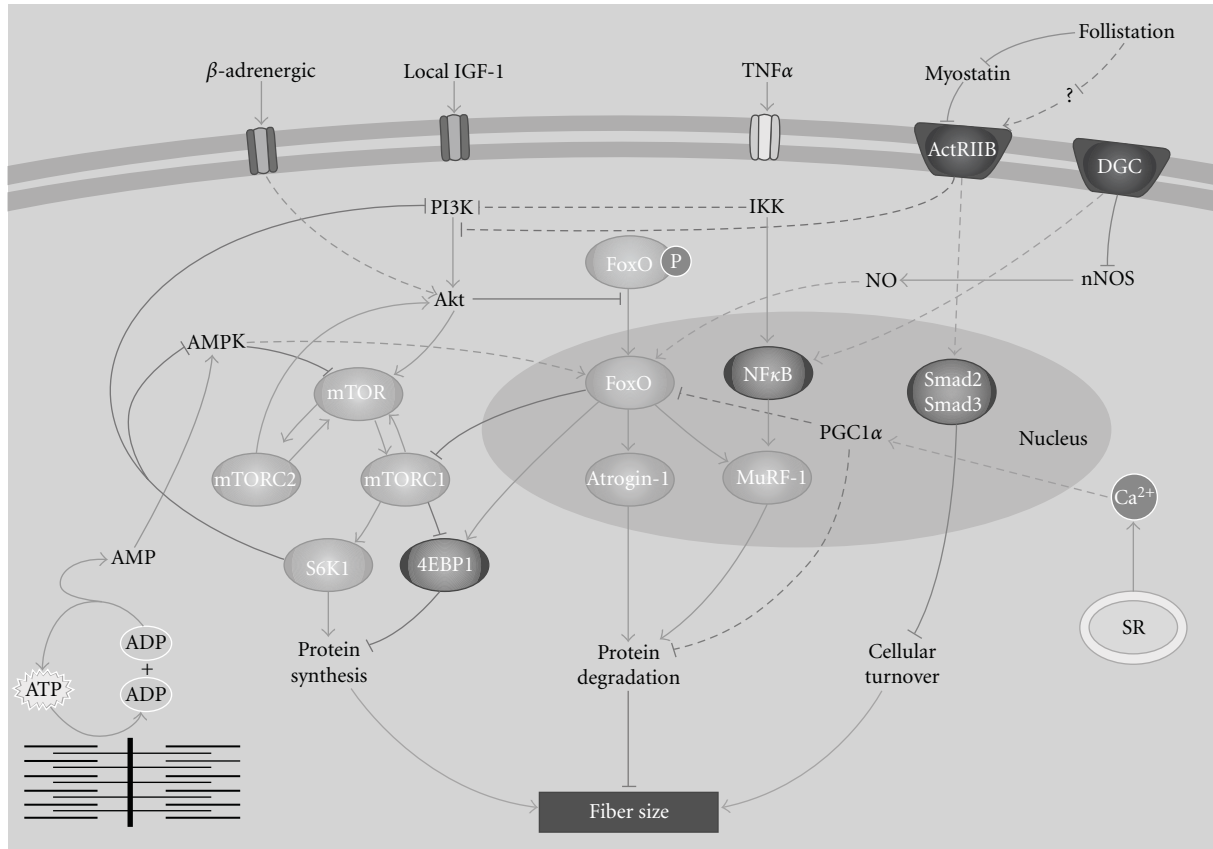


FIGURE 5: Net of signaling systems participating in regulation of fiber size of skeletal muscle under disuse atrophy. Pathways whose molecular function in the cell is not known are dashed [78].

cells silencing [103]. Thus, myostatin activity maintenance under disuse, possibly, promotes maintenance of low level of myofibers renewal and prevents potential increase in satellite cells proliferation and fusion.

At the same time, Smad proteins can recognize CAGAC DNA sequence but possess low affinity to it, so to interact with DNA Smad proteins need some DNA binding co-factors, which can help to recognize and regulate target genes [104]. Such mediators are proteins of the FoxO family [105]. Besides, Smads inhibitor, TGIF, was shown to be activated earlier than muscle mass loss becomes noticeable.

7. Autophagy: Lysosomal Proteins Degradation

Lysosomes are the cell organelles responsible for removal of other organelles and aggregated proteins. Autophagy is an integral property of muscle cells, which is confirmed by huge number of autophagosomes in humans with myopathies caused by different diseases or during pharmacological inhibition of lysosomal function by chloroquine, for instance [106]. However, lysosomal enzymes are differently activated during atrophy induced by denervation [107] and unloading [108]. According to biochemical and electron microscope data, lysosomal degradation of proteins is responsible mainly for denervation-induced atrophy [78, 107–109].

These results are in accordance with the data that chloroquine practically cannot block proteolysis during hypokinesia/hypogravity but inhibits it during soleus denervation [110]. Moreover, significant activation of Ca²⁺-dependent carboxylic proteases and decrease of total cathepsin B and D activity were observed under disuse stimulated by hindlimb unloading, while denervation-induced disuse caused the highest activity of the cathepsins [17]. At the same time, recently, cathepsin L quantity was shown to be increased during HS [58, 111]. Role of cathepsin L is unknown. Thus, increment of certain cathepsins concentration proves some lysosomal system activation during denervation-induced atrophy but does not have significant contribution of lysosomes to HS-induced atrophy [111]. Cathepsins are known to be inactivated at neutral pH in cytoplasm. Proteolysis with cathepsins is carried out inside the lysosomes; thus, they cannot degrade myofibril proteins despite of their activation. Therefore, lysosomal system contribution into catabolism of myofibril proteins during atrophy is not sufficient [112].

mTOR and PI3 K/Akt signaling systems are also involved in microtubules autophagy [113]. Recently, the results were obtained demonstrating coordination between lysosomal system and UPS during atrophy [114, 115]. Therefore, some genes related with autophagy, as well as MAFbx gene, are controlled by FoxO3 regulatory factor, and thus expression of FoxO1 and FoxO3 can be necessary for lysosomal proteolysis

induction mediated by activation of ubiquitin ligases MAFbx and MuRF-1 in cell culture and in vivo [91, 93]. At that, it is still unknown whether such interaction of these proteolytic systems takes place in skeletal muscles of animals under disuse.

8. Caspases

Caspases are known to cleave actomyosin to 14 kDa actin fragments, as was shown in culture of skeletal muscle cells on the model of serum deprivation [116]. Caspase-3 contribution to protein degradation by UPS in culture was 125%. The observed by Du et al. actomyosin cleavage was blocked by specific caspase-3 inhibitor. Cleaved actin fragments were also found in rat muscles after diabetes and chronic uremia [116]. Caspases were shown to be activated during rat hindlimb unloading [117, 118]. Interestingly, at the 5th day of HS, only caspase-3 content increased, while, at the 10th day of disuse, caspases-6 and 9 were activated. These data confirm that caspase-3 activates as through mitochondria-independent, so through mitochondria-dependent pathway during unloading caused by HS. However, the entire mechanism of mitochondria-independent caspase regulation needs further investigation. Physiological role of caspase content increment can be the myonuclei number regulation through apoptosis, which leads to synthesis activity decrease. Though, it was found that caspase-3 increase caused decrease in myonuclei number [119] and stimulated DNA fragmentation at the 14th day of HS [120]. Mechanisms of this phenomenon are also remained unclear.

9. Muscle Atrophy Is the Balance between Signaling Systems Involved in Regulation of Protein Synthesis and Proteolysis

Alterations of structure and function of skeletal muscle under functional unloading, so called, muscle plasticity, are caused not only by increment of muscle proteins degradation. It is better to say that disuse atrophy is the result of shift of the balance between protein synthesis and proteolysis towards increase in proteolysis and decrease of synthesis intensity. Main signaling system regulating protein synthesis in muscles is the Akt/mTOR pathway, which is activated when IGF-1 (insulin-like growth factor-1) binds with its receptor on myofiber membrane. This signaling cascade is responsible for stimulation of protein synthesis in skeletal muscle fibers realizing its effect particularly through stimulation of proliferation and fusion of satellite cells (Figure 5) [111]. mTOR (mammalian target of rapamycin) is a part of two multiprotein complexes, one of which is mTORC1 (sensitive to rapamycin). mTORC1 activates S6 K and 4EBP, through which Akt-FoxO signal is realized. mTOR effect on translation process and protein synthesis is realized through TORC1-dependent phosphorylation of ribosomal S6 kinases (S6 K1 and S6 K2) and 4EBP, a repressor of a cap-binding protein eIF4E. S6 K1 is an important component of Akt cascade, which is confirmed by experiments on mice S6 K1 knockouts. Those mice had very small fibers, and

could not respond to activated Akt and IGF-1 [121]. Thus, protein synthesis intensification through PI3 K/Akt/mTOR mechanism is realized by means of activation of S6 K1, eukaryotic factor of translation initiation 4E (eIF4E), and inhibition of translation regulator 4EBP1. At the same time, IGF-1/PI3 K/Akt pathway prevents atrophy development by inhibition (dephosphorylation by Akt) of transcription regulation factors FoxO1-3, stimulating their transition from nucleus to cytoplasm [93]. Activity of IGF-1 plays an important role during functional unloading, since ability of muscle cells to bind insulin increased noticeably under disuse. At that, total quantity of insulin receptors did not change [122]. At the same time, activity of PI3 K/Akt signaling cascade, which plays role of central regulator between insulin and IGF-1 receptor, and activated synthetic pathways in muscle, were shown to be diminished significantly [123, 124]. Moreover, it was clearly demonstrated that c-Jun NH₂-terminal kinase (JNK) significantly increased after 10 days of rat HS, as in predominantly fast [125, 126], so in predominantly slow muscles [127], on the models of animal HS [125, 127], cast immobilization [126], and denervation [128]. Independently of the model used increment in JNK level evidences that IRS-1 protein is phosphorylated, Akt activity is suppressed, and insulin resistance develops in the wasting muscle. Therefore, activation of PI3 K/Akt signaling pathway is important for disused muscle reloading. Nevertheless, it is not the only way of protein synthesis intensification. Eukaryotic initiation factor 4E (eIF4E), one of the components of eIF4F complex interacts with eIF3 complex, which regulates assembling of 43 S preinitiation complex (PIC) [129]. eIF3 directly captures 40 S ribosomal subunit stimulating its interaction with Met-tRNA-eIF2-GTP complex and with eIF1. Due to interaction of eIF3 and eIF4E-mRNA, mRNA binds 43 S ribosomal complex forming 48 S complex, which initiates synthesis of muscle proteins. Studies revealed 13 different subunits of eIF3 complex with molecular mass varying from 170 to 25 kDa. Five of these subunits form the main nucleus of the complex, and others have regulatory function. Role of one of these subunits, eIF3-f, is not known well, though in yeasts and coronaviruses, decrease of eIF3-f quantity leads to significant reduction of total protein content in dividing cells and to decrement of cytokines IL-6 and IL-8 [130]. IL-6, in its turn, is an essential factor of development of skeletal muscle hypertrophy mediated by proliferating satellite cells [131]. In humans, eIF3-f decrease is related to tumor development, while its overexpression suppresses cell growth and leads to apoptosis stimulation [65].

Small quantity of eIF3-f is found in myoblasts of skeletal muscles. Its concentration increases significantly during terminal differentiation and remains at the same level in adult muscle. Interestingly, eIF3-f binds MAFbx in skeletal muscle, which explains, probably, protein synthesis decrease during muscle atrophy of different nature [129]. MAFbx is known to stimulate polyubiquitination of eIF3-f with its following degradation by 26S proteasome. Therefore, decrease of MAFbx will lead to maintaining of eIF3-f level.

eIF3-f directly interacts with mTOR and S6 K1 stimulating assembling of preinitiation complex of translation of specific mRNA encoding proteins, which participate in

muscle hypertrophy. According to Csibi's data [129], inactive hypophosphorylated form of S6 K1 is physically bound to eIF3-f in the site of MAFbx and ubiquitin binding. Hence, MAFbx-initiated eIF3-f degradation must lead to S6 K1 inhibition during atrophy. Though it is still unknown whether MAFbx interacts with free-eIF3-f molecule or with the molecule bound to S6 K1. Thus, it is difficult to suppose in which direction shifts the balance between eIF3-f binding with the two ligands under disuse and which factors can affect this balance.

MAFbx has been considered as active proteolytic system member under functional unloading, while recent data confirm predominant role of MAFbx in suppression of protein synthesis at the stage of mRNA translation in case of its interaction with eIF3-f, or at the level of FoxO and MyoD activity inhibition [64, 129]. Thus, MAFbx should be considered as muscle atrophy marker rather than an index of proteolysis.

10. Ways to Suppress Expression of Ubiquitin Ligases under Functional Unloading

Chronic passive stretch of the muscle is supposed to be one of the most effective experimental approaches to prevent muscle atrophy [132]. First experiments with stretch combined with HS revealed marked protein synthesis intensification, while proteolysis, at least, during first 7 days, remained unchanged [132]. Meanwhile, our study of stretch combined with HS for 7 days showed twofold (and after 14 days of disuse with stretch threefold) increase in MuRF-1 and MAFbx expression in soleus [75]. At the same time, these effects were accompanied by significant rise of IGF-1 expression in soleus, which allows maintaining of proteolysis-synthesis balance in the stretched unloaded muscle with high UPS expression level. IGF-1 expression activation itself can promote decrease in the expression rate of ubiquitin ligases through the induction of Akt phosphorylation, as was described in [90].

Moreover, it was shown also that the stretch-induced dynamic redistribution of p94 is dependent on its protease activity and essential to protect muscle from degeneration, particularly under physical stress [133]. Though, we do not know whether the same phenomenon takes place during the unloaded muscle stretch.

Another possible way of protein synthesis maintaining in unloaded muscle can be injection of amino acids. Recently, it was shown that per oral administration of leucine amino acid during rat soleus immobilization significantly decreased expression rate of E3 ubiquitin ligases [134]. Mechanism of this phenomenon remains unclear.

Dependence of FoxO3 migration to the nucleus and inhibition of expression of E3 ubiquitin ligases on protective systems of myofibers was found in the experiments with plasmid transfection encoding heat shock protein 70 (HSP70). Four days of immobilization after such transfection revealed decrement of E3 ubiquitin ligases expression mediated by FoxO3 dephosphorylation [89]. We observed decrease of MuRF-1 and MAFbx expression in rat soleus under HS combined with application of NO donor, L-arginine. Evidently,

experimental intensification of NO production inhibited ubiquitin ligases expression [40].

11. Conclusion: Hypogravitational Atrophy of Skeletal Muscle Is a Sustainable Adaptation of Signaling Systems

Signaling systems in the cell and in fibers of skeletal muscle, in particular, are joined into extremely complex net. Change of one of its components will certainly lead to alteration of many others. At that, activity of all chains involved in the net is directed differently; therefore, any imbalance of the system should initiate processes of homeostasis maintaining. Functional unloading leads to atrophy of skeletal muscles, which manifests in increased proteolysis leading to decrease of fiber size, muscle mass loss, function deterioration, loss of Ca^{2+} sensitivity, and so forth. However, under disuse, balance between protein synthesis and proteolysis shifts so that muscle adapts to the altered circumstances. This conclusion is supported by accumulated knowledge about activity of signaling systems, which take part in proteolysis and synthesis of muscle proteins, as NFkB, for instance. Thus, under disuse, NFkB is activated independently of TNF α (decreasing IGF-1-dependent pathway), which may be important, because, in this case, a number of factors blocking PI3 K/Akt pathway and protein synthesis are activated. Thus, unchanged Akt level allows keeping phosphorylation level of FoxO3 and restraining the latter in myoplasm.

At the same time, NFkB does not stimulate MuRF-1 activity during hypokinesia/hypogravity [89], which can limit in some way total level of ubiquitin ligases activity. Consequently, predominant role of MAFbx in suppression of synthetic processes in muscle and NFkB transactivation under disuse prove adaptation of the muscle to functional unloading, rather than its negative reaction to lack of basement.

Thus, it is clear now that skeletal muscles do not degrade under disuse, they adapt to altered circumstances in a way different from that of atrophy development caused by other stimuli. Mechanism of development of skeletal muscle adaptation is extremely complicated and needs further studies to reveal key regulators, which can be affected further in order to prevent development or decrease of muscle atrophy intensity.

Acknowledgments

This work was supported by RFBR Grant 11 -04-01769 a.

References

- [1] D. B. Thomason and F. W. Booth, "Atrophy of the soleus muscle by hindlimb unweighting," *Journal of Applied Physiology*, vol. 68, no. 1, pp. 1–12, 1990.
- [2] V. J. Caiozzo, "Plasticity of skeletal muscle phenotype: mechanical consequences," *Muscle and Nerve*, vol. 26, no. 6, pp. 740–768, 2002.
- [3] E. R. Morey-Holton and R. K. Globus, "Hindlimb unloading rodent model: technical aspects," *Journal of Applied Physiology*, vol. 92, no. 4, pp. 1367–1377, 2002.

- [4] K. Yamashita-Goto, R. Okuyama, M. Honda et al., "Maximal and submaximal forces of slow fibers in human soleus after bed rest," *Journal of Applied Physiology*, vol. 91, no. 1, pp. 417–424, 2001.
- [5] L. Stevens, Y. Mounier, X. Holy, and M. Falempin, "Contractile properties of rat soleus muscle after 15 days of hindlimb suspension," *Journal of Applied Physiology*, vol. 68, no. 1, pp. 334–340, 1990.
- [6] A. I. Grigoriev and B. S. Shenkman, "Skeletal muscle during unloading," *Vestn. Russ. Acad. Sci. In Russian*, vol. 78, no. 4, pp. 337–345, 2008.
- [7] E. V. Ponomareva, V. V. Kravtsova, E. V. Kachaeva et al., "Contractile properties of the isolated rat musculus soleus and single skinned soleus fibers at the early stage of gravitational unloading: facts and hypotheses," *Biofizika*, vol. 53, no. 6, pp. 1087–1094, 2008 (Russian).
- [8] G. H. Templeton, M. Padalino, and J. Manton, "Influence of suspension hypokinesia on rat soleus muscle," *Journal of Applied Physiology Respiratory Environmental and Exercise Physiology*, vol. 56, no. 2, pp. 278–286, 1984.
- [9] F. Haddad, G. R. Adams, P. W. Bodell, and K. M. Baldwin, "Isometric resistance exercise fails to counteract skeletal muscle atrophy processes during the initial stages of unloading," *Journal of Applied Physiology*, vol. 100, no. 2, pp. 433–441, 2006.
- [10] A. I. Grigoriev, I. B. Kozlovskaia, and B. S. Shenkman, "The role of support afferents in organisation of the tonic muscle system," *Rossiiskii Fiziologicheskii Zhurnal Imeni I.M. Sechenova*, vol. 90, no. 5, pp. 508–521, 2004.
- [11] H. Vandenburg, J. Chroimiak, J. Shansky, M. del Tatto, and J. Lemaire, "Space travel directly induces skeletal muscle atrophy," *The FASEB Journal*, vol. 13, no. 9, pp. 1031–1038, 1999.
- [12] J. M. Steffen and X. J. Musacchia, "Spaceflight effects on adult rat muscle protein, nucleic acids, and amino acids," *American Journal of Physiology*, vol. 247, no. 16, pp. R728–R732, 1984.
- [13] S. R. Jaspers and M. E. Tischler, "Metabolism of amino acids by the atrophied soleus of tail-casted, suspended rats," *Muscle & Nerve*, vol. 9, pp. 554–561, 1986.
- [14] P. Zhang, M. Yang, H. Liu, L. Li, and X. Chen, Book of Abstracts of the 16th IAA Humans in Space Symposium, pp.53, 2007.
- [15] S. C. Bodine, T. N. Stitt, M. Gonzalez et al., "Akt/mTOR pathway is a crucial regulator of skeletal muscle hypertrophy and can prevent muscle atrophy in vivo," *Nature Cell Biology*, vol. 3, no. 11, pp. 1014–1019, 2001.
- [16] D. F. Goldspink, A. J. Morton, P. Loughna, and G. Goldspink, "The effect of hypokinesia and hypodynamia on protein turnover and the growth of four skeletal muscles of the rat," *Pflugers Archiv European Journal of Physiology*, vol. 407, no. 3, pp. 333–340, 1986.
- [17] D. Taillandier, E. Arousseau, D. Meynial-Denis et al., "Coordinate activation of lysosomal, Ca²⁺-activated and ATP-ubiquitin-dependent proteinases in the unweighted rat soleus muscle," *Biochemical Journal*, vol. 316, no. 1, pp. 65–72, 1996.
- [18] M. L. Urso, A. G. Scrimgeour, Y. W. Chen, P. D. Thompson, and P. M. Clarkson, "Analysis of human skeletal muscle after 48 h immobilization reveals alterations in mRNA and protein for extracellular matrix components," *Journal of Applied Physiology*, vol. 101, no. 4, pp. 1136–1148, 2006.
- [19] M. Ikemoto, T. Nikawa, S. Takeda et al., "Space shuttle flight (STS-90) enhances degradation of rat myosin heavy chain in association with activation of ubiquitin-proteasome pathway," *The FASEB Journal*, vol. 15, no. 7, pp. 1279–1281, 2001.
- [20] D. L. Enns, T. Raastad, I. Ugelstad, and A. N. Belcastro, "Calpain/calpastatin activities and substrate depletion patterns during hindlimb unweighting and reweighting in skeletal muscle," *European Journal of Applied Physiology*, vol. 100, no. 4, pp. 445–455, 2007.
- [21] J. G. Tidball and M. J. Spencer, "Expression of a calpastatin transgene slows muscle wasting and obviates changes in myosin isoform expression during murine muscle disuse," *Journal of Physiology*, vol. 545, no. 3, pp. 819–828, 2002.
- [22] D. E. Goll, V. F. Thompson, H. Li, W. Wei, and J. Cong, "The calpain system," *Physiological Reviews*, vol. 83, no. 3, pp. 731–801, 2003.
- [23] J. M. Steffen and X. J. Musacchia, "Disuse atrophy, plasma corticosterone, and muscle glucocorticoid receptor levels," *Aviation Space and Environmental Medicine*, vol. 58, no. 10, pp. 996–1000, 1987.
- [24] D. B. Thomason, R. E. Herrick, D. Surdyka, and K. M. Baldwin, "Time course of soleus muscle myosin expression during hindlimb suspension and recovery," *Journal of Applied Physiology*, vol. 63, no. 1, pp. 130–137, 1987.
- [25] A. Martonosi, A. R. de Boland, R. Boland, J. M. Vanderkooi, and R. A. Halpin, "The mechanism of Ca transport and the permeability of sarcoplasmic reticulum membranes," *Recent Advances in Studies on Cardiac Structure and Metabolism*, vol. 4, pp. 473–494, 1974.
- [26] S. Verjovski-Almeida and G. Inesi, "Rapid kinetics of calcium ion transport and ATPase activity in the sarcoplasmic reticulum of dystrophic muscle," *Biochimica et Biophysica Acta*, vol. 558, no. 1, pp. 119–125, 1979.
- [27] L. Stevens and Y. Mounier, "Ca²⁺ movements in sarcoplasmic reticulum of rat soleus fibers after hindlimb suspension," *Journal of Applied Physiology*, vol. 72, no. 5, pp. 1735–1740, 1992.
- [28] C. P. Ingalls, G. L. Warren, and R. B. Armstrong, "Intracellular Ca²⁺ transients in mouse soleus muscle after hindlimb unloading and reloading," *Journal of Applied Physiology*, vol. 87, no. 1, pp. 386–390, 1999.
- [29] B. Macintosh, A. McComas, and P. Gardiner, *Skeletal Muscle: Form and Function*, Human Kinetics, Champaign, Ill, USA, 2005.
- [30] A. M. Mukhina, A. V. Zhelezniakova, I. N. Kitina, B. S. Shenkman, and T. L. Nemirovskaia, "NFATc1 and slow-to-fast shift of myosin heavy chain isoforms under functional unloading of the rat m. soleus," *Biofizika*, vol. 51, no. 5, pp. 918–923, 2006.
- [31] S. Pierno, J. F. Desaphy, A. Liantonio et al., "Change of chloride ion channel conductance is an early event of slow-to-fast fibre type transition during unloading-induced muscle disuse," *Brain*, vol. 125, no. 7, pp. 1510–1521, 2002.
- [32] I. I. Krivoi, V. V. Kravtsova, E. G. Altaeva et al., "Decrease in the electrogenic contribution of Na,K-ATPase and resting membrane potential as a possible mechanism of calcium ion accumulation in filaments of the rat musculus soleus subjected to the short-term gravity unloading," *Biofizika*, vol. 53, no. 6, pp. 1051–1057, 2008 (Russian).
- [33] R. J. Zeman, T. Kameyama, and K. Matsumoto, "Regulation of protein degradation in muscle by calcium. Evidence for enhanced nonlysosomal proteolysis associated with elevated cytosolic calcium," *The Journal of Biological Chemistry*, vol. 260, no. 25, pp. 13619–13624, 1985.
- [34] J. E. Desmedt and K. Hainaut, "Regulation of ionized calcium in the cytosol of muscle cells during rest: action of dantrolene

- on the sarcoplasmic reticulum," *The Journal of Physiology*, vol. 257, pp. 87–107, 1976.
- [35] H. P. Rodemann, L. Waxman, and A. L. Goldberg, "The stimulation of protein degradation in muscle by Ca^{2+} is mediated by prostaglandin E2 and does not require the calcium-activated protease," *The Journal of Biological Chemistry*, vol. 257, no. 15, pp. 8716–8723, 1982.
- [36] B. E. García Díaz, S. Gauthier, and P. L. Davies, " Ca^{2+} dependency of calpain 3 (p94) activation," *Biochemistry*, vol. 45, no. 11, pp. 3714–3722, 2006.
- [37] D. L. Enns and A. N. Belcastro, "Early activation and redistribution of calpain activity in skeletal muscle during hindlimb unweighting and reweighting," *Canadian Journal of Physiology and Pharmacology*, vol. 84, no. 6, pp. 601–609, 2006.
- [38] B. S. Shenkman and T. L. Nemirovskaya, "Calcium-dependent signaling mechanisms and soleus fiber remodeling under gravitational unloading," *Journal of Muscle Research and Cell Motility*, vol. 29, no. 6–8, pp. 221–230, 2008.
- [39] X.-W. Ma, Q. Li, P.-T. Xu, L. Zhang, H. Li, and Z.-B. Yu, "Tetanic contractions impair sarcomeric Z-disk of atrophic soleus muscle via calpain pathway," *Molecular and Cellular Biochemistry*, vol. 354, no. 1–2, pp. 171–180, 2011.
- [40] Y. Lomonosova, G. R. Kalamkarov, A. E. Bugrova et al., "Protective effect of L-arginin on soleus proteins under functional unloading," *Biochemistry*, vol. 76, no. 5, pp. 571–580, 2011.
- [41] J. G. Tidball, E. Lavergne, K. S. Lau, M. J. Spencer, J. T. Stull, and M. Wehling, "Mechanical loading regulates NOS expression and activity in developing and adult skeletal muscle," *American Journal of Physiology*, vol. 275, no. 1, pp. C260–C266, 1998.
- [42] A. Moukhina, B. Shenkman, D. Blottner et al., "Effects of support stimulation on human soleus fiber characteristics during exposure to "dry" immersion," *Journal of Gravitational Physiology*, vol. 11, no. 2, pp. P137–P138, 2004.
- [43] H. Sorimachi, K. Kinbara, S. Kimura et al., "Muscle-specific calpain, p94, responsible for limb girdle muscular dystrophy type 2A, associates with connectin through IS2, a p94-specific sequence," *The Journal of Biological Chemistry*, vol. 270, no. 52, pp. 31158–31162, 1995.
- [44] R. M. Murphy, E. Verburg, and G. D. Lamb, " Ca^{2+} activation of diffusible and bound pools of μ -calpain in rat skeletal muscle," *The Journal of Physiology*, vol. 576, no. 2, pp. 595–612, 2006.
- [45] I. J. Smith and S. L. Dodd, "Calpain activation causes a proteasome-dependent increase in protein degradation and inhibits the Akt signalling pathway in rat diaphragm muscle," *Experimental Physiology*, vol. 92, no. 3, pp. 561–573, 2007.
- [46] L. Laure, N. Danièle, L. Suel et al., "A new pathway encompassing calpain 3 and its newly identified substrate cardiac ankyrin repeat protein is involved in the regulation of the nuclear factor- κ B pathway in skeletal muscle," *The FEBS Journal*, vol. 277, no. 20, pp. 4322–4337, 2010.
- [47] M. K. Miller, M. L. Bang, C. C. Witt et al., "The muscle ankyrin repeat proteins: CARP, ankrd2/Arpp and DARP as a family of titin filament-based stress response molecules," *Journal of Molecular Biology*, vol. 333, no. 5, pp. 951–964, 2003.
- [48] K. S. Litvinova, I. M. Vikhlyantsev, I. B. Kozlovskaya, Z. A. Podlubnaya, and B. S. Shenkman, "Effects of artificial support stimulation on fiber and molecular characteristics of soleus muscle in men exposed to 7-day dry immersion," *Journal of Gravitational Physiology*, vol. 11, no. 2, pp. P131–P132, 2004.
- [49] S. Lange, F. Xiang, A. Yakovenko et al., "Cell biology: the kinase domain of titin controls muscle gene expression and protein turnover," *Science*, vol. 308, no. 5728, pp. 1599–1603, 2005.
- [50] T. Centner, J. Yano, E. Kimura et al., "Identification of muscle specific ring finger proteins as potential regulators of the titin kinase domain," *Journal of Molecular Biology*, vol. 306, no. 4, pp. 717–726, 2001.
- [51] S. C. Kandarian and E. J. Stevenson, "Molecular events in skeletal muscle during disuse atrophy," *Exercise and Sport Sciences Reviews*, vol. 30, no. 3, pp. 111–116, 2002.
- [52] B. S. Shenkman, T. L. Nemirovskaya, I. N. Belozeroва et al., "Effects of Ca^{2+} -binding agent on unloaded rat soleus: muscle morphology and sarcomeric titin content," *European Space Agency*, no. 501, pp. 107–108, 2002.
- [53] B. S. Shenkman, K. S. Litvinova, T. L. Nemirovskaya, Z. A. Podlubnaya, I. M. Vikhlyantsev, and I. B. Kozlovskaya, "Afferent and peripheral control of muscle fiber properties during gravitational unloading," *Journal of Gravitational Physiology*, vol. 11, no. 2, pp. P111–P114, 2004.
- [54] K. Goto, R. Okuyama, M. Honda et al., "Profiles of connectin (titin) in atrophied soleus muscle induced by unloading of rats," *Journal of Applied Physiology*, vol. 94, no. 3, pp. 897–902, 2003.
- [55] H. Chang, L. Zhang, P.-T. Xu et al., "Nuclear translocation of calpain-2 regulates propensity toward apoptosis in cardiomyocytes of tail-suspended rats," *Journal of Cellular Biochemistry*, vol. 112, no. 2, pp. 571–580, 2011.
- [56] P. O. Hasselgren and J. E. Fischer, "Counter-regulatory hormones and mechanisms in amino acid metabolism with special reference to the catabolic response in skeletal muscle," *Current Opinion in Clinical Nutrition and Metabolic Care*, vol. 2, no. 1, pp. 9–14, 1999.
- [57] R. T. Jagoe and A. L. Goldberg, "What do we really know about the ubiquitin-proteasome pathway in muscle atrophy?" *Current Opinion in Clinical Nutrition and Metabolic Care*, vol. 4, no. 3, pp. 183–190, 2001.
- [58] S. H. Lecker, R. T. Jagoe, A. Gilbert et al., "Multiple types of skeletal muscle atrophy involve a common program of changes in gene expression," *The FASEB Journal*, vol. 18, no. 1, pp. 39–51, 2004.
- [59] M. D. Gomes, S. H. Lecker, R. T. Jagoe, A. Navon, and A. L. Goldberg, "Atrogin-1, a muscle-specific F-box protein highly expressed during muscle atrophy," *Proceedings of the National Academy of Sciences of the United States of America*, vol. 98, no. 25, pp. 14440–14445, 2001.
- [60] R. Medina, S. S. Wing, A. Haas, and A. L. Goldberg, "Activation of the ubiquitin-ATP-dependent proteolytic system in skeletal muscle during fasting and denervation atrophy," *Biomedica Biochimica Acta*, vol. 50, no. 4–6, pp. 347–356, 1991.
- [61] A. S. McElhinny, C. N. Perry, C. C. Witt, S. Labeit, and C. C. Gregorio, "Muscle-specific RING finger-2 (MURF-2) is important for microtubule, intermediate filament and sarcomeric M-line maintenance in striated muscle development," *Journal of Cell Science*, vol. 117, no. 15, pp. 3175–3188, 2004.
- [62] C. C. Gregorio, C. N. Perry, and A. S. McElhinny, "Functional properties of the titin/connectin-associated proteins, the muscle-specific RING finger proteins (MURFs), in striated muscle," *Journal of Muscle Research and Cell Motility*, vol. 26, no. 6–8, pp. 389–400, 2005.

- [63] S. W. Jones, R. J. Hill, P. A. Krasney, B. O'Conner, N. Peirce, and P. L. Greenhaff, "Disuse atrophy and exercise rehabilitation in humans profoundly affects the expression of genes associated with the regulation of skeletal muscle mass," *The FASEB Journal*, vol. 18, no. 9, pp. 1025–1027, 2004.
- [64] L. A. Tintignac, J. Lagirand, S. Batonnet, V. Sirri, M. P. Leibovitch, and S. A. Leibovitch, "Degradation of MyoD mediated by the SCF (MAFbx) ubiquitin ligase," *The Journal of Biological Chemistry*, vol. 280, no. 4, pp. 2847–2856, 2005.
- [65] J. Lagirand-Cantaloube, N. Offner, A. Csibi et al., "The initiation factor eIF3-f is a major target for Atrogin1/MAFbx function in skeletal muscle atrophy," *The EMBO Journal*, vol. 27, no. 8, pp. 1266–1276, 2008.
- [66] V. Kedar, H. McDonough, R. Arya, H. H. Li, H. A. Rockman, and C. Patterson, "Muscle-specific RING finger 1 is a bona fide ubiquitin ligase that degrades cardiac troponin I," *Proceedings of the National Academy of Sciences of the United States of America*, vol. 101, no. 52, pp. 18135–18140, 2004.
- [67] B. A. Clarke, D. Drujan, M. S. Willis et al., "The E3 Ligase MuRF1 degrades myosin heavy chain protein in dexamethasone-treated skeletal muscle," *Cell Metabolism*, vol. 6, no. 5, pp. 376–385, 2007.
- [68] D. L. Allen, E. R. Bandstra, B. C. Harrison et al., "Effects of spaceflight on murine skeletal muscle gene expression," *Journal of Applied Physiology*, vol. 106, no. 2, pp. 582–592, 2009.
- [69] S. M. Phillips, E. I. Glover, and M. J. Rennie, "Alterations of protein turnover underlying disuse atrophy in human skeletal muscle," *Journal of Applied Physiology*, vol. 107, no. 3, pp. 645–654, 2009.
- [70] M. Salanova, G. Schiffl, B. Püttmann, B. G. Schoser, and D. Blottner, "Molecular biomarkers monitoring human skeletal muscle fibres and microvasculature following long-term bed rest with and without countermeasures," *Journal of Anatomy*, vol. 212, no. 3, pp. 306–318, 2008.
- [71] T. Ogawa, H. Furochi, M. Mameoka et al., "Ubiquitin ligase gene expression in healthy volunteers with 20-day bedrest," *Muscle and Nerve*, vol. 34, no. 4, pp. 463–469, 2006.
- [72] K. A. Reich, Y. W. Chen, P. D. Thompson, E. P. Hoffman, and P. M. Clarkson, "Forty-eight hours of unloading and 24 h of reloading lead to changes in global gene expression patterns related to ubiquitination and oxidative stress in humans," *Journal of Applied Physiology*, vol. 109, no. 5, pp. 1404–1415, 2010.
- [73] P. A. Tesch, F. von Walden, T. Gustafsson, R. M. Linnehan, and T. A. Trappe, "Skeletal muscle proteolysis in response to short-term unloading in humans," *Journal of Applied Physiology*, vol. 105, no. 3, pp. 902–906, 2008.
- [74] M. D. de Boer, A. Selby, P. Atherton et al., "The temporal responses of protein synthesis, gene expression and cell signalling in human quadriceps muscle and patellar tendon to disuse," *The Journal of Physiology*, vol. 585, no. 1, pp. 241–251, 2007.
- [75] E. V. Kachaeva, O. V. Turtikova, T. A. Leinsoo, and B. S. Shenkman, "Insulin-like growth factor 1 and the key markers of proteolysis during the acute period of readaptation of the muscle atrophied as a result of unloading," *Biofizika*, vol. 55, no. 6, pp. 1108–1116, 2010.
- [76] M. Vermaelen, J.-F. Marini, A. Chopard, Y. Benyamin, J. Mercier, and C. Astier, "Ubiquitin targeting of rat muscle proteins during short periods of unloading," *Acta Physiologica Scandinavica*, vol. 185, no. 1, pp. 33–40, 2005.
- [77] L. Tskhovrebova and J. Trinick, "Muscle disease: a giant feels the strain," *Nature Medicine*, vol. 11, no. 5, pp. 478–479, 2005.
- [78] S. Schiaffino and HanzlikováVera, "Studies on the effect of denervation in developing muscle. II. The lysosomal system," *Journal of Ultrastructure Research*, vol. 39, no. 1-2, pp. 1–14, 1972.
- [79] S. H. Witt, H. Granzier, C. C. Witt, and S. Labeit, "MURF-1 and MURF-2 target a specific subset of myofibrillar proteins redundantly: towards understanding MURF-dependent muscle ubiquitination," *Journal of Molecular Biology*, vol. 350, no. 4, pp. 713–722, 2005.
- [80] A. S. Moriscot, I. L. Baptista, J. Bogomolovas et al., "MuRF1 is a muscle fiber-type II associated factor and together with MuRF2 regulates type-II fiber trophicity and maintenance," *Journal of Structural Biology*, vol. 170, no. 2, pp. 344–353, 2010.
- [81] S. Labeit, C. H. Kohl, C. C. Witt, D. Labeit, J. Jung, and H. Granzier, "Modulation of muscle atrophy, fatigue and MLC phosphorylation by MuRF1 as indicated by hindlimb suspension studies on MuRF1-KO mice," *Journal of Biomedicine and Biotechnology*, vol. 2010, Article ID 693741, 9 pages, 2010.
- [82] C. Bozzo, L. Stevens, L. Toniolo, Y. Mounier, and C. Reggiani, "Increased phosphorylation of myosin light chain associated with slow-to-fast transition in rat soleus," *American Journal of Physiology*, vol. 285, no. 3, pp. C575–C583, 2003.
- [83] M. J. Potthoff, H. Wu, M. A. Arnold et al., "Histone deacetylase degradation and MEF2 activation promote the formation of slow-twitch myofibers," *The Journal of Clinical Investigation*, vol. 117, no. 9, pp. 2459–2467, 2007.
- [84] U. Späte and P. C. Schulze, "Proinflammatory cytokines and skeletal muscle," *Current Opinion in Clinical Nutrition and Metabolic Care*, vol. 7, no. 3, pp. 265–269, 2004.
- [85] I. W. McKinnell and M. A. Rudnicki, "Molecular mechanisms of muscle atrophy," *Cell*, vol. 119, no. 7, pp. 907–910, 2004.
- [86] D. Cai, J. D. Frantz, N. E. Tawa et al., "IKK β /NF- κ B activation causes severe muscle wasting in mice," *Cell*, vol. 119, no. 2, pp. 285–298, 2004.
- [87] R. Bridge Hunter, E. J. Stevenson, C. Alan Koncarevi, H. Mitchell-Felton, D. A. Essig, and S. C. Kandarian, "Activation of an alternative NF- κ B pathway in skeletal muscle during disuse atrophy," *The FASEB Journal*, vol. 16, no. 6, pp. 529–538, 2002.
- [88] A. R. Judge, A. Koncarevic, R. B. Hunter, H. C. Liou, R. W. Jackman, and S. C. Kandarian, "Role for I κ B α , but not c-Rel, in skeletal muscle atrophy," *American Journal of Physiology*, vol. 292, no. 1, pp. C372–C382, 2007.
- [89] S. M. Senf, S. L. Dodd, J. M. McClung, and A. R. Judge, "Hsp70 overexpression inhibits NF- κ B and Foxo3a transcriptional activities and prevents skeletal muscle atrophy," *The FASEB Journal*, vol. 22, no. 11, pp. 3836–3845, 2008.
- [90] T. N. Stitt, D. Drujan, B. A. Clarke et al., "The IGF-1/PI3K/Akt pathway prevents expression of muscle atrophy-induced ubiquitin ligases by inhibiting FOXO transcription factors," *Molecular Cell*, vol. 14, no. 3, pp. 395–403, 2004.
- [91] K. H. Kaestner, W. Knöchel, and D. E. Martínez, "Unified nomenclature for the winged helix/forkhead transcription factors," *Genes and Development*, vol. 14, no. 2, pp. 142–146, 2000.
- [92] H. Huang and D. J. Tindall, "Regulation of FOXO protein stability via ubiquitination and proteasome degradation," *Biochimica et Biophysica Acta*, vol. 1813, no. 11, pp. 1961–1964, 2011.
- [93] M. Sandri, C. Sandri, A. Gilbert et al., "Foxo transcription factors induce the atrophy-related ubiquitin ligase atrogin-1 and cause skeletal muscle atrophy," *Cell*, vol. 117, no. 3, pp. 399–412, 2004.

- [94] Y. Kamei, S. Miura, M. Suzuki et al., "Skeletal muscle FOXO1 (FKHR) transgenic mice have less skeletal muscle mass, down-regulated type I (slow twitch/red muscle) fiber genes, and impaired glycemic control," *The Journal of Biological Chemistry*, vol. 279, no. 39, pp. 41114–41123, 2004.
- [95] C. De Alvaro, T. Teruel, R. Hernandez, and M. Lorenzo, "Tumor necrosis factor alpha produces insulin resistance in skeletal muscle by activation of inhibitor kappaB kinase in a p38 MAPK-dependent manner," *The Journal of Biological Chemistry*, vol. 279, no. 17, pp. 17070–17078, 2004.
- [96] C. Dogra, H. Changotra, N. Wedhas, X. Qin, J. E. Wergedal, and A. Kumar, "TNF-related weak inducer of apoptosis (TWEAK) is a potent skeletal muscle-wasting cytokine," *The FASEB Journal*, vol. 21, no. 8, pp. 1857–1869, 2007.
- [97] J. Hirosumi, G. Tuncman, L. Chang et al., "A central, role for JNK in obesity and insulin resistance," *Nature*, vol. 420, no. 6913, pp. 333–336, 2002.
- [98] F. Mourkioti, P. Kratsios, T. Luedde et al., "Targeted ablation of IKK2 improves skeletal muscle strength, maintains mass, and promotes regeneration," *The Journal of Clinical Investigation*, vol. 116, no. 11, pp. 2945–2954, 2006.
- [99] B. Han, M. J. Zhu, C. Ma, and M. Du, "Rat hindlimb unloading down-regulates insulin like growth factor-1 signaling and AMP-activated protein kinase, and leads to severe atrophy of the soleus muscle," *Applied Physiology, Nutrition and Metabolism*, vol. 32, no. 6, pp. 1115–1123, 2007.
- [100] R. Nakao, K. Hirasaka, J. Goto et al., "Ubiquitin ligase Cbl-b is a negative regulator for insulin-like growth factor 1 signaling during muscle atrophy caused by unloading," *Molecular and Cellular Biology*, vol. 29, no. 17, pp. 4798–4811, 2009.
- [101] C. McFarlane, A. Henneby, M. Thomas et al., "Myostatin signals through Pax7 to regulate satellite cell self-renewal," *Experimental Cell Research*, vol. 314, no. 2, pp. 317–329, 2008.
- [102] D. L. Allen and T. G. Unterman, "Regulation of myostatin expression and myoblast differentiation by FoxO and SMAD transcription factors," *American Journal of Physiology*, vol. 292, no. 1, pp. C188–C199, 2007.
- [103] S. McCroskery, M. Thomas, L. Maxwell, M. Sharma, and R. Kambadur, "Myostatin negatively regulates satellite cell activation and self-renewal," *Journal of Cell Biology*, vol. 162, no. 6, pp. 1135–1147, 2003.
- [104] J. Massagué, J. Seoane, and D. Wotton, "Smad transcription factors," *Genes and Development*, vol. 19, no. 23, pp. 2783–2810, 2005.
- [105] R. R. Gomis, C. Alarcón, W. He et al., "A FoxO-Smad syn-expression group in human keratinocytes," *Proceedings of the National Academy of Sciences of the United States of America*, vol. 103, no. 34, pp. 12747–12752, 2006.
- [106] T. Shintani and D. J. Klionsky, "Autophagy in health and disease: a double-edged sword," *Science*, vol. 306, no. 5698, pp. 990–995, 2004.
- [107] M. F. N. O'Leary and D. A. Hood, "Denervation-induced oxidative stress and autophagy signaling in muscle," *Autophagy*, vol. 5, no. 2, pp. 230–231, 2009.
- [108] M. E. Tischler, S. Rosenberg, S. Satarug et al., "Different mechanisms of increased proteolysis in atrophy induced by denervation or unweighting of rat soleus muscle," *Metabolism*, vol. 39, no. 7, pp. 756–763, 1990.
- [109] K. Furuno, M. N. Goodman, and A. L. Goldberg, "Role of different proteolytic systems in the degradation of muscle proteins during denervation atrophy," *The Journal of Biological Chemistry*, vol. 265, no. 15, pp. 8550–8557, 1990.
- [110] C. Deval, S. Mordier, C. Obled et al., "Identification of cathepsin L as a differentially expressed message associated with skeletal muscle wasting," *Biochemical Journal*, vol. 360, no. 1, pp. 143–150, 2001.
- [111] M. Sandri, "Signaling in muscle atrophy and hypertrophy," *Physiology*, vol. 23, no. 3, pp. 160–170, 2008.
- [112] D. E. Goll, G. Neti, S. W. Mares, and V. F. Thompson, "Myofibrillar protein turnover: the proteasome and the calpains," *Journal of Animal Science*, vol. 86, no. 14, pp. E19–E35, 2008.
- [113] A. Tassa, M. P. Roux, D. Attaix, and D. M. Bechet, "Class III phosphoinositide 3-kinase-Beclin1 complex mediates the amino acid-dependent regulation of autophagy in C₂C₂ myotubes," *Biochemical Journal*, vol. 376, no. 3, pp. 577–586, 2003.
- [114] C. Mammucari, G. Milan, V. Romanello et al., "FoxO3 controls autophagy in skeletal muscle in vivo," *Cell Metabolism*, vol. 6, no. 6, pp. 458–471, 2007.
- [115] J. Zhao, J. J. Brault, A. Schild et al., "FoxO3 coordinately activates protein degradation by the autophagic/lysosomal and proteasomal pathways in atrophying muscle cells," *Cell Metabolism*, vol. 6, no. 6, pp. 472–483, 2007.
- [116] J. Du, X. Wang, C. Miereles et al., "Activation of caspase-3 is an initial step triggering accelerated muscle proteolysis in catabolic conditions," *The Journal of Clinical Investigation*, vol. 113, no. 1, pp. 115–123, 2004.
- [117] P. Berthon, S. Duguez, F. B. Favier et al., "Regulation of ubiquitin-proteasome system, caspase enzyme activities, and extracellular proteinases in rat soleus muscle in response to unloading," *Pflugers Archiv European Journal of Physiology*, vol. 454, no. 4, pp. 625–633, 2007.
- [118] E. Vazeille, A. Codran, A. Claustre et al., "The ubiquitin-proteasome and the mitochondria-associated apoptotic pathways are sequentially downregulated during recovery after immobilization-induced muscle atrophy," *American Journal of Physiology*, vol. 295, no. 5, pp. E1181–E1190, 2008.
- [119] P. M. Siu, E. E. Pistilli, and S. E. Alway, "Apoptotic responses to hindlimb suspension in gastrocnemius muscles from young adult and aged rats," *American Journal of Physiology*, vol. 289, no. 4, pp. R1015–R1026, 2005.
- [120] C. Leeuwenburgh, C. M. Gurley, B. A. Strotman, and E. E. Dupont-Versteegden, "Age-related differences in apoptosis with disuse atrophy in soleus muscle," *American Journal of Physiology*, vol. 288, no. 5, pp. R1288–R1296, 2005.
- [121] M. Ohanna, A. K. Sobering, T. Lapointe et al., "Atrophy of S6K1^{-/-} skeletal muscle cells reveals distinct mTOR effectors for cell cycle and size control," *Nature Cell Biology*, vol. 7, no. 3, pp. 286–294, 2005.
- [122] E. J. Henriksen, M. E. Tischler, and D. G. Johnson, "Increased response to insulin of glucose metabolism in the 6-day unloaded rat soleus muscle," *The Journal of Biological Chemistry*, vol. 261, no. 23, pp. 10707–10712, 1986.
- [123] S. C. Bodine, E. Latres, S. Baumhueter et al., "Identification of ubiquitin ligases required for skeletal muscle atrophy," *Science*, vol. 294, no. 5547, pp. 1704–1708, 2001.
- [124] W. H. Shen, D. W. Boyle, P. Wisniewski, A. Bade, and E. A. Liechty, "Insulin and IGF-I stimulate the formation of the eukaryotic initiation factor 4F complex and protein synthesis in C2C12 myotubes independent of availability of external amino acids," *Journal of Endocrinology*, vol. 185, no. 2, pp. 275–289, 2005.
- [125] T. L. Hilder, J. C. L. Tou, R. E. Grindeland, C. E. Wade, and L. M. Graves, "Phosphorylation of insulin receptor substrate-1

- serine 307 correlates with JNK activity in atrophic skeletal muscle," *FEBS Letters*, vol. 553, no. 1-2, pp. 63–67, 2003.
- [126] S. Machida and F. W. Booth, "Changes in signalling molecule levels in 10-day hindlimb immobilized rat muscles," *Acta Physiologica Scandinavica*, vol. 183, no. 2, pp. 171–179, 2005.
- [127] K. Csukly, T. Marqueste, and P. Gardiner, "Sensitivity of rat soleus muscle to a mechanical stimulus is decreased following hindlimb unweighting," *European Journal of Applied Physiology*, vol. 95, no. 2-3, pp. 243–249, 2005.
- [128] P. K. Paul, S. K. Gupta, S. Bhatnagar et al., "Targeted ablation of TRAF6 inhibits skeletal muscle wasting in mice," *Journal of Cell Biology*, vol. 191, no. 7, pp. 1395–1411, 2010.
- [129] A. Csibi, L. A. Tintignac, M. P. Leibovitch, and S. A. Leibovitch, "eIF3-f function in skeletal muscles: to stand at the crossroads of atrophy and hypertrophy," *Cell Cycle*, vol. 7, no. 12, pp. 1698–1701, 2008.
- [130] C. Zhou, F. Arslan, S. Wee et al., "PCI proteins eIF3e and eIF3m define distinct translation initiation factor 3 complexes," *BMC Biology*, vol. 3, article 14, 2005.
- [131] A. L. Serrano, B. Baeza-Raja, E. Perdiguero, M. Jardí, and P. Muñoz-Cánoves, "Interleukin-6 is an essential regulator of satellite cell-mediated skeletal muscle hypertrophy," *Cell Metabolism*, vol. 7, no. 1, pp. 33–44, 2008.
- [132] P. Loughna, G. Goldspink, and D. F. Goldspink, "Effect of inactivity and passive stretch on protein turnover in phasic and postural rat muscles," *Journal of Applied Physiology*, vol. 61, no. 1, pp. 173–179, 1986.
- [133] K. Ojima, Y. Kawabata, H. Nakao et al., "Dynamic distribution of muscle-specific calpain in mice has a key role in physical-stress adaptation and is impaired in muscular dystrophy," *The Journal of Clinical Investigation*, vol. 120, no. 8, pp. 2672–2683, 2010.
- [134] I. L. Baptista, M. L. Leal, G. G. Artioli et al., "Leucine attenuates skeletal muscle wasting via inhibition of ubiquitin ligases," *Muscle and Nerve*, vol. 41, no. 6, pp. 800–808, 2010.

Research Article

Influences of Desmin and Keratin 19 on Passive Biomechanical Properties of Mouse Skeletal Muscle

Sameer B. Shah,^{1,2} James M. Love,¹ Andrea O'Neill,³ Richard M. Lovering,⁴
and Robert J. Bloch³

¹ Fischell Department of Bioengineering, University of Maryland, College Park, MD 20742, USA

² Departments of Orthopaedic Surgery and Bioengineering, University of California, San Diego, La Jolla, CA 92093, USA

³ Department of Physiology, University of Maryland School of Medicine, Baltimore, MD 21201, USA

⁴ Department of Orthopaedics, University of Maryland School of Medicine, Baltimore, MD 21201, USA

Correspondence should be addressed to Sameer B. Shah, sbs Shah@ucsd.edu

Received 28 May 2011; Accepted 10 September 2011

Academic Editor: J.-P. Jin

Copyright © 2012 Sameer B. Shah et al. This is an open access article distributed under the Creative Commons Attribution License, which permits unrestricted use, distribution, and reproduction in any medium, provided the original work is properly cited.

In skeletal muscle fibers, forces must be transmitted between the plasma membrane and the intracellular contractile lattice, and within this lattice between adjacent myofibrils. Based on their prevalence, biomechanical properties and localization, desmin and keratin intermediate filaments (IFs) are likely to participate in structural connectivity and force transmission. We examined the passive load-bearing response of single fibers from the extensor digitorum longus (EDL) muscles of young (3 months) and aged (10 months) wild-type, desmin-null, K19-null, and desmin/K19 double-null mice. Though fibers are more compliant in all mutant genotypes compared to wild-type, the structural response of each genotype is distinct, suggesting multiple mechanisms by which desmin and keratin influence the biomechanical properties of myofibers. This work provides additional insight into the influences of IFs on structure-function relationships in skeletal muscle. It may also have implications for understanding the progression of desminopathies and other IF-related myopathies.

1. Introduction

Lateral force transmission, both across the sarcolemma and within a single myofiber, is believed to be an important component of the biomechanical function of muscle [1–4]. Forces must be transmitted both between the plasma membrane and the intracellular myofibrillar lattice, and also within this lattice, from myofibril to myofibril. Based on their prevalence, biomechanical properties and localization, intermediate filaments (IFs) are strong candidates to regulate such lateral transmission. IFs composed of desmin and keratins 8 and 19 have been identified as key components of mature skeletal muscle [5–7]. Considerable evidence links these IFs to roles in structural connectivity and mechanical function.

Desmin, a type III IF expressed exclusively in striated muscle, localizes around Z-disks in the extramyofibrillar space, around mitochondria, at the periphery of cell nuclei,

and at costameres, which are periodic sarcolemmal protein complexes lying over the Z-disks and M-bands of peripheral myofibrils [8–14]. Structurally, the loss of desmin results in misaligned myofibrils and disrupted costameres [15, 16]. Mechanically, muscles lacking desmin display reduced maximal isometric force, increased fatigability, poor transverse and longitudinal coupling, and slight increases in passive stiffness, particularly in older animals [17–19]. Although there are discrepancies regarding the susceptibility of desmin-null muscles to injury, these may be attributable to differences in the strains of desmin-null mice probed, the identity of muscles tested, or injury protocols imposed [17, 18].

Keratin 19 (K19) and keratin 8 (K8), type I and type II IF proteins, respectively, are the best characterized of the keratins expressed in mature striated muscle. At the sarcolemma, K8 and K19 colocalize with and specifically interact with costameric proteins, including dystrophin,

overlying both the Z-disks and M-bands of adjacent myofibrils [20, 21]. Within the myofibrillar lattice, K19 and K8 concentrate primarily around Z-disks [21]. Structurally, the absence of K19 results in the partial disruption of costameres and the dramatic separation of the sarcolemma from adjacent myofibrils by a large gap within which mitochondria accumulate [18, 22]. A small but significant shift in the lateral spacing between myofibrils is also observed in the absence of K19; however, myofibrillar desmin localization is undisturbed [18, 22]. Physiologically, the absence of K19 results in decreased maximal isometric force and increased plasma creatine kinase levels [18, 22]. Double-null muscles, lacking both K19 and desmin, display increased susceptibility to injury and significant increases in membrane instability. Decreases in specific tension are greater than that of K19-null muscles, but equal to those in desmin-null muscles [18].

Given the possibility that extracellular matrix remodeling could influence the mechanical properties of whole muscle [23–25], experiments on single fibers have been performed to examine structural connectivity during passive mechanical stretch [26, 27]. Analysis of desmin-null fibers confirmed the necessity of desmin for myofibrillar and nuclear alignment during mechanical loading. Unlike observations in whole muscle, however, isolated desmin-null fibers do not appear to display misaligned costameres, even in the presence of considerable shear force. In addition, desmin-null fibers are more compliant than their wild-type counterparts.

In this study, we have extended the examination of biomechanical roles for IFs in single fibers. We investigated the structural changes and tensile load-bearing response of passively loaded fibers harvested from the extensor digitorum longus (EDL) muscles of young (3 months) and middle-aged (10 months) wild-type, desmin-null, K19-null, and desmin/K19 double-null FVB mice. We observed that, although fibers are more compliant in both desmin and K19-null knockout mice, the structural changes that occur within the two types of fibers during loading are different. Our data suggest that IFs influence force transmission in myofibers through multiple biomechanical pathways.

2. Methods

2.1. Animals. Female FVB mice homozygous for the desmin-null (*des* $-/-$), K19-null (K19 $-/-$), and desmin/K19 double-null genotypes were bred and genotyped as described previously [18] and compared to age- and sex-matched wild-type FVB mice (Taconic, Hudson, NY, USA). Mice were studied at two ages, 3 months and 10 months. They were euthanized by carbon dioxide inhalation immediately prior to tissue harvest. Institutional Animal Care and Usage (IACUC) Committees of the University of Maryland School of Medicine and the University of Maryland, College Park, approved all animal use protocols.

2.2. Fiber Dissection and Attachment to Mechanical Apparatus. Tissue harvest, muscle storage, and fiber dissection protocols have been described previously [27]. Briefly, EDL muscles were dissected from mouse hindlimbs, bathed in relaxing

solution for 60 min and placed in a glycerol-based storage solution for a minimum of 24 h and a maximum of one week at -20°C . All solutions were made in the presence of the protease inhibitor leupeptin. Segments of single intact fibers were carefully dissected and transferred in relaxing solution to a chamber housed in a custom-made mechanical apparatus. This apparatus is similar to that previously used [26, 27], with the only difference being the modification of the structural frame and stage insert to be mounted on an inverted wide-field fluorescence microscope (Nikon TE-2000PFS, Melville, NY, USA). Within the chamber, the segment was securely tied with 10-0 monofilament suture to pins projecting from a force transducer (Aurora Scientific 405A, Aurora, Ontario, Canada) and a rotational bearing (Newport MTRS, Irvine, Calif, USA). This configuration enabled the high-resolution imaging of fiber and sarcomere geometry during passive loading. To minimize any experimental artifacts associated with glycerol-mediated skinning of fibers during storage, segments displaying abnormal discoloration, localized swelling, or otherwise irregular geometry or appearance were discarded.

2.3. Passive Mechanical Protocol and Imaging. The fiber segment was brought to its resting length, determined as the knot-to-knot segment length at which passive tension was just measurable above the noise level of the force transducer. The segment was preconditioned by three loading cycles of 15% fiber strain, resulting in a change in resting length of $<3\%$ from the resting length before preconditioning. The segment was then loaded in increments of $\sim 10\%$ of the segment length at a rate of 0.05 mm/s. At each length, after two minutes of stress relaxation, images of the fiber were captured in a middle region of the fiber, and steady-state force (within 5% of the final force value) was recorded. During the 2 min of stress relaxation, the imaging field was adjusted to visualize the same region and focal plane of the fiber at each strain. Phase-contrast imaging was performed on an inverted microscope (Nikon TE-2000PFS, Melville, NY), using 10x and 20x CFI Plan Apo objectives (Nikon). Exposure times were 5–20 ms; image acquisition was controlled by Elements software (Nikon, Melville, NY, USA). A custom built environmental chamber (Precision Plastics, Beltsville, Md, USA) maintained temperature (25°C) and humidity during imaging.

2.4. Calculation of Biomechanical Parameters. Image analysis was performed using Elements software and Micron software (Westover Scientific, Mill Creek, Wash, USA). Fiber cross-sectional area was calculated using a circular approximation, based on diameters measured from a phase contrast image of the fiber at each strain. Area was multiplied by fiber length to estimate fiber volume, assuming a cylindrical fiber. Cauchy (true) stress (σ_C) was calculated by dividing force by the current cross-sectional area at each strain, and LaGrangian stress (σ_{LG}) was calculated by dividing force by the cross-sectional area of the undeformed fiber. Fiber strain (ϵ_F) was calculated as the ratio of the imposed deformation to the resting knot-to-knot fiber length. Sarcomere length (SL)

was calculated based on the average spacing between 20 consecutive Z-disks, as measured from phase images of fibers at each fiber strain. SL in different regions of the fiber varied by less than $0.1 \mu\text{m}$, and therefore SLs were measured at three locations per image and averaged. Sarcomere strain (ϵ_{SL}) was calculated as the ratio of the change in SL to the SL at resting fiber length. Strain in the sarcolemmal plasma membrane in the vicinity of the imaged sarcomeres, or local membrane strain, was calculated based on changes in the spacing between membrane markers, or pieces of residual debris on the external surface of the fiber; local membrane strain (ϵ_{M}) was calculated as the ratio of the change in spacing between membrane markers to marker spacing at resting fiber length. Radial strain (ϵ_{R}) was calculated as the ratio of the change in fiber diameter to the fiber diameter at resting fiber length. Poisson's ratio (ν) was calculated based on the power-law relationship between longitudinal and radial strain. Biomechanical parameters and their relationships with each other are summarized in Table 1.

2.5. Statistics. Regression analysis was performed using Excel (Microsoft, Seattle, Wash, USA). One-way ANOVAs examining the effect of genotype were performed independently on mechanical data from young and aged mice, since an additional double-null group was evaluated in aged mice. Data from double-null mice were not considered for subsequent two-way ANOVA analysis, which examined effects and interactions of age and genotype on mechanical parameters. ANOVA and post hoc two-tailed *t*-tests assuming unequal variance were performed using Prism (Graph Pad Software, Inc., La Jolla, Calif, USA). Values are given as mean \pm SEM.

3. Results

3.1. Intermediate Filament Influences on Passive Properties of Fibers from Aged Animals. We examined the response of EDL fibers harvested from 10-month-old wild-type, desmin-null, K19-null, and desmin/K19 double-null mice to tensile loading to examine the relative contributions of each intermediate filament to fiber passive mechanical properties. A summary and a brief description of measured and calculated parameters are provided in Table 1.

For stress-strain curves, regression coefficients were used to compare the relative compliance of fiber populations. Cauchy stress was plotted against fiber strain for each experiment and fit using quadratic regression (Figure 1(a), cf. [26]). Fibers from all genotypes displayed a strong quadratic relationship between stress and fiber strain ($r^2 > 0.78$ for all experiments), indicating an elastic modulus that varies linearly with strain. ANOVA revealed a significant effect of genotype on the quadratic regression coefficient ($P < 0.0001$). Post hoc comparison of the quadratic coefficients revealed that wild-type fibers were significantly stiffer than desmin-null ($P < 0.002$), K19-null ($P < 0.006$), and double-null ($P < 0.002$) fibers (Figure 1(b)). There were no significant differences in the quadratic regression coefficients of K19-null and desmin-null or desmin-null and double-null fibers. Interestingly, however, a significant difference

($P < 0.03$) was observed between K19-null and double-null fibers for Cauchy stress-strain curves.

To determine whether these differences in fiber populations were strictly a result of changes in fiber geometry or also inherent load-bearing ability, LaGrangian stress was plotted against fiber strain (Figure 1(c)). Use of the undeformed area to calculate stress had the effect of flattening the curves, so linear regression was used ($r^2 > 0.81$ for all experiments) to describe the relationship between stress and fiber strain. ANOVA again revealed a significant effect of genotype on the regression coefficient ($P < 0.0001$). Comparison of linear coefficients confirmed that wild-type fibers were significantly stiffer than desmin-null ($P < 0.005$), K19-null ($P < 0.007$), and double-null ($P < 0.004$) fibers (Figure 1(d)). There were no significant differences in the linear regression coefficients of K19-null and desmin-null, desmin-null and double-null, or K19-null and double-null fibers. Consistent with results from Cauchy stress-strain relationships, though, a strong but nonsignificant trend ($P < 0.09$) was observed for the latter.

Analysis of radial strain revealed additional differences in the mechanical response of fibers from different genotypes (Figure 1(e)). First-order exponential functions were used to describe the relationship between radial and longitudinal strains ($r^2 > 0.83$ for all experiments). Although, as expected, ANOVA revealed a significant effect of genotype on the exponential decay constant ($P < 0.04$), post hoc comparison (Figure 1(f)) revealed that wild-type fibers exhibited tighter coupling between longitudinal and radial strains than desmin-null ($P < 0.04$), but not K19-null ($P < 0.24$) fibers. Wild-type fibers also trended towards a higher time constant (tighter coupling) than double-null fibers, but were not significantly different ($P < 0.06$). As was the case for stress-strain relationships, there was no difference between the relationship between radial and longitudinal strain for desmin-null and double-null fibers.

We further examined the coupling of longitudinal and radial strains in the context of fiber anisotropy, by calculating Poisson's ratio. A power-law was used to fit the relationship between longitudinal and radial strain, with the exponent denoting Poisson's ratio for each fiber. R^2 values for each experiment were reasonably high ($r^2 > 0.62$), though not as strong as an exponential regression fit. For all genotypes, Poisson's ratios exceeded 0.5, indicating significant anisotropy. There were no significant differences in Poisson's ratio between any of the genotypes (Mean \pm SEM for wild-type: 0.81 ± 0.10 ; des $-/-$: 0.63 ± 0.08 ; ker $-/-$: 0.71 ± 0.05 ; double KO: 0.61 ± 0.04), though a trend towards a slightly higher Poisson's ratio was observed for wild-type fibers compared to double-null fibers ($P < 0.09$).

Consistent with the high Poisson's ratios, when changes in fiber volume were plotted against longitudinal strain, each genotype displayed a decrease in volume with increasing strain, indicating that loading was not isovolumic. This decrease was usually linear, and therefore linear regression was used to fit this data ($r^2 > 0.68$). Wild-type fibers displayed the most dramatic decrease in volume (Mean slope \pm SEM: -0.38 ± 0.11), though there were no significant differences in first-order regression slopes between any of the genotypes (des $-/-$: -0.16 ± 0.05 ; ker $-/-$: -0.22 ± 0.04 ;

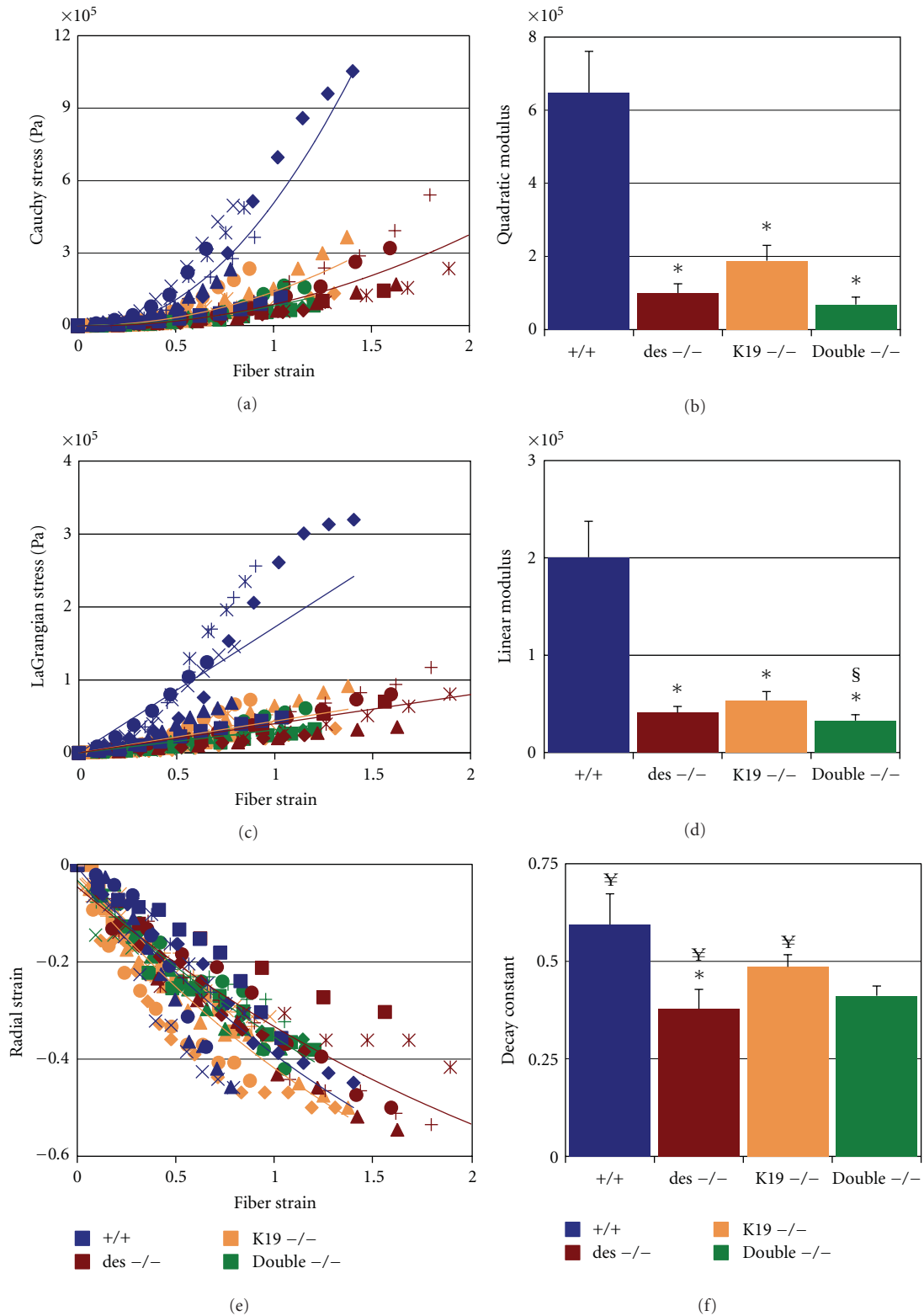


FIGURE 1: Mechanical response of fibers from aged animals. Raw data (a, c, e) and regression coefficients (b, d, f) for (a-b) Cauchy stress-fiber strain (quadratic regression); (c-d) LaGrangian stress-fiber strain (linear regression); (e-f) radial strain-fiber strain (exponential regression) for fibers from 10-month-old wild-type (blue), desmin-null (red), K19-null (orange), and double-null (green) animals ($n = 7$ fibers/genotype). Different symbols within a color group represent data from individual experiments. Displayed regression lines in (a), (c), and (e) represent averaged coefficients for individual experiments reported in (b), (d), and (f). * Indicates significant difference from wild-type; § indicates significant difference from K19-null; ¥ indicates significant difference from corresponding genotype in younger animals. P values are reported in the text.

TABLE 1: Summary and explanation of biomechanical parameters.

Parameter (units)	Symbol	Formula	Lay description of parameter and relevance
Force (N)	F	—	Nonnormalized force
Undeformed fiber length (m)	L_o	—	Initial knot-knot fiber length
Undeformed diameter (m)	d_o	—	Initial fiber diameter
Undeformed area (m ²)	A_o	—	Initial fiber cross-sectional area
Deformed fiber length (m)	L_f	—	Fiber length following longitudinal deformation
Deformed diameter (m)	d_f	—	Fiber diameter following longitudinal deformation
Deformed area (m ²)	A_f	—	Fiber cross-sectional area following longitudinal deformation
Longitudinal fiber strain (dimensionless)	ϵ_L	$(L_f - L_o)/L_o$	Normalized longitudinal deformation—percentage fiber extension
Fiber volume	V_f	$L_f * A_d$	Fiber volume after deformation, assuming a cylindrical geometry
Radial strain (dimensionless)	ϵ_R	$d_f - d_o/d_o$	Normalized lateral deformation—percentage reduction in fiber diameter following longitudinal deformation; increased radial strain represents stronger coupling between longitudinal and lateral responses.
Cauchy (true) stress (Pa)	σ_C	F/A_d	Force normalized to deformed area—couples force generation to changes in 3D-fiber geometry
LaGrangian stress (Pa)	σ_{LG}	F/A_o	Force normalized to undeformed area—measure of inherent load-bearing ability, decoupled from changes in 3D-fiber geometry
Poisson's ratio (dimensionless)	ν	$(1 + \epsilon_L) = (1 + \epsilon_L)^{-\nu}$	Measure of relation between longitudinal strain and radial strain—lateral strain transmission

TABLE 2: Summary of parameters that display significant post hoc differences ($P < 0.05$) between genotypes for fibers harvested from aged mice. Raw data, means, and standard errors are provided in Figure 1. Parameters that display non-significant trends ($P < 0.09$) are provided in parentheses. NS: No significant difference.

Genotype	des -/-	K19 -/-	Double -/-
+/+	$\sigma_{LG}, \sigma_C, \epsilon_R$	σ_{LG}, σ_C	$\sigma_{LG}, \sigma_C, (\epsilon_R), (\nu), (V_f)$
des -/-		NS	NS
K19 -/-			$\sigma_C, (\sigma_{LG}), (\epsilon_R)$

double KO: -0.13 ± 0.04). As for Poisson's ratio, a trend towards a slightly higher magnitude of regression slope was observed for wild-type fibers compared to double-null fibers ($P < 0.08$). Significant differences between parameters are summarized in Table 2.

3.2. Intermediate Filament Influences on Passive Properties of Fibers from Young Animals. Passive biomechanical analysis was then performed on EDL fibers harvested from 3-month-old wild-type, desmin-null, and K19-null mice, to probe whether phenotypes observed in the older 10-month-old animals originate at earlier time points. As was observed for

older animals, fibers from all genotypes displayed a strong quadratic relationship between Cauchy stress and fiber strain ($r^2 > 0.82$ for all experiments; Figure 2(a)) and a linear relationship between LaGrangian stress and fiber strain ($r^2 > 0.86$ for all experiments; Figure 2(c)). For both Cauchy and LaGrangian stress-strain, ANOVA revealed a significant effect of genotype on regression coefficients (quadratic: $P < 0.002$; linear: $P < 0.0002$, resp.). Post hoc comparison of the quadratic coefficients revealed that wild-type fibers were significantly stiffer than desmin-null ($P < 0.01$) and K19-null ($P < 0.01$) fibers (Figure 2(b)). Similarly, comparison of linear coefficients confirmed that wild-type fibers were significantly stiffer than desmin-null ($P < 0.01$) and K19-null ($P < 0.01$) fibers (Figure 2(d)).

Analysis of radial strain in fibers from younger animals, in contrast to observations in fibers from older animals, also did not reveal any differences between desmin-null and K19-null genotypes (Figure 2(e)). First-order exponential functions were again used to describe the relationship between radial and longitudinal strain ($r^2 > 0.78$ for all experiments). ANOVA revealed a significant effect of genotype on the exponential decay constant ($P < 0.0003$). Post hoc comparison of the time constants revealed that wild-type fibers exhibited a stronger inverse relationship, and

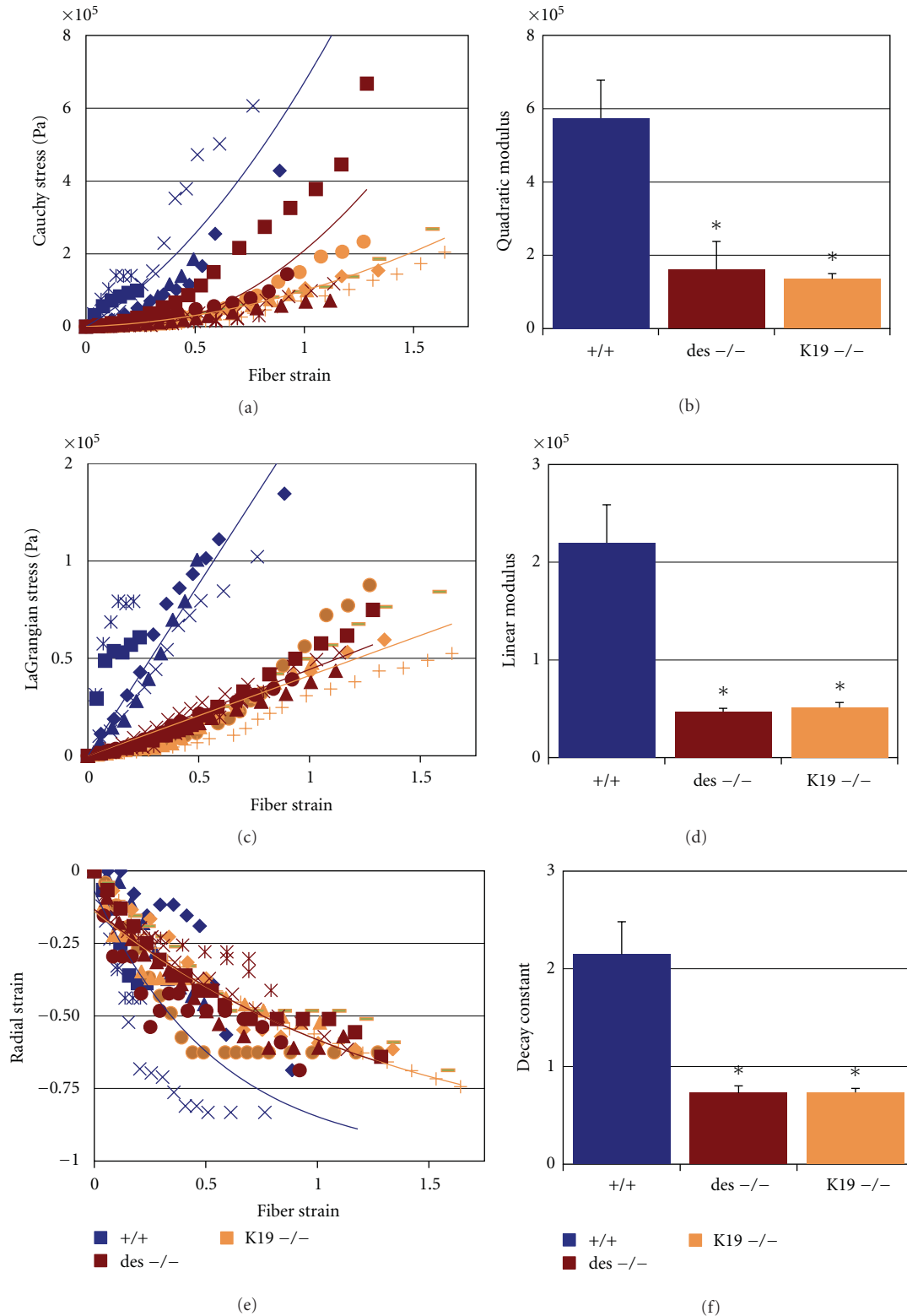


FIGURE 2: Mechanical response of fibers from young animals. Raw data (a, c, e) and regression coefficients (b, d, f) for (a-b) Cauchy stress-fiber strain (quadratic regression); (c-d) LaGrangian stress-fiber strain (linear regression); (e-f) radial strain-fiber strain (exponential regression) for fibers from 3-month-old wild-type (blue), desmin-null (red), and K19-null (orange) animals ($n = 5$ fibers/genotype). Different symbols within a color group represent data from individual experiments. Displayed regression lines in (a), (c), and (e) represent averaged coefficients for individual experiments reported in (b), (d), and (f). * indicates significant difference from wild-type. P values are reported in the text.

TABLE 3: Summary of parameters that display significant post hoc differences ($P < 0.05$) between genotypes for fibers harvested from young mice. Raw data, means, and standard errors are provided in Figure 2. NS: no significant difference.

Genotype	des $-/-$	K19 $-/-$
+/+	$\sigma_{LG}, \sigma_C, \epsilon_R, \nu,$ V_f	$\sigma_{LG}, \sigma_C, \epsilon_R, \nu, V_f$
Des $-/-$		NS

thus tighter coupling, between longitudinal and radial strains than desmin-null ($P < 0.01$) and K19-null ($P < 0.01$) fibers (Figure 1(f)).

This finding was consistent with our analysis of Poisson’s ratio. As for fibers from older animals, regression revealed a power-law relationship between longitudinal and radial strains ($r^2 > 0.61$), and Poisson’s ratios for all genotypes far exceeded 0.5, indicating considerable anisotropy. There were no significant differences in Poisson’s ratio between desmin-null and K19-null genotypes (Mean \pm SEM for des $-/-$: 1.08 ± 0.12 ; ker $-/-$: 1.19 ± 0.08), but the Poisson’s ratio of wild-type fibers (2.43 ± 0.33) was significantly higher than those of both desmin-null and K19-null fibers ($P < 0.02$). With respect to changes in volume in response to loading, as for older animals, all genotypes decreased in volume with increased deformation, and wild-type fibers displayed the most dramatic decrease in volume (Mean slope \pm SEM: -1.08 ± 0.19). This decrease was significantly greater ($P < 0.01$) than that in both desmin-null and K19-null fibers (des $-/-$: 0.24 ± 0.05 ; ker $-/-$: 0.24 ± 0.02). Significant differences between parameters are summarized in Table 3.

Though we have not yet compared the properties of fibers in 10-month-old to 3-month-old double-null mice, we confirmed differences in passive mechanical parameters between young and aged wild-type, desmin-null, and K19-null mice using two-way ANOVA. Effects of genotype ($P < 0.0001$), but no effect of age and no interaction were found on stress-strain and volume-strain relationships. However, a significant effect of genotype ($P < 0.0001$) and age ($P < 0.0001$) and an interaction between genotype and age ($P < 0.0001$) were observed for the coupling between radial strain and longitudinal strain as indicated by both exponential and power-law relationships. Post hoc analysis revealed a significant reduction in the exponential time constant and Poisson’s ratio of longitudinal and radial strain for wild-type (exp: $P < 0.008$; Poisson’s ratio: $P < 0.006$), desmin-null (exp: $P < 0.005$; Poisson’s ratio: $P < 0.02$), and K19-null (exp: $P < 0.001$; Poisson’s ratio: $P < 0.001$) fibers from aged mice compared to their younger counterparts (Figures 1(e) and 1(f) versus Figures 2(e) and 2(f)).

3.3. Structural Bases for Differences in Biomechanical Properties. In an effort to elucidate potential structural bases for differences in passive mechanical function between genotypes, we used phase-contrast microscopy to image the response of fibers from 10-month-old animals of each genotype at higher resolution (Figures 3–7). Wild-type fibers displayed well aligned Z-disks, even at high fiber strains

(Figure 4). In contrast, desmin-null fibers displayed the characteristic “basket-weave” pattern of misaligned myofibrils (Figure 5). Despite the misalignment of myofibrils in desmin-null mice, local sarcomere strain scaled consistently with fiber strain in both wild-type and desmin-null fibers (Figures 3(a), 3(b), 4, and 5). Additionally, membrane strain was also tightly correlated with sarcomere strain in both wild-type and desmin-null fibers, indicating continuity between the sarcolemma and myofibrillar lattice (Figures 3(c) and 3(d)).

In contrast, K19-null fibers appeared to have well aligned myofibrils, even in the presence of considerable shear (Figure 6). Though differences did not reach statistical significance due to the small sample size, there was considerable discontinuity between fiber strain and sarcomere strain for K19-null fibers compared to wild-type or desmin-null fibers (variability of each genotype in Figures 3(a) and 3(b); examples in Figures 4–6). Examination of the entire length of the fiber at multiple time points during experimentation suggested that this was not simply an artifact of fiber slippage at the knots or visible damage outside of the imaging window (Figures 6(b) and 6(c)). Additionally, similar to findings in desmin-null fibers, the absence of K19 did not appear to disrupt coupling between the sarcolemma and the contractile apparatus significantly, based on the strong correlation between local membrane strain and sarcomere strain (Figures 3(c) and 3(d)).

Double-null fibers, as expected, displayed phenotypes from both desmin-null and K19-null fibers. Visually, a lack of Z-disk alignment similar to that in desmin-null fibers was observed (Figure 7). As in K19-null fibers, however, there was also considerable discontinuity between fiber strain and sarcomere strain in double-null fibers (Figures 3(a), 3(b), and 7). As for all genotypes, there was no apparent decoupling between the sarcolemma and underlying myofibrils (Figures 3(c) and 3(d)).

4. Discussion

We characterized the mechanical response of skeletal muscle fibers from wild-type, desmin-null, K19-null, and desmin/K19 double-null mice to passive tensile loading. Using a mechanical testing device that also enabled high-resolution imaging, we also characterized structural changes in fibers from each genotype during deformation. Our study extends previous work describing the roles of IFs in skeletal muscle morphology and function [15, 17–22, 26] by showing that IFs comprised of desmin and of keratins each contribute to the biomechanical integrity of myofibrils in the sarcoplasm and their links to the sarcolemma. Our work also demonstrates that the weakening of these links in myofibers null for either of these proteins becomes more pronounced in older mice.

Experiments on wild-type and desmin-null fibers from 3-month-old and 10-month-old FVB mice confirmed and extended our previous characterization of fibers of these genotypes from 129/SVJ mice [26]. Reported regression coefficients and magnitudes for Cauchy stresses, LaGrangian

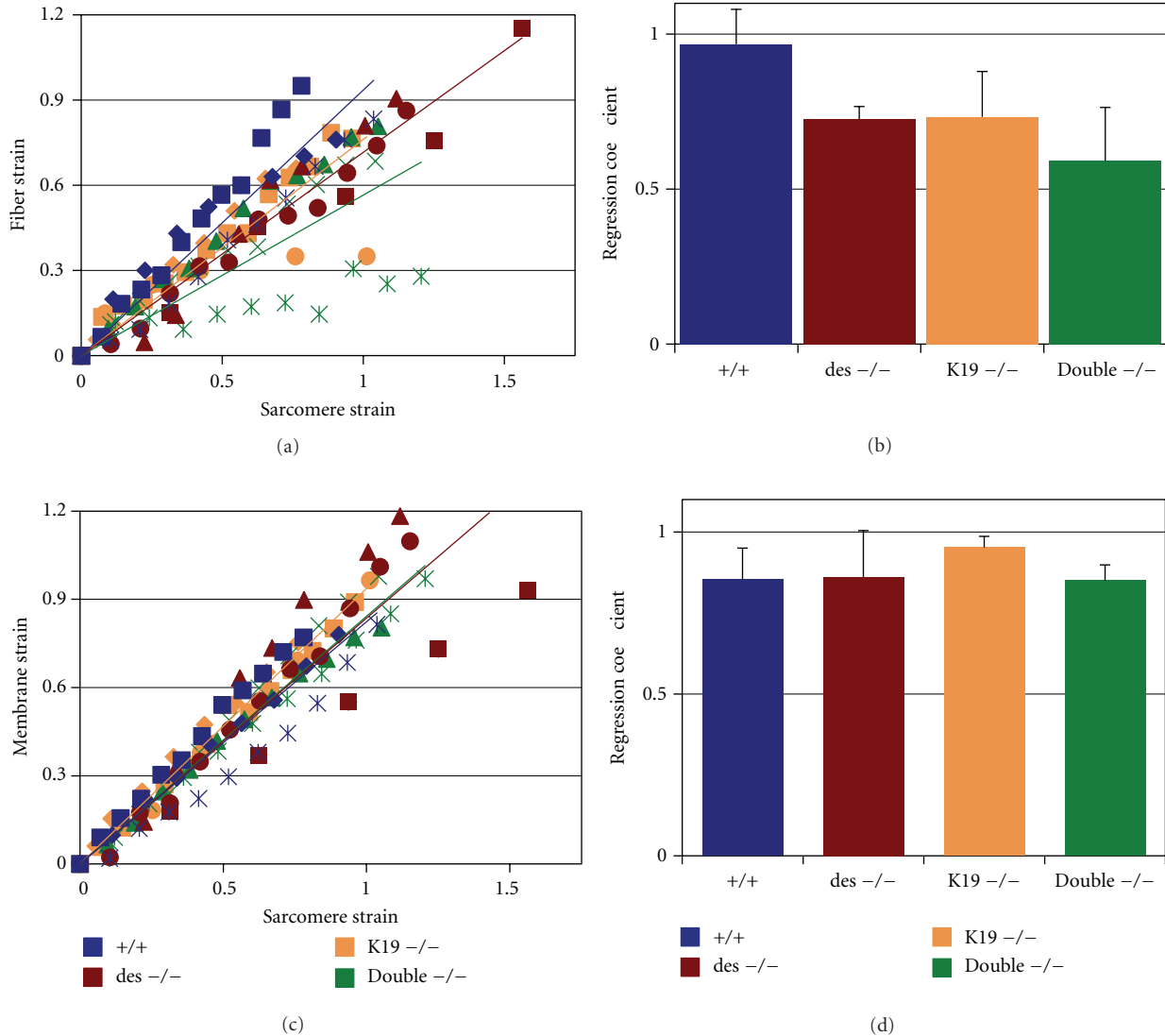


FIGURE 3: Relationships between global fiber strain and local membrane and sarcomere strain. Raw data (a, c) and regression coefficients (b, d) for (a-b) fiber strain-sarcomere strain; (c-d) membrane strain-sarcomere strain for fibers from 10-month-old wild-type (blue), desmin-null (red), K19-null (orange), and double-null (green) animals ($n = 3$ fibers/genotype). Different symbols within a color group represent data from individual experiments. Displayed regression lines in (a) and (c) represent averaged coefficients for individual experiments reported in (b) and (d).

stresses, and radial strains are consistent with those previously reported, suggesting that the murine strain does not influence passive mechanical properties in skeletal muscle. Differences in elastic moduli between wild-type and desmin-null fibers, reported for both LaGrangian and Cauchy stress-strain curves, indicate a role for desmin in both defining inherent load-bearing capabilities within the muscle fiber and regulating changes in fiber geometry that further influence force transmission (Figures 1(a)–1(d), and 2(a)–2(d)). The latter finding is also consistent with significantly decreased coupling between longitudinal and radial strains and reduced changes in volume following loading in desmin-null fibers compared to wild-type (Figures 1(e), 1(f), 2(e), and 2(f), Poisson's ratios).

Given the misalignment of Z-disks observed in single fibers and in whole muscle (Figure 5; [15, 16, 18, 26]), it is likely that a major site of desmin's influence on force transmission is within the myofibrillar lattice. Within this region, desmin enhances the effectiveness in transmission of shear loads and coordinates tensile load-bearing between myofibrils. However, it remains an open question whether desmin also influences force transmission at the sarcolemma. On one hand, this study reports a strong correlation of membrane strain and sarcomere strain (Figures 3(c) and 3(d)). This would suggest limited influence of desmin at the sarcolemma, consistent with the tight coupling between Z-disks and costameric proteins observed in single desmin-null EDL fibers [26], and intact costameres in quadriceps muscle

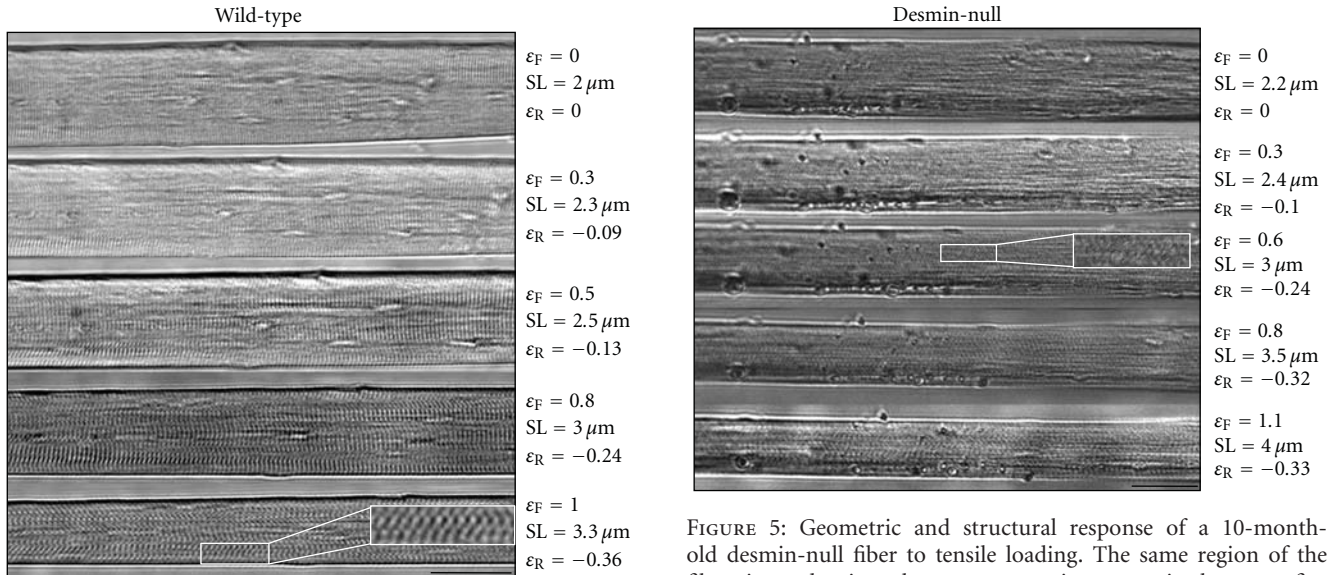


FIGURE 4: Geometric and structural response of a 10-month-old wild-type fiber to tensile loading. The same region of the fiber, imaged using phase-contrast microscopy, is shown at five different deformations. Fiber strains, radial strains, and sarcomere lengths are reported to the right of the fiber for each deformation. The fiber displays well aligned Z-lines (dark vertical stripes), consistently increasing sarcomere strain, and decreasing fiber diameter with increased fiber deformation. A sample region of the fiber that displays particularly well aligned Z-lines that are experiencing some shear, inferred through the slanting of Z-lines, is marked with a white box. The boxed region has been computationally enlarged 2x for clarity. At high strains ($\epsilon_F > 0.8$), artifactual thickening of Z-lines occurs due to shear-induced offsets of Z-lines in deeper regions of the fiber. Bar = 50 μm .

FIGURE 5: Geometric and structural response of a 10-month-old desmin-null fiber to tensile loading. The same region of the fiber, imaged using phase-contrast microscopy, is shown at five different deformations. Fiber strains, radial strains, and sarcomere lengths are reported to the right of the fiber for each deformation. The fiber displays misaligned Z-lines, but consistently increasing sarcomere strain and decreasing fiber diameter with increased fiber deformation. Misalignment is characterized by a striking basketweave pattern where no clear Z-line orientation may be inferred. A sample region of the fiber that displays this pattern is marked with a white box, and may be compared to the well aligned region shown in Figure 4. The boxed region has been computationally enlarged 2x for clarity. Desmin-null fibers display dramatically more debris on their external membrane compared to wild-type fibers. This observation is consistent with the increased “stickiness” experienced during fiber dissection, possibly resulting from differences in extracellular matrix composition. Bar = 50 μm .

from desmin-null mice [15]. On the other hand, significant costamere disruption is seen in tibialis anterior and EDL muscle [15], suggesting that desmin does, in fact, influence costamere, and thus membrane, coupling to the underlying myofibrillar lattice.

Examination of K19-null fibers from three-month-old FVB mice indicated, for the first time, a role for keratins in regulating the passive mechanical properties of muscle. Similar to desmin-null fibers, K19-null fibers are more compliant than wild-type fibers, based on LaGrangian and Cauchy stress-strain curves (Figures 1(a)–1(d), and 2(a)–2(d)). In addition, K19-null fibers from younger mice exhibit poor coupling between longitudinal and radial strain (Figures 2(e) and 2(f), Poisson’s ratios). Interestingly, coupling between longitudinal and radial strain, and thus perhaps the efficiency of lateral force transmission, decreases for all genotypes with aging (Figures 1(e), 1(f), 2(e), and 2(f), Poisson’s ratios). This may be a result of myofibril loss and a consequent increase in intramyofibrillar space [28, 29]. In contrast to desmin-null fibers, though, coupling between longitudinal and radial strain was not significantly decreased in 10-month-old K19-null fibers compared to wild-type fibers (Figures 1(e) and 1(f)), and Z-disks appeared to

remain well aligned, suggesting different mechanisms by which K19 and desmin influence passive biomechanical properties. Taken together, these results raise the possibility that genotypic differences in longitudinal and radial coupling may in part be a result of differences in Z-disk connectivity, both longitudinally and laterally [16, 18, 22, 26].

Also unlike desmin-null fibers, K19-null fibers reveal a poor correlation between fiber strain and sarcomere strain (Figures 3(a), 3(b), 5, and 6). The reason for this lack of correlation remains unclear. Based on disrupted costameres and the dramatic accumulation of mitochondria in some subsarcolemmal regions of K19-null muscle [22], decoupling between the membrane and myofibrillar response to deformation was predicted; however, coupling between the plasma membrane and the contractile apparatus does not appear to be dramatically disrupted, at least over a length scale of 100–200 μm (Figures 3(c) and 3(d)). There are at least two reasonable explanations for this paradox, which are also applicable to understanding desmin-mediated connectivity at the costameres. First, when disrupted costameres have been observed in whole muscle sections [15, 22], there appear to be at least a few costameres in a given fiber that are intact. This limited connectivity may be sufficient to

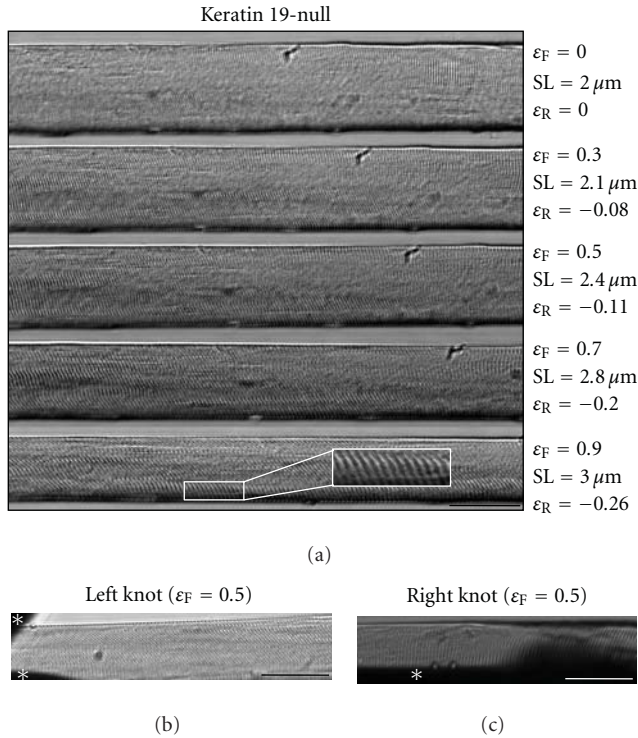


FIGURE 6: Geometric and structural response of a 10-month-old K19-null fiber to tensile loading. (a) The same region of the fiber, imaged using phase-contrast microscopy, is shown at five different deformations. Fiber strains, radial strains, and sarcomere lengths are reported to the right of the fiber for each deformation. The fiber displays aligned Z-lines, but discontinuity between fiber deformation and sarcomere strain. This fiber also displays considerable shear, as seen by the slanting of Z-lines (dark lines). A sample region of the fiber that displays particularly well aligned Z-lines that are experiencing some shear is marked with a white box. The boxed region has been computationally enlarged 2x for clarity. There is no slippage or damage of the fiber at the (b) left edge or (c) right edge, imaged in the vicinity of the knot and pins (starred black regions in the periphery of the image) at a moderate fiber strain of 0.5. This may be concluded from the gradual reduction in of the slant of Z-disks away from the knot, which is located to the left in (b) and to the right in (c). Bar = $50 \mu\text{m}$.

tether the membrane to the underlying cytoskeleton, though not necessarily strongly or effectively. The fraction of intact costameres is likely to be even higher in successfully teased (i.e., more robust) single fibers from IF-null muscles (this study, [26]), further enhancing apparent connectivity. The second explanation arises from the fact that multiple structural proteins, including other intermediate filaments such as K8, localize to costameres and thus likely contribute to the mechanical properties of the connection between individual costameres and underlying Z-disks (cf. [30, 31]). In this case, costameres may still be weakly coupled to myofibrils via remaining or compensatory structural proteins. Examination of more subtle differences in connectivity at the scale of individual or a few sarcomeres under conditions of radial tensile loading (e.g., [30]) may reveal differences in

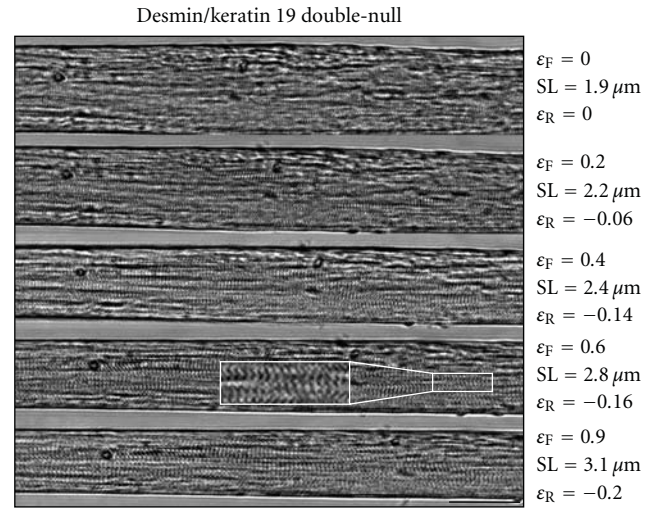


FIGURE 7: Geometric and structural response of a 10-month-old double-null fiber to tensile loading. The same region of the fiber, imaged using phase-contrast microscopy, is shown at five different deformations. Fiber strains, radial strains, and sarcomere lengths are reported to the right of the fiber for each deformation. Fiber displays both misaligned Z-lines as well as discontinuity between fiber, sarcomere, and radial strains. A sample region of the fiber that displays the basketweave pattern characteristic of misalignment is marked with a white box. The boxed region has been also computationally enlarged 2x for clarity. As for desmin-null fibers, double-null fibers display dramatically more debris on their external membrane compared to wild-type fibers. Bar = $50 \mu\text{m}$.

local compliance that could then underlie differences in the efficiency of lateral force transmission.

Additional insight into the different roles of desmin and keratin emerged from the examination of desmin/K19 double-null fibers in 10-month-old mice. The similar fiber compliance of double-null fibers and desmin-null fibers, but increased compliance compared to K19-null fibers (Figures 1(a)–1(d)) parallels decreased myofibrillar organization within desmin-null and double-null fibers compared to K19-null fibers (Figures 5–7). Our findings in single myofibers are also consistent with biomechanical results in whole muscle, where deficits in specific tension are similar and more severe in desmin-null and double-null tibialis anterior muscle than in K19-null muscle [18]. These data support the hypothesis that myofibrils must be engaged and coordinated to maximally support mechanical loads. It will be interesting to continue the characterization of double-null fibers in younger mice, where phenotypic differences between desmin-null and K19-null fibers were not significant, to address developmental differences in IF function.

Collectively, integration of mechanical and structural data from this work and previous studies support a model in which membrane-myofibril connectivity, guided by two sets of IFs, composed of keratins and of desmin, dictates the radial transmission of tensile and shear loads into and out of the cell. In an outside-in model, this connectivity would enable the recruitment of longitudinal load-bearing

structures, predominantly coordinated by desmin, within the myofibrillar lattice. Conversely, in an inside-out model, connectivity between myofibrils and the membrane would enable the reliable transmission of myofibrillar forces, again coordinated by desmin, to the extracellular matrix.

Finally, this work illustrates the importance of studying single muscle fibers to the interpretation of biomechanical data from knockout models. Increased passive compliance measured in desmin-null fibers (Figures 1 and 2; [26]) is contrary to the increased passive stiffness reported in desmin-null muscles [17, 32]. These differences are most likely due to secondary remodeling of extracellular matrix, though this remains to be tested directly. Given the increasing relevance of extracellular matrix remodeling to our understanding of myopathies and muscular dystrophies [23–25], comparative studies between single fibers and whole muscle or fiber bundles may reveal interesting and important details regarding roles of intermediate filaments in initiating physiologically relevant extracellular signaling pathways.

5. Conclusions

We have characterized the structural and mechanical response of single fibers from wild-type, desmin-null, K19-null, and desmin/K19 double-null mice to passive tensile loading. Through this work, we provide the first direct evidence, in an experimental system free from influences of the extracellular matrix, that desmin and keratin 19 differentially influence passive force transmission in single muscle fibers. Our work has strong implications for our understanding of the role of intermediate filaments on structure-function relationships in skeletal muscle. In addition, our work is important for interpreting structural and biomechanical changes resulting from desminopathies and other myopathies linked to intermediate filaments and their associated proteins [33–37].

Acknowledgments

The authors acknowledge contributions to device modification by Jiemin Wu. This research was supported by grant 1R01AR055928 to RJB and SBS, and K01AR053235 and 1R01AR059179 to RML, from NIAMS/NIH, and grant 69236 to RJB from the Muscular Dystrophy Association.

References

- [1] R. J. Monti, R. R. Roy, J. A. Hodgson, and V. R. Edgerton, "Transmission of forces within mammalian skeletal muscles," *Journal of Biomechanics*, vol. 32, no. 4, pp. 371–380, 1999.
- [2] J. G. Tidball, "Force transmission across muscle cell membranes," *Journal of Biomechanics*, vol. 24, supplement 1, pp. 43–52, 1991.
- [3] R. J. Bloch and H. Gonzalez-Serratos, "Lateral force transmission across costameres in skeletal muscle," *Exercise and Sport Sciences Reviews*, vol. 31, no. 2, pp. 73–78, 2003.
- [4] S. F. Street, "Lateral transmission of tension in frog myofibers: a myofibrillar network and transverse cytoskeletal connections are possible transmitters," *Journal of Cellular Physiology*, vol. 114, no. 3, pp. 346–364, 1983.
- [5] R. J. Bloch, Y. Capetanaki, A. O'Neill et al., "Costameres: repeating structures at the sarcolemma of skeletal muscle," *Clinical Orthopaedics and Related Research*, no. 403, pp. S203–S210, 2002.
- [6] Y. Capetanaki, R. J. Bloch, A. Kouloumenta, M. Mavroidis, and S. Psarras, "Muscle intermediate filaments and their links to membranes and membranous organelles," *Experimental Cell Research*, vol. 313, no. 10, pp. 2063–2076, 2007.
- [7] D. Paulin and Z. Li, "Desmin: a major intermediate filament protein essential for the structural integrity and function of muscle," *Experimental Cell Research*, vol. 301, no. 1, pp. 1–7, 2004.
- [8] B. L. Granger and E. Lazarides, "Desmin and vimentin coexist at the periphery of the myofibril Z disc," *Cell*, vol. 18, no. 4, pp. 1053–1063, 1979.
- [9] F. L. Richardson, M. H. Stromer, T. W. Huiatt, and R. M. Robson, "Immunoelectron and immunofluorescence localization of desmin in mature avian muscles," *European Journal of Cell Biology*, vol. 26, no. 1, pp. 91–101, 1981.
- [10] K. T. Tokuyasu, A. H. Dutton, and S. J. Singer, "Immunoelectron microscopic studies of desmin (skeletin) localization and intermediate filament organization in chicken skeletal muscle," *Journal of Cell Biology*, vol. 96, no. 6, pp. 1727–1735, 1983.
- [11] K. Wang and R. Ramirez-Mitchell, "A network of transverse and longitudinal intermediate filaments is associated with sarcomeres of adult vertebrate skeletal muscle," *Journal of Cell Biology*, vol. 96, no. 2, pp. 562–570, 1983.
- [12] J. V. Pardo, J. D. Siliciano, and S. W. Craig, "Vinculin is a component of an extensive network of myofibril-sarcolemma attachment regions in cardiac muscle fibers," *Journal of Cell Biology*, vol. 97, no. 4, pp. 1081–1088, 1983.
- [13] J. V. Pardo, J. D. Siliciano, and S. W. Craig, "A vinculin-containing cortical lattice in skeletal muscle: transverse lattice elements ("costameres") mark sites of attachment between myofibrils and sarcolemma," *Proceedings of the National Academy of Sciences of the United States of America*, vol. 80, no. 4, pp. 1008–1012, 1983.
- [14] D. J. Milner, M. Mavroidis, N. Weisleder, and Y. Capetanaki, "Desmin cytoskeleton linked to muscle mitochondrial distribution and respiratory function," *Journal of Cell Biology*, vol. 150, no. 6, pp. 1283–1297, 2000.
- [15] A. O'Neill, M. W. Williams, W. G. Resneck, D. J. Milner, Y. Capetanaki, and R. J. Bloch, "Sarcolemmal organization in skeletal muscle lacking desmin: evidence for cytokeratins associated with the membrane skeleton at costameres," *Molecular Biology of the Cell*, vol. 13, no. 7, pp. 2347–2359, 2002.
- [16] S. B. Shah, F. C. Su, K. Jordan et al., "Evidence for increased myofibrillar mobility in desmin-null mouse skeletal muscle," *Journal of Experimental Biology*, vol. 205, part 3, pp. 321–325, 2002.
- [17] M. Sam, S. Shah, J. Fridén, D. J. Milner, Y. Capetanaki, and R. L. Lieber, "Desmin knockout muscles generate lower stress and are less vulnerable to injury compared with wild-type muscles," *American Journal of Physiology—Cell Physiology*, vol. 279, no. 4, pp. C1116–C1122, 2000.
- [18] R. M. Lovering, A. O'Neill, J. M. Muriel, B. L. Prosser, J. Strong, and R. J. Bloch, "Physiology, structure, and susceptibility to injury of skeletal muscle in mice lacking keratin 19-based and desmin-based intermediate filaments," *American Journal of Physiology—Cell Physiology*, vol. 300, no. 4, pp. C803–C813, 2011.

- [19] A. M. Boriek, Y. Capetanaki, W. Hwang et al., “Desmin integrates the three-dimensional mechanical properties of muscles,” *American Journal of Physiology—Cell Physiology*, vol. 280, no. 1, pp. C46–C52, 2001.
- [20] M. R. Stone, A. O’Neill, D. Catino, and R. J. Bloch, “Specific interaction of the actin-binding domain of dystrophin with intermediate filaments containing keratin 19,” *Molecular Biology of the Cell*, vol. 16, no. 9, pp. 4280–4293, 2005.
- [21] J. A. Ursitti, P. C. Lee, W. G. Resneck et al., “Cloning and characterization of cytokeratins 8 and 19 in adult rat striated muscle: interaction with the dystrophin glycoprotein complex,” *Journal of Biological Chemistry*, vol. 279, no. 40, pp. 41830–41838, 2004.
- [22] M. R. Stone, A. O’Neill, R. M. Lovering et al., “Absence of keratin 19 in mice causes skeletal myopathy with mitochondrial and sarcolemmal reorganization,” *Journal of Cell Science*, vol. 120, part 22, pp. 3999–4008, 2007.
- [23] J. M. Boer, E. J. de Meijer, E. M. Mank, G. B. van Ommen, and J. T. den Dunnen, “Expression profiling in stably regenerating skeletal muscle of dystrophin-deficient mdx mice,” *Neuromuscular Disorders*, vol. 12, supplement 1, pp. S118–S124, 2002.
- [24] M. Marotta, C. Ruiz-Roig, Y. Sarria et al., “Muscle genome-wide expression profiling during disease evolution in mdx mice,” *Physiological Genomics*, vol. 37, no. 2, pp. 119–132, 2009.
- [25] G. A. Meyer and R. L. Lieber, “Elucidation of extracellular matrix mechanics from muscle fibers and fiber bundles,” *Journal of Biomechanics*, vol. 44, no. 4, pp. 771–773, 2011.
- [26] S. B. Shah, J. Davis, N. Weisleder et al., “Structural and functional roles of desmin in mouse skeletal muscle during passive deformation,” *Biophysical Journal*, vol. 86, no. 5, pp. 2993–3008, 2004.
- [27] S. B. Shah and R. L. Lieber, “Simultaneous imaging and functional assessment of cytoskeletal protein connections in passively loaded single muscle cells,” *Journal of Histochemistry and Cytochemistry*, vol. 51, no. 1, pp. 19–29, 2003.
- [28] S. Bensamoun, L. Stevens, M. J. Fleury, G. Bellon, F. Goubel, and M. C. H. B. Tho, “Macroscopic-microscopic characterization of the passive mechanical properties in rat soleus muscle,” *Journal of Biomechanics*, vol. 39, no. 3, pp. 568–578, 2006.
- [29] T. Ansved and L. Edstrom, “Effects of age on fibre structure, ultrastructure and expression of desmin and spectrin in fast- and slow-twitch rat muscles,” *Journal of Anatomy*, vol. 174, pp. 61–79, 1991.
- [30] K. P. García-Pelagio, R. J. Bloch, A. Ortega, and H. González-Serratos, “Biomechanics of the sarcolemma and costameres in single skeletal muscle fibers from normal and dystrophin-null mice,” *Journal of Muscle Research and Cell Motility*, vol. 31, no. 5-6, pp. 323–336, 2011.
- [31] G. A. Meyer, B. Kiss, S. R. Ward, D. L. Morgan, M. S. Z. Kellermayer, and R. L. Lieber, “Theoretical predictions of the effects of force transmission by desmin on intersarcomere dynamics,” *Biophysical Journal*, vol. 98, no. 2, pp. 258–266, 2010.
- [32] J. Anderson, Z. Li, and F. Goubel, “Passive stiffness is increased in soleus muscle of desmin knockout mouse,” *Muscle and Nerve*, vol. 24, no. 8, pp. 1090–1092, 2001.
- [33] B. L. Banwell, “Intermediate filament-related myopathies,” *Pediatric Neurology*, vol. 24, no. 4, pp. 257–263, 2001.
- [34] K. Nowak, K. McCullagh, E. Poon, and K. E. Davies, “Muscular dystrophies related to the cytoskeleton/nuclear envelope,” *Novartis Foundation Symposium*, vol. 264, pp. 98–111, 2005.
- [35] D. Paulin, A. Huet, L. Khanamyrian, and Z. Xue, “Desminopathies in muscle disease,” *Journal of Pathology*, vol. 204, no. 4, pp. 418–427, 2004.
- [36] D. J. Blake and E. Martin-Rendon, “Intermediate filaments and the function of the dystrophin-protein complex,” *Trends in Cardiovascular Medicine*, vol. 12, no. 5, pp. 224–228, 2002.
- [37] H. H. Goebel and I. A. P. Warlo, “Progress in desmin-related myopathies,” *Journal of Child Neurology*, vol. 15, no. 9, pp. 565–572, 2000.

Review Article

Physiology and Pathophysiology of CLC-1: Mechanisms of a Chloride Channel Disease, Myotonia

Chih-Yung Tang¹ and Tsung-Yu Chen²

¹Department of Physiology, College of Medicine, National Taiwan University, Taipei 10051, Taiwan

²Center for Neuroscience and Department of Neurology, University of California, Davis, CA 95618, USA

Correspondence should be addressed to Chih-Yung Tang, tang@ntu.edu.tw

Received 26 April 2011; Revised 18 July 2011; Accepted 10 September 2011

Academic Editor: Lars Larsson

Copyright © 2011 C.-Y. Tang and T.-Y. Chen. This is an open access article distributed under the Creative Commons Attribution License, which permits unrestricted use, distribution, and reproduction in any medium, provided the original work is properly cited.

The CLC-1 chloride channel, a member of the CLC-channel/transporter family, plays important roles for the physiological functions of skeletal muscles. The opening of this chloride channel is voltage dependent and is also regulated by protons and chloride ions. Mutations of the gene encoding CLC-1 result in a genetic disease, myotonia congenita, which can be inherited as an autosomal dominant (Thomsen type) or an autosomal recessive (Becker type) pattern. These mutations are scattered throughout the entire protein sequence, and no clear relationship exists between the inheritance pattern of the mutation and the location of the mutation in the channel protein. The inheritance pattern of some but not all myotonia mutants can be explained by a working hypothesis that these mutations may exert a “dominant negative” effect on the gating function of the channel. However, other mutations may be due to different pathophysiological mechanisms, such as the defect of protein trafficking to membranes. Thus, the underlying mechanisms of myotonia are likely to be quite diverse, and elucidating the pathophysiology of myotonia mutations will require the understanding of multiple molecular/cellular mechanisms of CLC-1 channels in skeletal muscles, including molecular operation, protein synthesis, and membrane trafficking mechanisms.

1. Introduction

Chloride (Cl^-) channels are membrane proteins that consist of Cl^- -permeation pores. Different types of human cells express Cl^- channels in the cell membrane for various physiological purposes. In the last several decades, ion channels that conduct cations, such as sodium (Na^+), potassium (K^+) or calcium (Ca^{2+}) channels, have been studied more extensively than anion channels. Nonetheless, Cl^- channels are as abundant as cation channels, and they also participate in many important physiological tasks, including the maintenance of normal cellular excitability, the control of neurotransmitter release, and the transport of ions across epithelial cells, to name a few. The aim of this paper is to provide an up-to-date overview of the mechanism and the consequence of the disruption of Cl^- channel function. We will focus on the physiology and pathophysiology of a Cl^- channel critical for the function of skeletal muscles, the CLC-1 Cl^- channel.

Cl^- is the most abundant anion in most organisms. In adult mammalian cells, the extracellular concentration of Cl^- is significantly higher than its intracellular counterpart, resulting in a negative Cl^- equilibrium potential (E_{Cl}) that is exquisitely determined by an intracellular Cl^- concentration. Two secondary active transport systems contribute the most to the regulation of the cytoplasmic Cl^- level. The Na^+ - K^+ - Cl^- cotransporter (NKCC) normally accumulates Cl^- in the cell [1], whereas the K^+ - Cl^- co-transporter (KCC) usually transports Cl^- out of the cell [2]. Most epithelial cells express predominantly NKCC and display an E_{Cl} positive to the resting potential [3, 4]. In contrast, the majority of mature neurons have an enhanced expression of KCC, and therefore manifest a quite negative E_{Cl} —sometimes even more negative than the resting potential [3, 5]. In skeletal muscle, despite the presence of both NKCC and KCC, the contribution of secondary active transporters to E_{Cl} is rather small, mainly due to the presence of an extraordinarily high Cl^- permeability that is virtually impossible to be counteracted

by active transporters [6–9]. The E_{Cl} in skeletal muscle is thus mainly set by passive electrochemical equilibrium of Cl^- according to the resting membrane potential which is primarily determined by K^+ equilibrium potential (E_K). Recent evidence, however, supports the idea that the secondary active transporter NKCC may modulate the membrane potential of skeletal muscle via its Cl^- import function [10–12]. Indeed, the muscle resting potential is never the same as the value of E_K while the E_{Cl} has been shown to be slightly more positive than the resting membrane potential [13]. Furthermore, the value of the intracellular Cl^- activity has been shown to be slightly higher than would be expected for a passive Cl^- distribution [13]. These observations underscore the contribution of the chloride conductance in determining the resting membrane potential of skeletal muscles.

2. Physiological Roles of CLC-1 Channels in Skeletal Muscles

Because of a large membrane Cl^- conductance, up to 80% of the resting sarcolemmal conductance [14–16], a relatively negative E_{Cl} explains the physiological role of Cl^- channels in the cell membrane of skeletal muscles (sarcolemma). For example, activation of Cl^- channels is essential for ensuring the electrical stability of skeletal muscle by resetting its membrane excitability to the resting state after firing an action potential. Furthermore, a significant Cl^- conductance is also located in the transverse-tubule system [15, 17–19], indicating that the presence of an effective Cl^- homeostasis system is crucial for the generation and propagation of action potential in both the sarcolemmal and the transverse-tubule system. Finally, emerging evidence suggests that disruptions of the balance of ion channel functions in sarcolemma may contribute to skeletal muscle fatigue [19–21]. During intensive firing of muscle action potentials, K^+ ions tend to accumulate in the extracellular space up to 10 mM as the extracellular volume of skeletal muscles is limited. The increase of extracellular K^+ concentration results in depolarization of membrane potential, and, consequently, a partial inactivation of voltage-gated Na^+ channels. If the Na^+ channels that remain active fail to generate a sufficient Na^+ inward current to overcome the shunting currents mediated by the resting sarcolemmal Cl^- conductance, the firing of action potential is not possible, thereby leading to muscle fatigue.

Although various types of Cl^- channels are expressed in skeletal muscles, the most abundant Cl^- channel in the sarcolemma is CLC-1 [4, 22], which is a member of the CLC-channel/transporter family. The mammalian CLC family consists of nine members: CLC-1, CLC-2, CLC-3, CLC-4, CLC-5, CLC-6, CLC-7, CLC-Ka, and CLC-Kb [22–24]. Among these members, CLC-1, CLC-2, CLC-Ka, and CLC-Kb are Cl^- channels, predominantly residing in the plasma membrane. The rest of the CLC members (CLC-3 to CLC-7) are thought to be transporters, mostly located in intracellular organelles. Like bacterial CLC proteins [25], these mammalian CLC transporters are thought to mediate

the counter transport of H^+ and Cl^- ; that is, they are Cl^-/H^+ antiporters [26, 27].

Among the four plasma membrane CLC-channels, CLC-Ka and CLC-Kb channels are involved in transepithelial transport in the kidney and the inner ear [4, 28]. CLC-2 channels can be activated by hyperpolarization, cell swelling, and extracellular acidification [29, 30]. Northern analysis indicates that brain, kidney, and intestine express relatively high levels of CLC-2 channels, although these channels are broadly expressed in various tissues as well [31]. In contrast, CLC-1 channels are most abundantly expressed in the skeletal muscle [32]. A very low level of CLC-1 expression, however, has been reported in kidney, heart, smooth muscle, and, more recently, glial cells [32, 33]. Since the CLC-1 channel is the major sarcolemmal Cl^- conductance, mutations of the gene encoding this Cl^- channel lead to a significant muscle hyperexcitability in humans, mice, and other animals [34–38], a situation known as “myotonia” [32, 39]. Myotonia is a muscle disease due to hyper-excitability of skeletal muscles. Therefore, this disease can be caused either by the gain of function of Na^+ channels or a loss of function of Cl^- channels in the sarcolemma of skeletal muscles. In the following sections we will focus on the defect of CLC-1, starting with the CLC-1’s molecular properties.

3. Molecular Biophysics of CLC-1 Channels

CLC-1 is a voltage-gated channel, and the open probability of CLC-1 channels increases with membrane depolarization. The functional study of CLC-1 at the single-channel level is challenging due to the small single-channel conductance of this channel. Therefore, many functional properties of CLC-1 are inferred from those found in its fish homologue, the *Torpedo* CLC-0 Cl^- channel [23]. One unique functional feature in CLC-channels is that the channel opens to two current levels separated by equidistance in the single-channel recording trace (Figure 1). This feature has been identified as the consequence of a “double-barreled” channel opening, first found in CLC-0 in early 1980s [40, 41]. Later single-channel recordings confirmed that the opening of CLC-1 channels also fluctuates between three different conductance levels (Figure 1(a)), corresponding to the three functional states: two pores closed; one open and one closed; and, finally, both pores open [42]. These functional recordings of CLC-0 and CLC-1 channels foretold the recent structural findings from bacterial CLC proteins in which two identical Cl^- -transport pathways were found in one CLC functional unit [43, 44].

The opening and closure of the two pores in CLC-0 and CLC-1 channels are controlled by two distinct gating mechanisms [23]. One of these gating mechanisms controls the opening and closure of two pores simultaneously, and is therefore called “common gate”. In addition, each pore is also controlled by a “fast gate” that operates independently from the partner fast-gate. Thus, the activation of the Cl^- conducting pathway of CLC-1 channels requires the opening of both the common gate and the fast gate. The open-close transition of the fast gate operates at a time scale of

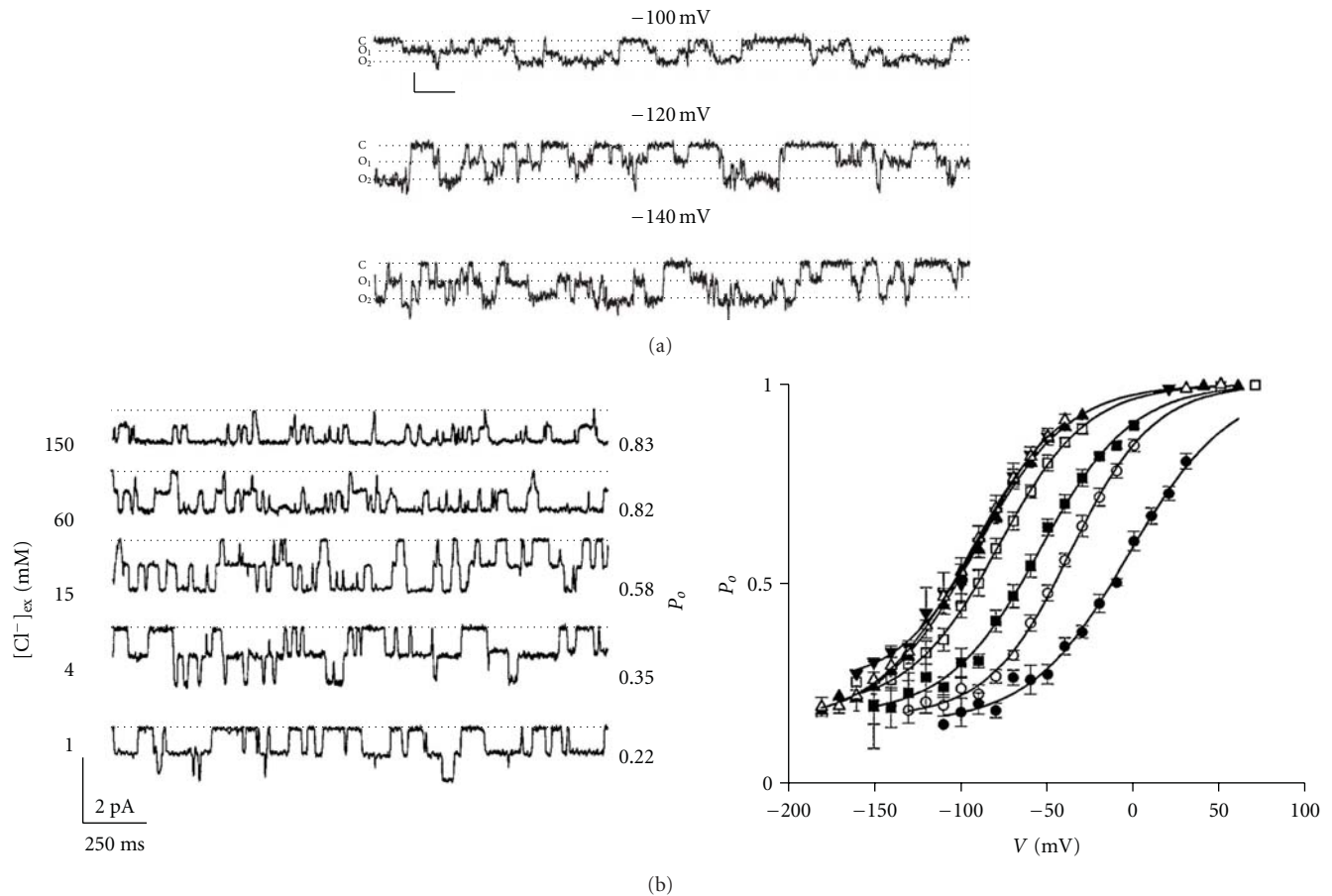


FIGURE 1: Molecular functions of CLC-channels. (a) Single-channel recordings of CLC-1 showing the “double-barreled” behavior. Dotted lines depict the three current levels: C: closed state, O1: one protopore open, and O2: both protopores open. Horizontal and vertical scale bars represent 200 ms and 0.2 pA, respectively. Notice that the three current levels are separated in equi-distance. Figure, taken from Saviane et al. [42] (© Rockefeller University Press, 1999). (b) Effects of extracellular Cl⁻ on the fast-gate open probability of the *Torpedo* CLC-0 Cl⁻ channel. Left panel shows single-channel recordings of CLC-0 at different extracellular Cl⁻ concentrations indicated on the left. The calculated open probabilities of the fast gate in each Cl⁻ concentration are shown on the right. Membrane potentials in all recordings are -60 mV. Right panel shows a summarized result for the Cl⁻ effect on the fast-gate P_o -V curve. The extracellular Cl⁻ concentrations are 300 mM and those indicated in the left panel. As the extracellular Cl⁻ concentration is reduced (from 300 mM to 1 mM), the fast-gate P_o -V curve is shifted to the more depolarized membrane potential. A similar Cl⁻ effect on the fast-gate P_o -V curve has been observed in CLC-1. Figures, taken from Chen and Miller [45] (© Rockefeller University Press, 1996).

milliseconds at negative membrane potentials. At the peak of the action potential, the opening kinetics of CLC-1 can be in the submillisecond range. Thus, the opening of CLC-1's fast-gate can counteract the depolarization generated by the opening of Na⁺ channels during an action potential. This gating mechanism is thus important for CLC-1 channels to control the action potential in skeletal muscles. Mutations that reverse the voltage dependence of CLC-1 channels result in certain forms of myotonia (see below) because these mutant channels are unable to open after membrane depolarization. In addition to the control by membrane potentials, the fast-gating is also regulated by Cl⁻ and H⁺ [46, 47]. The regulation of CLC-1 and CLC-0 channels by Cl⁻ and H⁺ is thought to bear an evolutionary relationship to the Cl⁻/H⁺ counter transport function of their CLC transporter counterparts [48], although the exact link

between the channel-gating mechanism and the Cl⁻/H⁺-antiporter mechanism is not known. Interestingly, a recent crystallographic study of a prokaryotic CLC protein provided a potential mechanism for the exchange stoichiometry of 2 Cl⁻ for 1 H⁺ [49]. The voltage dependence of the fast gating is similar to that found in voltage-gated cation channels; namely, the open probability (P_o) is higher at more depolarized membrane potentials [40, 41, 45, 50, 51]. However, unlike voltage-gated cation channels with the “S4” transmembrane segment serving as the “voltage sensor” [52], there is no such structure in CLC-0 and CLC-1 channels. The voltage-dependent activation of the fast gate of CLC-0 and CLC-1 is likely to arise from the coupling of Cl⁻ transport with the gating process [45, 46, 53]. This gating-permeation coupling mechanism was first proposed by Pusch and his colleague [53], who demonstrated that the P_o -V

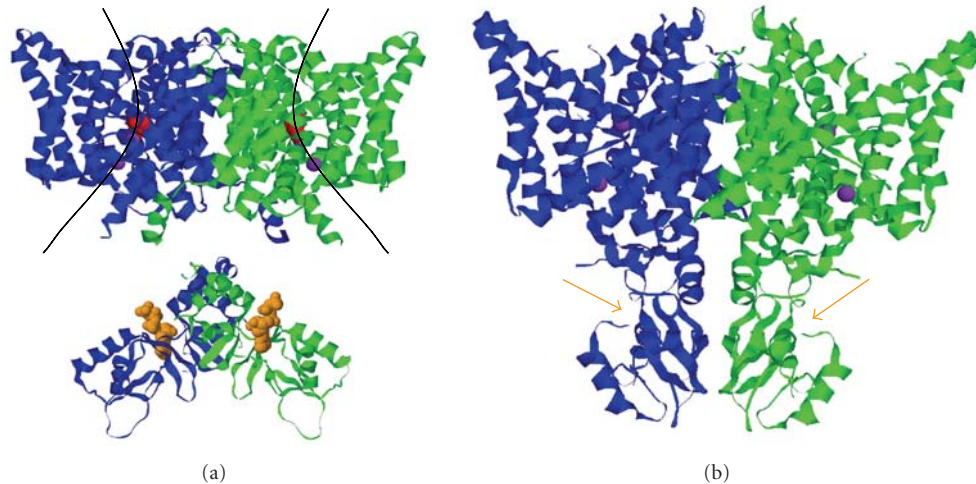


FIGURE 2: Molecular architecture of mammalian CLC molecules. (a) The composite structure of a generic CLC molecule consists of two parts: the membrane region, represented by the crystal structure of *E. coli* CLC molecule (CLC-ec1) (top), and the cytoplasmic domain represented by the crystal structure of the cytoplasmic domain of CLC-5. The two subunits are colored in green and blue, respectively. The two curve lines in the membrane portion roughly depict the transport pathways of Cl^- ions (purple spheres). Red residues are Glu 148 of CLC-ec1, which correspond to Glu 232 of CLC-1. The negatively charged side chain of this residue obstructs the ion-transport pathway, and therefore is hypothesized to be the fast gate of CLC-channels. The two space-filled molecules in orange color in the cytoplasmic domains (one in each subunit) are ATP molecules seen in the crystal structure of the CLC-5's cytoplasmic domain. Binding of ATP to CLC-1 inhibits the common gating of CLC-1. (b) X-ray crystal structure of CmCLC, a CLC protein from a thermophilic red alga *Cyanidioschyzon merolae*. Orange arrows point to the ATP-binding sites.

curve of the fast gating of CLC-0 channels was shifted toward a more depolarized membrane potential by reducing the extracellular Cl^- concentration. At a constant voltage, therefore, reducing the extracellular Cl^- concentration inhibits the opening of the fast gate. More detailed experiments at the single-channel level (Figure 1(b)) further showed that extracellular Cl^- increases the open probability of the fast-gate by increasing the opening rate of the fast gate [45]. Later experiments also revealed the same dependent fast gating mechanism for CLC-1 channels [46]. To explain this gating effect, investigators have proposed a model in which the binding of Cl^- to the channel pore opens the fast gate and the movement of Cl^- across membrane electric field constitutes the fundamental mechanism for the observed voltage dependence [23]. This hypothesis was formulated before the crystal structure of CLC molecules became available. Later structural information from crystallographic studies of bacterial CLC proteins revealed that the transport pathway of CLC molecules appear to be obstructed by the negatively charged side chain of a glutamate residue, and Cl^- in the pore may compete with this glutamate side chain [43, 44].

4. Structural/Functional Relationship of CLC-1 Channels

The gene of the human CLC-1 channel encodes a transmembrane protein consisting of 991 amino acids (AA). The protein can be roughly divided into two parts, the amino (N)-terminal transmembrane portion (up to ~ 590 AA.) and the carboxyl (C)-terminal cytoplasmic portion (Figure 2).

Although the molecular structure of CLC-1 has not been solved, recent breakthroughs in obtaining the crystal structure of bacteria CLC proteins [43, 44] and the crystal structures of the C-terminal cytoplasmic domain of several vertebrate CLC molecules, such as CLC-0 [54], CLC-5 [55] and CLC-K [56], have provided insightful structural information for other homologous CLC molecules. The CLC protein from *E. coli* (CLC-ec1) consists of only ~460 AA, which form a structure corresponding to the N-terminal transmembrane portion of CLC-1 [44] (Figure 2(a), upper panel). This part of the channel protein is composed of eighteen α -helices (helices 1 to 18, or helices A to R), seventeen of which being membrane associated (helix A is not inserted into the membrane). Most of these helices are not perpendicular to the membrane, but severely tilted. Moreover, many of these helices do not span the entire width of the lipid membrane (Figure 2(a), upper panel). The most interesting feature of the transmembrane portion of CLC molecules is that a glutamate residue located at the beginning of helix N (helix 14) protrudes its negatively charged side chain into the Cl^- -permeation pathway (Figure 2(a), red residues in the upper panel). With the glutamate side chain blocking the Cl^- -permeation pore, Cl^- permeation is not possible [44]. Mutation of this glutamate residue to a neutral amino acid in CLC-channels results in channels that appear to have a fully open pore. The side chain of this glutamate residue is therefore thought to be the gate that controls each individual protopore. It is also thought that the competition of Cl^- with this glutamate side-chain may underlie the aforementioned gating permeation mechanism thoroughly characterized for CLC-0 and CLC-1 channels [23, 57–59].

The C-terminal half of CLC-1 (from ~AA 591 to the C-terminus) is believed to be entirely located in the cytoplasmic side of the membrane (Figure 2(a), lower panel). This structure of the C-terminal cytoplasmic domain was initially solved in several mammalian CLC molecules independent of the transmembrane domain. A most recent crystallographic study revealed the structure of CmCLC, a CLC protein from thermophilic alga that consists of a transmembrane region and a C-terminal cytoplasmic domain [49]. The transmembrane and cytoplasmic domains of the CmCLC structure are similar to those solved previously in other CLC proteins, including the extensive helical architecture in the transmembrane region and the characteristic cystathionine β -synthase (CBS) domains in the cytoplasmic region (Figure 2(b)). Thus, it is very likely that the C-terminal cytoplasmic domain of CLC-1, like those in other mammalian CLC molecules, also contains two tandem CBS domains that are folded into a potential ATP-binding site. It has been shown that cytoplasmic ATP can inhibit the current of CLC-1 channels in acidic pH conditions [60–62], and the crystal structure of the C-terminal region of the CLC-5 protein revealed an ATP molecule bound to the predicted ATP-binding site formed by the two tandem CBS domains [55] (Figure 2(a), lower panel). The inhibition of CLC-1 channels by ATP is therefore thought to be due to a direct ATP binding to the C-terminus of protonated CLC-1 channels. Experimental evidence shows that the effect of intracellular ATP is to make the opening of the common gate more difficult [61]. The mechanism of common gating of CLC-channels is not clear, but it has been proposed that this gating mechanism may involve the relative motion of the two channel subunits, including the movement of the C-terminal cytoplasmic domain [63]. The inhibition of the common gating by cytoplasmic ATP is consistent with the structural feature that the ATP-binding site is located in the C-terminal cytoplasmic region of CLC-1 channels.

During vigorous muscle activities, ATP level in fast-twitch muscle fibers is significantly lowered [64], which in turn reduces ATP inhibition of CLC-1 channels. This enhanced activation of CLC-1 channels is expected to decrease muscle excitability, a potential cell protection mechanism during metabolic stress that may contribute to the development of muscle fatigue [65]. As discussed above, muscle fatigue may also be caused by partial Na^+ channel inactivation as a result of the accumulation of extracellular k^+ ions after multiple action potentials. Moreover, intensive exercise leads to muscle acidosis [66, 67], which in the presence of ATP, may result in CLC-1 channel inhibition [60]. This down regulation of membrane Cl^- conductance will notably reduce the input conductance of sarcolemma and consequently increase the likelihood of spike induction for the Na^+ channels that remain active, and may therefore serve as a physiological response to prevent the development of muscle fatigue.

5. Pathophysiology of Myotonia Congenita

In humans, mutations in the skeletal muscle CLC-1 gene (*CLCN1*) on chromosome 7 have been linked to a hereditary

muscle disease, myotonia congenita [68]. Myotonia can be defined as a hyperexcitability of the plasma membrane of skeletal muscle fibers. Myotonia is due to an electrical instability of the muscle membrane itself, leading to repetitive action potentials with a single stimulus (“myotonic runs”). Myotonia congenita was one of the first human diseases proven to be caused by an ion-channel defect (channelopathy). This discovery was based on studies in goats with hereditary myotonia that closely resembled myotonia congenita in humans [69–71]. Subsequent studies also demonstrated that there was indeed a reduced Cl^- conductance in goat and human myotonic muscle fibers and that normal muscle fibers exhibited myotonic features when Cl^- was replaced with an impermeant anion [14, 72]. This myotonia-like phenomenon induced by low concentrations of Cl^- can be accounted for by the aforementioned Cl^- -dependent gating mechanism for CLC-1 channels.

Human myotonia congenita can be inherited in an autosomal recessive (Becker type) or autosomal dominant (Thomsen type) manner [73]. By now, more than 100 different mutations in the *CLCN1* gene have been identified in patients with myotonia congenita [74–76]. Myotonia-causing mutations are scattered over the entire sequence of the channel protein, both in the transmembrane region and in the cytosolic N-terminal and C-terminal parts. They include nonsense, splice-site, and frameshift mutations that truncate the channel protein. Truncation mutations are always associated with recessive myotonia, except when they are very close to the C-terminus. Missense mutations can be associated with either recessive or dominant inheritance. Mutations with dominant inheritance are less frequent. With the exception of truncations very close to the C-terminus of CLC-1 channels, all dominant mutations are missense mutations. Recessive mutations are more diverse; they can be associated with truncations, insertions, splice defects, missense, or nonsense/stop errors. Therefore, it is not possible to predict on the basis of the mutation location or the mutation type whether the inheritance will be dominant or recessive.

For the autosomal dominant form of myotonia, patients are expected to carry the heterozygous *CLCN1* genotype: one copy each of the wild-type and the mutant allele. Regarding the molecular mechanism of myotonia congenita, a loss-of-function phenotype of the mutant *CLCN1* gene certainly supports haploinsufficiency as a reasonable mechanism causing the malfunction of muscles. For many other cases of disease-related mutations, however, a total loss of functional CLC-1 channels on only one allele does not lead to myotonia [32, 36]. It has been suggested that dominant myotonia is due to dominant-negative effects of the mutant subunit on the wild-type subunit coexpressed in the muscles of heterozygous patients. On the other hand, lots of *CLCN1* gene mutations result in recessive myotonia, and the mutant proteins do not have dominant negative effects. A likely reason for a lack of dominant negative effects for these recessive mutants is the inability of truncated proteins to associate with the wild-type subunit [74].

Therefore, a current working hypothesis on the molecular basis for the inheritance of myotonia congenita is that

the inheritance pattern of a mutation is predominantly determined by the functional consequence of the mutation on the gating of CLC-1 channels: those mutations that affect the common gate lead to an autosomal-dominant inheritance pattern, whereas those affecting individual protopores only result in a recessive pattern [42, 77]. As described above, a functional CLC-1 channel is a homodimer. With the exception of truncations very close to the C-terminus of CLC-1 channels, all dominant mutations are missense mutations. Almost all these mutations shift the voltage-dependence of gating of the channel towards positive voltages so that the activity of the mutant channels is insufficient to cause membrane repolarization [53]. The dominant-negative effect of these mutations on the heterodimeric channel is due to the fact that the common-gate controlling both protopores is affected by the mutation in the mutant subunit [42]. Indeed, many, but not all, mutations in dominant myotonia are due to mutations of residues close to the subunit interface [74, 75, 78]. Consistent with this observation, site-directed mutagenesis of residues lining subunit interface affects the common gate of CLC-1 [79, 80]. On the other hand, as the ion-conducting pore of CLC-1 is entirely contained within each subunit of the dimer [43, 81], mutations affecting the function of one protopore are unlikely to affect the conductance of the second subunit in wild-type/mutant hetero dimeric channels and therefore will generally lack dominant-negative effects. For example, the equivalent residue of CLC-1's M485 in bacterial CLC proteins is located in the ion-transport pathway. In heterologous expression systems, the mutation M485V in CLC-1 drastically changed the single-channel conductance and the voltage-dependent gating of homodimeric mutant CLC-1 channels [82]. This mutation, however, displays a recessive inheritance pattern. As both alleles are mutated in patients with recessive myotonia, a total loss of CLC-1 channel function may ensue. In contrast, by assuming equal association affinity for both wild-type and mutant subunits in the dimeric channel architecture, at least 25% of wild-type currents will still remain in heterozygous patients carrying dominant-negative mutations. Accordingly, recessive myotonia is clinically more severe than the dominant Thomsen form.

In addition to faulty channel gating, other mechanisms may also contribute to the pathophysiology of myotonia congenita [83]. For example, several recessive *CLCN1* mutations (e.g., Y150C, V165G, F167L, V236L, Y261C, V327I, and F413C) have been shown to yield functional CLC-1 channels with biophysical properties either only slightly different or virtually indistinguishable from those of wild-type channels [75]. Similarly, some dominant *CLCN1* mutations (e.g., R338Q, F428S, and T550M) have been shown to display no detectable gating defects upon forming heterodimers with their wild-type counterparts [84, 85]. By no means can the foregoing dominant negative mechanism explain the inheritance patterns of these mutations. These examples clearly demonstrate that the effect of myotonia-related mutations cannot be simply attributed to the disruption of the gating of CLC-1 channels. Several novel mutations in the *CLCN1* gene have recently been identified in Taiwanese patients

suffering from myotonia congenita [86, 87]. Interestingly, one of the detected mutations, fs793X, was found in a Taiwanese family with dominant inheritance pattern [87]. However, the same mutation was previously found in an recessive Italian pedigree [88]. This is only one of the several examples showing that the same mutations are associated with recessive myotonia in some families, but with dominant myotonia in others [77, 89, 90]. This dual inheritance pattern again demonstrates the inadequacy of the gating hypothesis and further highlights the importance of other pathophysiological mechanisms of myotonia congenita. It is likely that some myotonia congenita-related mutations may (i) result in aberrant biogenesis and subunit assembly and/or (ii) lead to a defective membrane targeting subcellular localization patterns of CLC-1 channels. Indeed, three myotonia-related mutations in the distal C-terminus of CLC-1 channels have been shown to have a reduction of protein expression in the surface membrane [83]. Thus, the underlying mechanisms of myotonia due to CLC-1 channelopathy are likely to be quite diverse.

6. Clinical Correlation

Myotonia is characterized by the impaired relaxation of skeletal muscle following sudden voluntary contraction. As discussed above, CLC-1 conductance contributes up to 80% of the resting membrane conductance in normal skeletal muscle. Myotonia-causing mutations in the *CLCN1* gene therefore lead to a significant reduction in resting membrane conductance, thereby increasing the input resistance of skeletal muscle [72, 91]. Consequently, a smaller membrane depolarization (threshold potential) will be sufficient to trigger an action potential, that is, muscle excitability will be enhanced. This scenario explains why a single nerve stimulus elicited a train of action potentials in muscle fibers from myotonic goats; in contrast, the same stimulus only induced a single action potential in normal muscle fibers [70].

Another important role of CLC-1 conductance in muscle is to counteract the depolarizing effect of tubular K^+ accumulation during intensive firing of action potentials [70]. As the extracellular volume in the transverse-tubule system of skeletal muscles is limited, K^+ ions tend to accumulate in the extracellular space during intensive firing of muscle action potentials. This increase in extracellular K^+ normally has little effect on the membrane potential due to the presence of high CLC-1 conductance. In myotonic muscle, however, a small accumulation of tubular K^+ will result in a significant membrane depolarization. In the presence of rapid successions of action potentials, summation of these K^+ accumulation-induced membrane depolarization may trigger spontaneous muscle action potentials, thereby manifesting myotonia symptoms such as muscle stiffness after voluntary contraction. Hence, the medication of choice for myotonic patients usually involves drugs that suppress muscle excitability via inhibition of voltage-gated Na^+ channels [92].

The muscle stiffness of myotonia can gradually be relieved by exercise (the so-called "warm-up" phenomenon) [93]. One plausible mechanism of the warm-up is the

enhanced activity of the muscle Na^+/K^+ -ATPase induced by exercise, which facilitates the clearance of extracellular K^+ from transverse-tubules. A recent study in myotonic patients, however, failed to support this hypothesis [94], indicating that the precise mechanism of warm-up is still unclear.

Also elusive are the rationales for several other clinical manifestations of myotonia congenita. For example, the recessive myotonia is usually more common in men than in women, and for female patients of dominant myotonia, the symptoms become worse during pregnancy [75]. It has been suggested that the observed gender difference may arise from the modulation of CLC-1 channel function by sex hormones [95]. In addition, recessive but not dominant myotonia is often associated with transient muscle weakness on the initiation of movement [75, 96], a defect that is not predicted by enhanced muscle excitability. Obviously, a combination of biophysical and cell biological studies in both *in vitro* and *in vivo* models will be required for better understanding of the clinical symptoms of myotonia congenita.

7. Concluding Remarks

CLC-1 channels play a crucial role in setting membrane excitability in skeletal muscle. Despite of the numerous documentations of the association between *CLCN1* mutations and myotonia congenita, elucidation of the mechanistic link between genetic defects and pathogenesis is still at the primitive stage. One major limitation to our better understanding of this issue lies in the fact that protein biosynthetic pathways as well as subcellular localization patterns of CLC-1 channels *in situ* remain obscure. For example, even though a significant Cl^- conductance has been identified in the transverse-tubule system, it remains inconclusive whether CLC-1 channels are actually expressed in the transverse-tubule system. In the ADR (arrested development of righting response) mouse that has been used as a model for recessive myotonia [34, 69], immunohistochemistry of muscle cryosection located CLC-1 channels primarily in the outer, sarcolemmal membrane, but not in the transverse-tubule of skeletal muscle [97]. A similar conclusion on sarcolemmal localization of CLC-1 channels was recently reported in flexor digitorum brevis muscle fibers of wild-type mice as well [98]. Biophysical and pharmacological studies in a skinned rat skeletal muscle, however, demonstrated that the transverse-tubule Cl^- channel conductance was blocked by 9-AC, low intracellular pH, and protein kinase C activators [18, 19, 96], all of which are known to affect the properties of CLC-1 channels observed in the heterologous expression system [32, 60, 61, 99]. As has been previously proposed [19, 100], this apparent discrepancy may arise from the possibility that the transverse-tubule system expresses certain splice variants of CLC-1 channels that lack the epitope for the antibody used in the immunofluorescence study, or that the surrounding microenvironment in the transverse-tubule system prevents the antibody from properly recognizing the epitope in CLC-1 channels *in situ*. The field thus requires more extensive studies on not only the gating mechanisms but also the biosynthetic process and subcellular localization of CLC-1 channels.

Myotonia congenita, therefore, is still in lack of a standard, effective treatment. The field thus begs for further research efforts in multiple directions. At the molecular level, the mechanistic principles underlying the operation of CLC-1 need to be further examined. At the cellular level, the protein biosynthesis mechanisms of CLC-1 (protein biogenesis, membrane trafficking, as well as subcellular localization patterns *in situ*), although drawing much research attention recently, remain obscure and need more in-depth investigations. At the clinical level, many myotonia-associated symptoms require better understanding of their pathophysiological mechanisms. Through elucidations of the physiological roles of CLC-1 and the pathophysiological mechanisms of the CLC-1 channelopathy, the therapeutic strategies for myotonia congenita will eventually be illuminated.

Acknowledgments

The authors thank Dr. Tzyh-Chang Hwang for critical readings of the paper. The research in Dr. Chih-Yung Tang's laboratory is supported by a Grant (NSC 96-2320-B-002-069-MY3) from National Science Council of Taiwan, while the work of Dr. Tsung-Yu Chen's laboratory is supported by a Grant (R01GM065447) from National Institutes of Health of USA.

References

- [1] J. M. Russell, "Sodium-potassium-chloride cotransport," *Physiological Reviews*, vol. 80, no. 1, pp. 211–276, 2000.
- [2] N. C. Adragna, M. di Fulvio, and P. K. Lauf, "Regulation of K-Cl cotransport: from function to genes," *Journal of Membrane Biology*, vol. 201, no. 3, pp. 109–137, 2004.
- [3] G. Gamba, "Molecular physiology and pathophysiology of electroneutral cation-chloride cotransporters," *Physiological Reviews*, vol. 85, no. 2, pp. 423–493, 2005.
- [4] T. J. Jentsch, T. Maritzen, and A. A. Zdebik, "Chloride channel diseases resulting from impaired transepithelial transport or vesicular function," *Journal of Clinical Investigation*, vol. 115, no. 8, pp. 2039–2046, 2005.
- [5] J. A. Payne, C. Rivera, J. Voipio, and K. Kaila, "Cation-chloride co-transporters in neuronal communication, development and trauma," *Trends in Neurosciences*, vol. 26, no. 4, pp. 199–206, 2003.
- [6] A. L. Hodgkin and P. Horowicz, "The influence of potassium and chloride ions on the membrane potential of single muscle fibres," *Journal of Physiology*, vol. 148, pp. 127–160, 1959.
- [7] R. H. Adrian, "Potassium chloride movement and the membrane potential of frog muscle," *Journal of Physiology*, vol. 151, pp. 154–185, 1960.
- [8] R. H. Adrian, "Internal chloride concentration and chloride efflux of frog muscle," *Journal of Physiology*, vol. 156, pp. 623–632, 1961.
- [9] A. F. Dulhunty, "The dependence of membrane potential on extracellular chloride concentration in mammalian skeletal muscle fibres," *Journal of Physiology*, vol. 276, pp. 67–82, 1978.
- [10] R. J. G. Foppen, H. G. J. van Mil, and J. S. van Heukelom, "Effects of chloride transport on bistable behaviour of the

- membrane potential in mouse skeletal muscle," *Journal of Physiology*, vol. 542, no. 1, pp. 181–191, 2002.
- [11] R. J. G. Foppen, "In skeletal muscle the relaxation of the resting membrane potential induced by K(+) permeability changes depends on Cl(-) transport," *Pflugers Archiv*, vol. 447, no. 4, pp. 416–425, 2004.
- [12] J. Gallaher, M. Bier, and J. S. van Heukelom, "The role of chloride transport in the control of the membrane potential in skeletal muscle—theory and experiment," *Biophysical Chemistry*, vol. 143, no. 1-2, pp. 18–25, 2009.
- [13] C. C. Aickin, W. J. Betz, and G. L. Harris, "Intracellular chloride and the mechanism for its accumulation in rat lumbrical muscle," *Journal of Physiology*, vol. 411, pp. 437–455, 1989.
- [14] S. H. Bryant and A. Morales-Aguilera, "Chloride conductance in normal and myotonic muscle fibres and the action of monocarboxylic aromatic acids," *Journal of Physiology*, vol. 219, no. 2, pp. 367–383, 1971.
- [15] A. F. Dulhunty, "Distribution of potassium and chloride permeability over the surface and T-tubule membranes of mammalian skeletal muscle," *Journal of Membrane Biology*, vol. 45, no. 3-4, pp. 293–310, 1979.
- [16] A. H. Bretag, "Muscle chloride channels," *Physiological Reviews*, vol. 67, no. 2, pp. 618–724, 1987.
- [17] P. T. Palade and R. L. Barchi, "Characteristics of the chloride conductance in muscle fibers of the rat diaphragm," *Journal of General Physiology*, vol. 69, no. 3, pp. 325–342, 1977.
- [18] J. R. Coonan and G. D. Lamb, "Effect of transverse-tubular chloride conductance on excitability in skinned skeletal muscle fibres of rat and toad," *Journal of Physiology*, vol. 509, part 2, pp. 551–564, 1998.
- [19] T. L. Dutka, R. M. Murphy, D. G. Stephenson, and G. D. Lamb, "Chloride conductance in the transverse tubular system of rat skeletal muscle fibres: importance in excitation-contraction coupling and fatigue," *Journal of Physiology*, vol. 586, no. 3, pp. 875–887, 2008.
- [20] T. H. Pedersen, O. B. Nielsen, G. D. Lamb, and D. G. Stephenson, "Intracellular acidosis enhances the excitability of working muscle," *Science*, vol. 305, no. 5687, pp. 1144–1147, 2004.
- [21] S. P. Cairns and M. I. Lindinger, "Do multiple ionic interactions contribute to skeletal muscle fatigue?" *Journal of Physiology*, vol. 586, no. 17, pp. 4039–4054, 2008.
- [22] T. J. Jentsch, V. Stein, F. Weinreich, and A. A. Zdebik, "Molecular structure and physiological function of chloride channels," *Physiological Reviews*, vol. 82, no. 2, pp. 503–568, 2002.
- [23] T. Y. Chen, "Structure and function of CLC channels," *Annual Review of Physiology*, vol. 67, pp. 809–839, 2005.
- [24] T. J. Jentsch, M. Poët, J. C. Fuhrmann, and A. A. Zdebik, "Physiological functions of CLC Cl- channels gleaned from human genetic disease and mouse models," *Annual Review of Physiology*, vol. 67, pp. 779–807, 2005.
- [25] A. Accardi and C. Miller, "Secondary active transport mediated by a prokaryotic homologue of CLC Cl- channels," *Nature*, vol. 427, no. 6977, pp. 803–807, 2004.
- [26] A. Picollo and M. Pusch, "Chloride/proton antiporter activity of mammalian CLC proteins CLC-4 and CLC-5," *Nature*, vol. 436, no. 7049, pp. 420–423, 2005.
- [27] O. Scheel, A. A. Zdebik, S. Lourdel, and T. J. Jentsch, "Voltage-dependent electrogenic chloride/proton exchange by endosomal CLC proteins," *Nature*, vol. 436, no. 7049, pp. 424–427, 2005.
- [28] O. Devuyt and W. B. Guggino, "Chloride channels in the kidney: lessons learned from knockout animals," *American Journal of Physiology—Renal Physiology*, vol. 283, no. 6, pp. F1176–F1191, 2002.
- [29] J. Cuppoletti, K. P. Tewari, A. M. Sherry, and D. H. Malinowska, "Activation of human CLC-2 Cl- channels: implications for cystic fibrosis," *Clinical and Experimental Pharmacology and Physiology*, vol. 27, no. 11, pp. 896–900, 2000.
- [30] K. Strange, "Of mice and worms: novel insights into CLC-2 anion channel physiology," *News in Physiological Sciences*, vol. 17, no. 1, pp. 11–16, 2002.
- [31] A. Thiemann, S. Grunder, M. Pusch, and T. J. Jentsch, "A chloride channel widely expressed in epithelial and non-epithelial cells," *Nature*, vol. 356, no. 6364, pp. 57–60, 1992.
- [32] K. Steinmeyer, C. Ortland, and T. J. Jentsch, "Primary structure and functional expression of a developmentally regulated skeletal muscle chloride channel," *Nature*, vol. 354, no. 6351, pp. 301–304, 1991.
- [33] X. D. Zhang, S. Morishima, Y. Ando-Akatsuka et al., "Expression of novel isoforms of the CLC-1 chloride channel, in astrocytic glial cells in vitro," *GLIA*, vol. 47, no. 1, pp. 46–57, 2004.
- [34] K. Steinmeyer, R. Klocke, C. Ortland et al., "Inactivation of muscle chloride channel by transposon insertion in myotonic mice," *Nature*, vol. 354, no. 6351, pp. 304–308, 1991.
- [35] M. C. Koch, K. Steinmeyer, C. Lorenz et al., "The skeletal muscle chloride channel in dominant and recessive human myotonia," *Science*, vol. 257, no. 5071, pp. 797–800, 1992.
- [36] M. Gronemeier, A. Condie, J. Prosser, K. Steinmeyer, T. J. Jentsch, and H. Jockusch, "Nonsense and missense mutations in the muscular chloride channel gene Clc- 1 of myotonic mice," *Journal of Biological Chemistry*, vol. 269, no. 8, pp. 5963–5967, 1994.
- [37] C. L. Beck, C. Fahlke, and A. L. George Jr., "Molecular basis for decreased muscle chloride conductance in the myotonic goat," *Proceedings of the National Academy of Sciences of the United States of America*, vol. 93, no. 20, pp. 11248–11252, 1996.
- [38] T. H. Rhodes, C. H. Vite, U. Giger, D. F. Patterson, C. Fahlke, and A. L. George Jr., "A missense mutation in canine CLC-1 causes recessive myotonia congenita in the dog," *FEBS Letters*, vol. 456, no. 1, pp. 54–58, 1999.
- [39] C. Fahlke, R. Rüdell, N. Mitrovic, M. Zhou, and A. L. George Jr., "An aspartic acid residue important for voltage-dependent gating of human muscle chloride channels," *Neuron*, vol. 15, no. 2, pp. 463–472, 1995.
- [40] C. Miller, "Open-state substructure of single chloride channels from Torpedo electroplax," *Philosophical Transactions of the Royal Society of London B*, vol. 299, no. 1097, pp. 401–411, 1982.
- [41] C. Miller and M. M. White, "Dimeric structure of single chloride channels from Torpedo electroplax," *Proceedings of the National Academy of Sciences of the United States of America*, vol. 81, no. 9, pp. 2772–2775, 1984.
- [42] C. Saviane, F. Conti, and M. Pusch, "The muscle chloride channel CLC-1 has a double-barreled appearance that is differentially affected in dominant and recessive myotonia," *Journal of General Physiology*, vol. 113, no. 3, pp. 457–468, 1999.
- [43] R. Dutzler, E. B. Campbell, M. Cadene, B. T. Chait, and R. MacKinnon, "X-ray structure of a CLC chloride channel at 3.0 Å reveals the molecular basis of anion selectivity," *Nature*, vol. 415, no. 6869, pp. 287–294, 2002.
- [44] R. Dutzler, E. B. Campbell, and R. MacKinnon, "Gating the selectivity filter in CLC chloride channels," *Science*, vol. 300, no. 5616, pp. 108–112, 2003.

- [45] T. Y. Chen and C. Miller, "Nonequilibrium gating and voltage dependence of the ClC-0 Cl⁻ channel," *Journal of General Physiology*, vol. 108, no. 4, pp. 237–250, 1996.
- [46] G. Y. Rychkov, M. Pusch, D. S. J. Astill, M. L. Roberts, T. J. Jentsch, and A. H. Bretag, "Concentration and pH dependence of skeletal muscle chloride channel ClC-1," *Journal of Physiology*, vol. 497, part 2, pp. 423–435, 1996.
- [47] M. F. Chen and T. Y. Chen, "Different fast-gate regulation by external Cl⁻ and H⁺ of the muscle-type ClC chloride channels," *Journal of General Physiology*, vol. 118, no. 1, pp. 23–32, 2001.
- [48] C. Miller, "ClC chloride channels viewed through a transporter lens," *Nature*, vol. 440, no. 7083, pp. 484–489, 2006.
- [49] L. Feng, E. B. Campbell, Y. Hsiung, and R. MacKinnon, "Structure of a eukaryotic ClC transporter defines an intermediate state in the transport cycle," *Science*, vol. 330, no. 6004, pp. 635–641, 2010.
- [50] W. Hanke and C. Miller, "Single chloride channels from Torpedo electroplax. Activation by protons," *Journal of General Physiology*, vol. 82, no. 1, pp. 25–45, 1983.
- [51] Y. W. Lin, C. W. Lin, and T. Y. Chen, "Elimination of the slow gating of ClC-0 chloride channel by a point mutation," *Journal of General Physiology*, vol. 114, no. 1, pp. 1–12, 1999.
- [52] B. Hille, *Ion Channels of Excitable Membranes*, Sinauer Associates, Inc., Sunderland, Mass, USA, 2001.
- [53] M. Pusch, K. Steinmeyer, M. C. Koch, and T. J. Jentsch, "Mutations in dominant human myotonia congenita drastically alter the voltage dependence of the ClC-1 chloride channel," *Neuron*, vol. 15, no. 6, pp. 1455–1463, 1995.
- [54] S. Meyer and R. Dutzler, "Crystal structure of the cytoplasmic domain of the chloride channel ClC-0," *Structure*, vol. 14, no. 2, pp. 299–307, 2006.
- [55] S. Meyer, S. Savaresi, I. C. Forster, and R. Dutzler, "Nucleotide recognition by the cytoplasmic domain of the human chloride transporter ClC-5," *Nature Structural and Molecular Biology*, vol. 14, no. 1, pp. 60–67, 2007.
- [56] S. Markovic and R. Dutzler, "The structure of the cytoplasmic domain of the chloride channel ClC-Ka reveals a conserved interaction interface," *Structure*, vol. 15, no. 6, pp. 715–725, 2007.
- [57] T. Y. Chen, "Coupling gating with ion permeation in ClC channels," *Science's STKE*, vol. 2003, no. 188, p. e23, 2003.
- [58] R. Dutzler, "The structural basis of ClC chloride channel function," *Trends in Neurosciences*, vol. 27, no. 6, pp. 315–320, 2004.
- [59] R. Dutzler, "Structural basis for ion conduction and gating in ClC chloride channels," *FEBS Letters*, vol. 564, no. 3, pp. 229–233, 2004.
- [60] B. Bennetts, M. W. Parker, and B. A. Cromer, "Inhibition of skeletal muscle ClC-1 chloride channels by low intracellular pH and ATP," *Journal of Biological Chemistry*, vol. 282, no. 45, pp. 32780–32791, 2007.
- [61] P. Y. Tseng, B. Bennetts, and T. Y. Chen, "Cytoplasmic ATP inhibition of ClC-1 is enhanced by low pH," *Journal of General Physiology*, vol. 130, no. 2, pp. 217–221, 2007.
- [62] X. D. Zhang, P. Y. Tseng, and T. Y. Chen, "ATP inhibition of ClC-1 is controlled by oxidation and reduction," *Journal of General Physiology*, vol. 132, no. 4, pp. 421–428, 2008.
- [63] E. A. Bykova, X. D. Zhang, T. Y. Chen, and J. Zheng, "Large movement in the C terminus of ClC-0 chloride channel during slow gating," *Nature Structural and Molecular Biology*, vol. 13, no. 12, pp. 1115–1119, 2006.
- [64] C. Karatzaferi, A. de Haan, R. A. Ferguson, W. van Mechelen, and A. J. Sargeant, "Phosphocreatine and ATP content in human single muscle fibres before and after maximum dynamic exercise," *Pflügers Archiv*, vol. 442, no. 3, pp. 467–474, 2001.
- [65] B. Bennetts, G. Y. Rychkov, H. L. Ng et al., "Cytoplasmic ATP-sensing domains regulate gating of skeletal muscle ClC-1 chloride channels," *Journal of Biological Chemistry*, vol. 280, no. 37, pp. 32452–32458, 2005.
- [66] A. Roos and W. F. Boron, "Intracellular pH transients in rat diaphragm muscle measured with DMO," *American Journal of Physiology*, vol. 235, no. 1, pp. C49–C54, 1978.
- [67] J. R. Wilson, K. K. McCully, D. M. Mancini, B. Boden, and B. Chance, "Relationship of muscular fatigue to pH and diprotonated P(i) in humans: a ³¹P-NMR study," *Journal of Applied Physiology*, vol. 64, no. 6, pp. 2333–2339, 1988.
- [68] K. Jurkat-Rott, H. Lerche, and F. Lehmann-Horn, "Skeletal muscle channelopathies," *Journal of Neurology*, vol. 249, no. 11, pp. 1493–1502, 2002.
- [69] R. J. Lipicky and S. H. Bryant, "Sodium, potassium, and chloride fluxes in intercostal muscle from normal goats and goats with hereditary myotonia," *Journal of General Physiology*, vol. 50, no. 1, pp. 89–111, 1966.
- [70] R. H. Adrian and S. H. Bryant, "On the repetitive discharge in myotonic muscle fibres," *Journal of Physiology*, vol. 240, no. 2, pp. 505–515, 1974.
- [71] R. H. Adrian and M. W. Marshall, "Action potentials reconstructed in normal and myotonic muscle fibres," *Journal of Physiology*, vol. 258, no. 1, pp. 125–143, 1976.
- [72] R. J. Lipicky, S. H. Bryant, and J. H. Salmon, "Cable parameters, sodium, potassium, chloride, and water content, and potassium efflux in isolated external intercostal muscle of normal volunteers and patients with myotonia congenita," *Journal of Clinical Investigation*, vol. 50, no. 10, pp. 2091–2103, 1971.
- [73] L. J. Ptacek, K. J. Johnson, and R. C. Griggs, "Genetics and physiology of the myotonic muscle disorders," *The New England Journal of Medicine*, vol. 328, no. 7, pp. 482–489, 1993.
- [74] M. Pusch, "Myotonia caused by mutations in the muscle chloride channel gene ClCN1," *Human Mutation*, vol. 19, no. 4, pp. 423–434, 2002.
- [75] E. Colding-Jørgensen, "Phenotypic variability in myotonia congenita," *Muscle and Nerve*, vol. 32, no. 1, pp. 19–34, 2005.
- [76] C. Lossin and A. L. George Jr., "Myotonia congenita," *Advances in Genetics*, vol. 63, pp. 25–55, 2008.
- [77] C. Kubisch, T. Schmidt-Rose, B. Fontaine, A. H. Bretag, and T. J. Jentsch, "ClC-1 chloride channel mutations in myotonia congenita: variable penetrance of mutations shifting the voltage dependence," *Human Molecular Genetics*, vol. 7, no. 11, pp. 1753–1760, 1998.
- [78] D. Fialho, S. Schorge, U. Pucovska et al., "Chloride channel myotonia: exon 8 hot-spot for dominant-negative interactions," *Brain*, vol. 130, no. 12, pp. 3265–3274, 2007.
- [79] A. Accardi, L. Ferrera, and M. Pusch, "Drastic reduction of the slow gate of human muscle chloride channel (ClC-1) by mutation C277S," *Journal of Physiology*, vol. 534, no. 3, pp. 745–752, 2001.
- [80] M. Duffield, G. Rychkov, A. Bretag, and M. Roberts, "Involvement of helices at the dimer interface in ClC-1 common gating," *Journal of General Physiology*, vol. 121, no. 2, pp. 149–161, 2003.
- [81] F. Weinreich and T. J. Jentsch, "Pores formed by single subunits in mixed dimers of different ClC chloride channels," *Journal of Biological Chemistry*, vol. 276, no. 4, pp. 2347–2353, 2001.

- [82] B. Wollnik, C. Kubisch, K. Steinmeyer, and M. Pusch, "Identification of functionally important regions of the muscular chloride channel CLC-1 by analysis of recessive and dominant myotonic mutations," *Human Molecular Genetics*, vol. 6, no. 5, pp. 805–811, 1997.
- [83] M. J. Macías, O. Tejjido, G. Zifarelli et al., "Myotonia-related mutations in the distal C-terminus of CLC-1 and CLC-0 chloride channels affect the structure of a poly-proline helix," *Biochemical Journal*, vol. 403, no. 1, pp. 79–87, 2007.
- [84] F. F. Wu, A. Ryan, J. Devaney et al., "Novel CLCN1 mutations with unique clinical and electrophysiological consequences," *Brain*, vol. 125, no. 11, pp. 2392–2407, 2002.
- [85] J. Zhang, S. Bendahhou, M. C. Sanguinetti, and L. J. Ptáček, "Functional consequences of chloride channel gene (CLCN1) mutations causing myotonia congenita," *Neurology*, vol. 54, no. 4, pp. 937–942, 2000.
- [86] S. B. Jou, L. I. Chang, H. Pan, P. R. Chen, and K. M. Hsiao, "Novel CLCN1 mutations in Taiwanese patients with myotonia congenita," *Journal of Neurology*, vol. 251, no. 6, pp. 666–670, 2004.
- [87] H. C. Kuo, K. M. Hsiao, L. I. Chang, T. H. You, T. H. Yeh, and C. C. Huang, "Novel mutations at carboxyl terminus of CLC-1 channel in myotonia congenita," *Acta Neurologica Scandinavica*, vol. 113, no. 5, pp. 342–346, 2006.
- [88] F. Sangiuolo, A. Botta, A. Mesoraca et al., "Identification of five new mutations and three novel polymorphisms in the muscle chloride channel gene (CLCN1) in 20 Italian patients with dominant and recessive myotonia congenita. Mutations in brief no. 118. Online," *Human Mutation*, vol. 11, no. 4, p. 331, 1998.
- [89] A. L. George Jr., K. Sloan-Brown, G. M. Fenichel, G. A. Mitchell, R. Spiegel, and R. M. Pascuzzi, "Nonsense and missense mutations of the muscle chloride channel gene in patients with myotonia congenita," *Human Molecular Genetics*, vol. 3, no. 11, pp. 2071–2072, 1994.
- [90] C. Meyer-Kleine, K. Steinmeyer, K. Ricker, T. J. Jentsch, and M. C. Koch, "Spectrum of mutations in the major human skeletal muscle chloride channel gene (CLCN1) leading to myotonia," *American Journal of Human Genetics*, vol. 57, no. 6, pp. 1325–1334, 1995.
- [91] S. H. Bryant, "Cable properties of external intercostal muscle fibres from myotonic and nonmyotonic goats," *Journal of Physiology*, vol. 204, no. 3, pp. 539–550, 1969.
- [92] G. Meola and V. Sansone, "Therapy in myotonic disorders and in muscle channelopathies," *Neurological Sciences*, vol. 21, no. 5, pp. S953–S961, 2000.
- [93] R. Rudel and F. Lehmann-Horn, "Membrane changes in cells from myotonia patients," *Physiological Reviews*, vol. 65, no. 2, pp. 310–356, 1985.
- [94] M. C. P. van Beekvelt, G. Drost, G. Rongen, D. F. Stegeman, B. G. M. van Engelen, and M. J. Zwarts, "Na⁺-K⁺-ATPase is not involved in the warming-up phenomenon in generalized myotonia," *Muscle and Nerve*, vol. 33, no. 4, pp. 514–523, 2006.
- [95] D. Fialho, D. M. Kullmann, M. G. Hanna, and S. Schorge, "Non-genomic effects of sex hormones on CLC-1 may contribute to gender differences in myotonia congenita," *Neuromuscular Disorders*, vol. 18, no. 11, pp. 869–872, 2008.
- [96] D. L. R. Rayan and M. G. Hanna, "Skeletal muscle channelopathies: nondystrophic myotonias and periodic paralysis," *Current Opinion in Neurology*, vol. 23, no. 5, pp. 466–476, 2010.
- [97] C. A. Gurnett, S. D. Kahl, R. D. Anderson, and K. P. Campbell, "Absence of the skeletal muscle sarcolemma chloride channel CLC-1 in myotonic mice," *Journal of Biological Chemistry*, vol. 270, no. 16, pp. 9035–9038, 1995.
- [98] J. D. Lueck, A. E. Rossi, C. A. Thornton, K. P. Campbell, and R. T. Dirksen, "Sarcolemmal-restricted localization of functional CLC-1 channels in mouse skeletal muscle," *Journal of General Physiology*, vol. 136, no. 6, pp. 597–613, 2010.
- [99] A. Rosenbohm, R. Rüdell, and C. Fahlke, "Regulation of the human skeletal muscle chloride channel hCLC-1 by protein kinase C," *Journal of Physiology*, vol. 514, part 3, pp. 677–685, 1999.
- [100] E. C. Aromataris and G. Y. Rychkov, "CLC-1 chloride channel: matching its properties to a role in skeletal muscle," *Clinical and Experimental Pharmacology and Physiology*, vol. 33, no. 11, pp. 1118–1123, 2006.

Research Article

Obscurin Depletion Impairs Organization of Skeletal Muscle in Developing Zebrafish Embryos

Maide Ö. Raeker¹ and Mark W. Russell^{1,2}

¹Department of Pediatrics and Communicable Diseases, University of Michigan, Ann Arbor, MI 48109, USA

²Cellular and Molecular Biology Graduate Program, University of Michigan, Ann Arbor, MI 48109, USA

Correspondence should be addressed to Mark W. Russell, mruss@med.umich.edu

Received 2 May 2011; Revised 10 July 2011; Accepted 27 July 2011

Academic Editor: Robert J. Bloch

Copyright © 2011 M. Ö. Raeker and M. W. Russell. This is an open access article distributed under the Creative Commons Attribution License, which permits unrestricted use, distribution, and reproduction in any medium, provided the original work is properly cited.

During development, skeletal myoblasts differentiate into myocytes and skeletal myotubes with mature contractile structures that are precisely oriented with respect to surrounding cells and tissues. Establishment of this highly ordered structure requires reciprocal interactions between the differentiating myocytes and the surrounding extracellular matrix to form correctly positioned and well-organized attachments from the skeletal muscle to the bony skeleton. Using the developing zebrafish embryo as a model, we examined the relationship between new myofibril assembly and the organization of the membrane domains involved in cell-extracellular matrix interactions. We determined that depletion of obscurin, a giant muscle protein, resulted in irregular cell morphology and disturbed extracellular matrix organization during skeletal muscle development. The resulting impairment of myocyte organization was associated with disturbance of the internal architecture of the myocyte suggesting that obscurin participates in organizing the internal structure of the myocyte and translating those structural cues to surrounding cells and tissues.

1. Introduction

Skeletal muscle function is dependent upon stable connections from the contractile elements that generate force to the bony skeleton that translates that force into movement. Efficient transmission of that contractile force is enabled by a highly organized arrangement of support structures both within and around the actin-myosin array. Through these supporting elements, the actin-myosin array within the cell is directly connected to the extracellular matrix (ECM). These connections occur both along the axis of contraction at the myotendinous junction (MTJ), where the muscle inserts into a fibrous tendon that attaches to the bony skeleton, and radially at specialized membrane domains like the costameres [1, 2], where the muscle attaches to surrounding fibrous sheaths called the endomysium and the perimysium. The importance of muscle-ECM connections to muscle structure and function is evident from the number of myopathies and muscular dystrophies, including Duchenne muscular dystrophy, that result from disturbance of the multiprotein complexes that support the linkage [3].

The primary site of force transmission from the muscle to the ECM, and ultimately to the bony skeleton, occurs at the myotendinous junctions. Despite the importance of the MTJ to muscle function, relatively little is known about how it is formed. What is known has been derived from studies in zebrafish where visualization of embryos during development has allowed direct observation of the dynamic process of MTJ formation and skeletal muscle development [4]. As with other vertebrates, truncal skeletal muscle in the zebrafish is primarily derived from repeating structures called somites. The mesenchymal cells of the somite give rise to the myotome, which will differentiate into skeletal myocytes that span the length of the somite and insert into the fibrous sheaths that form at the anterior and posterior somite boundaries [5]. These muscle-matrix connections are the structural and functional equivalents of the MTJs that form in higher vertebrates [6].

Previous studies have determined that Eph/Ephrin signaling initiates integrin clustering along the nascent somite border concomitant with the earliest indication of border

formation and shortly after that fibronectin matrix is assembled. Integrins are cell-matrix adhesion molecules that form heterodimeric transmembrane units which bind to components of the extracellular matrix including collagen and fibronectin. Laminin is secondarily deposited at the somite boundary where it serves as a ligand for α -dystroglycan of the dystrophin-associated glycoprotein complex during progressive maturation of the MTJ [7]. A zebrafish model of Duchenne muscular dystrophy, the *sapje* mutant which has a truncating mutation of dystrophin, forms MTJs at the somite boundary but these attachments are unstable, leading to muscle detachment and myocyte death [8].

The finding of MTJ instability in the zebrafish model of DMD suggested that this may be an important mechanism of muscle injury in patients with this disorder. This was a somewhat unexpected finding as MTJs had been difficult to study in DMD patients or mammalian animal models which had focused on the effects of dystrophin loss on the composition and function of lateral muscle-ECM attachments within the costameres [9]. It also indicated that the formation and composition of myofibril-membrane attachments may be similar whether they form along the longitudinal axis of the cell at the MTJ or along the lateral aspect of the myocyte, where dystrophin and the dystrophin-associated glycoprotein complex are enriched. The lateral connections occur primarily at the costameres overlying the sarcomere at the level of the Z disk [2]. As with the MTJ, the transmembrane adhesive contacts at the costameres include the integrin-based and dystrophin-associated glycoprotein complexes. These transmembrane systems are linked to each other and to the actin cytoskeleton by an array of cytoskeletal adaptors including vinculin, talin, ILK, and filamin. The adaptor proteins regulate the adhesive properties of the connections and allow the scaffolding of signaling molecules at these sites.

What is not well understood is how these myocyte-ECM attachments are positioned and assembled relative to the underlying myofibrils, and whether or not these processes are similar for axial (MTJ) and radial (costameric) connections. In this paper, we used a zebrafish morphant phenotype with impaired MTJ formation and skeletal muscle disorganization [10] to examine the elements required for muscle-ECM attachment and for the coordination of myofibril organization across adjacent myocytes. We determined that the giant structural and signaling protein obscurin has an important role in promoting the organization of the extracellular matrix at the terminal ends of the myocyte and in supporting myofibril-membrane interactions that lead to alignment of myofibrils both within and across myocytes. As myocyte-extracellular matrix connections have critical roles in force transduction defining the processes that promote and sustain these connections will have important implications for the understanding the pathogenesis of, and developing new treatment strategies for, a range of myopathies and muscular dystrophies.

2. Methods

2.1. Zebrafish Maintenance and Breeding. Wild-type adult zebrafish were maintained as described previously [10, 11].

2.2. Morpholino Oligonucleotide Microinjection. The obscurin A antisense morpholino (MO2 from [12]) targeting the 5'UTR site and a standard control morpholino (5'-CCTCTTACCTCAGTTACAATTTATA-3') were designed by GENE TOOLS, LLC (Philomath, Ore, USA). The MOs were dissolved to a stock concentration of 3 mM in distilled water and diluted to 1.5 and 3 ng/nL. A 2.5 nL aliquot of diluted morpholinos were injected into 1–4-cell-stage embryos using a nanoliter 2000 injector (World Precision Instruments). A Leica MZ16F dissecting microscope equipped with DFC340 FX camera was used to visualize the embryos.

2.3. mRNA Injections. A *lyn-GFP* (pCS-memb-mCherry + *lyn-eGFP*) construct, kindly provided by Dr. Phil Elks (University of Sheffield), was linearized with NotI and capped mRNA was generated using the mMESSAGE mMACHINE SP6 kit (Ambion, Austin, Tex, USA). The *lyn-GFP* mRNA was injected at an amount of 62.5 pg/embryo alone and together with obscurin A morpholino. A pCS2 + *itga5emGFP* construct, kindly provided by Dr. Scott Holley (Yale University), was linearized with NotI and transcribed with SP6 polymerase using the mMESSAGE mMACHINE SP6 kit from Ambion. The *itga5-GFP* mRNA was injected at a 250 pg/embryo amount alone and together with obscurin A morpholino.

2.4. Wholmount Immunostaining and In Situ Hybridization. Embryos were fixed for 6 hr with 4% paraformaldehyde (PFA) in PBS and labeled with the following antibodies: obscurin (directed at the C terminal region where the small ankyrins bind (kindly provided by Dr. Robert Bloch, University of Maryland)) 1 : 10, fibronectin (Sigma) 1 : 50, laminin (Sigma) 1 : 50, F59 (Developmental Hybridoma Bank, University of Iowa) 1 : 10, α -actinin (Sigma) 1 : 100, vinculin (Sigma) 1 : 50, talin (Sigma) 1 : 50, dystrophin (Clone MANDRA1, Sigma) 1 : 50, and α -dystroglycan (Millipore) 1 : 20. Secondary antibodies Alexa 640, Alexa 594, and Alexa 488 from Molecular Probes were diluted to 1 : 150 to reveal staining. Embryos were mounted onto slides using ProLong Gold Antifade Reagent (Molecular Probes) and visualized on an Olympus FV-500 confocal microscope. Digoxigenin-labeled antisense RNA probes were synthesized from cDNA clones of *MyoD*, *Notc5*, *Notch6*, and obscurin A by *in vitro* transcription using T3 and T7 polymerases and DIG RNA labeling kit (Boehringer-Mannheim). Embryos were fixed in 4% PFA for 5 hours at room temperature and subjected to *in situ* hybridization with the above RNA probes. Stained embryos were visualized on an Olympus BX-51 light microscope.

2.5. RNA Isolation and RT-PCR. To determine the onset of obscurin A expression, total RNA was isolated from uninjected embryos at 3, 4.5, 6, 8.5, 10, 11.5, 13, 15, 24, 33, and 72 hours after fertilization (hpf) using Qiagen RNeasy Mini Kit (Qiagen Inc., USA). RNA concentration and purity was determined by optical density reading at 260 nm and the ratio of 260/280 nm absorbance, respectively. For all time points, with the exception of 8.5 hpf, a total of 75 ng RNA was used in a 25- μ L reaction volume to synthesize

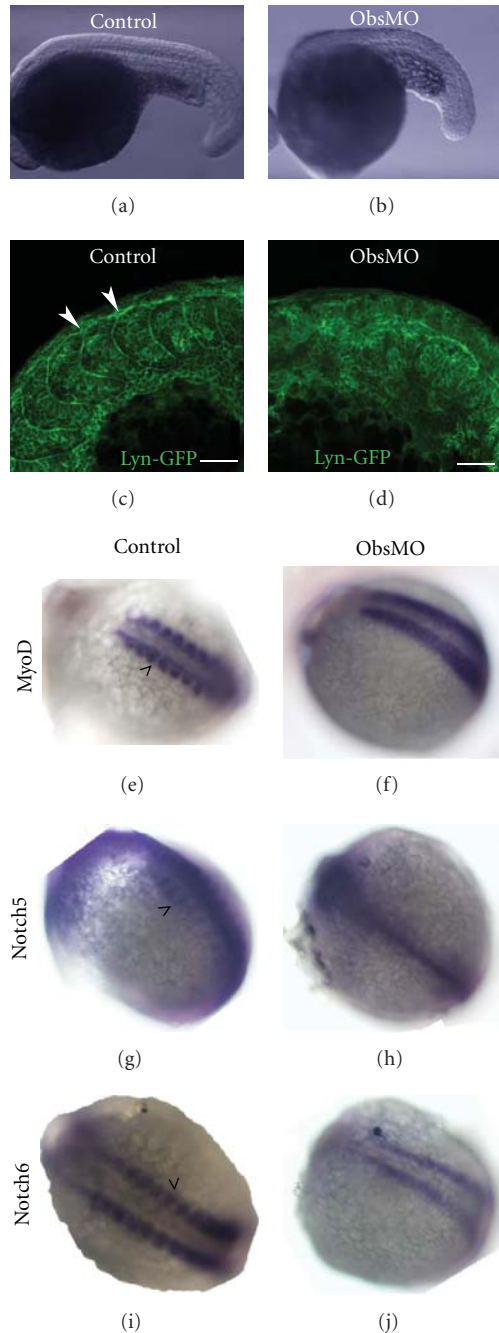


FIGURE 1: Obscurin A depletion results in abnormalities of myotome development. (a, b) Compared to control embryos at 20 hpf, an obscurin-A-depleted embryo (ObsMO) demonstrates shortening of the tail and indistinct somite boundaries. The skeletal muscle abnormalities are associated with irregularities of cell morphology as noted by cell membrane localization of lyn-GFP (c, d). Note that in control embryos, (c) lyn-GFP accumulates at the somite boundary (arrowheads). In morphant embryos (d), distinct somite boundaries are difficult to identify. (e–j) RNA *in situ* hybridization using riboprobes for *MyoD*, *Notch5*, and *Notch6* in control (e)–(i) and obscurin A (f), (h), (j) morphant embryos demonstrate maintained expression but diminished periodicity of these somite markers suggesting preserved myocyte commitment but impaired somite organization in the setting of obscurin depletion. Scale bars are 50 μm (a)–(d) and 500 μm (e)–(j).

cDNA using the iScript One-Step RT-PCR kit with SYBR green (Bio-Rad Laboratories, Hercules, Calif, USA). Due to a very low RNA concentration in the isolate, about 15 ng of RNA was used in the reaction mix for 8 hpf time point. A 350 bp (forward primer, 5'-GCCTGACCTGCG-CGATTGTGA; reverse primer, 5'-GAGCGCTGGGAGAGG-GAGGAC) and a 250 bp (forward primer, 5'GCACCAAAC-CCACCAAATCCA; reverse primer, 5'GCGCCCTCCTCA-TCCACACG), zebrafish obscurin A cDNA fragments were amplified by PCR. As a control, two reactions were prepared: one without RNA and one without reverse transcriptase. Zebrafish β -Actin (forward primer, 5'-CCGTGAACATCA-AGGAGAAGCT; reverse primer, 5'-TCGTGGATACCG-CAAGATTCC) was used as an internal control.

2.6. *Electron Microscopy*. Electron microscopy was performed as previously described [10]. Briefly, embryos at 72 hpf were fixed with 2.5% glutaraldehyde and 2.0% paraformaldehyde and postfixed in 1% osmium tetroxide. After washing, they were stained with saturated uranyl acetate and embedded in Epon 812. Ultrathin sections were prepared and stained with saturated uranyl acetate and lead citrate. The sections were examined with a Philips CM100 transmission electron microscope, at an accelerating voltage of 60 kV. The distance between the myofibrils in adjacent myocytes was measured from the transverse sections at the minimal distance between the two myofibrils. Z disk offset was measured in superficial myofibrils from two adjacent myocytes. In both control- and obscurin-depleted embryos, a minimum of 30 myocyte pairs were measured at 24 and 72 hpf.

3. Results

3.1. *Obscurin A Depletion Phenotype*. To examine the relationship between the myofibril and the organization of specialized membrane compartments during muscle development, we used a previously described morphant model [10] in which depletion of a myofibrillar protein, obscurin [13, 14], led to the impairment of the organization of the myotendinous junction, which is formed through the interactions of specialized membrane domain of the myocyte with the extracellular matrix. As previously noted, obscurin A morphant embryos were shorter, with marked abnormalities in tail and skeletal muscle morphology (Figure 1). These included both abnormalities of tissue architecture (irregular and deficient somite boundaries) and cellular organization (impaired SR organization, increased incidence of breaks in the transverse alignment of adjacent myofibrils, and irregularities of myofibril bundling) [10].

In obscurin morphant embryos, defects were noted in the developing myotome prior to the onset of myofibrillogenesis. Somite markers *MyoD*, *Notch5*, and *Notch6* were expressed in both the control and obscurin-A-depleted embryos, but the periodicity of their expression, namely, the absence of expression at the future somite boundaries, was impaired in the obscurin A morphants (Figure 1). Since this defect in myotome organization would suggest an important role

for obscurin A very early in skeletal muscle development, prior to the onset of myofibrillogenesis, we sought to precisely define the onset and localization of obscurin A expression very early in embryogenesis. Using RT-PCR, RNA *in situ* hybridization and whole mount immunostaining, we determined that obscurin A is expressed very early during somitogenesis and that it first localizes to the newly forming somite boundaries, see supplementary materials available at doi:10.1155/2011/479135 (Supplemental Figure 1).

To examine the role of obscurin A in promoting the changes in cell morphology that permit the formation of the somite boundary, control and obscurin A morphant embryos were injected with lyn-GFP mRNA and fixed at 18, 24, and 48 hpf. Lyn is a member of the Src family of receptor tyrosine kinases that is associated with cell surface receptors [15] and has been used to help track changes in cell morphology during development [16]. Lyn localized to the cell membranes of the developing myoblasts and accumulated at the nascent somite boundaries (Figure 2(a)). In the younger somites, myoblasts (future fast-twitch skeletal muscle) were rounded and began to elongate after the development of the somite boundary (Figure 2(b)), eventually spanning the distance between the anterior and posterior boundaries and inserting into the fibrous matrix forming at the boundary. In obscurin-A-depleted embryos, fewer nascent boundaries could be identified (Figure 2(d)). In the more severely affected embryos, the cells remained rounded and no defined boundaries were noted (Figure 2(g)). In the mildly affected embryos, irregular boundaries did form (Figure 2(e)) and were associated with local elongation of the adjacent cells. In the absence of a defined boundary, cells initially remained rounded (Figures 2(e) and 2(h)), eventually elongating in the more mature somites (Figures 2(e) and 2(f)). This suggests that somite boundary formation (and the associated extracellular matrix organization) promotes cell elongation but that cell elongation can progress in the absence of the somite boundaries potentially as a result of positional cues from surrounding cells.

3.2. Clustering of Integrins. Previous studies have noted that integrin clustering precedes fibronectin matrix accumulation at the nascent somite boundary [17] and helps facilitate tissue remodeling during development by translating cell contact-mediated signals into cellular cytoskeletal reorganization. Therefore, we examined the localization of $\alpha 5$ -integrin, which participates in somite boundary formation [18, 19] during early skeletal muscle differentiation. Using a GFP-tagged $\alpha 5$ -integrin expression construct, we noted that $\alpha 5$ -integrin clustering at the nascent somite boundary closely preceded organization of the fibronectin matrix and elongation of the cells at the developing boundary (Figure 3). As noted previously, depletion of the giant protein obscurin with a morpholino targeting the 5' untranslated region of the obscurin A isoform resulted in marked abnormalities of somite boundary and MTJ formation [10]. This provided unique opportunity to observe the progression of MTJ maturation and define the elements required for the process. Depletion of obscurin revealed that integrin clustering, fibronectin organization, and cellular remodeling are closely

interrelated processes. In response to obscurin depletion, integrin clustering was impaired resulting in diminished fibronectin matrix organization and abnormalities of cell morphology. In those regions with preserved integrin clustering, a fibronectin matrix was organized and cells began to elongate. In the absence of integrin clustering, there was no organization of a fibronectin matrix and cells remained rounded. This is consistent with prior studies which have proposed that cytoskeletal actin reorganization and cellular remodeling during myoblast differentiation are dependent on the organization of the fibronectin matrix [20]. The findings also suggest that obscurin, which is expressed at very low levels prior to myoblast differentiation, may have a role in supporting the early cellular events that lead to apical clustering of integrins.

3.3. Organization of the Fibronectin Matrix and Its Relationship to Nascent Myofibrils. Given the potential role of fibronectin in determining myocyte morphology and skeletal muscle organization [20], the relationship between fibronectin organization and new myofibril assembly was examined during early skeletal muscle differentiation. Fibronectin was organized first immediately adjacent to the notochord, prior to the appearance of a clear striated pattern of myosin heavy chain or α -actinin immunostaining in assembling myofibrils of slow-twitch skeletal muscle. Alpha-actinin appeared first as closely and irregularly spaced punctuate spots that were gradually organized into distinct Z disk structures in the more mature somites (data not shown). In contrast, very early in myofibrillogenesis, myosin heavy chain II (sarcomeric myosin) was diffusely distributed along the length of the myofibril (Figure 4). As myofibril assembly progressed, myosin becomes restricted to nascent A bands before demonstrating the double-banded pattern with mid-A-band clearing characteristic of mature F59 antibody-staining pattern which recognizes an epitope within the myosin motor domain. In response to obscurin depletion, there was a normal progression of M band organization despite the noted irregularities of fibronectin matrix deposition and myocyte morphology. Of note, in response to obscurin depletion, there was delayed bundling of nascent myofibrils into larger units even at relatively advanced stages of myofibrillogenesis, A bands from adjacent myofibrils remained spatially distinct. The delayed structural integration of adjacent myofibrils is consistent with the abnormalities in the lateral alignment of myofibrils that was previously noted in response to obscurin depletion [10]. Therefore, fibronectin matrix organization precedes the formation of mature, striated myofibrils, and despite the effects of obscurin on the fibronectin matrix, the progression of thick filament organization proceeds to structural maturity.

3.4. Deposition of Laminin. Laminin deposition at the MTJ closely followed fibronectin organization and persisted after fibronectin downregulation (Figure 5). In embryos subject to obscurin depletion, fibronectin matrix organization was severely reduced. In contrast, while laminin deposition was irregular, it did accumulate normally in those regions where fibronectin was detected. This indicates that fibronectin

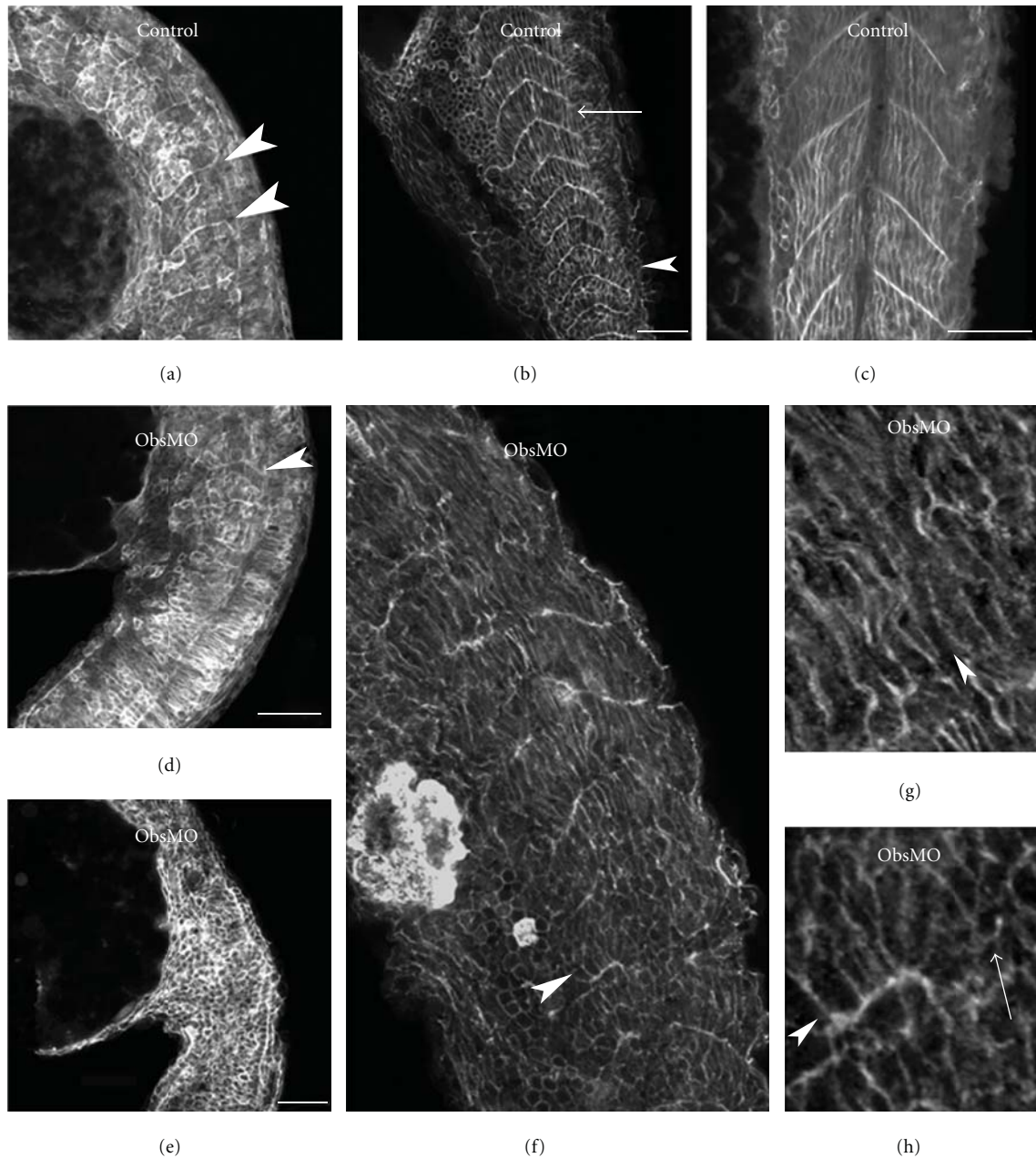


FIGURE 2: Obscurin A depletion results in abnormalities in the tissue architecture of skeletal muscle. Control (a)–(c) and obscurin A morphant (d)–(h) embryos were injected with a mRNA encoding for lyn-GFP and fixed at 18 (a), (d), (g), 24 (b), (e)–(h), and 48 (c) hpf. (a) Lyn is incorporated into the membrane and accumulates along the somite boundaries as they form (arrowheads). (b) As the myocytes mature, they transition from rounded morphology (arrowhead) and elongate (arrow) to span the length of the developing myotome to insert into the ECM at the MTJ. (c) By 48 hpf, all the fast-twitch skeletal myocytes have elongated. (d) In response to obscurin depletion, only rare somite boundaries (arrowhead) were noted. (e) In a more severely affected obscurin morphant embryo, no nascent somite boundaries are detected and the myoblasts remain rounded. (f) As development proceeds in a mildly affected obscurin morphant embryo, patchy development of nascent MTJs reveals a close relationship between apical lyn accumulation and cell elongation (arrowhead). (g) In the more mature somites, myocyte elongation proceeds in the absence of apical lyn clustering (arrowheads). (h) In a younger somite, myoblast elongation (arrowhead) preferentially occurs at the site of apical lyn clustering while other cells remain rounded (arrow). Scale bars are 50 μm (a)–(f) and 10 μm (g), (h).

matrix organization supports and may be required for laminin deposition as has been previously suggested [5]. Furthermore, although obscurin participates in integrin clustering and fibronectin matrix organization, the subsequent

recruitment of laminin to areas of fibronectin accumulation is likely to be independent of obscurin A function. Laminin deposition preceded formation of striated myofibrils in fast-twitch skeletal muscle. In the regions of reduced,

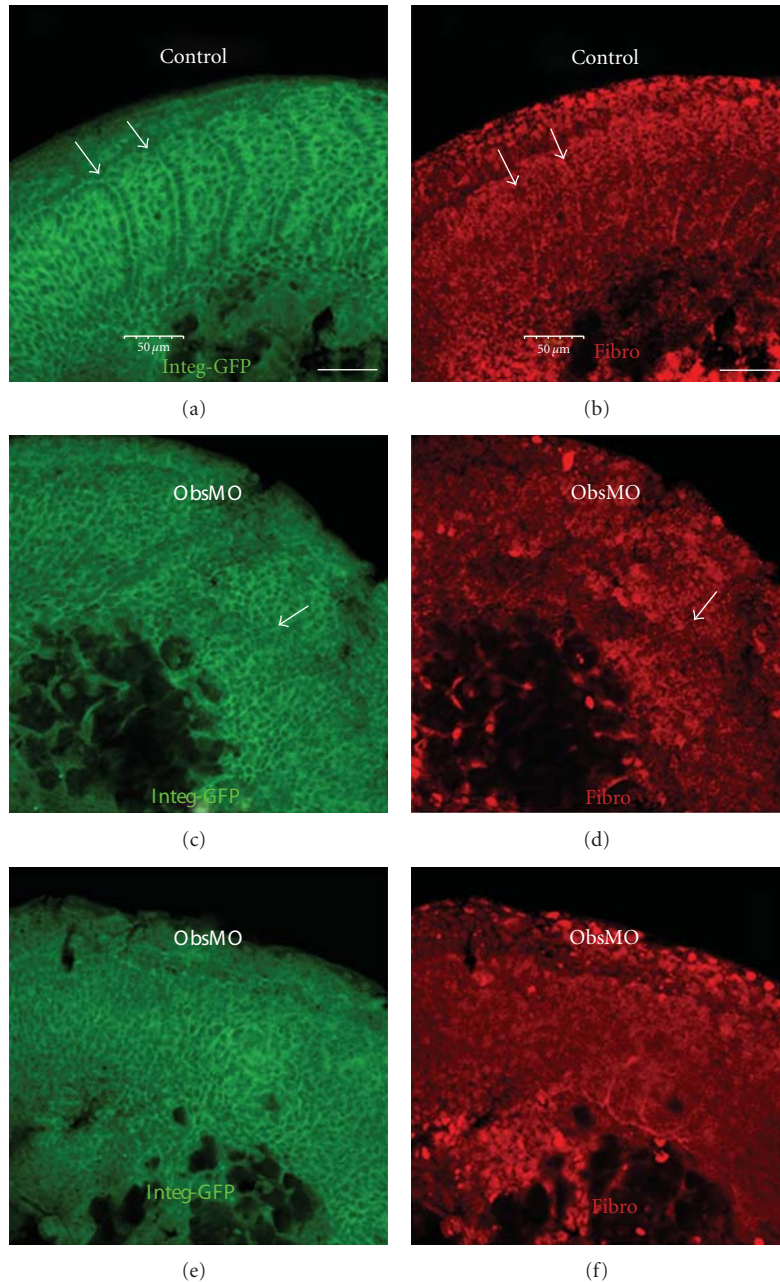


FIGURE 3: Integrin clustering is impaired in zebrafish embryos depleted of obscurin A. Zebrafish embryos were injected with GFP- $\alpha 5$ -integrin mRNA and then immunolabeled with anti-GFP (green: (a), (c), (e)) and antifibronectin (red: (b), (d), (f)) antibodies at 18 hours after fertilization (hpf). (a), (b) In control embryos, fibronectin matrix is organized at sites where $\alpha 5$ -integrin has clustered along a nascent somite boundaries (arrows). (c)–(e) In mildly affected (c), (d) and more markedly affected (e), (f) obscurin-A-depleted embryos, there is reduced apical clustering of integrins along nascent boundaries, although in the few instances where there is significant integrin clustering, fibronectin is organized ((c), (d): arrows). Scale bars are 50 μm .

fibronectin/laminin deposition, myofibrillogenesis appeared to be delayed, as regions with more abundant laminin deposition demonstrated more rapid development of mature myofibrils. However, by 72 hours, even those regions with markedly reduced laminin deposition demonstrated mature myofibril development.

3.5. Recruitment of Intracellular Adaptors to the Cell-ECM Adhesion Complex. To determine the order of incorporation

of other components of the adhesion complex and examine their relative distribution to MTJ and costameric sites, immunolocalization of talin and vinculin, components of the adherens junctions, was performed. Both talin and vinculin localized to the MTJ nearly concurrently with the timing of laminin deposition (Figure 6). However, as skeletal muscle differentiation preceded their localization, patterns were distinct. Talin was noted to localize very early to membrane domains, and potentially to cytoskeletal structures,

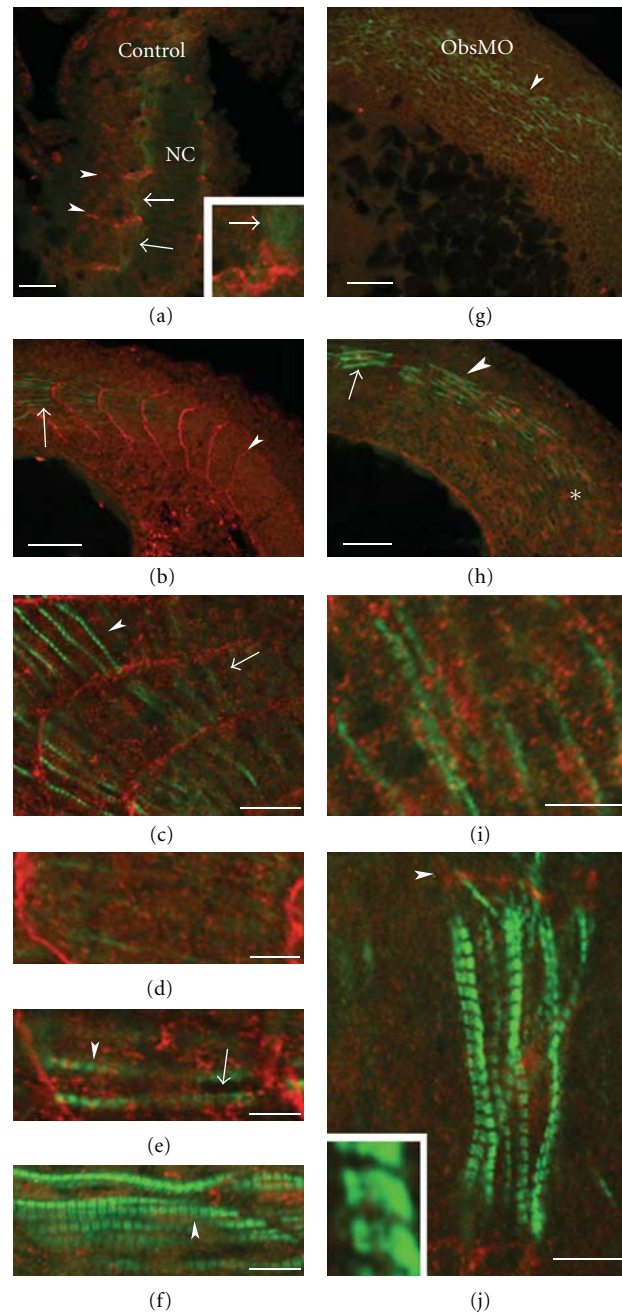


FIGURE 4: Organization of the fibronectin matrix precedes new myofibril assembly. Zebrafish embryos at 14 (a), 20 (b)–(e), (g), 24 (f), (h)–(j) hpf were immunolabeled for fibronectin (red) and slow-twitch myosin heavy chain (F59 antibody) (green). (a) Fibronectin organizes next to the notochord (NC) at nascent somite boundaries (arrowheads). Myosin heavy chain is still diffusely localized (arrows: (a) and inset) as the fibronectin matrix is organizing. (b) In a control embryo, the fibronectin matrix (arrowhead) is organized at the somite boundary before assembly of mature myofibrils in slow-twitch skeletal muscle of the younger somites at the right of the panel. (c) At higher magnification, continuous bands of myosin staining (arrow) are noted extending between the organized fibronectin matrix at either end of the myocytes before organizing into a striated pattern (arrowhead). (d)–(f) As development proceeds, MHC localization transitions from a diffuse distribution (arrows) along new myofibrils to a distinct restriction to the A band (arrowheads) and finally to a mature “double-banded” pattern ((f): arrowhead) with central clearing in the region of the future M band. By comparison, obscurin A depletion (g)–(j) affects fibronectin matrix organization and results in reduced organization of the MHC filaments. (g)–(j) Myofibril maturation can progress from immature myofibrils ((g), (h): arrowheads) to mature myofibrils ((h): arrow) even with a reduced and poorly organized fibronectin matrix (i). However, myofibrillogenesis proceeds more rapidly in regions with preserved fibronectin deposition ((j): arrowhead). Note the fibronectin organization at the terminal ends of the myofibrils (j). Lateral bundling of myofibrils appeared to be delayed in response to obscurin depletion as noted by the gaps between the A bands of neighboring but not yet fused myofibrils (inset of (j)). Scale bars are 50 μm (b), (h), 20 μm (a), and 10 μm (c), (d), (e), (f), (i), (j). Insets in (a) and (j) are 3x magnification of the larger image.

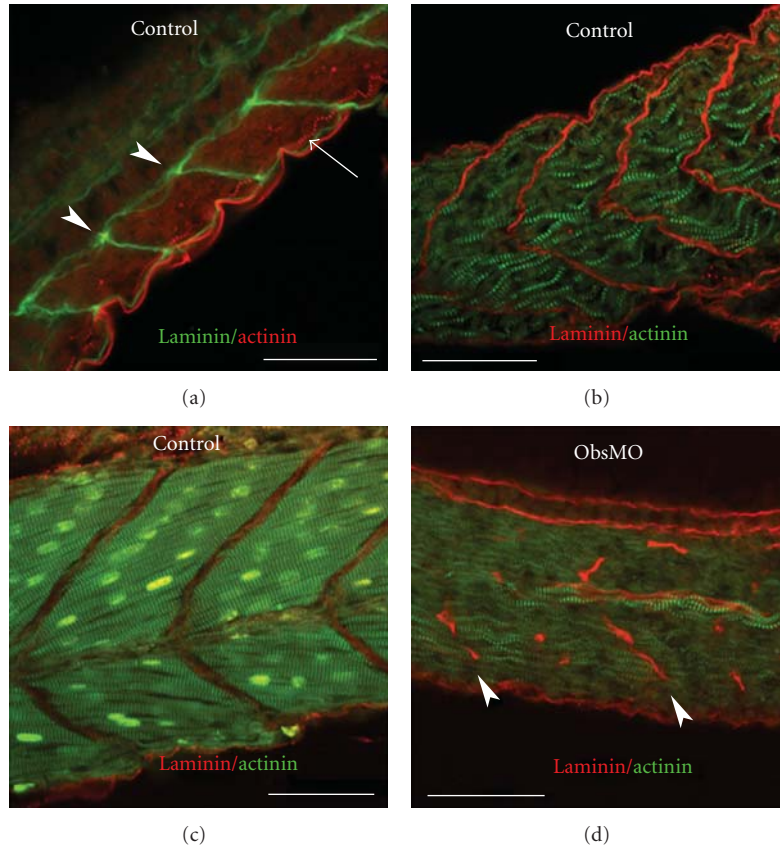


FIGURE 5: Laminin deposition precedes but is not a requirement for fast-twitch skeletal muscle myofibrillogenesis. Zebrafish embryos were immunolabeled for laminin ((a): green; (b), (c), (d): red) and α -actinin ((a): red; (b), (c), (d): green) at 20 (a), 24 (b), (d), and 48 (c) hpf. (a) A mature laminin matrix has formed at the somite/myotome boundaries (arrowheads) and along the surface of the myotome prior to fast-twitch skeletal muscle myofibrillogenesis. By this time, slow-twitch skeletal muscle has migrated to its superficial location within the myotome (arrow). As fast-twitch skeletal muscle myofibrillogenesis progresses, laminin persists at the somite boundary at 24 (b) and 48 (c) hpf. In response to obscurin A depletion (d), laminin accumulates normally at the irregularly localized and incomplete MTJs (arrowheads). Fast-twitch skeletal muscle myofibrillogenesis is delayed in the regions lacking laminin deposition but does eventually proceed. Scale bars are 50 μ m (a), (b), (d) and 30 μ m (c).

overlying the Z disk. In contrast, vinculin did not demonstrate significant striated patterning by 72 hours after-fertilization and instead became progressively more concentrated at the MTJ. Vinculin patterning in the obscurin morphant embryos was irregular in distribution but normal in its accumulation at the MTJ. Likewise, talin localized normally to domains overlying the Z disk and to the MTJ in obscurin morphant embryos. However, there were areas of laminin deposition that lacked significant talin accumulation suggesting a potential delay or irregularity in adhesion complex assembly in response to obscurin A depletion.

3.6. Localization of Dystrophin and α -Dystroglycan Is Obscurin A Dependent. Dystrophin is a cytoskeletal protein that links the actin cytoskeleton to the membrane-bound dystrophin-associated glycoprotein complex (DGC). α -DG, a member of DGC, is a cell surface receptor for various ECM molecules including laminins, agrin, and perlecan. Previous studies indicate that the DGC participates in the organization of, and attachment of the myocyte to, laminin on the cell surface. Since dystrophin and α -DG are impor-

tant components of the costameres and the myotendinous junctions, we examined their localization in control and obscurin A morphant embryos at 24 hpf (Figure 7). In control morpholino-injected embryos, both dystrophin and α -DG localized to the MTJ as has been previously noted [21, 22]. In obscurin-A-depleted embryos, however, the localization of dystrophin is less distinct and α -DG could not be detected at the somite boundaries. Since even the most severely affected obscurin A morphant embryos form irregular somite boundaries, the marked decrease in α -DG staining suggested a specific destabilization of the DGC in the obscurin morphants.

3.7. Obscurin A Depletion Results in Impaired Relationships between the Myofibril and Overlying Sarcolemma. It has been postulated that ankyrin within the sarcolemma and the subsarcolemmal spectrin cytoskeleton are involved in establishing the membrane microdomains overlying the superficial myofibrils [23]. Since obscurin A interacts with both ankyrin within the sarcolemma [12, 24, 25] and titin within the sarcomere [14, 26], it was a good candidate to link

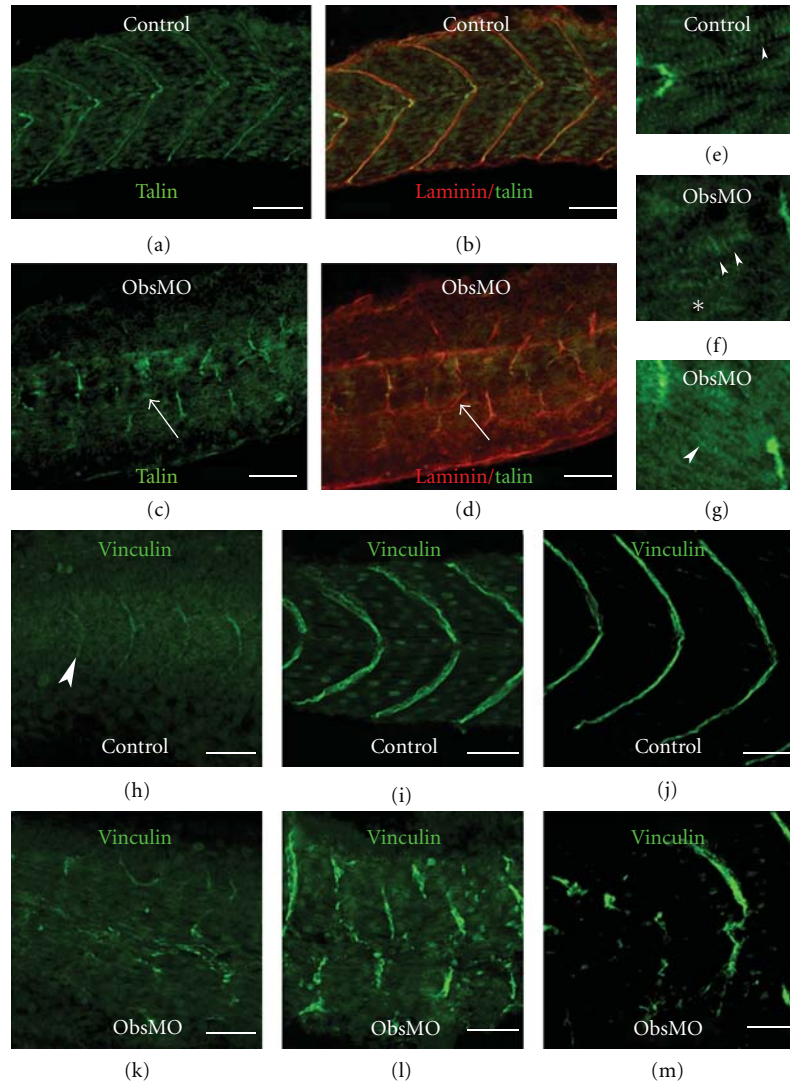


FIGURE 6: Overlapping localization of talin and vinculin during early skeletal muscle development. Control (a), (b), (e), (h)–(j) and obscurin A morphant (c), (d), (f), (g), (k)–(m) embryos were immunostained for talin ((a)–(g): green) and laminin ((b), (d): red) or vinculin ((h)–(m): green) at 24 (a)–(h), (k), 48 (i), (l), or 72 (j), (m) hpf. (a) In a control embryo, talin localizes to the MTJ and overlying the myofibrils at 24 hpf. (b) At the MTJ, talin localizes immediately adjacent to laminin. (c), (d) In obscurin A morphant embryos at 24 hpf, talin does localize to the irregularly organized MTJs but there are regions in which laminin has been deposited where talin has not yet accumulated (arrow). (e), (f) In control and obscurin A morphant embryos, talin localizes overlying the Z disk (arrowheads) although there are regions of diffuse talin localization in the morphant (asterisk) that were not noted in the control. (g) In newly forming myofibrils talin localizes along the myofibril (arrowhead) before achieving a striated pattern overlying the Z disk. No talin localization was noted overlying the mid-A-band. (h), (k) Like talin, vinculin localized to the somite boundary/MTJ ((h): arrowhead) at 24 hpf in both control (h) and morphant (k) embryos. (i), (l), (j), (m) By 48 hpf, there is progressive accumulation of vinculin at the MTJ in control (i) and morphant (l) embryos with nearly exclusive localization to the MTJ by 72 hpf in both control (j) and morphant (m) embryos. Scale bars are 50 μm . Panels (e)–(g) are 3x magnifications of the corresponding regions of (a), (c), and (d).

these two cellular compartments during early myofibril assembly. If obscurin A was required for this process, then its depletion might result in aberrant patterning of the sarcolemma overlying the myofibril and reduced association of the myofibril with the membrane. Examination of transverse sections of zebrafish skeletal muscle by transmission electron microscopy revealed that, as in control embryos (Figure 8(a)), new myofibril assembly in obscurin-A-depleted embryos occurred adjacent to the sarcolemma, preferentially at sites where three cells were in direct contact

(Figure 8(b)). However, there appeared to be reduced association of the myofibrils with the membrane, as new myofibril bundles were noted at a distance from the sarcolemma (Figures 8(c) and 8(d)). Patterning of internal membranes was also affected, as the sarcoplasmic reticulum was deficient, irregularly patterned and not consistently closely associated with the myofibrils in obscurin-depleted embryos.

Similar findings were noted on longitudinal sections. In control embryos, new myofibril assembly occurred in the subsarcolemmal space. Interestingly, there was a relatively

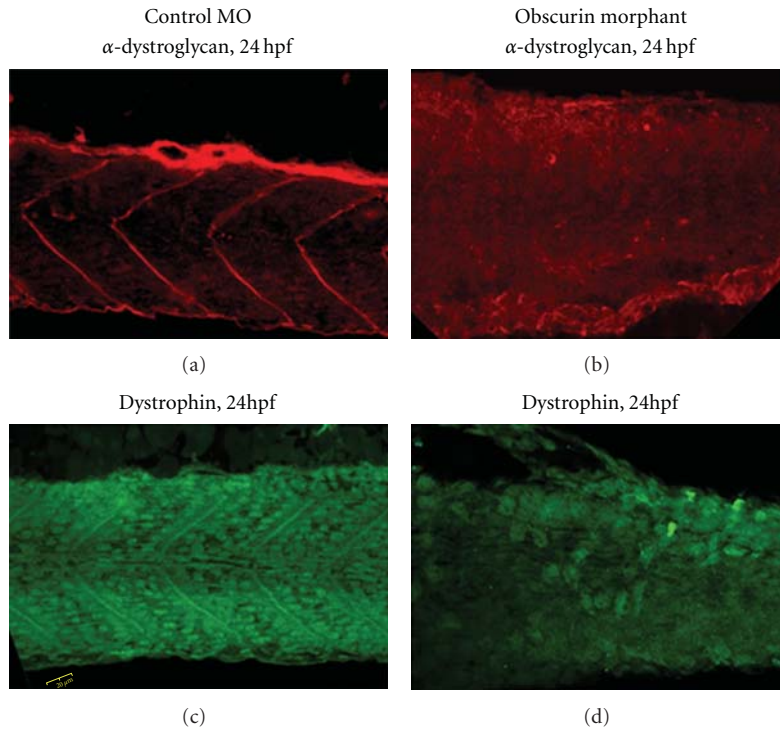


FIGURE 7: Obscurin depletion leads to marked reduction in localization of α -dystroglycan and dystrophin to the myotendinous junction. α -dystroglycan (α -DG) (a), (b) and dystrophin (c), (d) are abundant at the myotendinous junctions (MTJ) in control (a), (c) but not obscurin morphant embryos (b), (d). Note that in the obscurin-depleted embryos, α -DG and dystrophin are not noted even in the disorganized MTJs of the targeted embryos suggesting a specific destabilization of dystrophin-associated glycoprotein complex (DGC) in response to decreased obscurin expression.

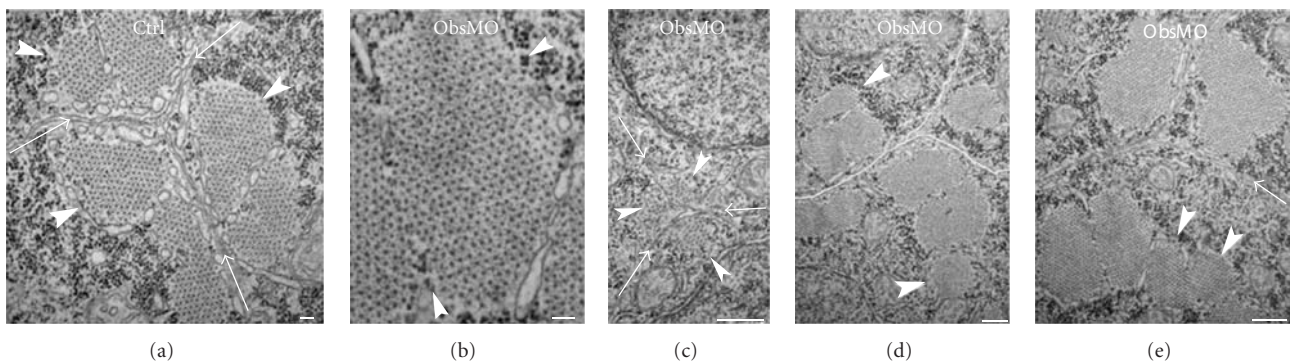


FIGURE 8: Obscurin depletion affects membrane-myofibril interactions. Skeletal muscle from 24 hpf zebrafish embryos were evaluated by transmission electron microscopy. (a) New myofibril assembly (arrowheads) occurs along the sarcolemma (arrows), preferentially at the intersection of three myocytes. Note the well-formed sarcoplasmic reticulum that encircles the new myofibrils. (b)–(e) In obscurin A morphant embryos, the sarcoplasmic reticulum is less well developed and less closely associated with the myofibril (b). Myofibril assembly still preferentially occurs at the sarcolemmal intersections ((c): arrowheads). However, frequent “internal myofibrils” form ((d): arrowheads) and distances between superficial myofibrils and the membrane increase ((e): arrowheads). Scale bars are 100 nm (a), (b) and 500 nm (c), (d).

consistent relationship between the superficial myofibrils of two adjacent cells. Although the distance from the myofibril to the membrane was variable, the distance between myofibrils in adjoining myocytes was within a relatively narrow range in control embryos (Figures 9(a) and 10(a)). In obscurin-depleted embryos, the relationship was much more variable (Figures 9(b)–9(d)). By 72 hpf, myofibrils filled

the sarcoplasm and the distance between the superficial myofibrils in adjoining cells had decreased in both control and obscurin-depleted embryos, although remained more variable in obscurin-depleted embryos (Figure 10(b)).

The coordination of myofibril assembly across myocytes included a consistent relationship between the level of the Z disks. While the myofibrils were not aligned precisely in

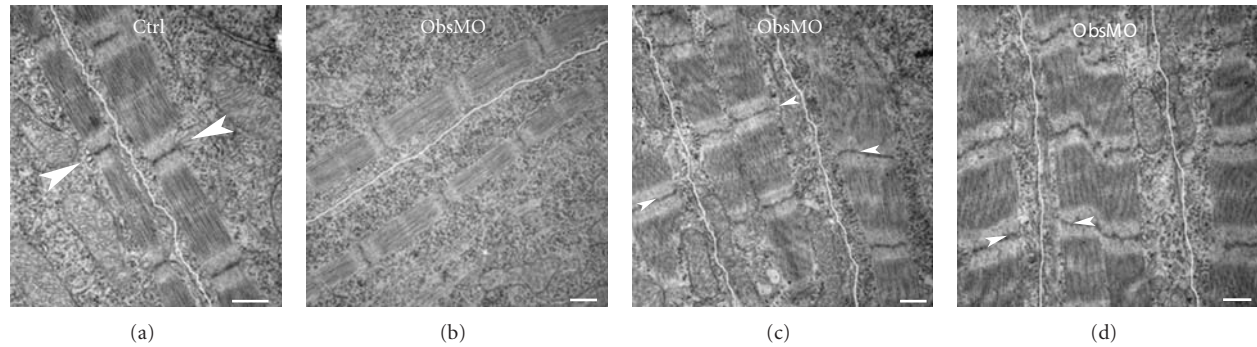


FIGURE 9: New myofibril assembly occurs along the sarcolemma with a consistent relationship between myofibrils in adjacent myocytes. Skeletal muscles from 20 hpf zebrafish embryos were evaluated by transmission electron microscopy. (a) In control (Ctrl) embryos, new myofibril assembly occurs along the sarcolemma (white line) with a slight offset in the alignment of the Z disks (arrowheads). (b)–(d) In obscurin morphant (ObsMO) embryos, myofibril assembly continues to occur adjacent to the sarcolemma (white lines) but there is a greater distance and a greater variability in the distance between superficial myofibrils in adjacent cells. There was also a greater variability in the alignment of Z disks across adjacent myocytes, ranging from very offset ((c): arrowheads) to nearly precisely aligned ((d): arrowheads). Scale bars are 500 nm.

register, the offset in the level of Z disks was within a relatively narrow range in control embryos but much more variable in obscurin-depleted muscle (Figures 9(a) and 10(c)). By 72 hpf, the Z disk offset had decreased in both control and obscurin-depleted embryos but remained more variable in the setting of diminished obscurin expression (Figure 10(d)).

Impairment of the coordination of myofibrillar architecture across myocytes also resulted in an inconsistent relationship between the axis of contraction in adjacent myocytes (Figure 11). In control embryos, the axis of contraction in adjacent myocytes was essentially parallel; the difference in axis of orientation between two adjacent myocytes (a myocyte pair) was $1.7 \pm 1.8^\circ$ in control embryos and $7.6 \pm 7.7^\circ$ in obscurin depleted embryos (*t*-test: $P < 0.01$). The impaired myocyte-myocyte relationships resulted in significant myocyte and myofibril disorganization across the muscle unit (Figures 11(b) and 11(c)).

4. Discussion

The assembly of new myofibrils within myocytes and the organization of the extracellular matrix surrounding the myocyte are dynamic and closely interrelated processes. Using a morphant phenotype with impaired MTJ formation and myofibril disarray, we examined the relationship between these processes during skeletal muscle development. We demonstrated that the organization of skeletal muscle during development is a highly orchestrated process that involves both outside-in and inside-out signals between the cell and the extracellular environment. Outside-in signals from the extracellular environment result in changes to myocyte morphology and promote new myofibril assembly; in return, inside-out signals organize the extracellular matrix and coordinate the assembly and organization of myofibrils across cells and tissues. Obscurin A appears to have an important role in these processes in zebrafish skeletal muscle, potentially mediating interactions between integrins and the ECM that regulate transmembrane communication and translate internal cellular structure into tissue organization.

Obscurin A is expressed early in the development, before somitogenesis begins, and our data indicate that it is required for the initial somite boundary morphogenesis. In the developing myotome, it initially localizes to the future somite boundary before localizing to newly assembling myofibrils that is form in the subsarcolemmal space. Expression patterns of MyoD, Notch5, and Notch6 indicate that loss of obscurin A disrupts somite segmentation but does not affect myotome specification or myoblast commitment. Colocalization of integrins and obscurin A at the future somite boundary, where myofibril assembly initiates, and along the sarcolemma, where the initiation and propagation of new myofibril assembly occurs, suggests that there may be an important relationships between integrins and obscurin A in promoting new myofibril assembly and organization. It has been proposed that integrin adhesion complexes along the lateral sarcolemma help nucleate new myofibril assembly. These early integrin-myofibril connections have been termed “protocostameres,” since they will ultimately develop into the multicomponent linkage complexes characteristic of mature costameres [27]. Integrin signaling may be capable of coordinating the assembly process in neighboring cells, as suggested by the consistent relationship of Z disks on either side of apposed sarcolemmal membranes very early in myofibrillogenesis. A coordinated patterning of the newly assembling myofibrils in neighboring cells mediated by integrin transmembrane contacts within the sarcolemma would account for consistent relationship of the sarcomeres from one myocyte to the next. The offset of the Z disks in adjacent myocytes was more evident early in development and could not be correlated with distance to the MTJ indicating that it was more likely to be an inherent property of the myocyte. The reason for the offset and the molecular mechanism that supports it is not known but integrins may have a role since transinhibition by integrins have been demonstrated to inhibit integrin clustering on neighboring cells [17]. This transinhibition may inhibit integrin clustering overlying the Z disk if it is at exactly the same level as the superficial Z disk of the myofibril in the neighboring myocyte.

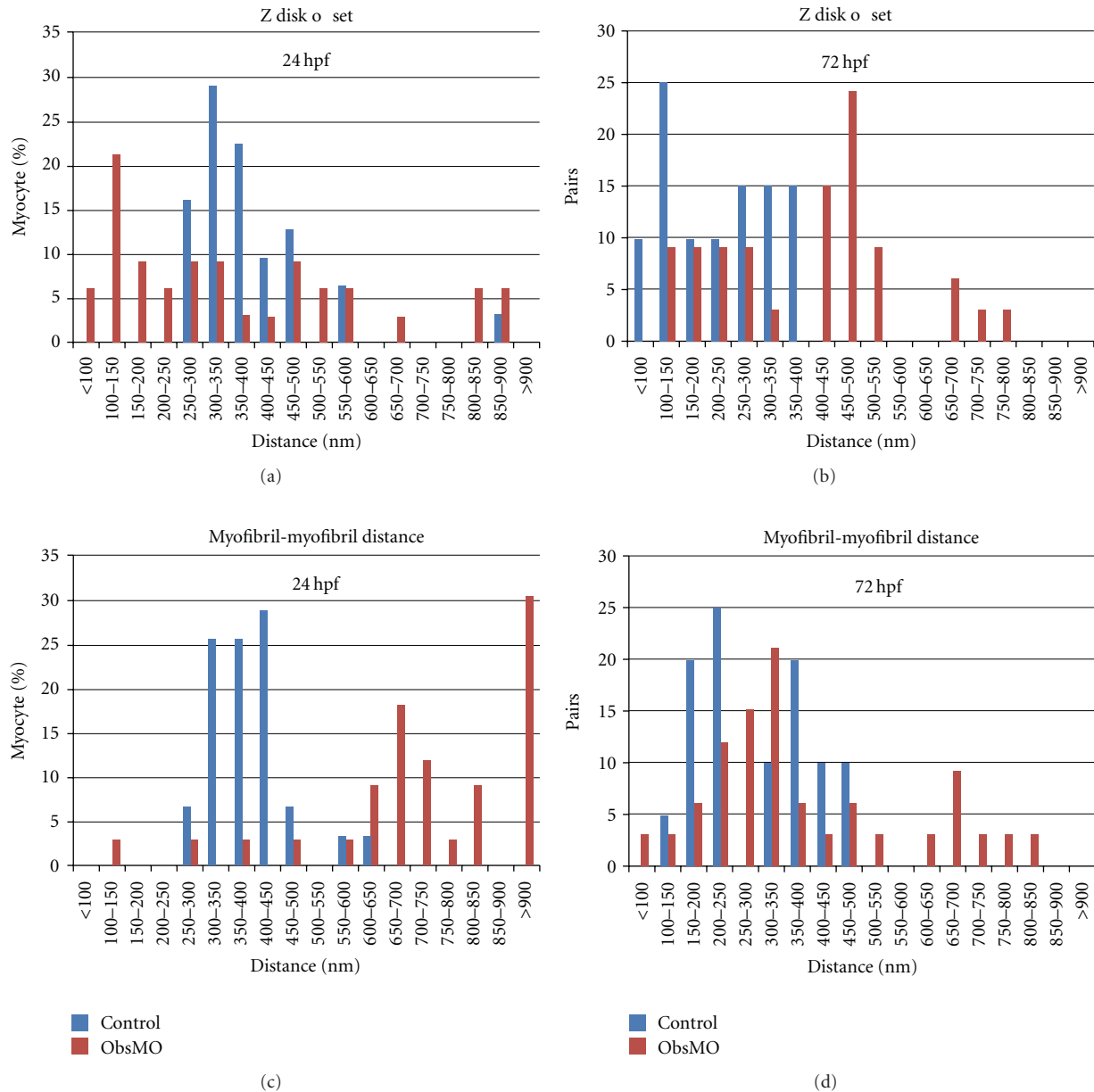


FIGURE 10: Obscurin depletion results in greater variability in the relationship between superficial myofibrils in adjacent myocytes. (a) At 24 hpf, obscurin morphant embryos (red bars) demonstrate a greater variability in Z disk alignment than control embryos (blue bars). Note that in the majority of myocyte pairs evaluated, the superficial myofibrils demonstrate a Z disk offset of approximately 250–500 nm in control embryos. (b) By 72 hpf, the Z disk offset has been significantly reduced in control embryos but was still quite variable in obscurin morphant embryos. (c) Similarly, at 24 hpf in control embryos (blue bars), there was a consistent distance between the superficial myofibrils in adjacent myocytes. However, in obscurin morphant embryos, the distance is significantly greater and more variable. (d) By 72 hpf, the distance between superficial myofibrils has been reduced in control and obscurin morphant embryos but remains more variable in the obscurin morphants.

The potential role of obscurin A in regulating integrin-based adhesion complexes is supported by studies on Unc-89. *C. elegans* mutants lacking Unc-89 have defects in M band assembly, thick filament organization and locomotion (leading to its classification as one of the *uncoordinated* family of proteins) [28, 29]. It has been noted to participate in the recruitment of actopaxin, a binding partner of the adherens junction adapter protein paxillin [30], to the

sarcolemma [31]. More recently, the kinase domains of Unc-89 were determined to interact with SCPL-1 [32, 33] which in turn has been demonstrated to complex with Lim-9 to interact with Unc-96 and Unc-97 (PINCH) [34], components of a cytoskeletal network that links integrin adhesion complex assembly [35] to thick filament organization [34] in *C. elegans*. That these integrin-based adhesion complexes participate in the transmission of force from the sarcomere

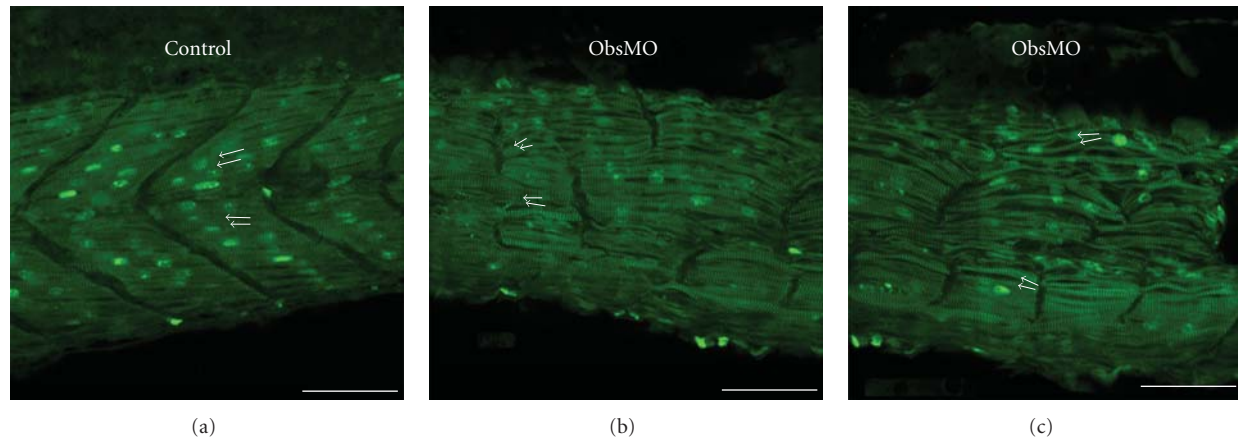


FIGURE 11: Obscurin depletion results in diminished alignment of myofibrils in adjacent myocytes. (a) At 48 hpf, myofibrils in adjacent myocytes are aligned (arrows) along a nearly identical axis of contraction. (b), (c) In obscurin morphant embryos, there is a loss of the precise parallel alignment (arrows) of myofibrils in adjacent myocytes. Scale bars are 50 μm .

to the extracellular environment to elicit movement has been supported by the genetic characterization of *C.elegans* mutant embryos, known as *pat* (for *paralyzed arrested at twofold*) mutants, with a paralyzed phenotype [36]. Mutations of beta integrin (*pat-3*), alpha integrin (*pat-2*), integrin-linked kinase (*pat-4*), and actopaxin (*pat-6*) all impair the assembly of integrin adhesion complexes and all result in a paralyzed phenotype [37]. In *C.elegans*, integrin complexes are found at the cytoplasmic interface of the dense bodies (corresponding to vertebrate Z disks) and the M bands [38]. In vertebrates, integrins are localized to the myotendinous junctions and to the costameres, sites of force transmission and signaling between the myocyte and the ECM. It is important to note that, although obscurin is primarily considered an M band protein, it localizes overlying the Z disk early in myofibril assembly [14] and some isoforms are noted at the Z disk or Z/I junction in mature myofibrils [39].

The importance of the integrin–fibronectin attachments to myofibril organization was demonstrated in two zebrafish models. In zebrafish embryos depleted of TGFBI, an extracellular matrix protein that binds to integrins and is expressed in response to TGF-beta signaling [16], skeletal muscle formed normal appearing MTJs and myofibrils assembled in the subsarcolemmal space but the myofibrils did not remain closely attached to the sarcolemma, and there was markedly reduced myofibril content. Similarly, zebrafish depleted of fibronectin demonstrated reduced myofibril content and organization [20] further supporting the role of integrin-mediated ECM adhesion as an important regulator of myofibril organization. The obscurin-A-depleted embryos demonstrated very similar findings, consistent with disturbance of the fibronectin-integrin-TGFBI axis. As with the TGFBI embryos, obscurin-depleted myofibrils formed but did not consistently remain closely associated with the membrane, and the resulting myocyte/myofibril disorder was reminiscent of embryos lacking fibronectin.

5. Conclusions

Our studies are consistent with the previously described models of new myofibril assembly which have proposed a multistep process by which myofibrils organize along the sarcolemma [40–42]. Our studies suggest that formation of new myofibrils in the subsarcolemmal space promotes coordinated organization of the myofibril, the overlying sarcolemma, and surrounding extracellular matrix. These interactions, which depend in part on obscurin, facilitate organization of myofibrils and myocytes across the muscle permitting efficient muscle contraction and striated muscle function. Such coordinate changes in myofibrillar and ECM remodeling will be important not only during development but in the adaptation of muscle (both cardiac and skeletal) to tissue injury or increases in physiologic demand. Therefore, the role of obscurin in facilitating interactions between the myofibril and the ECM through the sarcolemma indicates that it may be an important therapeutic target in preventing muscle injury and promoting muscle repair.

Acknowledgments

The authors would like to acknowledge Ashley Bieniek for her assistance with the care of the zebrafish. The work was supported by funds from the Aaron Stern Professorship (MWR) and the NIH (HL075093). We would like to thank Dr. Scott Holley and Dr. Robert Bloch for reagents and helpful comments.

References

- [1] R. J. Bloch, Y. Capetanaki, A. O'Neill et al., "Costameres: repeating structures at the sarcolemma of skeletal muscle," *Clinical Orthopaedics and Related Research*, no. 403, pp. S203–S210, 2002.
- [2] J. V. Pardo, J. D. Siliciano, and S. W. Craig, "A vinculin-containing cortical lattice in skeletal muscle: transverse lattice

- elements (“costameres”) mark sites of attachment between myofibrils and sarcolemma,” *Proceedings of the National Academy of Sciences of the United States of America*, vol. 80, no. 4 I, pp. 1008–1012, 1983.
- [3] E. M. McNally and P. Pytel, “Muscle diseases: the muscular dystrophies,” *Annual Review of Pathology*, vol. 2, pp. 87–109, 2007.
- [4] L. Durbin, C. Brennan, K. Shiomi et al., “Eph signaling is required for segmentation and differentiation of the somites,” *Genes and Development*, vol. 12, no. 19, pp. 3096–3109, 1998.
- [5] C. J. Snow and C. A. Henry, “Dynamic formation of microenvironments at the myotendinous junction correlates with muscle fiber morphogenesis in zebrafish,” *Gene Expression Patterns*, vol. 9, no. 1, pp. 37–42, 2009.
- [6] C. A. Henry, I. M. McNulty, W. A. Durst, S. E. Munchel, and S. L. Amacher, “Interactions between muscle fibers and segment boundaries in zebrafish,” *Developmental Biology*, vol. 287, no. 2, pp. 346–360, 2005.
- [7] B. D. Crawford, C. A. Henry, T. A. Clason, A. L. Becker, and M. B. Hille, “Activity and distribution of paxillin, focal adhesion kinase, and cadherin indicate cooperative roles during zebrafish morphogenesis,” *Molecular Biology of the Cell*, vol. 14, no. 8, pp. 3065–3081, 2003.
- [8] D. I. Bassett, R. J. Bryson-Richardson, D. F. Daggett, P. Gautier, D. G. Keenan, and P. D. Currie, “Dystrophin is required for the formation of stable muscle attachments in the zebrafish embryo,” *Development*, vol. 130, no. 23, pp. 5851–5860, 2003.
- [9] S. Ehmer, R. Herrmann, R. Bittner, and T. Voit, “Spatial distribution of β -spectrin in normal and dystrophic human skeletal muscle,” *Acta Neuropathologica*, vol. 94, no. 3, pp. 240–246, 1997.
- [10] M. O. Raeker, F. Su, S. B. Geisler et al., “Obscurin is required for the lateral alignment of striated myofibrils in zebrafish,” *Developmental Dynamics*, vol. 235, no. 8, pp. 2018–2029, 2006.
- [11] M. O. Raeker, A. N. Bieniek, A. S. Ryan, H. J. Tsai, K. M. Zahn, and M. W. Russell, “Targeted deletion of the zebrafish obscurin A RhoGEF domain affects heart, skeletal muscle and brain development,” *Developmental Biology*, vol. 337, no. 2, pp. 432–443, 2010.
- [12] P. Bagnato, V. Barone, E. Giacomello, D. Rossi, and V. Sorrentino, “Binding of an ankyrin-1 isoform to obscurin suggests a molecular link between the sarcoplasmic reticulum and myofibrils in striated muscles,” *Journal of Cell Biology*, vol. 160, no. 2, pp. 245–253, 2003.
- [13] M. W. Russell, M. O. Raeker, K. A. Korytkowski, and K. J. Sonneman, “Identification, tissue expression and chromosomal localization of human Obscurin-MLCK, a member of the titin and Dbl families of myosin light chain kinases,” *Gene*, vol. 282, no. 1-2, pp. 237–246, 2002.
- [14] P. Young, E. Ehler, and M. Gautel, “Obscurin, a giant sarcomeric Rho guanine nucleotide exchange factor protein involved in sarcomere assembly,” *Journal of Cell Biology*, vol. 154, no. 1, pp. 123–136, 2001.
- [15] Y. Yamanashi, S.-I. Fukushige, and K. Semba, “The yes-related cellular gene lyn encodes a possible tyrosine kinase similar to p56(lck),” *Molecular and Cellular Biology*, vol. 7, no. 1, pp. 237–243, 1987.
- [16] H. R. Kim and P. W. Ingham, “The extracellular matrix protein TGFBI promotes myofibril bundling and muscle fibre growth in the zebrafish embryo,” *Developmental Dynamics*, vol. 238, no. 1, pp. 56–65, 2009.
- [17] D. Julich, A. P. Mould, E. Koper, and S. A. Holley, “Control of extracellular matrix assembly along tissue boundaries via integrin and Eph/Ephrin signaling,” *Development*, vol. 136, no. 17, pp. 2913–2921, 2009.
- [18] S. Koshida, Y. Kishimoto, H. Ustumi et al., “Integrin α 5-dependent fibronectin accumulation for maintenance of somite boundaries in zebrafish embryos,” *Developmental Cell*, vol. 8, no. 4, pp. 587–598, 2005.
- [19] D. Julich, R. Geisler, S. A. Holley et al., “Integrin α 5 and delta/notch signaling have complementary spatiotemporal requirements during zebrafish somitogenesis,” *Developmental Cell*, vol. 8, no. 4, pp. 575–586, 2005.
- [20] C. J. Snow, M. T. Peterson, A. Khalil, and C. A. Henry, “Muscle development is disrupted in zebrafish embryos deficient for fibronectin,” *Developmental Dynamics*, vol. 237, no. 9, pp. 2542–2553, 2008.
- [21] M. J. Parsons, I. Campos, E. M. A. Hirst, and D. L. Stemple, “Removal of dystroglycan causes severe muscular dystrophy in zebrafish embryos,” *Development*, vol. 129, no. 14, pp. 3505–3512, 2002.
- [22] F. Bolanos-Jimenez, A. Bordais, M. Behra et al., “Molecular cloning and characterization of dystrophin and Dp71, two products of the Duchenne Muscular Dystrophy gene, in zebrafish,” *Gene*, vol. 274, pp. 217–226, 2001.
- [23] P. M. Bennett, A. J. Baines, M. C. Lecomte, A. M. Maggs, and J. C. Pinder, “Not just a plasma membrane protein: in cardiac muscle cells alpha-II spectrin also shows a close association with myofibrils,” *Journal of Muscle Research and Cell Motility*, vol. 25, no. 2, pp. 119–126, 2004.
- [24] A. A. Hopitzan, A. J. Baines, and E. Kordeli, “Molecular evolution of ankyrin: gain of function in vertebrates by acquisition of an obscurin/titin-binding-related domain,” *Molecular Biology and Evolution*, vol. 23, no. 1, pp. 46–55, 2006.
- [25] A. Kontrogianni-Konstantopoulos, E. M. Jones, D. B. Van Rossum, and R. J. Bloch, “Obscurin is a ligand for small ankyrin 1 in skeletal muscle,” *Molecular Biology of the Cell*, vol. 14, no. 3, pp. 1138–1148, 2003.
- [26] M. L. Bang, T. Centner, F. Fornoff et al., “The complete gene sequence of titin, expression of an unusual \approx 700-kDa titin isoform, and its interaction with obscurin identify a novel Z-line to I-band linking system,” *Circulation Research*, vol. 89, no. 11, pp. 1065–1072, 2001.
- [27] J. C. Sparrow and F. Schock, “The initial steps of myofibril assembly: integrins pave the way,” *Nature Reviews Molecular Cell Biology*, vol. 10, no. 4, pp. 293–298, 2009.
- [28] G. M. Benian, T. L. Tinley, X. Tang, and M. Borodovsky, “The *Caenorhabditis elegans* gene unc-89, required for muscle M-line assembly, encodes a giant modular protein composed of Ig and signal transduction domains,” *Journal of Cell Biology*, vol. 132, no. 5, pp. 835–848, 1996.
- [29] R. H. Waterston, J. N. Thomson, and S. Brenner, “Mutants with altered muscle structure in *Caenorhabditis elegans*,” *Developmental Biology*, vol. 77, no. 2, pp. 271–302, 1980.
- [30] S. N. Nikolopoulos and C. E. Turner, “Actopaxin, a new focal adhesion protein that binds paxillin LD motifs and actin and regulates cell adhesion,” *Journal of Cell Biology*, vol. 151, no. 7, pp. 1435–1447, 2000.
- [31] X. Lin, H. Qadota, D. G. Moerman, and B. D. Williams, “C. elegans PAT-6/actopaxin plays a critical role in the assembly of integrin adhesion complexes in vivo,” *Current Biology*, vol. 13, no. 11, pp. 922–932, 2003.
- [32] G. Xiong, H. Qadota, K. B. Mercer, L. A. McGaha, A. F. Oberhauser, and G. M. Benian, “A LIM-9 (FHL)/SCPL-1 (SCP) complex interacts with the C-terminal protein kinase regions of UNC-89 (obscurin) in *Caenorhabditis elegans* muscle,” *Journal of Molecular Biology*, vol. 386, no. 4, pp. 976–988, 2009.

- [33] H. Qadota, L. A. McGaha, K. B. Mercer, T. J. Stark, T. M. Ferrara, and G. M. Benian, "A novel protein phosphatase is a binding partner for the protein kinase domains of UNC-89 (obscurin) in *Caenorhabditis elegans*," *Molecular Biology of the Cell*, vol. 19, no. 6, pp. 2424–2432, 2008.
- [34] H. Qadota, K. B. Mercer, R. K. Miller, K. Kaibuchi, and G. M. Benian, "Two LIM domain proteins and UNC-96 link UNC-97/PINCH to myosin thick filaments in *Caenorhabditis elegans* muscle," *Molecular Biology of the Cell*, vol. 18, no. 11, pp. 4317–4326, 2007.
- [35] K. R. Norman, S. Cordes, H. Qadota, P. Rahmani, and D. G. Moerman, "UNC-97/PINCH is involved in the assembly of integrin cell adhesion complexes in *Caenorhabditis elegans* body wall muscle," *Developmental Biology*, vol. 309, no. 1, pp. 45–55, 2007.
- [36] B. D. Williams and R. H. Waterston, "Genes critical for muscle development and function in *Caenorhabditis elegans* identified through lethal mutations," *Journal of Cell Biology*, vol. 124, no. 4, pp. 475–490, 1994.
- [37] H. Qadota and G. M. Benian, "Molecular structure of sarcomere-to-membrane attachment at M-lines in *C. elegans* muscle," *Journal of Biomedicine and Biotechnology*, vol. 2010, Article ID 864749, 9 pages, 2010.
- [38] D. G. Moerman and B. D. Williams, "Sarcomere assembly in *C. elegans* muscle," *WormBook*, pp. 1–16, 2006.
- [39] A. L. Bowman, A. Kontrogianni-Konstantopoulos, S. S. Hirsch et al., "Different obscurin isoforms localize to distinct sites at sarcomeres," *FEBS Letters*, vol. 581, no. 8, pp. 1549–1554, 2007.
- [40] J. W. Sanger, J. Wang, B. Holloway, A. Du, and J. M. Sanger, "Myofibrillogenesis in skeletal muscle cells in zebrafish," *Cell Motility and the Cytoskeleton*, vol. 66, no. 8, pp. 556–566, 2009.
- [41] A. Du, J. M. Sanger, and J. W. Sanger, "Cardiac myofibrillogenesis inside intact embryonic hearts," *Developmental Biology*, vol. 318, no. 2, pp. 236–246, 2008.
- [42] J. W. Sanger, S. Kang, C. C. Siebrands et al., "How to build a myofibril," *Journal of Muscle Research and Cell Motility*, vol. 26, no. 6–8, pp. 343–354, 2005.

Research Article

Diffusion Tensor MRI to Assess Damage in Healthy and Dystrophic Skeletal Muscle after Lengthening Contractions

Alan B. McMillan,¹ Da Shi,¹ Stephen J. P. Pratt,² and Richard M. Lovering²

¹Department of Diagnostic Radiology, University of Maryland School of Medicine, Baltimore, MD 21201, USA

²Department of Orthopaedics, University of Maryland School of Medicine, Baltimore, MD 21201, USA

Correspondence should be addressed to Richard M. Lovering, rlovering@som.umaryland.edu

Received 13 May 2011; Revised 2 July 2011; Accepted 4 August 2011

Academic Editor: Robert J. Bloch

Copyright © 2011 Alan B. McMillan et al. This is an open access article distributed under the Creative Commons Attribution License, which permits unrestricted use, distribution, and reproduction in any medium, provided the original work is properly cited.

The purpose of this study was to determine if variables calculated from diffusion tensor imaging (DTI) would serve as a reliable marker of damage after a muscle strain injury in dystrophic (*mdx*) and wild type (WT) mice. Unilateral injury to the tibialis anterior muscle (TA) was induced *in vivo* by 10 maximal lengthening contractions. High resolution T1- and T2-weighted structural MRI, including T2 mapping and spin echo DTI was acquired on a 7T small animal MRI system. Injury was confirmed by a significant loss of isometric torque (85% in *mdx* versus 42% in WT). Greater increases in apparent diffusion coefficient (ADC), axial, and radial diffusivity (AD and RD) of the injured muscle were present in the *mdx* mice versus controls. These changes were paralleled by decreases in fractional anisotropy (FA). Additionally, T2 was increased in the *mdx* mice, but the spatial extent of the changes was less than those in the DTI parameters. The data suggest that DTI is an accurate indicator of muscle injury, even at early time points where the MR signal changes are dominated by local edema.

1. Introduction

The muscular dystrophies (MDs) are a heterogeneous group of inherited disorders characterized by progressive weakness and degeneration of skeletal muscles. Duchenne muscular dystrophy (DMD), the most common form of MD, is an X-linked disorder that was first described over a century ago [1]. DMD is caused by the absence of dystrophin, a 427 kDa protein found on the cytoplasmic surface of the plasma membrane of muscle fibers (the sarcolemma) in skeletal and cardiac muscle. It is well established that the absence of dystrophin leads to the impaired linkage between the cytoskeleton and the extracellular matrix protein laminin, which is thought to result in fragility of the sarcolemma and a disruption in the proper transmission of force during contraction.

Muscle strains are one of the most common complaints treated by physicians [2]. When an activated muscle lengthens because the external load exceeds the tension generated by the muscle contraction, this is termed a lengthening (“eccentric”) contraction. The force generated during a max-

imal lengthening contraction is at least twofold the force developed during a maximal isometric contraction; therefore lengthening contractions are more likely to produce damage than either isometric or concentric contractions [3]. Eccentric contractions are especially harmful to dystrophic muscle [4, 5].

Plain films, or X-rays, are not very useful for imaging muscle pathology, unless heterotopic bone formation has occurred within the muscle. Diagnosis of acute muscle strains is still typically made based on physical examination and patient history, but muscle injuries can be detected with MR imaging methods [6]. As noninvasive technology continues to improve and imaging, such as magnetic resonance imaging (MRI), becomes more commonplace, these tools will play a greater role in diagnosis, prognosis, and in rehabilitation planning [7]. Unlike X-rays, MRI offers superb tissue contrast and has high sensitivity to the hemorrhage and edema that follow muscle injuries. This, together with the capability to evaluate multiple arbitrary anatomic planes, make it the ideal technique to evaluate muscle injuries. Because of the similarities between muscle injury and muscle

disease, MRI may yield useful information for both of these conditions.

Conventionally, muscle strains are revealed best by T2-weighted MRI images, which optimize contrast between injured muscles with edema (increased signal intensity) and normal uninjured muscles. More recently, diffusion tensor imaging (DTI) has been explored as a more accurate marker for muscle damage compared to T2-weighted MRI [8]. The variables obtained with DTI, at least in other tissues such as the brain [9], show a strong and rapid response to damage, whereas the T2 signal can take a prolonged period to change. DTI is based on measurement of the apparent diffusion of water in tissues. Self-diffusion of water in tissue is restricted by membranes, resulting in an apparent diffusion coefficient (ADC) that is lower than the free diffusion coefficient and is orientation dependent for elongated structures. In short, DTI can be used to determine the three-dimensional architecture of skeletal muscle [10, 11] as well as provide useful information regarding muscle damage [12].

The purpose of this study was to determine if measurements obtained from DTI would serve as a reliable marker of damage after a muscle strain injury in dystrophic (*mdx*) and control mice. We hypothesize that DTI biomarkers would provide a more informative assessment of muscle injury than T2 and that these measures will further elucidate the increased susceptibility to injury of the *mdx* model.

2. Materials and Methods

2.1. Injury. All protocols were approved by the University of Maryland Institutional Animal Care & Use Committee (IACUC). The injury model results in a significant and reproducible injury and has been described in detail previously [13–16]. Briefly, 5 adult healthy (C57BL/10ScSn) and 5 dystrophic (C57BLScSn-DMD^{*mdx*}) male mice were purchased (The Jackson Laboratory, Bar Harbor, Me) and were approximately 8 weeks old at the start of experiments. Before each injury protocol, mice were anesthetized (~4–5% isoflurane in an induction chamber, then ~2% isoflurane via a nosecone for maintenance) using a precision vaporizer (cat no. 91103, Vet Equip, Inc, Pleasanton, Calif). Sterile ophthalmic cream (Paralube Vet Ointment, PharmaDerm, Floham Park, NJ) was applied to each eye to protect the corneas from drying. During the procedure, the animal was kept warm by use of a heat lamp.

With the animal supine, the hindlimb was stabilized, and the foot was secured onto a plate, the axis of which was attached to a stepper motor (model T8904, NMB Technologies, Chatsworth, Calif) and a torque sensor (QWFK-8M, Sensotec) to measure torque. The fibular nerve was stimulated via subcutaneous needle electrodes (J05 Needle Electrode Needles, 36BTP, Jari Electrode Supply, Gilroy, Calif), and proper electrode position was determined by a series of isometric twitches. Impulses generated by an S48 square pulse stimulator (Grass Instruments, West Warwick, RI) were 1 ms in duration and passed through a PSIU6 stimulator isolation unit (Grass Instruments, West Warwick, RI). In addition to visual confirmation of isolated dorsiflexion,

an increase in twitch torque in response to increasing voltage indicated that opposing plantarflexor muscles were not being simultaneously stimulated [17].

The majority of torque produced by the dorsiflexors is from the tibialis anterior muscle (TA) [18], and we have shown previously that this model results in injury to this muscle [15, 16, 19, 20]. A custom program based on commercial software (Labview version 8.5, National Instruments, Austin, Tex) was used to synchronize contractile activation and the onset of ankle rotation. Injury resulted from 10 forced lengthening (plantarflexion) contractions through a 0°–70° arc of motion (with the foot orthogonal to the tibia, considered 0°). A sham procedure was performed whereby the identical protocol was performed (including stimulation), but without lengthening.

2.2. Outcome Measures. A maximal isometric contraction (200 ms duration) of the dorsiflexors was used to measure maximal torque before injury. For each animal, maximal isometric torque was also measured 5 minutes after injury (to measure force lost due to injury). All isometric contractions were performed with the ankle at 20° into plantarflexion, a position that results in optimal force production.

2.3. In Vivo Imaging. High resolution MRI (magnetic resonance imaging) was performed on a Bruker Biospin (Billerica, Mass) 7.0 Tesla MR system equipped with a 12 cm gradient insert (660 mT/m maximum gradient, 4570 T/m/s maximum slew rate) running Paravision 5.0 software to assess muscle damage on the day of injury. An MR-compatible small-animal monitoring and gating system (SA Instruments, Inc.) was used to monitor respiration rate and body temperature. Body temperature was maintained at 36–37°C using a warm water circulator. A custom-made holder was used to position the mouse in the supine position with both legs parallel to the bore of the magnet from knee to foot. Two hours after injury [21], animals were placed inside the scanner, with a four-channel receive-only surface coil placed anterior to the TA. Anesthesia was maintained using 2% isoflurane and was adjusted to maintain a safe respiration rate.

After imaging localizers, the following MR scans were performed: T1-weighted rapid acquisition with relaxation enhancement (RARE) with the following parameters: TE = 9.52 ms, TR = 1800, echo train length = 4, NA = 8, in-plane resolution 100 × 100 μm, and slice thickness = 750 μm; dual echo PD/T2 RARE: TE = 19.0/57.1 ms, TR = 5000 ms, echo train length = 4, NA = 1, in-plane resolution 100 × 100 μm, and slice thickness = 750 μm. Spin echo (SE) diffusion tensor image data was acquired using 12 noncolinear directions: b -value = 350 s/mm⁻², TE = 26 ms, TR = 4500 ms, NA = 1, in-plane resolution 150 × 150 μm, and slice thickness = 750 μm. Multislice multiecho (MSME) T2 mapping image data was acquired in the same slice positions as the DTI data using 16 TEs = 11.4 ms to 182.5 ms with ΔTE = 11.4 ms, TR = 10000 ms, NA = 1, in-plane resolution 150 × 150 μm, and slice thickness = 750 μm.

T2 mapping was performed using custom software written in MATLAB (The Mathworks; Natick, Mass) using

nonlinear least squares to fit the measured data at each pixel to the canonical T2 signal equation. Diffusion tensor reconstruction and tractography was performed using TrackVis (Martinos Center for Biomedical Imaging; Massachusetts General Hospital; Boston, Mass) and MATLAB to calculate mean diffusivity (MD), fractional anisotropy (FA), radial diffusivity (RD), and axial diffusivity (AD) images. A region of interest (ROI) in the TA and tractography was used to guide bilateral segmentation of the TA. Diffusion tensor tractography was calculated using the fiber assignment by continuous tracking (FACT) method [22] with a termination criteria of an angle greater than 35° , followed by subsequent spline filtering. Tracts were restricted to those traveling through several transverse slices of manually traced regions of interest within each of the left and right TAs. This was used to create an image mask for each muscle, which was then divided into proximal, middle, and distal sections of approximately equal length. Finally, the masks were used to calculate average measurements of MD, FA, RD, AD, and T2 within each section of the injured and uninjured muscle. These measurements were compared between normal and dystrophic mice for both the uninjured and the injured side using a Wilcoxon Rank Sum test.

2.4. Histology. After MR and functional data were collected, anesthetized animals were fixed with 4% paraformaldehyde via perfusion through the left ventricle to preserve tissue morphology. TAs were harvested, weighed, snap frozen in liquid nitrogen, and then stored at -80°C . Animals not perfused fixed were euthanized by carbon dioxide inhalation followed by decapitation. To study the integrity of the muscle fiber membrane, additional mice ($n = 3$ each group) received an intraperitoneal injection of 1% Evans blue dye (EBD; Sigma, St. Louis, Mo) (wt/vol) in phosphate-buffered saline (PBS, pH 7.4) at a volume of 1% body mass (BM) (1 mg EBD/0.1 mL PBS/10 g BM). This solution was sterilized by passage through a Millex-GP 0.22 μm filter (Millipore, Bedford, Mass) and administered 24 h before death of the animal to assure a good signal [23]. EBD binds to albumin and is detected by fluorescence microscopy (at 568 nm) in the extracellular space. Presence of the protein-bound dye inside the muscle fiber indicates damage to the sarcolemma. Here, the sections were assessed blindly, and the myofibers were judged in a binary fashion, as positive or negative for intracellular EBD.

Transverse sections were cut on a cryostat (10 μm thickness) and collected onto glass slides (Superfrost Plus; VWR, West Chester, Pa). For EBD-injected tissue, myofibers with dye-labeled sarcoplasm were quantified in cross-sections under fluorescence optics [16, 24]. At least 400 fibers in 10 optical fields were assessed in 3 mice; results are expressed as percent labeled fibers. In sections from muscles without EBD, sections were stained with hematoxylin and eosin (H&E) for tissue evaluation. Sections were randomized and viewed at 100x magnification in a Zeiss Axioskop light microscope, and pictures were taken with a digital camera (AxioCam HR using AxioVision 3.0). Each optical field contained an

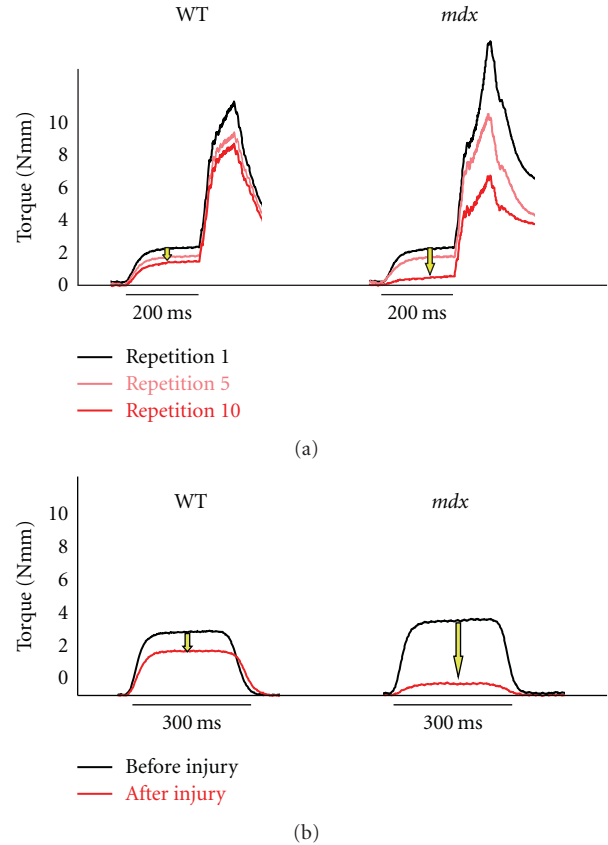


FIGURE 1: Mice lacking dystrophin are more susceptible to injury. Producing the injury, the fibular (aka peroneal) nerve was used to stimulate the dorsiflexor muscles supramaximally while moving the plate forced the foot into plantar flexion. Injury was induced by 10 large strain lengthening (“eccentric”) contractions through a 70° arc of motion. Maximal isometric torque was measured before and after injury in wild type (WT) and mice lacking dystrophin (*mdx*). The dorsiflexors were maximally activated isometrically for 200 ms prior to movement and then forcibly stretched through a 70° arc of plantarflexion at $900^\circ/\text{s}$. (a) Trace recordings of torque lengthening contractions (superimposed on a maximal lengthening contraction for 200 ms) for repetitions 1, 5, and 10 (black, pink, and red lines, resp.). (b) Maximal isometric torque was recorded at optimal length (L_0) before (black line) and after (red line) injury. Note that *mdx* muscles generate at least the same absolute force, but they consistently showed a significant drop in torque (yellow arrow) compared to the wild-type muscles, with an average loss of 85% compared to 32% ($P < 0.01$) in normal mice. Not only do the *mdx* muscles sustain more force loss, but this usually occurs very early in the protocol (after the first few, resp.). $*=P < 0.05$.

average of 38 ± 7 fibers, and more than 45 fields were counted per muscle.

3. Results

To induce injury in the tibialis anterior muscle (TA), we superimposed a lengthening contraction onto a maximal isometric contraction (Figure 1(a)). To assess the amount of injury, we measured maximal torque before and after

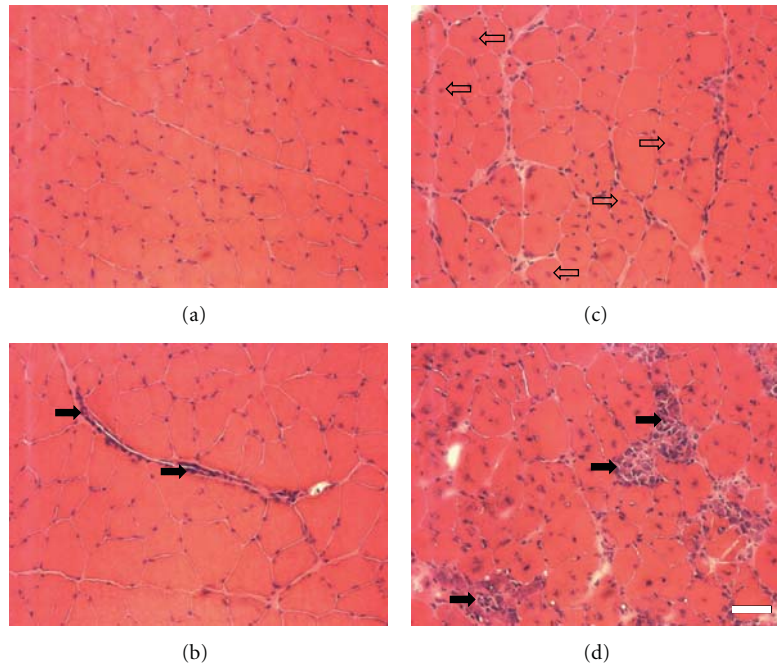


FIGURE 2: Histopathology related to injury. (a) cross-section of normal healthy TA muscle from a wild-type mouse. Skeletal muscle fibers are multinucleated and the nuclei stain blue; the sarcoplasm of each cell stains pink. (b) cross-section from a wild-type TA after injury. There was only minimal evidence of perivascular inflammation (arrows) in the wild-type tissue after injury. (c) cross-section from TA muscle of an *mdx* mouse. Even without injury, there is mild inflammation, slight increase in endomysial connective tissue, heterogeneity in fiber size, and many centrally nucleated fibers (CNFs, open arrows), all indicative of ongoing degeneration/regeneration within the muscle. (d) cross-section from an *mdx* TA after injury. Even with a protocol that produces mild changes in morphology to healthy muscle, the *mdx* muscle suffers much more damage, such as myonecrosis, myophagocytosis, and foci of inflammation surrounding individual muscle fibers (closed arrows). Scale bar = 40 μm .

injury (Figure 1(b)). While the mechanism of injury was identical between animals, the injury was much more severe in dystrophic mice, with an average force loss of 85%, compared to 42% ($P < 0.05$) in normal mice.

Histological changes paralleled functional changes to some extent. For H&E staining, there was only minimal evidence of perivascular inflammation in the wild-type tissue after injury (Figure 2(b)) compared to undisturbed healthy muscle (Figure 2(a)). Even without injury, centrally nucleated fibers, fiber size variation, mild inflammation, and slight increases in endomysial connective tissue in the uninjured *mdx* mice are all consistent with ongoing muscle damage and regeneration (Figure 2(c)). In contrast, the myonecrosis, myophagocytosis, and foci of inflammation surrounding individual muscle fibers seen in the injured *mdx* muscle (Figure 2(d)) are all consistent with acute muscle injury. The amount of membrane damage, as evidenced by the number of fibers with intracellular EBD, also reflected the magnitude of functional injury (Figures 3(a)–3(e)). In wild-type tissue sections (Figure 3(a)), there were few fibers that could be found to have intracellular EBD (1%); however after the relatively mild injury protocol (Figure 3(b)), the number of fibers with membrane damage did not increase significantly ($13 \pm 2\%$, $P < 0.06$). The uninjured *mdx* tissue (Figure 3(c)) already had a small amount of EBD-positive fibers ($11 \pm 4\%$, $P < 0.05$), but there was almost a 5-fold

increase in the number of fibers with membrane damage after injury ($49 \pm 8\%$, $P < 0.05$, Figure 3(d)).

MRI revealed a clear increase on the T2 signal after injury (Figures 4(a) and 4(b)). Quantitative changes in T2 are apparent in Figures 4(c) and 4(d), where the expected T2 signal was fit across multiple echo times in T2-weighted images [25]. There was no significant difference in parameters between the injured and uninjured leg in the normal mice. Further, there were no significant differences in any of the measured parameters for the TA between normal and dystrophic mice in the uninjured side. However, there were marked differences in parameters in the injured side between normal and dystrophic mice and between the injured and uninjured leg in the dystrophic mice (Table 1). As in prior studies [14], the sham animals did not have an increase in T2 signal by the time imaging was performed.

Figure 5 shows a representative picture of 3D tractography. When comparing parameter of diffusion on the injured side, dystrophic mice showed significantly increased MD and AD and decreased FA ($P < 0.05$) in the proximal and middle TA compared to wild-type uninjured mice. These differences were much more marked than the more limited differences we measured with T2. While not significant, RD trended toward increased values. These data are plotted against force loss in Figure 6. DTI tractography (see Figure 5, e.g.) was used to visualize the TAs.

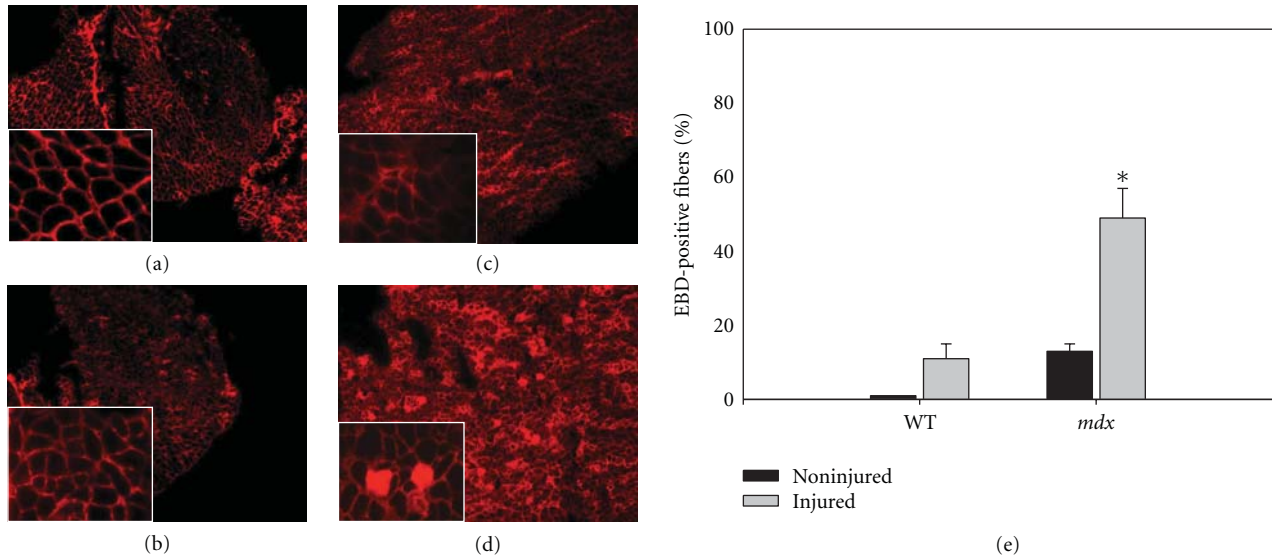


FIGURE 3: Membrane stability in muscle fibers before and after injury. Evans Blue Dye (EBD) was used to evaluate sarcolemmal integrity within the TA muscles of mice after injury. EBD is detected under fluorescence microscopy (568 nm, insets show high magnification) and the presence of the protein-bound dye inside the muscle fiber indicates damage to the sarcolemma. (a) cryosection of an uninjured wild-type TA muscle from animals injected with EBD. (b) cryosection of an injured wild-type TA; the injury protocol used here was not enough to cause significant membrane damage in wild-type muscle. (c) cryosection of an uninjured *mdx* TA from animals injected with EBD. (d) cryosection of an injured wild-type TA; intracellular EBD indicates damage to the sarcolemma, which occurred frequently in the *mdx* injured muscles. (e) Histogram showing quantification of EBD-positive fibers. Without injury, the number of EBD-positive (EBD+) fibers was not significantly different between wild type and *mdx*. Only the *mdx* animals showed a significant increase in the number of positively labeled fibers after injury. Scale bar = 200 μm . *: significant difference from noninjured, $P < 0.05$.

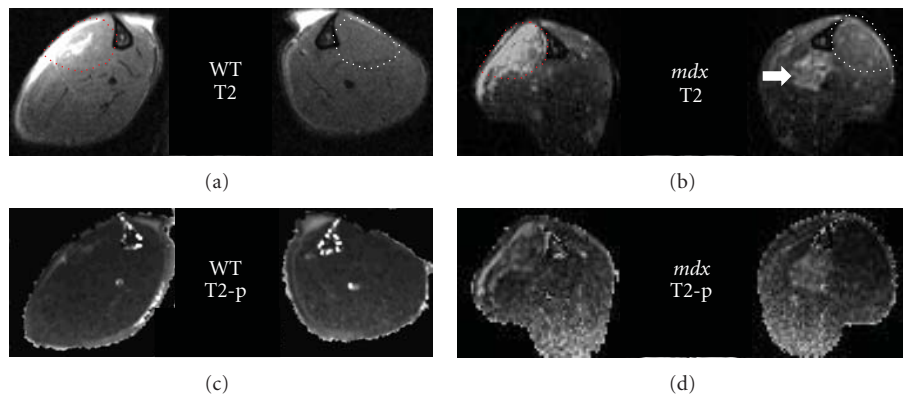


FIGURE 4: Representative T2-weighted and T2-parametric images. (a) Example of a T2-weighted image (T2) after injury in the wild-type (WT) mouse. The injured TA (dotted red circle) is easily discerned from the TA on the control side (dotted white circle) based on the increased T2 signal, presumably due to edema. (b) Even in noninjured *mdx* muscle, there are regions of hyperintensity (arrow), a characteristic finding in dystrophic muscle. (c-d) Example of a T2 parametric image (T2-p) after injury in the wild-type and *mdx* mouse.

4. Discussion

Since X-rays reveal little regarding skeletal muscle anatomy or function, muscle injury is still typically diagnosed by taking a history and performing a physical examination. However, modalities such as MRI are becoming more affordable and more commonplace, and there is a surge of interest in using them to learn more about both muscle injury and muscle disease. Acute muscle strain injury is a stochastic event, and that would not be ethical or desirable

to induce in human subjects; therefore most human studies involve imaging after “eccentric exercise” or “exertional muscle injury” (i.e., overuse type injuries). By using an established animal model to induce an acute contraction-induced injury, we were able to compare changes in muscle function, *in vivo* imaging, and histology shortly after injury. Our injury method clearly resulted in muscle damage, as indicated by the measurable loss of force, changes in H&E staining, and an uptake of EBD by injured muscle fibers, as well as marked changes in MRI parameters, especially DTI.

TABLE 1: Quantitative data between control (wild-type) and dystrophic (*mdx*) TA muscles without and with injury. Except for RD, all the calculated water diffusion characteristics were significantly altered ($P < 0.05$) after injury, and to a greater extent in *mdx* muscles. There was a trend toward increased RD, but this was not significant (NS) at $P < 0.05$.

	<i>mdx</i> noninjured versus wt noninjured	wt injured versus noninjured	<i>mdx</i> injured versus wt injured	<i>mdx</i> injured versus noninjured
Whole MD (mm ² /s)	NS	NS	† (0.00163 ± 0.00012 versus 0.00143 ± 0.000087)	† (0.00163 ± 0.00012 versus 0.00140 ± 0.00013)
Proximal MD (mm ² /s)	NS	NS	† (0.00165 ± 0.00011 versus 0.00143 ± 0.00012)	NS
Middle MD (mm ² /s)	NS	NS	† (0.00161 ± 0.00013 versus 0.00140 ± 0.00011)	NS
Distal MD (mm ² /s)	NS	NS	NS	NS
Whole AD (mm ² /s)	NS	NS	† (0.00139 ± 0.00010 versus 0.00118 ± 0.000056)	† (0.00139 ± 0.00010 versus 0.00113 ± 0.000011)
Proximal AD (mm ² /s)	NS	NS	† (0.00140 ± 0.000082 versus 0.00117 ± 0.000097)	† (0.00140 ± 0.000082 versus 0.00115 ± 0.000014)
Middle AD (mm ² /s)	NS	NS	† (0.00137 ± 0.00011 versus 0.00116 ± 0.000076)	† (0.00137 ± 0.00011 versus 0.00113 ± 0.000010)
Distal AD (mm ² /s)	NS	NS	NS	NS
Whole FA	NS	NS	† (0.287 ± 0.013 versus 0.329 ± 0.031)	† (0.287 ± 0.013 versus 0.349 ± 0.021)
Proximal FA	NS	NS	† (0.282 ± 0.017 versus 0.333 ± 0.015)	† (0.282 ± 0.017 versus 0.348 ± 0.040)
Middle FA	NS	NS	† (0.287 ± 0.018 versus 0.330 ± 0.027)	† (0.287 ± 0.018 versus 0.341 ± 0.022)
Distal FA	NS	NS	NS	NS
Whole RD (mm ² /s)	NS	NS	NS	NS
Proximal RD (mm ² /s)	NS	NS	NS	NS
Middle RD (mm ² /s)	NS	NS	NS	NS
Distal RD (mm ² /s)	NS	NS	NS	NS
Whole T2 (ms)	NS	NS	NS	NS
Proximal T2 (ms)	NS	NS	† (38.93 ± 2.57 versus 29.93 ± 5.35)	NS
Middle T2 (ms)	NS	NS	NS	NS
Distal T2 (ms)	NS	NS	NS	NS

Explanation of DTI parameters (apply to all but the last 4 lines, which report data for T2): MD: mean diffusivity; measure of total diffusion within a voxel; AD: axial diffusivity; diffusion along the longitudinal axis; FA: fractional anisotropy; the fraction of unidirectional diffusion; RD: radial diffusivity; diffusion occurring perpendicular to a track; T2: a time constant describing the exponential decay of signal.

There is a growing number of animal studies that use MRI to assess muscle injury; however, these include such methods as overuse (running downhill), myotoxins, denervation, hindlimb suspension reloading, and ischemia-reperfusion [8, 12, 26–31], rather than by acute muscle strain injury. This can make reproducibility and even relevance to functional outcome difficult to determine. Our *in vivo* animal model of injury provides several advantages, such as the ability to study exclusively one type of contraction (eccentric), to measure force directly from an individual muscle, and to characterize the biochemical and morphological state of the muscle at defined times following injury and during recovery. Because the animal is anesthetized, we

can reliably induce damage to a single muscle group with a known velocity, arc of motion, and contractile level. Effort, such as in a maximal voluntary contraction (MVC), and pain are not confounding factors when assessing changes in function. Downhill treadmill running is an exercise that is sometimes used as an injury model, but there are problems with compliance [32]. The *in vivo* injury model provides a known dose of injury to a specific muscle group in all animals.

Regardless of the method used to induce damage, the T2 signal in MRI is typically increased significantly after muscle injury, but after some protocols there is a long-term persistence of this signal [33, 34], with a time scale that

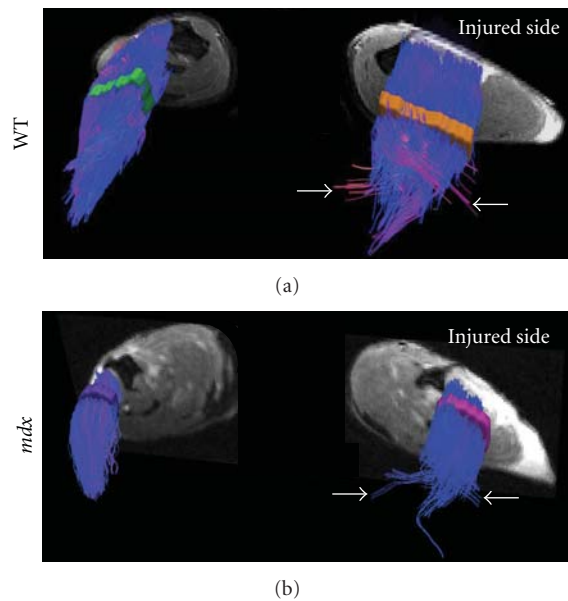


FIGURE 5: Muscle fiber tracking of the tibialis anterior (TA) muscle *in vivo*. Examples of “fiber tracking” from processed diffusion tensor imaging (DTI). The image shows modeling of fiber tracks based on the DTI data in the TA muscles of a wild-type (wt) mouse and an *mdx* mouse in the noninjured and injured sides. Even with this mild injury protocol that shows only minimal change in the T2 signal, the injured TA is readily identified by an apparent interruption in the vertical orientation of the tracks (arrows). Tractography is only a visual depiction of the DTI parameters. It is useful in providing accurate representation of the true anatomy of muscles but less so after injury. The colored bands are just where the regions of interest were drawn to outline the TA. Note that the *mdx* T2 image shows regions of hyperintensity, as seen in Figure 4.

is not in line with the temporal changes of inflammation and edema [28]. Although some studies have shown that T2 values gradually peak hours or days after injury [26, 30], these employed a myotoxin to injure the muscle. Myotoxins provide a model to study necrosis, inflammation, and massive degeneration and regeneration but do not provide a physiological model of injury. In a recent paper, Mathur et al. [32] used downhill running to study the changes in T2 after eccentric exercise of *mdx* mice. They used older animals (5–15 months) but still found that *mdx* mice were more susceptible to damage, with T2 returning to preexercise levels 10 days after exertion. Interestingly, they noted a strong relationship between the percent of EBD-positive area and the percentage of pixels with elevated T2 ($r = 0.79$). EBD binds to albumin, a blood plasma protein, and is detected by fluorescence microscopy in the extracellular space. Presence of the protein-bound dye inside a muscle fiber indicates damage to the sarcolemma. Since albumin is a relatively large protein (~67 kDa), their findings suggest that downhill running results in relatively large sarcolemmal tears of damaged myofibers.

McIntosh et al. [35] provided one of the first studies to use MRI to assess skeletal muscle in *mdx* mice. These authors noted heterogeneous signal intensity on T2-weighted images

in *mdx* hindlimb muscles. These foci of high intensity were subsequently confirmed by Walter et al. [36], who used more advanced techniques to obtain higher resolution images as well to quantify the changes in the T2 signal that occurred in the *mdx* (and *ysg*^{-/-}) mice compared to controls. Walter et al. also showed that delivery of *ysg* by AAV (adenoassociated virus) into hindlimb muscles was not only able to rescue to phenotype (i.e., return of normal histology) but also restored the T2 properties of skeletal muscle.

DTI parameters have been compared to longitudinal sections of the rat TA, the results of which show that DTI directions actually represent the local orientation of fibers in the rat TA muscle [37]. Damon et al. have used DTI fiber tracking successfully to measure pennation angles of myofibers in human skeletal muscle [10, 11, 38, 39], and subsequent studies have also used DTI in mice, both for three-dimensional reconstruction of fiber tracks [40] and as a measure of damage induced by ischemia reperfusion [8]. Heemskerk et al. provide an excellent description of measured changes in DTI parameters after ischemia-reperfusion type of injury in mouse skeletal muscle [12]. They found that DTI indices changed in response to ischemia-reperfusion and that the indices correlated with histopathology, although they caution against overinterpretation since their study was not designed to achieve exact correlation. Such correlation requires optimal MRI protocols, an exact spatial correspondence between histology and MRI slices, and specific immunohistochemical labeling to identify specific cell types.

One can use DTI to compare muscle architecture of dystrophic and healthy hindlimb muscles of mice *in vivo*. This could be extremely valuable to muscle physiologists who need to obtain the cross-sectional area (CSA) of a muscle to calculate the “specific force” (force normalized to CSA) without removing the muscles. In addition to the computer-generated models of fiber tracks, we were able to collect quantifiable data. Using our injury model, the diffusion parameters (decrease in FA and increases in MD and AD) and T2 findings are consistent with increased edema. However, the lack of significant changes in RD may suggest increased diffusion along the sarcolemma as a result of cell swelling. Interestingly, significant changes in DTI parameters were evident in the middle and proximal sections of the TA, and significant T2 changes were evident in the proximal TA. Such findings support earlier work suggesting that damage to the myofibers is not limited to the muscle-tendon junction, where soreness often occurs [14].

There are certain limitations to any study of muscle injury and disease. In addition to technical issues involved with imaging [41], position of the limb [42], and the lack of any single biological marker to explain the loss of force after injury [43, 44], one must still use caution when interpreting T2 intensity or DTI findings. The exact meaning of T2 changes are still to be elucidated [28, 32, 45]. While tractography corresponds to normal anatomy, there is a tendency after injury for the more superficial fascicles to appear abnormal (Figure 5, arrows). This three-dimensional reconstruction can appear to have fibers that “punch through” the strong connective tissue (epimysium) that surrounds that muscle and enter into the space occupied

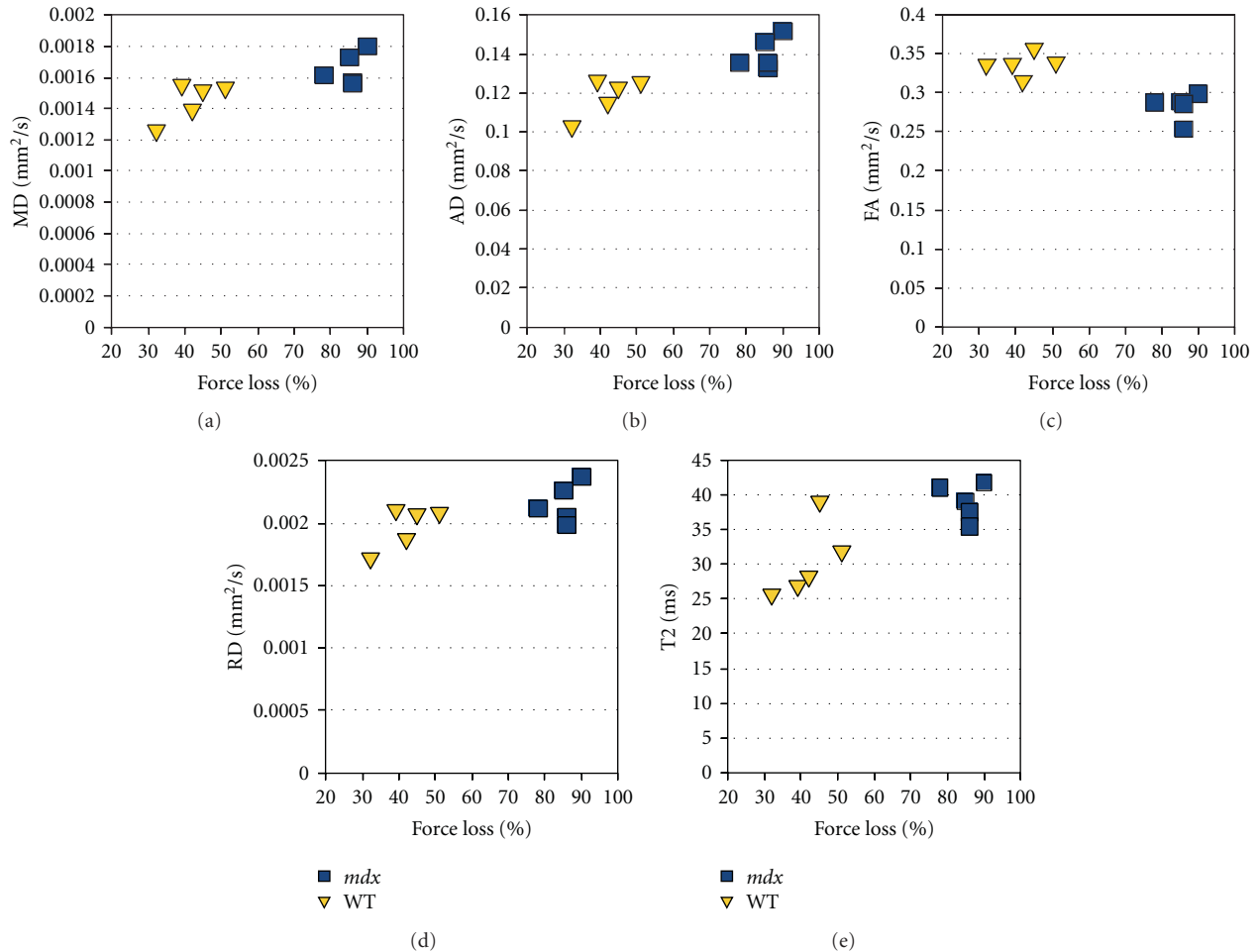


FIGURE 6: Diffusion tensor imaging (DTI) parameters after injury. Parameters (y -axis, in mm^2/s) for the proximal section of TA muscles from wild-type (yellow triangles) and *mdx* (blue squares) mice are plotted against force loss (x -axis, in % loss compared to pre-injury torque). Parameters include (a) mean diffusivity (MD), (b) axial diffusivity (AD), (c) fractional anisotropy (FA), (d) radial diffusivity (RD). (e) shows T2 (ms) also presented plotted against force loss. Presenting the data in this way, one can see that as there is a loss in force, there is a greater change in the diffusion parameters for the *mdx* mice than with the wild-type mice.

by another muscle, when indeed this is not the case. This is likely to be even more of a problem when using DTI on patients with DMD, as they have significant progressive damage over time and a gradual replacement of muscle tissue by fat, something that does not occur in the *mdx* mouse model of DMD. Such issues are still being worked on and can hopefully be resolved. However, this change in normal direction of myofibers is clearly indicative of damage, and tractography in healthy muscle is still a useful tool to obtain volume in order to calculate “specific force” (force per unit cross-sectional area).

In summary, we have used MRI to study injured muscle by observing edema and muscle fiber diffusion changes with T2 and DTI sequences, respectively. DTI exhibited significant changes in both the middle and proximal sections of the TA, whereas T2 changes were only significant in the proximal section. This is, to the best of our knowledge, the first animal study to use DTI in a reliable and valid animal model of eccentric injury. The results suggest that DTI is a reliable

marker in the assessment of acute muscle injury, even at early time points where the MR signal changes are dominated by local edema.

Acknowledgment

This work was supported by Grants to RML from the National Institutes of Health (K01AR053235 and 1R01AR059179).

References

- [1] G. Duchenne, *De l'électrisation localisée et de son application à la pathologie et à la thérapeutique*, Bailliere et Fils, Paris, France, 1861.
- [2] W. E. Garrett Jr., “Muscle strain injuries,” *American Journal of Sports Medicine*, vol. 24, pp. S2–S8, 1996.
- [3] K. D. Hunter and J. A. Faulkner, “Pliometric contraction-induced injury of mouse skeletal muscle: effect of initial

- length," *Journal of Applied Physiology*, vol. 82, no. 1, pp. 278–283, 1997.
- [4] C. Dellorosso, R. W. Crawford, J. S. Chamberlain, and S. V. Brooks, "Tibialis anterior muscles in mdx mice are highly susceptible to contraction-induced injury," *Journal of Muscle Research and Cell Motility*, vol. 22, no. 5, pp. 467–475, 2001.
 - [5] B. J. Petrof, J. B. Shrager, H. H. Stedman, A. M. Kelly, and H. L. Sweeney, "Dystrophin protects the sarcolemma from stresses developed during muscle contraction," *Proceedings of the National Academy of Sciences of the United States of America*, vol. 90, no. 8, pp. 3710–3714, 1993.
 - [6] K. P. Speer, J. Lohnes, W. E. Garrett Jr., and E. Eriksson, "Radiographic imaging of muscle strain injury," *American Journal of Sports Medicine*, vol. 21, no. 1, pp. 89–96, 1993.
 - [7] D. G. Blankenbaker and A. A. De Smet, "MR imaging of muscle injuries," *Applied Radiology*, vol. 33, no. 4, pp. 14–26, 2004.
 - [8] A. M. Heemskerk, M. R. Drost, G. S. Van Bochove, M. F. M. Van Oosterhout, K. Nicolay, and G. J. Strijkers, "DTI-based assessment of ischemia-reperfusion in mouse skeletal muscle," *Magnetic Resonance in Medicine*, vol. 56, no. 2, pp. 272–281, 2006.
 - [9] C. H. Sotak, "The role of diffusion tensor imaging in the evaluation of ischemic brain—a review," *NMR in Biomedicine*, vol. 15, no. 7-8, pp. 561–569, 2002.
 - [10] B. M. Damon, Z. Ding, A. W. Anderson, A. S. Freyer, and J. C. Gore, "Validation of diffusion tensor MRI-based muscle fiber tracking," *Magnetic Resonance in Medicine*, vol. 48, no. 1, pp. 97–104, 2002.
 - [11] A. M. Heemskerk, T. K. Sinha, K. J. Wilson, Z. Ding, and B. M. Damon, "Quantitative assessment of DTI-based muscle fiber tracking and optimal tracking parameters," *Magnetic Resonance in Medicine*, vol. 61, no. 2, pp. 467–472, 2009.
 - [12] A. M. Heemskerk, G. J. Strijkers, M. R. Drost, G. S. Van Bochove, and K. Nicolay, "Skeletal muscle degeneration and regeneration after femoral artery ligation in mice: monitoring with diffusion MR imaging," *Radiology*, vol. 243, no. 2, pp. 413–421, 2007.
 - [13] R. M. Lovering, A. O'Neill, J. M. Muriel, B. L. Prosser, J. Strong, and R. J. Bloch, "Physiology, structure, and susceptibility to injury of skeletal muscle in mice lacking keratin 19-based and desmin-based intermediate filaments," *American Journal of Physiology*, vol. 300, no. 4, pp. C803–C813, 2011.
 - [14] R. M. Lovering, A. B. Mcmillan, and R. P. Gullapalli, "Location of myofiber damage in skeletal muscle after lengthening contractions," *Muscle and Nerve*, vol. 40, no. 4, pp. 589–594, 2009.
 - [15] R. M. Lovering, J. A. Roche, R. J. Bloch, and P. G. De Deyne, "Recovery of function in skeletal muscle following 2 different contraction-induced injuries," *Archives of Physical Medicine and Rehabilitation*, vol. 88, no. 5, pp. 617–625, 2007.
 - [16] R. M. Lovering and P. G. De Deyne, "Contractile function, muscle eccentric contraction-induced injury," *American Journal of Physiology*, vol. 286, no. 2, pp. C230–C238, 2004.
 - [17] I. A. Barash, L. Mathew, A. F. Ryan, J. Chen, and R. L. Lieber, "Rapid muscle-specific gene expression changes after a single bout of eccentric contractions in the mouse," *American Journal of Physiology*, vol. 286, no. 2, pp. C355–C364, 2004.
 - [18] C. P. Ingalls, G. L. Warren, J. Z. Zhang, S. L. Hamilton, and R. B. Armstrong, "Dihydropyridine and ryanodine receptor binding after eccentric contractions in mouse skeletal muscle," *Journal of Applied Physiology*, vol. 96, no. 5, pp. 1619–1625, 2004.
 - [19] M. Hakim, W. Hage, R. M. Lovering, C. T. Moorman, L. A. Curl, and P. G. De Deyne, "Dexamethasone and recovery of contractile tension after a muscle injury," *Clinical Orthopaedics and Related Research*, no. 439, pp. 235–242, 2005.
 - [20] R. M. Lovering, M. Hakim, C. T. Moorman, and P. G. De Deyne, "The contribution of contractile pre-activation to loss of function after a single lengthening contraction," *Journal of Biomechanics*, vol. 38, no. 7, pp. 1501–1507, 2005.
 - [21] R. M. Lovering, J. A. Roche, M. H. Goodall, B. B. Clark, and A. Mcmillan, "An in vivo rodent model of contraction-induced injury and non-invasive monitoring of recovery," *Journal of Visualized Experiments*, no. 51, 2011.
 - [22] S. Mori, B. J. Crain, V. P. Chacko, and P. C. M. Van Zijl, "Three-dimensional tracking of axonal projections in the brain by magnetic resonance imaging," *Annals of Neurology*, vol. 45, no. 2, pp. 265–269, 1999.
 - [23] P. W. Hamer, J. M. McGeachie, M. J. Davies, and M. D. Grounds, "Evans Blue Dye as an in vivo marker of myofibre damage: optimising parameters for detecting initial myofibre membrane permeability," *Journal of Anatomy*, vol. 200, no. 1, pp. 69–79, 2002.
 - [24] M. R. Stone, A. O'Neill, R. M. Lovering et al., "Absence of keratin 19 in mice causes skeletal myopathy with mitochondrial and sarcolemmal reorganization," *Journal of Cell Science*, vol. 120, no. 22, pp. 3999–4008, 2007.
 - [25] H. K. Kim, T. Laor, P. S. Horn, J. M. Racadio, B. Wong, and B. J. Dardzinski, "T2 mapping in Duchenne muscular dystrophy: distribution of disease activity and correlation with clinical assessments," *Radiology*, vol. 255, no. 3, pp. 899–908, 2010.
 - [26] K. T. Mattila, R. Lukka, T. Hurme, M. Komu, A. Alanen, and H. Kalimo, "Magnetic resonance imaging and magnetization transfer in experimental myonecrosis in the rat," *Magnetic Resonance in Medicine*, vol. 33, no. 2, pp. 185–192, 1995.
 - [27] C. Sébrié, B. Gillet, J. P. Lefaucheur, A. Sébille, and J. C. Beloeil, "Mouse muscle regeneration: an in vivo 2D 1H magnetic resonance spectroscopy (MRS) study," *FEBS Letters*, vol. 423, no. 1, pp. 71–74, 1998.
 - [28] T. Marqueste, B. Giannesini, Y. Le Fur, P. J. Cozzone, and D. Bendahan, "Comparative MRI analysis of T2 changes associated with single and repeated bouts of downhill running leading to eccentric-induced muscle damage," *Journal of Applied Physiology*, vol. 105, no. 1, pp. 299–307, 2008.
 - [29] J. Zhang, G. Zhang, B. Morrison, S. Mori, and K. A. Sheikh, "Magnetic resonance imaging of mouse skeletal muscle to measure denervation atrophy," *Experimental Neurology*, vol. 212, no. 2, pp. 448–457, 2008.
 - [30] A. Wishnia, H. Alameddine, S. Tardif de Géry, and A. Leroy-Willig, "Use of magnetic resonance imaging for noninvasive characterization and follow-up of an experimental injury to normal mouse muscles," *Neuromuscular Disorders*, vol. 11, no. 1, pp. 50–55, 2001.
 - [31] T. N. Frimel, G. A. Walter, J. D. Gibbs, G. S. Gaidosh, and K. Vandenborne, "Noninvasive monitoring of muscle damage during reloading following limb disuse," *Muscle and Nerve*, vol. 32, no. 5, pp. 605–612, 2005.
 - [32] S. Mathur, R. S. Vohra, S. A. Germain et al., "Changes in muscle T2 and tissue damage after downhill running in mdx mice," *Muscle and Nerve*, vol. 43, no. 6, pp. 878–886, 2011.
 - [33] J. L. Fleckenstein, P. T. Weatherall, R. W. Parkey, J. Payne, and R. M. Peschock, "Sports-related muscle injuries: evaluation with MR imaging," *Radiology*, vol. 172, no. 3, pp. 793–798, 1989.
 - [34] F. G. Shellock, T. Fukunaga, J. H. Mink, and V. R. Edgerton, "Exertional muscle injury: evaluation of concentric versus

- eccentric actions with serial MR imaging,” *Radiology*, vol. 179, no. 3, pp. 659–664, 1991.
- [35] L. M. McIntosh, R. E. Baker, and J. E. Anderson, “Magnetic resonance imaging of regenerating and dystrophic mouse muscle,” *Biochemistry and Cell Biology*, vol. 76, no. 2-3, pp. 532–541, 1998.
- [36] G. Walter, L. Cordier, D. Bloy, and H. L. Sweeney, “Noninvasive monitoring of gene correction in dystrophic muscle,” *Magnetic Resonance in Medicine*, vol. 54, no. 6, pp. 1369–1376, 2005.
- [37] C. C. Van Donkelaar, L. J. G. Kretzers, P. H. M. Bovendeerd et al., “Diffusion tensor imaging in biomechanical studies of skeletal muscle function,” *Journal of Anatomy*, vol. 194, no. 1, pp. 79–88, 1999.
- [38] J. H. Kan, A. M. Heemskerk, Z. Ding et al., “DTI-based muscle fiber tracking of the quadriceps mechanism in lateral patellar dislocation,” *Journal of Magnetic Resonance Imaging*, vol. 29, no. 3, pp. 663–670, 2009.
- [39] D. A. Lansdown, Z. Ding, M. Wadlington, J. L. Hornberger, and B. M. Damon, “Quantitative diffusion tensor MRI-based fiber tracking of human skeletal muscle,” *Journal of Applied Physiology*, vol. 103, no. 2, pp. 673–681, 2007.
- [40] A. M. Heemskerk, G. J. Strijkers, A. Vilanova, M. R. Drost, and K. Nicolay, “Determination of mouse skeletal muscle architecture using three-dimensional diffusion tensor imaging,” *Magnetic Resonance in Medicine*, vol. 53, no. 6, pp. 1333–1340, 2005.
- [41] B. M. Damon, “Effects of image noise in muscle diffusion tensor (DT)-MRI assessed using numerical simulations,” *Magnetic Resonance in Medicine*, vol. 60, no. 4, pp. 934–944, 2008.
- [42] U. Sinha, S. Sinha, J. A. Hodgson, and R. V. Edgerton, “Human soleus muscle architecture at different ankle joint angles from magnetic resonance diffusion tensor imaging,” *Journal of Applied Physiology*, vol. 110, no. 3, pp. 807–819, 2011.
- [43] G. L. Warren, C. P. Ingalls, D. A. Lowe, and R. B. Armstrong, “What mechanisms contribute to the strength loss that occurs during and in the recovery from skeletal muscle injury?” *Journal of Orthopaedic and Sports Physical Therapy*, vol. 32, no. 2, pp. 58–64, 2002.
- [44] D. L. Morgan and D. G. Allen, “Early events in stretch-induced muscle damage,” *Journal of Applied Physiology*, vol. 87, no. 6, pp. 2007–2015, 1999.
- [45] R. A. Meyer and B. M. Prior, “Functional magnetic resonance imaging of muscle,” *Exercise and Sport Sciences Reviews*, vol. 28, no. 2, pp. 89–92, 2000.

Research Article

Tissue Expression and Actin Binding of a Novel N-Terminal Utrophin Isoform

Richard A. Zuellig,¹ Beat C. Bornhauser,² Ralf Amstutz,²
Bruno Constantin,³ and Marcus C. Schaub⁴

¹Department of Endocrinology and Diabetes, University Hospital Zurich, 8091 Zurich, Switzerland

²Department of Oncology, University Children's Hospital, University of Zurich, 8032 Zurich, Switzerland

³Institut de Physiologie et Biologie Cellulaire, UMR CNRS/Université de Poitiers 6187, 86022 Poitiers Cedex, France

⁴Institute of Pharmacology and Toxicology, University of Zurich, Winterthurerstrasse 190, 8057 Zurich, Switzerland

Correspondence should be addressed to Marcus C. Schaub, schaub@pharma.uzh.ch

Received 1 June 2011; Revised 13 July 2011; Accepted 14 July 2011

Academic Editor: J.-P. Jin

Copyright © 2011 Richard A. Zuellig et al. This is an open access article distributed under the Creative Commons Attribution License, which permits unrestricted use, distribution, and reproduction in any medium, provided the original work is properly cited.

Utrophin and dystrophin present two large proteins that link the intracellular actin cytoskeleton to the extracellular matrix via the C-terminal-associated protein complex. Here we describe a novel short N-terminal isoform of utrophin and its protein product in various rat tissues (N-utro, 62 kDa, amino acids 1–539, comprising the actin-binding domain plus the first two spectrin repeats). Using different N-terminal recombinant utrophin fragments, we show that actin binding exhibits pronounced negative cooperativity (affinity constants $K_1 = \sim 5 \times 10^6$ and $K_2 = \sim 1 \times 10^5 \text{ M}^{-1}$) and is Ca^{2+} -insensitive. Expression of the different fragments in COS7 cells and in myotubes indicates that the actin-binding domain alone binds exclusively to actin filaments. The recombinant N-utro analogue binds in vitro to actin and in the cells associates to the membranes. The results indicate that N-utro may be responsible for the anchoring of the cortical actin cytoskeleton to the membranes in muscle and other tissues.

1. Introduction

Utrophin and dystrophin are large (395 and 427 kDa, resp.) modular proteins that link the cytoskeletal F-actin filaments to the plasmalemma. The C-terminal portion including the cysteine-rich domain associates with over a dozen of different scaffold and signaling proteins (utrophin-/dystrophin-associated protein complexes, UAPC and DAPC). These complexes are coupled via the transmembranous beta-dystroglycan to alpha-dystroglycan and to the extracellular matrix (ECM) proteins. At their N-terminus, both proteins contain a homologous actin-binding domain composed of a pair of calponin homology motifs (CH1 and CH2 in tandem) that are connected to the long sequence of spectrin-like triple helical repeats, 22 in utrophin and 24 in dystrophin. The spectrin repeat sequences are interspersed by hinges (H1–H5) giving these structural molecules flexibility (Figure 1). Thus, these two cytoskeletal proteins directly link the intra-

cellular cytoskeleton to the ECM in muscle and nonmuscle tissues.

In striated muscle, full-length dystrophin (Dp427) localises to the inner side of the plasma membrane (sarcolemma) with its N-terminus binding to nonmuscle beta- and gamma-actin in the costameres which physically couple to the Z-disc of force-generating myofibres [1]. Dp427 is thought to provide mechanical stability for the muscle fibre and the necessary flexibility of its anchoring to the surrounding ECM during contraction and extension; in fact, it may act as a cellular “shock-absorber” [2, 3]. Loss of functional Dp427 causes severe muscle wasting in the fatal Duchenne’s muscular dystrophy (DMD). The muscle symptoms can be improved, at least in the dystrophic mdx mouse model, by transgenic expression of Dp427 or by expression of engineered shorter versions of dystrophin comprising the essential constituents for binding to actin and the sarcolemma [4–6]. In addition, overexpression of full-length

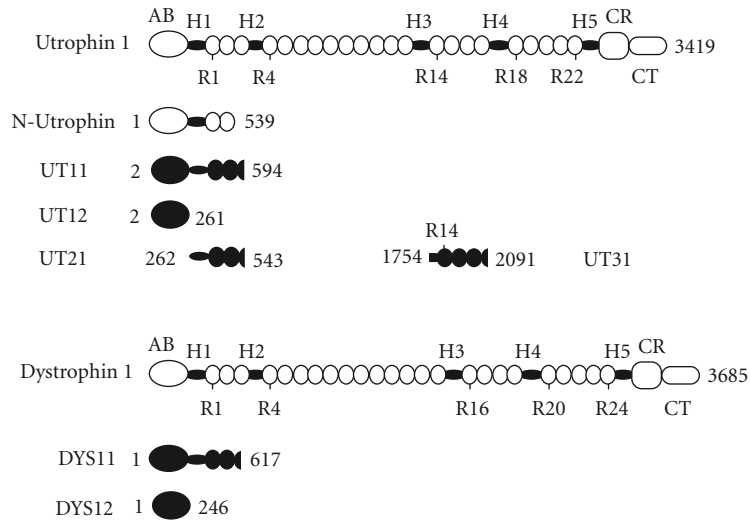


FIGURE 1: Domain structure of utrophin (rat) and dystrophin (human). Numbers denote amino acid (aa) residues according to rat utrophin. The short N-terminal utrophin isoform (N-utro) extends from aa 1 to 539. The black sections UT11, UT12, UT21, UT31, and DYS12 were used for heterologous expression in bacteria and eukaryotic cells. The recombinant proteins were used for production of antibodies, for in vitro actin-binding studies, and for eukaryotic cell transfection. AB, actin-binding domain; H1–H5, hinge regions; R1–R24, spectrin-like triple helical repeats; CR, cysteine-rich domain; CT, C-terminal domain.

utrophin (Up395) in Fiona mice lacking Dp427 localises along the sarcolemma resulting in complete recovery of normal mechanical functions and prevents the occurrence of muscular dystrophy [7, 8]. The Fiona mouse line overexpresses Up395 under a human alpha-actin promoter in skeletal muscle, but not in the heart, over 20 times compared to control mice.

Based on the homologous domain structure (Figure 1) and the high amino acid (aa) sequence similarity, utrophin and dystrophin are expected to serve comparable functions. In fact, in fetal animals utrophin prevails and localises to the sarcolemma like dystrophin in the adult. During postnatal maturation of striated muscle, Up395 disappears from the sarcolemma and becomes restricted to the neuromuscular (NMJ) and myotendinous junctions [9]. Thus, utrophin can functionally replace dystrophin. Nevertheless, there are significant differences between the two during spatiotemporal development, in tissue and subcellular localisation, in isoform complement, and, on a molecular level, in actin-binding properties [4, 10–12]. DMD (X-linked recessive disorder) is the most common lethal disease in childhood concerning 1 in 3500 boys. In addition, about one-third of DMD patients display mental retardation related to alterations in integrated brain circuits [13]. This points to vital functions of these skeletal proteins other than muscle membrane stability.

The DMD gene localises to human chromosome Xp21 and comprises 79 exons and at least 7 internal promoters [14]. The protein Dp427 is mainly expressed in skeletal and cardiac muscle and to a lesser extent in the nervous system. It derives from three independent promoters (M: muscle; B: brain; P: cerebellar Purkinje cells) consisting of spliced unique first exons that regulate specific expression. In adult skeletal muscle, Dp427 is located at the sarcolemma and in the troughs of the postsynaptic membrane. Its N-terminal

actin-binding domain contains aa 1–246 (Figure 1). Four shorter nonmuscle products harboring the cysteine-rich and C-terminal domains, but lacking the N-terminal actin binding domain, are expressed from downstream promoters and have been named according to their molecular weights, Dp260, Dp140, Dp116, and Dp71 [14, 15]. Dp71 has been detected in cardiac muscle and most nonmuscle tissues including brain, retina, kidney, liver, and lung [11, 12, 16, 17].

The gene of utrophin, paralogous to DMD, is located on human chromosome 6q24 containing 75 exons and 6 internal promoters [18, 19]. Up395 is named utrophin because of its ubiquitous tissue distribution in comparison to Dp427. Expression of Up395 is driven by two independent promoters UtrnA and UtrnB [20]. The UtrnA protein is the main isoform in adult skeletal muscle and appears in the NMJ at the crests of the postsynaptic membrane folds in association with the nicotinic acetylcholine receptors (AChR). The UtrnB isoform is found enriched in vascular endothelium. Both Up395 isoforms are, however, found in brain structures and in many other tissues as well [11, 20]. As for the DMD gene, the internal utrophin promoters give rise to several shorter C-terminal isoforms with preservation of the cysteine-rich and the C-terminal domains, which correspond to the similar short isoforms from dystrophin and thus also lack the N-terminal actin-binding domain [14, 19, 21]. Up140 corresponds to DP140, Up113 (also called G-utrophin) to Dp116, and Up71 to Dp71.

While no short N-terminal dystrophin isoform is known, we have described the cloning of a transcript from the utrophin locus in rat C6 glioma cells which codes for a short N-terminal utrophin isoform (N-utro). N-Utro aa 1–539 comprises the actin-binding domain (Ch1 and CH2) plus the first two spectrin-like repeats (Figure 1) [22].

By immunoblotting with monoclonal antibodies (mABs) against aa 1–261 (N-terminal actin-binding domain) of utrophin, a 62 kDa fragment was earlier detected in rat C6 glioma cells [23]. This finding suggested the existence of a truncated N-terminal form of utrophin that was confined to the glioma cells. Indeed, its apparent molecular mass in sodium dodecyl sulfate polyacrylamide gel electrophoresis (SDS-PAGE) precisely matches that of N-utro. Here we confirm the expression of mRNA for N-utro in all rat tissues examined including skeletal and cardiac muscle, brain, kidney, and liver. The expression of the N-utro protein could be verified in cardiac muscle and kidney.

Recombinant utrophin fragments aa 2–594 (corresponding to N-utro), aa 2–261 (actin-binding domain), aa 262–543 (first two spectrin repeats), aa 1754–2091 (spectrin repeats R14–R16), and the dystrophin fragment aa 1–246 (actin-binding domain) were heterologously expressed in *E. coli* and in eukaryotic cells (Figure 1, black domains). These fragments were used for production of polyclonal antibodies (pABs) and for testing actin-binding function. Transfection of COS7 cells and myoblasts allowed to follow intracellular localisation by immunostaining. As this novel N-terminal fragment (N-utro) is added to the panoply of the short utrophin isoform family, it is important to characterise its genetics and functional potential.

2. Material and Methods

2.1. Recombinant Protein Expression. Three fragments from rat utrophin (UT11, UT12, and UT31) and two from human muscular dystrophin (DYS11 and DYS12) were cloned into pQE vectors (Qiagen) for expression in *Escherichia coli* M15[pREP4] (Figure 1). This provides a MRGSH6 tag at the Nterminus of the proteins. In order to maintain the correct reading frame, one to two additional amino acids (aa) appeared between the tag and the in-frame proteins (see below). For DYS12, the DNA coding for aa 1–246 was cloned into the blunted BamHI site of pQE-32 after PCR amplification from a human dystrophin minigene with the following sense and antisense primers 5'-ATGCTT-TGGTGGGAAGAAGTA-3' and 5'-TATTCAATGCTCACT-TGTTGAGGC-3', respectively. The dystrophin minigene in pUC18 (44) was kindly provided by Dr. S. J. Winder. The other four pQE expression plasmids contain DNA fragments obtained by restriction digestion. For the DYS11 plasmid which codes for aa 1–617, the minigene was digested with NcoI, blunted, and digested with NarI, and the resulting NarI-NcoI-fragment was ligated into the NarI HincII-site of the DYS12 plasmid; the UT11 plasmid coding for aa 2–594 is a blunted EaeI-EaeI-fragment of clone α -213 ligated into the blunted BamHI site of pQE-30; for production of the UT12 plasmid coding for aa 2–261, clone α -213 was digested with BsaHI, blunted, digested again with StuI, and the thus resulting StuI-BsaHI fragment was then ligated into the StuI-HincII site of the UT11 plasmid; for the UT31 plasmid coding for aa 1754–2091, the clone α -215 was first digested with BamHI to produce a 2.7 kb fragment that was subcloned into a pBluescript II SK vector (Stratagene Ltd) from which a BamHI-HincII fragment was ligated into the BamHI-HincII

site of pBluescript II SK again from which a BamHI-KpnI fragment was ligated into the BamHI-KpnI site of pQE-31.

All ligation junctions were sequenced for checking the correct reading frame. Due to restriction cloning, a variable number of vector-derived aa were attached to the C-terminus of the proteins. The following final expression constructs were obtained (numbers in brackets refer to the rat utrophin or human dystrophin primary structure):

UT11: MRGSH6GS-(2–594)-RSACELGTP
GRPAAKLN,

UT12: MRGSH6GS-(2–261)-GPAAKLN,

UT31: MRGSH6T-(1754–2091)-SRGGPVPRV
DLQPSLIS,

DYS11: MRGSH6GI-(1–617)-DLQPSLIS,

DYS12: MRGSH6GI-(1–246).

All five described plasmids could be expressed in *Escherichia coli* by induction with isopropyl- β -D-1-thiogalactopyranoside (IPTG) and purified by affinity chromatography on Ni-nitrilotriacetic acid agarose (Qiagen). UT11, UT12, and DYS12 were purified under native conditions by elution with 200 mM imidazole (example given in Figure 2). UT31 and DYS11 could only be extracted and purified under denaturing condition in 8 M urea with elution from the affinity column at pH 4.5. All protein preparations were tested by SDS-PAGE. Protein concentrations were determined by the Bradford test [24] with BSA as standard and by UV absorption at E280 with extinction coefficients of 87'580 M⁻¹cm⁻¹ for UT11, 39'620 for UT12, 52'040 for DYS12, and 106'700 for DYS11 as derived from GCG software.

2.2. RNA Isolation. RNA was isolated from different rat tissues, brain, heart, kidney, liver, skeletal muscle, and C6 glioma cells [25] and passed twice over an oligo(dT) cellulose column (New England Biolabs) for preparation of poly(A)⁺ RNA [26].

2.3. RT-PCR. 1 μ g poly(A)⁺ RNA was mixed with 1 μ g pd(N)₆ or with 0.86 μ g oligo(dT)_{12–18} primers, in water and incubated for 5 min at 70°C. The reverse transcription was done according to manufacturer manual; in brief, the RNA-primer complex was mixed with 200 U M-MLV reverse transcriptase (Promega, USA), 500 μ M dNTPs each, 50 mM Tris-Cl pH 8.3, 75 mM KCl, 3 mM MgCl₂, 10 mM DTT, 25 μ L reaction volume. First strand cDNA was synthesised at 37°C for 2 h, stopped with 45 μ L 77 mM EDTA/0.23 M NaOH, and heated to 95°C for 5 min. After mixing with 18 μ L 1 M Tris-Cl pH 8.0, the first strand cDNA was extracted with equal volumes of phenol, phenol/chloroform, and chloroform, precipitated with ethanol/NH₄Ac and resolved in 50 μ L TE.

PCR was performed in a volume of 50 μ L containing 1 U Taq polymerase (HotStar, Qiagen), 200 μ M dNTPs each, 0.3 μ M primer each, 1x PCR buffer (Qiagen), 1 μ L first strand cDNA. Cycles were 95°C 10 min, followed by 40 cycles 30 sec 94°C, 30 sec 60°C, 60 sec 72°C. PCR products were analysed on a 1% agarose gel (see Table 1).

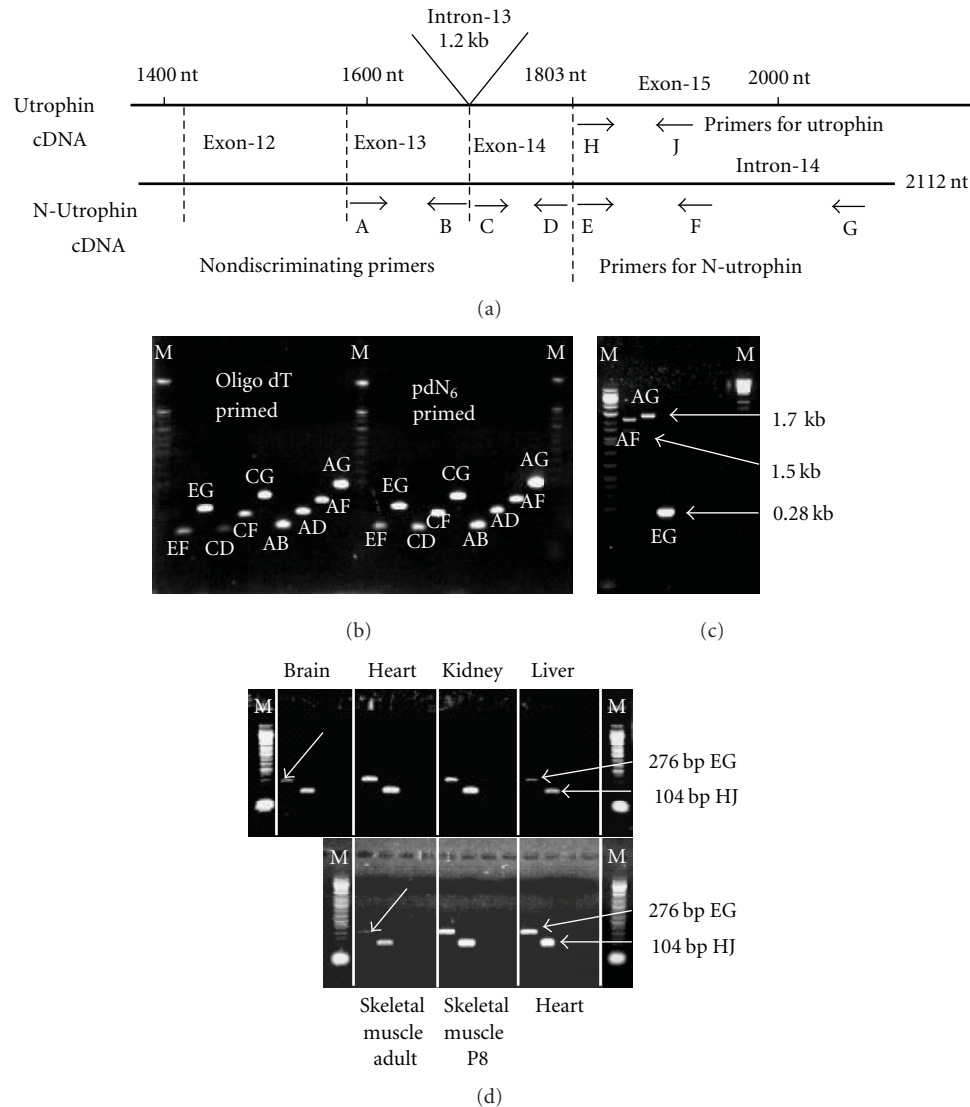


FIGURE 2: Detection of the mRNA for the N-utrophin isoform and for full-length Up395 in rat tissues by RT-PCR and electrophoresis in 1% agarose with ethidium bromide. (a) Organisation of mRNA for full-length utrophin (upper line) and for N-utrophin (lower line) with direction of primers (lettered arrows) and exon borders (dashed lines). Sequence homology breaks down at nucleotide (nt) 1803. Nondiscriminating primers (A, B, C, D) recognise both isoforms, while primers (E, F, G) are specific for N-utrophin, and primers (H, J) are specific for full-length utrophin. The genomic DNA contains intron-13 of 1.2 kilobases (kb) between exon-13 and 14. Exon numbering is in homology to that of dystrophin. (b) RT-PCR (40 cycles) products ranging in size from 100 to 500 base pairs (bp) from poly(A)⁺ RNA of rat kidney primed with either oligo(dT) or pd(N)₆. (c) RT-PCR (40 cycles) products (AF and AG) from genomic rat liver DNA display sizes of 1.5 and 1.7 kb containing intron-13 which adds 1.2 kb to each fragment. Product (EG) of 0.28 kb is specific for N-utrophin as control. The three black lanes between EG and the markers (M) are controls with the same primer pairs but without DNA. (d) RT-PCR (30 cycles) products (EG specific for N-utrophin and HJ specific for full-length utrophin) in different tissues. Black lanes are negative controls without reverse transcriptase. Note the larger amount of N-utrophin message in skeletal muscle of young rats (postnatal day 8) as compared to adult (arrow). Pairs of letters denote primer pairs; M stands for DNA markers.

2.4. Western Blots. Rat tissues from liver, brain, kidney, heart, skeletal muscle, aorta, and uterus were collected, immediately frozen in liquid nitrogen, and crushed to powder using a mortar. 100 μ L tissue lysis buffer per 10 mg tissue was added (62.5 mM Tris-Cl pH 6.8, 5% sucrose, 5 mM EDTA, 2% SDS and protease inhibitor (Complete Mini, Roche)), and the lysate was homogenised three times for 20 sec with a polytron (Kinematica) and centrifuged at 20,000 g for 5 min at 4°C. The supernatant was collected and used for analysis.

Lysates were boiled in 50 mM Tris-Cl pH 6.8, 2% SDS, 5% glycerol, 10 mM DTT and run on 4–15% gradient SDS-PAGE [27]. Blotting of the gel was performed in 7 mM Tris, 87.5 mM glycine, pH 8.3 (without methanol) using a Mini Trans-Blot Cell (BioRad). After staining with Ponceau-S, the membranes were cut into appropriate lanes for incubations with different antibodies and antisera (see legends of Figure 3). After incubation with the primary antibodies and a horseradish-peroxidase- (HRP-) labelled secondary antibody

TABLE 1: Primer used for PCR (for localisation of primers along the cDNA, see Figure 2(a)).

Forward primer	Backward primer
A Rut13F	B Rut23B
C Rut14F	D Rut24B
E Rut18F	F Rut25B
	G Rut28B
H Rut19F	J Rut41B
PCR product size	
A-B: 110 bp	
A-D: 215 bp	
A-F: 326 bp	
A-G: 499 bp	
C-D: 96 bp	
C-F: 207 bp	
C-G: 380 bp	
E-F: 103 bp	
E-G: 276 bp	
H-J: 104 bp	
Primer sequence	
Forward primer	
RUT 13F	5' CAA AGT GAC CTC GAA GCT GAG C 3' rat utrophin 1587→1608
RUT 14F	5' GGG TGA GCG CTG GAC AGC TG 3' rat utrophin 1706→1725
RUT 18F	5' GTG CAA CGA CCA TCC ATC AAG G 3' rat N-utrophin 1810→1831
RUT 19F	5' GTC TTT TGG AAG CTT GGC TCA CC 3' rat utrophin 1804→1826
Backward primer	
RUT 23B	5' AAC TGA TCT TCC AAA ACA GCT GTG 3' rat utrophin 1673←1696
RUT 24B	5' TGT TCT TCC AAT AAT TCC TGC CAC 3' rat N-utrophin 1778←1801
RUT 25B	5' TTC CAG AGC TCT CAC TAC AGA AG 3' rat N-utrophin 1890←1912
RUT 28B	5' CCC CAG AAT TAC GAA GGT CAC AC 3' rat N-utrophin 2063←2085
RUT 41B	5' CAG ACG CCG GAC ACT GAC ACC 3' rat utrophin 1887←1907

detection was performed by SuperSignal chemiluminescence (Pierce). The different membrane lanes were precisely re-joined together and exposed to Fuji's medical X-ray film (Fuji Photo Film). Controls were done by omission of the first antibody, by using preimmune serum (not shown) and by competition with the appropriate antigen, 10 $\mu\text{g}/\text{mL}$ (Figure 3). Molecular weight markers spanning the range from 14.4 kDa lysozyme up to 200 kDa myosin were used (BioRad, broad-range markers).

2.5. Antibodies and Antisera. Antibodies used were monoclonal Abs (mAb) NCL-DYS1 (Novocastra Laboratories), anti-actin monoclonal IgM (Amersham Life Science), goat anti-rabbit IgG-HRP (Pierce) and goat anti-mouse IgM-HRP (Pierce). New Zealand white rabbits and guinea pigs were immunised with purified recombinant UT11 and UT31 together with Freund's adjuvant [22]. Prior to immunisation the 26 N-terminal aa of recombinant UT11 and UT31, were sequenced for confirmation. The recombinant proteins were run on 10% SDS-PAGE and eluted for sequencing after electroblotting onto polyvinylidene difluoride membranes.

2.6. Actin-Binding Assay. Actin-binding assays were done according to Zuellig et al. [22]. Binding results are given as affinity constant K which corresponds to the reciprocal value of the dissociation constant K_D . In brief, varying concentrations of the recombinant protein fragments UT11, UT12, DYS12, or BSA in actin-binding buffer (50 mM Tris-maleate pH 7.4, 0.1 M NaCl, 1 mM ATP, 1 mM DTT, and either 0.5 mM CaCl_2 , 2 mM MgCl_2 or 5 mM EGTA, 6 mM MgCl_2 were dialysed for 15 hours with one buffer change at 4°C. Purified F-actin (6 μM) [28] from rabbit fast skeletal muscle was added and the samples incubated for 30 min at 25°C in 100 μL volume. Cosedimentation was carried out in a Beckman TLA-100 tabletop ultracentrifuge for 30 min at 100,000 g at 25°C. Equal amounts of supernatant and pellet were run on 10% SDS-PAGE, stained with Coomassie Blue R250, and analysed with the Image Analysis System MCID/M2 (Imaging Research) integrating the area of the protein bands.

For the EGTA studies, the fragments (all 10 μM) were dialysed at 4°C for 40 h with three buffer changes into a buffer containing 50 mM HEPES/NaOH pH 7.4, 0.1 M NaCl,

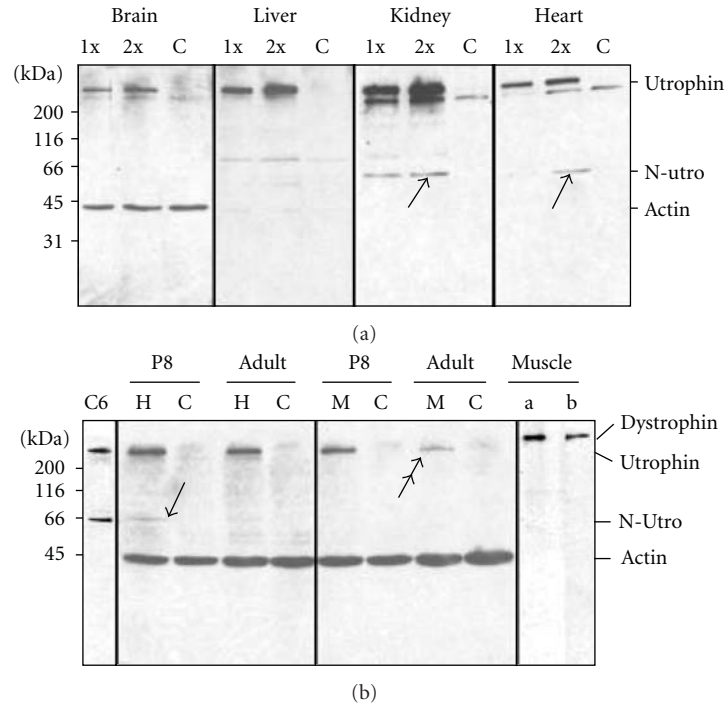


FIGURE 3: Immunoblots of rat tissues for full-length utrophin and N-utrophin (4–10% SDS-PAGE). (a) Adult tissues with protein loads of $\sim 45 \mu\text{g}$ (1x), $\sim 90 \mu\text{g}$ (2x), and $\sim 90 \mu\text{g}$ for C. All lanes stem from one gel blotted onto nitrocellulose membrane. After staining with Ponceau-S, the membrane was cut for separate immunostaining (1x and 2x together plus lane C separate). Lanes 1x and 2x were incubated with anti-UT11. Anti-UT11 recognises full-length ($\sim 395 \text{ kDa}$) and N-utrophin ($\sim 65 \text{ kDa}$). C Lanes present competition by preincubation of the serum with recombinant UT11 antigen ($10 \mu\text{L}/\text{mL}$ serum) before loading onto the blot. In addition, actin ($\sim 44 \text{ kDa}$) was visualised in brain tissue by mixing anti-actin antibody with anti-UT11. Finally, the differently incubated membrane lanes were precisely joined together for exposure on X-ray films. Full-length utrophin is seen in all tissues and N-utrophin in kidney and heart. Competition with UT11 antigen removes full-length and N-utrophin. The second lower band underneath the full-length utrophin may represent a degradation product which is, however, only partially removed by antigen competition. (b) The same approach was employed with the gel comprising H, M, and C, except that anti-actin antibody was added to all lanes for loading control and as internal molecular size marker. Protein load was $\sim 90 \mu\text{g}$ protein of heart (H) and muscle (M) from young (8 days postnatal) and adult tissues. N-Utrophin can only be seen as a faint band in young heart tissue (arrow). The band of full-length utrophin is greatly reduced in adult muscle (double arrow) and abolished by competition in all samples labeled with C. For comparison, C6 rat glioma cells stained with anti-UT11 displaying full-length and N-utrophin as well as adult muscle stained with anti-DYS12 (a) and NCL-DYS1 (b) derived from different gels are included.

1 mM ATP, 1 mM DTT, 6 mM MgCl_2 , and the corresponding combination of EGTA/ CaCl_2 (in mM) 0/0.5, 0.5/1.0, 1.0/1.5, 5.0/6.0. Purified F-actin ($10 \mu\text{M}$) was added and processed as described above.

For the calmodulin (Sigma-Aldrich) studies, the procedure was as described above except the actin and UT11 or UT12 concentrations were kept constant at $10 \mu\text{M}$, and the buffer for dialysis and binding contained the following combinations of EGTA/ CaCl_2 /calmodulin (all in mM) 0/1/0, 1/0/0.2, 0/1/0.2, 1/2/0.2.

2.7. Circular Dichroism. Five mM dithiothreitol was added to the purified recombinant proteins before dialysis into 10 mM Tris-Cl, pH 7.4, plus either 0.5 mM CaCl_2 or 1 mM EGTA plus 1.5 mM CaCl_2 for 40 hours with three buffer changes at 4°C . Samples were analysed by circular dichroism at 25°C in a Jasco J 715 spectropolarimeter with a path length of 1 mm. Samples from two different preparations were analysed at a concentration range of 1.5–3.1 μM with scanning from 260 to 190 nm. Data was processed according to [29] and the alpha-helix content derived by infinite analysis.

2.8. Eukaryotic Expression Vectors. pBSGFP was constructed by cutting pEGFP-N1 (Clontech Laboratories, Inc.) with EcoRI and NotI, isolating the 0.7 kb EGFP-coding sequence, and ligating it into the EcoRI-NotI site of pBluescript II SK⁻ (Stratagene Ltd). pBK Δ lacI was generated by cutting pBK-CMV (Stratagene Ltd) with the restriction enzymes NheI-XbaI and religating the 4.27 kb fragment. pEUT11-Flag contains the rat utrophin sequence from aa 1 to 543 followed by the Flag peptide (DYKDDDDK); the rat utrophin sequence from clone $\alpha 213$ [22] was amplified by PCR with the primers Rut15F: 5'-TACCATGGACGGGCACCTTG-3' (NcoI, nt189- \rightarrow 210) and Rut26B: 5'-ATGCGGC-CGCTACTTATCGTCGTCATCCTTGTAATC-AGCTTCCA-AAAGACACTGTTC-3' (NotI, FlagTag, nt1817- \rightarrow 1797); the resulting product was ligated into the NcoI-NotI site of pBSGFP resulting in pBSx Δ EUT11-Flag. This vector was cut with Bsp120I and NotI, the resulting 1.7 kb fragment with part of the 5'UTR, the utrophin sequence, and the FlagTag was ligated into the Bsp120I and NotI site of pBK Δ lacI vector pEUT12 Flag contains the rat utrophin sequence 1–261 followed by the Flag peptide and was constructed the same

way as pEUT11 Flag with the primer Rut15F and Rut27B: 5'-ATGCGGCCGCTACTTATCGTCGTCATCCTTGTAATC-GTCTATAGTGACTTGCTGAGG-3' (NotI, *FlagTag*, nt 971–>951) pEUT21 Flag contains the rat utrophin sequence 262–543 followed by the Flag peptide and was constructed the same way as pEUT11-Flag with the primer Rut16F: 5'-TACCATGGCCATTCGAGAGGTGGAGACG-3' (NcoI, nt 972–>992) and Rut26B.

2.9. Cell Culture. COS7 cells (ATCC-Nr: CRL 1651) were cultivated at 37°C/5%CO₂ in Dulbecco's modified Eagle's medium (DMEM, Sigma-Aldrich) supplemented with 10% FCS (Sera-Tech), nonessential amino acids (Sigma-Aldrich), and freshly added L-glutamine (complete DMEM).

Primary cultures of mammalian skeletal muscle cells were initiated from neonatal myogenic cells obtained by trypsinisation of muscle pieces from hind limbs of 1- to 3-day-old neonatal rats. For three days following plating, cells were maintained in growth medium (300 µM Ca²⁺), consisting of HAM F12 (Invitrogen SARL, Cergy Pontoise/France) with 10% heat-inactivated horse serum (Invitrogen SARL), 10% fetal calf serum (Invitrogen SARL), and 1% antibiotics. Myoblasts underwent myogenesis in differentiation medium (1.8 mM Ca²⁺), containing DMEM (Invitrogen SARL) supplemented with 5% heat-inactivated horse serum. After 48 h of culture, this control medium (DMEM + serum) was used to promote the formation of myotubes, which occur within 15 to 18 h. The fusion-promoting conditions were provided by the presence of a higher calcium concentration (1,8 mM) and horse serum. This medium exchange was used as time zero for the differentiation.

2.10. Transfections. COS7 cells were seeded at 2 × 10⁵ cells per dish (4 cm diameter) and grown over night. The next day, they were used for transfections. 3 µg plasmid DNA in 75 µL DMEM were mixed with 6 µL Superfect Transfection Reagent (Qiagen) vortexed and incubated for 7 min at 37°C. After washing the cells once with PBS, 0.5 mL DMEM mixed with the DNA-Superfect complex was added and the cells incubated for 3 h at 37°C/5%CO₂. The cell were washed twice with PBS, and 2 mL complete DMEM per dish was added and the cells cultivated for 24–48 h. After 48 h of culture, myotube formation was induced which occurs within 15–18 h. Two days later, the cells were used for immunocytochemistry.

Proliferating myoblasts were transfected with the plasmid cDNA by the Effectene Reagent kit (Qiagen, Courtaboeuf, France). Cells were cultured for 36 hours on glass coverslips (50 × 10⁴ cells) in proliferating medium. Cells were rinsed twice in fresh culture medium, and transfection of 1 µg of plasmid cDNA per 35 mm plastic dish was performed in the presence of 8 µL enhancer for compacting cDNA and 10 µL of the effectene cationic lipid. Following a 16 hour incubation, the transfection mixture was replaced with fresh complete proliferating medium.

2.11. Immunocytochemistry. COS7 cells were washed 3 times for 2 min with PBS and fixed in 4% paraformaldehyde, 0.15 M sodium phosphate buffer pH 7.4 for 15 min, washed

3 times 2 min with PBS, and permeabilised with 0.1% Triton-X-100 in 10% normal goat serum (Sera-Tech) in PBS for 10 min. Primary antibodies were applied in PBS, 10% normal goat serum for 1 h at RT. Cells were washed 3 times 2 min with PBS, then the second antibodies were added in PBS, 10% normal goat serum for 1 h at RT. Cells were washed 3 times 2 min with PBS, then they were covered with glycerol gelatine (Merck) and viewed with a Carl Zeiss Axioplan2 microscope. Antibodies used were anti-FLAG-M2 mouse monoclonal antibody (Stratagene Ltd.), rabbit anti-UT11, rabbit anti-UT31, goat anti-mouse IgM conjugated to Oregon green (Molecular Probes Inc.) goat anti-rabbit conjugated to Cy3 (Jackson Immunoresearch Lab.) F-actin was visualised with rhodamine-phalloidin (Molecular Probes Inc.).

Myoblasts and myotubes were fixed with 4% paraformaldehyde in TBS (20 mM Tris-HCl, pH 7.5, 150 mM NaCl, 2 mM EGTA, 2 mM MgCl₂) for 20 min at room temperature, washed three times with TBS, and incubated with 0.5% Triton X-100/TBS for 10 min to improve permeability to the reagents. After 10 min of exposure to a blocking solution (TBS containing 1% bovine serum albumin; Sigma), fixed cells were incubated 1 h with an anti-Flag-M2 monoclonal mouse antibody (1 : 1000). Samples were then exposed 1 h in the dark to a 1 : 200 diluted FITC-conjugated goat anti-mouse antibody (Jackson Immunoresearch, West Grove, Pa, USA) altogether with TRITC-conjugated phalloidin (Sigma) for directly staining F-actin microfilaments. Samples were mounted using Vectashield mounting medium (Vector, Burlingame, Calif, USA). The immunolabelled samples were examined by confocal laser scanning microscopy (CLSM) using a BioRad MRC 1024 ES (BioRad, Hemel Hempstead, UK) equipped with an argon-krypton gas laser. The TRITC fluorochrome was excited with the 568 nm yellow line, and the emission of the dye was collected via a photomultiplier through a 585 nm long pass filter. The FITC fluorochrome was excited with the 488 nm blue line, and the emission of the dye was collected via a photomultiplier through a 522 nm band pass filter. Data were acquired using an inverted microscope (Olympus IX70, Tokyo, Japan) through a ×60 oil immersion lens and processed with the Laser Sharp software, version 3.0 (BioRad). All the images were performed at equal excitation intensities (10% of the laser power) with a variable confocal aperture, a gain of 1500 and a black level of –3.

2.12. Statistics. Data evaluation was done using nonlinear regression analyses with GraphPad Prism version 2 (GraphPad Software). Values are mean ± standard error of the mean. Statistical analysis was performed using ANOVA and unpaired Student's *t*-test. Significance was accepted at *P* < 0.05.

3. Results

3.1. mRNA of N-Terminal Utrophin Isoform (N-Utro, aa 1–539) in Different Tissues. We previously described the message and protein of the short isoform N-utro in C6 rat glioma cells [22]. Here, we identify its presence in different rat tissues. 1st strand cDNA prepared from tissue

poly(A)⁺ RNA served as template for specific probing for the occurrence of N-utro mRNA by PCR. The schematic cDNA structures for full-length utrophin (Up395) and N-utro in the region of interest around nucleotide 1803 are given in Figure 2(a). The two sequences are identical down to nt 1802 where the deviation from Up395 begins in N-utro with GTA, immediately followed by the stop codon TGA. The protein sequence of N-utro is thus identical to that of Up395 except for the last residue which in N-utro is Val instead of Cys in Up395. N-Utro comprises the two calponin homology domains, CH1 and CH2, followed by the first two spectrin-like repeats and ends with amino acid (aa) residue 539 (Figure 1). The GT motif at the start of the sequence diversion could represent an unused splice donor site, followed by intron material that is completely different from the sequence in Up395 [22]. This allowed the construction of forward and backward primers specific for either the N-utro or the Up395 sequence in order to identify the respective molecular species by PCR (Figure 2(a)). Putative exon-intron boundaries (dashed lines) are given in analogy to their positions in the dystrophin gene.

The 1st strand cDNA was obtained from rat kidney poly(A)⁺ RNA, primed with either oligo(dT) or pd(N)6. As oligo(dT) priming starts at the 3' end and might some times stop within the sequence, we also employed pd(N)6 random hexadeoxynucleotide for priming which starts at corresponding sites along the sequence [30]. On agarose gels, all primer pairs yielded the same distinct bands with both methods in RT-PCR (Figure 2(b)). The AB product is a 110 bp fragment encoded by exon-13, AD comprises exon-13 plus exon-14, and CD only exon-14. All three fragments are shared by Up395 and N-utro. In contrast, the products AF, AG, CF, and CG comprising exon-13 and/or exon-14 plus different lengths of intron-14 are specific for N-utro. EF and EG derive from the N-utro-specific intron-14. To rule out possible transcription artefacts and to confirm correctly spliced N-utro RNA, genomic rat liver DNA was directly subjected to PCR with the following primer pairs, AF, AG, and EG, (Figure 2(c)). Both the AF and AG products comprise now the 1.2 kb intron-13 (see Figure 2(a)) increasing their size with a corresponding slower electrophoretic migration in the agarose gel (from 0.3 kb to 1.5 kb for AF and from 0.5 kb to 1.7 for AG). The size of EG remains unchanged since it derives entirely from intron-14. Thus, splicing N-utro from genomic DNA does not alter fragment size.

For detection of the N-utro splice variant poly(A)⁺ RNA was isolated from different tissues and pd(N)6-primed for production of 1st strand cDNAs. These were subjected to RT-PCR with primers yielding the products EG (276 bp) specific for N-utro and HJ (104 bp) specific for full-length Up395 (Figure 2(d)). Both species are seen in all tissues examined, brain, heart, kidney, liver, and skeletal muscle. The message for N-utro (EG) appeared in all tissues lower than for those Up395 (HJ). Different primer pairs do, however, not allow comparative quantification since expression efficacy may vary between different primer pairs. On the other hand, the N-utro message (primer pair EG) was clearly fainter in adult skeletal muscle than in muscle from 8 days old rats or in adult heart. The same holds for the full-length-utrophin Up395-

specific primer pair HJ. Quantitative comparison between one primer pair from the same gel under identical conditions is valid.

3.2. Utrophin and N-Utro Protein in Different Tissues. Western blots on 4–15% gradient SDS-PAGE were performed with all tissues where the mRNAs for Up395 and N-utro have been analysed (Figure 3). The polyclonal antibodies (pABs) raised against the recombinant utrophin fragments and DYS12 proved specific and did not cross-react. Probing with anti-UT11 clearly revealed Up395 in all tissues (Figures 3(a) and 3(b)) including C6 rat glioma cells which was added for comparison (Figure 3(b)). As expected, Up395 was drastically reduced in adult (double arrowhead) skeletal muscle when compared to muscle from 8 days old rats (P8). The protein bands migrating at ~62 kDa indicated by arrows in heart and kidney may represent the N-utro protein as they coincide in position with the N-utro band in C6 cells. Furthermore, the disappearance of the bands of Up395 and N-utro by competition with an excess of UT11 antigen (columns headed by C) supports the suggestion that the band at ~62 kDa indeed represents the N-utro protein. Together with the fact that the message for the N-utro isoform is well expressed in these tissues (kidney and heart in Figure 2(d)), the corresponding protein we observed seems to represent N-utro. The higher molecular weight bands between Up395 and N-utro in heart and kidney are only partially outcompeted by UT11 antigen and may thus represent utrophin degradation products comprising the N-terminal portion or nonspecific cross-reactions by the primary antiserum or the secondary antibodies. For positioning of full-length dystrophin (Dp427) in relation to Up395 adult muscle, samples were immunostained by anti-DYS12 (a, in Figure 3(b)) and by the commercial monoclonal NCL-DYS1 antibody stemming from aa 1181–1388 in the spectrin repeats 8 and 9 of the rod (b, in Figure 3(b)). The actin stained with a monoclonal IgM antibody in brain (Figure 3(a)), muscle, and heart (Figure 3(b)), was used for loading control and as intrinsic molecular weight marker.

In general, the levels of mRNAs need not necessarily correspond to the amount of protein expression. Nevertheless, it was reported that in human NCL-60 cancer cells 65% of the genes showed statistically significant transcript-protein correlation [31]. We, thus, estimated the relative content of Up395 by semiquantitative immunoblot densitometry in the various tissues from 2 to 8 days young and 6 to 8 weeks adult rats (Table 2). Staining intensities (\pm SEM) were all expressed in relation to that of adult liver tissue which was taken as 100. For calibration, liver and/or adult heart tissue was included in all electrophoretic runs. The results indicate that young and adult liver and brain tissue comprise similar amounts of Up395 protein, while young and adult kidney and heart as well as young skeletal muscle display significantly higher values. In adult muscle, Up395 is down to 10% of that found in young muscle as expected. The high Up395 content in adult aortic and uterine tissue is given for comparison. The content of N-utro was generally too low for

TABLE 2: Content of full-length utrophin in tissues from young (2–8 days of age) and adult (6–8 weeks old) rats. Averages of densitometric evaluation of immunoblots (SEM is given for averages from 5 experiments or more; number n of experiments in brackets). Values of adult liver are set at 100. For comparison, averages of 3 experiments are given for aorta and uterus. Relative band intensities are always determined in runs together with adult liver and/or heart for calibration. For experimental details, see the Methods section.

Tissue		Young		Adult
Liver	(5)	117 ± 24*	(17)	100
Brain	(5)	139 ± 22*	(5)	105 ± 13*
Kidney	(5)	229 ± 29	(6)	278 ± 27
Heart	(8)	362 ± 38	(11)	299 ± 14
Skeletal muscle	(12)	211 ± 18	(20)	21.0 ± 1.5**
Aorta	—	—	(3)	569
Uterus	—	—	(3)	539

(*) Significantly lower ($P < 0.002$) than young and adult heart and adult kidney. (**) Significantly lower ($P < 0.0001$) than any other tissue with n of 5 or higher.

quantitative assessment (Figure 3). The relatively high Up395 content in adult heart and kidney and in young muscle coincides with the brightest transcript bands for Up395 in the agarose gels (HJ product in Figure 2(d)) pointing to a correlation between message and protein expression. An absolute protein content for Up395 of 0.0006% of total protein was determined in adult mouse skeletal muscle [2, 32]. This is around 30 times less than dystrophin in adult muscle (~0.02%) and would allow to translate the relative values from Table 2 into approximate protein content in the different tissues.

3.3. Actin Binding of N-Terminal Fragments of Utrophin and Dystrophin. Two types of recombinant N-terminal fragments were prepared from utrophin and dystrophin for in vitro actin-binding studies (Figure 1). UT12 (coding for aa 2–261 = 31.6 kDa) and DYS12 (aa 1–246 = 29.9 kDa) comprise the actin-binding domain (CH1 and CH2) alone. Second, UT11 (aa 2–594 = 71.1 kDa) contains in addition the first hinge region followed by two spectrin-like repeats plus 68 aa running into spectrin repeat-3. This fragment is taken as analogue to the N-terminal utrophin isoform (N-utro) earlier isolated from C6 rat glioma cells which comprises the two spectrin-like repeats plus 13 aa of repeat-3. As mentioned above, its primary sequence is identical to that of rat utrophin except for the last residue of Cys instead of Val. All three recombinant fragments bearing a His-tag (MRGSH6GS-) at their N-terminus for affinity purification on Ni-nitrilotriacetic acid (Ni-NTA) agarose column could be eluted with 200 mM imidazole under native conditions. The affinity purification from expression in *E. coli* is shown in SDS-PAGE (Figure 4). The electrophoretic mobility of the purified protein fragments is also revealed by immunoreaction with a mAb against the His-tag. Despite its calculated molecular mass of 71.1 kDa, UT11 persistently migrated at a somewhat lower position (with an apparent molecular mass of ~62 kDa) in SDS-PAGE. The

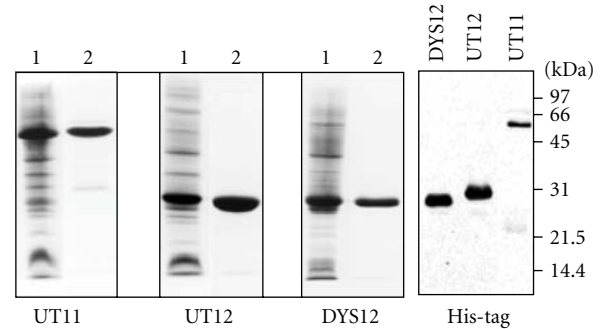


FIGURE 4: Expression and purification of the recombinant utrophin (UT11 and UT12) and dystrophin (DYS12) fragments used for in vitro actin-binding studies. Fragments were expressed in *E. coli* by induction with isopropyl- β -D-1-thiogalactopyranoside (IPTG), subsequently purified by Ni-NTA (Ni-nitrilotriacetic acid) affinity chromatography, and finally checked on 10% SDS-PAGE. Protein staining with Coomassie brilliant blue R250 of bacterial expression (lanes 1) and purified fragments (lanes 2). The fragments were also immunostained with an anti-His-tag mAb.

DYS11 plasmid coding for aa 1–617 (74.0 kDa) presents the homologue to UT11 in utrophin. Unfortunately, the protein could only be extracted and eluted from Ni-NTA agarose under denaturing conditions in 8 M urea and pH 4.5. DYS11 could, therefore, not be used for actin-binding studies. Renaturation by dialysis gradually approaching “native” conditions without urea and pH 7 was unsuccessful.

Actin binding was assessed for UT11 (aa 2–594), UT12 (aa 2–261), and DYS12 (1–246) by high-speed (30 min at 1000,000 g and 25°C) cosedimentation with fast rabbit skeletal muscle actin filaments (see Material and Methods section). SDS-PAGE was performed by loading equal volumes of supernatant and resuspended pellet. Densitometric evaluation was executed after rigorously controlled staining and destaining conditions yielding a linear relationship from 0.2 to 10 μ g of protein under the assumption that all proteins stained with equal intensity. Actin concentration was always kept constant and thus served as internal loading standard, while the potential ligand was varied. BSA (~67 kDa) and tropomyosin (subunit chain ~33 kDa) were run with all series in parallel for negative and positive controls of the binding as well as control sedimentation of the ligands in the absence of actin. The electrophoretic runs of an example of UT12 binding to actin together with BSA as a control are given in Figure 5. While BSA at all concentrations occurs unbound in the supernatant (Figure 5(b)), the bound as well as the unbound portion of UT12 increase with ascending ligand concentration (Figure 5(a)). Traces of probably non-polymerised actin were occasionally seen in the supernatants, never, however, exceeding 2% of total actin.

Binding data and Scatchard plots of all experiments with UT11, UT12, and DYS12 are given in Figure 6. All three protein fragments exhibit saturation binding independent of Ca^{2+} with UT11 and UT12, while DYS12 binding was Ca^{2+} -sensitive (inhibition with EGTA). UT11 and UT12 both display a concave curve in the Scatchard plot indicating a

TABLE 3: Actin binding of recombinant protein fragments of utrophin and dystrophin. Parameters are derived from the binding data given in Figure 6.

Recombinant protein	Amino acids	Affinity constants (M^{-1})		Binding sites per actin monomer		Correlation coefficient (r)	Total actin monomers per ligand at high affinity	Total actin monomer per ligand at saturation
		K_1	K_2	n_1	n_2			
UT11	2–594	6.3×10^6	9.3×10^4	0.04	0.28	0.93	25	3.1
UT12	2–261	4.6×10^6	2.5×10^5	0.14	0.62	0.98	7	1.3
DYS12	1–246	1.3×10^5	3.7×10^5	1.90 (n_1 plus n_2)		0.98	—	1.9

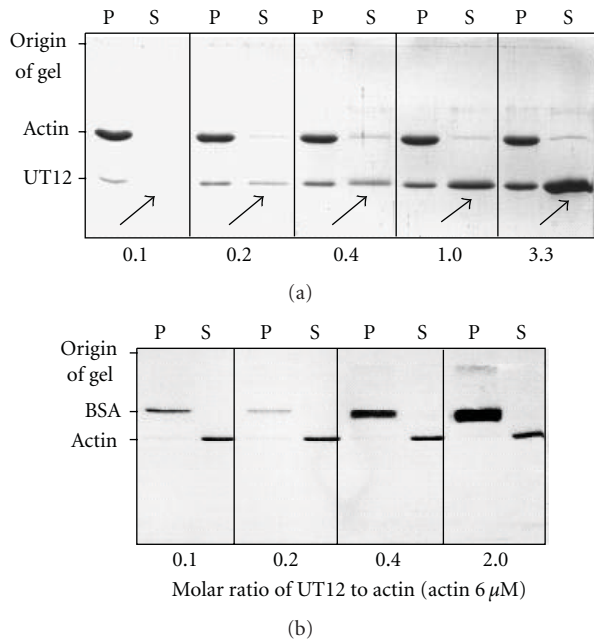


FIGURE 5: Binding assay by cosedimentation of F-actin with UT12 and BSA for control. 10% SDS-PAGE with protein staining by Coomassie brilliant blue R250. Pellet (P) and supernatant (S) fractions with different molar ratios of UT12 (a) or BSA (b) to actin in the presence of 2 mM $MgCl_2$ and 0.5 mM $CaCl_2$. UT12 and BSA varied from 0.6 up to 19 μM . Actin was held constant at 6 μM . The positions of UT12, BSA, and actin are indicated at the left. Arrows point to unbound UT12 in the supernatant. At all concentrations, no BSA was bound to actin.

high affinity and a second lower affinity (Figures 6(b) and 6(d)). The binding parameters derived from Figure 6 are summarised in Table 2. The affinity constant K corresponds to the reciprocal value of the dissociation constant K_D . The higher affinity constant K_1 is for both UT fragments around $5\text{--}6 \times 10^6 M^{-1}$. The second lower K_2 is for UT11 about 70 times lower and for UT12 about 20 times lower. Concave Scatchard curves imply either the existence of two types of binding sites on filamentous actin (F-actin), or ligand-induced negative cooperativity. The two parts of the Scatchard curves for UT11 and UT12 are sufficiently distinct to allow separate evaluation. One molecule of UT11 binds with high affinity per 25 actin monomers, while UT12

binds per 7 actin monomers with high affinity (Table 3). This high stoichiometric relation is greatly reduced at full saturation binding involving the two affinities together. Then one molecule of UT11 binds per 3.1 actin monomers, and UT12 binds per ~ 1.3 actin monomers. The lower binding stoichiometry for UT12 conforms to that reported for the recombinant utrophin fragment (aa 1–261) which corresponds to UT12 [33]. Winder and coworkers [34] have reported an affinity of $\sim 5 \times 10^4 M^{-1}$ for the binding of the N-terminal utrophin fragment (aa 1–261) to muscle F-actin with a stoichiometry of almost 1:2. Its affinity is, however, ~ 100 times lower than that reported here for K_1 and still 5 times lower than that of K_2 .

In contrast to the utrophin fragments, DYS12 (aa 1–246 = actin binding domain) binding to F-actin in the absence of EGTA displays a sigmoidal saturation curve with a lower slope at the beginning that increases with rising ligand concentration before saturation sets (Figure 6(e)). Such a sigmoidal binding curve is characteristic for positive cooperativity and yields a typical convex Scatchard's plot (Figure 6(f)) with a Hill coefficient of 1.52. The combined binding constant for DYS12 is $2\text{--}3 \times 10^5 M^{-1}$, and one DYS12 molecule binds per 2 actin monomers. Reported stoichiometries for recombinant N-terminal protein fragments from utrophin (aa 1–261) and dystrophin (aa 1–246) are 1:1 and 2:1, respectively, [10, 33] which agrees with our results given here. Affinities around $8 \times 10^4 M^{-1}$ have been published for several in vitro actin-binding studies with fragments from utrophin and dystrophin [33]. Our K_1 values for UT11 and UT12 are definitely higher by more than an order of magnitude (Table 3). On the other hand, the binding affinity of our DYS12 with a His-tag at its N-terminus is close to $7.3 \times 10^4 M^{-1}$ reported [35] for a corresponding N-terminal dystrophin peptide (aa 1–246) with the His-tag at its C-terminus and also close to $5.3 \times 10^4 M^{-1}$ published for an untagged N-terminal peptide (aa 1–246) [36]. It may, therefore, be concluded that an attached His-tag does not grossly affect actin binding.

The apparent Ca^{2+} sensitivity of DYS12 binding to actin (inhibited by EGTA) concealed a peculiarity we first were not aware of. In order to evaluate the free Ca^{2+} ion concentration critical for the actin binding of DYS12, cosedimentation assays were performed in a Ca^{2+} -EGTA buffer system with 5 mM EGTA and varying amounts of Ca^{2+} . Surprisingly, at all free Ca^{2+} ion concentrations up to 1 mM, the binding of

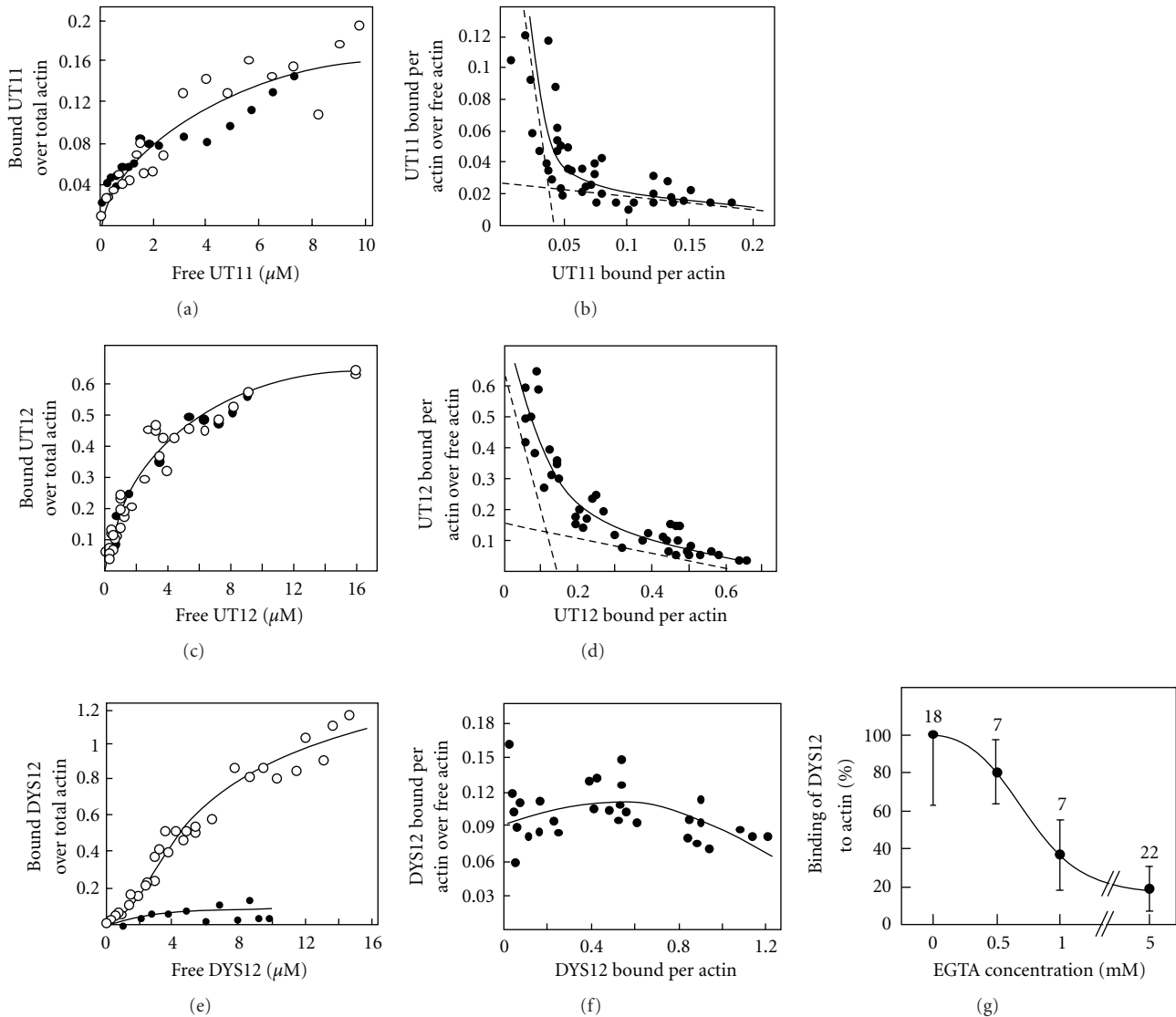


FIGURE 6: Binding of utrophin and dystrophin fragments to actin by cosedimentation. Assays were carried out in 2 mM MgCl₂ and 0.5 mM CaCl₂ (O) or 6 mM MgCl₂ and 5 mM EGTA (•). Saturation curves for binding of UT11 (a), UT12 (c), and DYS12 (e) at the left side with the corresponding Scatchard plots at the right (b, d, f). The binding curves resulted from 7 separate experiments each. All data points (•) are incorporated in the Scatchard plots except for DYS12 in the presence of EGTA. The concave Scatchard curves (b, d) indicate the presence of a higher and a lower affinity due to either two classes of binding sites or, alternatively, negative cooperativity. The convex curve (f) suggests positive cooperativity of DYS12 binding. Binding of DYS12 to actin was also measured with increasing concentrations of EGTA (g) in the presence of 1 mM CaCl₂ in excess over the EGTA. Numbers at data points refer to the number of experiments. Error bars indicate SEM with $P < 0.001$ for 0 and 0.5 versus 1.0 and 5.0 mM EGTA. The small differences between 0 versus 0.5 and 1.0 versus 5.0 mM EGTA were not significant. For further explanation, see the text.

DYS12 never exceeded 30% of the maximal level obtained in the absence of EGTA (data not shown). Therefore, in further series of experiments, the EGTA concentration was varied with always 0.5 mM CaCl₂ in excess over EGTA. The results in Figure 6(g) indicate that the actin binding decreases significantly at EGTA concentrations higher than 0.5 mM. No recovery of the actin binding was observed after removal of EGTA by dialysis in the presence of 0.5 mM CaCl₂. Actin sedimentation was not affected by the presence of EGTA at any concentration used. EGTA up to 5 mM never had

an affect on actin binding either of UT11 nor UT12. For a rough estimation of possible protein structural changes, circular dichroism (CD) measurements were performed on UT12 and DYS12 in the absence of EGTA but with 0.5 mM Ca²⁺ and in the presence of 1.0 mM EGTA plus 1.5 mM Ca²⁺ (spectra not shown). Both fragments exhibited a double minimum under both conditions typical for proteins with a high alpha-helical content. The results revealed a decrease of alpha helix content by 16% for UT12 and by 18% for DYS12 in the presence of EGTA with CaCl₂ in excess (Table 4).

TABLE 4: Circular dichroism parameters of UT12 and DYS12 in the presence and the absence of EGTA each with an excess of 0.5 mM CaCl₂ (spectrum analysis from 190 to 260 nm, for details see the Method section).

	UT12	UT12/EGTA	DYS12	DYS12/EGTA
Alpha helix	60.0	50.9	62.4	51.1
Beta Sheet	0.3	0	0	0
Turn	12.7	19.2	14.0	23.2
Random	26.4	29.9	23.6	25.7
Total	100	100	100	100
RMS*	7.406	19.824	10.238	16.711

*RMS: root mean square for performance quality.

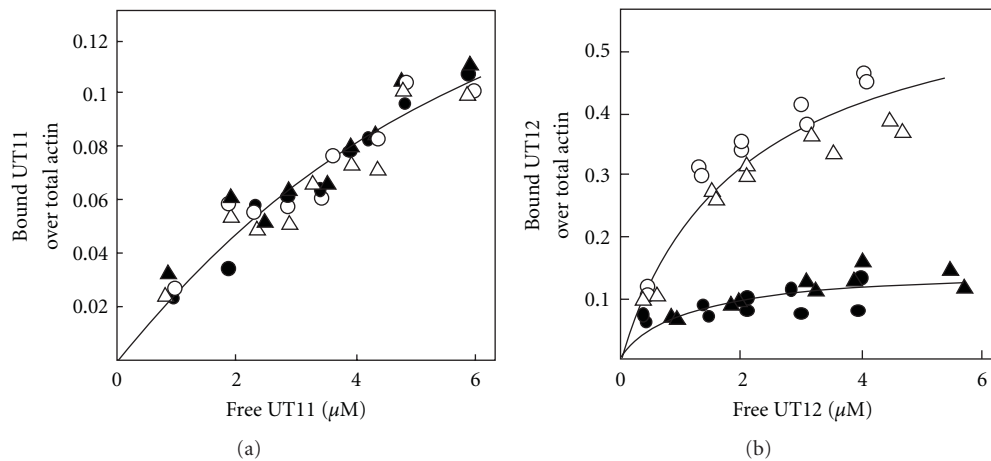


FIGURE 7: Effects of calmodulin and calcium on binding of UT11 and UT12 to actin. Calmodulin plus EGTA does not inhibit actin binding (open symbols). Calmodulin plus Ca²⁺ (black symbols) does not inhibit actin binding of UT11 (a), but binding of UT12 is inhibited (b). Incubation conditions: (O) Ca²⁺ 1 mM; (Δ) calmodulin 0.2 mM plus EGTA 1 mM; (\bullet) calmodulin 0.2 mM plus Ca²⁺ 1 mM; (\blacktriangle) calmodulin 0.2 mM, Ca²⁺ 2 mM plus EGTA 1 mM (for further explanation see the text).

The reduction of alpha-helix was compensated for by an increase in turns. The decrease in alpha-helix is of similar magnitude in the two proteins and does not explain the selective impairment of EGTA on the actin-binding function of DYS12.

Winder and Kendrick-Jones [37] reported that actin binding of recombinant UTR261 (aa 1–261) was inhibited by calmodulin in the presence of Ca²⁺, but not in its absence. We reproduced this result with the corresponding UT12 (aa 2–261) without and with additional EGTA (Figure 7(b)). Surprisingly, calmodulin plus Ca²⁺ and also calmodulin, 2 mM Ca²⁺ plus 1 mM EGTA, which both inhibited binding of UT12 did not affect actin binding of UT11 bearing two spectrin repeats (Figure 7(a)).

3.4. Immunolocalisation of UT11, UT12, and UT21 in COS7 Cells and Myotubes. For evaluation of intracellular localisation of the actin binding domain alone (EUT12, aa 1–261), the actin-binding domain plus the first two spectrin repeats (EUT11, aa 1–543) and the two first spectrin repeats R1 and R2 alone (EUT21, aa 262–543) were inserted into eukaryotic plasmids for transfection to COS7 cells (Figure 8) as well as to myoblasts (Figure 9). For unambiguous recognition, all three recombinant fragments were fused to the “FLAG”

peptide (-DYKDDDDK) at their C-terminus which can be detected by anti-Flag M2 mAb. Actin was visualised in double staining with rhodamine-phalloidin. Transfection efficiency was directly assessed by fluorescence microscopy in a number of experiments in which a GFP containing second plasmid was included. The transfected cells displayed unaltered shape and growth compared to nontransfected cells in phase contrast analysis.

COS7 cells are derived from monkey’s kidney and immortalised by an origin-defective mutant of SV40 [38]. These cells are often used for transfection with recombinant plasmids, and during growth they readily adhere to glass and plastic surfaces. Spread on the substratum the cells display a fibroblast-like appearance (Figures 8(a), 8(c), and 8(e) at the right). The cytoskeletal actin (probably beta- and gamma-actin) appears in stress fibre structures and in densely organised cortical cytoskeleton along the cell surface membrane. In the left vertical row (a–f), anti-FLAG staining reveals the recombinant utrophin proteins. EUT12 (actin-binding domain) follows the same pattern by staining all actin structures outside the cell nucleus (Figures 8(c) and 8(d)). EUT21 (first two spectrin repeats) localises in the cell nucleus and does not associate with actin (Figures 8(e) and 8(f)). Anti-UT31 (against the rod) faintly stains endogenous full-length

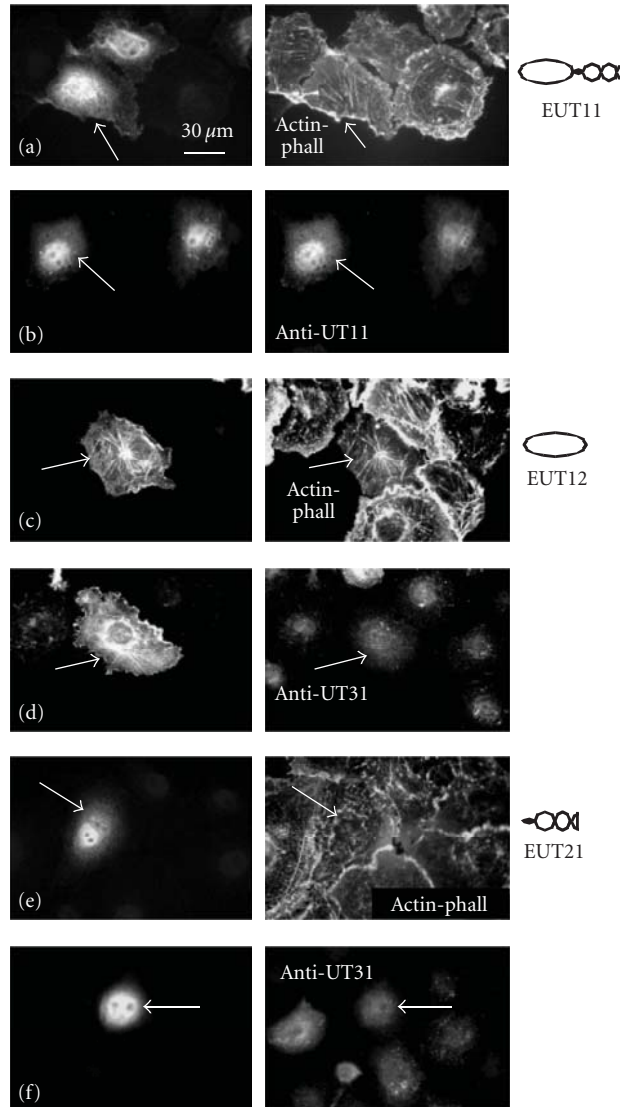


FIGURE 8: Intracellular sorting of utrophin fragments by expression of eukaryotic vectors in COS7 cells (EUT11, EUT12, and EUT21, all carrying the FLAG-tag at the C-terminus). Cells in the vertical row at the left are all stained with the anti-Flag M2 mAb ((a), (b), (c), (d), (e), (f)). Rhodamine-phalloidin staining for actin displays stress fibres and a dense cortical actin cytoskeleton along the cell membranes in the COS7 cells spreading on the substratum ((a), (c), (e) at the right). Anti-UT11 recognises full-length utrophin and N-utrophin giving intensive staining in and around the nucleus that results from the heterologously expressed EUT11 plus the endogenous utrophin ((b) at the right). Anti-UT31 (spectrin 14–16 in the rod) stains COS7 cells diffusely throughout the cytoplasm without marking any defined actin structures ((d), (f) at the right). EUT21 (first two spectrin domains) exclusively concentrates in the nuclei ((e), (f)). EUT12 (actin-binding domain alone) precisely traces the actin microfilaments and the cortical cytoskeletal structures ((c), (d)). For further explanation see the text.

utrophin (Up395) in the entire cell (d the at right). EUT11 (actin-binding plus two spectrin domains) is found in and around the cell nucleus but also throughout the cell body and faintly along the membrane (Figures 8(a) and 8(b)). This distribution of the FLAG-labeled EUT11 is underlined by anti-UT11 (b the at right) that intensely stains EUT11 plus the endogenous utrophin. Taken together, only the isolated actin-binding domain of utrophin (EUT12) clearly associates with stress fibres and submembranous cortical actin structures. The relatively diffuse staining of Up395 with anti-UT11 and anti-UT31 throughout the cells lets assume that additional portions of the intact molecule other than the

actin and the first two spectrin domains must be involved in specific target sorting.

Transfection with the cDNA plasmids encoding the utrophin fragments EUT11, EUT12, and EUT21 fused to the FLAG Tag was performed on myoblasts from neonatal rat hindleg muscle in primary cell cultures. After 48 h of culture, myotube formation was induced, and two days later the fixed cells were immunostained for the utrophin fragments with FITC-conjugated AB and with TRITC-conjugated phalloidin for F-actin microfilaments. Staining patterns were assessed by confocal laser scanning microscopy (Figure 9). The anti-Flag stained utrophin fragments are displayed in the left

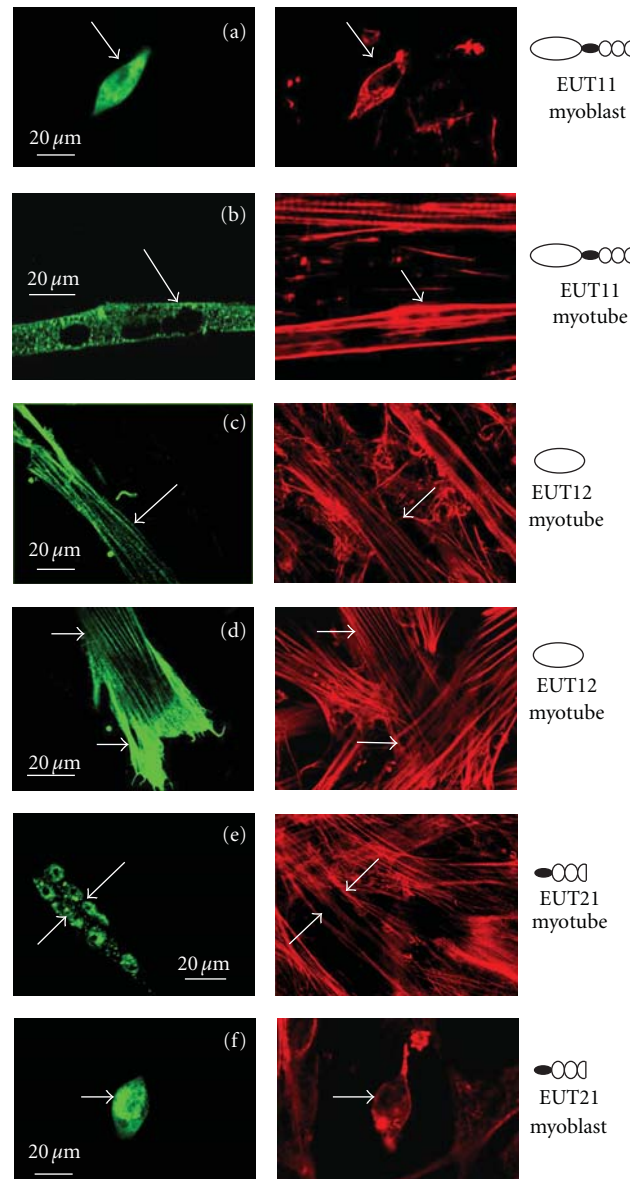


FIGURE 9: Intracellular sorting of utrophin fragments by expression of eukaryotic vectors in myoblast and myotube primary cultures (EUT11, EUT12, and EUT21, all carrying the FLAG-tag at the C-terminus). In each picture in the left vertical row ((a)–(f)), one transfected cell (green) is present stained with anti-FLAG for the corresponding utrophin fragment. Staining with rhodamine-phalloidin for actin reveals a variable number of red cells in each picture ((b)–(e) in the right vertical row) indicating that the transfected cells often fuse with nontransfected cells when forming myotubes. EUT11 and EUT21 solidly stain nucleus and cytoplasm in single spindle-shaped myoblasts. EUT12 (actin-binding domain) sharply stains actin microfilaments ((c) and (d)) superimposable to the red pattern of actin stain ((c) and (d) at the right). EUT12 also concentrates in regions where actin may attach to the substratum (d). EUT11 distributes over the cytoplasm in a diffuse and punctate manner (b) leaving the myotube nuclei unstained. In contrast, EUT21 is almost exclusively confined to the cell nuclei. For further explanations, see the Methods section and the text.

vertical row in green, while F-actin is stained in red in the right vertical row. In all cases there appears only one transfected green cell (Figures 9(b)–9(e)). Evidently the transfected myoblasts often fuse to myotubes together with nontransfected cells. In the spindle-shaped myoblasts (Figures 9(a) and 9(f)), staining for EUT11 and EUT21 fills the entire cell including the nucleus. The myotubes (Figures 9(b)–9(e)) display a rich filamentous actin structural network, probably mostly nonmuscle beta- and gamma-isoforms of the cortical

cytoskeleton. Sarcomere structures are not yet visible except for just a beginning in the nontransfected myotube in red at the top of Figure 9(b). EUT12 (actin-binding domain) staining precisely follows the actin structures throughout the myotubes and becomes especially dense at the ends where the cells adhere to the substratum (Figures 9(c) and 9(d)). EUT11 staining does not follow the actin filaments but remains diffuse and punctate, sparing out the nuclei. Its staining pattern suggests that EUT11 may attach to the

myotube surface membrane. EUT21 seems almost entirely confined to a row of nuclei in Figure 9(e).

The general staining patterns of the three recombinant fragments from the N-terminal utrophin region in myotubes and in COS7 cells are similar in kind. The isolated actin-binding domain (EUT12) clearly associates with F-actin structures in both cell types, while the other two protein fragments more variably appear in the cytoplasm, along the membranes or in the cell nuclei.

4. Discussion

4.1. mRNA and N-Utro Protein in Rat Tissues. The occurrence of message and protein of a novel N-terminal short utrophin isoform (N-utro) in different rat tissues is reported here for the first time. In addition, its intracellular sorting as well as in vitro actin-binding properties was examined. The message for full-length utrophin (Up395) is the highest in cardiac muscle, in skeletal muscle of early postnatal animals, and in kidney. It is apparently lower in adult skeletal muscle, brain, and liver (product HJ in Figure 2(d)). Although a quantitative correlation between protein and message can often not be demonstrated, in this case the Up395 content (expressed relative to that in adult liver) was significantly higher in those tissues where the message was also higher (Table 1). This correlation between message and protein is remarkable in view of the notorious difficulties encountered with quantitative immunoblotting involving transfer of large proteins such as Up395 to nitrocellulose membranes for electrophoresis. Correspondingly, the protein N-utro could be only visualised by immunoblots in those tissues with the highest message levels for kidney and cardiac muscle (Figure 3). In the other, tissues its content was too low for detection.

4.2. Actin Binding. Since N-utro is the only N-terminal short isoform possessing the actin-binding domain known so far, extensive binding studies were done with the recombinant analogue UT11 (aa 2–594, actin-binding domain plus two spectrin repeats) in comparison to UT12 (aa 2–261) and DYS12 (1–246), the latter two comprising the actin-binding domain alone (Figures 6 and 7 plus Table 3). Several of the findings presented here shed light on fundamental differences in actin-binding function between these N-terminal fragments of utrophin and dystrophin.

First, the high- and low-binding affinities for UT11 and UT12 greatly affect the stoichiometric relation of ligand to actin. With the high affinity, UT11 binds to every 25th actin and UT12 to every 7th actin. The two additional spectrin repeats in UT11 differentiate the two utrophin fragments from one another. These two motifs of UT11 must be responsible for the more extended spacing of this ligand as compared to UT12. With saturation binding the second lower affinity reduces the spacing of the ligands along the F-actin filament to ~ 3 actin per UT11 and close to one actin per UT12. In our experiments, there were no additional proteins present such a tropomyosin or troponin components that could impart a defined spacing periodicity. Thus, the high affinity binding results suggest that UT11 with two spectrin

repeats affects the actin filament binding properties over a distance of 25 actin monomers. But on increasing ligand saturation, additional UT11 molecules seem able to associate with actin at lower affinity in between those already bound with high affinity. The overall stoichiometry is, thus, reduced to three actin monomers per UT11. A similar deliberation applies to the shorter UT12 without spectrin repeats. With high affinity, the actin-binding domain alone affects the accessibility of 7 actins in the filament, while on saturation including low-affinity binding, the stoichiometry drops to $\sim 1:1$. Taken together, our results suggest, under the assumption of indistinguishable binding sites of the individual actin monomers in the filament, that the distinct lower affinity is induced by the binding of the ligands UT11 and UT12 with high affinity. Furthermore, in view of the different spacing induced by UT11 or UT12 binding with high affinity, it seems most unlikely that a second class of defined binding sites with lower intrinsic affinity exists along the actin filament. Several reports on N-terminal utrophin and dystrophin fragments mention similar actin-binding affinities in the range of $\sim 10^5 \text{ M}^{-1}$ and similar stoichiometries for binding saturation as given here [33–35, 39]. However, these published binding affinities may routinely represent the lower values at full saturation, while the higher values at low ligand concentrations of utrophin fragments may have been overlooked. Actin-binding studies have mostly been performed with skeletal muscle alpha-actin. Yet the cytoskeletal Up395 and Dp427 primarily interact in vivo with cytosolic beta- and gamma-actin which are ubiquitously expressed. Even in striated muscle, the cortical gamma cytoskeletal actin in the costameres between the sarcolemma and the Z-disks presents the interaction partner for Up395 and Dp427 [40]. Nevertheless, the different actin isoforms share over 93% sequence identity and can replace each other to a large extent [40]. Reassuringly, it was reported that the binding characteristics of utrophin and dystrophin and their fragments to nonmuscle actin are almost identical to those with skeletal muscle actin [8, 33–35]. The binding affinities are in some cases slightly higher for cytoplasmic than for skeletal muscle actin.

Second, in stark contrast to the negative cooperativity in the binding of the utrophin N-terminal fragments, DYS12 binds to actin filaments with moderately positive cooperativity (Hill coefficient of 1.5) and a stoichiometry at saturation of one ligand per two actin monomers. Positive cooperativity with a Hill coefficient of 3.5 was also reported for actin binding of the dystrophin fragment (aa 1–246) that corresponds to UT12 [6, 36]. Tropomyosin was reported to affect neither affinity nor stoichiometry in the binding of dystrophin in vitro [39, 41]. Curious enough, Up395 and Dp427 both bind to actin by lateral association along the actin filament but do not compete in their binding with one another [2]. Dp427 comprises 5 basic spectrin repeats within the stretch of R11 to R17 in the middle of the rod. This spectrin repeat stretch firmly associates with F-actin and reinforces the binding of the N-terminal domain to actin. The actin interaction of the spectrin repeat region is salt dependent pointing to its electrostatic nature. The two actin-binding regions in dystrophin are separated by ~ 1200 aa. Ervasti has presented a

model for dystrophin as molecular shock absorber during muscle contraction. On stretch the electrostatic interaction of the positively charged spectrin repeats would slide along the negative surface of the actin filament and, thus, dampen elastic recoil [2]. This is not the case with Up395. Up395 lacks the basic nature of the corresponding spectrin repeats in the middle of the rod, and, consequently, this stretch does not interact with actin [42]. Instead, the 10 spectrin repeats immediately following the N-terminal actin-binding domain firmly interact with actin and stabilise the binding. This interaction is not salt dependent and, thus, may be of hydrophobic nature. The N-terminal domain and the following spectrin repeats function as a single contiguous unit [43]. This is compatible with the notion that UT11 with the two first spectrin repeats occupies more actin monomers than UT12. Consequently, it may be speculated that intact Up395, because of its contiguous binding region from the N-terminus through to spectrin repeat R10, does not function as molecular shock absorber but rather as stabiliser of cortical actin filaments in costameres and in the postsynaptic membranes of NMJs [2, 4].

Finally, we assessed potential regulation by Ca^{2+} and calmodulin of fragment binding to actin. The actin binding of UT11 and UT12 proved to be independent of Ca^{2+} and not affected by EGTA. However, the interaction of DYS12 with actin is virtually abolished in the presence of more than 0.5 mM EGTA even in the simultaneous presence of 0.5 mM CaCl_2 in excess. It was not possible to restore the binding function to DYS12 by gradually removing EGTA in dialysis. Molecular parameters derived from circular dichroism measurements indicated a reduction of alpha-helix content by around 17% for both fragments in the presence of 5 mM EGTA plus 6 mM CaCl_2 . This does not explain the selective abolition of DYS12 actin binding by EGTA. The inhibition of actin binding of UTR261 (or UT12) by calmodulin in the presence of Ca^{2+} was suggested to be due to its competitive binding to the CH1 domain [37]. Immediately upstream of the actin-binding sequence-2 (ABS2) near the C-terminus of CH1 localises a highly hydrophobic stretch of 15 aa that may accommodate calmodulin complexed to Ca^{2+} . It is speculated that this represents a mode of regulation *in vivo* for the interaction of the N-terminal utrophin with actin. Our results indicate, however, that the two spectrin-like repeats in UT12 are sufficient to prevent such a calmodulin/ Ca^{2+} mode of regulation. *In vivo* with Up395 running along the actin filament firmly bound from its N-terminal actin-binding domain through to spectrin repeat R10, it is unlikely that this part of the molecule responds to subtle Ca-calmodulin regulation. Furthermore, these findings are of particular interest in relation to the novel N-utro isoform.

4.3. Intracellular Sorting of N-Terminal Utrophin Fragments. To define their intracellular localization, COS7 cells and skeletal muscle myoblasts were transfected with the eukaryotic vectors of N-terminal utrophin fragments bearing the FLAG-Tag at their C-terminus for immunodetection:

EUT11 (aa 1–543, CH1-CH2 actin-binding domain plus first two spectrin repeats);

EUT12 (aa 1–261, CH1-CH2 actin-binding domain alone);

EUT21 (aa 262–543, the first two spectrin repeats alone).

After spreading on the substratum, the COS7 cells display a fibroblast-like appearance as revealed by staining of the actin cytoskeleton with rhodamine-phalloidin (Figure 8). Differentiation and myotube formation were induced in the myoblasts by adding 1.8 mM CaCl_2 and horse serum (Figure 9). As soon as the spindle-shaped diffusely staining myoblasts fuse to myotubes, an intensely stained cytoskeleton develops with cytoplasmic actin filaments filling the entire tubes. Only in one nontransfected myotube an early expression of sarcomeric striation can be seen (Figure 9(b)). In both types of cells, the transfected EUT12 neatly tracks the actin cytoskeleton and accumulates at the edges where the myotubes attach to the substratum. In the myotubes, the actin fibres could serve as scaffold for the nascent myofibrils as we have described earlier for the remodeling of rat cardiomyocytes in long-term culture [44]. Recombinant UTR261-GST (glutathione S-transferase) fusion-protein microinjected into chick embryo fibroblasts was shown to label stress fibres and focal contacts [34]. The diffuse staining for EUT11 comes as a surprise. Its repartition extends throughout the cells. In the myotube, it leaves the nuclei unstained and probably lines the membranes. Intact Up395 recognised by anti-UT31 against the rod domain (spectrin repeats R14–R16) presents a discrete, diffuse staining throughout the COS7 cells (Figures 8(d) and 8(f)). This indicates that Up395 probably also lines the cell membrane attached to the cortical actin cytoskeleton, but it does not mark any stress fibre-like structures. Yet another feature holds for EUT21 which distinctly marks the nuclei, probably invading them.

Taken together, the staining pattern of EUT12 for actin filaments and of EUT11 for membranes may be interpreted as follows. The actin-binding domain alone (UT12 and EUT12) binds to actin filaments with high affinity in a Ca^{2+} -independent manner. The actin binding plus first two spectrin domains (UT11 and EUT11) associate with membranes preventing the N-terminus to bind to actin stress fibre-like structures, though the N-terminus may still bind strongly to the cortical actin network lining the membranes. In other words, the two spectrin repeats associated with membranes, prevent the N-terminus from going astray by following the actin filaments throughout the cell body. UT11 and EUT11 correspond to the N-utro isoform, whose genomic derivation and protein we have described here. Thus, N-utro (1–539) may function as an ultrashort linker between cortical actin and the membranes. These properties may gain functional significance when N-utro was present in sufficiently high concentration. In molecular terms, N-utro is ~6 times smaller than full-length Up395 and could represent a significant molecular fraction. Moreover, its repartition in different tissues could be concentrated at specific subcellular structures such as neural synapses or in epithelial and endothelial cell systems involved in barrier, secretory, and resorptive function as in kidney nephrons,

vasculature, or blood-brain barrier. In all these cases, scaffold and signaling platforms require highly specialised subcellular localisation for interaction with myriads of proteins and other components [11, 12, 16, 17, 45].

5. Conclusions

We describe here a novel type of utrophin isoform that derives from its N-terminus (N-utro). The various C-terminal isoforms of utrophin and dystrophin correspond to each other except for Dp260 which has no analogue in utrophin. N-Utro also presents an exception as no analogous N-terminal isoform from dystrophin is known so far. N-utro has no relation to the utrophin/dystrophin-associated protein complex. Consequently, the function of N-utro seems to differ from that of the full-length or C-terminal isoforms. Our immunocytochemical results indicate that N-utro could be responsible for the anchoring of the cortical actin cytoskeleton to the membranes. Possible association of N-utro with additional proteins other than actin needs further exploration.

Acknowledgments

The authors thank Dr. M. Vasak and M. Knipp (Department of Biochemistry, University of Zurich, Switzerland) for help with the CD analysis, Dr. G. Frank (Institute of Molecular Biology and Biophysics, ETH Zurich, Switzerland) for microsequencing the purified recombinant proteins, Dr. S. J. Winder (Department of Biomedical Science, University of Sheffield, UK) for providing the human dystrophin minigene, and T. Grampp for skilled technical assistance. They are grateful for financial support by the Roche Research Foundation, Basel, Switzerland; Swiss Foundation for Research on Muscle Diseases, Basel, Switzerland; Hartmann Mueller Foundation, Zurich, Switzerland.

References

- [1] J. M. Ervasti, "Costameres: the Achilles' heel of Herculean muscle," *Journal of Biological Chemistry*, vol. 278, no. 16, pp. 13591–13594, 2003.
- [2] I. N. Rybakova, J. L. Humston, K. J. Sonnemann, and J. M. Ervasti, "Dystrophin and utrophin bind actin through distinct modes of contact," *Journal of Biological Chemistry*, vol. 281, no. 15, pp. 9996–10001, 2006.
- [3] D. G. Allen and N. P. Whitehead, "Duchenne muscular dystrophy—what causes the increased membrane permeability in skeletal muscle?" *International Journal of Biochemistry and Cell Biology*, vol. 43, no. 3, pp. 290–294, 2010.
- [4] J. M. Ervasti, "Dystrophin, its interactions with other proteins, and implications for muscular dystrophy," *Biochimica et Biophysica Acta*, vol. 1772, no. 2, pp. 108–117, 2007.
- [5] M. Guglieri and K. Bushby, "Molecular treatments in Duchenne muscular dystrophy," *Current Opinion in Pharmacology*, vol. 10, no. 3, pp. 331–337, 2010.
- [6] E. Le Rumeur, S. J. Winder, and J. -F. Hubert, "Dystrophin: more than just the sum of its parts," *Biochimica et Biophysica Acta*, vol. 1804, no. 9, pp. 1713–1722, 2010.
- [7] J. Tinsley, N. Deconinck, R. Fisher et al., "Expression of full-length utrophin prevents muscular dystrophy in mdx mice," *Nature Medicine*, vol. 4, no. 12, pp. 1441–1444, 1998.
- [8] I. N. Rybakova, J. R. Patel, K. E. Davies, P. D. Yurchenco, and J. M. Ervasti, "Utrophin binds laterally along actin filaments and can couple costameric actin with sarcolemma when over-expressed in dystrophin-deficient muscle," *Molecular Biology of the Cell*, vol. 13, no. 5, pp. 1512–1521, 2002.
- [9] A. Clerk, G. E. Morris, V. Dubowitz, K. E. Davies, and C. A. Sewry, "Dystrophin-related protein, utrophin, in normal and dystrophic human fetal skeletal muscle," *Histochemical Journal*, vol. 25, no. 8, pp. 554–561, 1993.
- [10] A. J. Sutherland-Smith, C. A. Moores, F. L. M. Norwood et al., "An atomic model for actin binding by the CH domains and spectrin-repeat modules of utrophin and dystrophin," *Journal of Molecular Biology*, vol. 329, no. 1, pp. 15–33, 2003.
- [11] C. Perronnet and C. Vaillend, "Dystrophins, utrophins, and associated scaffolding complexes: role in mammalian brain and implications for therapeutic strategies," *Journal of Biomedicine and Biotechnology*, vol. 2010, Article ID 849426, 19 pages, 2010.
- [12] T. Haenggi and J. M. Fritschy, "Role of dystrophin and utrophin for assembly and function of the dystrophin glycoprotein complex in non-muscle tissue," *Cellular and Molecular Life Sciences*, vol. 63, no. 14, pp. 1614–1631, 2006.
- [13] J. Donders and C. Taneja, "Neurobehavioral characteristics of children with duchenne muscular dystrophy," *Child Neuropsychology*, vol. 15, no. 3, pp. 295–304, 2009.
- [14] T. S. Khurana and K. E. Davies, "Pharmacological strategies for muscular dystrophy," *Nature Reviews Drug Discovery*, vol. 2, no. 5, pp. 379–390, 2003.
- [15] S. J. Winder, "The membrane-cytoskeleton interface: the role of dystrophin and utrophin," *Journal of Muscle Research and Cell Motility*, vol. 18, no. 6, pp. 617–629, 1997.
- [16] T. Haenggi, A. Soontornmalai, M. C. Schaub, and J. M. Fritschy, "The role of utrophin and Dp71 for assembly of different dystrophin-associated protein complexes (DPCs) in the choroid plexus and microvasculature of the brain," *Neuroscience*, vol. 129, no. 2, pp. 403–413, 2004.
- [17] T. Haenggi, M. C. Schaub, and J. M. Fritschy, "Molecular heterogeneity of the dystrophin-associated protein complex in the mouse kidney nephron: differential alterations in the absence of utrophin and dystrophin," *Cell and Tissue Research*, vol. 319, no. 2, pp. 299–313, 2005.
- [18] T. M. Nguyen, T. T. Le, D. J. Blake, K. E. Davies, and G. E. Morris, "Utrophin, the autosomal homologue of dystrophin, is widely-expressed and membrane-associated in cultured cell lines," *FEBS Letters*, vol. 313, no. 1, pp. 19–22, 1992.
- [19] D. J. Blake, J. N. Schofield, R. A. Zuellig et al., "G-utrophin, the autosomal homologue of dystrophin Dp116, is expressed in sensory ganglia and brain," *Proceedings of the National Academy of Sciences of the United States of America*, vol. 92, no. 9, pp. 3697–3701, 1995.
- [20] A. P. Weir, E. A. Burton, G. Harrod, and K. E. Davies, "A- and B-utrophin have different expression patterns and are differentially up-regulated in mdx muscle," *Journal of Biological Chemistry*, vol. 277, no. 47, pp. 45285–45290, 2002.
- [21] J. Wilson, W. Putt, C. Jimenez, and Y. H. Edwards, "Up71 and Up140, two novel transcripts of utrophin that are homologues of short forms of dystrophin," *Human Molecular Genetics*, vol. 8, no. 7, pp. 1271–1278, 1999.
- [22] R. A. Zuellig, B. C. Bornhauser, I. Knuesel, F. Heller, J. M. Fritschy, and M. C. Schaub, "Identification and characterisation of transcript and protein of a new short N-terminal utrophin isoform," *Journal of Cellular Biochemistry*, vol. 77, no. 3, pp. 418–431, 2000.
- [23] T. M. Nguyen, T. R. Helliwell, C. Simmons et al., "Full-length and short forms of utrophin, the dystrophin-related protein," *FEBS Letters*, vol. 358, no. 3, pp. 262–266, 1995.

- [24] M. M. Bradford, "A rapid and sensitive method for the quantitation of microgram quantities of protein utilizing the principle of protein dye binding," *Analytical Biochemistry*, vol. 72, no. 1-2, pp. 248-254, 1976.
- [25] J. H. Han, C. Stratowa, and W. J. Rutter, "Isolation of full-length putative rat lysophospholipase cDNA using improved methods for mRNA isolation and cDNA cloning," *Biochemistry*, vol. 26, no. 6, pp. 1617-1625, 1987.
- [26] J. Sambrook, E. F. Fritsch, and T. Maniatis, *Molecular Cloning: A Laboratory Manual*, Cold Spring Harbor Laboratory, Cold Spring Harbor, NY, USA, 1989.
- [27] U. K. Laemmli, "Cleavage of structural proteins during the assembly of the head of bacteriophage T4," *Nature*, vol. 227, no. 5259, pp. 680-685, 1970.
- [28] J. D. Pardee and J. A. Spudich, "Purification of muscle actin," *Methods in Cell Biology*, vol. 24, pp. 271-289, 1982.
- [29] J. T. Yang, C. S. C. Wu, and H. M. Martinez, "Calculation of protein conformation from circular dichroism," *Methods in Enzymology*, vol. 130, no. C, pp. 208-269, 1986.
- [30] D. K. Nam, S. Lee, G. Zhou et al., "Oligo(dT) primer generates a high frequency of truncated cDNAs through internal poly(A) priming during reverse transcription," *Proceedings of the National Academy of Sciences of the United States of America*, vol. 99, no. 9, pp. 6152-6156, 2002.
- [31] U. T. Shankavaram, W. C. Reinhold, S. Nishizuka et al., "Transcript and protein expression profiles of the NCI-60 cancer cell panel: an integromic microarray study," *Molecular Cancer Therapeutics*, vol. 6, no. 3, pp. 820-832, 2007.
- [32] K. Ohlendieck and K. P. Campbell, "Dystrophin constitutes 5% of membrane cytoskeleton in skeletal muscle," *FEBS Letters*, vol. 283, no. 2, pp. 230-234, 1991.
- [33] C. A. Moores and J. Kendrick-Jones, "Biochemical characterisation of the actin-binding properties of utrophin," *Cell Motility and the Cytoskeleton*, vol. 46, no. 2, pp. 116-128, 2000.
- [34] S. J. Winder, L. Hemmings, S. K. Maciver et al., "Utrophin actin binding domain: analysis of actin binding and cellular targeting," *Journal of Cell Science*, vol. 108, no. 1, pp. 63-71, 1995.
- [35] B. A. Renley, I. N. Rybakova, K. J. Amann, and J. M. Ervasti, "Dystrophin binding to nonmuscle actin," *Cell Motility and the Cytoskeleton*, vol. 41, no. 3, pp. 264-270, 1998.
- [36] M. Way, B. Pope, R. A. Cross, J. Kendrick-Jones, and A. G. Weeds, "Expression of the N-terminal domain of dystrophin in *E. coli* and demonstration of binding to F-actin," *FEBS Letters*, vol. 301, no. 3, pp. 243-245, 1992.
- [37] S. J. Winder and J. Kendrick-Jones, "Calcium/calmodulin-dependent regulation of the NH₂-terminal F-actin binding domain of utrophin," *FEBS Letters*, vol. 357, no. 2, pp. 125-128, 1995.
- [38] Y. Gluzman, "SV40-transformed simian cells support the replication of early SV40 mutants," *Cell*, vol. 23, no. 1, pp. 175-182, 1981.
- [39] E. Fabbriozio, A. Bonet-Kerrache, J. J. Leger, and D. Mornet, "Actin-dystrophin interface," *Biochemistry*, vol. 32, no. 39, pp. 10457-10463, 1993.
- [40] B. J. Perrin and J. M. Ervasti, "The actin gene family: function follows isoform," *Cytoskeleton*, vol. 67, no. 10, pp. 630-634, 2010.
- [41] I. N. Rybakova and J. M. Ervasti, "Dystrophin-glycoprotein complex is monomeric and stabilizes actin filaments in vitro through a lateral association," *Journal of Biological Chemistry*, vol. 272, no. 45, pp. 28771-28778, 1997.
- [42] K. J. Amann, A. W. X. Guo, and J. M. Ervasti, "Utrophin lacks the rod domain actin binding activity of dystrophin," *Journal of Biological Chemistry*, vol. 274, no. 50, pp. 35375-35380, 1999.
- [43] I. N. Rybakova and J. M. Ervasti, "Identification of spectrin-like repeats required for high affinity utrophin-actin interaction," *Journal of Biological Chemistry*, vol. 280, no. 24, pp. 23018-23023, 2005.
- [44] M. E. Eppenberger, I. Hauser, T. Baechi et al., "Immunocytochemical analysis of the regeneration of myofibrils in long-term cultures of adult cardiomyocytes of the rat," *Developmental Biology*, vol. 130, no. 1, pp. 1-15, 1988.
- [45] I. Knuesel, B. C. Bornhauser, R. A. Zuellig, F. Heller, M. C. Schaub, and J. M. Fritschy, "Differential expression of utrophin and dystrophin in CNS neurons: an in situ hybridization and immunohistochemical study," *Journal of Comparative Neurology*, vol. 422, no. 4, pp. 594-611, 2000.

Methodology Report

A High-Throughput Solid-Phase Microplate Protein-Binding Assay to Investigate Interactions between Myofilament Proteins

Brandon J. Biesiadecki¹ and J.-P. Jin²

¹Department of Physiology and Cell Biology, The Ohio State University, Columbus, OH 43210, USA

²Department of Physiology, Wayne State University School of Medicine, Detroit, MI 48201, USA

Correspondence should be addressed to Brandon J. Biesiadecki, biesiadecki.1@osu.edu

Received 25 May 2011; Accepted 24 August 2011

Academic Editor: Xupei Huang

Copyright © 2011 B. J. Biesiadecki and J.-P. Jin. This is an open access article distributed under the Creative Commons Attribution License, which permits unrestricted use, distribution, and reproduction in any medium, provided the original work is properly cited.

To understand the structure-function relationship of muscle-regulatory-protein isoforms, mutations, and posttranslational modifications, it is necessary to probe functional effects at the level of the protein-protein interaction. Traditional methodologies assessing such protein-protein interactions are laborious and require significant amounts of purified protein, while many current methodologies require costly and specialized equipment or modification of the proteins, which may affect their interaction. To address these issues, we developed a novel method of microplate-based solid-phase protein-binding assay over the recent years. This method assesses specific protein-protein interactions at physiological conditions, utilizes relatively small amounts of protein, is free of protein modification, and does not require specialized instrumentation. Here we present detailed methodology for the solid-phase protein-binding assay with examples that we have successfully applied to quantify interactions of myofilament-regulatory proteins. We further provide considerations for optimization of the assay conditions and its broader application in studies of other protein-protein interactions.

1. Introduction

To ultimately understand the structure-function relationship resulting from protein isoform variation, mutation, and posttranslational modification, one must be able to quantify the functional effect of the structural alteration on the interaction of the protein with its binding proteins. Traditional methodologies used to investigate these interactions, such as equilibrium dialysis and affinity chromatography, rely on large amounts of proteins, are time consuming, and are labor intensive. While newer methodologies such as Förster resonance energy transfer or surface plasmon resonance utilize less protein and can be of high throughput, they rely on specialized, costly equipment and/or modification of the target protein with labeling that by itself may alter the protein-protein interaction to be investigated.

Over the past number of years, we have developed a novel microplate-based solid-phase protein-protein binding assay. This assay requires no specialized equipment, uses a minimal amount of protein, is rapid throughput, does

not rely on modification of the target protein, and results in quantitative measurements. In this assay one of the proteins of interest is noncovalently immobilized to a solid phase followed by incubation with a soluble binding partner protein dissolved in a physiological solution. Binding is then detected via an antibody against the soluble partner protein using enzyme-linked immunosorbent assay (ELISA). Here we present the detailed methodology for this novel high-throughput protein-binding assay that we have successfully employed for investigating myofilament protein binding, including troponin T to tropomyosin [1–3] and troponin T to troponin I [1, 2, 4]. The assay is also highly effective in revealing the functional effects of muscle myofilament protein alternative splicing variants [1, 2], phosphorylation [5], restrictive proteolysis [4, 6], point mutations [7], as well as the effects of solution salt, metal ions, or pH on myofilament protein binding [8–11]. In addition, this methodology has also been used to study the binding of calponin [12, 13] and titin motifs [14] to F-actin. Beyond these applications this assay can readily be extended to study

the interactions of nonmuscle proteins. Any protein binding pair can be analyzed provided that a specific antibody against one of the proteins is available.

In this paper we first discuss traditional protein-binding assays and use this background to present the general concepts of the microplate ELISA-based solid-phase protein-binding assay. We then provide detailed methodology to conduct a simple binary solid-phase binding assay. Finally, we will discuss modifications expanding on the simple binary binding experiment and optimization of the assay conditions.

2. Traditional Protein-Protein Binding Assays

Classical assays to measure the interaction and binding of one protein to another largely consist of two main methodologies: (1) equilibrium dialysis and (2) affinity chromatography. These two methodologies rely on different principals to separate bound from nonbound interacting proteins.

To determine the affinity of two proteins for each other by equilibrium dialysis, the experimental proteins of known concentration are placed in two chambers separated from each other by a membrane permeable to only one of the proteins. The permeable protein is then allowed to diffuse across the membrane and bind the nonpermeable protein. Once the permeable protein achieves equilibrium between the two chambers, its free concentration is determined in the chamber lacking the impermeable protein. Following dialysis of the protein pair at appropriate concentrations, the binding affinity of the pair can be determined. The dialysis can be conducted with one or more variants of one of the two proteins for comparison. Equilibrium dialysis, thus, provides the affinity of one protein for another at equilibrium between association and disassociation in solution. Although the data generated by equilibrium dialysis is quantitatively informative, a major limitation of this method is that it requires a size difference between the two binding proteins to be distinguishable by the dialysis membrane. The downfall of this method also includes its labor-intensive nature and its requirement for large amounts of the proteins.

The other commonly used traditional protein binding assay is affinity chromatography. Affinity chromatography requires immobilization of one protein to a support resin that is usually packed into a column for chromatographic analysis. The binding partner protein in solution is then incubated with the protein-resin conjugate at sufficient concentration and contact time to saturate its binding to the immobilized protein. The binding affinity between the two proteins is then assessed by step or continuous gradient elution with a buffer condition that weakens the protein-protein interaction and the strength of elution necessary to achieve peak dissociation of the bound protein determined. Once the bound protein is completely eluted, the column can be reequilibrated and a similar measurement conducted for another or variant partner protein. Unlike the solution steady-state binding measured in the equilibrium dialysis method, affinity chromatography measures a nonequilibrium disassociation rate from a maximally bound state.

Therefore, by its nature this assay only investigates the disassociation characteristic of the two proteins. Further drawbacks of this methodology include the measurement of only relative affinity and the necessity of chemically coupling one of the proteins to a support resin, which by itself may affect the structure and function of the immobilized protein.

3. The Microplate Solid-Phase Protein-Binding Assay

The solid-phase protein-binding assay was developed as an alternate methodology to assess association and disassociation of protein-protein interactions using relatively small amounts of protein without specialized equipment [9]. The basis for the solid-phase protein-binding assay is derived from ELISA-based methodology. The rationale for designing the protein-binding assay based on ELISA, a well-established immunological assay, is that the antibody-antigen interaction measured by various immunological detection methods is basically a protein-protein interaction. The assay consists of three main components. The first is immobilization of a protein to the wells of an assay plate by noncovalent coating. The second is the protein-protein interaction. The third is detection of the bound protein. As a basis for our discussion, we will first describe details of a standard solid-phase protein-binding assay followed by variants of the assay for extending its applications.

The simplest and most widely used format is the binary binding assay that measures the interaction between two proteins, one *immobilized* and the other *free* in solution. This assay format is commonly used to compare the binding interactions between an immobilized protein to two or more variants of a soluble partner protein. However, the assay can be designed such that the variant proteins are either in the solution or immobilized position.

Although simple in its design, the binary assay format (Figure 1(a)) demonstrates the basis of the solid phase protein binding assay. In this experimental system a single protein is noncovalently coated through absorption to the well surface of a 96-well polystyrene (*not polypropylene*) assay plate. Excess free protein in solution is subsequently removed and the wells are washed. The remaining available binding surfaces of the wells are blocked with a non-interacting protein such as bovine serum albumin (BSA) often together with a nonionic detergent. The plate is then washed again followed by adding serial dilutions of the binding partner protein to the wells and incubated allowing equilibrium binding with the immobilized protein to be reached. Remaining free protein in solution is then removed followed by washes, and the portion of the partner protein bound to the immobilized protein is quantified through detection via an antibody specific to the binding partner protein.

The detection employs an enzyme-linked antibody approach. The enzyme, for example, horse radish peroxidase (HRP), can be directly conjugated to the detecting antibody; however, it is more convenient to use an enzyme-conjugated second antibody. In this setting a primary antibody specifically recognizing the bound protein is used as the detecting

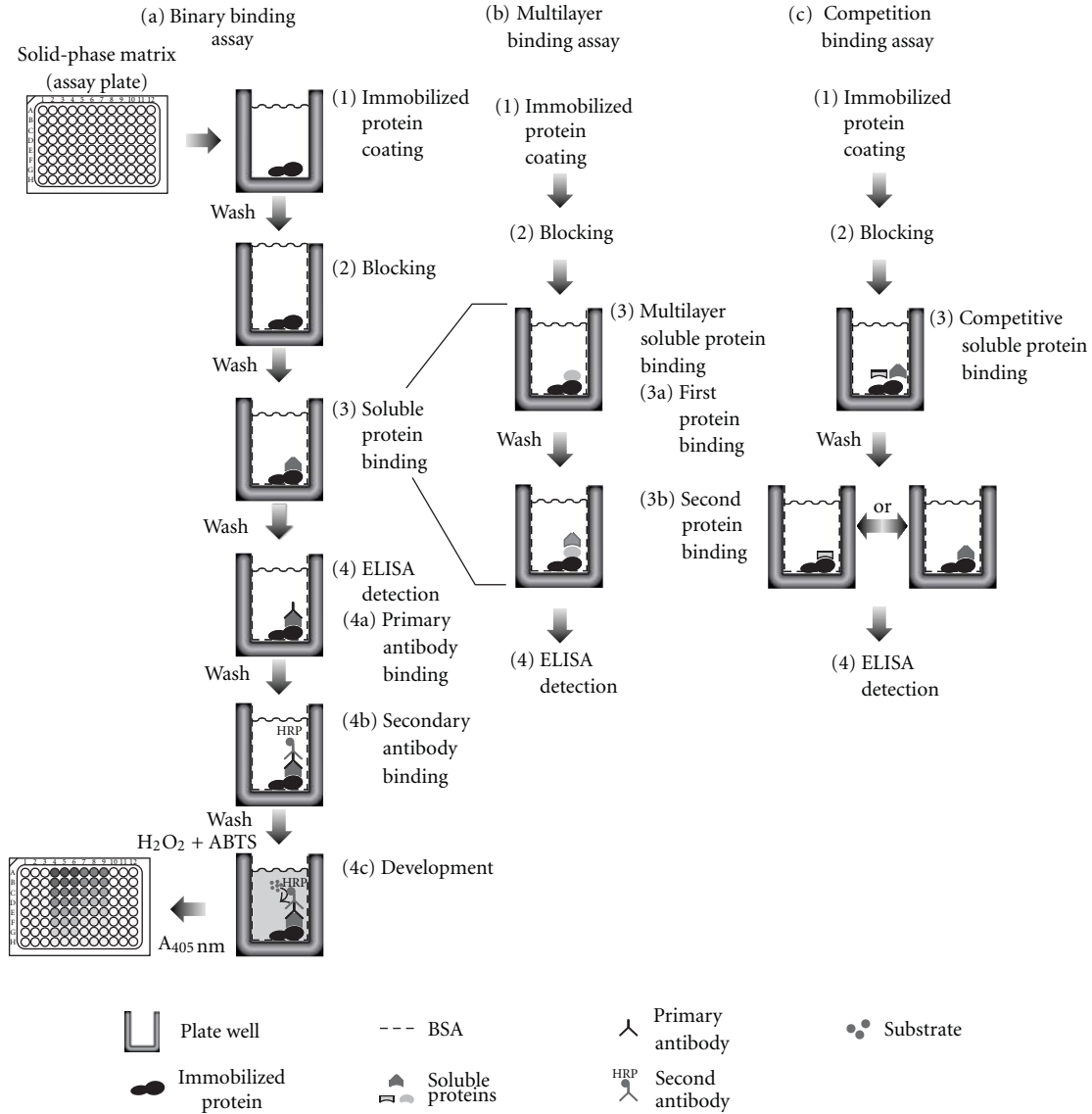


FIGURE 1: Solid-phase protein-binding assay method. (a) Binary binding assay to quantify the interaction between an immobilized protein and an interacting soluble protein. (1) The immobilized protein of interest is maximally coated into the wells of a 96 well assay plate. (2) Unbound protein is removed by washing, and remaining surfaces blocked with a nonspecific protein. (3) The plate is washed, and binding is evaluated by incubation with serial dilutions of a soluble interacting protein. (4) Following another wash to remove unbound interacting protein, bound protein is detected by ELISA with a primary antibody against the interacting protein, a HRP-conjugated second antibody and substrate development to quantify bound protein by absorbance. (b) Multilayer binding assay to quantify the interaction between an immobilized protein and two related interacting soluble proteins. The multilayer protein binding is conducted similar to the binary binding assay in (a) with the exception that, following binding of the first soluble protein and washes, the wells are incubated with another protein that binds the first protein bound to the immobilized protein followed by ELISA quantification. (c) Competitive binding assay to quantify the interaction between an immobilized protein and an interacting soluble binding protein in the presence of varied amounts of a second binding protein. Protein coating and blocking are conducted as in (a) and (b) with the exception that during the soluble protein binding step, addition of the first interacting protein of interest is conducted at a constant concentration in the presence of serial concentrations of a competitive binding protein. Resultant binding of the constant concentration of the first binding protein of interest to the immobilized protein is then quantified by ELISA with a specific antibody. ELISA quantification of the degree of competition will be detected by decreases in the final reading of absorbance.

antibody, and excess antibody is removed by washes. Subsequently an enzyme-conjugated second antibody recognizing the detecting primary antibody is added for another step of incubation followed by washes to remove excess second antibody. Finally, a substrate development reaction is conducted

and quantified using a microplate reader. The amount of the bound enzyme-linked second antibody is in direct proportion to the amount of bound primary detecting antibody that is determined by the amount of the soluble partner protein remaining bound to the immobilized protein. As the

result of this direct relationship between the bound protein and enzyme-linked secondary antibody, the intensity of the color or fluorescence product produced from the substrate reaction is quantitatively dependent on the amount of the soluble protein remaining bound to the immobilized protein. By plotting the microplate readings against the concentration of the free protein used in the equilibrium binding step, the association AND disassociation features can be compared between two or more variants of the proteins studied.

4. Experimental Procedure

As outlined above, Figure 1(a) shows the basic design of the solid-phase protein-protein binding assay consisting of a binary protein-binding experiment. The design of the binary binding experiment investigates the binding characteristics between two proteins, one of which is immobilized in the wells of microplate and allowed to incubate with the binding partner protein in solution. A thorough understanding of this basic experimental setting will provide the foundation for understanding more sophisticated designs derived from it. For this reason we will first present the binary binding assay protocol and then the application of this methodology to other designs.

As routinely employed in our laboratories, the binary protein-binding experiment consists of coating the immobilized protein through noncovalent absorption, binding of the partner protein, and indirect ELISA detection of the protein binding. This section will describe the detailed protocol to conduct the binary binding assay similar to that described in our previous publications [2, 9, 15].

4.1. Specific Materials

- (i) 96-well polystyrene microtitering plates.
- (ii) Multichannel pipette in the 100–200 μL range.
- (iii) Squishing wash bottle. A standard 500 mL laboratory wash bottle that can be used to provide a consistent stream of wash buffer from a spout to fill the wells of the assay plate.
- (iv) Buffer A (Buf A; 100 mM KCl, 3 mM MgCl_2 , and 10 mM PIPES, pH 7.0) can be made as a 5x stock, stable at room temperature. This buffer is used for the study of myofilament proteins. It should be modified according to the proteins to be studied. Neutral or alkaline pH is required for proper coating of the immobilized protein to the plate. A concentration of 3–6 M urea can be included for the coating of less soluble proteins. Neutral pH should be used for the urea-coating buffer to avoid carbamylation of the protein. Most proteins will refold well following immobilization during the blocking step after urea is removed.
- (v) Buffer T (Buf T; buffer A + 0.1% Tween-20).
- (vi) Buffer B (Buf B; buffer T + 0.1% BSA).
- (vii) Substrate solution (2,2'-azino-bis(3-ethylbenzothiazoline-6-sulfonic acid (ABTS)/ H_2O_2) is used for

horseradish peroxidase-conjugated first or second antibody). 0.04% ABTS diammonium is dissolved in 65.7 mM citric acid monohydrate, 34 mM sodium citrate dihydrate, pH 4.0, adjusted with sodium citrate dihydrate. The substrate stock should be made in autoclaved, deionized water with autoclaved tools to avoid peroxidase contamination and stored at -20°C in aliquots of the volume for individual experiments. Before use the substrate solution is brought to room temperature and immediately prior to its application, 0.03% H_2O_2 added.

- (viii) Microplate reader capable of reading absorbance at 415 nm or 405 nm (for the ABTS substrate).
- (ix) Primary antibody against the soluble protein to be studied. Although it is necessary to have a specific antibody against one of the proteins to be studied, current methods of generating recombinant fusion proteins with a tag, such as FLAG or His₆₋₈, and the availability of antibodies against such tags allow this approach to be applied to a wide range of protein interactions, overcoming the restriction from the availability of a specific antibody.
- (x) Horseradish peroxidase-conjugated second antibody that recognizes the primary antibody species (e.g., goat anti-mouse IgG horseradish peroxidase conjugated secondary antibody) was used in our studies employing mouse monoclonal primary antibodies.

4.2. Assay Design. A practical binary protein-binding assay design consists of eight dilutions of the soluble binding protein in triplicate. The 8 \times 12 well format of the 96-well microplate should be considered in the assay design. For example, the immobilized protein can be arranged in columns (A to H) and incubated with eight serial dilutions of the soluble variant proteins. The assay design should also include control columns for each variant protein consisting of the serial diluted soluble protein incubated in triplicate wells without immobilized protein. Figure 2 illustrates the 96-well microplate layout of a typical binary binding experiment conducted in triplicate for two variant soluble proteins.

4.3. Immobilization of Protein to the Microplate. It is preferred that the single partner protein is selected to be the immobilized protein with the two or more variant binding proteins incubated in the soluble phase. This strategy will ensure a uniform level of the coated protein for the comparison among the variants of the binding protein. However, multiple variants of the proteins to be studied may be coated under similar conditions for incubation with a single soluble partner protein as well. Standard coating of the immobilized protein occurs through absorption to the wells of the assay plate based on hydrophobic interactions between the plastic surface of the assay plate and the nonpolar amino acid residues of the protein to be immobilized.

The coating of the immobilized protein onto the wells of a microtiter plate is performed at 100 μL /well with 2–5 $\mu\text{g}/\text{mL}$

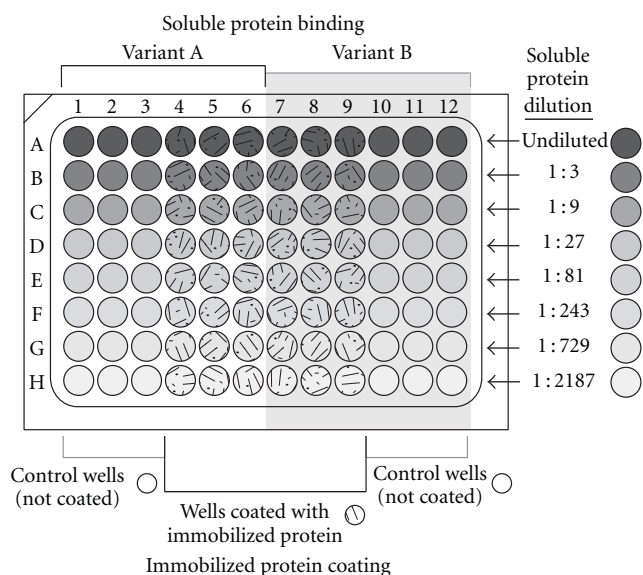


FIGURE 2: Representative design of a 96-well microtitering plate assay for binary binding consisting of an immobilized protein incubated with two variant soluble interacting proteins in 8 serial concentrations of triplicate wells. Immobilized protein is equally and maximally coated in the experimental wells, rows A to H and columns 4 to 9. Columns 1 to 3 and 10 to 12 are left uncoated (incubated with coating buffer only) as controls. Following coating all wells are blocked, and the wells in columns 1 to 6 are incubated with serial dilutions, one dilution per row, of one of the soluble proteins, and wells in columns 7 to 12 are incubated with serial dilutions of the other soluble protein variant. All wells are then processed uniformly for ELISA detection.

protein in Buf A by incubation at 4°C sealed overnight. Coating conducted at these protein concentrations is in excess of the amount able to bind the plate well for most proteins of 10–200 kDa in size. The use of excess amount of protein for coating exploits conditions to ensure saturated coating to minimize variation of the assay.

Most small proteins or peptide fragments are sufficiently immobilized to the plate well to allow a robust assay. In the case that simple hydrophobic absorption does not result in a sufficient amount and strength of coating; microplates with added reactive groups for covalent conjugation may be considered (see Section 4.10).

4.4. Blocking of the Coated Plate. To begin protein binding, the well contents of the microplate are emptied by shaking into a sink, and the remaining solution removed by tapping onto a stack of paper towels. The plate is then washed once rapidly to avoid protein drying by the addition of a volume of Buf T sufficient to fill each well using a squishing bottle (see Section 4.6). Following filling of the wells, the washing buffer is emptied as above, tapped dry, and the wells are blocked with 150 μL /well 1% BSA in Buf T by incubation at room temperature for 1 hr sealed. When dealing with limited protein material, the coating protein solution may be recovered for reuse, although the resulting coating capacity may decrease.

4.5. Protein Binding. Following emptying of the blocking solution from the wells and tapping, the plate is washed three times with Buf T to remove free protein (see Section 4.6). Serial dilutions of the binding partner protein solution in Buf B are then added to the wells at 100 μL /well and incubated with the immobilized protein at room temperature for 2 hrs sealed. A typical binding assay designed for myofilament proteins consists of free protein concentrations starting from 0.5–1 μM and eight 3-fold serial dilutions (Figure 2).

4.6. Washing. Following protein-binding incubation, the plate is washed as follows. The well contents are emptied by shaking into the sink, the remaining solution is removed by tapping onto paper towels, and the plate is washed a total of three times with Buf T in a total period of 10 min. The lag time between emptying the well to filling with Buf T should be as short as possible to avoid drying of the binding protein on the plate resulting in high background.

Washing is conducted using a squishing bottle by applying a consistent stream of Buf T to sequentially fill the wells without overflowing. Accurate filling is critical for the first wash to avoid spilling over trace amount of the binding protein between wells, especially from high to low concentration and from positive to negative control wells. It is useful to start the wash stream outside of the plate and then move sequentially through the wells delivering a continuing stream of wash solution while moving from well to well. It is helpful to hold the plate slightly tilted, beginning filling from the lower-side rows. This will help avoid spillover from entering into empty wells without further dilution. After the first filling, the washing buffer is immediately removed followed by the second wash. This will limit the time for any spillover protein to interact at a significant concentration with the immobilized protein in unwanted wells. The plate is then allowed to incubate at room temperature for approximately 3 min. The wash procedure is repeated for the 3rd time and allowed to incubate approximately 4 min before final removal of the washing buffer as above.

The washing condition is an important factor in determining the effectiveness and stringency of the assay by eliminating nonspecific binding while quantitatively evaluating the dissociation of specific binding between the protein pair. Using appropriate washing conditions will allow evaluating the coupling strength of the two proteins studied. More stringent separation by increasing the number of buffer changes, duration of the washes, and/or the detergent concentration will differentially affect weak and strong bindings as a sensitive method to reveal differences among protein variants of interest. It is worth noting that no single washing condition fits all protein-protein interactions, and the wash strength should be evaluated empirically.

4.7. ELISA Detection. The partner protein specifically bound to the immobilized protein is detected using an ELISA procedure in which an antibody recognizing the partner

protein is the primary reagent (Figure 1(a)). Following the final wash to remove unbound partner protein a predetermined, constant dilution of the primary antibody in Buf B is added to all the wells at 100 $\mu\text{L}/\text{well}$ using a multi-channel pipette and incubated sealed at room temperature for 1 hr. The working concentration of the primary antibody should be predetermined to give a final absorbance of around 1.0 by ELISA titration against the partner protein directly coated to a microplate in the same buffer system, incubation, and washing conditions. The antibody solution should be added quickly such that the well contents do not dry out. The plate is then washed 3 times in 10 min as described in the Washing Section. A constant dilution of HRP-conjugated second antibody against the primary antibody in Buf B is added to all the wells at 100 $\mu\text{L}/\text{well}$ and incubated at room temperature for 45 min. Similar to that of the primary antibody, the second antibody's working concentration should be determined empirically. The plate is then washed 3 times in 10 min as described in the Washing Section (see Section 4.10) prior to adding 100 $\mu\text{L}/\text{well}$ of the ABTS- H_2O_2 substrate solution.

The substrate reaction is incubated at room temperature with periodic mixing (e.g., 2-3 seconds shaking in the plate reader) and the color development monitored by absorbance reading at 415 nm or 405 nm using a microplate reader at several time intervals (e.g., 5, 10, 15, 20, 25, and 30 min). The well of highest absorbance is then plotted against time and a time point chosen for analysis before deviation from linear color development. Under typical assay conditions, this will be between 10 to 20 minutes of development. The time of development should also be such that the absorbance reading remains within the reliable reading range of the microplate reader, less than 2.0 for most instruments. If the color development is too quick and the absorbance values too high, the concentration of the primary and/or second antibody should be decreased.

4.8. Data Analysis. Background absorbance for each serial dilution of the binding protein is determined from 3 control wells not coated with immobilized protein but processed the same as the assays wells. Absorbance of the 3 control wells is averaged, and this value is subtracted from data readings for that dilution. Resultant absorbance values at the highest concentration of each binding protein are averaged as the maximum (100%) binding for that protein. It is important to only compare the absolute values of the maximal binding from experiments conducted at the same time to avoid the effect of day-to-day variations. Background-subtracted absorbance values for each dilution of the binding protein are then normalized to the average maximal binding value and the titration curve plotted against a log scale of the dilution concentrations. The curve is then fit to determine the soluble protein concentration required to reach 50% maximal binding. Although it is best to compare the 50% maximal binding values of protein variants from the same assay, it is possible to compare day-to-day results as long as the reagents, incubation times, washing stringency, and room temperature remain consistent (Figure 3).

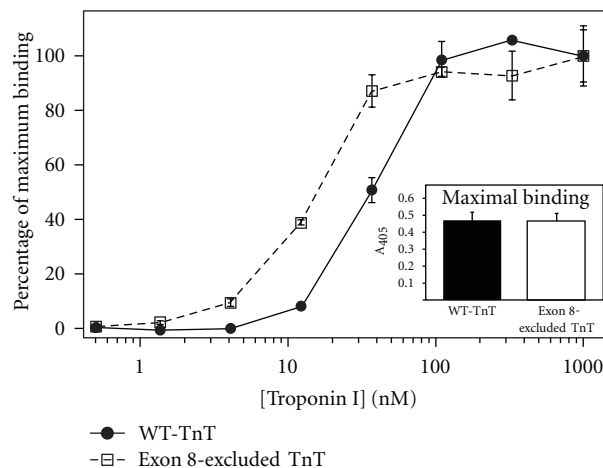


FIGURE 3: A set of typical, original protein-protein binding curves demonstrating the altered binding of an exon 8-excluded cardiac troponin T (exon 8-excluded TnT, white square) to the interacting protein troponin I in comparison with wild-type cardiac troponin T (WT-TnT, black circle). The troponin T variants are configured as the immobilized protein and troponin I the soluble protein. The normalized binding curves demonstrate exon 8-excluded TnT bound with higher affinity to troponin I compared to WT-TnT as evident by the lower concentration required for 50% maximal binding. Absolute absorbance of the maximal binding is shown in the inset demonstrating that both exon 8-excluded TnT and WT-TnT exhibited similar coupling strength to troponin I.

The above procedure provides relative comparisons between two or more binding protein variants for their interaction with the immobilized protein. With a standard curve produced with known concentrations of the binding partner protein, this approach can be employed to gain quantification of the partner in an unknown sample of purified protein, body fluid, or tissue homogenate.

4.9. Data Interpretation. The molar concentration required for 50% maximal binding of the soluble partner protein to the immobilized protein reflects the on-rate of their association at equilibrium and is a representative of the binding affinity (K_d). Although the strength and time of washing will affect the nonequilibrium disassociation of the binding protein, these conditions affect all samples similarly. Thus, the initial binding between the immobilized and free proteins during equilibrium incubation is determined by the intrinsic affinity between the protein pair.

On the other hand, the level of maximal binding of the soluble partner protein to a given amount of the immobilized protein represents their coupling strength or resistance to the washes. In contrast to the maximally saturated binding achieved during the equilibrium incubation step, during washes the absence of free soluble binding protein produces nonequilibrium dissociation. Thus, this coupling strength determined in the solid-phase protein-binding assay employing stringent washing-separation steps reflects the off-rate of the protein pair's binding. In the assay system,

immobilized protein coating is conditioned to a maximum, and binding of the partner protein at high concentration reflects saturated binding. Therefore, similar to that in affinity chromatography, the disassociation resulting from wash separation conditions is a highly sensitive measure to provide information of the disassociation rate (K_d) of the protein pair studied. Washing strength can, therefore, be altered to exploit coupling strength differences between protein variants.

4.10. Optimizing Assay Conditions. A number of conditions can be modified to optimize the solid-phase protein-binding assay allowing investigation of a number of specific protein-protein interactions, including nonmuscle proteins. Unlike most traditional protein binding assays, a unique advantage of the microplat-based protein binding assay is that it allows different buffer conditions during the incubation and washing steps. For example, one may coat a low-solubility protein to the plate by dissolving it in a modified coating buffer containing high salt and/or 3–6 M urea. The salt and urea will then be washed away, and the following binding assay can be performed in physiological buffers. Another example is that reducing agents may be included for coating and protein-binding steps but removed before the antibody incubation steps (reducing agents will dissociate the quaternary structure of immunoglobulins). Further examples include the use of different buffer conditions for the equilibration protein-binding step and the washing steps that determine the stringency for separately investigating association and dissociation rates.

Other optimizations include adaptations for small peptides. Small peptides that are weak in hydrophobic absorption may be immobilized as a conjugate with a carrier protein. Small peptides may also be immobilized through a specific interaction such as the use of biotin-streptavidin system. Microtiter assay plates of varied surface chemistry can be used to enhance the coating of the immobilized protein. For example, covalent bonding of peptides can be achieved via precoating the plate with a hydrophilic polymer such as soluble dextran treated with 2,2,2-trifluoroethanesulphonyl chloride (tresyl chloride) to activate hydroxyl groups [16].

As discussed above, separation strength can be varied by altering the number, time, or stringency of the washes to exploit the properties of the interaction between the protein pair studied. Issues of low amounts of protein binding can be overcome by employing detection methods of increased sensitivity. For example, higher concentrations of the primary and/or secondary antibodies may be used. Alternatively, instead of ABTS, *o*-phenylenediamine (OPD) or 3,3',5',5'-tetramethylbenzidine (TMB) can be employed as the substrate to increase detection sensitivity of weaker binding protein pairs. If labeling a protein does not interfere with its binding, the binding partner protein can directly be labeled by conjugation to a fluorescent tag and its binding to the immobilized protein detected by measuring fluorescence of the bound protein.

Taken together the adaptability of the solid-phase protein-binding assay offers significant flexibility to develop

specifically optimized experiments allowing for the investigation of a wide range of proteins under varied conditions.

5. Extended Assay Configurations

As presented above, the simple binary protein-binding assay can provide significant information regarding differences in the interaction of one protein with another. Additionally the solid-phase protein-binding assay is amendable to provide information on more than binary protein-protein interactions. With appropriate optimization, other protein-protein interactions of increased complexity can be studied using this approach. One or both of the binding partners may be a protein complex as long as a suitable antibody is available for the ELISA detection [17]. This methodology can also be readily applied to multilayer binding assays and competition assays. In the multilayer binding assay an additional protein binding step can be added to evaluate the binding among the subunits of a multiprotein complex (Figure 1(b)). We have successfully employed a similar multilayer assay in our laboratory investigating the binding of tropomyosin and troponin T in the presence of filamentous actin (unpublished data). Likewise, other multi-protein complexes or binding cofactors could similarly be investigated.

In the competition assay, binding of a partner protein at a constant concentration to the immobilized protein is carried out in the presence of serial concentrations of a competitive protein (Figure 1(c)). Using a specific primary antibody to detect the partner protein, its affinity to the immobilized protein relative to that of the competitive protein can be assessed. The competition assay design can be modified to study the blocking effect of a protein, a peptide, or a small-molecule ligand on the binding of the partner protein to the immobilized protein. The competition assay is also applicable not only to two proteins but also to two isoforms of the same protein [18] or different posttranslational modifications [19] to assess the effect of the modification on binding.

The competition assay is also amendable to study the spatial relationship between a protein-binding site and an antibody-binding site [19]. Using a monoclonal or anti-peptide antibody against a known epitope of structural and/or functional interests, the assay can be extended to identify binding partners of the protein in a complex mixture through competitive blocking of the antibody epitope by protein binding. Likewise, substrate-enzyme interactions could be investigated using a similar competitive approach by employing an antibody against the catalytic site. When an antibody probe is available, the competitive assay configuration is likewise applicable to study the interactions between proteins and cofactors.

6. Special Cautions

Although the solid-phase protein-binding assay is readily amendable to a number of different situations, a few key points must be observed to ensure success. Importantly, reducing agents must be excluded from all buffers for the primary antibody incubation and subsequent steps. The

inclusion of reducing agents in these steps will disrupt immunoglobulin disulfide bonds destroying the ability of the antibody to detect the bound protein and, thus, rendering no signal. Furthermore, although employing methods of increased sensitivity can help with detection of low-affinity binding, this methodology, applying high stringent washes, is most effective in studying high-affinity binding events.

7. Conclusions

We have presented detailed methodology of a novel solid-phase binding assay to assess protein-protein interactions emphasizing examples using muscle regulatory proteins. This assay expands on previous methodologies to provide a simple and high-throughput assay to assess protein-protein interactions in solution. In contrast to many other current methods that process a few samples a time, this approach readily handles hundreds of assay wells by a single operator in a days time using common laboratory equipment. By employing the adaptations and optimizations discussed, this assay should be readily applicable to the quantitative assessment of other nonmuscle proteins interactions.

Abbreviations

ELISA: Enzyme-linked immunosorbent assay
 HRP: Horse radish peroxidase
 ABTS: 2,2'-Azino-bis(3-ethylbenzo-thiazoline-6-sulfonic acid)
 BSA: Bovine serum albumin.

Acknowledgment

This work was supported by the National Institutes of Health Grants HL-091056 (to B. J. Biesiadecki), AR048816, HL-078773, HL-086720, and HL-098945 (to J.-P. Jin).

References

- [1] B. J. Biesiadecki, B. D. Elder, Z. B. Yu, and J. P. Jin, "Cardiac troponin T variants produced by aberrant splicing of multiple exons in animals with high instances of dilated cardiomyopathy," *Journal of Biological Chemistry*, vol. 277, no. 52, pp. 50275–50285, 2002.
- [2] B. J. Biesiadecki and J. P. Jin, "Exon skipping in cardiac troponin T of turkeys with inherited dilated cardiomyopathy," *Journal of Biological Chemistry*, vol. 277, no. 21, pp. 18459–18468, 2002.
- [3] J. P. Jin and S. M. Chong, "Localization of the two tropomyosin-binding sites of troponin T," *Archives of Biochemistry and Biophysics*, vol. 500, no. 2, pp. 144–150, 2010.
- [4] B. J. Biesiadecki, K. L. Schneider, Z. B. Yu, S. M. Chong, and J. P. Jin, "An R111C polymorphism in wild turkey cardiac troponin I accompanying the dilated cardiomyopathy-related abnormal splicing variant of cardiac troponin T with potentially compensatory effects," *Journal of Biological Chemistry*, vol. 279, no. 14, pp. 13825–13832, 2004.
- [5] B. You, G. Yan, Z. Zhang et al., "Phosphorylation of cardiac troponin I by mammalian sterile 20-like kinase 1," *Biochemical Journal*, vol. 418, no. 1, pp. 93–101, 2009.
- [6] Z. Zhang, B. J. Biesiadecki, and J. P. Jin, "Selective deletion of the NH2-terminal variable region of cardiac troponin T in ischemia reperfusion by myofibril-associated μ -calpain cleavage," *Biochemistry*, vol. 45, no. 38, pp. 11681–11694, 2006.
- [7] P. L. Engel, T. Kobayashi, B. Biesiadecki et al., "Identification of a region of troponin I important in signaling cross-bridge-dependent activation of cardiac myofilaments," *Journal of Biological Chemistry*, vol. 282, no. 1, pp. 183–193, 2007.
- [8] J. P. Jin, S. M. Chong, and M. M. Hossain, "Microtiter plate monoclonal antibody epitope analysis of Ca²⁺- and Mg²⁺-induced conformational changes in troponin C," *Archives of Biochemistry and Biophysics*, vol. 466, no. 1, pp. 1–7, 2007.
- [9] J. P. Jin and K. Wang, "Nebulin as a giant actin-binding template protein in skeletal muscle sarcomere. Interaction of actin and cloned human nebulin fragments," *FEBS Letters*, vol. 281, no. 1-2, pp. 93–96, 1991.
- [10] O. Ogut and J. P. Jin, "Developmentally regulated, alternative RNA splicing-generated pectoral muscle-specific troponin T isoforms and role of the NH2-terminal hypervariable region in the tolerance to acidosis," *Journal of Biological Chemistry*, vol. 273, no. 43, pp. 27858–27866, 1998.
- [11] O. Ogut and J. P. Jin, "Expression, zinc-affinity purification, and characterization of a novel metal-binding cluster in troponin T metal-stabilized alpha-helical structure and effects of the NH2-terminal variable region on the conformation of intact troponin T and its association with tropomyosin," *Biochemistry*, vol. 35, no. 51, pp. 16581–16590, 1996.
- [12] J. P. Jin, M. P. Walsh, C. Sutherl, and W. Chen, "A role for serine-175 in modulating the molecular conformation of calponin," *Biochemical Journal*, vol. 350, no. 2, pp. 579–588, 2000.
- [13] J. P. Jin, D. Wu, J. Gao, R. Nigam, and S. Kwong, "Expression and purification of the h1 and h2 isoforms of calponin," *Protein Expression and Purification*, vol. 31, no. 2, pp. 231–239, 2003.
- [14] J. P. Jin, "Cloned rat cardiac titin class I and class II motifs. Expression, purification, characterization, and interaction with F-actin," *Journal of Biological Chemistry*, vol. 270, no. 12, pp. 6908–6916, 1995.
- [15] J. Wang and J. P. Jin, "Conformational modulation of troponin T by configuration of the NH2-terminal variable region and functional effects," *Biochemistry*, vol. 37, no. 41, pp. 14519–14528, 1998.
- [16] K. Gregorius, S. Mouritsen, and H. I. Elsner, "Hydrocoating: a new method for coupling biomolecules to solid phases," *Journal of Immunological Methods*, vol. 181, no. 1, pp. 65–73, 1995.
- [17] Z. Zhang, S. Akhter, S. Mottl, and J. P. Jin, "Calcium-regulated conformational change in the C-terminal end segment of troponin I and its binding to tropomyosin," *FEBS Journal*, vol. 278, no. 18, pp. 3348–3359, 2011.
- [18] O. Ogut and J. P. Jin, "Cooperative interaction between developmentally regulated troponin T and tropomyosin isoforms in the absence of F-actin," *Journal of Biological Chemistry*, vol. 275, no. 34, pp. 26089–26095, 2000.
- [19] S. Akhter, Z. Zhang, and J. P. Jin, "The NH2-terminal extension regulates molecular conformation and function of cardiac troponin I," *Biophysical Journal*, vol. 100, no. 3, supplement, pp. 370a–371a, 2011.

Research Article

Dynamic Changes in Sarcoplasmic Reticulum Structure in Ventricular Myocytes

Amanda L. Vega, Can Yuan, V. Scott Votaw, and Luis F. Santana

Department of Physiology & Biophysics, University of Washington, Box 357290, Seattle, WA 98195, USA

Correspondence should be addressed to Luis F. Santana, santana@u.washington.edu

Received 29 April 2011; Accepted 9 August 2011

Academic Editor: Xupei Huang

Copyright © 2011 Amanda L. Vega et al. This is an open access article distributed under the Creative Commons Attribution License, which permits unrestricted use, distribution, and reproduction in any medium, provided the original work is properly cited.

The fidelity of excitation-contraction (EC) coupling in ventricular myocytes is remarkable, with each action potential evoking a $[Ca^{2+}]_i$ transient. The prevalent model is that the consistency in EC coupling in ventricular myocytes is due to the formation of fixed, tight junctions between the sarcoplasmic reticulum (SR) and the sarcolemma where Ca^{2+} release is activated. Here, we tested the hypothesis that the SR is a structurally inert organelle in ventricular myocytes. Our data suggest that rather than being static, the SR undergoes frequent dynamic structural changes. SR boutons expressing functional ryanodine receptors moved throughout the cell, approaching or moving away from the sarcolemma of ventricular myocytes. These changes in SR structure occurred in the absence of changes in $[Ca^{2+}]_i$ during EC coupling. Microtubules and the molecular motors dynein and kinesin 1 (Kif5b) were important regulators of SR motility. These findings support a model in which the SR is a motile organelle capable of molecular motor protein-driven structural changes.

1. Introduction

The sarcoplasmic reticulum (SR) is an intracellular organelle that forms an intricate tubular network throughout ventricular myocytes. A critical function of the SR is to store and release Ca^{2+} . The SR is a structurally diverse organelle that consists of junctional, corbular, and network SR. The network SR is formed by a series of interconnected tubules that span the region between the transverse-tubules (T-tubules). The junctional SR is where this organelle forms specialized junctions with the sarcolemmal T-tubules, which result in the close juxtaposition (≈ 15 nm) of ryanodine-sensitive Ca^{2+} channels (RyRs) in the SR and sarcolemmal voltage-gated L-type Ca^{2+} channels [1, 2]. Corbular SR is a protrusion from the SR network that expresses RyRs but does not make junctions with the sarcolemma.

During excitation-contraction (EC) coupling, membrane depolarization opens L-type Ca^{2+} channels near the junctional SR. This allows a small amount of Ca^{2+} to enter the small cytosolic volume that separates the SR and the T-tubule sarcolemma, rising local $[Ca^{2+}]_i$ beyond a threshold

for RyRs activation via the mechanism of Ca^{2+} -induced Ca^{2+} release (CICR) [3]. Local $[Ca^{2+}]_i$ elevations resulting from the activation of a small cluster of RyRs are called “ Ca^{2+} sparks” [4]. Synchronous activation of multiple Ca^{2+} sparks by L-type Ca^{2+} channels produces a global rise in $[Ca^{2+}]_i$ that initiates myocardial contraction. The coupling strength between L-type Ca^{2+} channels and RyRs is critically dependent on the proximity and stability of the T-tubule/sarcolemmal-SR junction [5, 6].

EC coupling in ventricular myocytes is remarkably reliable. That is, an action potential invariably evokes a whole-cell $[Ca^{2+}]_i$ transient that results in contraction. Under steady-state conditions, the amplitude of the whole-cell $[Ca^{2+}]_i$ transient and contraction remains virtually unchanged for long periods of time. A recent study examined the biophysical basis for the fidelity of action potential-evoked $[Ca^{2+}]_i$ transient and contraction [7]. This study suggested that the probability of Ca^{2+} spark activation (P_s) by nearby L-type Ca^{2+} channels is very high (≈ 1) during the plateau of the ventricular action potential. Because the P_s during EC coupling is dependent on the separation between

L-type Ca^{2+} channels and RyRs, these findings suggest that the T-tubule sarcolemma-SR junction is a functionally stable structure at least over relatively short periods of time (i.e., minutes). At present, however, the SR structural dynamics in living ventricular myocytes have not been examined.

In this study, we used electron, confocal, and total internal reflection fluorescence (TIRF) microscopy to address this fundamental issue. Our data suggest that the SR in neonatal and adult cardiac myocytes forms a vast, yet dynamic network with mobile SR elements that contain functional RyRs. The microtubule network and the molecular motors dynein and kinesin 1 (referred as Kif5b) regulate SR motility. Interestingly, rearrangements in SR structure were more pronounced in neonatal than in adult myocytes. These findings support a model in which the SR is a motile organelle capable of undergoing rapid microtubule-associated molecular motor protein-driven structural reorganization.

2. Methods

2.1. Isolation of Ventricular Myocytes. Animals were handled according to the guidelines of the University of Washington Institutional Animal Care and Use Committee. Hearts were obtained from adult male Sprague Dawley rats or neonatal mice (<72 hours postpartum) euthanized by a lethal intraperitoneal injection of pentobarbital or decapitation, respectively. Single adult and neonatal ventricular myocytes were enzymatically isolated and kept in short-term culture as previously described [8–10].

2.2. Plasmid Construction and Production of Adenovirus Expressing tRFP-SR and Kif5b. The tagged red fluorescent protein (tRFP) was genetically modified to contain an N-terminal calreticulin signal sequence and a C-terminal ER retention signal, KDEL [11]. A cartoon of our tRFP-SR construct is presented in Figure 2(a). Human Kif5b was a generous gift of Dr. Ronald Vale (University of San Francisco, CA, USA). We constructed a dominant version of Kif5b as previously described [12] and fused blue fluorescent protein (BFP) to the N-terminus of Kif5b-WT and Kif5b-DN. Adenoviruses expressing tRFP-SR, Kif5b-WT, and Kif5b-DN were generated using the ViraPower Adenoviral Expression System kit in accordance with manufacturer's instructions (Invitrogen, Carlsbad, CA, USA). Isolated neonatal and adult cardiac ventricular myocytes were infected with tRFP-SR, Kif5b-WT, or Kif5b-DN, and experiments were conducted 48 hours postinfection unless otherwise indicated.

2.3. Confocal, Total Internal Reflection Fluorescence Imaging and Analysis. For all experiments, cells were perfused with a physiological saline solution containing in mM: KCl 5, NaCl 140, MgCl_2 1, Glucose 10, HEPES, 10 and CaCl_2 2, pH 7.4 with NaOH. All experiments were performed at room temperature (22–25°C). Images were acquired using a confocal or total internal reflection fluorescence (TIRF) microscope. Confocal imaging was performed using a Bio-Rad Radiance 2000, Nikon Swept Field, or Nikon A1R-S1 confocal microscopes with a Nikon 60× oil immersion lens

(NA = 1.4). The TIRF microscope has a PlanApo (60×; NA = 1.45) oil immersion lens, an Andor iXON CCD camera, and a TILL photonics TIRF illuminator. Images were collected every 10 seconds, unless otherwise indicated. The potential for focus drift during time-lapse microscopy was minimized using Nikon's Perfect Focus System, which provides continuous, real-time focus drift correction caused by thermal and mechanical conditions. Analysis was performed on cells that showed no signs of focus drift.

Confocal and TIRF images were quantitatively analyzed using National Institutes of Health ImageJ software. Circular SR bouton distances, velocities, and trajectory mapping were performed using the Manualtracking plug-in. To measure change in tRFP-SR fluorescence, we identified prominent peaks using a top-hat filter with a 5×5 pixel window. Thresholds for the top-hat filter were determined per image to generate a full cell profile. A site was counted as having changed if at least one of the frames of a trace exceeded 3 standard deviations (SD) above or below the mean. To measure SR structural change of adult ventricular myocytes, we used an analysis for quantifying change in transverse-tubule structure [13]. Briefly, tRFP-SR myocytes were processed using fast Fourier transform (FFT) to convert two-dimensional images into frequency domain and its corresponding power spectrum (Figure 7(b)) allowing us to determine the spatial regularity of SR structure and the absolute value of the magnitude of the first harmonic (SR_{Power}) via Gaussian fitting with pCLAMP 10 software (Axon Instruments). The graphs shown in Figure 7(c) were fit with either a single Gaussian or sum of two Gaussian functions using Graphpad Prism v5.0a (GraphPad, La Jolla, CA, USA).

To measure changes in $[\text{Ca}^{2+}]_i$, ventricular myocytes were loaded with the free-acid or AM form of the fluorescent Ca^{2+} indicator Fluo-4 as previously described [4]. $[\text{Ca}^{2+}]_i$ signals were imaged using confocal or TIRF microscopy. For the experiments in which a TIRF microscope was used, the perforated patch-clamp technique was used to control membrane potential. The patch pipette solution was composed in mM: amphotericin B (30 $\mu\text{g}/\text{mL}$), penta-potassium form of fluo-4 (100 μM), CsCl 20, Aspartic acid 110, MgCl_2 1, HEPES 10, MgATP_5 , CaCl_2 2.94, EGTA 10, and pH 7.2 with CsOH. TIRF images were acquired at 30–60 Hz using TILL Image software. Confocal images were acquired using a Nikon swept field or Olympus FV1000 confocal microscope.

TIRF and confocal images were analyzed with custom software written in IDL language (Research Systems, Boulder, CO, USA). Briefly, background-subtracted fluorescence signals were normalized by dividing the fluorescence (F) intensity at each time point by the resting fluorescence (F_0) intensity. Fluorescent signals were calibrated using the “pseudo-ratio” equation [4]:

$$[\text{Ca}^{2+}]_i = \frac{K_d(F/F_0)}{\left(K_d/[\text{Ca}^{2+}]_{i,\text{rest}} + 1 - (F/F_0)\right)}, \quad (1)$$

where F is the fluorescence intensity, F_0 is the resting fluorescence, K_d is the dissociation constant of Fluo4 (1100 nM), and $[\text{Ca}^{2+}]_{i,\text{rest}}$ is resting Ca^{2+} concentration (150 nM).

2.4. Ryanodine Labeling. Live-cell labeling of ryanodine receptors was accomplished by incubating neonatal myocytes with 100 nM BODIPY-FL-X ryanodine (Invitrogen) for 10 minutes at room temperature in Hanks Balanced Salt Solution (HBSS; Invitrogen). Excess BODIPY-FL-X ryanodine was removed by washing cells 3 times, 10 minutes each, with HBSS prior to imaging. For adult ventricular myocytes, the concentration of BODIPY-FL-X-ryanodine was reduced to 50 nM, and the incubation period was reduced to 5 minutes at room temperature.

2.4.1. Electron Microscopy and Immunogold Labeling. Neonatal ventricular myocytes infected with tRFP-SR were fixed with 2.5% glutaraldehyde in PBS (10 mM phosphate buffer/150 mM NaCl, pH 7.4) for 30 minutes followed with 0.1% NaBH₄ in 0.1 M PB (phosphate buffer, pH 7.4) for 15 minutes to inactivate aldehydes. Cells were then fixed with 0.5% osmium tetroxide in PB for 15 minutes, subjected to graded dehydration and flat embedded in a mixture of Spur resin and Eponate 12 resin (Ted Pella, Redding, CA, USA). Ultrathin sections (70 nm) were poststained in 4% uranyl acetate and lead citrate. The samples were viewed on a JEOL JSM 6300F scanning electron microscope with digital image capture. Immunogold labeling of tRFP-SR was performed on tRFP-SR-infected neonatal mouse myocytes grown on coverslips using silver enhancement as previously described [14, 15] and prepared for electron microscopy as described above. The primary antibody, rabbit anti-tRFP (Evrogen, Joint Stock, Russia), was used in 1 : 5000 dilution and the secondary antibody, ultrasmall gold-conjugated F(ab)² fragment of goat anti-rabbit IgG (Aurion, Electron Microscopy Services, Hatfield, PA, USA) was used in a 1 : 100 dilution.

2.4.2. Statistics. Statistical significance was assessed by ANOVA analysis of all data points with pairwise comparisons completed as a posttest, with significance defined as *P* value less than 0.05. Data are presented as mean ± SEM. The asterisk (*) symbol is used in the figures to illustrate a significant difference between groups.

3. Results

3.1. SR Ca²⁺ Release Is the Principal Contributor to [Ca²⁺]_i Variance during EC Coupling. We imaged action potential-evoked [Ca²⁺]_i transients in adult and neonatal ventricular myocytes loaded with the fluorescent indicator fluo-4 AM (Figure 1). Action potentials were evoked via field stimulation at a frequency of 1 Hz. The mean [Ca²⁺]_i transient amplitude was 508 ± 28 and 705 ± 67 nM in adult (*n* = 9) and neonatal (*n* = 12) ventricular myocytes, respectively. The amplitude of these [Ca²⁺]_i transients did not change over a 5-minute period (Figure 1(a), left panel). Indeed, the coefficient of variation (i.e., standard deviation ÷ mean) of the [Ca²⁺]_i transient peak amplitude over this period of time was 0.12 ± 0.2 and 0.18 ± 0.03 in adult and neonatal ventricular myocytes, respectively (*P* < 0.05) (Figure 1(a), right panel).

To determine the time course and origin of beat-to-beat variations in [Ca²⁺]_i, we generated signal-averaged [Ca²⁺]_i records (Figure 1(b)) and their associated variance (σ^2) (Figure 1(c)) from neonatal and adult ventricular myocytes before and after the application of the SERCA pump inhibitor thapsigargin (1 μM). The variance of the [Ca²⁺]_i transient under control conditions ($\sigma_{\text{transient}}^2$) is defined by the following equation:

$$\sigma_{\text{transient}}^2 = \sigma_{\text{SR}}^2 + \sigma_{\text{influx}}^2, \quad (2)$$

where σ_{SR}^2 and σ_{influx}^2 are the variance of SR Ca²⁺ release and Ca²⁺ influx, respectively. $\sigma_{\text{transient}}^2$ and σ_{influx}^2 can be experimentally determined from the [Ca²⁺]_i transients before and after application of thapsigargin. Thus, $\sigma_{\text{SR}}^2 = \sigma_{\text{transient}}^2 - \sigma_{\text{influx}}^2$. Our analysis indicate that $\sigma_{\text{transient}}^2$ increased during the onset of the [Ca²⁺]_i transient. Consistent with the coefficient of variation data above, peak $\sigma_{\text{transient}}^2$ was larger in neonatal (20,111 ± 234 nM²) than in adult (5066 ± 74 nM²) ventricular myocytes. Thapsigargin significantly reduced mean peak [Ca²⁺]_i transient amplitude to 225 ± 9 and 420 ± 39 nM of adult and neonatal ventricular myocytes. Furthermore, σ_{influx}^2 was 8963 ± 39 nM² and 509 ± 9.01 nM² in neonatal and adult ventricular myocytes. Thus, σ_{SR}^2 is 4557 nM² in adult myocytes and 11148 nM² in neonatal myocytes. These data suggest that the majority of the $\sigma_{\text{transient}}^2$ in adult (~90%) and neonatal myocytes (~55%) originates from variations in Ca²⁺ release from the SR.

3.2. Network, Junctional, and SR Boutons in Living Ventricular Myocytes. Changes in the spatial organization of the SR could be a potential contributor to variations in Ca²⁺ release from this organelle during EC coupling. To investigate this issue, we infected ventricular myocytes with an adenoviral vector expressing the tag red fluorescent protein (tRFP-SR) [16] with a calreticulin entrance sequence in its N-terminal and a four-amino-acid sequence (KDEL) in its C-terminal that signals its retention in the SR lumen [11] (Figure 2(a)).

Confocal imaging revealed that tRFP-SR fluorescence was confined to the nuclear envelope and a vast, seemingly interconnected tubular SR network that extended throughout neonatal and adult ventricular myocytes (Figures 2(b)-2(c)). In neonatal ventricular myocytes, the width of these SR tubules at 50% fluorescence amplitude ranged from 0.6 to 3 μm with a mean of 0.8 ± 0.1 μm (*n* = 120 sites) (Figure 2(b), green). In contrast, adult ventricular myocytes expressing tRFP-SR did not show the convoluted, irregular reticular pattern observed in neonatal myocytes (Figures 2(b)-2(c)). Instead, as previously reported by others [1, 17], the SR forms terminals (i.e., junctional SR) with a periodic distribution of about 1.8 μm along the longitudinal axis of the cell. The diameter of these terminals ranged from 0.8 to 1.2 μm (Figure 2(c), green). The junctional SR at opposite ends of each sarcomere was interconnected by “network” SR.

We observed multiple bright structures protruding from the SR network of neonatal and adult ventricular myocytes (Figures 2(b)-2(c)). We refer to these structures as corbular SR boutons [1, 18]. Corbular SR boutons varied in length

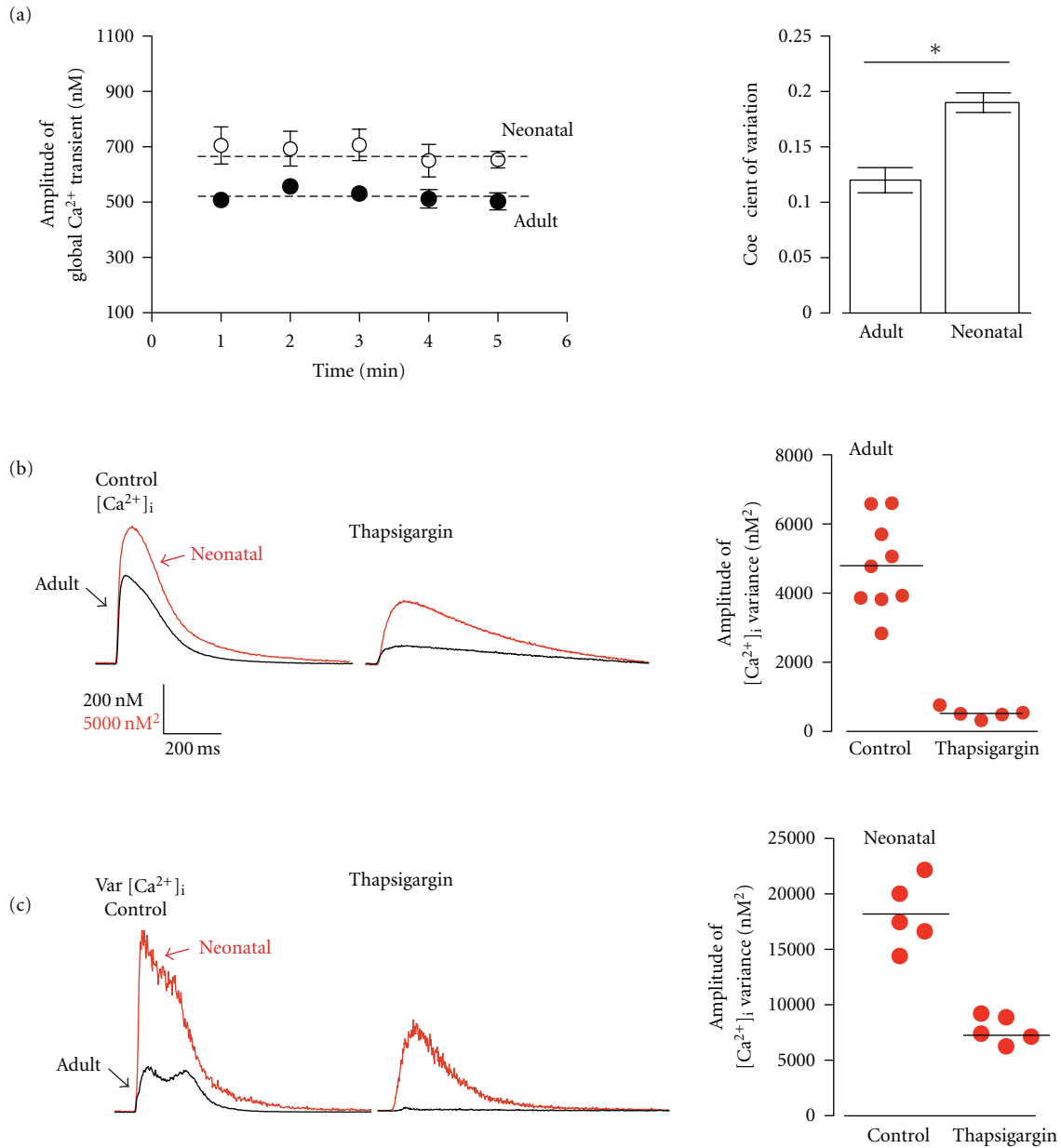


FIGURE 1: Beat-to-beat fidelity of EC coupling in ventricular myocytes. (a) Average peak amplitude of action potential evoked (1 Hz) global Ca^{2+} transients (nM) from adult (closed circles) and neonatal (open circles) ventricular myocytes measured at 1 minute interval for five minutes and corresponding coefficient of variation among the adult and neonatal myocyte population. Dashed line represents average peak $[\text{Ca}^{2+}]_i$ signal over 5 minutes. (b) Representative $[\text{Ca}^{2+}]_i$ transient of adult and neonatal myocytes. (c) Representative $[\text{Ca}^{2+}]_i$ signal variance of adult and neonatal ventricular myocytes and the distribution of peak amplitude $[\text{Ca}^{2+}]_i$ variance (nM^2) of adult ventricular myocytes in the presence and absence of the SR Ca^{2+} pump inhibitor thapsigargin ($1 \mu\text{M}$).

from 1 to $2 \mu\text{m}$ (mean = $1.2 \pm 0.1 \mu\text{m}$; $n = 79$) and from 0.5 to $0.7 \mu\text{m}$ in width (mean = $0.63 \pm 0.07 \mu\text{m}$, $n = 79$). The spatial distribution of tRFP-SR and structure of corbular SR boutons was examined with ultrahigh resolution, using conventional and immunogold electron microscopy (EM) (Figures 2(d)-2(e)). The SR/ER was identified in EM images using two generally accepted criteria. First, it is an intracellular membranous organelle that forms a cell-wide network that is continuous with the nuclear membrane. Second, it

has multiple electron-dense particles (likely ribosomes and RyRs) embedded in its membrane.

Consistent with our confocal data, EM images showed multiple Ω -shaped boutons within the SR and rough ER of non-permeabilized myocytes (boxes in Figure 2(d)). tRFP-SR-associated immunogold particles were also found to be broadly distributed through the perinuclear, network, and junctional, corbular SR of permeabilized myocytes (Figure 2(e) inset; arrows indicate immunogold particles).

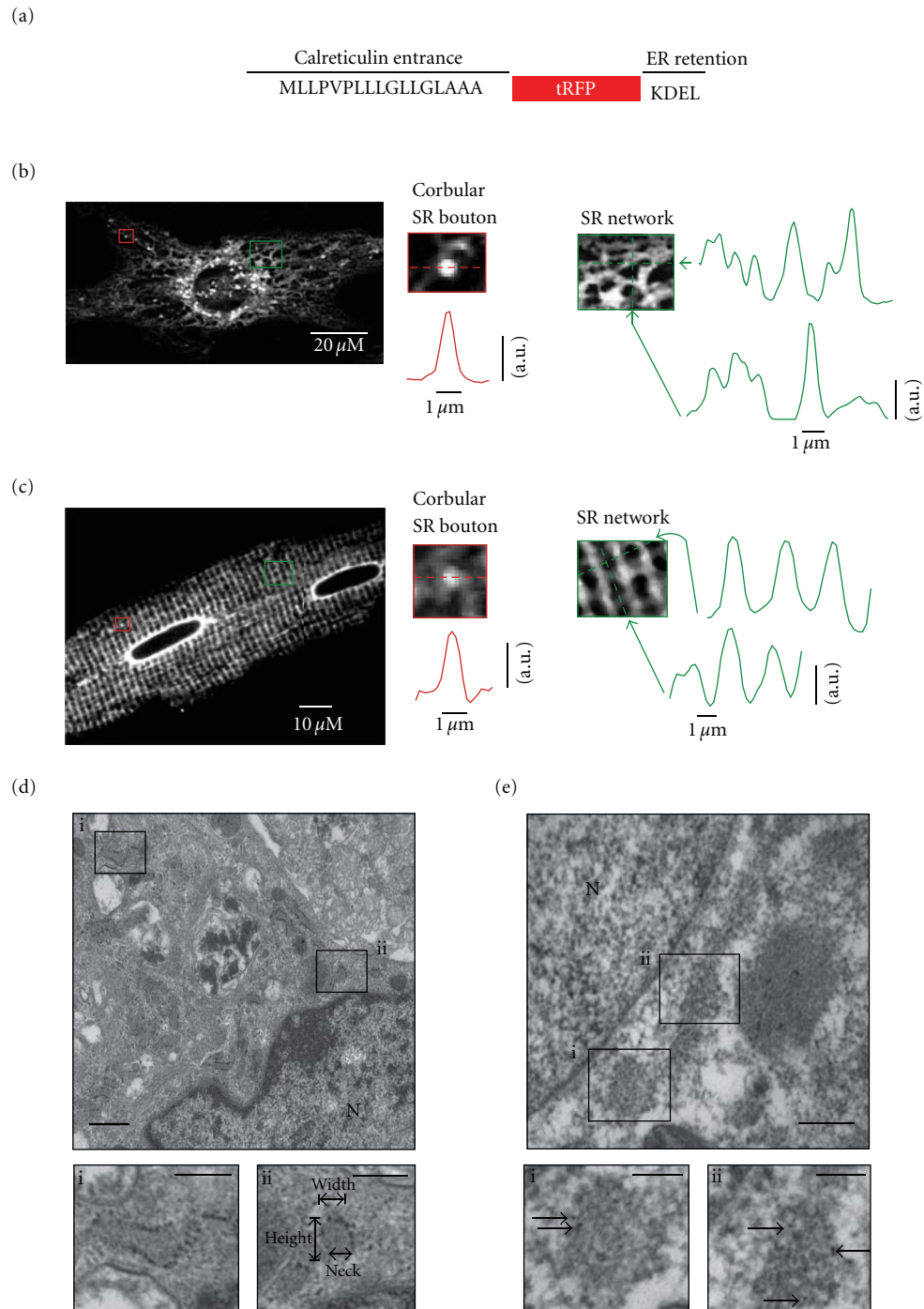


FIGURE 2: Imaging of network, junctional, and corbular SR boutons in living and fixed ventricular myocytes. (a) A cartoon of the tRFP-SR construct. (b) Confocal image of representative living neonatal ventricular myocyte expressing tRFP-SR. (c) Confocal images of representative living adult ventricular myocyte. Insets show zooms of a corbular SR bouton (red box) and SR network (green box) in these cells. Graphs show fluorescence intensity profile in the region in the image marked by arrows. (d) Electron microscopy image of non-permeabilized neonatal ventricular myocytes infected with tRFP-SR (scale bar = 1 μ m; N = nucleus). Insets depict invaginations of the endoplasmic/sarcoplasmic reticulum (scale bar = 100 nm). Panel Dii shows an example of how the dimensions of SR boutons were made. (e) Immunogold labeling of tRFP-SR (arrows of insets) from a permeabilized neonatal ventricular myocyte infected with tRFP-SR depicting invaginations of the endoplasmic/sarcoplasmic reticulum (scale bar = 500 nm and 100 nm (insets); N = nucleus).

Analysis of these EM images indicated that corbular SR had a height and maximum width of 25 ± 5 nm and 1.1 ± 0.1 μm ($n = 50$), respectively. The diameter at the “neck” of the corbular SR, where they connect to the SR network, was 156 ± 5 nm. Figure 2(d)ii shows the location of these structures in an electron micrograph from a representative myocyte.

3.3. The SR of Ventricular Myocytes Is Motile. Having found a strategy to monitor SR ultrastructure in living ventricular myocytes, we tested the hypothesis that the SR of neonatal and adult ventricular myocytes is a structurally inert organelle. To do this, time-lapse confocal microscopy was performed using neonatal and adult ventricular myocytes expressing tRFP-SR (Figures 3 and 4). Contrary to our hypothesis, we found a significant level of mobility and reorganization within the SR of ventricular myocytes. Corbular SR boutons moved frequently and for relatively long distances (see Movie 1 in Supplementary Material available online at doi: 10.1155/2011/382586).

Figures 3(a)–3(d) shows two-dimensional confocal images from representative neonatal and adult ventricular myocytes expressing tRFP-SR at various time points after the beginning of imaging. Motile corbular SR boutons are identified in each image with circles of varied colors. We tracked the position of the epicenter of each corbular SR bouton over time. The lines connected to each circle illustrate the trajectories of each of the corbular SR boutons in these images. We found that corbular SR boutons moved exclusively within the SR network of neonatal and adult ventricular myocytes. Furthermore, our analysis suggests that the trajectories and velocities of corbular SR boutons were highly variable. Accordingly, individual corbular SR boutons did not move at a constant speed, with periods of rapid mobility often followed by periods of slowed movements or even stasis (Figures 3(b)–3(d)). For example, while the *corbular SR bouton i* (green) in the neonatal myocyte in Figures 3(a)–3(b) only moved 0.8 μm at a maximum velocity of 0.06 $\mu\text{m/s}$, *corbular SR bouton ii* (orange) in the same cell moved a total of ≈ 10 μm at a maximum velocity of 0.18 $\mu\text{m/s}$ over a period of 300 seconds.

Motile corbular SR boutons were also observed in the SR of adult ventricular myocytes, albeit with a lower frequency than in neonatal myocytes (Figures 3(c)–3(d)). An example of a motile corbular SR bouton in an adult myocyte is shown in Figure 3(c). The green line shows the trajectory of this specific corbular SR bouton. Like neonatal corbular SR boutons, the velocity and distance traveled by this adult corbular SR bouton was variable. It moved with a maximum velocity of 0.06 $\mu\text{m/s}$ and traveled ≈ 8 μm over a period of 300 seconds (Figure 3(d)).

Motile corbular SR boutons moved faster in neonatal (0.045 ± 0.01 $\mu\text{m/s}$, $n = 250$) than in adult ventricular myocytes (0.020 ± 0.004 $\mu\text{m/s}$, $n = 50$; $P < 0.05$) (Figure 3(e)). The maximum velocity reached by corbular SR boutons was 0.6 $\mu\text{m/s}$. Neonatal and adult neonatal SR boutons traveled distances of up to 30 μm in a period of 300 seconds (Figure 3(f)). The distance traveled for a corbular SR bouton in a continuous movement event (called “step distance”)

in adult and neonatal myocytes ranged from 0.3 to 4.2 μm (Figure 3(g)).

We found that changes in SR structure were not limited to motile SR boutons but included changes in the structure of the SR network of neonatal and ventricular myocytes. An example of this is shown in Figures 4(a)–4(b) and Movie 2 in Supplementary Material. Site *i* in Figure 4(a) is an area of the SR network of a neonatal ventricular myocyte, where an SR tubule bifurcates into two branches. Time-lapse confocal microscopy of this site showed the formation of a new connection between two adjacent SR branches. In site *ii*, we were able to capture the sequence of events that likely lead to the formation of these SR connections. The corbular SR bouton marked by the red arrow elongated finally fusing with a neighboring section of SR network. Figure 4(b) shows a similar set of events, but in an adult ventricular myocyte.

We also detected fluctuations of tRFP-SR fluorescence presumably resulting from changes in SR structure in these cells. An example of this type of phenomenon is shown in Figure 4(c) (see also Movie 3 in Supplementary Material). Surface plots of sites *i* and *ii* in this adult ventricular myocyte revealed dynamic fluctuations in tRFP-SR fluorescent suggesting structural changes in the junctional SR.

We used TIRF microscopy to resolve subtle changes in SR morphology within the subsarcolemmal space of neonatal and adult ventricular myocytes (Figure 5). In our TIRF microscope, excitation is limited to an evanescent field of about 100 nm from the coverslip. Thus, the axial resolution of the TIRF microscope (≈ 0.1 μm) is nearly an order of magnitude higher than our confocal microscope (≈ 1.1 μm). In neonatal myocytes, we observed multiple motile SR projections into the subsarcolemmal space per cell (Figure 5(a); see also Movie 4 in Supplementary Material). Interestingly, these SR structures moved laterally as well as in and out of the evanescent field, suggesting that in neonatal myocytes the SR is forming and dissolving SR-sarcolemma junctions on a regular basis. A similar observation was made using adult ventricular myocytes (Figure 5(b)). Collectively, these confocal and TIRF data suggest that the SR is a dynamic organelle that frequently forms and dissolves SR-sarcolemmal junctions in neonatal and adult ventricular myocytes.

3.4. Motile Corbular SR Boutons Express Functional Ryanodine Receptors. We investigated whether the corbular SR boutons and junctional SR observed with confocal and TIRF microscopy contained functional RyRs (Figure 6). To do this, we labeled living neonatal and adult ventricular myocytes expressing tRFP-SR with BODIPY-Ryanodine (100 nM neonatal, 50 nM adult) (Figures 6(a) and 6(c)). The Pearson's coefficient between tRFP-SR with BODIPY-Ryanodine signals in neonatal and adult ventricular myocytes was 0.69 and 0.80 , respectively. We performed simultaneous time-lapse confocal microscopy imaging of our neonatal ventricular myocytes labeled with BODIPY-RyR. The representative two-dimensional confocal images of the cell presented in Figure 6(a) are shown at various time points (Figure 6(b), see also Movie 5 in Supplementary Material). We found

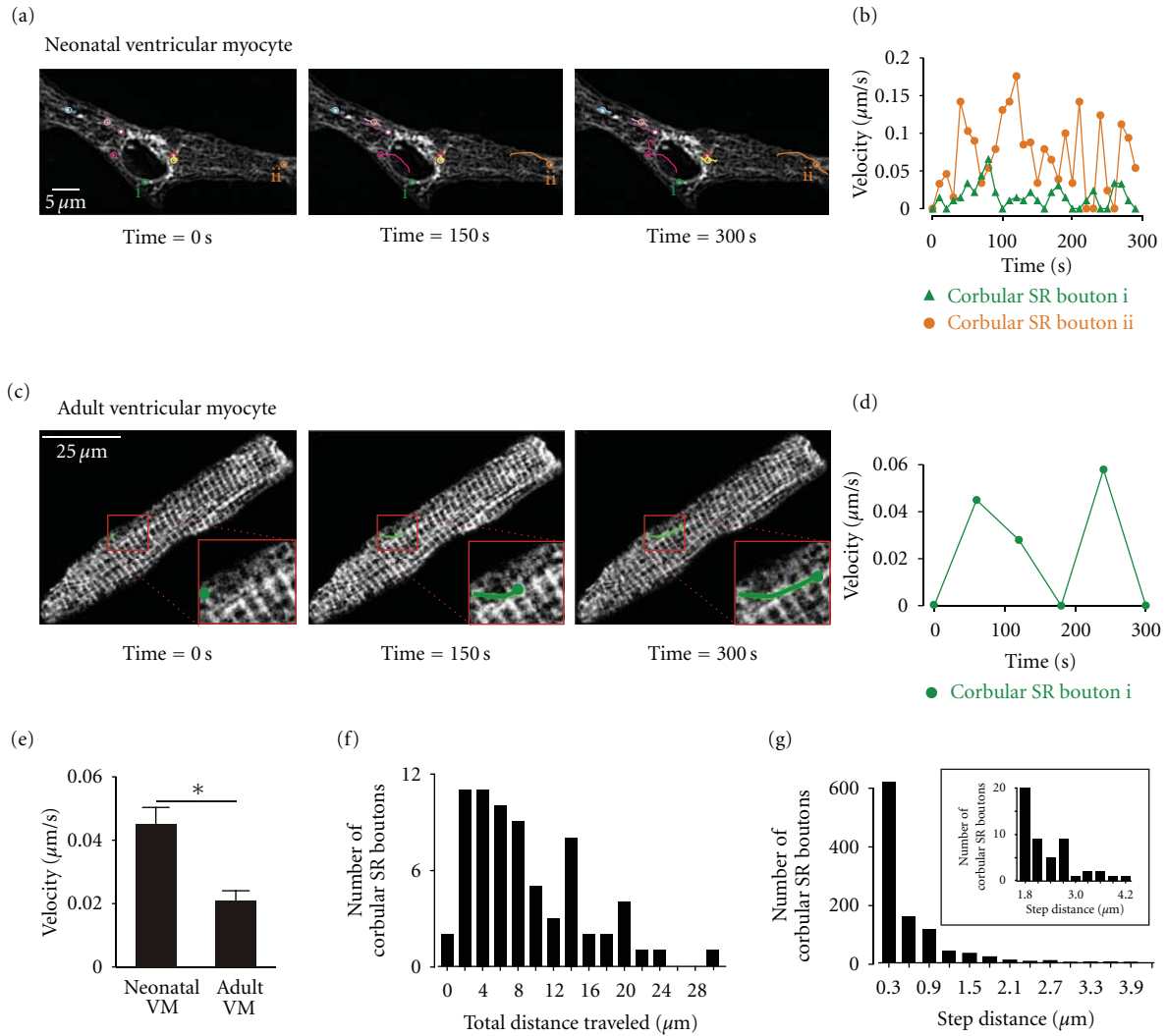


FIGURE 3: Motile corbular SR boutons in neonatal and adult ventricular myocytes. (a) Time-lapse confocal images of a neonatal ventricular myocytes expressing tRFP-SR. Images shown were obtained 0, 150, and 300 seconds after the initiation of the experiment. Motile corbular SR boutons are labeled with colored circles. (b) Plot of the velocity of corbular SR boutons *i* and *ii* as a function of time. (c) Time-course of corbular SR bouton motility in a representative adult ventricular myocyte expressing tRFP-SR. The insets in the lower right corner of each image show an expansion of the region in the cell marked by the red box. (d) Plot of velocity of this corbular SR bouton as a function of time. (e) Bar plot of the mean velocity of corbular SR boutons in neonatal and adult ventricular myocytes (**P* < 0.05). (f) Histogram of the total distance traveled over a period of 300 seconds of 79 corbular SR boutons in adult and neonatal ventricular myocytes. (g) Histogram of the step distance traveled by corbular SR boutons. The inset shows an expanded view of the region of the histogram from 1.8 to 4.2 μm .

that BODIPY-RyR labeled structures moved with corbular SR boutons and along the tracks of the tRFP-SR labeled SR network at varying speeds over time. As described previously, we tracked the position and distance traveled of the epicenter of each corbular SR bouton labeled with BODIPY-RyR and compared them to unlabeled control cells. Labeled and unlabeled SR boutons traveled similar distances over a period of 300 seconds. These data suggest that tRFP-SR with BODIPY-Ryanodine colocalize in neonatal and adult ventricular myocytes and ryanodine receptors are expressed in diverse structures (i.e., network, junctional, and boutons) and are mobile within the SR of ventricular myocytes.

Next, we tested the hypothesis that motile SR boutons express functional RyRs. Consistent with this, we recorded

spontaneous Ca^{2+} sparks from motile SR boutons (Figures 6(d)-6(e)). For example, the corbular SR bouton marked with a green dot in Figure 6(d) moved at a velocity of up to $0.004 \mu\text{m/s}$ and multiple Ca^{2+} sparks were recorded from this site. As shown in Figure 6(e), Ca^{2+} sparks were also recorded from corbular SR boutons in adult myocytes. In combination with the data above, these findings suggest that mobile corbular SR boutons express functional ryanodine receptors in ventricular myocytes.

3.5. *The Microtubule Network and Microtubule-Associated Motors Dynein and Kif5b Regulate SR Motility in Ventricular Myocytes.* We investigated the mechanisms underlying SR

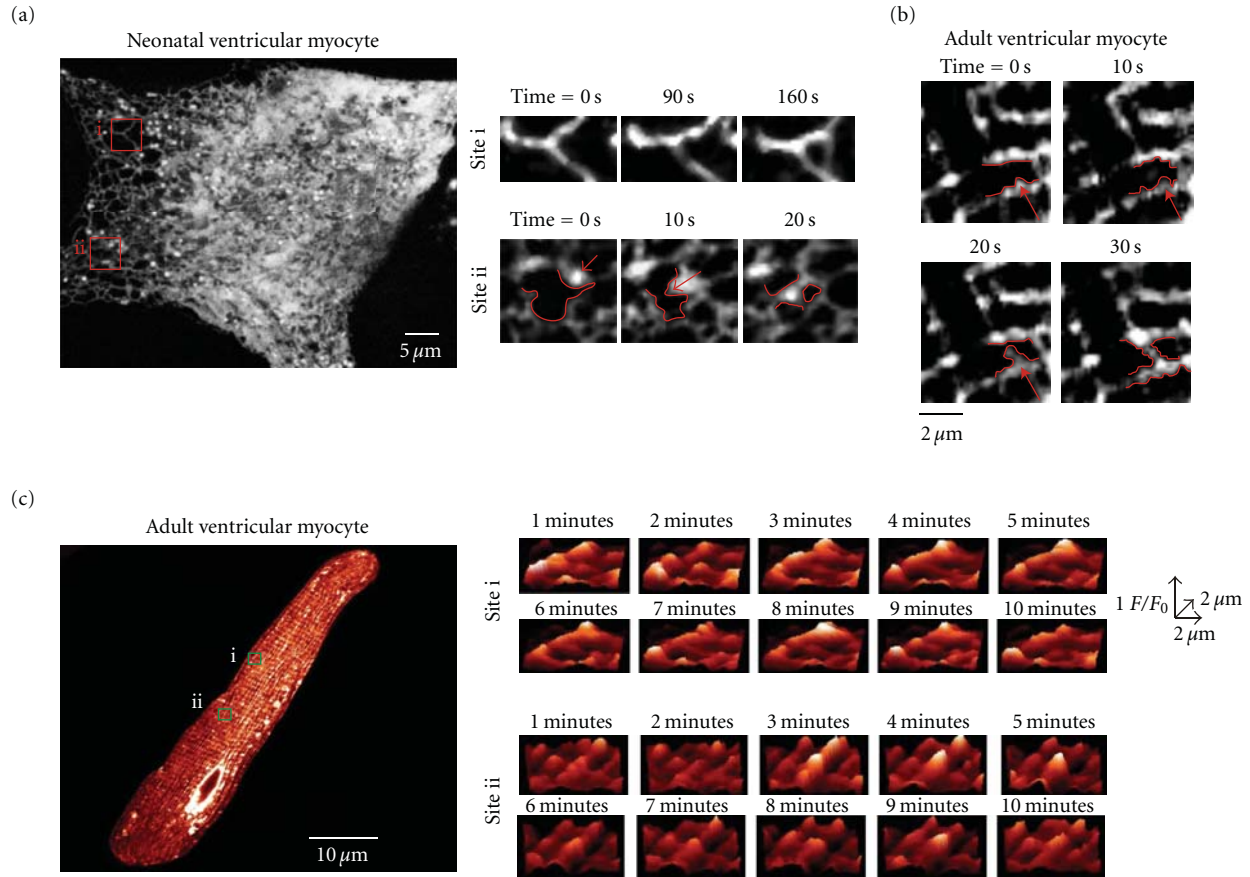


FIGURE 4: Dynamic remodeling of the SR network of neonatal and adult ventricular myocyte. (a) Confocal image of a neonatal ventricular myocytes expressing tRFP-SR. Images to the left show expanded views of sites i and ii at various time points. The red arrow in site ii marks a corbular SR bouton. Redlines delineate a portion of the SR network and shows elongation and subsequent fusion of this SR bouton to an adjacent SR tubule. (b) Time-lapse confocal imaging of a region of an adult ventricular myocyte expressing tRFP-SR. Redlines delineate a portion of the SR network and shows elongation and subsequent fusion of SR tubule to an adjacent SR tubule. (c) Confocal image of an adult ventricular myocyte. Surface plots at multiple time points of sites i and ii are shown to the right of this image.

motility in ventricular myocytes. Previous studies have implicated the microtubule network and the molecular motor dynein in the regulation of ER structure and motility in nonmuscle cells [19–22]. Thus, we examined the effects of the microtubule disruptor nocodazole (10 μM) on the SR of neonatal and adult ventricular myocytes expressing tRFP-SR. We found that incubation with 10 μM nocodazole for 2 hours induced significant SR fragmentation in neonatal ventricular myocytes (Figure 7(a)).

Nocodazole also seemed to alter SR organization in adult ventricular myocytes (Figures 7(b) and 7(c)). To quantify changes in SR-structure in adult ventricular myocytes, where the SR is organized in a well-defined periodic pattern, we implemented an analysis similar to the one used by Wei et al. [13], to monitor transverse tubule periodicity in ventricular myocytes. Briefly, this analysis involves a Fast Fourier Transform (FFT) analysis of tRFP-SR images, which are converted into a frequency domain that quantifies periodicity. The first harmonic, which centers at 1.7 μm, is the strongest periodicity of the SR-network based upon the spacing between each harmonic (Figure 7(b)). The magnitude of

the 1st harmonic, or SR_{Power} , provides a quantitative index for SR structural periodicity. In this analysis, a decrease in SR_{Power} would represent a decrease in SR periodicity and hence its structural integrity. We found that under control conditions the histogram of SR_{Power} values could be fit with a single Gaussian function with a center at 1.70 μm ($n = 17$). However, in nocodazole-treated cells the SR_{Power} was shifted towards lower SR_{Power} values than under control conditions. Indeed, the SR_{Power} of nocodazole treated cells could be fit with the sum of two Gaussian functions with centers at 0.88 and 1.53 μm ($n = 30$) (Figure 7(c)). These data suggest that microtubules play a critical role in the maintenance of the structural integrity of the SR network in ventricular myocytes.

Next, we tested the hypothesis that inhibition of the microtubule-associated molecular motor proteins dynein and Kif5b would decrease SR motility. We investigated whether inhibition of the retrograde molecular motor, dynein with erythro-9-(2-hydroxy-3-nonyl) adenine (EHNA) [23] would decrease SR motility in neonatal ventricular myocytes (Figures 8(a) and 8(c)). Confocal images were collected at

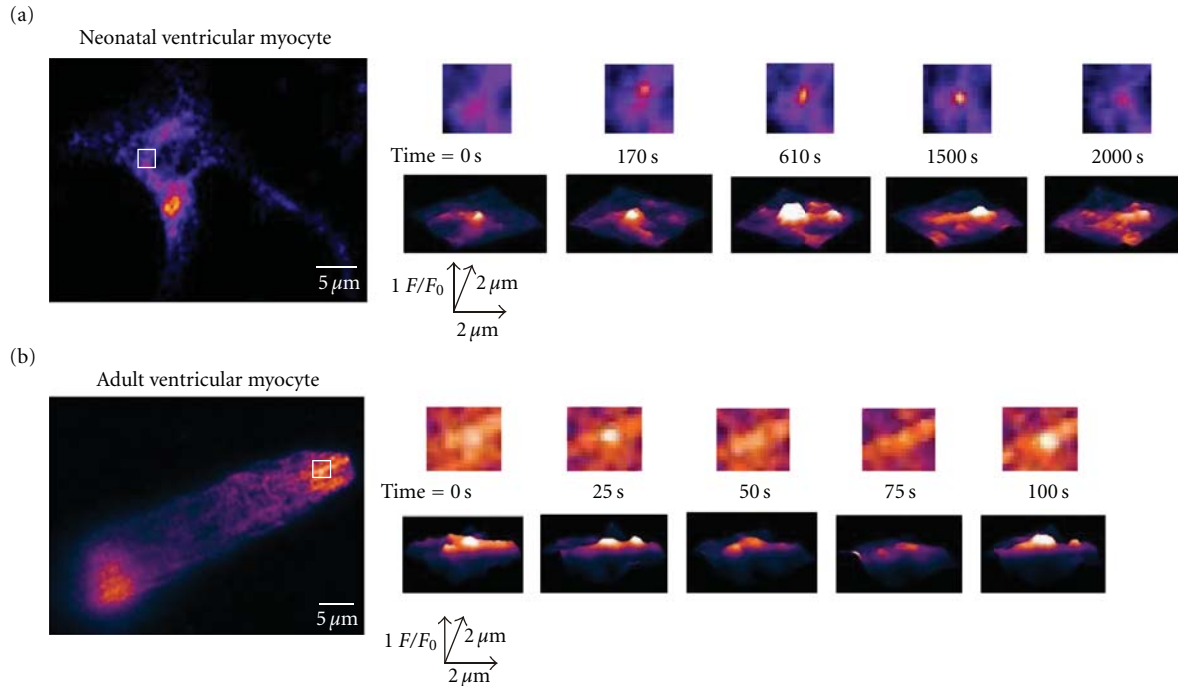


FIGURE 5: TIRF imaging of submembrane SR motility in neonatal and adult ventricular myocytes. (a) TIRF images of representative neonatal ventricular myocyte expressing tRFP-SR. (b) TIRF image of representative adult ventricular myocyte expressing tRFP-SR. Images to the right are two dimensional images (top row) and surface plots of the region delineated by the white.

various time points over a period of 120 minutes in the presence or absence of $30 \mu\text{M}$ EHNA. Figure 8(a) shows a representative neonatal myocytes before (control) and after the application of EHNA. We mapped the trajectories of corbular SR boutons under control conditions and in the presence of EHNA with colored lines. Note that although corbular SR boutons were observed after incubation with EHNA, motility was significantly reduced (Figure 8(a)). Indeed, EHNA significantly decreased the total distance traveled by neonatal corbular SR boutons by $\approx 57\%$ from $6.27 \pm 0.44 \mu\text{m}$ (control, $n = 6$) to $2.69 \pm 0.34 \mu\text{m}$ (EHNA, $n = 16$) ($P < 0.05$) (Figure 8(c)).

To examine whether the anterograde microtubule-associated molecular motor protein Kif5b alters SR dynamics, we generated two adenovirus constructs of wild type and a dominant-negative form of Kif5b lacking the motor domain [12] fused to BFP at the N-terminus (Kif5b-WT and Kif5b-DN) and infected ventricular myocytes simultaneously with Kif5b-BFP and tRFP-SR adenoviruses (Figure 8(b)). The Pearson's coefficient between tRFP-SR and Kif5b-WT-BFP or Kif5b-DN-BFP was 0.82 and 0.81, respectively (Figure 8(b)). These data suggest that the molecular motor Kif5b associates with the diverse structures of the SR network (i.e., network, junctional, and boutons) in ventricular myocytes. Importantly, we found that expression of Kif5b-DN-BFP significantly decreased the total distance traveled by neonatal corbular SR boutons by $\approx 60\%$ from $7.01 \pm 0.31 \mu\text{m}$ (control, $n = 6$) to $2.78 \pm 0.2 \mu\text{m}$ (Kif5b-DN-BFP, $n = 6$) ($P < 0.05$) (Figure 8(c)).

Finally, we investigated the effects of the dynein inhibitor EHNA on junctional SR in adult ventricular myocytes (Figure 8(d)). We focused on the junctional SR and not on SR boutons because, as noted above, the latter are less frequently observed in adult than in neonatal myocytes. For this analysis, we calculated the percent of junctional SR sites throughout the cell that, over time, underwent fluorescence fluctuations that exceeded 3 standard deviations above or below the mean local tRFP-SR fluorescence. Junctional SR sites were identified automatically with the use of a 5×5 top-hat detection filter. Using this analysis, we found that, under control conditions, $4.7 \pm 0.2\%$ ($n = 20,000$ sites from 6 cells) of isolated sites experienced change in tRFP-SR fluorescence in the junctional SR that exceeded the detection threshold. Consistent with the neonatal data above, application of $30 \mu\text{M}$ EHNA decreased the number of fluctuating junctional SR sites by $45 \pm 0.1\%$ ($P < 0.05$). Collectively, these data suggest that the microtubule network and the molecular motors dynein and Kif5b play a critical role in SR motility of ventricular myocytes.

4. Discussion

This study provides the first characterization of SR structure in living neonatal and adult ventricular myocytes. The main findings of this study were fourfold. First, the SR forms a vast network that is structurally diverse and dynamic. Second, we discovered that corbular SR boutons move throughout

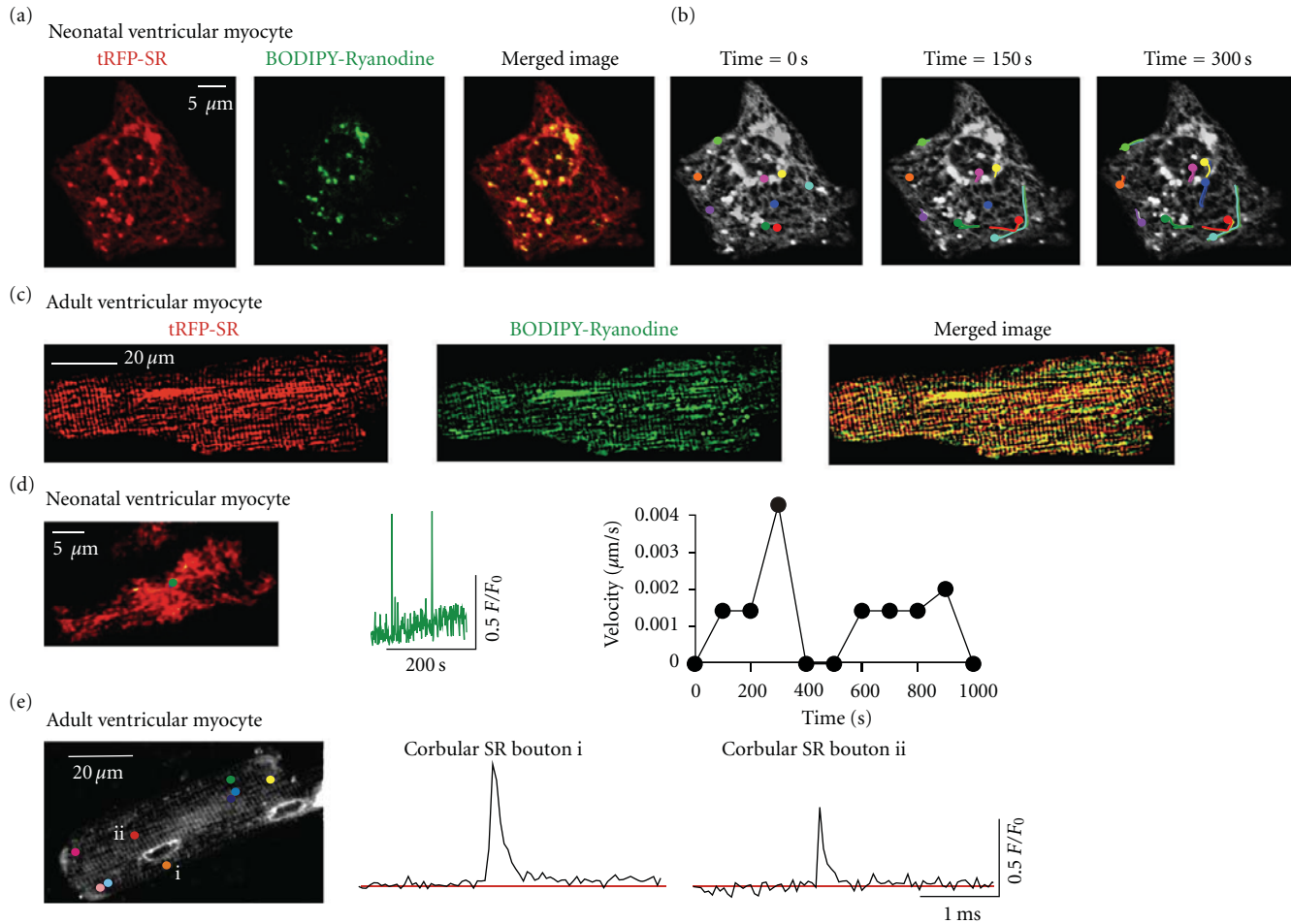


FIGURE 6: Expression of functional ryanodine receptors in motile corbular SR boutons. (a) Confocal image of a neonatal ventricular myocyte expressing tRFP-SR (left), labeled with BODIPY FL-X Ryanodine (center) and merged image (right). (b) Time-lapse confocal images of neonatal ventricular myocyte from panel A expressing tRFP-SR and labeled with BODIPY FL-X Ryanodine. Images shown were obtained 0, 150, and 300 seconds after the initiation of the experiment. Motile corbular SR boutons are labeled with colored circles. (c) Confocal image of adult ventricular myocyte expressing tRFP-SR (left), labeled with BODIPY FL-X Ryanodine (center) and merged image (right). (d) TIRF image (left) of a representative neonatal myocyte expressing tRFP-SR loaded with fluo-4. Green dot represents corbular SR bouton of interest. The plot in the center shows the time course of Ca^{2+} spark activity in this corbular SR bouton. The plot to the left shows the velocity of the corbular SR bouton marked by the green dot as a function of time. (e) Confocal image (left) of a representative adult ventricular myocyte expressing tRFP-SR loaded with fluo-4 AM. Colored dots mark corbular SR boutons in this cell. The two plots in this panel show the time-course of spontaneous Ca^{2+} sparks in corbular SR boutons *i* and *ii*.

the cell and express functional RyR. Third, by simultaneously imaging $[\text{Ca}^{2+}]_i$ and tRFP-SR, we discovered that the amplitude of the evoked whole-cell $[\text{Ca}^{2+}]_i$ transient remains unchanged even though the SR is undergoing significant remodeling. These data suggest that a static SR network is not required for stable EC coupling in ventricular myocytes. Fourth, SR structure and motility are dependent on an intact microtubule network and the retrograde and anterograde microtubule-associated motors dynein and Kif5b.

Electron microscopy and immunofluorescence approaches have been extensively employed to study SR structure in cardiac muscle [1, 24–26]. These studies have led to the formulation of a model of the SR and its involvement in EC coupling. In this model, the SR is comprised of interconnected longitudinal tubules that terminate in dilated

sacs that come into close apposition (≈ 15 nm) to the sarcolemma. RyRs are expressed in this junctional SR. Together, the junctional SR, RyRs, and nearby sarcolemmal L-type Ca^{2+} channel form a signaling unit called a “couplon”. The formation of SR-sarcolemmal junctions that underlies the couplon is proposed to be a multistep process [27, 28]. The first event in development of the junctional SR is the “docking” of the SR membrane to the sarcolemma via the protein junctophilin 2. Following the establishment of the SR-sarcolemmal junctions in embryonic myocytes, the proteins calsequestrin, junction, and triadin are targeted and organized within the SR. The arrival of the RyRs and L-type Ca^{2+} channels and final organization of the macromolecular complex that comprises a Ca^{2+} release unit within the junctional SR lead to a couplon.

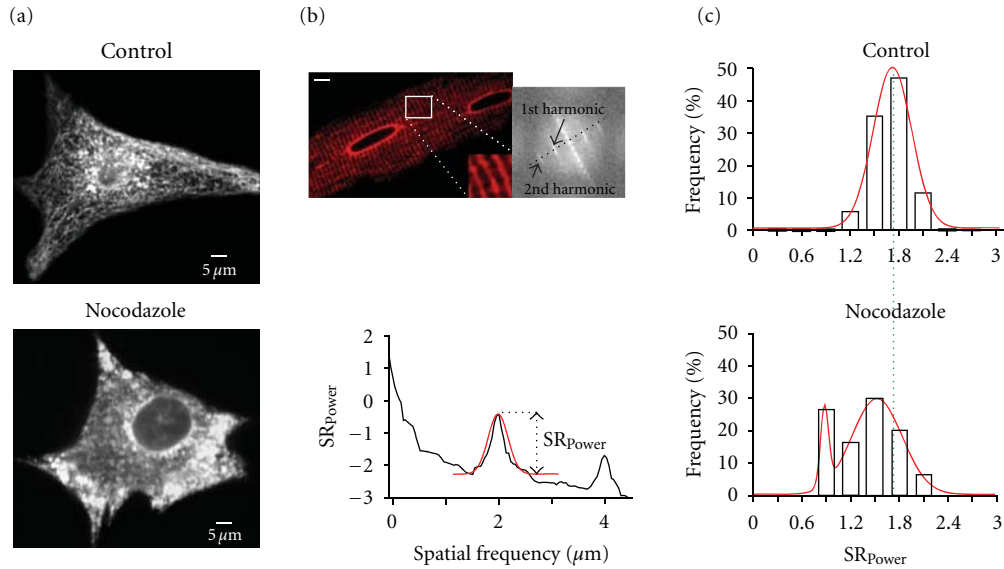


FIGURE 7: Microtubules regulate SR structure in neonatal and adult ventricular myocytes. (a) Confocal images of a neonatal ventricular myocyte expressing tRFP-SR in the absence (top; control) or presence of $10\ \mu\text{M}$ nocodazole (bottom). (b) Confocal image of an adult ventricular myocyte expressing tRFP-SR. The inset shows a zoomed-in region of the cell delineated by the white box. The image to the left is a 2D Fourier transformation of the confocal image. (c) Histograms of SR_{power} values in control and nocodazole-treated adult ventricular myocytes. Dashed green line shows global shift in SR_{power} distributions in nocodazole-treated myocytes from the center ($1.7\ \mu\text{m}$) of control myocytes. Solid red lines represent fits to the data with single (control; center = $1.7\ \mu\text{m}$) and dual (nocodazole; center peak 1 = $0.88\ \mu\text{m}$, center peak 2 = $1.53\ \mu\text{m}$) Gaussian functions.

Our data suggest that these SR structures are highly dynamic. This is analogous to what has been described for the endoplasmic reticulum (ER) in nonmuscle cells [20, 29]. The SR is considered to be a specialized derivation of the endoplasmic reticulum (ER) that is dedicated to Ca^{2+} storage and release for the regulation of muscle contraction and EC coupling. The ER of nonmuscle cells is known to have a convoluted structure that is continually reorganizing its structure and moving toward and away from the plasma membrane over time in a variety of living nonmuscle cell models [20, 29]. Our data suggest that like the ER, the SR has the capacity to remodel.

Our results demonstrate that the mean $[\text{Ca}^{2+}]_i$ transient amplitude achieves high fidelity yet also displays beat-to-beat variation in $[\text{Ca}^{2+}]_i$. Interestingly, the variance of the $[\text{Ca}^{2+}]_i$ attributable to SR Ca^{2+} release was nearly 4-fold larger than adult myocytes. This coincides with a higher degree of SR motility in neonatal than in adult myocytes. Although the exact sources for $[\text{Ca}^{2+}]_i$ variance during EC coupling are unclear, it is intriguing to speculate that variations in SR motility of neonatal and adult ventricular myocytes could be a contributing factor.

Similar to studies of the regulation of ER motility [19–22, 29], we demonstrate that the microtubule network regulates SR motility. Although a direct interaction between the microtubule network and the SR has not been shown, it has been postulated to be necessary to mechanically regulate the SR and T-tubule sarcolemma for proper regulation of Ca^{2+} spark activation and termination [30]. Indeed, perturbation of the microtubule network has been shown to

alter L-type Ca^{2+} current, $[\text{Ca}^{2+}]_i$ transients [30], Ca^{2+} sparks [31], and action potential waveform [32]. Our results suggest intact microtubules are necessary for maintenance of SR ultrastructure.

Kif5b has been implicated in ER motility in nonmuscle cells [29] and in the trafficking of Kv1.5 channels in heterologous cells and rat ventricular myocytes [12]. Likewise, the retrograde motor protein, dynein, has been previously shown to affect the trafficking of Kv1.5 channels in heterologous cells and rat cardiac myocytes [33, 34] and ClC-2 chloride channel in hippocampus [35]. Interestingly, we found that expression of a dominant-negative Kif5b and inhibition of dynein decreased. At present, however, the specific role of Kif5b and dynein in SR motility, couplon formation, and EC coupling is unknown. Future studies should examine the role of microtubules and molecular motor proteins in these important issues.

On the basis of these findings, we propose a new model for the role and regulation of SR structure and motility in EC coupling in ventricular myocytes (Figure 8(e)). In this model, the SR forms a vast interconnected network with distinct microdomains (i.e., junctional domains, corbular domains) throughout the ventricular myocyte. The position of SR structures likely depends on the relative activities of microtubule-associated Kif5b (anterograde motor), and dynein (retrograde motor) regulate SR structure and motility. We propose that the function of these structural rearrangements would include formation of new interconnections with neighboring SR network, formation of new junctions between SR and sarcolemma (i.e., couplons), and

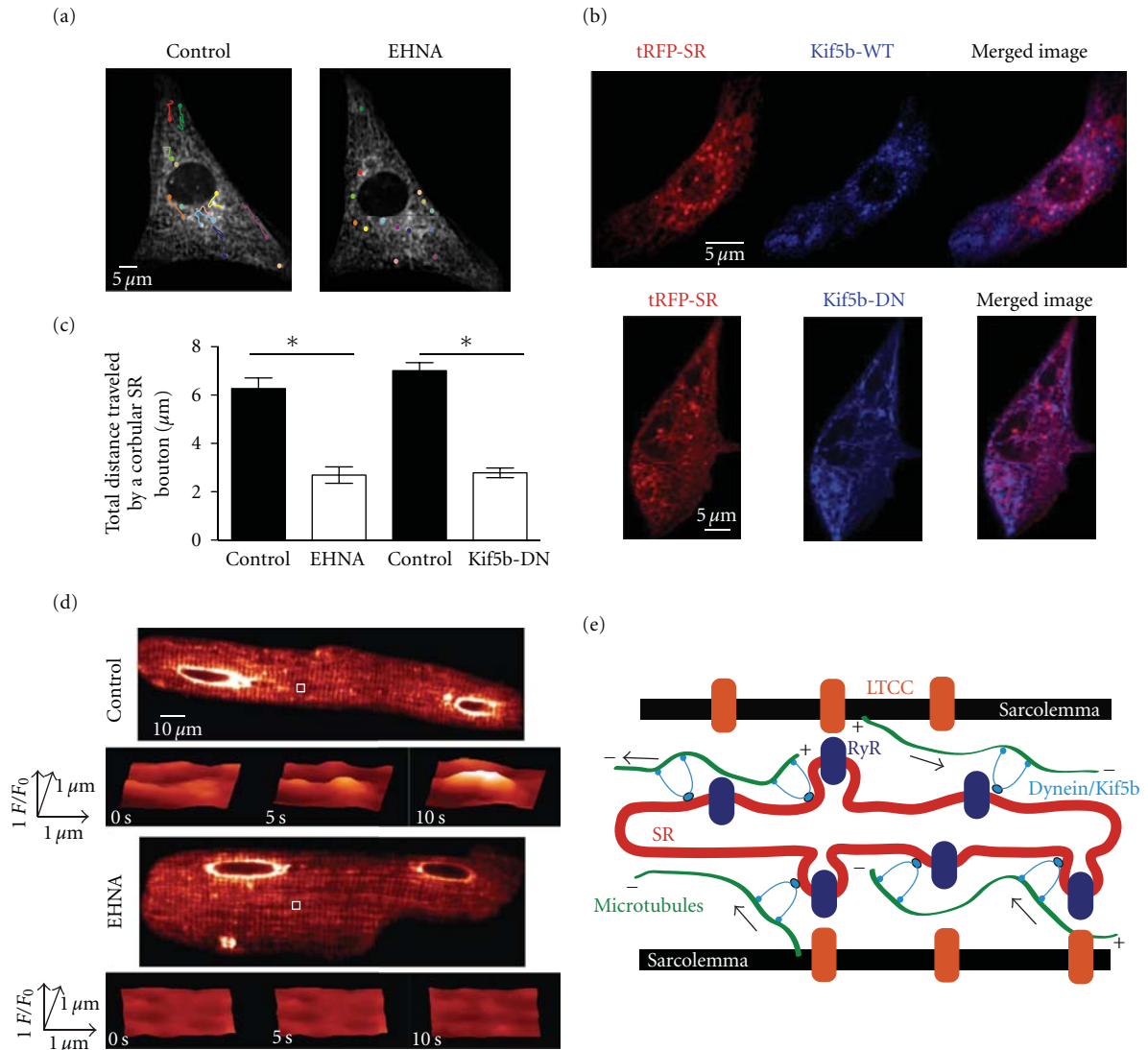


FIGURE 8: The microtubule-associated motors dynein and Kif5b regulate SR motility in ventricular myocytes. (a) Confocal image of neonatal ventricular myocyte expressing tRFP-SR under control conditions and after 120 minutes of 30 μM EHNA perfusion. Corbular SR boutons are identified with colored circles. (b) Confocal images of neonatal ventricular myocyte expressing tRFP-SR (left) and Kif5b-WT-BFP (top/center) or Kif5b-DN-BFP (bottom/center). The images to the right were generated by merging the tRFP-SR and Kif5b-BFP images. (c) Bar plot of the mean total distance traveled by corbular SR boutons before and after EHNA perfusion and myocytes infected with tRFP-SR (control) and myocytes infected with tRFP-SR and Kif5b-DN-BFP. (d) Confocal images showing tRFP-SR fluorescence of adult ventricular myocytes under control conditions (top) and incubated in the presence of 30 μM EHNA (bottom). Surface plots show the time-course of fluorescence intensity in the region delineated by the white box. (e) Cartoon depicting a hypothetical model for the regulation of SR structure and motility in ventricular myocytes (LTCC = L-type Ca^{2+} channel; RyR = ryanodine receptor).

possibly regulation of trafficking of important EC coupling proteins through the SR bouton. An important implication of this model is that the exquisite fidelity of the $[\text{Ca}^{2+}]_i$ transient in ventricular myocytes is not likely produced by the activation of Ca^{2+} release from a permanently static SR structure. Rather, it may result from the activation of a temporally averaged number of SR Ca^{2+} release units from the formation and dissolution of SR-sarcolemmal junctions that are sensitive to perturbations in the microtubule network such as those observed in cardiac pathology.

5. Limitations

All studies that use cultured ventricular myocytes and pharmacological agents should be interpreted cautiously. For example, cultured adult ventricular myocytes undergo deterioration of their T-tubules and experience electrophysiological changes [36, 37]. Furthermore, it is important to note that although EHNA is known to disrupt the ATPase activity of dynein [23, 35, 38], it also inhibits phosphodiesterases in cardiac myocytes [39]. Thus, we cannot rule

out the possibility that a nondynein molecular motor that is modulated by cAMP levels is involved in SR motility. In spite of these limitations, we contend that novel insights into the bases of SR structure in ventricular myocytes have been obtained in the present experiments. These insights should form the bases of new hypotheses that can be best tested in appropriate animal models.

6. Summary and Conclusions

The present study suggests that normal cardiovascular function is accomplished via complex regulation of SR ultrastructure, $[Ca^{2+}]_i$, and contraction. Our study offers a novel conceptual model on the regulation of SR dynamics in ventricular myocytes. Based on this model, we propose that the fidelity of the $[Ca^{2+}]_i$ transient is not likely produced by the activation of Ca^{2+} release from a permanently static SR but rather may result from the activation of temporally averaged number of SR Ca^{2+} release units forming and dissolving SR-sarcolemmal junctions that are sensitive to perturbations of the microtubule network. Our results and proposal merit further investigation.

Acknowledgments

The authors thank Mr. Edward Cheng and Drs. Rose Dixon, Carmen A. Ufret-Vincenty, Manuel F. Navedo, and Madeline Nieves-Cintrón for reading this paper. Ms. Stephanie Lara helped with electron microscopy. The study was supported by Grants from NIH (HL85686 and T32-HL07828) and the AHA (0840094N).

References

- [1] C. Franzini-Armstrong, F. Protasi, and V. Ramesh, "Shape, size, and distribution of Ca^{2+} release units and couplons in skeletal and cardiac muscles," *Biophysical Journal*, vol. 77, no. 3, pp. 1528–1539, 1999.
- [2] C. Franzini-Armstrong and F. Protasi, "Ryanodine receptors of striated muscles: a complex channel capable of multiple interactions," *Physiological Reviews*, vol. 77, no. 3, pp. 699–729, 1997.
- [3] A. Fabiato, "Calcium-induced release of calcium from the cardiac sarcoplasmic reticulum," *American journal of physiology*, vol. 245, no. 1, pp. C1–C14, 1983.
- [4] H. Cheng, W. J. Lederer, and M. B. Cannell, "Calcium sparks: elementary events underlying excitation-contraction coupling in heart muscle," *Science*, vol. 262, no. 5134, pp. 740–744, 1993.
- [5] A. M. Gómez, H. H. Valdivia, H. Cheng et al., "Defective excitation-contraction coupling in experimental cardiac hypertrophy and heart failure," *Science*, vol. 276, no. 5313, pp. 800–806, 1997.
- [6] C. Soeller and M. B. Cannell, "Numerical simulation of local calcium movements during L-type calcium channel gating in the cardiac diad," *Biophysical Journal*, vol. 73, no. 1, pp. 97–111, 1997.
- [7] M. Inoue and J. H. B. Bridge, " Ca^{2+} sparks in rabbit ventricular myocytes evoked by action potentials: involvement of clusters of L-type Ca^{2+} channels," *Circulation Research*, vol. 92, no. 5, pp. 532–538, 2003.
- [8] E. Devic, Y. Xiang, D. Gould, and B. Kobilka, " β -Adrenergic receptor subtype-specific signaling in cardiac myocytes from $\beta 1$ and $\beta 2$ adrenoceptor knockout mice," *Molecular Pharmacology*, vol. 60, no. 3, pp. 577–583, 2001.
- [9] T. Shioya, "A simple technique for isolating healthy heart cells from mouse models," *Journal of Physiological Sciences*, vol. 57, no. 6, pp. 327–335, 2007.
- [10] Y. Y. Zhou, S. Q. Wang, W. Z. Zhu et al., "Culture and adenoviral infection of adult mouse cardiac myocytes: methods for cellular genetic physiology," *American Journal of Physiology—Heart and Circulatory Physiology*, vol. 279, no. 1, pp. H429–H436, 2000.
- [11] L. Fliegel, K. Burns, D. H. MacLennan, R. A. F. Reithmeier, and M. Michalak, "Molecular cloning of the high affinity calcium-binding protein (calreticulin) of skeletal muscle sarcoplasmic reticulum," *Journal of Biological Chemistry*, vol. 264, no. 36, pp. 21522–21528, 1989.
- [12] A. D. Zadeh, Y. Cheng, H. Xu et al., "Kif5b is an essential forward trafficking motor for the Kv1.5 cardiac potassium channel," *Journal of Physiology*, vol. 587, no. 19, pp. 4565–4574, 2009.
- [13] S. Wei, A. Guo, B. Chen et al., "T-tubule remodeling during transition from hypertrophy to heart failure," *Circulation Research*, vol. 107, no. 4, pp. 520–531, 2010.
- [14] R. C. Balijepalli, J. D. Foell, D. D. Hall, J. W. Hell, and T. J. Kamp, "Localization of cardiac L-type Ca^{2+} channels to a caveolar macromolecular signaling complex is required for $\beta 2$ -adrenergic regulation," *Proceedings of the National Academy of Sciences of the United States of America*, vol. 103, no. 19, pp. 7500–7505, 2006.
- [15] H. Yi, J. L. M. Leunissen, G. M. Shi, C. A. Gutekunst, and S. M. Hersch, "A novel procedure for pre-embedding double immunogold-silver labeling at the ultrastructural level," *Journal of Histochemistry and Cytochemistry*, vol. 49, no. 3, pp. 279–284, 2001.
- [16] E. M. Merzlyak, J. Goedhart, D. Shcherbo et al., "Bright monomeric red fluorescent protein with an extended fluorescence lifetime," *Nature Methods*, vol. 4, no. 7, pp. 555–557, 2007.
- [17] P. Asghari, M. Schulson, D. R. L. Scriven, G. Martens, and E. D. W. Moore, "Axial tubules of rat ventricular myocytes form multiple junctions with the sarcoplasmic reticulum," *Biophysical Journal*, vol. 96, no. 11, pp. 4651–4660, 2009.
- [18] M. S. Forbes and N. Sperlakis, "The membrane systems and cytoskeletal elements of mammalian myocardial cells," *Cell and Muscle Motility*, vol. 3, pp. 89–155, 1983.
- [19] C. M. Waterman-Storer and E. D. Salmon, "Endoplasmic reticulum membrane tubules are distributed by microtubules in living cells using three distinct mechanisms," *Current Biology*, vol. 8, no. 14, pp. 798–806, 1998.
- [20] C. Lee and L. B. Chen, "Dynamic behavior of endoplasmic reticulum in living cells," *Cell*, vol. 54, no. 1, pp. 37–46, 1988.
- [21] M. Terasaki, L. B. Chen, and K. Fujiwara, "Microtubules and the endoplasmic reticulum are highly interdependent structures," *Journal of Cell Biology*, vol. 103, no. 4, pp. 1557–1568, 1986.
- [22] M. J. Woźniak, B. Bola, K. Brownhill, Y. C. Yang, V. Levakova, and V. J. Allan, "Role of kinesin-1 and cytoplasmic dynein in endoplasmic reticulum movement in VERO cells," *Journal of Cell Science*, vol. 122, no. 12, pp. 1979–1989, 2009.
- [23] P. Bouchard, S. M. Penningroth, A. Cheung, C. Gagnon, and C. W. Bardin, "Erythro-9-[3-(2-hydroxynonyl)]adenine is an inhibitor of sperm motility that blocks dynein ATPase and protein carboxylmethylase activities," *Proceedings of the*

- National Academy of Sciences of the United States of America*, vol. 78, no. 2, pp. 1033–1036, 1981.
- [24] B. E. Flucher and C. Franzini-Armstrong, “Formation of junctions involved in excitation-contraction coupling in skeletal and cardiac muscle,” *Proceedings of the National Academy of Sciences of the United States of America*, vol. 93, no. 15, pp. 8101–8106, 1996.
- [25] D. R. L. Scriven, P. Dan, and E. D. W. Moore, “Distribution of proteins implicated in excitation-contraction coupling in rat ventricular myocytes,” *Biophysical Journal*, vol. 79, no. 5, pp. 2682–2691, 2000.
- [26] I. D. Jayasinghe, M. B. Cannell, and C. Soeller, “Organization of ryanodine receptors, transverse tubules, and sodium-calcium exchanger in rat myocytes,” *Biophysical Journal*, vol. 97, no. 10, pp. 2664–2673, 2009.
- [27] N. Chopra, T. Yang, P. Asghari et al., “Ablation of triadin causes loss of cardiac Ca²⁺ release units, impaired excitation-contraction coupling, and cardiac arrhythmias,” *Proceedings of the National Academy of Sciences of the United States of America*, vol. 106, no. 18, pp. 7636–7641, 2009.
- [28] C. Franzini-Armstrong, F. Protasi, and P. Tijskens, “The assembly of calcium release units in cardiac muscle,” *Annals of the New York Academy of Sciences*, vol. 1047, pp. 76–85, 2005.
- [29] B. Bola and V. Allan, “How and why does the endoplasmic reticulum move?” *Biochemical Society Transactions*, vol. 37, no. 5, pp. 961–965, 2009.
- [30] A. M. Gómez, B. G. Kerfant, and G. Vassort, “Microtubule disruption modulates Ca²⁺ signaling in rat cardiac myocytes,” *Circulation Research*, vol. 86, no. 1, pp. 30–36, 2000.
- [31] G. Iribe, C. W. Ward, P. Camelliti et al., “Axial stretch of rat single ventricular cardiomyocytes causes an acute and transient increase in Ca²⁺ spark rate,” *Circulation Research*, vol. 104, no. 6, pp. 787–795, 2009.
- [32] B. G. Kerfant, G. Vassort, and A. M. Gómez, “Microtubule disruption by colchicine reversibly enhances calcium signaling in intact rat cardiac myocytes,” *Circulation Research*, vol. 88, no. 7, pp. E59–E65, 2001.
- [33] M. E. Loewen, Z. Wang, J. Eldstrom et al., “Shared requirement for dynein function and intact microtubule cytoskeleton for normal surface expression of cardiac potassium channels,” *American Journal of Physiology—Heart and Circulatory Physiology*, vol. 296, no. 1, pp. H71–H83, 2009.
- [34] W. S. Choi, A. Khurana, R. Mathur, V. Viswanathan, D. F. Steele, and D. Fedida, “Kv1.5 surface expression is modulated by retrograde trafficking of newly endocytosed channels by the dynein motor,” *Circulation Research*, vol. 97, no. 4, pp. 363–371, 2005.
- [35] S. U. Dhani, R. Mohammad-Panah, N. Ahmed, C. Ackerley, M. Ramjeesingh, and C. E. Bear, “Evidence for a functional interaction between the ClC-2 chloride channel and the retrograde motor dynein complex,” *Journal of Biological Chemistry*, vol. 278, no. 18, pp. 16262–16270, 2003.
- [36] J. S. Mitcheson, J. C. Hancox, and A. J. Levi, “Cultured adult cardiac myocytes: future applications, culture methods, morphological and electrophysiological properties,” *Cardiovascular Research*, vol. 39, no. 2, pp. 280–300, 1998.
- [37] R. N. Leach, J. C. Desai, and C. H. Orchard, “Effect of cytoskeleton disruptors on L-type Ca channel distribution in rat ventricular myocytes,” *Cell Calcium*, vol. 38, no. 5, pp. 515–526, 2005.
- [38] S. M. Penningroth, “Erythro-9-[3-(2-hydroxynonyl)]adenine and Vanadate as probes for microtubule-based cytoskeletal mechanochemistry,” *Methods in Enzymology*, vol. 134, pp. 477–487, 1986.
- [39] P. F. Mery, C. Pavoine, F. Pecker, and R. Fischmeister, “Erythro-9-(2-hydroxy-3-nonyl)adenine inhibits cyclic GMP-stimulated phosphodiesterase in isolated cardiac myocytes,” *Molecular Pharmacology*, vol. 48, no. 1, pp. 121–130, 1995.

Review Article

Planar Cell Polarity Signaling Pathway in Congenital Heart Diseases

Gang Wu,^{1,2} Jiao Ge,¹ Xupei Huang,² Yimin Hua,¹ and Dezhi Mu^{1,3}

¹Department of Pediatrics, West China Second University Hospital, Sichuan University, Chengdu, Sichuan 610041, China

²Department of Biomedical Science, College of Medicine, Florida Atlantic University, Boca Raton, FL 33431, USA

³Department of Neurology, Newborn Brain Research Institute, University of California, San Francisco, CA 94143, USA

Correspondence should be addressed to Yimin Hua, kk.hhua99@gmail.com and Dezhi Mu, dezhi.mu@ucsf.edu

Received 21 July 2011; Accepted 31 August 2011

Academic Editor: J.-P. Jin

Copyright © 2011 Gang Wu et al. This is an open access article distributed under the Creative Commons Attribution License, which permits unrestricted use, distribution, and reproduction in any medium, provided the original work is properly cited.

Congenital heart disease (CHD) is a common cardiac disorder in humans. Despite many advances in the understanding of CHD and the identification of many associated genes, the fundamental etiology for the majority of cases remains unclear. The planar cell polarity (PCP) signaling pathway, responsible for tissue polarity in *Drosophila* and gastrulation movements and cardiogenesis in vertebrates, has been shown to play multiple roles during cardiac differentiation and development. The disrupted function of PCP signaling is connected to some CHDs. Here, we summarize our current understanding of how PCP factors affect the pathogenesis of CHD.

1. Introduction

Congenital heart disease (CHD), the most common disorder of congenital disease in humans, occurs in approximately 1% of live births [1, 2]. Among many types of CHDs, septation and alignment defects make up the largest group of CHDs, including ventricular and atrial septal defects, tetralogy of Fallot, and double-outlet right ventricle defects [3]. In particular, congenital defects that involve the outflow tract are especially prevalent, including defects of the transposition of the great arteries (TGA), double outlet right ventricle (DORV), and persistent truncus arteriosus (PTA), where a single outflow tract vessel is observed in place of the normal aorta and pulmonary artery [4].

The prognosis, morbidity, and mortality are dependent on the type, size, location, number of defects, and the associated anomalies [5]. CHD represents the cause of one-tenth of all infant deaths worldwide and is the leading noninfectious cause of death in the first year of life [6]. Of great concern to pediatricians and cardiac surgeons are outflow tract defects, because babies that suffer from these problems typically require urgent and complex surgeries shortly after birth.

In recent years, a correlation has been made between dysregulation of the planar cell polarity signaling pathway and CHD.

2. Cardiac Development

2.1. Early Heart Development. In vertebrates, the heart is the first organ to form and has a vital role in the distribution of nutrients and oxygen in the embryo [7]. Formation of the vertebrate heart can be subdivided into distinct but partially overlapping phases, such as specification of cardiac progenitors and the formation of the linear heart tube by cell migration and morphogenetic movements, followed by cardiac looping, chamber formation, septation, and maturation [8].

Myocardial cells are derived from the mesoderm, which emerge from the primitive streak during gastrulation. Later, these cells migrate from the streak in an anterior-lateral direction to positions under the headfolds forming two groups of cells on either side of the midline [9]. The cells then extend across the midline to develop a crescent-shaped epithelium called the cardiac crescent, which fuses at the midline to form the early heart tube [7] called the primary heart field or the first heart field (FHF). These cells will form the left ventricle.

During the formation of a mature heart, the linear heart tube subsequently expands. This is achieved by two mechanisms: cell proliferation and recruitment of additional cells. The latter cells originate in the second heart field (SHF) a cardiac precursor cell population distinct from the first heart

field [10]. SHF will mainly develop into the outflow tract (OFT) and the right ventricle, but also into both atria [11]. Also, as demonstrated in the chicken system, cells of the SHF populate the right ventricle [12]. Frog hearts contain a single ventricle; therefore, cells of the SHF exclusively end up in the OFT [13].

2.2. Outflow Tract Formation. OFT formation involves interactions between diverse cell types in the region of the pharyngeal splanchnic mesenchyme and in SHF that gives rise to the myocardium of the OFT and its endothelial lining [14, 15]. Cardiac neural crest (CNC) cell-derived mesenchyme also plays an important role [16]. These cells form the greater part of the outflow tract cushions, and if they are removed physically or genetically, then outflow tract septation fails [17, 18].

OFT is normally divided by the fusion of a series of ridges or cushions within itself. There are two mechanisms. In the early stages, the dominant mechanism is myocardialization [19]. First during myocardialization, the cells within the thin layer of OFT myocardium fail to adhere to one another tightly. Then, the cells stop behaving like an epithelium and, instead, show protrusive activity and move into the adjacent outflow tract cushions. Thus, the cushions become directly populated by cardiomyocytes [20]. It is thought that myocardialization shares characteristics with the convergent and extension (CE) process, at least with respect to the polarized migration of cells [20]. Direct invasion, the second mechanism, may be complemented by the recruitment of cushion mesenchymal cells into the muscle lineage [21].

3. The Planar Cell Polarity Signaling Pathway

Signaling by ligands of the Wnt family, which controls cell proliferation and patterning, is important for a variety of crucial cell changes and morphogenetic events in development. Two branches of the Wnt pathway exist: a β -catenin-dependent canonical pathway and β -catenin-independent noncanonical pathways [22, 23]. Noncanonical Wnt signaling has been shown to be inhibitory for canonical Wnt signaling through multiple mechanisms [24]. In zebrafish, Wnt genes that activate the noncanonical Wnt pathway are pipetail/Wnt5 [25] and silberblick/Wnt11 [26].

Noncanonical Wnt pathways, also called the planar cell polarity (PCP) signaling pathway, work on planar cell polarity in *Drosophila* and gastrulation movements and cardiogenesis in vertebrates [27–29].

PCP signaling involves a multiprotein complex that associates at the cell membrane. This complex involves the core proteins Frizzled (Fz), Dishevelled (Dvl), Prickle (Pk), Vangl/Strabismus (Vangl), Celsr/Flamingo (Celsr), and Diego (Dgo). In addition, Scribble (Scrib) [30, 31] and Ptk7 [32] are also regarded as the PCP proteins. Formation of the multiprotein complex is thought to modulate the pathway, rather than the components being members of a linear pathway. Vangl/Pk are thought to antagonize Fz/Dvl signaling [20]. PCP pathways are important in polarized cell migration and organ morphogenesis through activation of cytoskeletal pathways, such as those involving the small GTPases RhoA

and cdc42, Rho kinase (ROCK), protein kinase C (PKC), and Jun N-terminal kinase (JNK) [4, 22].

Molecules involved in the PCP pathway commonly fall into 1 of these 3 categories: (1) the “upstream” factors in charge of the coordination of the planar polarity across the whole tissue (i.e., some atypical cadherins like Dachous and Fat [33]); (2) the so-called “core polarity genes” that provide intrinsic polarization cues within single cells through their uneven subcellular localization; and (3) the tissue-specific factors needed for the emergence of the polarized structures characteristic of each cell type [34, 35].

4. Planar Cell Polarity Signaling Pathway in CHD

Normal cardiac development is dependent on PCP signaling [3, 20, 36, 37], which contributes to correct cardiac specification in the mesodermal germ layer [8]. If the correct expression of proteins in PCP signaling is disrupted, then defects may be seen in the heart.

4.1. Vang-Like 2. Vertebrates have two Vang-like (Vangl) genes, Vangl1 and Vangl2, which are homologs of the *Drosophila* gene *Van Gogh/Strabismus (Vang/Stbm)*. Vang mutations disrupt the organization of various epithelial structures, causing characteristic swirled patterns of hairs on wing cells and disorientation of eye ommatidia [38]. Vangl1 and Vangl2 proteins share ~70% sequence similarity, which underlies their conserved functions: Vangl1 and Vangl2 proteins bind to three mammalian Dvl proteins, and Lp mutations engineered in Vangl1 or Vangl2 abrogate interaction with Dvl [39]. The *Vangl2* gene encodes a membrane protein comprising four transmembrane domains and a large intracellular domain with a PDZ-domain-binding motif at its carboxy terminus [40]. Mutations in *Vangl2* can cause neural tube defects and cardiac abnormalities [41]. Loop-tail (Lp), a naturally occurring mouse mutant, develops severe cardiovascular defects in association with abnormal midline development [40, 42], and is often used when studying of Vangl2.

4.2. Outflow Tract. Vangl2 plays an important role in the development of the outflow tract for the following reasons: Vangl2 is strongly expressed in the outflow tract myocardium, including the cells that migrate into the outflow tract cushions [36]. Conspicuous abnormalities are found in the outflow tract of Lp mutants [3], and similarities exist between myocardialization of the OFT and the CE movement during gastrulation, in which Vangl2 is generally thought to be correlated [20].

Complex cardiovascular defects can be found in Lp homozygotes, including double-outlet right ventricle defects, with obligatory peri-membrane ventricular septal defects, and double-sided aortic arch defects, with associated abnormalities in the aortic arch arteries [3]. During the myocardialization of the Lp mice, both the extension of polarized membrane protrusions and the reorganization of the actin cytoskeleton are inhibited in myocardial cells at the muscle-cushion tissue, strongly suggesting that this is a defect in

cell polarity and/or cell movement, rather than some other aspect of cell behavior [20]. RhoA and ROCK1 [43], the downstream mediators of the PCP signaling pathway, are required as well for Vangl2 function [36]. However, the Tetralogy of Fallot (ToF) abnormality, resulting from disturbances of morphogenetic processes in OFT development [44], does not show any specific mutations in Vangl2 gene that are responsible for the ToF phenotype [45]. Further research could include the possible role of other PCP components expressed in the development of the outflow tract [45]. Furthermore, a typical PCP phenotype in a mouse mutant for the Sec24b gene has been reported, including abnormally small ventricles and abnormally arranged OFT vessels [46]. Sec24b is a component of the coat protein complex II (COPII) that is essential for intracellular endoplasmic-reticulum- (ER-) to-Golgi protein transport [47]. In Sec24b mutation mice, both abnormal Vangl2 expression or localization were detected; however, this abnormal expression or localization of Vangl2 may only be partially responsible for the Sec24b mutation caused cardiac defects [46].

As for Vangl1, its role in OFT is much smaller than Vangl2. No cardiac outflow abnormalities were detected in *Vangl1^{gt/+}*, *Vangl2^{l⁺/+}* double heterozygotes, or in *Vangl1^{gt/gt}* homozygotes, only an aberrant right subclavian artery was found in the former, suggesting that the two genes genetically interact to regulate the proper development of the extra-cardiac structures [41].

4.3. Coronary Circulation. The coronary arteries that channel oxygen rich blood throughout the ventricular myocardium are formed from cells that originally derive from a region of the splanchnic mesoderm known as the proepicardium [48, 49]. Vangl2-PCP signaling can play a noncell autonomous role in coronary artery formation [50]. For example, in the animals with Lp/Lp hearts, the coronary vessels fail to develop a normal smooth muscle cell layer and instead develop enlarged ectopic vessels in the subepicardium. Reduced fibronectin deposition, because of loss of functional vangl2 in the subepicardial space, is associated with limited migration of epicardially derived cells (EPDCs) into the ventricular myocardium and likely contributes to those defects [50]. Fibronectin deposition has also been shown to be deficient at tissue boundaries in *Xenopus* embryos in which Vangl2 is disrupted and PCP signaling is abnormal [51, 52]. These defects were associated with defects in the polarized cell movements during the process of CE, which resembles the Lp/Lp heart, where fibronectin deposition is reduced at the epicardial-myocardial boundary and cell migration is impaired [50].

Similarly, mice deficient in connexin 43 also have defects in epicardial cell polarization, migration, and early remodeling of the coronary vascular plexus [53, 54]. However, aberrant expression of planar cell polarity pathway components was not detected in the connexin 43 knockout hearts, so it is currently unclear whether and how connexin 43 interacts with the planar cell polarity pathway [55].

4.4. Diversin/Inversin. The vertebrate ankyrin repeat protein, Diversin, is related to the *Drosophila* protein Diego, which

controls PCP during fly development [56]. Diversin also acts in the canonical Wnt signaling pathway, where its centrosomal localization is crucial for its function in Wnt signaling [57]. Diversin is a modular protein containing N-terminal ankyrin repeats, a central casein kinase-binding domain, and a C-terminal domain that binds axin/conductin [58].

Early zebrafish embryos injected with Diversin mRNA that encodes a protein lacking the ankyrin repeat domain, Div- Δ ANK, were found to develop cardiac bifida [59]; however, those cardiac bifida can be rescued by coinjection of an activated form of RhoA (RhoA-V14), suggesting that Diversin controls heart formation through RhoA [59]. Cardiac bifida in fish is generated when the bilateral heart anlagen fail to fuse because of defective migration of myocardial precursors to the dorsal midline [60, 61], which is regulated by PCP signaling [28]. These results suggest that Diversin can play a role in heart through PCP in the downstream of RhoA.

Meanwhile, Diversin and Dishevelled are accepted as mutually dependent players within the PCP signaling pathway. The Diversin orthologue of *Drosophila*, Diego, genetically interacts with and physically binds to Dishevelled [62]. However, during cardiogenesis, coinjection of both dominant-negative molecules, Div- Δ ANK and Dvl- Δ DEP, did not synergize, suggesting that both Diversin and Dishevelled control heart formation and PCP signaling in zebrafish embryogenesis by similar mechanisms [59].

In the *inv/inv* mouse, carrying an insertional mutation in the *inversin* gene, some cardiopulmonary malformations were found, which are not rare in the mutant mice. The *inv/inv* mice have a propensity for defects in the development of the right ventricular OFT and the interventricular septum.

4.5. Dishevelled. Dishevelled (*dsh* in *Drosophila* or *Dvl* in mice) proteins, of which three have been identified in humans and mice, are highly conserved components of both the canonical Wnt pathway [63], and the PCP pathway [64]. They function as essential scaffolding proteins that interact with diverse proteins, including kinases, phosphatases, and adaptor proteins [65, 66].

In zebrafish, it is reported that injection of the dominant-negative Dishevelled lacking the DEP domain (Dvl- Δ DEP) into zebrafish embryos induced cardiac bifida phenotypes and CE defects. Dishevelled regulates heart formation via the activation of RhoA. Meanwhile, during cardiogenesis, Div- Δ ANK and Dvl- Δ DEP, the frequency of cardiac bifida was not increased [28].

In mice, mutations in the *Dvl2* gene, one of three vertebrate homologues of *Drosophila* Dishevelled, developed OFT defects similar to those seen in Lp mice, including double-outlet right ventricle and ventricular septal defects [37]. *Dvl1/Dvl2* double mutants develop the neural tube defect craniorachischisis [37], which is associated with disruption of PCP signaling in mice [40]. Since both Vangl2 and *Dvl2* are expressed in the OFT myocardium [36], *Dvl2* is suggested to act in PCP pathway in OFT. The PCP signaling pathway can regulate cell migration processes during gastrulation and neural crest cell migration in vertebrates [22, 67]. *Dvl2* is a core PCP member in canonical Wnt signaling. But *Dvl2* is

also suggested to influence OFT formation through neural crest cell migration in PCP signaling since a defect is found in cardiac neural crest development during OFT formation in *Dvl2* null mutants [37].

Dvl3^{-/-} mice died perinatally with cardiac OFT abnormalities, and the mutants displayed a misorientated stereocilia in the organ of Corti, suggesting that *Dvl3* is required for cardiac OFT development in the PCP pathway [64]. However, OFT in *Dvl3*^{-/-} mice were not due to an absence of CNC or SHF Cells. Moreover, *Dvl2*^{+/-}; *Dvl3*^{+/-} mice can survive to adulthood and are fertile. In an inbred background, conotruncal abnormalities were seen, while *Dvl2*^{+/-}; *Dvl3*^{-/-} hearts had similar morphologies to *Dvl3*^{-/-} hearts, suggesting *Dvls* are functionally redundant [64].

4.6. *Wnt5a* and *Wnt11*. In vertebrates, *Wnt5a* and *Wnt11* can activate the Wnt/JNK pathway, which resembles the PCP pathway in *Drosophila* [68]. *Wnt5a* [69, 70] and *Wnt11* [4, 29, 69–72] represent the PCP pathway that have been implicated in cardiogenesis.

4.6.1. *Wnt5a*. *Wnt5a* primarily signals through the PCP signaling pathway, although it also has the potential to activate the canonical Wnt signaling pathway [73], by functioning as an antagonist of the canonical Wnts [74]. A mutation in *Wnt5a* in mice can lead to PTA. In the model, *Wnt5a* produced in the OFT, by cells originating from the pharyngeal mesoderm, signals adjacent CNC cells during the formation of the aortopulmonary septum through a PCP pathway via localized intracellular increases in Ca²⁺ [16].

Wnt5a is thought to be supportive but not required for cardiogenesis [8] because in discussing Notch signaling in cardiac progenitors, *Wnt5a* synergizes with BMP6 and *Sfrp1* to promote formation of troponin-positive cells, likely through noncanonical Wnt signaling activities. However, adding individually *sFRP1*, *Wnt5a*, and BMP6 does not significantly increase cardiac development [75].

4.6.2. *Wnt11*. *Wnt11* is a secreted protein that signals through the PCP pathway and is a potent modulator of cell behavior and movement. In human, mouse, and chicken, there is a single *Wnt11* gene, and in *Xenopus* and zebrafish, there are two, *Wnt-11* and *Wnt-11R* [71]. *Wnt11* can activate PCP signaling and at the same time inhibit Wnt signaling [24]. *Wnt-11* shows a spatiotemporal pattern of expression that correlates with cardiac specification [76, 77] and loss-of-function experiments also demonstrated that *Wnt11* is required for normal heart development and cardiac marker gene expression [29, 78]. *Wnt11* leads to cardiac specification in the PCP pathway [68] and is conserved [29].

The mouse *Wnt11* gene is expressed within or in close proximity to the precardiac mesoderm, and later in the myocardium of the primitive heart tube [79]. Thus, the *Wnt-11* expression domain overlaps with the first and secondary heart fields that contribute to the majority of the tissues establishing the heart [69–71, 79]. At later stages, *Wnt11* is expressed in OFT, where both *Wnt5a* and *Wnt11* signaling have morphogenetic roles [4, 16]. Interestingly, human

Wnt11 has been reported to be expressed in the adult heart [80].

In cell culture models, *Wnt11* signaling determines the fate of the cardiomyocytes and promotes differentiation of the already committed cardiomyocytes, a conclusion based in part on its capacity to induce the expression of certain cardiac transcription factor genes [29, 81–85], suggesting that *Wnt11* signaling may have a broader role in the control of mammalian heart development [86].

5. Heart Morphogenesis

In *Xenopus*, *Wnt11-R* is expressed in neural tissue, dorsal mesenchyme derived from the dermatome region of the somites, the brachial arches, and the muscle layer of the heart, similar to the expression patterns reported for mouse and chicken *Wnt11* [72]. Inhibition of *Wnt11-R* function using morpholino oligomers causes defects in heart morphogenesis, in fact, 10% of the hearts exhibit a pronounced cardiac bifida phenotype, suggesting *Wnt11-R* functions in regulation of cardiac morphogenesis [72].

In cardiocytes of *Xenopus*, *Wnt11* is required for heart formation and is sufficient to induce a contractile tissue in embryonic explants by PCP signaling which involves protein kinase C and Jun amino-terminal kinase [29].

When embryos injected with *Wnt11-R* MO on one side only were examined in section, it was clear that the myocardial layer on the injected side was thicker than on the control side. This is also visible in double-sided MO1-injected embryos. Quantitation of differentiated myocardium showed that the area of the *Wnt11-R*-depleted side was 26% larger than the control side [72].

However, in a mouse model in which *Wnt-11* function has been inactivated, *Wnt-11* signaling serves as a critical cell adhesion cue for the organization of the cardiomyocytes in the developing ventricular wall. In the absence of *Wnt-11*, the coordinated organization, intercellular contacts, colocalized expression of the cell adhesion components N-cadherin and b-catenin, and the cytoskeleton of the differentiating ventricular cardiomyocytes are all disturbed. Moreover, the ventricular wall lacking *Wnt-11* signaling is thinner [86].

5.1. Outflow Tract. *Wnt11* signaling can affect extracellular matrix composition, cytoskeletal rearrangements and polarized cell movement required for morphogenesis of the cardiac OFT [4]. In fact, *Wnt11* plays this role in the integration and crosstalk between three major signaling pathways: Wnt pathway, PCP pathway, and TGF β signaling. In *Wnt11* mutants, penetrance of the outflow tract phenotype was 100% accompanied by ventricular septal defects (VSD) [4].

5.2. *Ptk7*. Protein tyrosine kinase 7 (*Ptk7*) is a transmembrane protein containing seven extracellular immunoglobulin domains and a kinase homology domain [87]. *Ptk7* is regarded as a regulator of PCP signaling that could modulate the *dsh* localization as well as the interaction with pathway-specific effector proteins [87], while someone regarded it as an essential component of PCP pathway [32]. In *Xenopus*, *Ptk7* is required for neural convergent extension [88] and

can regulate neural crest migration by recruiting dishevelled (dsh) to the plasma membrane [89].

In chick, disruption of off-track (the chick Ptk7 homologue) causes abnormal heart development [90]. In mouse, *chuzhoi* (*chz*) mutants, carrying a splice site mutation in *Ptk7*, exhibit several defects in cardiovascular development, including OFT defects with VSD, while they exhibit minor defects in neural crest cell distribution [89]. A genetic interaction between *chuzhoi* mutants and both *Vangl2^{L-P}* and *Celsr1^{Crsh}* mutants was demonstrated, strengthening the hypothesis that *chuzhoi* is involved in regulating the PCP pathway [89].

5.3. Scribble. Scrib (also known as Scrb1) is orthologous to the *Drosophila scribble* gene, which regulates apical-basal polarity and functions as a tumor suppressor, regulating cell growth; *scribble* mutants exhibit disrupted cellular architecture [91–93]. Scrib is a putative cytoplasmic protein and is a member of the LAP protein family that is characterized by the presence of four PDZ domains. Scrib plays essential roles in cell-cell adhesion [94]. In human, hScrib protein displays highly polarized localization in mammalian epithelial cells and could play an important role in the suppression of human tumors [93]. Scrib has not been implicated in planar cell polarity [95], although some scholars identify it as PCP protein [30, 31].

In mutations in mouse Scrib (circle tail mutant, *Crc*), cardiac looping and chamber expansion are disrupted and abnormal development of the arterial wall and early abnormalities in myocardial organization are found. Finally, spectrum of congenital heart defects are developed, such as smaller and abnormally shaped ventricular chambers, cardiovascular defects, and atrioventricular septal defects [96], suggesting that *Crc* can develop heart malformations and cardiomyopathy attributable to abnormalities in cardiomyocyte organization within the early heart tube [96].

The mechanism of Scrib involved in heart development may refer to N-cadherin. The integrity of the heart tube is dependent on N-cadherin, which is tightly localized to the lateral membranes of cardiomyocytes from the earliest time of heart tube formation [97]. The N-cadherin zebrafish mutant can develop a disorganized myocardium with abnormally shaped and loosely-aggregated cardiomyocytes [98], which is very similar to *Crc*. Scrib is required for the correct localization of N-cadherin and β -catenin at the lateral cell membrane in the primitive myocardium [96].

Moreover, Scrib and *Vangl2* can interact in heart development. Scrib is required for the correct localization of *Vangl2* within the membrane compartments of cardiomyocytes and that Scrib is acting to direct the PCP pathway in the developing myocardium. Double heterozygosity for mutations in both Scrib and *Vangl2* can cause cardiac defects similar to those found in homozygous mutants for each gene but without other major defects. Those are in accord with the fact [31] that proteins interact physically through discrete PDZ-binding domains, observed in yeast 2 hybrid and coimmunoprecipitation studies [99], in addition, heterozygotes (*Lp⁺,Crc⁺*) also exhibit craniorachischisis, which is equal in

severity to either *Crc/Crc* or *Lp/Lp* mice [100], suggesting the overlapping expression of *Scrb1* with *Vangl2*.

6. Conclusions

The planar cell polarity (PCP) pathway is a highly conserved signaling pathway that mediates changes in cell polarity and cell motility during cardiogenesis, through activation of cytoskeletal pathways, such as RhoA and Rho kinase (ROCK). Several components of the pathway are expressed within the developing heart, and the disrupted function of pathway members in chick, *Xenopus*, zebrafish, and mouse are associated with some heart defect, which leads to congenital heart disease (CHD). The interaction of proteins within the PCP pathway and the intercross of the PCP pathway with the other pathways such as the Wnt signaling pathway are also demonstrated. No genes within the PCP pathway that cause cardiovascular defects in humans have been described thus far.

Abbreviations

PCP:	Planar cell polarity
CHD:	Congenital heart disease
FHF:	First heart field
SHF:	Second heart field
CNC:	Cardiac neural crest
OFT:	Outflow tract
CE:	Convergent and extension
EPDCs:	Epicardially derived cells.

Acknowledgments

This work was supported by National Science Foundation of China (no. 30825039, no. 31171020, and no. 30973236 to Dezhi Mu; no. 30872545 and no. 81070136 to Yimin Hua), and Program of Changjiang Scholars and Innovative Research Team in University (IRT0935). Gang Wu and Jiao Ge contributed equally to the study.

References

- [1] S. M. Reamon-Buettner, K. Spanel-Borowski, and J. Borlak, "Bridging the gap between anatomy and molecular genetics for an improved understanding of congenital heart disease," *Annals of Anatomy*, vol. 188, no. 3, pp. 213–220, 2006.
- [2] M. D. Reller, M. J. Strickland, T. Riehle-Colarusso, W. T. Mahle, and A. Correa, "Prevalence of congenital heart defects in metropolitan atlanta, 1998–2005," *Journal of Pediatrics*, vol. 153, no. 6, pp. 807–813, 2008.
- [3] D. J. Henderson, S. J. Conway, N. D. E. Greene et al., "Cardiovascular defects associated with abnormalities in midline development in the Loop-tail mouse mutant," *Circulation Research*, vol. 89, no. 1, pp. 6–12, 2001.
- [4] W. Zhou, L. Lin, A. Majumdar et al., "Modulation of morphogenesis by noncanonical Wnt signaling requires ATF/CREB family-mediated transcriptional activation of TGF β 2," *Nature Genetics*, vol. 39, no. 10, pp. 1225–1234, 2007.
- [5] H. S. Khalil, A. M. Saleh, and S. N. Subhani, "Maternal obesity and neonatal congenital cardiovascular defects," *International Journal of Gynecology and Obstetrics*, vol. 102, no. 3, pp. 232–236, 2008.

- [6] J.-B. Huang, Y.-L. Liu, and X.-D. Lv, "Pathogenic mechanisms of congenital heart disease," *Fetal and Pediatric Pathology*, vol. 29, no. 5, pp. 359–372, 2010.
- [7] M. Buckingham, S. Meilhac, and S. Zaffran, "Building the mammalian heart from two sources of myocardial cells," *Nature Reviews Genetics*, vol. 6, no. 11, pp. 826–837, 2005.
- [8] S. Gessert and M. Kühl, "The multiple phases and faces of Wnt signaling during cardiac differentiation and development," *Circulation Research*, vol. 107, no. 2, pp. 186–199, 2010.
- [9] P. P. L. Tam, M. Parameswaran, S. J. Kinder, and R. P. Weinberger, "The allocation of epiblast cells to the embryonic heart and other mesodermal lineages: the role of ingression and tissue movement during gastrulation," *Development*, vol. 124, no. 9, pp. 1631–1642, 1997.
- [10] A. F. M. Moorman, V. M. Christoffels, R. H. Anderson, and M. J. B. van den Hoff, "The heart-forming fields: one or multiple?" *Philosophical Transactions of the Royal Society B*, vol. 362, no. 1484, pp. 1257–1265, 2007.
- [11] C. L. Cai, X. Liang, Y. Shi et al., "Isl1 identifies a cardiac progenitor population that proliferates prior to differentiation and contributes a majority of cells to the heart," *Developmental Cell*, vol. 5, no. 6, pp. 877–889, 2003.
- [12] M. S. Rana, N. C. A. Horsten, S. Tesink-Taekema, W. H. Lamers, A. F. M. Moorman, and M. J. B. van den Hoff, "Trabeculated right ventricular free wall in the chicken heart forms by ventricularization of the myocardium initially forming the outflow tract," *Circulation Research*, vol. 100, no. 7, pp. 1000–1007, 2007.
- [13] S. Gessert and M. Kühl, "Comparative gene expression analysis and fate mapping studies suggest an early segregation of cardiogenic lineages in *Xenopus laevis*," *Developmental Biology*, vol. 334, no. 2, pp. 395–408, 2009.
- [14] D. Srivastava and E. N. Olson, "A genetic blueprint for cardiac development," *Nature*, vol. 407, no. 6801, pp. 221–226, 2000.
- [15] K. R. Chien, "Myocyte survival pathways and cardiomyopathy: implications for trastuzumab cardiotoxicity," *Seminars in Oncology*, vol. 27, no. 6, pp. 9–14, 2000.
- [16] J. R. Schleiffarth, A. D. Person, B. J. Martinsen et al., "Wnt5a is required for cardiac outflow tract septation in mice," *Pediatric Research*, vol. 61, no. 4, pp. 386–391, 2007.
- [17] M. L. Kirby, T. F. Gale, and D. E. Stewart, "Neural crest cells contribute to normal aorticopulmonary septation," *Science*, vol. 220, no. 4601, pp. 1059–1061, 1983.
- [18] V. Kaartinen, M. Dudas, A. Nagy, S. Sridurongrit, M. M. Lu, and J. A. Epstein, "Cardiac outflow tract defects in mice lacking ALK2 in neural crest cells," *Development*, vol. 131, no. 14, pp. 3481–3490, 2004.
- [19] B. P. T. Kruithof, M. J. B. van den Hoff, A. Wessels, and A. F. M. Moorman, "Cardiac muscle cell formation after development of the linear heart tube," *Developmental Dynamics*, vol. 227, no. 1, pp. 1–13, 2003.
- [20] D. J. Henderson, H. M. Phillips, and B. Chaudhry, "Vang-like 2 and noncanonical Wnt signaling in outflow tract development," *Trends in Cardiovascular Medicine*, vol. 16, no. 2, pp. 38–45, 2006.
- [21] B. P. T. Kruithof, M. J. B. van den Hoff, S. Tesink-Taekema, and A. F. M. Moorman, "Recruitment of intra- and extracardiac cells into the myocardial lineage during mouse development," *Anatomical Record, Part A*, vol. 271, no. 2, pp. 303–314, 2003.
- [22] M. T. Veeman, J. D. Axelrod, and R. T. Moon, "A second canon: functions and mechanisms of β -catenin-independent Wnt signaling," *Developmental Cell*, vol. 5, no. 3, pp. 367–377, 2003.
- [23] C. Y. Logan and R. Nusse, "The Wnt signaling pathway in development and disease," *Annual Review of Cell and Developmental Biology*, vol. 20, pp. 781–810, 2004.
- [24] P. Maye, J. Zheng, L. Li, and D. Wu, "Multiple mechanisms for Wnt11-mediated repression of the canonical Wnt signaling pathway," *Journal of Biological Chemistry*, vol. 279, no. 23, pp. 24659–24665, 2004.
- [25] B. Kilian, H. Mansukoski, F. C. Barbosa, F. Ulrich, M. Tada, and C. P. Heisenberg, "The role of Ppt/Wnt5 in regulating cell shape and movement during zebrafish gastrulation," *Mechanisms of Development*, vol. 120, no. 4, pp. 467–476, 2003.
- [26] C.-P. Heisenberg, M. Tada, G. J. Rauch et al., "Silberblick/Wnt11 mediates convergent extension movements during zebrafish gastrulation," *Nature*, vol. 405, no. 6782, pp. 76–81, 2000.
- [27] T. J. Klein and M. Mlodzik, "Planar cell polarization: an emerging model points in the right direction," *Annual Review of Cell and Developmental Biology*, vol. 21, pp. 155–176, 2005.
- [28] T. Matsui, A. Raya, Y. Kawakami et al., "Noncanonical Wnt signaling regulates midline convergence of organ primordia during zebrafish development," *Genes and Development*, vol. 19, no. 1, pp. 164–175, 2005.
- [29] P. Pandur, M. Läsche, L. M. Eisenberg, and M. Kühl, "Wnt-11 activation of a non-canonical Wnt signalling pathway is required for cardiogenesis," *Nature*, vol. 418, no. 6898, pp. 636–641, 2002.
- [30] M. Montcouquiol, R. A. Rachel, P. J. Lanford, N. G. Copeland, N. A. Jenkins, and M. W. Kelley, "Identification of Vangl2 and Scrb1 as planar polarity genes in mammals," *Nature*, vol. 423, no. 6936, pp. 173–177, 2003.
- [31] E. E. Davis and N. Katsanis, "Cell polarization defects in early heart development," *Circulation Research*, vol. 101, no. 2, pp. 122–124, 2007.
- [32] V. S. Golubkov, A. V. Chekanov, P. Cieplak et al., "The Wnt/planar cell polarity protein-tyrosine kinase-7 (PTK7) is a highly efficient proteolytic target of membrane type-1 matrix metalloproteinase: implications in cancer and embryogenesis," *Journal of Biological Chemistry*, vol. 285, no. 46, pp. 35740–35749, 2010.
- [33] M. Simons and M. Mlodzik, "Planar cell polarity signaling: from fly development to human disease," *Annual Review of Genetics*, vol. 42, pp. 517–540, 2008.
- [34] J. M. Pérez-Pomares, "Myocardial-coronary interactions: against the canon," *Circulation Research*, vol. 102, no. 5, pp. 513–515, 2008.
- [35] H. Strutt and D. Strutt, "Long-range coordination of planar polarity in *Drosophila*," *BioEssays*, vol. 27, no. 12, pp. 1218–1227, 2005.
- [36] H. M. Phillips, J. N. Murdoch, B. Chaudhry, A. J. Copp, and D. J. Henderson, "Vangl2 acts via RhoA signaling to regulate polarized cell movements during development of the proximal outflow tract," *Circulation Research*, vol. 96, no. 3, pp. 292–299, 2005.
- [37] N. S. Hamblet, N. Lijam, P. Ruiz-Lozano et al., "Dishevelled 2 is essential for cardiac outflow tract development, somite segmentation and neural tube closure," *Development*, vol. 129, no. 24, pp. 5827–5838, 2002.

- [38] E. Torban, C. Kor, and P. Gros, "Van Gogh-like2 (Strabismus) and its role in planar cell polarity and convergent extension in vertebrates," *Trends in Genetics*, vol. 20, no. 11, pp. 570–577, 2004.
- [39] E. Torban, H. J. Wang, N. Groulx, and P. Gros, "Independent mutations in mouse *Vangl2* that cause neural tube defects in Looptail mice impair interaction with members of the Dishevelled family," *Journal of Biological Chemistry*, vol. 279, no. 50, pp. 52703–52713, 2004.
- [40] Z. Kibar, K. J. Vogan, N. Groulx, M. J. Justice, D. A. Underhill, and P. Gros, "Ltap, a mammalian homolog of *Drosophila Strabismus/Van Gogh*, is altered in the mouse neural tube mutant Loop-tail," *Nature Genetics*, vol. 28, no. 3, pp. 251–255, 2001.
- [41] E. Torban, A. M. Patenaude, S. Leclerc et al., "Genetic interaction between members of the *Vangl* family causes neural tube defects in mice," *Proceedings of the National Academy of Sciences of the United States of America*, vol. 105, no. 9, pp. 3449–3454, 2008.
- [42] Z. Kibar, S. Salem, C. Bosoi et al., "Contribution of *VANGL2* mutations to isolated neural tube defects," *Clinical Genetics*, vol. 80, no. 1, pp. 76–82, 2011.
- [43] J. Shi, L. Zhang, and L. Wei, "Rho-kinase in development and heart failure: insights from genetic models," *Pediatric Cardiology*, vol. 32, no. 3, pp. 297–304, 2011.
- [44] J. P. Starr, "Tetralogy of Fallot: yesterday and today," *World Journal of Surgery*, vol. 34, no. 4, pp. 658–668, 2010.
- [45] E. Erdal, C. Erdal, G. Bulut et al., "Mutation analysis of the *Vangl2* coding region revealed no common cause for tetralogy of fallot," *Journal of International Medical Research*, vol. 35, no. 6, pp. 867–872, 2007.
- [46] C. Wansleben, H. Feitsma, M. Montcouquiol, C. Kroon, E. Cuppen, and F. Meijlink, "Planar cell polarity defects and defective *Vangl2* trafficking in mutants for the COPII gene *Sec24b*," *Development*, vol. 137, no. 7, pp. 1067–1073, 2010.
- [47] K. Sato and A. Nakano, "Mechanisms of COPII vesicle formation and protein sorting," *FEBS Letters*, vol. 581, no. 11, pp. 2076–2082, 2007.
- [48] A. Wessels and J. M. Pérez-Pomares, "The epicardium and epicardially derived cells (EPDCs) as cardiac stem cells," *Anatomical Record, Part A*, vol. 276, no. 1, pp. 43–57, 2004.
- [49] H. E. Olivey, L. A. Compton, and J. V. Barnett, "Coronary vessel development: the epicardium delivers," *Trends in Cardiovascular Medicine*, vol. 14, no. 6, pp. 247–251, 2004.
- [50] H. M. Phillips, V. Hildreth, J. D. Peat et al., "Non-cell-autonomous roles for the planar cell polarity gene *vangl2* in development of the coronary circulation," *Circulation Research*, vol. 102, no. 5, pp. 615–623, 2008.
- [51] T. Goto, L. Davidson, M. Asashima, and R. Keller, "Planar cell polarity genes regulate polarized extracellular matrix deposition during frog gastrulation," *Current Biology*, vol. 15, no. 8, pp. 787–793, 2005.
- [52] J. B. Wallingford, "Vertebrate gastrulation: polarity genes control the matrix," *Current Biology*, vol. 15, no. 11, pp. R414–R416, 2005.
- [53] D. Y. Rhee, X. Q. Zhao, R. J. B. Francis, G. Y. Huang, J. D. Mably, and C. W. Lo, "Connexin 43 regulates epicardial cell polarity and migration in coronary vascular development," *Development*, vol. 136, no. 18, pp. 3185–3193, 2009.
- [54] D. L. Walker, S. J. Vacha, M. L. Kirby, and C. W. Lo, "Connexin43 deficiency causes dysregulation of coronary vasculogenesis," *Developmental Biology*, vol. 284, no. 2, pp. 479–498, 2005.
- [55] H. E. Olivey and E. C. Svensson, "Epicardial-myocardial signaling directing coronary vasculogenesis," *Circulation Research*, vol. 106, no. 5, pp. 818–832, 2010.
- [56] F. Feiguin, M. Hannus, M. Mlodzik, and S. Eaton, "The ankyrin repeat protein *diego* mediates frizzled-dependent planar polarization," *Developmental Cell*, vol. 1, no. 1, pp. 93–101, 2001.
- [57] K. Itoh, A. Jenny, M. Mlodzik, and S. Y. Sokol, "Centrosomal localization of *Diversin* and its relevance to Wnt signaling," *Journal of Cell Science*, vol. 122, no. 20, pp. 3791–3798, 2009.
- [58] T. Schwarz-Romond, C. Asbrand, J. Bakkers et al., "The ankyrin repeat protein *diversin* recruits casein kinase I ϵ to the β -catenin degradation complex and acts in both canonical Wnt and Wnt/JNK signaling," *Genes and Development*, vol. 16, no. 16, pp. 2073–2084, 2002.
- [59] H. Moeller, A. Jenny, H. J. Schaeffer et al., "Diversin regulates heart formation and gastrulation movements in development," *Proceedings of the National Academy of Sciences of the United States of America*, vol. 103, no. 43, pp. 15900–15905, 2006.
- [60] D. Y. R. Stainier, "Zebrafish genetics and vertebrate heart formation," *Nature Reviews Genetics*, vol. 2, no. 1, pp. 39–48, 2001.
- [61] C. Thisse and L. I. Zon, "Organogenesis—heart and blood formation from the zebrafish point of view," *Science*, vol. 295, no. 5554, pp. 457–462, 2002.
- [62] A. Jenny, J. Reynolds-Kenneally, G. Das, M. Burnett, and M. Mlodzik, "Diego and Prickle regulate frizzled planar cell polarity signalling by competing for Dishevelled binding," *Nature Cell Biology*, vol. 7, no. 7, pp. 691–697, 2005.
- [63] C. Gao and Y.-G. Chen, "Dishevelled: the hub of Wnt signaling," *Cellular Signalling*, vol. 22, no. 5, pp. 717–727, 2010.
- [64] S. L. Etheridge, S. Ray, S. Li et al., "Murine dishevelled 3 functions in redundant pathways with dishevelled 1 and 2 in normal cardiac outflow tract, cochlea, and neural tube development," *PLoS Genetics*, vol. 4, no. 11, Article ID e1000259, 2008.
- [65] C. C. Malbon and H.-Y. Wang, "Dishevelled: a mobile scaffold catalyzing development," *Current Topics in Developmental Biology*, vol. 72, pp. 153–166, 2005.
- [66] J. B. Wallingford and R. Habas, "The developmental biology of Dishevelled: an enigmatic protein governing cell fate and cell polarity," *Development*, vol. 132, no. 20, pp. 4421–4436, 2005.
- [67] J. de Calisto, C. Araya, L. Marchant, C. F. Riaz, and R. Mayor, "Essential role of non-canonical Wnt signalling in neural crest migration," *Development*, vol. 132, no. 11, pp. 2587–2597, 2005.
- [68] P. Pandur, D. Maurus, and M. Kühl, "Increasingly complex: new players enter the Wnt signaling network," *BioEssays*, vol. 24, no. 10, pp. 881–884, 2002.
- [69] L. M. Eisenberg and C. A. Eisenberg, "Wnt signal transduction and the formation of the myocardium," *Developmental Biology*, vol. 293, no. 2, pp. 305–315, 2006.
- [70] E. D. Cohen, Y. Tian, and E. E. Morrissy, "Wnt signaling: an essential regulator of cardiovascular differentiation, morphogenesis and progenitor self-renewal," *Development*, vol. 135, no. 5, pp. 789–798, 2008.
- [71] T. Brade, J. Männer, and M. Kühl, "The role of Wnt signalling in cardiac development and tissue remodelling in the mature heart," *Cardiovascular Research*, vol. 72, no. 2, pp. 198–209, 2006.

- [72] R. J. Garriock, S. L. D'Agostino, K. C. Pilcher, and P. A. Krieg, "Wnt11-R, a protein closely related to mammalian Wnt11, is required for heart morphogenesis in *Xenopus*," *Developmental Biology*, vol. 279, no. 1, pp. 179–192, 2005.
- [73] A. J. Mikels and R. Nusse, "Purified Wnt5a protein activates or inhibits beta-catenin-TCF signaling depending on receptor context," *PLoS Biology*, vol. 4, no. 4, article e115, 2006.
- [74] M. A. Torres, J. A. Yang-Snyder, S. M. Purcell, A. A. DeMarais, L. L. McGrew, and R. T. Moon, "Activities of the Wnt-1 class of secreted signaling factors are antagonized by the Wnt-5A class and by a dominant negative cadherin in early *Xenopus* development," *Journal of Cell Biology*, vol. 133, no. 5, pp. 1123–1137, 1996.
- [75] V. C. Chen, R. Stull, D. Joo, X. Cheng, and G. Keller, "Notch signaling respecifies the hemangioblast to a cardiac fate," *Nature Biotechnology*, vol. 26, no. 10, pp. 1169–1178, 2008.
- [76] K. E. Schroeder, M. L. Condic, L. M. Eisenberg, and H. J. Yost, "Spatially regulated translation in embryos: asymmetric expression of maternal Wnt-11 along the dorsal-ventral axis in *Xenopus*," *Developmental Biology*, vol. 214, no. 2, pp. 288–297, 1999.
- [77] M. Ku and D. A. Melton, "Xwnt-11: a maternally expressed *Xenopus* wnt gene," *Development*, vol. 119, no. 4, pp. 1161–1173, 1993.
- [78] B. A. Afouda, J. Martin, F. Liu, A. Ciau-Uitz, R. Patient, and S. Hoppler, "GATA transcription factors integrate Wnt signalling during heart development," *Development*, vol. 135, no. 19, pp. 3185–3190, 2008.
- [79] A. Kispert, S. Vainio, L. Shen, D. H. Rowitch, and A. P. McMahon, "Proteoglycans are required for maintenance of Wnt-11 expression in the ureter tips," *Development*, vol. 122, no. 11, pp. 3627–3637, 1996.
- [80] H. Kirikoshi, H. Sekihara, and M. Katoh, "Molecular cloning and characterization of human WNT11," *International Journal of Molecular Medicine*, vol. 8, no. 6, pp. 651–656, 2001.
- [81] S. Ueno, G. Weidinger, T. Osugi et al., "Biphasic role for Wnt/ β -catenin signaling in cardiac specification in zebrafish and embryonic stem cells," *Proceedings of the National Academy of Sciences of the United States of America*, vol. 104, no. 23, pp. 9685–9690, 2007.
- [82] C. A. Eisenberg and L. M. Eisenberg, "WNT11 promotes cardiac tissue formation of early mesoderm," *Developmental Dynamics*, vol. 216, no. 1, pp. 45–58, 1999.
- [83] M. P. Flaherty, A. Abdel-Latif, Q. Li et al., "Noncanonical Wnt11 signaling is sufficient to induce cardiomyogenic differentiation in unfractionated bone marrow mononuclear cells," *Circulation*, vol. 117, no. 17, pp. 2241–2252, 2008.
- [84] M. Koyanagi, J. Haendeler, C. Badorff et al., "Non-canonical Wnt signaling enhances differentiation of human circulating progenitor cells to cardiomyogenic cells," *Journal of Biological Chemistry*, vol. 280, no. 17, pp. 16838–16842, 2005.
- [85] H. Terami, K. Hidaka, T. Katsumata, A. Iio, and T. Morisaki, "Wnt11 facilitates embryonic stem cell differentiation to Nkx2.5-positive cardiomyocytes," *Biochemical and Biophysical Research Communications*, vol. 325, no. 3, pp. 968–975, 2004.
- [86] I. I. Nagy, A. Railo, R. Rapila et al., "Wnt-11 signalling controls ventricular myocardium development by patterning N-cadherin and β -catenin expression," *Cardiovascular Research*, vol. 85, no. 1, pp. 100–109, 2010.
- [87] I. Shnitsar and A. Borchers, "PTK7 recruits dsh to regulate neural crest migration," *Development*, vol. 135, no. 24, pp. 4015–4024, 2008.
- [88] X. Lu, A. G. M. Borchers, C. Jolicoeur, H. Rayburn, J. C. Baker, and M. Tessier-Lavigne, "PTK7/CCK-4 is a novel regulator of planar cell polarity in vertebrates," *Nature*, vol. 430, no. 6995, pp. 93–98, 2004.
- [89] A. Paudyal, C. Damrau, V. L. Patterson et al., "The novel mouse mutant, *chuzhoi*, has disruption of Ptk7 protein and exhibits defects in neural tube, heart and lung development and abnormal planar cell polarity in the ear," *BMC Developmental Biology*, vol. 10, article 87, 2010.
- [90] T. Toyofuku, H. Zhang, A. Kumanogoh et al., "Dual roles of Sema6D in cardiac morphogenesis through region-specific association of its receptor, Plexin-A1, with off-track and vascular endothelial growth factor receptor type 2," *Genes and Development*, vol. 18, no. 4, pp. 435–447, 2004.
- [91] D. Bilder and N. Perrimon, "Localization of apical epithelial determinants by the basolateral PDZ protein Scribble," *Nature*, vol. 403, no. 6770, pp. 676–680, 2000.
- [92] D. Bilder, M. Li, and N. Perrimon, "Cooperative regulation of cell polarity and growth by *Drosophila* tumor suppressors," *Science*, vol. 289, no. 5476, pp. 113–116, 2000.
- [93] L. E. Dow, A. M. Brumby, R. Muratore et al., "hScrib is a functional homologue of the *Drosophila* tumour suppressor Scribble," *Oncogene*, vol. 22, no. 58, pp. 9225–9230, 2003.
- [94] Y. Qin, C. Capaldo, B. M. Gumbiner, and I. G. Macara, "The mammalian Scribble polarity protein regulates epithelial cell adhesion and migration through E-cadherin," *Journal of Cell Biology*, vol. 171, no. 6, pp. 1061–1071, 2005.
- [95] J. N. Murdoch, D. J. Henderson, K. Doudney et al., "Disruption of scribble (*Scrb1*) causes severe neural tube defects in the circletail mouse," *Human Molecular Genetics*, vol. 12, no. 2, pp. 87–98, 2003.
- [96] H. M. Phillips, H. J. Rhee, J. N. Murdoch et al., "Disruption of planar cell polarity signaling results in congenital heart defects and cardiomyopathy attributable to early cardiomyocyte disorganization," *Circulation Research*, vol. 101, no. 2, pp. 137–145, 2007.
- [97] L.-L. Ong, N. Kim, T. Mima, L. Cohen-Gould, and T. Mikawa, "Trabecular myocytes of the embryonic heart require N-cadherin for migratory unit identity," *Developmental Biology*, vol. 193, no. 1, pp. 1–9, 1998.
- [98] B. Bagatto, J. Francl, B. Liu, and Q. Liu, "Cadherin2 (N-cadherin) plays an essential role in zebrafish cardiovascular development," *BMC Developmental Biology*, vol. 6, article 23, 2006.
- [99] M. Montcouquiol, N. Sans, D. Huss et al., "Asymmetric localization of Vangl2 and Fz3 indicate novel mechanisms for planar cell polarity in mammals," *Journal of Neuroscience*, vol. 26, no. 19, pp. 5265–5275, 2006.
- [100] J. N. Murdoch, R. A. Rachel, S. Shah et al., "Circletail, a new mouse mutant with severe neural tube defects: chromosomal localization and interaction with the loop-tail mutation," *Genomics*, vol. 78, no. 1-2, pp. 55–63, 2001.

Research Article

Effects of Theophylline on Anesthetized Malignant Hyperthermia-Susceptible Pigs

Marko Fiege, Ralf Weisshorn, Kerstin Kolodzie, Frank Wappler, and Mark U. Gerbershagen

Department of Anesthesiology, Hospital Itzehoe, Robert-Koch-Straße 2, 25524 Itzehoe, Germany

Correspondence should be addressed to Marko Fiege, m.fiege@kh-itzehoe.de

Received 12 May 2011; Accepted 23 August 2011

Academic Editor: Lars Larsson

Copyright © 2011 Marko Fiege et al. This is an open access article distributed under the Creative Commons Attribution License, which permits unrestricted use, distribution, and reproduction in any medium, provided the original work is properly cited.

Background. Theophylline was shown to induce contracture development in porcine malignant hyperthermia (MH) susceptible (MHS) skeletal muscles in vitro. The purpose of the current study was to investigate the in vivo effects of theophylline in MHS and MH normal (MHN) swine. **Methods.** MH-trigger-free general anesthesia was performed in MHS and MHN swine. Theophylline was administered intravenously in cumulative doses up to $93.5 \text{ mg} \cdot \text{kg}^{-1}$. The clinical occurrence of MH was defined by changes of central-venous pCO_2 , central-venous pH, and body core temperature. **Results.** Theophylline induced comparable clinical alterations in the anesthetized MHS and MHN swine, especially in regard to hemodynamic data. No pig developed hypermetabolism and/or MH according to defined criteria. All animals died with tachycardia followed by ventricular fibrillation. **Conclusions.** The cumulative theophylline doses used in this study were much higher than doses used therapeutically in humans, as demonstrated by measured blood concentrations. Theophylline is thus not a trigger of MH in genetically determined swine.

1. Introduction

Malignant hyperthermia (MH) is an autosomally inherited, potentially lethal myopathy with a heterogeneous etiology that is usually triggered by volatile anesthetics and depolarizing muscle relaxants [1]. It is widely accepted that susceptibility to MH is caused by abnormal Ca^{2+} metabolism within the skeletal-muscle fiber. The site of the defect in MH appears to lie in the Ca^{2+} release mechanism of the sarcoplasmic reticulum (SR) in skeletal muscle, namely, in the complex of the dihydropyridine (DHPR) and ryanodine receptors (RyR).

Ca^{2+} homeostasis in skeletal muscle is regulated by a variety of intracellular second-messenger systems. Alterations in some second-messenger systems have been found to be associated with MH [2, 3]; the cyclic AMP (cAMP) system also seems to be affected in MH. In skeletal-muscle cells from MH-susceptible (MHS) patients and animals, higher cAMP levels were measured compared to normal (MHN) subjects [4–7].

The mode of action of methylxanthines such as caffeine and theophylline is concentration dependent [8]. While

they act by adenosine-receptor antagonism at lower concentrations, at higher concentrations they are also unspecific phosphodiesterase (PDE) inhibitors. PDE inhibitors produce a receptor-independent increase in Ca^{2+} release from the SR via the RyR in cardiac muscle by decreasing the rate of cAMP degradation. This effect could also be demonstrated in skeletal muscle as an increase in isometric contraction after application of PDE inhibitors [9, 10].

Theophylline (1,3-dimethylxanthine) was shown to induce contracture development in porcine skeletal muscle in vitro [11]. Furthermore, clear differences could be demonstrated between MHN and MHS muscle: MHS muscle developed significantly greater contractures compared to MHN specimens after bolus administration of $3 \text{ mmol} \cdot \text{L}^{-1}$ or $5 \text{ mmol} \cdot \text{L}^{-1}$ theophylline. These results were comparable with in vitro contracture tests (IVCTs) with caffeine and could be explained by the chemical analogies of both substances. In contrast to caffeine, however, theophylline is a widely used pharmaceutical substance. The purpose of the current study was to investigate the in vivo effects of theophylline in MHS and MHN swine.

2. Methods

After approval by the animal research committee of the University Hospital Hamburg-Eppendorf, 6 MHN German Landrace pigs weighing 39–48 kg, aged 3–5 months, and 6 MHS Pietrain pigs weighing 26–33 kg, aged 3–5 months, from a special breeding farm (Research Station Thalhausen, Technical University Munich, Germany) were investigated. Prior to the study, in all animals genomic DNA was isolated from blood preserved in ethylenediaminetetraacetic acid to check for the presence of the Arg615-Cys point mutation on chromosome 6, indicating MH susceptibility [12].

Swine were fasted overnight with free access to water. General anesthesia was induced by administration of ketamine $10 \text{ mg}\cdot\text{kg}^{-1}$ intramuscularly (Ketavet, Pharmacia & Upjohn, Erlangen, Germany). After insertion of a venous cannula into an ear vein, anesthesia was deepened with propofol $10 \text{ mg}\cdot\text{kg}^{-1}$ (Diprivan 2%, Astra-Zeneca, Plankstadt, Germany) and fentanyl $10 \mu\text{g}\cdot\text{kg}^{-1}$ (Fentanyl-Janssen, Janssen-Cilag, Neuss, Germany) intravenously (i.v.). After tracheotomy and intubation, the lungs were mechanically ventilated with an air/oxygen mixture (fraction of inspired oxygen (FiO_2) 0.4). Anesthesia was maintained with propofol $10 \text{ mg}\cdot\text{kg}^{-1}\cdot\text{h}^{-1}$ and fentanyl $50 \mu\text{g}\cdot\text{kg}^{-1}\cdot\text{h}^{-1}$. Neuro-muscular blocking drugs were not administered. A multilumen central-venous line was inserted into the right internal-jugular vein. One lumen was used for withdrawal of blood samples and measurement of central-venous pressure (CVP), the second for administration of theophylline and fluid infusion ($5\text{--}10 \text{ mL}\cdot\text{kg}^{-1}\cdot\text{h}^{-1}$ Ringer's solution), and the third for administration of anesthetics. Cannulas were inserted into both femoral arteries: one was used for withdrawal of blood samples, the other for continuous measurement of arterial pressure and body core temperature (PiCCO, Pulsion Medical Systems, Munich, Germany). Normothermia was maintained by forced-air warming, and rectal and intravascular body temperatures were measured continuously.

A blood-gas analyzer (ABL625, Radiometer, Copenhagen, Denmark) was used for monitoring arterial and venous oxygen saturation, oxygen partial pressure (pO_2), carbon dioxide partial pressure (pCO_2), pH, and potassium and lactate levels. Mechanical ventilation was adjusted to maintain venous pCO_2 at $46 \pm 4 \text{ mmHg}$; the body core temperature was adjusted to $37.5 \pm 0.2^\circ\text{C}$ before the experiment was started. Once a steady state was achieved for at least 30 minutes, baseline values were recorded for all variables.

Theophylline (Bronchoparat, Klinge Pharma, Munich, Germany) $1.0 \text{ mg}\cdot\text{kg}^{-1}$ was administered as an i.v. bolus. Subsequent doses were given every 10 minutes to reach cumulative doses of 3.5, 8.5, 18.5, 33.5, 53.5, and $93.5 \text{ mg}\cdot\text{kg}^{-1}$. The clinical occurrence of MH was defined by the development of two of three conditions: central-venous $\text{pCO}_2 \geq 75 \text{ mmHg}$, central-venous $\text{pH} \leq 7.20$, and an increase of intravascular body core temperature by $\geq 2.0^\circ\text{C}$ as measured using the PiCCO system.

During the experiments, hemodynamic variables (heart rate (HR), mean arterial pressure (MAP), CVP, cardiac output), end-tidal CO_2 concentration (etCO_2), rectal and

intravascular body temperature ($^\circ\text{C}$), blood-gas concentrations (O_2 saturation (SaO_2), pCO_2 , pH), and lactate levels were measured every 5 minutes. Every 10 minutes, blood samples were taken for gas-chromatographic measurement of theophylline concentrations. After all experiments were completed, the pigs were killed using 10% magnesium chloride solution i.v.

Statistical evaluation was performed using a computer-based program (StatView 4.57, Abacus Concepts, Berkeley, CA). All data are presented as median and range. Inter-group variations were calculated with the Mann-Whitney test; intragroup differences were calculated with analysis of variance for repeated measures. If appropriate, subsequent comparisons were performed using Scheffé's posthoc method. Results were considered significant if P values were less than 0.05.

3. Results

Theophylline induced comparable clinical alterations in the anesthetized MHS and MHN swine, especially in regard to hemodynamic data. However, significant differences could not be found between MHS and MHN swine. Moreover, no pig developed hypermetabolism and/or MH according to the defined criteria. Furthermore, clinical signs of muscular alterations, for example, general muscle rigidity, were not observed in any swine. After cumulative administration of $93.5 \text{ mg}\cdot\text{kg}^{-1}$, all animals died with tachycardia and hypotension followed by ventricular fibrillation. The main results are summarized in Figure 1.

The pCO_2 and venous pH did not change after administration of theophylline (Figures 1(a) and 1(b)). The baseline body temperatures of the MHS (37.5°C ($36.6\text{--}38.6^\circ\text{C}$)) and MHN swine (37.4°C ($35.8\text{--}37.8^\circ\text{C}$)) as well as lactate levels of $1.8 \text{ mmol}\cdot\text{L}^{-1}$ ($0.4\text{--}3.4 \text{ mmol}\cdot\text{L}^{-1}$) in MHS and $1.8 \text{ mmol}\cdot\text{L}^{-1}$ ($0.8\text{--}6.5 \text{ mmol}\cdot\text{L}^{-1}$) in MHN animals remained unchanged. The HR of all swine increased at cumulative doses of $93.5 \text{ mg}\cdot\text{kg}^{-1}$ theophylline (Figure 1(c)), while the MAP decreased. In MHS swine MAP decreased from 84.5 mmHg ($60\text{--}104 \text{ mmHg}$) to 65.5 mmHg ($48\text{--}67 \text{ mmHg}$) after administration of $93.5 \text{ mg}\cdot\text{kg}^{-1}$ theophylline. In MHN swine the decrease was more marked, from 84 mmHg ($67\text{--}98 \text{ mmHg}$) to 53.5 mmHg ($50\text{--}68 \text{ mmHg}$).

There were no differences in blood theophylline concentrations between MHS and MHN swine. A mean blood concentration of $13.9 \text{ mg}\cdot\text{mL}^{-1}$ ($12.3\text{--}16.2 \text{ mg}\cdot\text{mL}^{-1}$) theophylline was found after 30 minutes and a cumulative dose of $8.5 \text{ mg}\cdot\text{kg}^{-1}$ (Figure 1(d)). These concentrations lie within the therapeutic range for humans ($8\text{--}20 \text{ mg}\cdot\text{kg}^{-1}$). Ten minutes after the last dose ($93.5 \text{ mg}\cdot\text{kg}^{-1}$) the mean blood concentration was $122.4 \text{ mg}\cdot\text{mL}^{-1}$ ($99.3\text{--}154.4 \text{ mg}\cdot\text{mL}^{-1}$).

4. Discussion

The cytoplasmic Ca^{2+} concentration is regulated by a variety of intracellular second-messenger systems. Alterations in second-messenger systems, for example, the serotonin system or inositol polyphosphates, have been found to be associated with MH [2, 3]. The cAMP system also appears

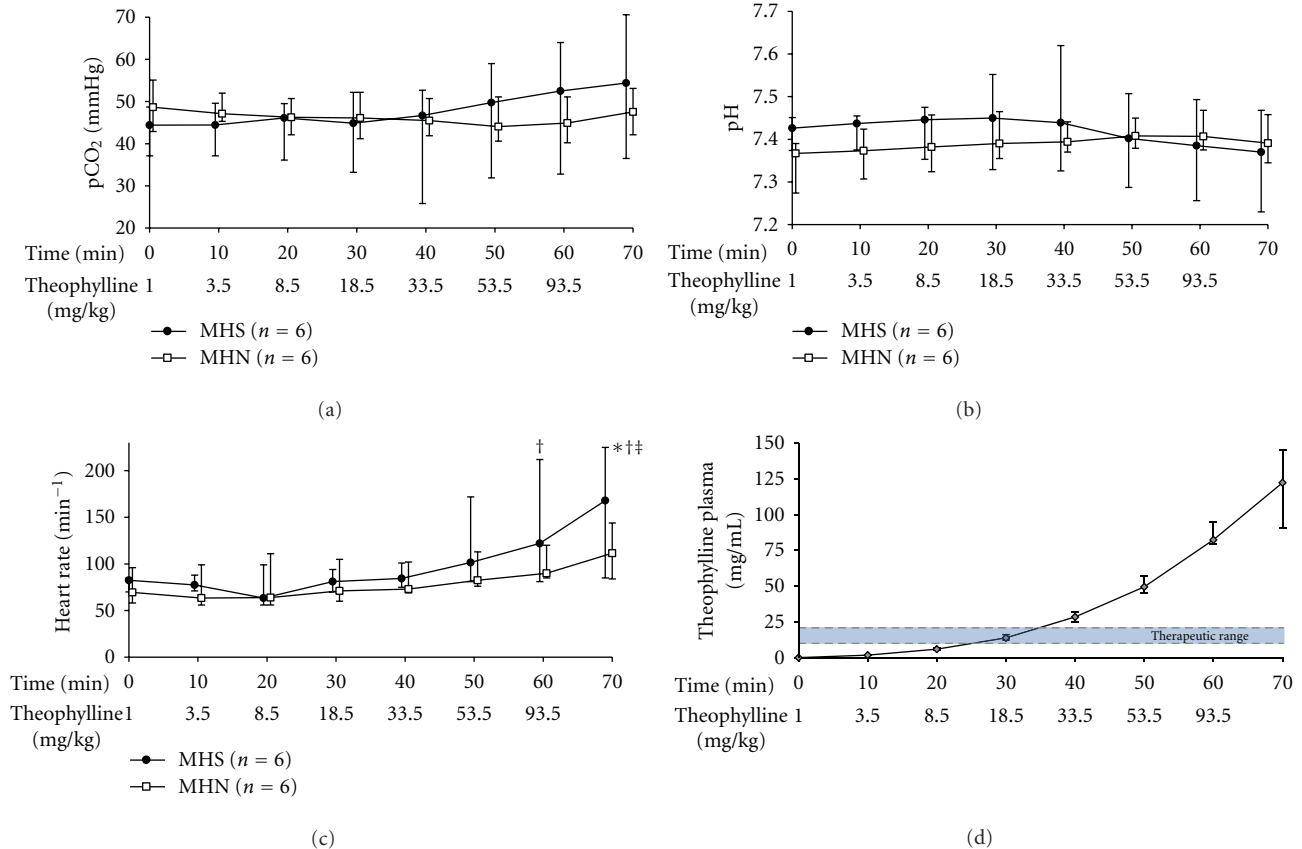


FIGURE 1: Central-venous pCO₂ (a), central-venous pH (b), heart rate (c), and plasma theophylline concentration (d) following cumulative intravenous administration of theophylline in malignant hyperthermia-susceptible (MHS) and normal (MHN) swine. Shown are median ± range. **P* < 0.05 MHS versus MHN; †*P* < 0.05 MHS versus 0 minutes; ‡*P* < 0.05 MHN versus 0 minutes.

to be altered in MH [4–7]. Higher cytoplasmic cAMP content and adenylyl-cyclase activity have been found in MHS compared to MHN patients. Additionally, serum cAMP concentrations during and after physical exercise increased more and for longer time periods in MHS compared to MHN patients [6]. One mode of action of methylxanthines is the unspecific inhibition of PDEs, which leads to enhancement of cytoplasmic cAMP. Furthermore, a MH-specific effect of the methylxanthine caffeine is well known and is used as a gold standard in the IVCTs for the diagnosis of MH [10, 13].

There are several case reports describing patients who developed MH-like symptoms without receiving the classic trigger substances such as succinylcholine or volatile anesthetics [1]. However, MH symptoms are largely unspecific. The clinical presentation of theophylline intoxication can be very similar to MH, for example, with tachycardia, hyperthermia, dehydration, convulsions, and coma as well as skeletal-muscle cramps and rhabdomyolysis. In individual cases, hypermetabolic theophylline overdoses have been treated successfully with dantrolene [14]. Therefore, a possible trigger mechanism of theophylline for MH was suggested [15].

The MH trigger potential of methylxanthines has been tested in several animal studies. Aminophylline induced MH-like symptoms in anesthetized rabbits, but a genetic basis

of MH susceptibility in these animals was not examined in this study [16]. In MHS swine, i.v. and oral administration of caffeine potentiated the development of MH crises induced by halothane and succinylcholine [17]. It was therefore suggested that caffeine may reduce the threshold of MH trigger agents. Furthermore, the detection of specific in vitro effects of theophylline in porcine skeletal-muscle preparations supported the hypothesis of an MH trigger potential for methylxanthines [11].

In this study, theophylline was not a trigger of MH in susceptible swine. No significant differences between MHS and MHN swine or symptoms of hypermetabolism could be found during cumulative administration of theophylline. The therapeutic blood level of theophylline in humans is estimated at between 8.0 and 20.0 mg·mL⁻¹. After cumulative administration of 93.5 mg theophylline, the swine in our study died in hemodynamic decompensation. The mean blood level measured at this time was 122.4 mg·mL⁻¹ (99.3–154.4 mg·mL⁻¹) or 0.68 mmol·L⁻¹ (0.55–0.86 mmol·L⁻¹) theophylline. A direct comparison between in vivo blood concentrations and concentrations in IVCTs is impossible. However, in vitro contracture development in isolated porcine MHS muscle specimens started at concentrations of 3.0 mmol·L⁻¹ theophylline. Therefore, it could be speculated that the in vivo theophylline concentrations in this study

were high enough to kill the animals, but too low to trigger MH.

Theophylline induces a sympathoadrenergic response comparable with a strong stress reaction. Stress is a well-known trigger of MH in swine, whereas the role of stress in human MH is still unclear [9, 18]. Considering the results of this study, theophylline might be a cofactor in the induction of MH in humans, but does not appear to be a primary trigger of MH.

References

- [1] F. Wappler, "Anesthesia for patients with a history of malignant hyperthermia," *Current Opinion in Anaesthesiology*, vol. 23, no. 3, pp. 417–422, 2010.
- [2] J. Scholz, U. Troll, J. Schulte Am Esch et al., "Inositol-1,4,5-trisphosphate and malignant hyperthermia," *The Lancet*, vol. 337, no. 8753, article 1361, 1991.
- [3] F. Wappler, M. Fiege, and J. Schulte am Esch, "Pathophysiological role of the serotonin system in malignant hyperthermia," *British Journal of Anaesthesia*, vol. 87, no. 5, pp. 794–798, 2001.
- [4] J. H. Willner, C. C. Cerri, and D. S. Wood, "High skeletal muscle adenylate cyclase in malignant hyperthermia," *The Journal of Clinical Investigation*, vol. 68, no. 5, pp. 1119–1124, 1981.
- [5] F. R. Ellis, P. J. Halsall, P. Allam, and E. Hay, "A biochemical abnormality found in muscle from unstressed malignant-hyperpyrexia-susceptible humans," *Biochemical Society Transactions*, vol. 12, no. 3, pp. 357–358, 1984.
- [6] A. Stanec and G. Stefano, "Cyclic AMP in normal and malignant hyperpyrexia susceptible individuals following exercise," *British Journal of Anaesthesia*, vol. 56, no. 11, pp. 1243–1246, 1984.
- [7] J. Scholz, M. Steinfath, N. Roewer et al., "Biochemical changes in malignant hyperthermia susceptible swine cyclic AMP, inositol phosphates, α_1 , β_1 - and β_2 -adrenoceptors in skeletal and cardiac muscle," *Acta Anaesthesiologica Scandinavica*, vol. 37, no. 6, pp. 575–583, 1993.
- [8] H. Scholz, "Inhibition of phosphodiesterases," *Zeitschrift fur Kardiologie*, vol. 83, no. 2, pp. 1–5, 1994.
- [9] J. Sawynok and T. L. Yaksh, "Caffeine as an analgesic adjuvant: a review of pharmacology and mechanisms of action," *Pharmacological Reviews*, vol. 45, no. 1, pp. 43–85, 1993.
- [10] H. Ørding, V. Brancadoro, S. Cozzolino et al., "In vitro contracture test for diagnosis of malignant hyperthermia following the protocol of the European MH group: results of testing patients surviving fulminant MH and unrelated low-risk subjects," *Acta Anaesthesiologica Scandinavica*, vol. 41, no. 8, pp. 955–966, 1997.
- [11] M. U. Gerbershagen, M. Fiege, R. Weißhorn, K. Kolodzie, and F. Wappler, "Theophylline induces contractures in porcine skeletal muscle preparations with the disposition to malignant hyperthermia," *Anesthesiologie Intensivmedizin Notfallmedizin Schmerztherapie*, vol. 39, no. 3, pp. 147–152, 2004.
- [12] J. Fujii, K. Otsu, F. Zorzato et al., "Identification of a mutation in porcine ryanodine receptor associated with malignant hyperthermia," *Science*, vol. 253, no. 5018, pp. 448–451, 1991.
- [13] M. G. Larach, J. R. Landis, J. S. Bunn, and M. Diaz, "Prediction of malignant hyperthermia susceptibility in low-risk subjects: an epidemiologic investigation of caffeine halothane contracture responses," *Anesthesiology*, vol. 76, no. 1, pp. 16–27, 1992.
- [14] M. J. A. Parr and S. M. Willatts, "Fatal theophylline poisoning with rhabdomyolysis. A potential role for dantrolene treatment," *Anaesthesia*, vol. 46, no. 7, pp. 557–559, 1991.
- [15] E. H. Flewellen and T. E. Nelson, "Is theophylline, aminophylline, or caffeine (methylxanthines) contraindicated in malignant hyperthermia susceptible patients?" *Anesthesia and Analgesia*, vol. 62, no. 1, pp. 115–118, 1983.
- [16] G. S. LeFever and H. Rosenberg, "Aminophylline, halothane, and malignant hyperpyrexia in the rabbit," *Fed Proc*, vol. 39, article 295, 1980.
- [17] J. W. Chapin, G. L. Chang, and D. W. Wingard, "Coffee (caffeine) and porcine malignant hyperthermia," *Anesthesiology*, vol. 55, no. 3, article A292, 1981.
- [18] R. Grinberg, G. Edelist, and A. Gordon, "Postoperative malignant hyperthermia episodes in patients who received 'safe' anaesthetics," *Canadian Anaesthetists Society Journal*, vol. 30, no. 3, pp. 273–276, 1983.

Review Article

Myosin Binding Protein-C: A Regulator of Actomyosin Interaction in Striated Muscle

Maegen A. Ackermann and Aikaterini Kontrogianni-Konstantopoulos

Department of Biochemistry and Molecular Biology, School of Medicine, University of Maryland, Baltimore, MD 21201, USA

Correspondence should be addressed to Aikaterini Kontrogianni-Konstantopoulos, akons001@umaryland.edu

Received 19 June 2011; Accepted 25 July 2011

Academic Editor: Robert J. Bloch

Copyright © 2011 M. A. Ackermann and A. Kontrogianni-Konstantopoulos. This is an open access article distributed under the Creative Commons Attribution License, which permits unrestricted use, distribution, and reproduction in any medium, provided the original work is properly cited.

Myosin-Binding protein-C (MyBP-C) is a family of accessory proteins of striated muscles that contributes to the assembly and stabilization of thick filaments, and regulates the formation of actomyosin cross-bridges, via direct interactions with both thick myosin and thin actin filaments. Three distinct MyBP-C isoforms have been characterized; cardiac, slow skeletal, and fast skeletal. Numerous mutations in the gene for cardiac MyBP-C (cMyBP-C) have been associated with familial hypertrophic cardiomyopathy (FHC) and have led to increased interest in the regulation and roles of the cardiac isoform. This review will summarize our current knowledge on MyBP-C and its role in modulating contractility, focusing on its interactions with both myosin and actin filaments in cardiac and skeletal muscles.

1. Introduction

Striated muscle cells contain a complex, highly ordered cytoskeleton, mainly composed of interdigitating thick myosin and thin actin filaments [1]. Muscle contraction and relaxation occurs by the sliding of myosin filaments past actin filaments under the strict regulation of their accessory proteins, which are responsible for their assembly and maintenance as well as the regulation of contractile activity [1].

Myosin-Binding protein-C (MyBP-C) comprises a family of accessory proteins of the thick myosin filaments that encompasses ~2% of the total myofibrillar protein [2]. To date, two major roles have been attributed to MyBP-C; it contributes to the regular organization and stabilization of thick filaments and modulates the formation of cross-bridges between myosin and actin, via direct interactions with both filamentous systems (as reviewed in [3, 4]). Within the sarcomere, MyBP-C localizes to the C-zone, the cross-bridges containing region of the A-band, in 7–9 transverse stripes that are ~43 nm apart [5–7].

Three MyBP-C isoforms have been identified; cardiac, slow skeletal, and fast skeletal (cMyBP-C, sMyBP-C, and fMyBP-C), encoded by different genes localizing to human

chromosomes 11, 12, and 19, respectively [8, 9]. The core structure of MyBP-C is composed of seven immunoglobulin (Ig) domains and three fibronectin type III (Fn-III) repeats, numbered from the NH₂-terminus as C1–C10 (Figure 1; [10]). A proline/alanine- (pro/ala-) rich motif and a conserved linker region, termed MyBP-C or M-motif, flank the first Ig domain, C1. Notably, both the cardiac and slow isoforms differ slightly from the core structure. cMyBP-C possesses three unique features, including an additional Ig domain at the extreme NH₂-terminus (termed C0), a 9-residue long insertion within the M-motif containing consensus phosphorylation sites and a 28-amino acid long loop in the middle of domain C5 [8, 11]. Conversely, sMyBP-C comprises a subfamily of four alternatively spliced variants (v), v1–v4, differing from one another due to the retention or exclusion of select exons encoding three novel insertions [12]. These are located at the very NH₂-terminus within the pro/ala- rich motif, the middle of domain C7, and the very COOH-terminus of the molecule, following the C10 domain (Figure 1; [12]). The presence of these insertions may result in different topographies and possibly functions of the sMyBP-C variants that contain them [12, 13]. Consistent with this, v1, which carries the COOH-terminal insertion preferentially localizes to the periphery of the M-band,

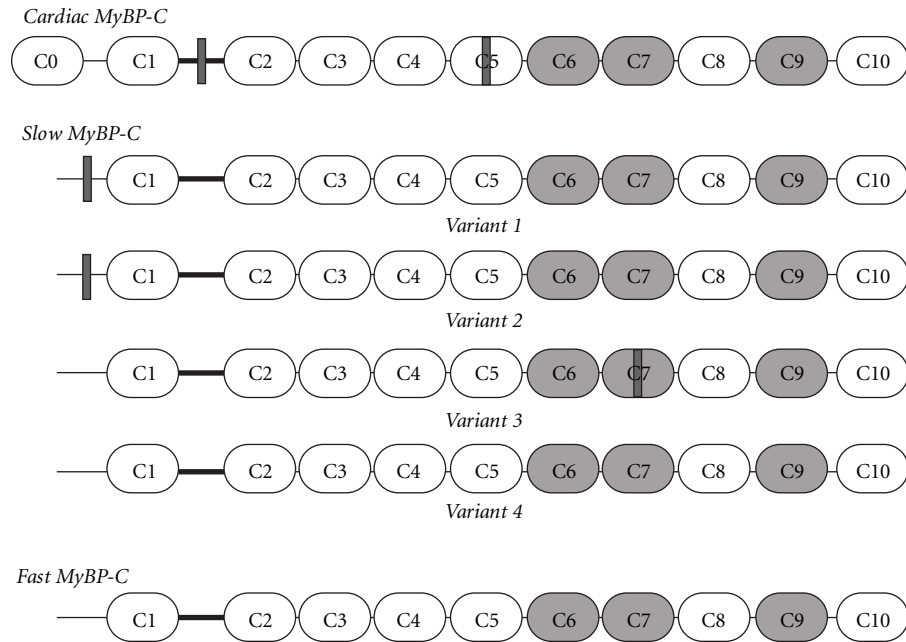


FIGURE 1: Schematic representation of the three MyBP-C isoforms. White and light grey ovals represent immunoglobulin and fibronectin type-III domains, respectively. The M-motif, flanked by domains C1 and C2 is denoted as a thick black line. Insertions specific to the cardiac isoform and slow variants are shown as dark grey rectangles.

rather than the C-zone, where it codistributes with its binding partners obscurin [13] and titin (our unpublished observations) and plays key roles in the structural integrity of M- and A-bands. The last Ig domain (C10) of sMyBP-C v1 interacts with the second Ig domain (Ig2) of obscurin [13]. Although the presence of the novel COOH-terminal insertion further strengthens this interaction, it is not required for binding. However, this novel motif is both necessary and sufficient to support binding of sMyBP-C v1 to the last Ig domain of titin, M10, which is a hotspot for mutations associated with tibial muscular dystrophy [14, 15]. Moreover, our laboratory has recently identified novel phosphorylation sites within the pro/ala- rich motif of the NH₂-terminus of sMyBP-C, specifically Ser-59, located in the novel NH₂-terminal insertion and Ser-62 are targets of PKA, while Ser-83 and Thr-84 are targets of PKC; Ser-204 is a substrate for both PKA and PKC [16]. Similar to its cardiac counterpart, phosphorylation of these sites may be essential in regulating the activities of sMyBP-C. Nevertheless, despite the differences in the core structure of the cardiac, slow, and fast MyBP-C proteins, they share a ~50% homology and a ~65% identity [12].

Although MyBP-C was identified over forty years ago as a contaminant of purified myosin [17], a better understanding of its physiology has emerged in the last two decades, paralleling the discovery of mutations in cMyBP-C that result in the development of familial hypertrophic cardiomyopathy (FHC; [18, 19]). Consequently, most of our knowledge originates from studies focusing on the cardiac form of the protein. This review will focus on the role of MyBP-C in regulating the formation of actomyosin cross-bridges via its direct interaction with both myosin and actin filaments.

2. Interactions of cMyBP-C with the Myosin Filament

Myosin is a hexameric protein consisting of two heavy chains (MHC) and two light chains (regulatory and essential, RLC and ELC, resp.). A dimer of heavy chains forms a coiled-coil helix that constitutes the rod or light meromyosin (LMM) segment of myosin [20]. Toward its NH₂-terminus, the helix unwinds and each MHC gives rise to a catalytic head, referred to as subfragment 1 (S1) that has ATPase activity and participates in the formation of cross-bridges with filamentous actin [21, 22]. The lever arm, referred to as subfragment 2 (S2), separates the S1 segment from the rod portion, and transduces the chemical energy from the hydrolysis of ATP into mechanical movement along the thin filament [23]. A pair of RLC and ELC binds in tandem to each head of the S1 segment modulating the speed and force of contraction [24, 25].

In addition to myosin light chains and actin, myosin is intimately associated with MyBP-C (Table 1 and Figure 2; [26]). The COOH-terminal C10 domain of all three MyBP-C isoforms harbors binding sites for the LMM portion of myosin [27]. Charged residues R1064, E1079, N1083, R1100, and R1101 present on the surface of the C10 domain of MyBP-C support an electrostatic interaction with residues 1554–1581 of the rod domain of myosin that has a modest affinity of ~3.5 μ M [28, 29]. Moreover, through domains C8–C10, MyBP-C interacts with titin, a giant sarcomeric protein spanning half a sarcomere, which is also tightly bound to the thick myosin filament [30]. Specifically, MyBP-C binds to the first Ig domain of an 11-domain superrepeat present in the A-band portion of titin [31]. Thus, it has been speculated

TABLE 1: Ligands of the cardiac isoform of MyBP-C.

<i>Cardiac MyBP-C</i>				
MyBP-C Domain	Ligand	Method	Affinity	Reference
C0	Myosin RLC	NMR, ITC	3.2 μ M	[32]
C1	Myosin S1-S2 hinge region	NMR		[33]
M-motif	Myosin S2	Cosedimentation assay, ITC	4.3 μ M	[34]
C2	Myosin S2	ITC, NMR	1.1 mM	[35]
C10	Myosin LMM	Cosedimentation	3.5 μ M	[28, 29, 36]
C0	F-actin	Co-IP, cosedimentation		[37]
C0 and C1	F-actin	Small angle neutron scattering		[38]
C0–C2	F-actin	Negative staining electron microscopy		[39]
C1–C2	F-actin	Cosedimentation	10 μ M	[40]
M-motif	F-actin	Cosedimentation		[41]
C5–C10	F-actin	Cosedimentation	4.3 μ M	[42]
C5	MyBP-C C8	Y2H, SPR	10 μ M	[43]
C7	MyBP-C C10	Y2H		[43]
C8–C10	Titin C-Zone 11-repeat super repeat	Dot-blot		[31]

Abbreviations used: RLC, regulatory light chain; NMR, nuclear magnetic resonance; ITC, isothermal calorimetry; LMM, light meromyosin; Co-IP, coimmunoprecipitation; Y2H, yeast 2 hybrid; SPR, surface plasmon resonance.

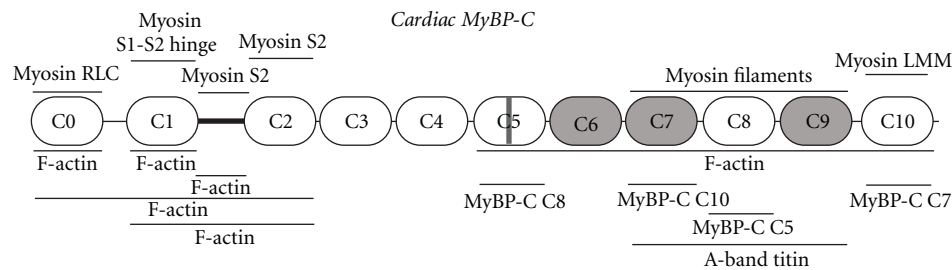


FIGURE 2: Schematic representation of cardiac MyBP-C, illustrating its domain architecture and known binding partners. Immunoglobulin and fibronectin type III domains are shown as white and grey ovals, respectively. The M-motif is denoted as a dark black line flanked by domains C1 and C2. The cardiac specific insertion within domain C5 is shown as a grey rectangle. Ligands for cMyBP-C are indicated at their sites of interaction.

that the repetitive binding of MyBP-C to the A-band portion of titin likely contributes to its periodicity within the C-zone [31]. Consistent with these findings, a number of studies have further shown that the COOH-terminal C8–C10 domains are necessary and sufficient to target MyBP-C to the A-band [44, 45].

While binding of the COOH-terminus of MyBP-C to the rod domain of myosin may contribute to the maintenance and stability of the thick filament, (reviewed in [3, 4]), binding of the NH₂-terminus of MyBP-C to myosin may mediate contractile regulation [3, 4]. Accordingly, a number of biochemical and structural studies have implicated the NH₂-terminal portion of cMyBP-C, containing domains C0–C2, in binding to the S2 region of myosin. Specifically, the M-motif located between the C1 and C2 Ig domains has been shown to bind directly to the NH₂-terminal 126 residues of the S2 fragment with an affinity of \sim 4.3 μ M [34]; this interaction is abolished by phosphorylation of

specific Ser residues within the M-motif of cMyBP-C via cAMP-dependent protein kinase [46–49]. Similarly, the C2 domain has been also shown to interact with the same 126 residues of the NH₂-terminus of the S2 fragment, albeit with considerably lower affinity (\sim 1.1 mM), compared to the M-motif [35]. Interestingly, molecular modeling has suggested that the interaction between the S2 portion of myosin and the C2 domain of cMyBP-C is mediated by polar residues [35]. On the other hand, the C1 domain of cMyBP-C has been reported to interact with the hinge region between the S1 heads and the S2 fragment [33], in close proximity to the myosin light chains, while a recent study reported that the first Ig domain of cMyBP-C, C0, binds to the RLCs with an affinity of \sim 3.2 μ M [32]. In support of this, overexpressed C0 targets to the A-band independently of the rest of the molecule, likely through its interaction with the RLCs [32].

Taken together, these findings strongly suggest that cMyBP-C may regulate the position and thus proximity of

the myosin S1 heads relative to the actin filament, through its interaction with the S2 region and the RLCs, therefore affecting the formation of actomyosin cross-bridges.

3. Interactions of cMyBP-C with the Actin Filament

In addition to the mounting experimental support indicating the intimate association of the NH₂-terminus of cMyBP-C with the S2 region of myosin, there is also significant evidence supporting its direct interaction with actin thin filaments. Early studies have shown that purified full-length cMyBP-C binds to filamentous actin (F-actin) [36, 50]. However, reconstituted thin filaments (i.e. preincubated with troponin and tropomyosin) fail to bind purified full length cMyBP-C in the presence of EDTA, a Ca²⁺ chelating agent, but binding is restored upon addition of Ca²⁺ [36, 50].

Further studies have recently begun to identify the actin-binding domain(s) of cMyBP-C through biochemical and structural approaches. Neutron scattering experiments have indicated that recombinant C0–C2 binds to F-actin in a repetitive manner, stabilizing it [38], while biochemical studies have shown that recombinant C0 is capable of directly interacting with F-actin [37]. Moreover, bacterially expressed C1–C2 associates with naked F-actin as well as reconstituted thin filaments, likely through the M-motif, exhibiting a binding affinity of ~10 μM to naked F-actin [40, 41]. This finding has been also substantiated by a recent study that used negative stain electron microscopy and three-dimensional reconstruction to show that bacterially expressed C0–C3 is well ordered on actin filaments near subdomain 1 [51].

Noticeably, some of the above studies report linear, nonsaturating binding, suggesting the presence of weak electrostatic interactions, as exemplified by the calculated micromolar affinity [41]. Consistent with this, these binding reactions depend largely on pH and ionic strength and are regulated by phosphorylation of cMyBP-C [42]. Thus, an increase in pH or ionic strength significantly decreases the capacity of the aforementioned cMyBP-C peptides to bind to F-actin [40–42]. Similarly, pretreatment of these recombinant peptides with PKA results in a dramatic reduction of their ability to associate with F-actin [41].

Importantly, a recent study by Rybakova and colleagues investigated the actin-binding capabilities of cMyBP-C across its entire length [42]. In support of previously published studies discussed above, the authors found that the NH₂-terminal domains of cMyBP-C bind to F-actin in a linear, nonsaturating manner, likely mediated by weak electrostatic interactions. However, recombinant full-length cMyBP-C, expressed in the baculovirus system, supported a direct and saturating interaction with F-actin with a calculated K_D of ~4.3 μM. Moreover, constructs lacking domains C0–C5 exhibited similar binding properties as full-length cMyBP-C [42]; this observation prompted the authors to conclude that the weak actin binding mediated by the NH₂-terminus of the molecule does not contribute significantly to the overall affinity of cMyBP-C for F-actin. Moreover, the authors

further showed that the actin binding supported by the COOH-terminal C6–C10 domains, unlike the NH₂-terminal C0–C2 domains, is independent of the regulatory elements, troponin and tropomyosin, of thin filaments, the levels of Ca²⁺, and the phosphorylation status of the M-motif [42]. Although the COOH-terminus of cMyBP-C exhibits a higher affinity for F-actin, the minimal binding region and its physiological relevance are still elusive. These open questions are especially important because the COOH-terminal domains C6–C10 also harbor binding sites for myosin and titin filaments (discussed above). Indeed, space constraints would favor dynamic rather than simultaneous interactions of the COOH-terminus of cMyBP-C with the actin, myosin, and titin filaments. However, three-dimensional reconstruction of thick filaments demonstrated that domains C7–C10 of cMyBP-C run along the length of the myosin rod [52], suggesting that its interaction with the LMM portion of myosin is not of dynamic nature.

Collectively these studies suggest the presence of various but weak binding sites for F-actin in the NH₂-terminus of cMyBP-C as well as the presence of a high affinity, saturating binding site in the COOH-terminus of the molecule. Obviously, more work is required before we can obtain a clear understanding of the physiological relevance of these interactions during muscle contraction and relaxation.

4. Interactions of Myosin and Actin Filaments with Skeletal Muscle MyBP-C

Early work has shown that the skeletal isoforms of MyBP-C also interact directly with both thick and thin filaments; however, their binding is much less characterized (Figure 3 and Table 2). Similar to cMyBP-C, the skeletal isoforms bind to the rod portion of sarcomeric myosin through their C10 domain and to the S2 region through their NH₂-terminus [27]. Further characterization of the NH₂-terminal binding has shown that the first two Ig domains of sMyBP-C (C1–C2) bind to the S2 region with an affinity of ~2.2 μM [26, 34]. In addition, native skeletal MyBP-C (presumably containing a mixture of the slow and fast isoforms) coaggregates with F-actin in a Ca²⁺ sensitive manner [50].

It becomes apparent from the above studies that our knowledge on the interaction of slow or fast MyBP-C with myosin and actin filaments is limited. There are several reasons for this. The identification of multiple mutations in the cardiac isoform that have been causally linked to the development of FHC is a major contributing factor that has shifted the interest of researchers towards cMyBP-C; however, this has recently changed, as mutations in sMyBP-C were identified in patients suffering from distal arthrogryposis type 1 (DA1), a disorder characterized by congenital contractures of the hands and feet ([53]; please see below). More importantly, the molecular diversity of the skeletal isoforms further complicates the relevant studies as there are at least five different skeletal forms of MyBP-C (one fast and four slow variants) that share homologous or common sequences, contain novel insertions in the NH₂- and COOH-termini, and may coexist in the same muscle,

TABLE 2: Ligands of the skeletal isoforms of MyBP-C.

MyBP-C Domain	Ligand	Skeletal MyBP-C		
		Method	Affinity	Reference
C1-C2	Myosin S2	Cosedimentation assay, ITC	2.2 μ M	[26, 34]
fast C10	Myosin filaments	Cosedimentation assay	0.5 μ M	[27]
Full length	F-actin	Cosedimentation		[36, 50]
Full length	Titin 11-domain super repeat	Dot-blot		[31, 54]
slow variant 1 C10 + insert	Obscurin Ig2	Y2H, pull down, overlay		[13]
slow variant 1 C10 + insert	FHL1	Y2H, pull down, Co-IP		[55]

Abbreviations used: RLC, regulatory light chain; NMR, nuclear magnetic resonance; ITC, isothermal calorimetry; LMM, light meromyosin; Co-IP, coimmunoprecipitation; Y2H, yeast 2 hybrid; SPR, surface plasmon resonance.

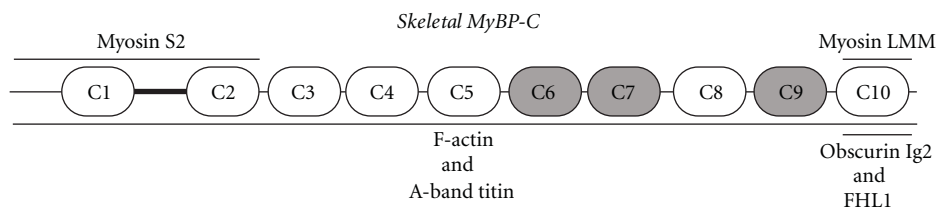


FIGURE 3: Schematic representation of the core structure of the skeletal isoforms of MyBP-C, depicting their identified binding partners. For ease of representation, the three novel insertions present in MyBP-C slow are not included in the schematic (for detailed description, please see Figure 1 and [12]). Immunoglobulin and fibronectin type III domains are presented as white and grey ovals, respectively. The M-motif is shown as a dark black line flanked by domains C1 and C2. Ligands for skeletal MyBP-C are denoted at their sites of interaction. Notably, obscurin and FHL1 are specific binding partners of v1, since their interactions depend on the presence of the novel COOH-terminal insertion, which is exclusively carried by v1, in addition to the C10 domain.

fiber, or even sarcomere [12]. Further detailed investigation is, therefore, necessary to evaluate the ability of each isoform to bind to myosin and actin filaments as well as the physiological significance of these interactions.

5. MyBP-C in Disease

During the last decade, an overwhelming number of mutations (~200) have been identified in the *MYBPC3* gene, which encodes the human cardiac MyBP-C protein. These include missense, nonsense, deletion/insertion, and frame-shift mutations and have been causally linked to the development of modest and late onset familial hypertrophic cardiomyopathy (FCH) [56–58]. The majority of the nonsense and frame-shift mutations result in truncated forms of the protein, that lack the COOH-terminus harboring binding sites for LMM, actin and titin, and thus negate the ability of cMyBP-C to associate with these filaments and regulate contractile activity [59]. Interestingly, these truncated peptides are often undetectable in patient biopsies, possibly due to transcriptional misregulation or rapid degradation [60]. Contrary to non-sense and frame shift mutations, missense mutations are generally associated with a less severe cardiomyopathic phenotype [58] and do not affect the structure or stability of the protein although some of them have been suggested to weaken myosin binding [33].

Moreover, recent genome wide linkage analysis revealed that mutations in the *MYBPC1* gene that encodes the human

skeletal MyBP-C slow protein lead to the development of distal arthrogyrosis type 1, an autosomal dominant disorder characterized by congenital contractures of the hands and feet [53]. Two missense mutations have been identified to date, W236R and Y856H, which are present in the M-motif and C8 domain, respectively [53]. Evaluation of skeletal muscle biopsies obtained from affected individuals revealed that slow twitch fibers were significantly smaller than fast twitch fibers. Importantly, the locations of these two mutations indicate possible alterations in the ability of sMyBP-C to interact with myosin or actin via its NH₂-terminus and to associate with the thick and titin filaments through its COOH-terminus.

The causal involvement of the MyBP-C family of proteins in the development of cardiac and skeletal myopathies, as exemplified by the aforementioned studies, clearly indicates that the members of this multifaceted and complex family are essential components and key regulators of muscle structure and function.

6. The Regulatory Activities of MyBP-C-Models and Perspectives

Through its dynamic interactions with myosin and actin filaments, MyBP-C affects the formation and cycling of cross-bridges in three distinct ways: (i) by maintaining the normal structure of myosin and actin filaments, (ii) by regulating the rate at which myosin and actin interact, and (iii) by

modulating the ATPase activity of myosin. Consistent with this, the addition of skeletal MyBP-C reduces the critical concentration necessary for myosin polymerization *in vitro* and results in the formation of longer and more uniform thick filaments [61, 62]. In addition, the NH₂-terminal region C0–C2 of cMyBP-C supports actin bundling *in vitro*, as evidenced by the increased turbidity of F-actin in the solution and the formation of significantly thicker actin filaments, as visualized by electron microscopy [41]. Notably, the effect of cMyBP-C on actin bundling is dependent on pH and regulated by phosphorylation events mediated by PKA [41]. Moreover, *in vitro* motility assays, examining the sliding of actin filaments over myosin heads in the presence of full-length or truncated forms of cMyBP-C revealed a significant reduction in their sliding velocity [40, 63, 64]. Notably, the degree of reduction was also dependent on the presence of the actin regulatory proteins, troponin, and tropomyosin; in their presence, there was a lesser effect on the decrease of actin motility over full-length myosin [63, 65], HMM [40] or S1 heads [64]. MyBP-C also modulates the ATPase activity of myosin, though in an indirect way, via interactions with both myosin and actin filaments supported by its NH₂-terminus. In agreement with this, purified sMyBP-C inhibited the ATPase activity of actin-activated myosin; however, native cMyBP-C moderately enhanced the actin-activated ATPase activity of myosin [66, 67]. Surprisingly though, recombinant cMyBP-C containing the C0–C2 region inhibited the ATPase activity of myosin in the presence of actin [40].

The majority of the aforementioned studies have been performed with native proteins obtained from different species or types of muscles, presumably due to ease of purification. However, Alyonycheva et al. have convincingly shown that the strength of the interaction between myosin and MyBP-C is considerably increased when both proteins are purified from the same source [68]. As such, cMyBP-C and skeletal MyBP-C bound with higher affinity to cardiac and skeletal myosin, respectively [68].

As our knowledge about the molecular and functional properties of MyBP-C broadens, it becomes apparent that through interactions supported by its COOH and NH₂ termini, MyBP-C contributes to the maintenance of the normal structure of thick filaments, and the regulation of cross-bridges formation and cycling. It has, therefore, been suggested that MyBP-C may serve as a linker, whereby its COOH-terminus is necessary for anchoring it to LMM in the A-band, leaving the NH₂-terminus available to modulate contractility through dynamic interactions with the head region of myosin and actin [4]. Consequently, Calaghan and colleagues proposed the “tether model” to explain how MyBP-C modulates the formation of actomyosin cross-bridges [69]. This model suggests that both myosin binding sites on MyBP-C act together by limiting the movement of the S1 heads relative to LMM and actin, thereby restricting the formation of actomyosin cross-bridges [69]. Phosphorylation of select Ser residues within the M-motif of cMyBP-C, mediated mainly by PKA, regulates the interaction between cMyBP-C and myosin by acting as an “on-off” switch. Consequently, when in the “on” or dephosphorylated state,

the NH₂-terminus of cMyBP-C binds to myosin and limits its interaction with actin, when in the “off” or phosphorylated state, myosin is free to interact with actin and form cross-bridges [70].

The tether model is centered on the dynamic and highly regulated interaction of MyBP-C with myosin and actin filaments. However, it is necessary to understand the orientation of MyBP-C within the sarcomere, as well. Two proposed models for the topology of MyBP-C have been suggested: a “collar model” in which a trimer of MyBP-C molecules wraps around the rod domain of myosin [43], and an “axial model”, where the COOH-terminus of MyBP-C runs along the length of the rod domain [71]. A stipulation of the collar model is that MyBP-C is required to dimerize [43]. In support of this, it has been shown that MyBP-C dimerizes through interactions mediated by domains C5 and C7 with C8 and C10, respectively [43, 72]. On the other hand, X-ray diffraction in combination with molecular and computational modeling studies support the axial model, suggesting that the last three domains of MyBP-C lay along the length of the myosin rod [71, 73]. Recently, a study using electron microscopy and three-dimensional reconstructions of cardiac thick filaments further demonstrated that the COOH-terminus of cMyBP-C runs along the rod domain surface of thick filaments [52]. Although MyBP-C dimerization is not essential for the arrangement of MyBP-C along the length of the myosin rod, the axial model does not negate its dimerization. Nevertheless, in both models the NH₂-terminus of MyBP-C extends into the interfilament space where it is accessible to bind to the S2 portion of myosin and actin. Physiological dynamic interactions of MyBP-C with myosin and actin are possible as the distance between thick and thin filaments is ~9–16 nm [74] and the length of extended MyBP-C is ~40 nm [75]. Therefore, MyBP-C is capable to span the interfilament space, enabling interactions with both actin and myosin filaments.

It is not without precedence that regulation of contractility occurs through dynamic interactions with both actin and myosin filaments, as the essential and regulatory light chains bind tightly to myosin, but also interact with actin [25, 76, 77]. Additionally, twitchin, a protein similar to titin, characterized in *C. elegans* as a thick filament regulatory protein, interacts with both myosin and actin in a phosphorylation-dependent manner to modulate cross-bridges formation [78, 79]. However, current models (as described above) to explain the mechanism of contractile regulation through dynamic binding to myosin and actin are lacking. Undoubtedly, more work is necessary in order to understand the precise mechanisms by which MyBP-C modulates contractility.

Acknowledgments

Our research has been supported by grants to A. Kontogianni Konstantopoulos from the National Institutes of Health (R01 AR52768) and to M. A. Ackermann from the National Institutes of Health (F32 AR058079).

References

- [1] K. A. Clark, A. S. McElhinny, M. C. Beckerle, and C. C. Gregorio, "Striated muscle cytoarchitecture: an intricate web of form and function," *Annual Review of Cell and Developmental Biology*, vol. 18, pp. 637–706, 2002.
- [2] G. Offer, C. Moos, and R. Starr, "A new protein of the thick filaments of vertebrate skeletal myofibrils. Extraction, purification and characterization," *Journal of Molecular Biology*, vol. 74, no. 4, pp. 653–676, 1973.
- [3] E. Flashman, C. Redwood, J. Moolman-Smook, and H. Watkins, "Cardiac myosin binding protein C: its role in physiology and disease," *Circulation Research*, vol. 94, no. 10, pp. 1279–1289, 2004.
- [4] C. E. Oakley, J. Chamoun, L. J. Brown, and B. D. Hambly, "Myosin binding protein-C: enigmatic regulator of cardiac contraction," *International Journal of Biochemistry and Cell Biology*, vol. 39, no. 12, pp. 2161–2166, 2007.
- [5] P. Bennett, R. Craig, R. Starr, and G. Offer, "The ultrastructural location of C-protein, X-protein and H-protein in rabbit muscle," *Journal of Muscle Research and Cell Motility*, vol. 7, no. 6, pp. 550–567, 1986.
- [6] F. A. Pepe, F. T. Ashton, C. Street, and J. Weisel, "The myosin filament. X. Observation of nine subfilaments in transverse sections," *Tissue and Cell*, vol. 18, no. 4, pp. 499–508, 1986.
- [7] F. A. Pepe and B. Drucker, "The myosin filament. III. C protein," *Journal of Molecular Biology*, vol. 99, no. 4, pp. 609–617, 1975.
- [8] M. Gautel, O. Zuffardi, P. Freiburg, and S. Labeit, "Phosphorylation switches specific for the cardiac isoform of myosin binding protein-C: a modulator of cardiac contraction?" *EMBO Journal*, vol. 14, no. 9, pp. 1952–1960, 1995.
- [9] F. E. Weber, K. T. Vaughan, F. C. Reinach, and D. A. Fischman, "Complete sequence of human fast-type and slow-type muscle myosin-binding-protein C (MyBP-C). Differential expression, conserved domain structure and chromosome assignment," *European Journal of Biochemistry*, vol. 216, no. 2, pp. 661–669, 1993.
- [10] S. Einheber and D. A. Fischman, "Isolation and characterization of a cDNA clone encoding avian skeletal muscle C-protein: an intracellular member of the immunoglobulin superfamily," *Proceedings of the National Academy of Sciences of the United States of America*, vol. 87, no. 6, pp. 2157–2161, 1990.
- [11] M. Yasuda, S. Koshida, N. Sato, and T. Obinata, "Complete primary structure of chicken cardiac C-protein (MyBP-C) and its expression in developing striated muscles," *Journal of Molecular and Cellular Cardiology*, vol. 27, no. 10, pp. 2275–2286, 1995.
- [12] M. A. Ackermann and A. Kontrogianni-Konstantopoulos, "Myosin binding protein-C slow: an intricate subfamily of proteins," *Journal of Biomedicine and Biotechnology*, vol. 2010, Article ID 652065, 10 pages, 2010.
- [13] M. A. Ackermann, L. Y. R. Hu, A. L. Bowman, R. J. Bloch, and A. Kontrogianni-Konstantopoulos, "Obscurin interacts with a novel isoform of MyBP-C slow at the periphery of the sarcomeric M-band and regulates thick filament assembly," *Molecular Biology of the Cell*, vol. 20, no. 12, pp. 2963–2978, 2009.
- [14] B. Udd, "Third filament diseases," *Advances in Experimental Medicine and Biology*, vol. 642, pp. 99–115, 2008.
- [15] B. Udd, H. Haravuori, H. Kalimo et al., "Tibial muscular dystrophy - from clinical description to linkage on chromosome 2q31," *Neuromuscular Disorders*, vol. 8, no. 5, pp. 327–332, 1998.
- [16] M. A. Ackermann and A. Kontrogianni-Konstantopoulos, "Myosin Binding Protein-C Slow is a Novel Substrate for Protein Kinase A (PKA) and C (PKC) in Skeletal Muscle," *Journal of proteome research*, vol. 10, no. 10, Article ID 652065, pp. 4547–4555, 2011.
- [17] R. Starr and G. Offer, "Polypeptide chains of intermediate molecular weight in myosin preparations," *FEBS Letters*, vol. 15, no. 1, pp. 40–44, 1971.
- [18] G. Bonne, L. Carrier, J. Bercovici et al., "Cardiac myosin binding protein-C gene splice acceptor site mutation is associated with familial hypertrophic cardiomyopathy," *Nature Genetics*, vol. 11, no. 4, pp. 438–440, 1995.
- [19] H. Watkins, D. Conner, L. Thierfelder et al., "Mutations in the cardiac myosin binding protein-C gene on chromosome 11 cause familial hypertrophic cardiomyopathy," *Nature Genetics*, vol. 11, no. 4, pp. 434–437, 1995.
- [20] T. Chakrabarty, M. Xiao, R. Cooke, and P. R. Selvin, "Holding two heads together: stability of the myosin II rod measured by resonance energy transfer between the heads," *Proceedings of the National Academy of Sciences of the United States of America*, vol. 99, no. 9, pp. 6011–6016, 2002.
- [21] I. Rayment, W. R. Rypniewski, K. Schmidt-Base et al., "Three-dimensional structure of myosin subfragment-1: a molecular motor," *Science*, vol. 261, no. 5117, pp. 50–58, 1993.
- [22] J. L. Woodhead, F. Q. Zhao, R. Craig, E. H. Egelman, L. Alamo, and R. Padrón, "Atomic model of a myosin filament in the relaxed state," *Nature*, vol. 436, no. 7054, pp. 1195–1199, 2005.
- [23] I. Rayment, H. M. Holden, M. Whittaker et al., "Structure of the actin-myosin complex and its implications for muscle contraction," *Science*, vol. 261, no. 5117, pp. 58–65, 1993.
- [24] B. A. Colson, M. R. Locher, T. Bekyarova et al., "Differential roles of regulatory light chain and myosin binding protein-C phosphorylations in the modulation of cardiac force development," *Journal of Physiology*, vol. 588, no. 6, pp. 981–993, 2010.
- [25] I. Morano, "Tuning the human heart molecular motors by myosin light chairs," *Journal of Molecular Medicine*, vol. 77, no. 7, pp. 544–555, 1999.
- [26] R. Starr and G. Offer, "The interaction of C-protein with heavy meromyosin and subfragment-2," *Biochemical Journal*, vol. 171, no. 3, pp. 813–816, 1978.
- [27] T. Okagaki, F. E. Weber, D. A. Fischman, K. T. Vaughan, T. Mikawa, and F. C. Reinach, "The major myosin-binding domain of skeletal muscle MyBP-C (C protein) resides in the COOH-terminal, immunoglobulin C2 motif," *Journal of Cell Biology*, vol. 123, no. 3, pp. 619–626, 1993.
- [28] E. Flashman, H. Watkins, and C. Redwood, "Localization of the binding site of the C-terminal domain of cardiac myosin-binding protein-C on the myosin rod," *Biochemical Journal*, vol. 401, no. 1, pp. 97–102, 2007.
- [29] C. A. Miyamoto, D. A. Fischman, and F. C. Reinach, "The interface between MyBP-C and myosin: site-directed mutagenesis of the CX myosin-binding domain of MyBP-C," *Journal of Muscle Research and Cell Motility*, vol. 20, no. 7, pp. 703–715, 1999.
- [30] A. Kontrogianni-Konstantopoulos, M. A. Ackermann, A. L. Bowman, S. V. Yap, and R. J. Bloch, "Muscle giants: molecular scaffolds in sarcomerogenesis," *Physiological Reviews*, vol. 89, no. 4, pp. 1217–1267, 2009.
- [31] A. Freiburg and M. Gautel, "A molecular map of the interactions between titin and myosin-binding protein C Implications for sarcomeric assembly in familial hypertrophic cardiomyopathy," *European Journal of Biochemistry*, vol. 235, no. 1-2, pp. 317–323, 1996.

- [32] J. Ratti, "Structure and interactions of myosin-binding protein c domain c0: cardiac-specific regulation of myosin at its neck?" *Journal of Biological Chemistry*, vol. 286, no. 14, pp. 12650–12658, 2011.
- [33] A. Ababou, E. Rostkova, S. Mistry, C. L. Masurier, M. Gautel, and M. Pfuhl, "Myosin binding protein C positioned to play a key role in regulation of muscle contraction: structure and interactions of domain C1," *Journal of Molecular Biology*, vol. 384, no. 3, pp. 615–630, 2008.
- [34] M. Gruen and M. Gautel, "Mutations in β -myosin S2 that cause familial hypertrophic cardiomyopathy (FHC) abolish the interaction with the regulatory domain of myosin-binding protein-C," *Journal of Molecular Biology*, vol. 286, no. 3, pp. 933–949, 1999.
- [35] A. Ababou, M. Gautel, and M. Pfuhl, "Dissecting the N-terminal myosin binding site of human cardiac myosin-binding protein C: structure and myosin binding of domain C2," *Journal of Biological Chemistry*, vol. 282, no. 12, pp. 9204–9215, 2007.
- [36] C. Moos, C. M. Mason, and J. M. Besterman, "The binding of skeletal muscle C-protein to F-actin, and its relation to the interaction of actin with myosin subfragment-1," *Journal of Molecular Biology*, vol. 124, no. 5, pp. 571–586, 1978.
- [37] I. Kulikovskaya, G. McClellan, J. Flavigny, L. Carrier, and S. Winegrad, "Effect of MyBP-C binding to actin on contractility in heart muscle," *Journal of General Physiology*, vol. 122, no. 6, pp. 761–774, 2003.
- [38] A. E. Whitten, C. M. Jeffries, S. P. Harris, and J. Trehwella, "Cardiac myosin-binding protein C decorates F-actin: implications for cardiac function," *Proceedings of the National Academy of Sciences of the United States of America*, vol. 105, no. 47, pp. 18360–18365, 2008.
- [39] R. W. Kensler, J. F. Shaffer, and S. P. Harris, "Binding of the N-terminal fragment C0-C2 of cardiac MyBP-C to cardiac F-actin," *Journal of Structural Biology*, vol. 174, no. 1, pp. 44–51, 2011.
- [40] M. V. Razumova, J. F. Shaffer, A. Y. Tu, G. V. Flint, M. Regnier, and S. P. Harris, "Effects of the N-terminal domains of myosin binding protein-C in an in vitro motility assay: evidence for long-lived cross-bridges," *Journal of Biological Chemistry*, vol. 281, no. 47, pp. 35846–35854, 2006.
- [41] J. F. Shaffer, R. W. Kensler, and S. P. Harris, "The myosin-binding protein C motif binds to F-actin in a phosphorylation-sensitive manner," *Journal of Biological Chemistry*, vol. 284, no. 18, pp. 12318–12327, 2009.
- [42] I. N. Rybakova, M. L. Greaser, and R. L. Moss, "Myosin binding protein C interaction with actin: characterization and mapping of the binding site," *The Journal of Biological Chemistry*, vol. 286, no. 3, pp. 2008–2016, 2011.
- [43] J. Moolman-Smook, E. Flashman, W. De Lange et al., "Identification of novel interactions between domains of myosin binding protein-C that are modulated by hypertrophic cardiomyopathy missense mutations," *Circulation Research*, vol. 91, no. 8, pp. 704–711, 2002.
- [44] R. Gilbert, J. A. Cohen, S. Pardo, A. Basu, and D. A. Fischman, "Identification of the A-band localization domain of myosin binding proteins C and H (MyBP-C, MyBP-H) in skeletal muscle," *Journal of Cell Science*, vol. 112, no. 1, pp. 69–79, 1999.
- [45] R. Gilbert, M. G. Kelly, T. Mikawa, and D. A. Fischman, "The carboxyl terminus of myosin binding protein C (MyBP-C, C-protein) specifies incorporation into the A-band of striated muscle," *Journal of Cell Science*, vol. 109, no. 1, pp. 101–111, 1996.
- [46] M. Gruen, H. Prinz, and M. Gautel, "cAPK-phosphorylation controls the interaction of the regulatory domain of cardiac myosin binding protein C with myosin-S2 in an on-off fashion," *FEBS Letters*, vol. 453, no. 3, pp. 254–259, 1999.
- [47] S. Sadayappan, J. Gulick, R. Klevitsky et al., "Cardiac myosin binding protein-C phosphorylation in a β -myosin heavy chain background," *Circulation*, vol. 119, no. 9, pp. 1253–1262, 2009.
- [48] S. Sadayappan, J. Gulick, H. Osinska et al., "Cardiac myosin-binding protein-C phosphorylation and cardiac function," *Circulation Research*, vol. 97, no. 11, pp. 1156–1163, 2005.
- [49] S. Sadayappan, H. Osinska, R. Klevitsky et al., "Cardiac myosin binding protein c phosphorylation is cardioprotective," *Proceedings of the National Academy of Sciences of the United States of America*, vol. 103, no. 45, pp. 16918–16923, 2006.
- [50] K. Yamamoto, "The binding of skeletal muscle C-protein to regulated actin," *FEBS Letters*, vol. 208, no. 1, pp. 123–127, 1986.
- [51] J. Y. Mun et al., "Electron microscopy and 3D reconstruction of F-actin decorated with cardiac myosin-binding protein C (cMyBP-C)," *Journal of Molecular Biology*, vol. 410, no. 2, pp. 214–225, 2011.
- [52] M. E. Zoghbi, J. L. Woodhead, R. L. Moss, and R. Craig, "Three-dimensional structure of vertebrate cardiac muscle myosin filaments," *Proceedings of the National Academy of Sciences of the United States of America*, vol. 105, no. 7, pp. 2386–2390, 2008.
- [53] C. A. Gurnett, D. M. Desruisseau, K. McCall et al., "Myosin binding protein C1: a novel gene for autosomal dominant distal arthrogyrosis type 1," *Human Molecular Genetics*, vol. 19, no. 7, pp. 1165–1173, 2010.
- [54] D. O. Fürst, U. Vinkemeier, and K. Weber, "Mammalian skeletal muscle C-protein: purification from bovine muscle, binding to titin and the characterization of a full-length human cDNA," *Journal of Cell Science*, vol. 102, no. 4, pp. 769–778, 1992.
- [55] M. J. McGrath, D. L. Cottle, M. A. Nguyen et al., "Four and a half LIM protein 1 binds myosin-binding protein C and regulates myosin filament formation and sarcomere assembly," *Journal of Biological Chemistry*, vol. 281, no. 11, pp. 7666–7683, 2006.
- [56] S. P. Harris, R. G. Lyons, and K. L. Bezold, "In the thick of it: HCM-causing mutations in myosin binding proteins of the thick filament," *Circulation Research*, vol. 108, no. 6, pp. 751–764, 2011.
- [57] T. Konno, S. Chang, J. G. Seidman, and C. E. Seidman, "Genetics of hypertrophic cardiomyopathy," *Current Opinion in Cardiology*, vol. 25, no. 3, pp. 205–209, 2010.
- [58] Q. Xu, S. Dewey, S. Nguyen, and A. V. Gomes, "Malignant and benign mutations in familial cardiomyopathies: insights into mutations linked to complex cardiovascular phenotypes," *Journal of Molecular and Cellular Cardiology*, vol. 48, no. 5, pp. 899–909, 2010.
- [59] C. E. Oakley, B. D. Hambly, P. M. Curmi, and L. J. Brown, "Myosin binding protein C: structural abnormalities in familial hypertrophic cardiomyopathy," *Cell Research*, vol. 14, no. 2, pp. 95–110, 2004.
- [60] W. Rottbauer, M. Gautel, J. Zehelein et al., "Novel splice donor site mutation in the cardiac myosin-binding protein-C gene in familial hypertrophic cardiomyopathy. Characterization of cardiac transcript and protein," *Journal of Clinical Investigation*, vol. 100, no. 2, pp. 475–482, 1997.
- [61] J. S. Davis, "Interaction of C-protein with pH 8.0 synthetic thick filaments prepared from the myosin of vertebrate skeletal muscle," *Journal of Muscle Research and Cell Motility*, vol. 9, no. 2, pp. 174–183, 1988.

- [62] J. F. Koretz, "Effects of C-protein on synthetic myosin filament structure," *Biophysical Journal*, vol. 27, no. 3, pp. 433–446, 1979.
- [63] W. Saber, K. J. Begin, D. M. Warshaw, and P. VanBuren, "Cardiac myosin binding protein-C modulates actomyosin binding and kinetics in the in vitro motility assay," *Journal of Molecular and Cellular Cardiology*, vol. 44, no. 6, pp. 1053–1061, 2008.
- [64] J. F. Shaffer, M. V. Razumova, A. Y. Tu, M. Regnier, and S. P. Harris, "Myosin S2 is not required for effects of myosin binding protein-C on motility," *FEBS Letters*, vol. 581, no. 7, pp. 1501–1504, 2007.
- [65] D. V. Shchepkin, G. V. Kopylova, L. V. Nikitina, L. B. Katsnelson, and S. Y. Bershitsky, "Effects of cardiac myosin binding protein-C on the regulation of interaction of cardiac myosin with thin filament in an in vitro motility assay," *Biochemical and Biophysical Research Communications*, vol. 401, no. 1, pp. 159–163, 2010.
- [66] K. Yamamoto and C. Moos, "The C-proteins of rabbit red, white, and cardiac muscles," *Journal of Biological Chemistry*, vol. 258, no. 13, pp. 8395–8401, 1983.
- [67] S. S. Margossian, "Reversible dissociation of dog cardiac myosin regulatory light chain 2 and its influence on ATP hydrolysis," *Journal of Biological Chemistry*, vol. 260, no. 25, pp. 13747–13754, 1985.
- [68] T. N. Alyonycheva, T. Mikawa, F. C. Reinach, and D. A. Fischman, "Isoform-specific interaction of the myosin-binding proteins (MyBPs) with skeletal and cardiac myosin is a property of the C-terminal immunoglobulin domain," *Journal of Biological Chemistry*, vol. 272, no. 33, pp. 20866–20872, 1997.
- [69] S. C. Calaghan, J. Trinick, P. J. Knight, and E. White, "A role for C-protein in the regulation of contraction and intracellular Ca²⁺ in intact rat ventricular myocytes," *Journal of Physiology*, vol. 528, no. 1, pp. 151–156, 2000.
- [70] L. Carrier, "Cardiac myosin-binding protein C in the heart," *Archives des Maladies du Cœur et des Vaisseaux*, vol. 100, no. 3, pp. 238–243, 2007.
- [71] J. M. Squire, P. K. Luther, and C. Knupp, "Structural evidence for the interaction of C-protein (MyBP-C) with actin and sequence identification of a possible actin-binding domain," *Journal of Molecular Biology*, vol. 331, no. 3, pp. 713–724, 2003.
- [72] E. Flashman, L. Korkie, H. Watkins, C. Redwood, and J. C. Moolman-Smook, "Support for a trimeric collar of myosin binding protein C in cardiac and fast skeletal muscle, but not in slow skeletal muscle," *FEBS Letters*, vol. 582, no. 3, pp. 434–438, 2008.
- [73] E. Rome, G. Offer, and F. A. Pepe, "X ray diffraction of muscle labelled with antibody to C protein," *Nature New Biology*, vol. 244, no. 135, pp. 152–154, 1973.
- [74] F. J. Julian, R. L. Moss, and G. S. Waller, "Mechanical properties and myosin light chain composition of skinned muscle fibres from adult and new-born rabbits," *Journal of Physiology*, vol. 311, pp. 201–218, 1981.
- [75] H. C. Hartzell and W. S. Sale, "Structure of C protein purified from cardiac muscle," *Journal of Cell Biology*, vol. 100, no. 1, pp. 208–215, 1985.
- [76] D. J. Timson, "Fine tuning the myosin motor: the role of the essential light chain in striated muscle myosin," *Biochimie*, vol. 85, no. 7, pp. 639–645, 2003.
- [77] G. P. Farman, M. S. Miller, M. C. Reedy et al., "Phosphorylation and the N-terminal extension of the regulatory light chain help orient and align the myosin heads in *Drosophila* flight muscle," *Journal of Structural Biology*, vol. 168, no. 2, pp. 240–249, 2009.
- [78] T. M. Butler, S. U. Mooers, S. R. Narayan, and M. J. Siegman, "The N-terminal region of twitchin binds thick and thin contractile filaments: redundant mechanisms of catch force maintenance," *Journal of Biological Chemistry*, vol. 285, no. 52, pp. 40654–40665, 2010.
- [79] D. Funabara, C. Hamamoto, K. Yamamoto et al., "Unphosphorylated twitchin forms a complex with actin and myosin that may contribute to tension maintenance in catch," *Journal of Experimental Biology*, vol. 210, no. 24, pp. 4399–4410, 2007.

Research Article

The Combined Effect of Electrical Stimulation and High-Load Isometric Contraction on Protein Degradation Pathways in Muscle Atrophy Induced by Hindlimb Unloading

Naoto Fujita,¹ Shinichiro Murakami,^{1,2} and Hidemi Fujino¹

¹ Department of Rehabilitation Science, Graduate School of Health Sciences Kobe University, 7-10-2 Tomogaoka, Suma-Ku, Kobe 654-0142, Japan

² Department of Physical Therapy, Himeji Dokkyo University, 7-2-1 Kamiono, Himeji 670-8524, Japan

Correspondence should be addressed to Hidemi Fujino, fujino@phoenix.kobe-u.ac.jp

Received 20 May 2011; Revised 1 August 2011; Accepted 1 August 2011

Academic Editor: J.-P. Jin

Copyright © 2011 Naoto Fujita et al. This is an open access article distributed under the Creative Commons Attribution License, which permits unrestricted use, distribution, and reproduction in any medium, provided the original work is properly cited.

High-load isometric exercise is considered an effective countermeasure against muscle atrophy, but therapeutic electrical stimulation for muscle atrophy is often performed without loading. In the present study, we investigated the combined effectiveness of electrical stimulation and high-load isometric contraction in preventing muscle atrophy induced by hindlimb unloading. Electrical stimulation without loading resulted in slight attenuation of muscle atrophy. Moreover, combining electrical stimulation with high-load isometric contraction enhanced this effect. In electrical stimulation without loading, inhibition of the overexpression of calpain 1, calpain 2, and MuRF-1 mRNA was confirmed. On the other hand, in electrical stimulation with high-load isometric contraction, inhibition of the overexpression of cathepsin L and atrogin-1 mRNA in addition to calpain 1, calpain 2, and MuRF-1 mRNA was confirmed. These findings suggest that the combination of electrical stimulation and high-load isometric contraction is effective as a countermeasure against muscle atrophy.

1. Introduction

Skeletal muscle atrophy results from a variety of conditions such as hindlimb unloading [1, 2], joint immobilization [3, 4], denervation [5, 6], and spinal cord injury [7–9]. Generally resistance exercise training is performed as an effective therapeutic intervention to prevent muscle atrophy induced by these diverse conditions. The effect of resistance exercise is known to be dependent on the intensity of muscle loading [10]. Isometric contraction exercise confers greater protection against muscle atrophy because isometric contraction is a higher-intensity activity than isotonic contraction [11, 12]. Additionally, muscle contraction using electrical stimulation has also been performed in cases in which it was impossible to perform voluntary limb movement such as denervation and spinal cord injury. Similarly to resistance exercise, the effectiveness of electrically stimulated muscle contraction is influenced by the intensity, including frequency [13, 14], number of contractions [5, 15], and chronaxie [6]. In performing different types of muscle contraction, it is

reported that electrical stimulation in isometric contraction is more effective in preventing muscle atrophy than that in isotonic contraction [7, 16].

We have investigated the effect of electrical stimulation on muscle atrophy and confirmed that electrical stimulation in isometric contraction can attenuate the decreases in muscle mass and muscle fiber cross-sectional area compared with electrical stimulation in isotonic contraction [17]. Although electrical stimulation in isometric contraction was effective in preventing muscle atrophy, it is still unclear what mechanisms underlie the beneficial effects of electrical stimulation. Three major protein degradation pathways are known to be implicated in muscle atrophy [18]: (1) the lysosomal protease pathway involving cathepsins, which were found to have increased activity in atrophied muscle [19]; (2) the calpain pathway involving calpain 1 and calpain 2, which are cytosolic calcium-dependent protease that are known to be increased in atrophied muscle [19]; (3) the ubiquitin-proteasome pathway, which involves 2 steps: conjugation of multiubiquitin moieties to the substrate and

degradation of the tagged protein by the 26S proteasome [20]. Muscle-specific ubiquitin ligases, atrogin-1/MAFbx (atrogin-1) and muscle RING finger 1 (MuRF-1), were found to be overexpressed in atrophied muscle [18]. If the relative contributions of the above-mentioned 3 major pathways to enhanced effectiveness of electrical stimulation on muscle atrophy by combined high-load isometric contraction can be verified, this will help establish muscle-specific therapeutic system. The purpose of the present study was to investigate the combined effect of electrical stimulation and high-load isometric contraction to prevent muscle atrophy with a focus on the 3 major protein degradation pathways.

2. Materials and Methods

2.1. Experimental Groups. Twenty-one adult male Wistar rats (Japan SLC, Shizuoka, Japan), weighing 282–301 g, were used in the present study. The animals were randomly divided into 4 groups: (1) control (Cont, $n = 7$), (2) hindlimb unloading (HU, $n = 7$), (3) hindlimb unloading plus electrical stimulation (ES, $n = 7$), and (4) hindlimb unloading plus the combination of electrical stimulation and high-load isometric contraction (ES + IM, $n = 7$) groups. This study was approved by the Institutional Animal Care and Use Committee and carried out according to the Kobe University Animal Experimentation Regulation. All experiments were conducted in accordance with the National Institute of Health (NIH) Guidelines for the Care and Use of Laboratory Animals (National Research Council, 1996).

2.2. Hindlimb Unloading. Hindlimb unloading was induced in animals by suspending their tails for 14 days, according to the method described by Morey et al. [21]. Briefly, each animal in the HU, ES, and ES + IM groups was fitted with a tail harness and was suspended by a string just high enough to prevent the hindlimbs from bearing weight on the floor or sides of the cage. The forelimbs were allowed to maintain contact with the floor of the cage, and the animals had full access to food and water. The animals in each group were housed in an isolated and environmental controlled room at $22 \pm 2^\circ\text{C}$ in a 12 h : 12 h light-dark cycle.

2.3. Electrical Stimulation Protocol. Electrical stimulation began the day after hindlimb unloading and continued for 13 consecutive days. The animals in the ES and ES + IM groups were anesthetized by an intraperitoneal injection of pentobarbital sodium, 40 mg/kg body weight, during electrical stimulation. The animals in the Cont and HU groups were anesthetized at the same frequency as the ES and ES + IM groups to exclude the influence of the anesthetic. Electrical stimulation equipment (SEN-3301; Nihon Kohden, Tokyo, Japan) that permitted changes in the electrical parameters was used to treat the tibialis anterior muscle percutaneously. Two surface electrodes were used to stimulate the tibialis anterior muscle. One electrode (5 cm in diameter) was positioned on the animal's back, and the other active electrode (3 mm in diameter) was adhered on the motor point of the tibialis anterior muscle. During the

electrical stimulation, the active electrode was maintained in contact with the skin overlying the tibialis anterior muscle perpendicular to the muscle fibers. The stimulation was a positive square wave with a pulse width of 0.1 ms, and the stimulation pulse amplitude was maintained at 4 mA. Each pulse was delivered at a frequency of 100 Hz. During the electrical stimulation, 1 s pulses were delivered every 3 s (time on: 1 s; time off: 2 s) for 1 min, followed by 5 min of rest. Six consecutive stimulation sessions were performed twice in a day, separated by a 9 h interval. This resulted in a total stimulation duration of 240 s in a day. In animals that underwent electrical stimulation, that is, ES group, the right tibialis anterior muscle was stimulated without ankle joint fixation to cause an isotonic contraction. Conversely, in the ES + IM group, the left ankle joint was fixed at 90° in a removable plaster cast during the electrical stimulation to cause high-load isometric contraction. In the rest time between sessions, the plaster cast was removed from the limb.

2.4. Sample Preparation and Histological Analysis. Twelve hours after the last stimulation, all animals were deeply anesthetized by an intraperitoneal injection of sodium pentobarbital, 50 mg/kg body weight, and then the tibialis anterior muscle was removed and weighed. Thereafter, the animals were sacrificed by an overdose of sodium pentobarbital. Isolated parts from the muscle sample (~ 15 mg) were kept in RNAlater solution (Ambion, Austin, Tex, USA) for total RNA isolation. The remaining muscle samples were immediately frozen in acetone, cooled in dry ice, and stored at -80°C until histological and western blot analysis.

Serial transverse sections of $10\ \mu\text{m}$ thickness were cut on a cryostat (CM-1510S; Leica Microsystems, Mannheim, Germany) from the middle part of the muscle belly in the tibialis anterior muscle at -25°C and mounted on glass slides. The sections were then stained for myofibrillar adenosine triphosphatase (ATPase) at pH 4.4 preincubation to categorize the muscle fiber as type I, IIA, or IIB on the basis of a previous study [22]. The sections stained by ATPase were used to determine the composition of muscle fiber types and to measure cross-sectional areas of each muscle fiber type. The sections were also stained for succinate dehydrogenase (SDH). Each muscle fiber was matched for ATPase and SDH stains, and fibers found to be lightly stained with ATPase and those darkly stained with SDH were omitted from the measurement of muscle fiber cross-sectional area. A measuring field was set over the entire muscle cross-section for the determination of muscle fiber type composition. At least 100 randomly selected cross-sectional areas of each muscle fiber type were investigated. The sections were measured using the ImageJ software program (NIH, Maryland, USA).

2.5. Western Blot Analysis. The frozen muscle samples were homogenized in ice-cold homogenizing buffer containing 20 mM Tris-HCl, pH 7.4, 25 mM KCl, 5 mM EDTA, 5 mM EGTA, 1 mM Dithiothreitol, and protease inhibitor cocktail (Nacalai tesque, Kyoto, Japan). The homogenates were centrifuged at 15,000 g for 25 min at 4°C . Total protein

TABLE 1: Body weight (g), wet weight (mg) of the tibialis anterior muscle, and ratio of wet weight to body weight (mg/g).

	Cont	HU	ES	ES + IM
Body weight, g	308 ± 3	246 ± 5*	238 ± 3*	238 ± 3*
Muscle wet weight, mg	539 ± 6	418 ± 4*	429 ± 12*	478 ± 12*†‡
Muscle wet weight to body ratio, mg/g	1.74 ± 0.02	1.70 ± 0.02	1.79 ± 0.03	2.00 ± 0.02*†‡

Values are the mean ± SEM. Cont: control group ($n = 14$); HU: hindlimb unloading for 14 days group ($n = 14$); ES: hindlimb unloading plus electrical stimulation group ($n = 7$); ES + IM: hindlimb unloading plus the combination of electrical stimulation and isometric contraction group ($n = 7$). *, †, and ‡ are significantly different from the Cont, HU, and ES groups, respectively, at $P < 0.05$.

concentration was determined by the use of a protein determination kit (BioRad, Calif, USA). The homogenates were solubilized in sample loading buffer containing 50 mM Tris-HCl, pH 6.8, 2% sodium dodecyl sulfate, 10% glycerol, 5% β -mercaptoethanol, and 0.005% bromophenol blue. The samples were boiled for 5 min at 60°C. Twenty micrograms of sample protein was subjected to SDS-PAGE and then transferred to PVDF membrane. Following overnight blocking step in 0.3% skimmed milk in PBST, the membranes were incubated with anticathepsin L (Abcam, Tokyo, Japan), anti-calpain 1 (Cell Signaling, Danvers, Mass, USA), anti-calpain 2 (Cell Signaling, Danvers, Mass, USA), and antiubiquitin (Stressgen, Plymouth Meeting, Pa, USA) at 4°C. Following overnight incubation, the membranes were incubated for 60 min at room temperature with anti-rabbit or anti-mouse IgG conjugated to horseradish peroxidase (GE Healthcare, Amersham, NJ, USA). The signals were detected using a chemiluminescent (ECL plus, GE Healthcare, Amersham, NJ, USA) and analyzed with an image reader (LAS-1000, Fujifilm, Tokyo, Japan).

2.6. Real-Time Quantitative Polymerase Chain Reaction (qPCR) Analysis. Total RNA was extracted from ~10 mg of each muscle using an extraction kit (QuickGene RNA tissue kit SII; Fujifilm, Tokyo, Japan). Reverse transcription was carried out using the High Capacity cDNA Archive Kit (Applied Biosystems, Foster City, Calif, USA), and then cDNA samples were stored at -20°C.

Expression levels of cathepsin L (Rn00565793_m1), calpain 1 (Rn00569689_m1), calpain 2 (Rn00567422_m1), atropin-1 (Rn00591730_m1), and MuRF-1 (Rn00590197_m1) mRNA were quantified by TaqMan Gene Expression Assays (Applied Biosystems). Each TaqMan probe and primer set was validated by performing qPCR with a series of cDNA template dilutions to obtain standard curves of threshold cycle time against relative concentration using the normalization gene 18S. qPCR was performed using PCR Fast Universal Master Mix (Applied Biosystems) in a MicroAmp 96-well reaction plate. Each well contained 1 μ L cDNA template, 10 μ L PCR Fast Master Mix, 8 μ L RNase-free water, and 1 μ L TaqMan Gene Expression Assays in a reaction volume of 20 μ L. All samples and nontemplate control reactions were performed in a 7500 Fast Sequence Detection System (Applied Biosystems) at 50°C for 2 min, 95°C for 10 min, followed by 40 cycles at 95°C for 15 s and 60°C for 1 min.

2.7. Statistical Analysis. The data are expressed as mean ± SEM. Significant differences between the 4 experimental

groups were analyzed using one-way analysis of variance followed by Tukey HSD post hoc test. Statistical significance was set at $P < 0.05$.

3. Results

3.1. Muscle Wet Weight. Body weight, muscle wet weight, and ratio of muscle wet weight to body weight are shown in Table 1. The values of body weight in the HU, ES, and HU+IM groups were significantly lower than that in the Cont group. The values of muscle wet weight in the HU, ES, and ES+IM groups were significantly lower than that in the Cont group. The value of muscle wet weight in the ES + IM group was significantly larger than that in the HU group, whereas there was no significant difference between the ES and HU groups. The value of muscle wet weight in the ES + IM group was significantly larger than that in the ES group. For the ratio of muscle wet weight to body weight, the value in the ES + IM group was significantly larger than that in the HU and ES groups.

3.2. Muscle Fiber Cross-Sectional Area. ATPase staining revealed that the tibialis anterior muscles were composed of type I (0.3–2.2%), type IIA (3.4–5.8%), and type IIB (92.4–96.2%) fibers (Figure 1), and there were no significant differences between the 4 groups. The sections in the ES and ES + IM groups did not have any histological signs of skeletal muscle injury.

The mean values of the cross-sectional area of the type I fibers in the HU and ES groups were significantly less than that in the Cont group, whereas there were no significant differences between the Cont and ES + IM groups (Figure 2(a)). The values in the ES and ES + IM groups were significantly larger than that in the HU group. The value in the ES + IM group was significantly larger than that in the ES group. In both the type IIA (Figure 2(b)) and IIB (Figure 2(c)) fibers, the mean fiber cross-sectional area values in the HU, ES, and ES + IM groups were significantly less than that in the Cont group. The mean values in the ES and ES + IM groups were significantly larger than that in the HU group, and the mean value in the ES + IM group was significantly larger than in the ES group.

3.3. Lysosomal Protease Pathway. For the expression level of cathepsin L protein, there were no significant differences between the 4 groups (Figure 3(a)). However, the expression level of cathepsin L mRNA in the HU group was increased by 2.25 ± 0.19 -fold compared with the Cont group

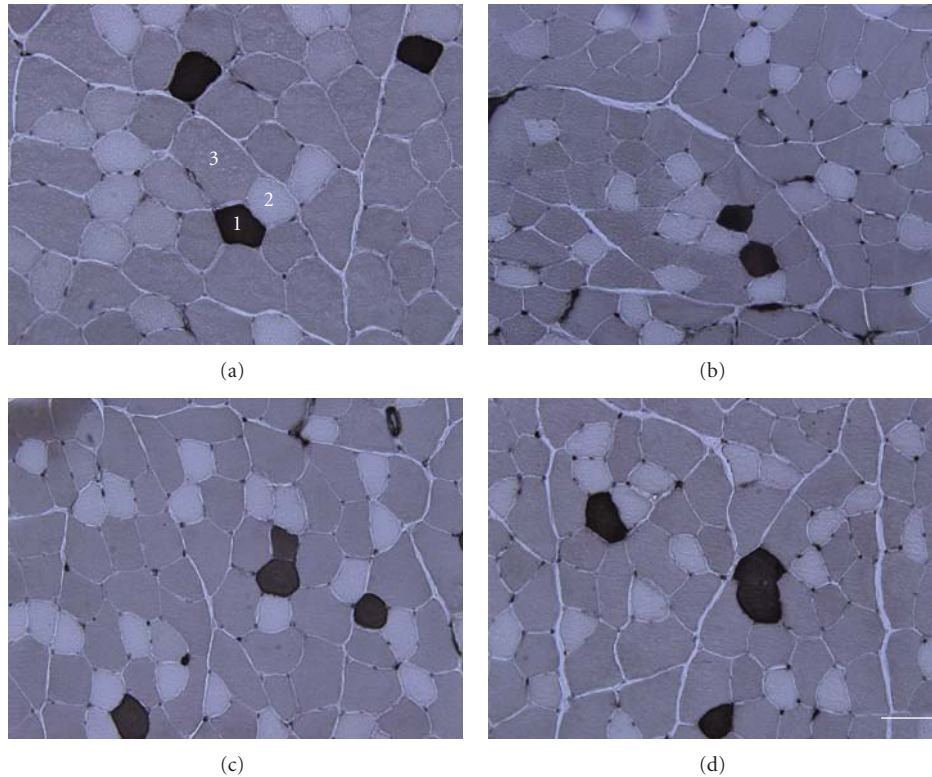


FIGURE 1: Transverse sections of the tibialis anterior muscle pretreated at pH 4.4 were assayed for myofibrillar ATPase staining. (a) Cont group; (b) HU group; (c) ES group; (d) ES + IM group. 1: type I; 2: type IIA; 3: type IIB. Bar = 50 μm .

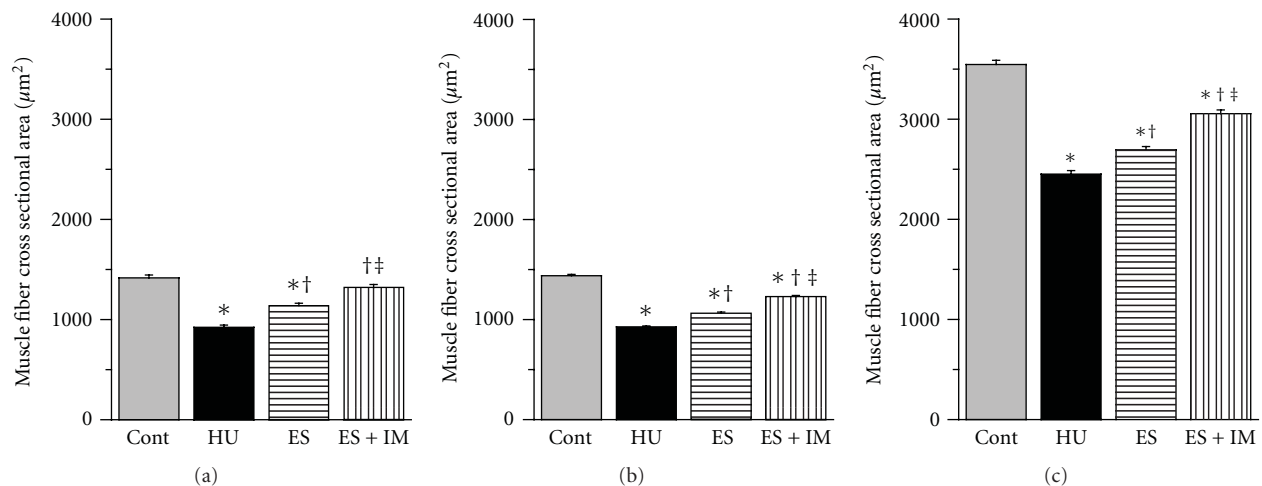


FIGURE 2: Cross-sectional area (μm^2) of type I (a), type IIA (b), and type IIB (c) fibers in the tibialis anterior muscle. Values are presented as the mean \pm SEM. *, †, and ‡ are significantly different from the Cont, HU, and ES groups, respectively, at $P < 0.05$. In each muscle fiber type, over 100 muscle fibers were measured.

(Figure 4(a)). There were no significant differences between the ES and HU groups. In contrast, the value in the ES + IM group was significantly less than that in the HU and ES groups and was maintained at the control group level.

3.4. Calpain Pathway. For the expression level of calpain 1 (Figure 3(b)) and calpain 2 (Figure 3(c)) proteins, the values

in the HU group were significantly higher than that in the Cont group. The values in the ES and ES + IM groups were significantly less than that in the HU group. However, there were no significant differences between the ES and ES + IM groups.

The expression levels of calpain 1 (Figure 4(b)) and calpain 2 (Figure 4(c)) mRNA in the HU group increased by

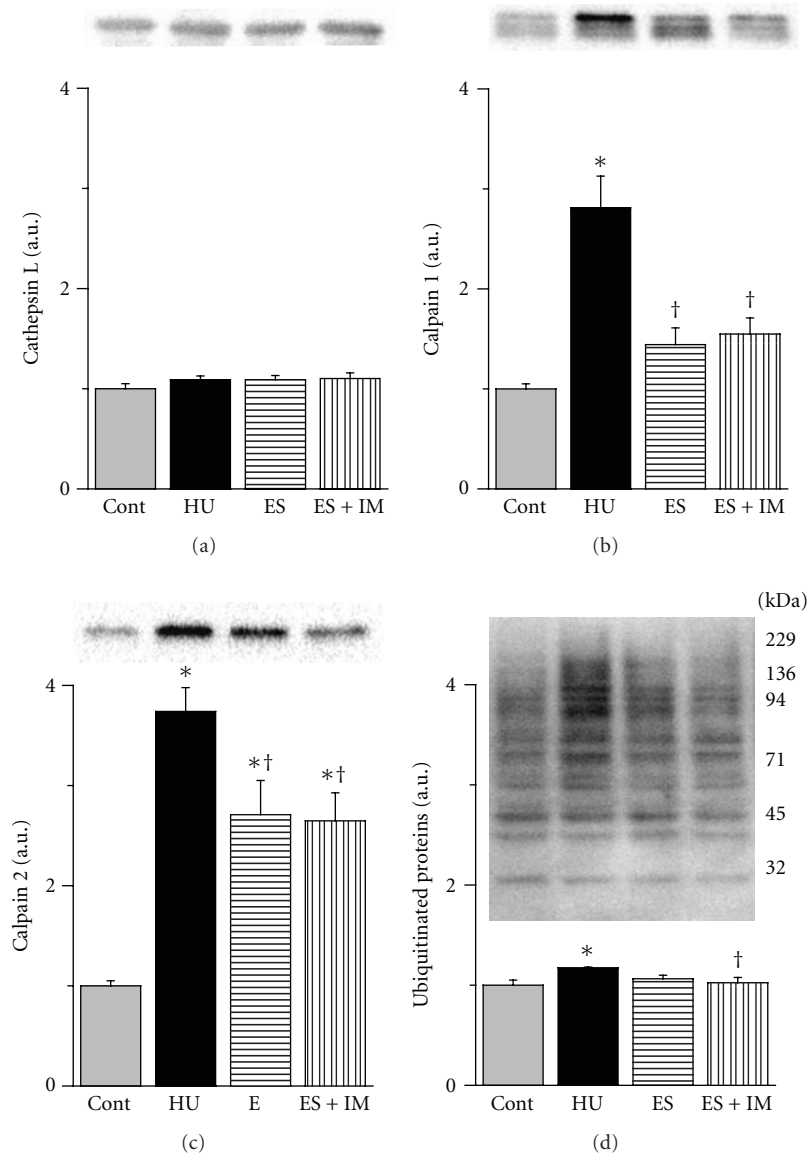


FIGURE 3: Expression levels of cathepsin L (a), calpain 1 (b), calpain 2 (c), and ubiquitinated proteins (d) in the tibialis anterior muscle and representative western blot. Values were calculated as the fold changes relative to the Cont and presented as the mean \pm SEM. * and † are significantly different from the Cont and HU groups, respectively, at $P < 0.05$. $N = 14$ in the Cont and HU groups, $n = 7$ in the ES and ES + IM groups.

1.28 ± 0.09 -fold and 2.5 ± 0.21 -fold compared with the Cont group, respectively. The levels of both calpain 1 and calpain 2 mRNA in the ES and ES + IM groups were significantly less than that in the HU. There were no significant differences between the ES and ES + IM groups.

3.5. Ubiquitin-Proteasome Pathway. For the expression level of ubiquitinated proteins, the value in the HU group was significantly higher than that in the Cont group (Figure 3(d)). Although there were no significant differences between the ES and HU groups, the value in the ES + IM group was significantly less than that in the HU group.

The expression level of atrogin-1 mRNA in the HU group increased by 2.71 ± 0.37 -fold compared with the Cont group (Figure 4(d)). Although there were no significant differences between the ES and HU groups, the value in the ES + IM group was significantly less than that in the HU group. The value in the ES + IM group appeared to be less than that in the ES group ($P = 0.0514$) and was maintained at the control group level. The expression level of MuRF-1 (Figure 4(e)) mRNA in the HU group increased by 1.83 ± 0.29 -fold compared with the Cont group. The values in the ES and ES + IM groups were significantly less than that in the HU group. There were no significant differences among the Cont, ES, and ES + IM groups.

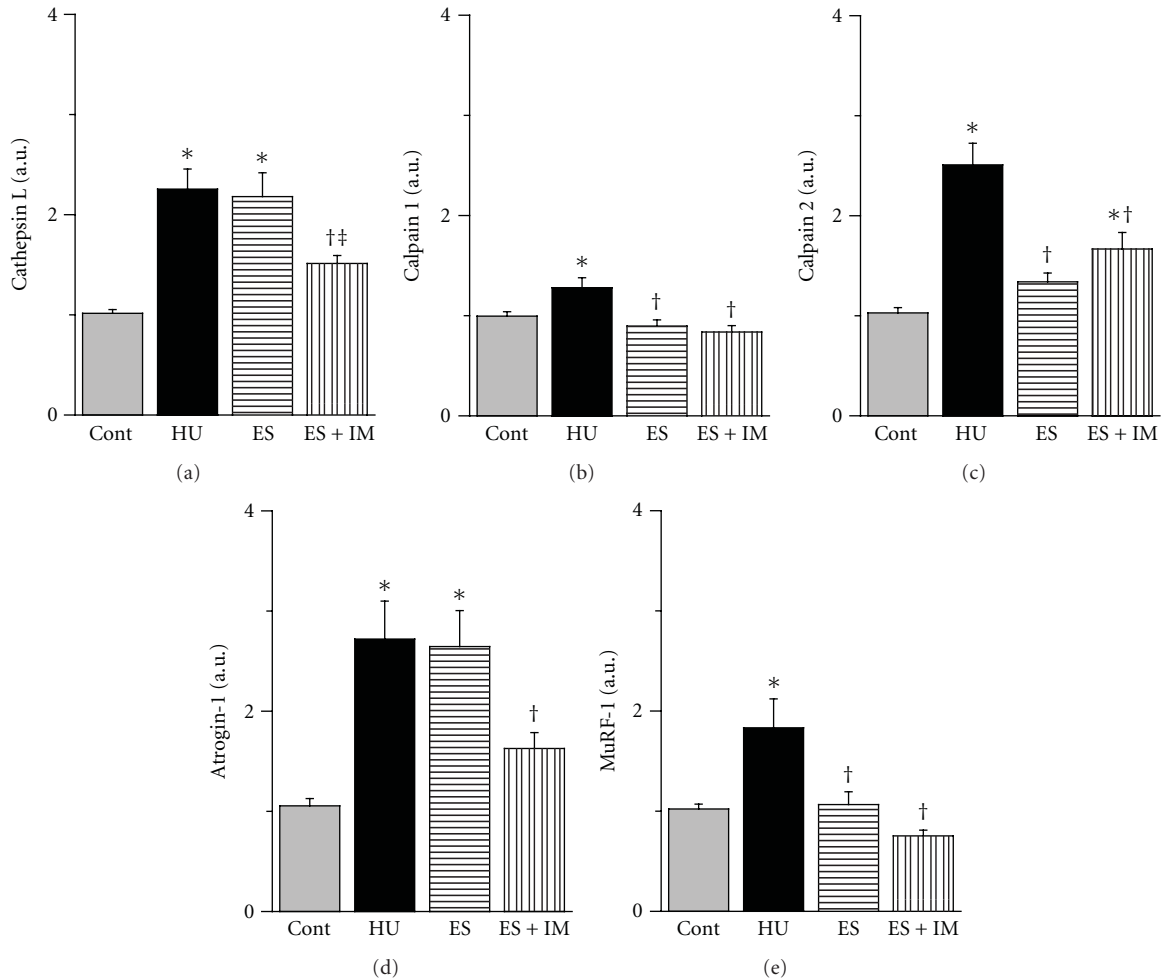


FIGURE 4: Expression levels of cathepsin L (a), calpain 1 (b), calpain 2 (c), atrogin-1/MAFbx (atrogin-1; d), and muscle RING finger-1 (MuRF-1; e) mRNA in the tibialis anterior muscle. Values were calculated as the fold changes relative to the Cont and presented as the mean \pm SEM. *, †, and ‡ are significantly different from the Cont, HU, and ES groups, respectively, at $P < 0.05$. $N = 14$ in the Cont and HU groups, $n = 7$ in the ES and ES + IM groups.

4. Discussion

In the present study, hindlimb unloading resulted in muscle atrophy of the tibialis anterior. Skeletal muscle atrophy is characterized by decreased protein synthesis and increased protein degradation. The decrease in protein synthesis reaches a peak within a few days after the start of unloading, whereas the increase in protein degradation reaches a peak 14 days after unloading [23]. Because hindlimb unloading was applied for 14 days in the present study, it was hypothesized that the increase in protein degradation was related closely rather than the decrease in protein synthesis to the atrophied tibialis anterior muscle. Three major protein degradation pathways are implicated in skeletal muscle atrophy resulting from a variety of disuse conditions (e.g., hindlimb unloading, immobilization, denervation, and spinal cord injury): the lysosomal protease pathway, the cytosolic calcium-dependent calpain pathway, and the ubiquitin-proteasome pathway [18]. In the present study, the expression level of

cathepsin L mRNA, one of the lysosomal proteases induced by hindlimb unloading [19], was increased by 2.25-fold in the HU group. Furthermore, hindlimb unloading evoked the overexpression of calpain 1 (1.28-fold) and calpain 2 (2.5-fold) mRNA. As for skeletal muscle atrophy-related ubiquitin ligases, the levels of atrogin-1 and MuRF-1 mRNA were increased by 2.71-fold and 1.83-fold, respectively, with hindlimb unloading. Therefore, it can be postulated that the decreases in muscle mass and muscle fiber cross-sectional areas in all types in the HU group were due to the activation of the 3 major protein degradation pathways.

Electrical stimulation in isotonic contraction in the ES group attenuated the decrease in the cross-sectional areas in all muscle fiber types induced by hindlimb unloading. Almost all results in the present study were consistent with those of Boonyarom et al. [14]. In the present study, the electrical stimulation in isotonic contraction was performed percutaneously during hindlimb unloading for 14 days. The inhibition of overexpression of calpain 1, calpain 2, and

MuRF-1 mRNA in the ES group may have contributed to the attenuation of muscle atrophy observed. However, the preventive effect of electrical stimulation on muscle atrophy in the ES group was not enough compared with the ES + IM group. Taillandier et al. [19] have reported that the inhibition of the calpain pathway failed to suppress protein degradation in atrophied muscle by unloading. In addition, the assembly and scaffolding of myofibrillar proteins such as nebulin, titin, and vinculin is known as calpains substrates [24], and the calpains are unable to degrade actin and myosin [25]. Because the most abundant proteins in muscle fiber are actin and myosin [18], the inhibition of calpains in atrophied muscle may have only a very little effect on the cross-sectional area of muscle fiber. Therefore, though this is just our speculation, the effect of electrical stimulation on muscle atrophy in the ES group was likely not based on the diminished expression of calpains mRNA, but that of MuRF-1.

The combination of electrical stimulation and high-load isometric contraction in the ES + IM group was more effective in preventing muscle atrophy than electrical stimulation in isotonic contraction in the ES group. Although the expression of ubiquitinated proteins in the ES group was of the same level as the HU group, the value in the ES + IM group was significantly less than that in the HU group. In the ES + IM group, there was inhibition of overexpression of cathepsin L and atrogen-1 mRNA in addition to calpain 1, calpain 2, and MuRF-1. Collectively, these results were contributive to the enhanced effect of electrical stimulation on muscle atrophy. However, it is reported that cathepsins are unable to degrade myofibrillar proteins; their major substrates are membrane proteins such as receptors, ligands, channels, and transporters [26]. Additionally, some studies have reported that, when lysosomal activity is inhibited, myofibrillar protein degradation rates are only slightly reduced [27, 28]. Therefore, the major factor underlying the enhanced preventive effect on muscle atrophy in the ES + IM group might not be diminished cathepsin L mRNA expression. Many previous studies have indicated that protein degradation during unloading occurs principally through the ubiquitin-proteasome pathway [18, 29, 30]; with respect to the ubiquitin-proteasome pathway in the ES + IM group, not only overexpression of MuRF-1 mRNA but also that of atrogen-1 was inhibited. Previous studies with MuRF-1 knockout mice have shown that the decrease in the muscle fiber cross-sectional area induced by hindlimb unloading [31] and denervation [32] were unable to prevent completely. Furthermore, Bodine et al. [33] compared atrogen-1 knockout and MuRF-1 knockout mice to show that the preventive effect on muscle atrophy is prominent in atrogen-1 knockout rather than in MuRF-1 knockout [33]. Therefore, there is a possibility that the differences between the ES and ES + IM groups are due to whether overexpression of both atrogen-1 and MuRF-1 mRNA was inhibited. However, this is just speculation, so there is a need for further study to show the evidence supporting this speculation.

5. Conclusion

Although electrical stimulation in isotonic contraction slightly attenuated muscle atrophy induced by hindlimb

unloading, the combination of electrical stimulation and high-load isometric contraction inhibited increases in all 3 protein degradation pathways linked to muscle atrophy and enhanced the effect of electrical stimulation to prevent muscle atrophy. Electrical stimulation in isotonic contraction attenuated only MuRF-1 mRNA overexpression, whereas the combination of electrical stimulation and high-load isometric contraction inhibited both atrogen-1 and MuRF-1 mRNA overexpression. The result of the electrical stimulation in isotonic contraction in this study is consistent with that of a previous study [34]. Macpherson et al. [34] investigated the effect of electrical stimulation in isotonic contraction on expression of the ubiquitin ligases in denervated muscle and showed that overexpression of MuRF-1 mRNA is relatively more inhibited than that of atrogen-1. Therefore, the findings of the present study suggest that when high-load isometric contraction is added to electrical stimulation, overexpression of not only MuRF-1 mRNA but also atrogen-1 is inhibited during unloading. It is still unknown what the differences are between the roles of atrogen-1 and MuRF-1 in the ubiquitin-proteasome pathway, and this requires further study. However, the combination of electrical stimulation and high-load isometric contraction is promising as an effective therapeutic intervention.

Acknowledgments

This study was supported by The Japanese Society of Physio Therapeutics and Grants-in-Aid for Scientific Research from the Japanese Ministry of Education, Culture, Sports, Science, and Technology.

References

- [1] H. Fujino, A. Ishihara, S. Murakami et al., "Protective effects of exercise preconditioning on hindlimb unloading-induced atrophy of rat soleus muscle," *Acta Physiologica*, vol. 197, no. 1, pp. 65–74, 2009.
- [2] I. Takeda, H. Fujino, S. Murakami, H. Kondo, F. Nagatomo, and A. Ishihara, "Thermal preconditioning prevents fiber type transformation of the unloading induced-atrophied muscle in rats," *Journal of Muscle Research and Cell Motility*, vol. 30, no. 3-4, pp. 145–152, 2009.
- [3] N. Fujita, T. Fujimoto, H. Tasaki, T. Arakawa, T. Matsubara, and A. Miki, "Influence of muscle length on muscle atrophy in the mouse tibialis anterior and soleus muscles," *Biomedical Research*, vol. 30, no. 1, pp. 39–45, 2009.
- [4] N. Fujita, T. Arakawa, T. Matsubara, H. Ando, and A. Miki, "Influence of fixed muscle length and contractile properties on atrophy and subsequent recovery in the rat soleus and plantaris muscles," *Archives of Histology and Cytology*, vol. 72, no. 3, pp. 151–163, 2009.
- [5] D. E. Dow, P. S. Cederna, C. A. Hassett, T. Y. Kostrominova, J. A. Faulkner, and R. G. Dennis, "Number of contractions to maintain mass and force of a denervated rat muscle," *Muscle and Nerve*, vol. 30, no. 1, pp. 77–86, 2004.
- [6] T. L. Russo, S. M. Peviani, C. M. Freria, D. Gigo-Benato, S. Geuna, and T. F. Salvini, "Electrical stimulation based on chronaxie reduces atrogen-1 and myod gene expressions in

- denervated rat muscle," *Muscle and Nerve*, vol. 35, no. 1, pp. 87–97, 2007.
- [7] R. R. Roy, H. Zhong, J. A. Hodgson et al., "Influences of electromechanical events in defining skeletal muscle properties," *Muscle and Nerve*, vol. 26, no. 2, pp. 238–251, 2002.
- [8] S. J. Kim, R. R. Roy, H. Zhong et al., "Electromechanical stimulation ameliorates inactivity-induced adaptations in the medial gastrocnemius of adult rats," *Journal of Applied Physiology*, vol. 103, no. 1, pp. 195–205, 2007.
- [9] S. J. Kim, R. R. Roy, J. A. Kim et al., "Gene expression during inactivity-induced muscle atrophy: effects of brief bouts of a forceful contraction countermeasure," *Journal of Applied Physiology*, vol. 105, no. 4, pp. 1246–1254, 2008.
- [10] K. J. Milne and E. G. Noble, "Exercise-induced elevation of HSP70 is intensity dependent," *Journal of Applied Physiology*, vol. 93, no. 2, pp. 561–568, 2002.
- [11] R. H. Fitts, "Effects of regular exercise training on skeletal muscle contractile function," *American Journal of Physical Medicine and Rehabilitation*, vol. 82, no. 4, pp. 320–331, 2003.
- [12] J. E. Hurst and R. H. Fitts, "Hindlimb unloading-induced muscle atrophy and loss of function: protective effect of isometric exercise," *Journal of Applied Physiology*, vol. 95, no. 4, pp. 1405–1417, 2003.
- [13] A. Misawa, Y. Shimada, T. Matsunaga, and K. Sato, "The effects of therapeutic electric stimulation on acute muscle atrophy in rats after spinal cord injury," *Archives of Physical Medicine and Rehabilitation*, vol. 82, no. 11, pp. 1596–1603, 2001.
- [14] O. Boonyarom, N. Kozuka, K. Matsuyama, and S. Murakami, "Effect of electrical stimulation to prevent muscle atrophy on morphologic and histologic properties of hindlimb suspended rat hindlimb muscles," *American Journal of Physical Medicine and Rehabilitation*, vol. 88, no. 9, pp. 719–726, 2009.
- [15] R. G. Dennis, D. E. Dow, and J. A. Faulkner, "An implantable device for stimulation of denervated muscles in rats," *Medical Engineering and Physics*, vol. 25, no. 3, pp. 239–253, 2003.
- [16] F. Haddad, G. R. Adams, P. W. Bodell, and K. M. Baldwin, "Isometric resistance exercise fails to counteract skeletal muscle atrophy processes during the initial stages of unloading," *Journal of Applied Physiology*, vol. 100, no. 2, pp. 433–441, 2006.
- [17] N. Fujita, S. Murakami, T. Arakawa, A. Miki, and H. Fujino, "The combined effect of electrical stimulation and resistance isometric contraction on muscle atrophy in rat tibialis anterior muscle," *Bosnian Journal of Basic Medical Sciences*, vol. 11, no. 2, pp. 74–79, 2011.
- [18] R. W. Jackman and S. C. Kandarian, "The molecular basis of skeletal muscle atrophy," *American Journal of Physiology—Cell Physiology*, vol. 287, no. 4, pp. C834–C843, 2004.
- [19] D. Taillandier, E. Arousseau, D. Meynial-Denis et al., "Coordinate activation of lysosomal, Ca²⁺-activated and ATP-ubiquitin-dependent proteinases in the unweighted rat soleus muscle," *Biochemical Journal*, vol. 316, part 1, pp. 65–72, 1996.
- [20] M. H. Glickman and A. Ciechanover, "The ubiquitin-proteasome proteolytic pathway: destruction for the sake of construction," *Physiological Reviews*, vol. 82, no. 2, pp. 373–428, 2002.
- [21] E. R. Morey, E. E. Sabelman, R. T. Turner, and D. J. Baylink, "A new rat model simulating some aspects of space flight," *Physiologist*, vol. 22, no. 6, pp. S23–S24, 1979.
- [22] K. Punkt, A. Naupert, and G. Asmussen, "Differentiation of rat skeletal muscle fibres during development and ageing," *Acta Histochemica*, vol. 106, no. 2, pp. 145–154, 2004.
- [23] D. B. Thomason and F. W. Booth, "Atrophy of the soleus muscle by hindlimb unweighting," *Journal of Applied Physiology*, vol. 68, no. 1, pp. 1–12, 1990.
- [24] J. Huang and N. E. Forsberg, "Role of calpain in skeletal-muscle protein degradation," *Proceedings of the National Academy of Sciences of the United States of America*, vol. 95, no. 21, pp. 12100–12105, 1998.
- [25] M. G. Thompson and R. M. Palmer, "Signalling pathways regulating protein turnover in skeletal muscle," *Cellular Signalling*, vol. 10, no. 1, pp. 1–11, 1998.
- [26] R. J. Mayer, "The meteoric rise of regulated intracellular proteolysis," *Nature Reviews Molecular Cell Biology*, vol. 1, no. 2, pp. 145–148, 2000.
- [27] K. Furuno and A. L. Goldberg, "The activation of protein degradation in muscle by Ca²⁺ or muscle injury does not involve a lysosomal mechanism," *Biochemical Journal*, vol. 237, no. 3, pp. 859–864, 1986.
- [28] M. E. Tischler, S. Rosenberg, S. Satarug et al., "Different mechanisms of increased proteolysis in atrophy induced by denervation or unweighting of rat soleus muscle," *Metabolism*, vol. 39, no. 7, pp. 756–763, 1990.
- [29] S. H. Lecker, V. Solomon, W. E. Mitch, and A. L. Goldberg, "Muscle protein breakdown and the critical role of the ubiquitin-proteasome pathway in normal and disease states," *Journal of Nutrition*, vol. 129, supplement 1, pp. 227S–237S, 1999.
- [30] R. T. Jagoe and A. L. Goldberg, "What do we really know about the ubiquitin-proteasome pathway in muscle atrophy?" *Current Opinion in Clinical Nutrition and Metabolic Care*, vol. 4, no. 3, pp. 183–190, 2001.
- [31] S. Labeit, C. H. Kohl, C. C. Witt, D. Labeit, J. Jung, and H. Granzier, "Modulation of muscle atrophy, fatigue and MLC phosphorylation by MuRF1 as indicated by hindlimb suspension studies on MuRF1-KO mice," *Journal of Biomedicine and Biotechnology*, vol. 2010, Article ID 693741, 2010.
- [32] A. S. Moriscot, I. L. Baptista, J. Bogomolovas et al., "MuRF1 is a muscle fiber-type II associated factor and together with MuRF2 regulates type-II fiber trophicity and maintenance," *Journal of Structural Biology*, vol. 170, no. 2, pp. 344–353, 2010.
- [33] S. C. Bodine, E. Latres, S. Baumhueter et al., "Identification of ubiquitin ligases required for skeletal muscle atrophy," *Science*, vol. 294, no. 5547, pp. 1704–1708, 2001.
- [34] P. C. D. Macpherson, X. Wang, and D. Goldman, "Myogenin regulates denervation-dependent muscle atrophy in mouse soleus muscle," *Journal of Cellular Biochemistry*, vol. 112, no. 8, pp. 2149–2159, 2011.

Review Article

The Dystrophin-Glycoprotein Complex in the Prevention of Muscle Damage

Jessica D. Gumerson¹ and Daniel E. Michele^{1,2}

¹Department of Molecular & Integrative Physiology, University of Michigan, Ann Arbor, MI 48109, USA

²Department of Internal Medicine, University of Michigan, 7732C Medical Science II, 1301 E Catherine Street, Ann Arbor, MI 48109-0622, USA

Correspondence should be addressed to Daniel E. Michele, dmichele@umich.edu

Received 13 May 2011; Accepted 3 July 2011

Academic Editor: Robert J. Bloch

Copyright © 2011 J. D. Gumerson and D. E. Michele. This is an open access article distributed under the Creative Commons Attribution License, which permits unrestricted use, distribution, and reproduction in any medium, provided the original work is properly cited.

Muscular dystrophies are genetically diverse but share common phenotypic features of muscle weakness, degeneration, and progressive decline in muscle function. Previous work has focused on understanding how disruptions in the dystrophin-glycoprotein complex result in muscular dystrophy, supporting a hypothesis that the muscle sarcolemma is fragile and susceptible to contraction-induced injury in multiple forms of dystrophy. Although benign in healthy muscle, contractions in dystrophic muscle may contribute to a higher degree of muscle damage which eventually overwhelms muscle regeneration capacity. While increased susceptibility of muscle to mechanical injury is thought to be an important contributor to disease pathology, it is becoming clear that not all DGC-associated diseases share this supposed hallmark feature. This paper outlines experimental support for a function of the DGC in preventing muscle damage and examines the evidence that supports novel functions for this complex in muscle that when impaired, may contribute to the pathogenesis of muscular dystrophy.

1. Introduction

Skeletal muscle is a dynamic tissue that routinely undergoes a significant degree of mechanical strain and cellular deformation with each contraction. In order to preserve normal skeletal muscle function throughout the lifetime of an individual, this complex tissue must be able to routinely undergo cell shortening and generate forces required for movement while at the same time limiting mechanical cellular injury and adapting to changing workloads. In muscular dystrophy, an imbalance between muscle damage or degeneration and muscle repair through stem-cell mediated regeneration is thought to contribute to the disease pathology and consequently results in a progressive decline in muscle function [1]. Mutations in a number of distinct genes can cause muscular dystrophy with varying degrees of severity, but precisely how each can negatively affect normal muscle function is unclear [2]. A significant number of muscular dystrophies result from mutations that affect the normal assembly of the dystrophin-glycoprotein complex at the sarcolemma in muscle. A longstanding hypothesis to

explain the high degree of muscle damage and degeneration observed in dystrophic muscle is that mutations affect the function of critical structural proteins in muscle and in some way compromises the mechanical stability of the muscle fiber and/or its sarcolemma. This exacerbates the damage that occurs during normal muscle contractions and initiates a lethal cascade of events that can cause death of the myofiber [3–5]. In support of this, early studies demonstrated an increase in the number of necrotic fibers in muscles from muscular dystrophy patients that likely resulted from irreparable membrane damage as a consequence of normal muscle activity [6]. However, rather than dystrophic muscle suffering from an increased susceptibility to external damage, alternative hypotheses exist that could account for increased cell death. For example, that causative mutations may affect either the resting homeostasis of muscle cells or alter the ability of the muscle to adapt and repair following a normal “dose” of muscle injury. Although the importance of the dystrophin-glycoprotein complex in maintaining sarcolemma integrity is well supported, alternative functions

for this complex have been proposed through the years and are now gaining significant experimental support [7, 8].

2. The Dystrophin-Glycoprotein Complex

The dystrophin-glycoprotein complex (DGC) is composed of several transmembrane and peripheral components and is highly expressed in the sarcolemma of skeletal muscle [9–11]. Mutations in genes that encode DGC components lead to the loss of either expression and/or function of the DGC in muscle. Dystroglycan is a protein central to this complex that spans the sarcolemma and binds to ligands in the surrounding basal lamina through α -dystroglycan and to dystrophin inside the cell through β -dystroglycan [12]. Dystrophin in turn binds to the submembrane actin and intermediate filament cytoskeleton within fibers, thereby completing a link between the cytoskeleton and the extracellular matrix [13, 14]. Costameres are concentrations of extracellular matrix receptor complexes that reside at the membrane in register with the Z-lines of sarcomeres within muscle fibers. The location of the DGC at costameres and the identification of its function as a link between the matrix and the cytoskeleton has led to the hypothesis that the DGC might be critical in mechanically stabilizing muscle or the sarcolemma during muscle contraction [12, 15].

In addition to dystroglycan and dystrophin, the core of this complex in skeletal muscle is also formed by four sarcoglycans (α , β , γ , and δ) and sarcospan, which are thought to contribute to stabilization of the complex within the sarcolemma. Mutations in either dystrophin or the sarcoglycans are associated with reduced expression or incomplete formation of the DGC [16–18] and are hypothesized to result in muscular dystrophy through a common mechanism which includes a reduction in dystroglycan function. Therefore, reduction in the connections between the cytoskeleton and the extracellular matrix appears critical to muscular dystrophies associated with the DGC.

In addition to primary mutations in DGC components, several causative mutations have also been identified in a group of glycosyltransferases, which have been shown to function in a common pathway to glycosylate α -dystroglycan. This O-linked glycosylation of α -dystroglycan is essential for enabling α -dystroglycan to function as an extracellular matrix receptor [19]. In these glycosylation-deficient muscular dystrophies, dystroglycan and the DGC are expressed and intact at the sarcolemma, but the loss of the ability of dystroglycan to bind laminin is sufficient to cause muscular dystrophy [20, 21]. These findings highlight specifically the interaction of the DGC with extracellular matrix as a critical function of the DGC in preventing muscular dystrophy.

In the dystroglycan glycosylation-deficient mice (LARGE^{myd}) electron microscopic analysis showed that the interaction of dystroglycan with laminin in the extracellular matrix appeared to tightly anchor the basal lamina to the sarcolemma [21]. This tight and regular interaction of dystroglycan with the basal lamina is proposed to protect the sarcolemma from expansion of small ruptures during mechanical activity. Mutations in dystroglycan

itself appear to be quite rare in humans, perhaps related to an essential role of dystroglycan in early development [22]. Only recently has a mutation in the dystroglycan gene been identified in muscular dystrophy patients and like previous glycosyltransferase mutations, the mutation appears to impair dystroglycan glycosylation and causes loss of function without impacting dystroglycan expression [23].

The heterotrimeric protein laminin-211 is a major component of the basal lamina surrounding adult muscle fibers that is bound by glycosylated α -dystroglycan (α -DG). Mutations in the *LAMA2* gene result in loss of laminin $\alpha 2$ expression and the most common form of congenital muscular dystrophy [24–26]. The identification of laminin $\alpha 2$ mutations only further reinforces the notion that any disruption of the connection between the muscle fiber cytoskeleton to the extracellular matrix through the DGC, whether it be reduced expression of the DGC, reduced ability of dystroglycan to interact with laminin, or loss of laminin itself from the basal lamina, is sufficient to cause muscular dystrophy.

Despite the first genetic identification of dystrophin as a causal gene in Duchenne muscular dystrophy more than two decades ago [27] and the identification of the DGC in years following [16], whether the DGC contributes purely a mechanical role in stabilizing the sarcolemma during normal contractions or imparts other significant functions in muscle still remains an area of active investigation. The identification of additional components of the DGC, such as sarcospan, dystrobrevins, and syntrophins, that do not appear to have a direct or essential role in the mechanical function of the DGC but instead appear to be docking sites for other intracellular signaling proteins [28], has fueled considerable interest in what other intracellular pathways may be affected in DGC-associated muscular dystrophies.

3. The DGC, Sarcolemma Integrity, and Contraction-Induced Muscle Injury

Even normal skeletal muscle is susceptible to mechanical damage, particularly during lengthening contractions, and immediate defects at the level of the sarcolemma [29], the *t*-tubules [30], or the contractile machinery [31] contribute to a transient decrease in the isometric force. Following repetitive lengthening contractions, there can also be considerable, prolonged injury and muscle dysfunction that results from muscle degeneration, swelling, and infiltration of inflammatory cells [32]. In most cases, muscle dysfunction caused by prolonged injury can be fully repaired over time by active muscle fiber regeneration from resident stem cells, known as satellite cells. This suggests that occasional sarcolemmal injuries, muscle damage, and their repair might be a critical component of the homeostasis of normal muscle.

Many of the early experiments that sought to identify the mechanism by which mutations affecting the DGC cause muscular dystrophy have utilized the *mdx* mouse model [33]. These mice harbor a null mutation in the dystrophin gene and although they do exhibit the clinical features observed in human patients, the severity is milder [34]. A role for

the function of dystrophin in maintaining the integrity of the sarcolemma during muscle contraction was supported by studies showing that *mdx* muscle was highly susceptible to lengthening contraction-induced injury performed *in vitro*, as compared to healthy control muscle. Muscle from *mdx* animals demonstrated an increased tendency to take up Procion orange dye from the bathing medium, which suggested an increase in sarcolemma permeability following contraction [4, 35]. When injected into *mdx* animals, the membrane-impermeant Evans blue dye was also selectively taken up by muscle fibers that appeared necrotic and were hypercontracted, which suggested that increased membrane permeability eventually resulted in cell death [36]. This further supported the hypothesis that muscle contractions produce membrane tears, which lead to an increase in permeability of the sarcolemma to calcium and small molecules and results in a greater degree of cell death in dystrophic muscle. Muscle from *mdx* mice also demonstrated a measurable deficit in force generation following an *in vivo* lengthening contraction protocol [37, 38]. These data support a function for dystrophin and the dystrophin-glycoprotein complex, at least partially, in protecting the sarcolemma during muscle contraction and suggest that, in its absence, the sarcolemma is more susceptible to damage by contractile forces, resulting in increased permeability of ions and small molecules, and eventual cell necrosis and muscle degeneration.

Further support for a critical role of membrane integrity in muscular dystrophies was gained from a different class of muscular dystrophies associated with mutations in the dysferlin gene. Mutations in dysferlin are associated with Miyoshi myopathy and limb girdle muscular dystrophy 2B in humans [39, 40]. Dysferlin is not associated with the DGC but appears to have homology to the vesicle protein, synaptotagmin, and therefore has been predicted to be important for mediating vesicle-mediated membrane repair. While the complete functions of dysferlin are still under investigation, dysferlin has been shown to be required for rapid resealing of the sarcolemma in a calcium-dependent manner following focal membrane damage [41]. Although muscle from dysferlin-null animals is not particularly susceptible to contraction-induced damage any more so than healthy muscle [42], a recent study demonstrated that recovery of muscle following damage required an immediate and transient membrane resealing event and that dysferlin-deficient muscle consequently took longer to recover [42, 43]. The identification of dysferlin as a potential mediator of membrane repair in muscle underlies the importance of sarcolemmal integrity and its maintenance by repair pathways as important mechanisms in which defects may result in muscle degeneration.

4. Does Contraction-Induced Injury Play a Causal Role in DGC-Associated Muscular Degeneration and Dystrophy?

While the generally accepted dogma is that mutations affecting the DGC render muscle more susceptible to

contraction-induced damage during mechanical stress [44], recent evidence from our laboratory suggests that not all muscles of dystrophic animals are equally affected. We reported that, in the LARGE^{myd} animal model of glycosyltransferase-deficient muscular dystrophy, typical fast-twitch muscles such as the EDL were weaker than control WT EDL muscles. Additionally, LARGE^{myd} EDL muscles demonstrated the increased susceptibility to contraction-induced injury typical of EDL muscles of *mdx* mice, as indicated by a dramatic loss of force following lengthening contraction that was significantly greater than controls [45]. However, a remarkably different phenotype was measured in soleus muscles, which are composed of mixtures of fast and slow fibers [45]. Although the contraction protocol resulted in a 26% force deficit in WT soleus muscle, there was no greater increase in force deficit observed in the soleus of LARGE^{myd} mice. Force deficits measured in WT soleus muscle were also higher than those measured in EDL muscle after two lengthening contractions, which suggested that the observed defect was not due to inherent differences in susceptibility to injury between the two muscle groups, nor to differences in dystroglycan glycosylation or laminin binding activity. However, the soleus of LARGE^{myd} animals was still weaker than WT muscle and dystrophic, as evidenced by an increase in degenerating fibers, accumulation of inflammatory cells, and the presence of centrally nucleated fibers. An explanation that accounts for the dystrophic features and fiber degeneration in the soleus muscle in the absence of any detectable increased susceptibility to contraction-induced injury has not been addressed.

A similar lack of increased susceptibility of muscle to contraction-induced muscle damage was previously demonstrated in the soleus of *mdx* mice, and the authors speculated that dystrophin was not essential for maintaining structural stability in the soleus muscle [37]. Utrophin, a homologue of dystrophin, has been shown to be upregulated in the absence of dystrophin [46] and is also more highly expressed in slow-twitch fibers [47] which may therefore confer a degree of stability in the soleus muscle of *mdx* mice that might explain this lack of susceptibility to contraction-induced injury. However, upregulation of utrophin cannot explain the results in LARGE^{myd} mice because, other than the loss of dystroglycan glycosylation, the DGC is assembled normally in LARGE^{myd} muscle [20, 21]. We found that another important laminin receptor in muscle, $\alpha 7\beta 1$ integrin, is expressed at much higher levels in the sarcolemma of soleus muscle as compared to other fast muscles [45]. Several reports have demonstrated that when the DGC is impaired, $\alpha 7$ or $\beta 1$ integrin is upregulated, which suggests that the two receptors may have at least some overlapping functions in muscle [48]. Susceptibility to contraction-induced injury was directly compared between $\alpha 7$ integrin-null and LARGE^{myd} mice using EDL muscle and only LARGE^{myd} muscle was shown to be more susceptible to injury [21]. This might suggest that interactions with laminin and dystroglycan are more important for mechanical stability than are the interactions between $\alpha 7\beta 1$ integrin and laminin. However, $\alpha 7\beta 1$ integrin expression in fast muscle is very low, and the comparison was only shown

in fast-twitch muscle, and not in the soleus muscle, which remains to be studied. Transgenic overexpression of $\alpha7$ integrin in dystrophin/utrophin double knockout mice can significantly improve muscle disease [49], but whether this beneficial effect is due to prevention of mechanical damage or effects on cell signaling has not been fully addressed. The potential role of integrins and the DGC in laminin-dependent signaling in muscle is discussed in greater detail in Section 6.

Muscle physiological studies have also been performed in an animal model of congenital muscular dystrophy, the *dy/dy* mouse, that harbors a null mutation in the *LAMA2* gene [24]. In contrast to the results demonstrated in *mdx* mice, laminin-deficient muscle does not exhibit a defect in sarcolemmal stability [50]. Both the EDL and soleus muscles were isolated from laminin-deficient mice and subjected to a moderate lengthening contraction protocol *in vitro* and neither demonstrated an increased susceptibility to injury over that observed in control muscle. As a means to amplify potentially subtle defects in these mice, the anesthetic halothane was used to increase fluidity of the lipid bilayer. Although this did cause an increase in force deficit following a lengthening contraction protocol, this deficit was still not any greater in laminin-deficient muscle [50]. Because contraction protocols can vary, sarcolemmal permeability was directly compared between three different mouse models of DGC-related muscular dystrophy, *mdx* [33] and two deficient in laminin, *dy/dy* [24] and *dy^{2j}/dy^{2j}* [25]. Animals were injected intravenously with Evans blue dye and muscles were analyzed several hours after injection. Muscles from *mdx* demonstrated an increase in dye uptake while dye uptake in laminin-deficient muscle was not different than control animals [51]. Additionally, positively stained fibers in *mdx* mice often appeared in groups of neighboring fibers, in contrast to the few individual fibers stained in laminin-deficient muscle, which appeared necrotic. However, laminin-deficient muscle still had dystrophic pathological features, which further supports the notion that, although disruption of the sarcolemma may contribute to the pathology of muscle disease, it is not essential.

Together, these studies demonstrate that membrane damage is not required for muscle degeneration and muscular dystrophy. Although mutations that compromise DGC function can leave muscle vulnerable to membrane damage, this is not true for all muscle groups, since the soleus muscle, despite demonstrating a susceptibility to injury in healthy muscle, does not show increased susceptibility in the absence of a functional DGC. Additionally, the number of fibers that may be damaged, as evidenced by dye uptake in *mdx* fast muscles, is not sufficient to explain the dramatic loss in force generation following injury [37]. Therefore, the DGC likely possesses other cellular functions in skeletal muscle that, when impaired, contribute to muscle degeneration and the dystrophic pathology. Potential alternative pathways and their experimental support are reviewed below.

5. Role of the DGC in Altered Calcium Homeostasis

Intracellular calcium is a critical mediator of several regulatory processes in skeletal muscle [52]. In dystrophic muscle, the concentration of intracellular calcium is elevated, and several potential sources for calcium entry have now been identified (Figure 1). Early studies of *mdx* muscle demonstrated that individual fibers that showed an elevation in intracellular calcium were also necrotic, which suggested that calcium entered through membrane tears as a direct result of dystrophin loss [53, 54]. Increased intracellular calcium in *mdx* muscle was later explained by an increase in sarcolemmal permeability attributed to calcium leak and stretched-activated channels [55, 56]. Stretch-activated channels can be blocked in *mdx* mice via oral delivery of streptomycin and results in a reduction in intracellular calcium and an improvement in force production [57]. In the same study, a decrease in intracellular calcium was not observed in streptomycin-treated control animals, which suggested that the activity of these channels was somehow enhanced in the absence of dystrophin.

The transient receptor potential (TRP) channels are a diverse family of ion channels composed of multiple subunits, that have also been identified as potential mediators of altered calcium homeostasis in dystrophic muscle [58]. Several TRP channels in the canonical subfamily (TRPC) are expressed in mouse skeletal muscle and TRPC1, TRPC4, and TRPC6 were initially identified as being potentially impaired in *mdx* muscle [59]. In a later study, expression of TRPC1 was shown to be increased in *mdx* muscle and the authors speculated that its activity may be increased due to additional upregulation of caveolin-3 and src, which contribute to the translocation of this channel to the sarcolemma [60]. Similarly, a stretch-activated TRP channel in the vanilloid receptor subfamily, TRPV2, has also been shown to be more highly expressed at the sarcolemma in *mdx* muscle. Inhibition of TRPV2 using a dominant negative genetic approach resulted in a restoration of normal intracellular calcium levels and an amelioration of dystrophic pathology in *mdx* mice [61].

Although the increased resting calcium concentration observed in the cytoplasm of dystrophic muscle may be the result of increased expression or activity of calcium channels at the sarcolemma, a recent study has demonstrated that an additional source of calcium entry may be due to defects at the level of the sarcoplasmic reticulum [62]. RyR1 channels isolated from *mdx* muscle were shown to be hypernitrosylated as a potential consequence of altered nitric oxide signaling downstream of dystrophin loss. This resulted in an increased leak of calcium ions from the sarcoplasmic reticulum, and pharmacological inhibition of RyR1 was shown to reduce muscle damage in *mdx* muscle.

While several of these studies noted an improvement in muscle health following inhibition of calcium entry in animal models of muscular dystrophy, an important study recently demonstrated that elevated calcium was sufficient to cause muscle damage in the absence of a genetic basis for muscular dystrophy [63]. The overexpression of TRPC3

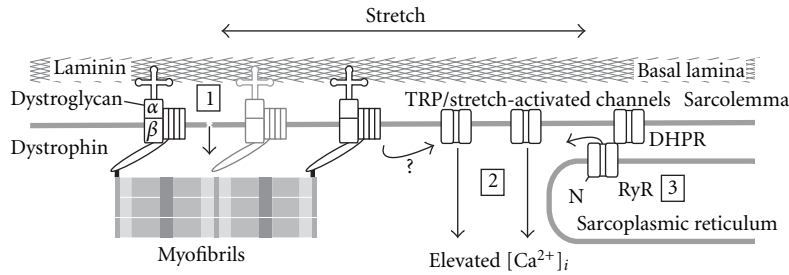


FIGURE 1: Sources of calcium entry in dystrophic muscle. (1) Disruptions to the DGC can result in instability of the sarcolemma that permits calcium entry through membrane tears when the sarcolemma is stretched during lengthening muscle contractions. (2) Activity of calcium leak, stretch-activated, and various TRP channels has been shown to be increased in dystrophin-deficient muscle and their inhibition *in vivo* can improve dystrophic pathology. (3) The ryanodine receptor has recently been shown to be hypernitrosylated in *mdx* muscle which may result in an increased leak of calcium from the sarcoplasmic reticulum.

in skeletal muscle resulted in a muscle wasting phenotype with defects similar to those observed in laminin-deficient muscle. Using gene expression profiling, this phenotype was also shown to be associated with altered expression of many genes, in a pattern that was strikingly similar to gene expression changes in δ -sarcoglycan deficient muscle. However, the muscle did not demonstrate any changes in expression of the DGC at the sarcolemma, which suggests that much of the muscle damage observed in DGC-related muscular dystrophies may be attributed to downstream defects in calcium homeostasis.

Elevated intracellular calcium can result in cellular damage in a number of ways that may underlie many of the defects observed in dystrophic muscle. When sustained, abnormal elevations in intracellular calcium can cause mitochondria to undergo permeability transition which can eventually lead to mitochondrially mediated apoptosis, involving swelling of the mitochondria, release of cytochrome *c*, and the activation of caspases [64]. Cyclophilin D is a mitochondrial enzyme that is important for regulating the mitochondrial permeability transition and genetic strategies have demonstrated that its absence renders mitochondria insensitive to calcium-induced cell death [65, 66]. Both δ -sarcoglycan-null and laminin-null mice have abnormally swollen mitochondria and the muscular dystrophy seen in both models can be partially alleviated by altering the pores mediating the mitochondrial permeability transition [67].

Another important downstream consequence of mitochondrial dysfunction is an increased production of reactive oxygen species (ROS), which can further exacerbate cellular damage [68]. Several studies have identified ROS as a potential mediator of muscle damage in the muscular dystrophies [69–71]. Antioxidant treatment of *mdx* mice has demonstrated mixed results but in some cases has lessened the symptoms of muscular dystrophy [71, 72]. In a model of muscular dystrophy not associated with DGC defects but instead caused by defective collagen IV, a component of the extracellular matrix, mitochondrial dysfunction was shown to be a major source of ROS. Additionally, when ROS production was suppressed, oxidation of myofibrillar proteins was reduced and improved contractile performance [73]. Therefore, cellular mechanisms downstream

of mitochondrial defects may be an important step in the process by which DGC mutations eventually result in myofiber damage and cause muscle disease.

Normal excitation-contraction coupling has been suggested to be affected by an increase in cellular calcium concentration and may also be an important contributor to muscle weakness in these diseases [74, 75]. Elevated calcium can also directly impair muscle function by increasing the activity of calcium-dependent proteases like calpains which can cleave myofibrillar proteins [76–78]. While the genetic and pharmacological inhibition of calpains may alleviate several pathological features in *mdx* muscle [79–81], such experiments have yielded inconsistent results and may be in part due to compensatory increases in calpain activity and/or a lack of efficacy of the proposed inhibitors [82].

Several of these studies have demonstrated that intracellular calcium is elevated in dystrophic muscle, and that this can lead to a number of deleterious effects to the cell and contribute to a decline in contractile function. More importantly, these studies have provided several alternatives by which calcium permeability and/or intracellular calcium may be increasing that are independent from direct entry of calcium through sarcolemma tears. However, it is still unclear just how distinct genetic mutations that affect the function of the DGC can alter activity of the various calcium channels that have been proposed. While inhibition of calcium entry has been shown to be beneficial in the animal models addressed, it is important to note that muscle disease was still present in these animals, albeit it to a lesser degree. This suggests that altered calcium homeostasis, whether it is through membrane tears or from altered activity of calcium channels, may not be the only mechanism downstream of genetic mutations that results in muscle damage.

6. Laminin-Dependent Intracellular Signaling through the DGC

Laminins exist as heterotrimeric proteins composed of specific combinations of α , β , and γ subunits and are differentially expressed in multiple cell types. Laminin-211 ($\alpha 2/\beta 1/\gamma 1$) is expressed in the extracellular matrix of adult skeletal muscle and is bound with high affinity by α -DG

and $\alpha 7\beta 1$ integrin. Mutations that affect $\alpha 2$ laminin, as is the case in the *dy/dy* mouse and in congenital muscular dystrophy 1A, result in muscular dystrophy as a result of lost interactions with either or both laminin receptors [24–26]. Although laminin is the major ligand of dystroglycan by which a connection is forged between the DGC and the extracellular matrix in skeletal muscle, laminin-211 deficient muscle is not susceptible to contraction-induced damage and does not typically show increased uptake of cell impermeant dye (reviewed in Section 4). Despite the lack of evidence for increased muscle damage, many fibers of laminin-deficient muscle are apoptotic [83], which is thought to significantly contribute to muscle disease. Both pharmacological and genetic inhibition of apoptosis (e.g., Bcl-2 overexpression, Bax inactivation) have been shown to ameliorate dystrophy in laminin- $\alpha 2$ -deficient animal models [84–87]. Because there appears to be a lack of sarcolemmal damage, the mechanism by which apoptosis occurs in this disease may be independent of elevations in intracellular calcium. Alternatively, increases in apoptosis may be due to disruptions in downstream cell survival signaling as a result of lost interactions between laminin and its two major receptors in skeletal muscle.

Potential increases in survival signaling through laminin receptors in muscle could be the basis for results of a recent study that demonstrated an improvement of dystrophy in *mdx* mice upon injection of soluble laminin-111, a laminin isoform not normally expressed in skeletal muscle [88]. While the mechanism of this effect is unclear, the benefit of laminin-111 injections may be due to either upregulation of $\alpha 7$ -integrin-mediated signaling or integrin-mediated stabilization of the sarcolemma [88]. However, a transgenic approach to deliver laminin-111 to skeletal muscle failed to benefit *mdx* mice [89] despite its rescue of muscular dystrophy in laminin- $\alpha 2$ -deficient muscle [90, 91]. So while laminin $\alpha 1$ and $\alpha 2$ are normally expressed in different tissues, they appear to be functionally similar in promoting muscle cell survival. Whether this important function of laminin in muscle can be targeted therapeutically in all forms of DGC-deficient muscular dystrophy is still debatable.

Integrins are formed as heterodimers of α and β subunits and the predominant alpha isoform expressed in differentiated skeletal muscle, $\alpha 7$ integrin, forms dimers with $\beta 1$ to form a laminin receptor. Mutations in $\alpha 7$ integrin result in muscular dystrophy in patients and in animal models, and a loss of $\alpha 7$ integrin in muscle has been shown to predominantly affect the structure and function of the myotendinous junction, where $\alpha 7\beta 1$ integrin is highly expressed [92–94]. $\alpha 7\beta 1$ integrin is also expressed at costameres and, similar to α -dystroglycan, can associate intracellularly with cytoskeletal proteins and may contribute to mechanical stability of the sarcolemma [48]. Animals lacking both dystrophin and $\alpha 7$ integrin display a much more severe form of muscular dystrophy than animals lacking either protein alone, which suggests that both laminin receptors may be required at the sarcolemma and can potentially compensate for one another [95]. Transgenic overexpression of $\alpha 7$ integrin can partially alleviate muscle disease in dystrophin/utrophin double knock-out mice independently of any change in expression of

DGC components [49, 96]. However, integrins are associated with a number of signaling pathways and can alter AKT and MAP kinase activity in a contraction-dependent manner [97]. Therefore, some of the improvement observed when integrins are overexpressed in dystrophic muscle may be in part due to changes in cell signaling rather than direct prevention of sarcolemma damage.

While the integrins may function as laminin-dependent signaling receptors in skeletal muscle [98], whether dystroglycan and the DGC may similarly participate in downstream signal transduction cascades is less clear. Rather than simply serving as a membrane “stabilizer”, dystrophin has also been proposed to serve as a sensor for membrane tension and function early in the development of skeletal muscle [99]. The authors of this early study proposed that this function of the DGC may be achieved through either interactions with stretch-activated cation channels or through regulation of a downstream signaling mechanism analogous to integrin signaling. Such signaling would likely be important for either growth of differentiated fibers or for mediating proliferation or fusion of satellite cells with regenerating fibers. Interestingly, when the dystroglycan gene was specifically targeted in differentiated skeletal muscle using cre-loxP-mediated recombination, the phenotype was surprisingly mild compared to other models of DGC-related muscular dystrophy [100]. The residual expression of dystroglycan in satellite cells suggested that dystroglycan might have an unappreciated role in this cell type, which could be important for either cell signaling within satellite cells or for interactions with the basal lamina [100]. However, how the DGC may be functioning in muscle regeneration is not known.

Given the critical role of laminin in promoting cell survival signaling in muscle and the existence of two possible receptors that might mediate its effects, dissecting the molecular mechanisms of each would certainly be a key advance towards understanding how disruptions can result in muscle disease. A truncated form of laminin- $\alpha 1$ was recently generated that lacks LG domains 4-5 and can prevent dystroglycan binding while retaining the LG domains necessary for laminin interactions with integrins. In contrast to full length laminin- $\alpha 1$, when this truncated laminin- $\alpha 1$ was transgenically expressed in laminin- $\alpha 2$ -deficient muscle, several fibers in select muscle groups were still apoptotic [101]. Because transgenic expression of full length laminin- $\alpha 1$ can fully rescue the *dy/dy* phenotype, this suggests that interactions between dystroglycan and laminin are also likely important for cell survival signaling. This is the first study to our knowledge that directly implicates dystroglycan in laminin dependent survival signaling in muscle *in vivo* and suggests that disruption of dystroglycan-dependent signaling may also contribute to the pathology of muscular dystrophy.

Several studies using primarily cell culture systems have shown that the DGC may be capable of participating as a scaffold for various signal transduction cascades (Figure 2). β -Dystroglycan is capable of binding multiple signaling and adaptor proteins known to be important for myoblast differentiation and cell survival signaling [102–105]. The c-terminus of β -dystroglycan contains a proline-rich region

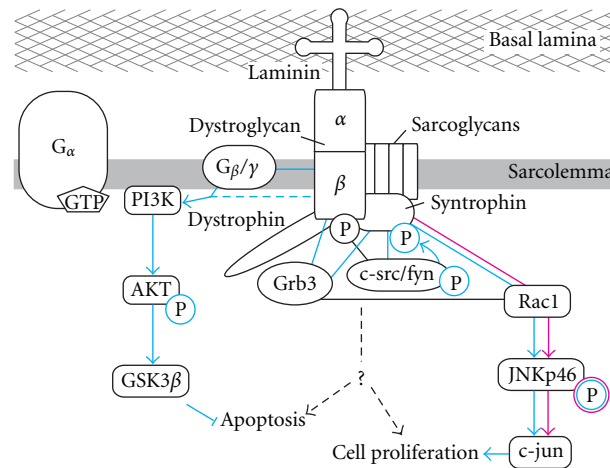


FIGURE 2: The dystrophin-glycoprotein complex may participate in laminin-dependent signaling in skeletal muscle. Interactions shown in blue indicate interactions that have been shown to be increased when laminin is bound to dystroglycan. Interactions in pink indicate those that have been shown to be increased following a muscle contraction protocol. Since the phosphorylation of β -dystroglycan can bind a number of other SH2-domain containing proteins and can also interact with Grb2, it may participate in additional signal transduction cascades that have not yet been identified. It is important to remember that in many cases, these interactions have been studied in cell culture systems and the relevance of these interactions in muscle *in vivo* has not been extensively studied.

that can bind Grb2, a well known adaptor protein [102, 106] and may be important for recruiting additional components of the MAP kinase pathway [104]. Dystroglycan can also be phosphorylated at tyrosine892 near the c-terminus of β -DG [103, 107] and may function to regulate interactions between dystrophin and caveolin-3 [107, 108]. This phosphorylation has also been shown to be adhesion dependent and enables dystroglycan to recruit several SH2-domain containing proteins, including c-Src and Fyn, to the sarcolemma [109]. In an unrelated study, these two kinases were also shown to be associated with the DGC and functioned to phosphorylate the DGC protein syntrophin [105]. In the presence of laminin, syntrophin was shown to associate with the DGC and mediate downstream Rac1 signaling that led to increased activity of c-jun. This result was suggested to explain how increased doses of laminin *in vitro* led to a dose-dependent increase in cell proliferation in C2C12 myoblasts [110]. An increase in Rac1 signaling was also observed following muscle contraction, which suggested that interactions between laminin and dystroglycan are important for enabling the DGC to function as a laminin-dependent mechanoreceptor [105].

The PI3K/AKT pathway is an important signaling pathway essential for muscle cell survival, growth, and hypertrophy that has been suspected to function downstream of the DGC. Disruption of laminin/dystroglycan binding *in vitro* by antibody blockade results in a decrease in PI3K-mediated phosphorylation of AKT and is associated with an increase in apoptosis [111]. This result may be mediated in part through interactions of the DGC with heterotrimeric G-proteins, which has also been shown to be laminin-dependent. In the presence of laminin, dystroglycan can be immunoprecipitated in a complex with $G\beta\gamma$ and PI3K and leads to an increase in AKT activation [112]. Therefore, the authors of this study concluded that, in

muscular dystrophies where the DGC is disrupted, loss of an interaction with $G\beta\gamma$ can impair PI3K signaling and may contribute to disease pathology. Several studies have demonstrated perturbations in AKT signaling in *mdx* muscle but generally have demonstrated an increase in AKT activity rather than a decrease that would be predicted by these cell culture studies [112, 113]. This potentially could be due to increased AKT signaling downstream of $\alpha7\beta1$ integrin, which is upregulated in *mdx* muscle [114] and has been shown to be beneficial when overexpressed in dystrophic muscle either directly [115] or downstream of IGF-1 [116–118].

While the potential loss of PI3K/AKT signaling downstream of laminin binding may impact muscle function through its effect on cell survival or growth, skeletal muscle function may also be compromised due to increases in activity of the ubiquitin-proteasome system (UPS) [119]. MuRF1 and MAFbx/atrogen-1 are important mediators of skeletal muscle atrophy that function to ubiquitinate target proteins which subsequently results in their destruction by the proteasome [119]. In a recent study, decreased phosphorylation of AKT was demonstrated in laminin-deficient muscle and was associated with an increase in total amount of ubiquitinated protein [120]. Additionally, pharmacological inhibition of the ubiquitin-proteasome pathway in laminin-deficient animals resulted in an amelioration of several pathological features of the disease. This led the authors to conclude that impaired laminin-dependent signaling in dystrophic muscle may also be impacting the UPS and contributing to muscle disease. Although a number of signaling pathways are known to be important for skeletal muscle growth, the exact contributions of disrupted dystroglycan-dependent or integrin-dependent signaling in dystrophic muscle still needs to be formally addressed.

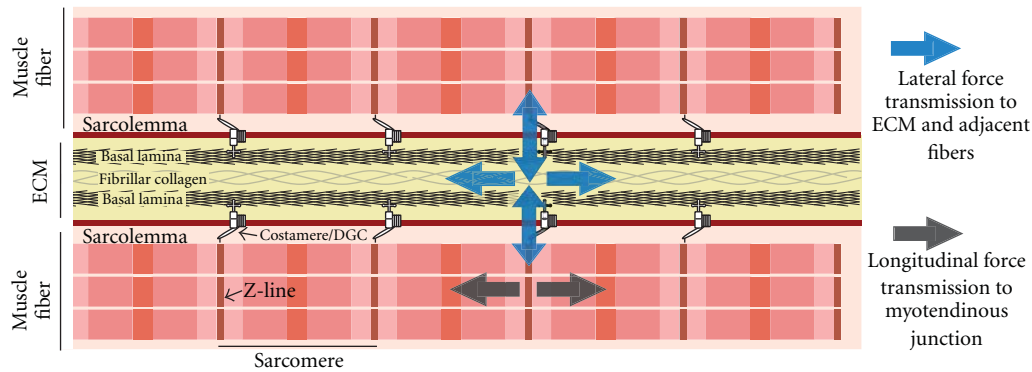


FIGURE 3: The dystrophin-glycoprotein complex transmits forces laterally at costameres in muscle. Longitudinal forces generated in sarcomeres are transmitted down myofibrils in muscle and forces are also transmitted laterally to the ECM and neighboring muscle fibers at costameres, at least in part through the dystrophin-glycoprotein complex (DGC). Recent data showing a loss of lateral force transmission in dystrophin-deficient muscle explains how the reduction or improper assembly of the DGC at the lateral membrane may contribute to overall muscle weakness and fragility.

7. Direct Role of the Dystrophin-Glycoprotein Complex in Force Transmission

While muscle damage is hypothesized to be important in the pathogenesis and progression of DGC-associated muscular dystrophy, dystrophic muscle displays considerable muscle weakness even in very early stages of the disease. This weakness, expressed as a reduction in specific force normalized to the cross sectional area of the muscle, occurs prior to muscular atrophy and can even be measured in the presence of pseudohypertrophy in early phases of the disease [121, 122]. Our studies and the studies of others, in soleus muscle of DGC-deficient muscular dystrophies, demonstrate that the soleus muscle is also weak and this weakness is completely independent of an increased susceptibility of the muscle to damage [38, 45]. Therefore, muscle damage that results as a consequence of contraction-induced injury cannot fully explain the muscle weakness in DGC-associated muscular dystrophy.

Given the location of the DGC at costameres in muscle, several investigators have hypothesized that the DGC might contribute to “lateral transmission of force” from the sarcomere to the lateral extracellular matrix [123–126]. While the concept of longitudinal force generated in sarcomeres and transmitted down myofibrils in muscle to the tendon is well studied, the concept of lateral force transmission is less well appreciated. This concept of lateral transmission of force in muscle was first described in frog muscle by Street in the early 1980’s [127]. In these studies, force was shown to be transmitted laterally from a single dissected fiber to the fibers flanking it in a muscle fiber bundle, with little or no decrement. Formal proof that the DGC was important in lateral transmission of force in muscle was lacking. Recently, we developed a novel yoke apparatus to directly measure the transmission of force from the muscle laterally to the extracellular matrix and the epimysium [128]. Applying this approach to *mdx* muscle, we showed for the first time that loss of DGC function in tibialis anterior muscles of *mdx* mice was sufficient to cause an approximately

40% loss in lateral force transmission in the muscles. While the precise contribution of each of the other components of the cytoskeleton, the costamere, and the extracellular matrix to the lateral transmission of force in muscle remains to be elucidated, the loss of lateral transmission of force may help explain how loss of the DGC at the lateral membrane contributes muscle weakness and fragility. Furthermore, the lateral transmission of force might be critical in transmitting force around the sites of focal myofiber injury in whole muscle and may help explain the markedly enhanced force deficits caused by lengthening contractions observed in fast muscles of DGC deficient animals (Figure 3).

8. Conclusions

Several studies have suggested that mutations affecting the DGC result in muscular dystrophy due to the importance of this complex in preserving sarcolemmal integrity. This role of the sarcolemma in muscular dystrophy is further supported by the observation that mutations that affect membrane repair can also result in muscle disease [40]. While several reports have demonstrated deficits in force production in dystrophic muscle in response to contraction-induced damage, it is not clear whether these defects are directly due to changes in sarcolemma integrity [37]. Additionally, mutations that affect the DGC have been shown to result in a muscle disease that variably affects the diaphragm, EDL, and soleus muscles. Therefore, an increased susceptibility to mechanical injury does not appear to be an essential step in the dystrophic process that leads to muscle weakness and the progressive decline in muscle function, and incidentally, cannot always account for other observed cellular disruptions such as differences in apoptosis.

An important downstream event that has been attributed to increased sarcolemma permeability through membrane tears is an increase in intracellular calcium. This rise in calcium is capable of negatively impacting skeletal muscle in a multitude of ways and may in fact be an important contributor to the pathology in these diseases. The

mechanism by which DGC mutations can alter the activity of calcium channels is not clear but would support a hypothesis that membrane damage is not an essential event that precedes changes in calcium permeability. Although changes in calcium permeability alone can result in muscle disease, it is unlikely that this is the sole mechanism by which DGC mutations result in muscular dystrophy since interventions that have restored calcium homeostasis have not completely eliminated the disease.

Another consequence of gene mutations that have been shown to be relevant to disease pathology in muscular dystrophy are disruptions in signaling pathways that may be essential to enable skeletal muscle to adapt and respond to ongoing cycles of contraction and relaxation. Laminin mutations result in muscle disease concomitant with increases in apoptosis and a recent study suggests that this defect may be mediated in part through the DGC. In light of emerging evidence that membrane damage is not essential, this gives credence to several *in vitro* studies that have suggested that dystroglycan and the DGC may be participating in cell survival signaling. Therefore, dystroglycan in combination with other components in the DGC may be serving a function similar to that of $\alpha\beta 1$ integrin, which has been more extensively demonstrated in mechano-related signaling [48, 49].

Many recent studies have demonstrated pharmacological and genetic interventions that have resulted in a dramatic improvement of the dystrophic pathology without any obvious protection of the sarcolemma from mechanical damage [129–131]. Discovery of additional signaling pathways directly downstream of the DGC, either those important for survival signaling or related to altered calcium homeostasis, may also serve as potential targets for pharmacological interventions to reduce disease pathology.

Acknowledgments

The authors would like to thank Zhyldyz Kabaeva for thoughtful discussion. J. D. Gumerson is currently supported by the University of Michigan Rackham Predoctoral Fellowship. This work was supported by NIH HL-080388 to D. E. Michele.

References

- [1] G. Q. Wallace and E. M. McNally, "Mechanisms of muscle degeneration, regeneration, and repair in the muscular dystrophies," *Annual Review of Physiology*, vol. 71, pp. 37–57, 2009.
- [2] E. M. McNally and P. Pytel, "Muscle diseases: the muscular dystrophies," *Annual Review of Pathology*, vol. 2, pp. 87–109, 2007.
- [3] R. D. Cohn and K. P. Campbell, "Molecular basis of muscular dystrophies," *Muscle and Nerve*, vol. 23, no. 10, pp. 1456–1471, 2000.
- [4] B. J. Petrof, J. B. Shrager, H. H. Stedman, A. M. Kelly, and H. L. Sweeney, "Dystrophin protects the sarcolemma from stresses developed during muscle contraction," *Proceedings of the National Academy of Sciences of the United States of America*, vol. 90, no. 8, pp. 3710–3714, 1993.
- [5] B. J. Petrof, "The molecular basis of activity-induced muscle injury in Duchenne muscular dystrophy," *Molecular and Cellular Biochemistry*, vol. 179, no. 1–2, pp. 111–123, 1998.
- [6] H. Moser, "Duchenne muscular dystrophy: pathogenetic aspects and genetic prevention," *Human Genetics*, vol. 66, no. 1, pp. 17–40, 1984.
- [7] D. G. Allen and N. P. Whitehead, "Duchenne muscular dystrophy—what causes the increased membrane permeability in skeletal muscle?" *International Journal of Biochemistry and Cell Biology*, vol. 43, no. 3, pp. 290–294, 2011.
- [8] C. L. Batchelor and S. J. Winder, "Sparks, signals and shock absorbers: how dystrophin loss causes muscular dystrophy," *Trends in Cell Biology*, vol. 16, no. 4, pp. 198–205, 2006.
- [9] M. Yoshida and E. Ozawa, "Glycoprotein complex anchoring dystrophin to sarcolemma," *Journal of Biochemistry*, vol. 108, no. 5, pp. 748–752, 1990.
- [10] K. P. Campbell and S. D. Kahl, "Association of dystrophin and an integral membrane glycoprotein," *Nature*, vol. 338, no. 6212, pp. 259–262, 1989.
- [11] C. Minetti, F. Beltrame, G. Marcenaro, and E. Bonilla, "Dystrophin at the plasma membrane of human muscle fibers shows a costameric localization," *Neuromuscular Disorders*, vol. 2, no. 2, pp. 99–109, 1992.
- [12] J. M. Ervasti and K. P. Campbell, "A role for the dystrophin-glycoprotein complex as a transmembrane linker between laminin and actin," *Journal of Cell Biology*, vol. 122, no. 4, pp. 809–823, 1993.
- [13] K. P. Campbell, "Three muscular dystrophies: loss of cytoskeleton-extracellular matrix linkage," *Cell*, vol. 80, no. 5, pp. 675–679, 1995.
- [14] M. R. Stone, A. O'Neill, D. Catino, and R. J. Bloch, "Specific interaction of the actin-binding domain of dystrophin with intermediate filaments containing keratin 19," *Molecular Biology of the Cell*, vol. 16, no. 9, pp. 4280–4293, 2005.
- [15] I. N. Rybakova, J. R. Patel, and J. M. Ervasti, "The dystrophin complex forms a mechanically strong link between the sarcolemma and costameric actin," *Journal of Cell Biology*, vol. 150, no. 5, pp. 1209–1214, 2000.
- [16] J. M. Ervasti and K. P. Campbell, "Membrane organization of the dystrophin-glycoprotein complex," *Cell*, vol. 66, no. 6, pp. 1121–1131, 1991.
- [17] E. Ozawa, Y. Mizuno, Y. Hagiwara, T. Sasaoka, and M. Yoshida, "Molecular and cell biology of the sarcoglycan complex," *Muscle and Nerve*, vol. 32, no. 5, pp. 563–576, 2005.
- [18] K. Ohlendieck and K. P. Campbell, "Dystrophin-associated proteins are greatly reduced in skeletal muscle from mdx mice," *Journal of Cell Biology*, vol. 115, no. 6, pp. 1685–1694, 1991.
- [19] F. Muntoni, S. Torelli, and M. Brockington, "Muscular dystrophies due to glycosylation defects," *Neurotherapeutics*, vol. 5, no. 4, pp. 627–632, 2008.
- [20] D. E. Michele, R. Barresi, M. Kanagawa et al., "Post-translational disruption of dystroglycan-ligand interactions in congenital muscular dystrophies," *Nature*, vol. 418, no. 6896, pp. 417–422, 2002.
- [21] R. Han, M. Kanagawa, T. Yoshida-Moriguchi et al., "Basal lamina strengthens cell membrane integrity via the laminin G domain-binding motif of α -dystroglycan," *Proceedings of the National Academy of Sciences of the United States of America*, vol. 106, no. 31, pp. 12573–12579, 2009.
- [22] R. A. Williamson, M. D. Henry, K. J. Daniels et al., "Dystroglycan is essential for early embryonic development: disruption of Reichert's membrane in *Dag1*-null mice," *Human Molecular Genetics*, vol. 6, no. 6, pp. 831–841, 1997.

- [23] Y. Hara, B. Balci-Hayta, T. Yoshida-Moriguchi et al., "A dystroglycan mutation associated with limb-girdle muscular dystrophy," *New England Journal of Medicine*, vol. 364, no. 10, pp. 939–946, 2011.
- [24] H. Xu, X. R. Wu, U. M. Wewer, and E. Engvall, "Murine muscular dystrophy caused by a mutation in the laminin $\alpha 2$ (*Lama2*) gene," *Nature Genetics*, vol. 8, no. 3, pp. 297–302, 1994.
- [25] Y. Sunada, S. M. Bernier, A. Utani, Y. Yamada, and K. P. Campbell, "Identification of a novel mutant transcript of laminin $\alpha 2$ chain gene responsible for muscular dystrophy and dysmyelination in *dy2j* mice," *Human Molecular Genetics*, vol. 4, no. 6, pp. 1055–1061, 1995.
- [26] A. Helbling-Leclerc, X. Zhang, H. Topaloglu et al., "Mutations in the laminin $\alpha 2$ -chain gene (*LAMA2*) cause merosin-deficient congenital muscular dystrophy," *Nature Genetics*, vol. 11, no. 2, pp. 216–218, 1995.
- [27] E. P. Hoffman, R. H. Brown Jr., and L. M. Kunkel, "Dystrophin: the protein product of the duchenne muscular dystrophy locus," *Cell*, vol. 51, no. 6, pp. 919–928, 1987.
- [28] T. Haenggi and J. M. Fritschy, "Role of dystrophin and utrophin for assembly and function of the dystrophin glycoprotein complex in non-muscle tissue," *Cellular and Molecular Life Sciences*, vol. 63, no. 14, pp. 1614–1631, 2006.
- [29] P. L. McNeil and R. Khakee, "Disruptions of muscle fiber plasma membranes: role in exercise-induced damage," *American Journal of Pathology*, vol. 140, no. 5, pp. 1097–1109, 1992.
- [30] C. P. Ingalls, G. L. Warren, J. H. Williams, C. W. Ward, and R. B. Armstrong, "E-C coupling failure in mouse EDL muscle after in vivo eccentric contractions," *Journal of Applied Physiology*, vol. 85, no. 1, pp. 58–67, 1998.
- [31] D. J. Newham, G. McPhail, K. R. Mills, and R. H. T. Edwards, "Ultrastructural changes after concentric and eccentric contractions of human muscle," *Journal of the Neurological Sciences*, vol. 61, no. 1, pp. 109–122, 1983.
- [32] P. M. Clarkson and M. J. Hubal, "Exercise-induced muscle damage in humans," *American Journal of Physical Medicine and Rehabilitation*, vol. 81, supplement 11, pp. S52–S69, 2002.
- [33] G. Bulfield, W. G. Siller, P. A. L. Wight, and K. J. Moore, "X chromosome-linked muscular dystrophy (*mdx*) in the mouse," *Proceedings of the National Academy of Sciences of the United States of America*, vol. 81, no. 4, pp. 1189–1192, 1984.
- [34] C. Pastoret and A. Sebille, "*mdx* mice show progressive weakness and muscle deterioration with age," *Journal of the Neurological Sciences*, vol. 129, no. 2, pp. 97–105, 1995.
- [35] P. Moens, P. H. Baatsen, and G. Marechal, "Increased susceptibility of EDL muscles from *mdx* mice to damage induced by contractions with stretch," *Journal of Muscle Research and Cell Motility*, vol. 14, no. 4, pp. 446–451, 1993.
- [36] R. Matsuda, A. Nishikawa, and H. Tanaka, "Visualization of dystrophic muscle fibers in *Mdx* mouse by vital staining with Evans blue: evidence of apoptosis in dystrophin-deficient muscle," *Journal of Biochemistry*, vol. 118, no. 5, pp. 959–964, 1995.
- [37] C. M. Consolino and S. V. Brooks, "Susceptibility to sarcomere injury induced by single stretches of maximally activated muscles of *mdx* mice," *Journal of Applied Physiology*, vol. 96, no. 2, pp. 633–638, 2004.
- [38] C. Dellorusso, R. W. Crawford, J. S. Chamberlain, and S. V. Brooks, "Tibialis anterior muscles in *mdx* mice are highly susceptible to contraction-induced injury," *Journal of Muscle Research and Cell Motility*, vol. 22, no. 5, pp. 467–475, 2001.
- [39] R. Bashir, S. Britton, T. Strachan et al., "A gene related to *Caenorhabditis elegans* spermatogenesis factor *fer-1* is mutated in limb-girdle muscular dystrophy type 2B," *Nature Genetics*, vol. 20, no. 1, pp. 37–42, 1998.
- [40] J. Liu, M. Aoki, I. Illa et al., "Dysferlin, a novel skeletal muscle gene, is mutated in Miyoshi myopathy and limb girdle muscular dystrophy," *Nature Genetics*, vol. 20, no. 1, pp. 31–36, 1998.
- [41] D. Bansal, K. Miyake, S. S. Vogel et al., "Defective membrane repair in dysferlin-deficient muscular dystrophy," *Nature*, vol. 423, no. 6936, pp. 168–172, 2003.
- [42] J. A. Roche, R. M. Lovering, and R. J. Bloch, "Impaired recovery of dysferlin-null skeletal muscle after contraction-induced injury in vivo," *NeuroReport*, vol. 19, no. 16, pp. 1579–1584, 2008.
- [43] J. A. Roche, R. M. Lovering, R. Roche, L. W. Ru, P. W. Reed, and R. J. Bloch, "Extensive mononuclear infiltration and myogenesis characterize recovery of dysferlin-null skeletal muscle from contraction-induced injuries," *American Journal of Physiology*, vol. 298, no. 2, pp. C298–C312, 2010.
- [44] K. E. Davies and K. J. Nowak, "Molecular mechanisms of muscular dystrophies: old and new players," *Nature Reviews Molecular Cell Biology*, vol. 7, no. 10, pp. 762–773, 2006.
- [45] J. D. Gumerson, Z. T. Kabaeva, C. S. Davis, J. A. Faulkner, and D. E. Michele, "Soleus muscle in glycosylation-deficient muscular dystrophy is protected from contraction-induced injury," *American Journal of Physiology*, vol. 299, no. 6, pp. C1430–C1440, 2010.
- [46] H. Tanaka, T. Ishiguro, C. Eguchi, K. Saito, and E. Ozawa, "Expression of a dystrophin-related protein associated with the skeletal muscle cell membrane," *Histochemistry*, vol. 96, no. 1, pp. 1–5, 1991.
- [47] A. O. Gramolini, G. Bélanger, J. M. Thompson, J. V. Chakkalal, and B. J. Jasmin, "Increased expression of utrophin in a slow vs. a fast muscle involves posttranscriptional events," *American Journal of Physiology*, vol. 281, no. 4, pp. C1300–C1309, 2001.
- [48] B. L. Hodges, Y. K. Hayashi, I. Nonaka, W. Wang, K. Arahata, and S. J. Kaufman, "Altered expression of the $\alpha 7\beta 1$ integrin in human and murine muscular dystrophies," *Journal of Cell Science*, vol. 110, no. 22, pp. 2873–2881, 1997.
- [49] D. J. Burkin, G. Q. Wallace, K. J. Nicol, D. J. Kaufman, and S. J. Kaufman, "Enhanced expression of the $\alpha 7\beta 1$ integrin reduces muscular dystrophy and restores viability in dystrophic mice," *Journal of Cell Biology*, vol. 152, no. 6, pp. 1207–1218, 2001.
- [50] S. I. Head, A. J. Bakker, and G. Liangas, "EDL and soleus muscles of the C57BL6J/*dy2j* laminin- $\alpha 2$ -deficient dystrophic mouse are not vulnerable to eccentric contractions," *Experimental Physiology*, vol. 89, no. 5, pp. 531–539, 2004.
- [51] V. Straub, J. A. Rafael, J. S. Chamberlain, and K. P. Campbell, "Animal models for muscular dystrophy show different patterns of sarcolemmal disruption," *Journal of Cell Biology*, vol. 139, no. 2, pp. 375–385, 1997.
- [52] E. R. Chin, "Intracellular Ca^{2+} signaling in skeletal muscle: decoding a complex message," *Exercise and Sport Sciences Reviews*, vol. 38, no. 2, pp. 76–85, 2010.
- [53] P. R. Turner, T. Westwood, C. M. Regen, and R. A. Steinhardt, "Increased protein degradation results from elevated free calcium levels found in muscle from *mdx* mice," *Nature*, vol. 335, no. 6192, pp. 735–738, 1988.
- [54] B. A. Valentine, B. J. Cooper, and E. A. Gallagher, "Intracellular calcium in canine muscle biopsies," *Journal of Comparative Pathology*, vol. 100, no. 3, pp. 223–230, 1989.

- [55] A. Franco Jr. and J. B. Lansman, "Calcium entry through stretch-inactivated ion channels in mdx myotubes," *Nature*, vol. 344, no. 6267, pp. 670–673, 1990.
- [56] P. Y. Fong, P. R. Turner, W. F. Denetclaw, and R. A. Steinhardt, "Increased activity of calcium leak channels in myotubes of Duchenne human and mdx mouse origin," *Science*, vol. 250, no. 4981, pp. 673–676, 1990.
- [57] E. W. Yeung, N. P. Whitehead, T. M. Suchyna, P. A. Gottlieb, F. Sachs, and D. G. Allen, "Effects of stretch-activated channel blockers on $[Ca^{2+}]_i$ and muscle damage in the mdx mouse," *Journal of Physiology*, vol. 562, no. 2, pp. 367–380, 2005.
- [58] D. E. Clapham, "TRP channels as cellular sensors," *Nature*, vol. 426, no. 6966, pp. 517–524, 2003.
- [59] C. Vandebrouck, D. Martin, M. C. V. Schoor, H. Debaix, and P. Gailly, "Involvement of TRPC in the abnormal calcium influx observed in dystrophic (mdx) mouse skeletal muscle fibers," *Journal of Cell Biology*, vol. 158, no. 6, pp. 1089–1096, 2002.
- [60] O. L. Gervasio, N. R. Whitehead, E. W. Yeung, W. D. Phillips, and D. G. Allen, "TRPC1 binds to caveolin-3 and is regulated by Src kinase—role in Duchenne muscular dystrophy," *Journal of Cell Science*, vol. 121, no. 13, pp. 2246–2255, 2008.
- [61] Y. Iwata, Y. Katanosaka, Y. Arai, M. Shigekawa, and S. Wakabayashi, "Dominant-negative inhibition of Ca^{2+} influx via TRPV2 ameliorates muscular dystrophy in animal models," *Human Molecular Genetics*, vol. 18, no. 5, pp. 824–834, 2009.
- [62] A. M. Bellinger, S. Reiken, C. Carlson et al., "Hypernitrosylated ryanodine receptor calcium release channels are leaky in dystrophic muscle," *Nature Medicine*, vol. 15, no. 3, pp. 325–330, 2009.
- [63] D. P. Millay, S. A. Goonasekera, M. A. Sargent, M. Maillet, B. J. Aronow, and J. D. Molkentin, "Calcium influx is sufficient to induce muscular dystrophy through a TRPC-dependent mechanism," *Proceedings of the National Academy of Sciences of the United States of America*, vol. 106, no. 45, pp. 19023–19028, 2009.
- [64] S. Orrenius, B. Zhivotovsky, and P. Nicotera, "Regulation of cell death: the calcium-apoptosis link," *Nature Reviews Molecular Cell Biology*, vol. 4, no. 7, pp. 552–565, 2003.
- [65] C. P. Baines, R. A. Kaiser, N. H. Purcell et al., "Loss of cyclophilin D reveals a critical role for mitochondrial permeability transition in cell death," *Nature*, vol. 434, no. 7033, pp. 658–662, 2005.
- [66] T. Nakagawa, S. Shimizu, T. Watanabe et al., "Cyclophilin D-dependent mitochondrial permeability transition regulates some necrotic but not apoptotic cell death," *Nature*, vol. 434, no. 7033, pp. 652–658, 2005.
- [67] D. P. Millay, M. A. Sargent, H. Osinska et al., "Genetic and pharmacologic inhibition of mitochondrial-dependent necrosis attenuates muscular dystrophy," *Nature Medicine*, vol. 14, no. 4, pp. 442–447, 2008.
- [68] V. M. Shkryl, A. S. Martins, N. D. Ullrich, M. C. Nowycky, E. Niggli, and N. Shirokova, "Reciprocal amplification of ROS and Ca^{2+} signals in stressed mdx dystrophic skeletal muscle fibers," *Pflugers Archiv European Journal of Physiology*, vol. 458, no. 5, pp. 915–928, 2009.
- [69] T. A. Rando, "Oxidative stress and the pathogenesis of muscular dystrophies," *American Journal of Physical Medicine and Rehabilitation*, vol. 81, supplement 11, pp. S175–S186, 2002.
- [70] N. P. Whitehead, E. W. Yeung, and D. G. Allen, "Muscle damage in mdx (dystrophic) mice: role of calcium and reactive oxygen species," *Clinical and Experimental Pharmacology and Physiology*, vol. 33, no. 7, pp. 657–662, 2006.
- [71] J. G. Tidball and M. Wehling-Henricks, "The role of free radicals in the pathophysiology of muscular dystrophy," *Journal of Applied Physiology*, vol. 102, no. 4, pp. 1677–1686, 2007.
- [72] T. M. Buetler, M. Renard, E. A. Offord, H. Schneider, and U. T. Ruegg, "Green tea extract decreases muscle necrosis in mdx mice and protects against reactive oxygen species," *American Journal of Clinical Nutrition*, vol. 75, no. 4, pp. 749–753, 2002.
- [73] S. Menazza, B. Blaauw, T. Tiepolo et al., "Oxidative stress by monoamine oxidases is causally involved in myofiber damage in muscular dystrophy," *Human Molecular Genetics*, vol. 19, no. 21, pp. 4207–4215, 2010.
- [74] R. M. Lovering, L. Michaelson, and C. W. Ward, "Malformed mdx myofibers have normal cytoskeletal architecture yet altered EC coupling and stress-induced Ca^{2+} signaling," *American Journal of Physiology*, vol. 297, no. 3, pp. C571–C580, 2009.
- [75] C. E. Woods, D. Novo, M. DiFranco, and J. L. Vergara, "The action potential-evoked sarcoplasmic reticulum calcium release is impaired in mdx mouse muscle fibres," *Journal of Physiology*, vol. 557, no. 1, pp. 59–75, 2004.
- [76] B. T. Zhang, S. S. Yeung, D. G. Allen, L. Qin, and E. W. Yeung, "Role of the calcium-calpain pathway in cytoskeletal damage after eccentric contractions," *Journal of Applied Physiology*, vol. 105, no. 1, pp. 352–357, 2008.
- [77] M. J. Spencer, D. E. Croall, and J. G. Tidball, "Calpains are activated in necrotic fibers from mdx dystrophic mice," *Journal of Biological Chemistry*, vol. 270, no. 18, pp. 10909–10914, 1995.
- [78] J. M. Alderton and R. A. Steinhardt, "Calcium influx through calcium leak channels is responsible for the elevated levels of calcium-dependent proteolysis in dystrophic myotubes," *Journal of Biological Chemistry*, vol. 275, no. 13, pp. 9452–9460, 2000.
- [79] M. J. Spencer and R. L. Mellgren, "Overexpression of a calpastatin transgene in mdx muscle reduces dystrophic pathology," *Human Molecular Genetics*, vol. 11, no. 21, pp. 2645–2655, 2002.
- [80] A. Briguët, M. Erb, I. Courdier-Fruh et al., "Effect of calpain and proteasome inhibition on Ca^{2+} -dependent proteolysis and muscle histopathology in the mdx mouse," *FASEB Journal*, vol. 22, no. 12, pp. 4190–4200, 2008.
- [81] M. A. Badalamente and A. Stracher, "Delay of muscle degeneration and necrosis in mdx mice by calpain inhibition," *Muscle and Nerve*, vol. 23, no. 1, pp. 106–111, 2000.
- [82] J. Selsby, K. Pendrak, M. Zadel et al., "Leupeptin-based inhibitors do not improve the mdx phenotype," *American Journal of Physiology*, vol. 299, no. 5, pp. R1192–R1201, 2010.
- [83] T. Mukasa, T. Momoi, and M. Y. Momoi, "Activation of caspase-3 apoptotic pathways in skeletal muscle fibers in laminin alpha 2-deficient mice," *Biochemical and Biophysical Research Communications*, vol. 260, no. 1, pp. 139–142, 1999.
- [84] M. Erb, S. Meinen, P. Barzaghi et al., "Omigapil ameliorates the pathology of muscle dystrophy caused by laminin- α 2 deficiency," *Journal of Pharmacology and Experimental Therapeutics*, vol. 331, no. 3, pp. 787–795, 2009.
- [85] M. Girgenrath, M. L. Beermann, V. K. Vishnudas, S. Homma, and J. B. Miller, "Pathology is alleviated by doxycycline in a laminin- α 2-null model of congenital muscular dystrophy," *Annals of Neurology*, vol. 65, no. 1, pp. 47–56, 2009.
- [86] M. Girgenrath, J. A. Dominov, C. A. Kostek, and J. B. Miller, "Inhibition of apoptosis improves outcome in a model of congenital muscular dystrophy," *Journal of Clinical Investigation*, vol. 114, no. 11, pp. 1635–1639, 2004.

- [87] P. H. Vachon, H. Xu, L. Liu et al., "Integrins ($\alpha7\beta1$) in muscle function and survival disrupted expression in merosin-deficient congenital muscular dystrophy," *Journal of Clinical Investigation*, vol. 100, no. 7, pp. 1870–1881, 1997.
- [88] J. E. Rooney, P. B. Guppur, and D. J. Burkin, "Laminin-111 protein therapy prevents muscle disease in the mdx mouse model for Duchenne muscular dystrophy," *Proceedings of the National Academy of Sciences of the United States of America*, vol. 106, no. 19, pp. 7991–7996, 2009.
- [89] K. I. Gawlik, B. M. Oliveira, and M. Durbeej, "Transgenic expression of laminin alpha 1 chain does not prevent muscle disease in the mdx mouse model for Duchenne muscular dystrophy," *American Journal of Pathology*, vol. 178, no. 4, pp. 1728–1737, 2011.
- [90] K. Gawlik, Y. Miyagoe-Suzuki, P. Ekblom, S. Takeda, and M. Durbeej, "Laminin $\alpha1$ chain reduces muscular dystrophy in laminin chain deficient mice," *Human Molecular Genetics*, vol. 13, no. 16, pp. 1775–1784, 2004.
- [91] K. I. Gawlik and M. Durbeej, "Transgenic overexpression of laminin $\alpha1$ chain in laminin $\alpha2$ chain-deficient mice rescues the disease throughout the lifespan," *Muscle and Nerve*, vol. 42, no. 1, pp. 30–37, 2010.
- [92] Y. K. Hayashi, F. L. Chou, E. Engvall et al., "Mutations in the integrin $\alpha7$ gene cause congenital myopathy," *Nature Genetics*, vol. 19, no. 1, pp. 94–97, 1998.
- [93] U. Mayer, G. Saher, R. Fässler et al., "Absence of integrin $\alpha7$ causes a novel form of muscular dystrophy," *Nature Genetics*, vol. 17, no. 3, pp. 318–323, 1997.
- [94] H. Nakashima, T. Kibe, and K. Yokochi, "Congenital muscular dystrophy caused by integrin $\alpha7$ deficiency," *Developmental Medicine and Child Neurology*, vol. 51, no. 3, p. 245, 2009.
- [95] J. E. Rooney, J. V. Welsler, M. A. Dechert, N. L. Flintoff-Dye, S. J. Kaufman, and D. J. Burkin, "Severe muscular dystrophy in mice that lack dystrophin and $\alpha7$ integrin," *Journal of Cell Science*, vol. 119, no. 11, pp. 2185–2195, 2006.
- [96] D. J. Burkin, G. Q. Wallace, D. J. Milner, E. J. Chaney, J. A. Mulligan, and S. J. Kaufman, "Transgenic expression of $\alpha7\beta1$ integrin maintains muscle integrity, increases regenerative capacity, promotes hypertrophy, and reduces cardiomyopathy in dystrophic mice," *American Journal of Pathology*, vol. 166, no. 1, pp. 253–263, 2005.
- [97] M. D. Boppart, D. J. Burkin, and S. J. Kaufman, " $\alpha7\beta1$ -Integrin regulates mechanotransduction and prevents skeletal muscle injury," *American Journal of Physiology*, vol. 290, no. 6, pp. C1660–C1665, 2006.
- [98] M. A. Schwartz, "Integrins and extracellular matrix in mechanotransduction," *Cold Spring Harbor Perspectives in Biology*, vol. 2, no. 12, p. a005066, 2010.
- [99] S. C. Brown and J. A. Lucy, "Dystrophin as a mechanochemical transducer in skeletal muscle," *BioEssays*, vol. 15, no. 6, pp. 413–419, 1993.
- [100] R. D. Cohn, M. D. Henry, D. E. Michele et al., "Disruption of Dag1 in differentiated skeletal muscle reveals a role for dystroglycan in muscle regeneration," *Cell*, vol. 110, no. 5, pp. 639–648, 2002.
- [101] K. I. Gawlik, M. Åkerlund, V. Carmignac, H. Elamaa, and M. Durbeej, "Distinct roles for laminin globular domains in laminin $\alpha1$ chain mediated rescue of murine laminin alpha 2 chain deficiency," *PLoS One*, vol. 5, no. 7, Article ID e11549, 2010.
- [102] B. Yang, D. Jung, D. Motto, J. Meyer, G. Koretzky, and K. P. Campbell, "SH3 domain-mediated interaction of dystroglycan and Grb2," *Journal of Biological Chemistry*, vol. 270, no. 20, pp. 11711–11714, 1995.
- [103] M. James, A. Nuttall, J. L. Ilesley et al., "Adhesion-dependent tyrosine phosphorylation of β -dystroglycan regulates its interaction with utrophin," *Journal of Cell Science*, vol. 113, no. 10, pp. 1717–1726, 2000.
- [104] H. J. Spence, A. S. Dhillon, M. James, and S. J. Winder, "Dystroglycan, a scaffold for the ERK-MAP kinase cascade," *EMBO Reports*, vol. 5, no. 5, pp. 484–489, 2004.
- [105] Y. Zhou, D. Jiang, D. B. Thomason, and H. W. Jarrett, "Laminin-induced activation of Rac1 and JNKp46 is initiated by Src family kinases and mimics the effects of skeletal muscle contraction," *Biochemistry*, vol. 46, no. 51, pp. 14907–14916, 2007.
- [106] K. Russo, E. Di Stasio, G. Macchia, and G. Rosa, "Characterization of the beta-dystroglycan-growth factor receptor 2 (Grb2) interaction," *Biochemical and Biophysical Research Communications*, vol. 274, no. 1, pp. 93–98, 2000.
- [107] J. L. Ilesley, M. Sudol, and S. J. Winder, "The interaction of dystrophin with β -dystroglycan is regulated by tyrosine phosphorylation," *Cellular Signalling*, vol. 13, no. 9, pp. 625–632, 2001.
- [108] J. L. Ilesley, M. Sudol, and S. J. Winder, "The WW domain: linking cell signalling to the membrane cytoskeleton," *Cellular Signalling*, vol. 14, no. 3, pp. 183–189, 2002.
- [109] F. Sotgia, H. Lee, M. T. Bedford, T. Petrucci, M. Sudol, and M. P. Lisanti, "Tyrosine phosphorylation of β -dystroglycan at its WW domain binding motif, PPxY, recruits SH2 domain containing proteins," *Biochemistry*, vol. 40, no. 48, pp. 14585–14592, 2001.
- [110] S. A. Oak, Y. W. Zhou, and H. W. Jarrett, "Skeletal muscle signaling pathway through the dystrophin glycoprotein complex and Rac1," *Journal of Biological Chemistry*, vol. 278, no. 41, pp. 39287–39295, 2003.
- [111] K. J. Langenbach and T. A. Rando, "Inhibition of dystroglycan binding to laminin disrupts the PI3K/AKT pathway and survival signaling in muscle cells," *Muscle and Nerve*, vol. 26, no. 5, pp. 644–653, 2002.
- [112] Y. Xiong, Y. Zhou, and H. W. Jarrett, "Dystrophin glycoprotein complex-associated G β subunits activate phosphatidylinositol-3-kinase/akt signaling in skeletal muscle in a laminin-dependent manner," *Journal of Cellular Physiology*, vol. 219, no. 2, pp. 402–414, 2009.
- [113] C. Dogra, H. Changotra, J. E. Wergedal, and A. Kumar, "Regulation of phosphatidylinositol 3-kinase (PI3K)/Akt and nuclear factor-kappa B signaling pathways in dystrophin-deficient skeletal muscle in response to mechanical stretch," *Journal of Cellular Physiology*, vol. 208, no. 3, pp. 575–585, 2006.
- [114] M. D. Boppart, D. J. Burkin, and S. J. Kaufman, "Activation of AKT signaling promotes cell growth and survival in $\alpha7\beta1$ integrin-mediated alleviation of muscular dystrophy," *Biochimica et Biophysica Acta*, vol. 1812, no. 4, pp. 439–446, 2011.
- [115] B. Blaauw, C. Mammucari, L. Toniolo et al., "Akt activation prevents the force drop induced by eccentric contractions in dystrophin-deficient skeletal muscle," *Human Molecular Genetics*, vol. 17, no. 23, pp. 3686–3696, 2008.
- [116] A. Kumar, J. Yamauchi, T. Girgenrath, and M. Girgenrath, "Muscle-specific expression of insulin-like growth factor 1 improves outcome in Lama2^{Dy-w} mice, a model for congenital muscular dystrophy type 1A," *Human Molecular Genetics*, vol. 20, no. 12, pp. 2333–2343, 2011.

- [117] E. R. Barton, L. Morris, A. Musaro, N. Rosenthal, and H. Lee Sweeney, "Muscle-specific expression of insulin-like growth factor I counters muscle decline in mdx mice," *Journal of Cell Biology*, vol. 157, no. 1, pp. 137–147, 2002.
- [118] T. Shavlakadze, J. White, J. F. Hoh, N. Rosenthal, and M. D. Grounds, "Targeted expression of insulin-like growth factor-I reduces early myofiber necrosis in dystrophic mdx mice," *Molecular Therapy*, vol. 10, no. 5, pp. 829–843, 2004.
- [119] D. J. Glass, "Signalling pathways that mediate skeletal muscle hypertrophy and atrophy," *Nature Cell Biology*, vol. 5, no. 2, pp. 87–90, 2003.
- [120] V. Carmignac, R. Quere, and M. Durbeej, "Proteasome inhibition improves the muscle of laminin $\alpha 2$ chain-deficient mice," *Human Molecular Genetics*, vol. 20, no. 3, pp. 541–552, 2011.
- [121] R. W. Grange, T. G. Gainer, K. M. Marschner, R. J. Talmadge, and J. T. Stull, "Fast-twitch skeletal muscles of dystrophic mouse pups are resistant to injury from acute mechanical stress," *American Journal of Physiology*, vol. 283, no. 4, pp. C1090–C1101, 2002.
- [122] D. A. Lowe, B. O. Williams, D. D. Thomas, and R. W. Grange, "Molecular and cellular contractile dysfunction of dystrophic muscle from young mice," *Muscle and Nerve*, vol. 34, no. 1, pp. 92–100, 2006.
- [123] R. J. Bloch, P. Reed, A. O'Neill et al., "Costameres mediate force transduction in healthy skeletal muscle and are altered in muscular dystrophies," *Journal of Muscle Research and Cell Motility*, vol. 25, no. 8, pp. 590–592, 2004.
- [124] J. M. Ervasti, "Costameres: the Achilles' heel of Herculean muscle," *Journal of Biological Chemistry*, vol. 278, no. 16, pp. 13591–13594, 2003.
- [125] R. J. Bloch and H. Gonzalez-Serratos, "Lateral force transmission across costameres in skeletal muscle," *Exercise and Sport Sciences Reviews*, vol. 31, no. 2, pp. 73–78, 2003.
- [126] A. C. Paul, P. W. Sheard, S. J. Kaufman, and M. J. Duxson, "Localization of $\alpha 7$ integrins and dystrophin suggests potential for both lateral and longitudinal transmission of tension in large mammalian muscles," *Cell and Tissue Research*, vol. 308, no. 2, pp. 255–265, 2002.
- [127] S. F. Street, "Lateral transmission of tension in frog myofibers: a myofibrillar network and transverse cytoskeletal connections are possible transmitters," *Journal of Cellular Physiology*, vol. 114, no. 3, pp. 346–364, 1983.
- [128] K. S. Ramaswamy, M. L. Palmer, J. H. van der Meulen et al., "Lateral transmission of force is impaired in skeletal muscles of dystrophic mice and very old rats," *Journal of Physiology*, vol. 589, no. 5, pp. 1195–1208, 2011.
- [129] C. M. Adamo, D. F. Dai, J. M. Percival et al., "Sildenafil reverses cardiac dysfunction in the mdx mouse model of Duchenne muscular dystrophy," *Proceedings of the National Academy of Sciences of the United States of America*, vol. 107, no. 44, pp. 19079–19083, 2010.
- [130] N. P. Evans, J. A. Call, J. Bassaganya-Riera, J. L. Robertson, and R. W. Grange, "Green tea extract decreases muscle pathology and NF- κ B immunostaining in regenerating muscle fibers of mdx mice," *Clinical Nutrition*, vol. 29, no. 3, pp. 391–398, 2010.
- [131] N. P. Whitehead, C. Pham, O. L. Gervasio, and D. G. Allen, "N-Acetylcysteine ameliorates skeletal muscle pathophysiology in mdx mice," *Journal of Physiology*, vol. 586, no. 7, pp. 2003–2014, 2008.

Methodology Report

Use of BODIPY (493/503) to Visualize Intramuscular Lipid Droplets in Skeletal Muscle

Espen E. Spangenburg,¹ Stephen J. P. Pratt,²
Lindsay M. Wohlers,¹ and Richard M. Lovering²

¹Department of Kinesiology, University of Maryland, School of Public Health, College Park, MD 20742, USA

²Department of Orthopaedics, University of Maryland, School of Medicine, Baltimore, MD 21201, USA

Correspondence should be addressed to Richard M. Lovering, rlovering@som.umaryland.edu

Received 1 May 2011; Revised 21 July 2011; Accepted 2 August 2011

Academic Editor: Robert J. Bloch

Copyright © 2011 Espen E. Spangenburg et al. This is an open access article distributed under the Creative Commons Attribution License, which permits unrestricted use, distribution, and reproduction in any medium, provided the original work is properly cited.

Triglyceride storage is altered across various chronic health conditions necessitating various techniques to visualize and quantify lipid droplets (LDs). Here, we describe the utilization of the BODIPY (493/503) dye in skeletal muscle as a means to analyze LDs. We found that the dye was a convenient and simple approach to visualize LDs in both sectioned skeletal muscle and cultured adult single fibers. Furthermore, the dye was effective in both fixed and nonfixed cells, and the staining seemed unaffected by permeabilization. We believe that the use of the BODIPY (493/503) dye is an acceptable alternative and, under certain conditions, a simpler method for visualizing LDs stored within skeletal muscle.

1. Introduction

Triacylglycerol (aka triglyceride, or TAG) storage is typically at its highest appreciable amounts in white adipose tissue. TAGs are stored within the organelles termed neutral lipid droplets (LDs). Previous studies have shown that under various conditions, appreciable LD accumulation can also occur in other tissues, such as skeletal muscle. The appearance of LDs in nonadipose depots is often referred to as “ectopic fat”. Increasing amounts of ectopic fat are associated with a number of clinical conditions, such as peripheral insulin resistance and muscular dystrophies [1–3]. Thus, the ability to measure or visualize the accumulation of stored TAG in the form of LDs in skeletal muscle is important.

Measurement of lipid accumulation within skeletal muscle has been performed using numerous different methodologies, each with their own strengths and weaknesses. Total TAG concentration can be quantified through biochemical extraction, magnetic spectroscopy, or visually analyzed with Oil Red O (ORO) or Nile Red histochemical staining of tissue sections [4]. Each approach has unique advantages and disadvantages. The use of ORO has become the most commonly used approach to visualize LDs within a section

of skeletal muscle [4–7]. Since LD frequency is correlated with the oxidative potential of the muscle fiber, there often is an uneven distribution of fibers that contain a significant amount of LDs within a whole muscle. Specifically, Van Loon et al. demonstrated that LD frequency is significantly higher in type I fibers compared to type II fibers, albeit there was no distinction between the subtypes of the type II fibers in this study [8]. Thus, it is often necessary to consider the amount of LDs in a fiber-by-fiber approach. Staining of the fibers allows the investigator to consider multiple labeling approaches for colocalization studies. This approach precludes experimental bias from extracellular TAG that is often found in skeletal muscle, but not within the muscle fiber itself.

The use of ORO as a means to measure LDs in a fiber-specific manner is a very powerful and useful technique for muscle biologists. However, the use of ORO is not without experimental disadvantages. For example, the tissue of interest requires fixation, preventing its use on live cells. In addition, completely dissolving ORO into solution can be challenging. It is typically dissolved in isopropanol, may require heating to encourage the process, and must be filtered afterwards, which often reduces the final concentration of

the solution. Once in solution, the ORO has a limited shelf life, thus requiring the solution to be remade frequently. Finally, the ORO staining process requires the handling and disposal of a significant amount of hazardous chemicals. For a number of years, adipocyte biologists have used an alternative approach to ORO to visualize LDs within adipocytes, specifically a cell permeable lipophilic fluorescence dye, BODIPY (493/503), which emits bright green fluorescence [9]. The dye stains neutral LDs in live or fixed cells and can be successfully coupled with other staining and/or labeling approaches. An advantage of the dye is that it requires little effort to place into solution and, unlike ORO, does not need to be made “fresh” for each use.

The purpose of this paper is to demonstrate the use of BODIPY (493/503) to image LDs within skeletal muscle fibers as an alternative to ORO. In order to determine its flexibility of use, we examined the use of BODIPY (493/503) under a variety of conditions that included frozen muscle and freshly cultured single muscle fibers.

2. Methods

2.1. Animals. A variety of skeletal muscles were removed from male Sprague-Dawley rats (~275 g) and male C57BL/10ScSn mice (~32 g) while under inhalation anesthesia (~3–5% isoflurane via a nosecone using a precision vaporizer, cat # 91103, Vet Equip, Inc, Pleasanton, Calif, USA) just prior to sacrifice. All animal procedures were approved by the Animal Care and Use Committee at the University of Maryland.

2.2. Muscle Fiber Sections. Rat tibialis anterior (TA) muscles were isolated and frozen in liquid nitrogen-cooled isopentane. They were stored at -80°C , and transverse sections were cut on a cryostat ($10\ \mu\text{m}$ thick) and collected onto glass slides (Superfrost Plus; VWR, Westchester, Pa, USA).

2.3. Single Fiber Isolation. Intact single muscle fibers were isolated from the flexor digitorum brevis (FDB) muscle of adult mice according to previously described techniques [10]. Briefly, surgically excised FDB muscles were incubated in dissociation media (DM) containing DMEM, $1\ \mu\text{L}/\text{mL}$ gentamycin, 0.2% BSA, and 4 mg/mL of collagenase A (Sigma, C0130). FDB muscles were placed in a 35 mm dish with 4 mLs DM and then in an incubator (37° , 5% CO_2) for 2 hours. Following the dissociation, muscles were placed in a new 35 mm plate with fresh media and triturated with a small bore (~1 mm) fire polished glass transfer pipette to yield single FDB myofibers. Following the trituration process, fibers were plated onto extracellular matrix- (ECM, Sigma E1270) coated dishes (Matek, P35G-1.0-14-C). Fibers were allowed to incubate overnight before staining and/or immunolabeling. Some dishes were incubated overnight in a high-fat media containing equal molar concentrations of palmitate (PA) and oleate (OA) (0.5 mM of each thus a final concentration 1.0 mM) to induce LD formation in the fibers. The palmitate and oleate were conjugated to 2% fatty acid-free bovine serum albumin which would be expected to result in a final ratio of NEFA to BSA of 2.5:1.0, as previously

described [11]. We have found no evidence of toxicity when cells are treated with both palmitate and oleate, although we have found evidence of toxicity if cells are treated with palmitate alone.

2.4. BODIPY (493/503) Staining and Visualization. BODIPY (D3922, Molecular Probes, Carlsbad, Calif, USA) (excitation wavelength 480 nm, emission maximum 515 nm), was diluted in PBS or DMSO at a concentration of 1 mg/mL and applied to cross sections or FDB fibers, respectively, for 30 mins. We assessed both fixed (4% paraformaldehyde for 5 mins) and unfixed sections, as well as fixed (4% paraformaldehyde for 5 mins) and live FDB fibers; 4,6-diamidino-2-phenylindole (DAPI) was used to identify nuclei. Following fixation, samples were washed 3 times in phosphate-buffered saline (PBS) for 10 mins. Some cross sections were stained with 5 $\mu\text{g}/\text{mL}$ rhodamine-labeled succinylated wheat germ agglutinin (WGA, RL1022S; Vector Laboratories, Burlingame, Calif, USA), and some were labeled with antibodies (monoclonal slow myosin, M4276, Sigma, St Louis, Mo, USA) to identify slow (Type I) muscle fibers. For immunolabeling, sections were washed for 10 minutes in 100 mmol glycine phosphate-buffered saline (glycine PBS), blocked for 1 hour in 1% bovine serum albumin PBS (BSA-PBS), and then incubated for 2 hours with primary antibodies diluted to 2 mg/mL in PBS. The tissue sections were then washed 3 times with 1% BSA/PBS for 10 minutes before incubation with species-specific secondary antibodies coupled to Alexa dye 568 (Invitrogen, Carlsbad, Calif, USA) (dilution of 1:100). All samples were mounted in VECTASHIELD (Vector Laboratories) and covered with glass cover slips (No. 1, VWR). We examined samples under epifluorescent optics, and digital images were obtained with a Zeiss 510 confocal laser scanning microscope.

2.5. Oil Red O Staining. Serial sections ($10\ \mu\text{M}$) from frozen rat TA muscle were used. The first half of the serial sections were stained with BODIPY as described above. The remaining samples were air dried onto a glass slide and then fixed in formalin for 5 minutes, followed by a 1 minute wash with tap water. Next, slides were rinsed with 60% isopropanol then stained with a filtered 5% Oil Red O solution for 30 minutes. After Oil Red O staining, slides were rinsed with 60% isopropanol. All samples were mounted in VECTASHIELD (Vector Laboratories), covered with glass cover slips (No. 1, VWR), and mounted with Permount (Biomed, Burlingame, Calif, USA).

3. Results

BODIPY (493/503) has become the standard dye utilized by scientists to study LDs within adipocytes. In this study, we sought to demonstrate that this compound can be used to visualize LDs in skeletal muscle tissue. Using the BODIPY (493/503), we were able to detect visible LDs through standard epifluorescence and confocal microscopy in sections of whole rat muscle and live cultured mouse single fibers. Using cross sections of a soleus muscle taken

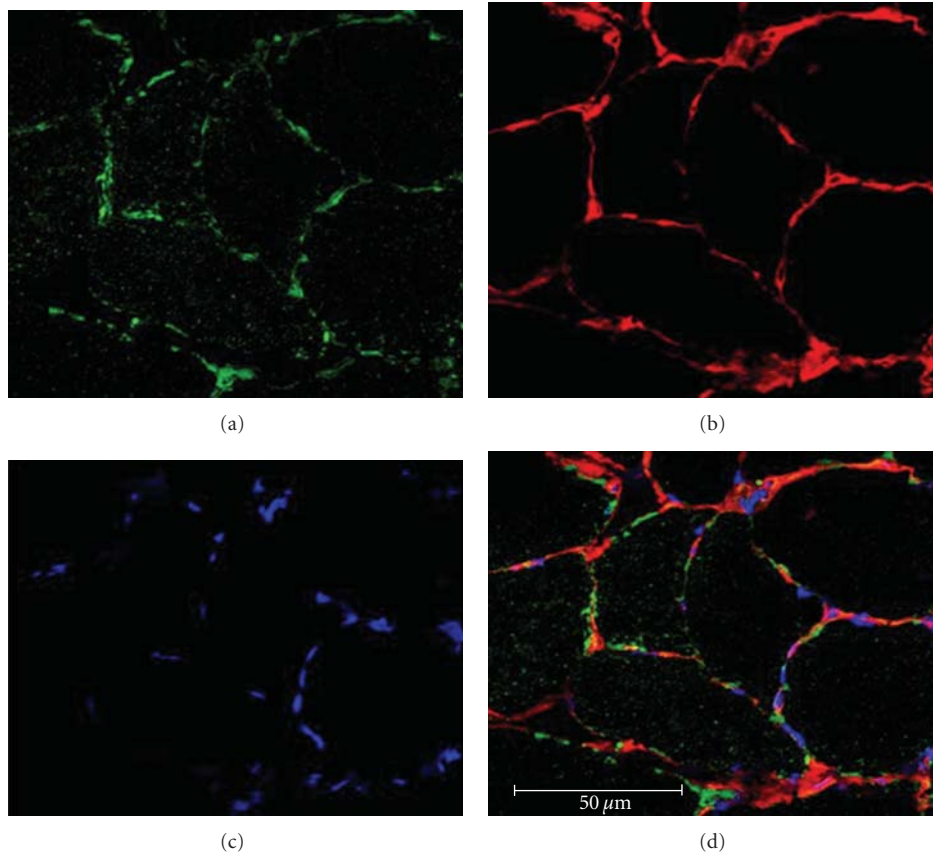


FIGURE 1: Staining of neutral lipid droplets (LDs) with BODIPY (493/503) in cross section of rat soleus muscle demonstrates staining within the fiber, but especially under the surrounding sarcolemma. (a) Fibers stained with BODIPY (green) demonstrate the appearance of spherical LDs within the muscle fibers as previously described with Oil Red O staining procedures. (b) To provide anatomical localization, the membrane is labeled with wheat germ agglutinin (WGA)-Alexa Fluor 594 (red). (c) Nuclei were stained with DAPI (Blue). (d) Merged triple label image of the muscle section. All images were taken at 63x, and a scale bar is provided for reference.

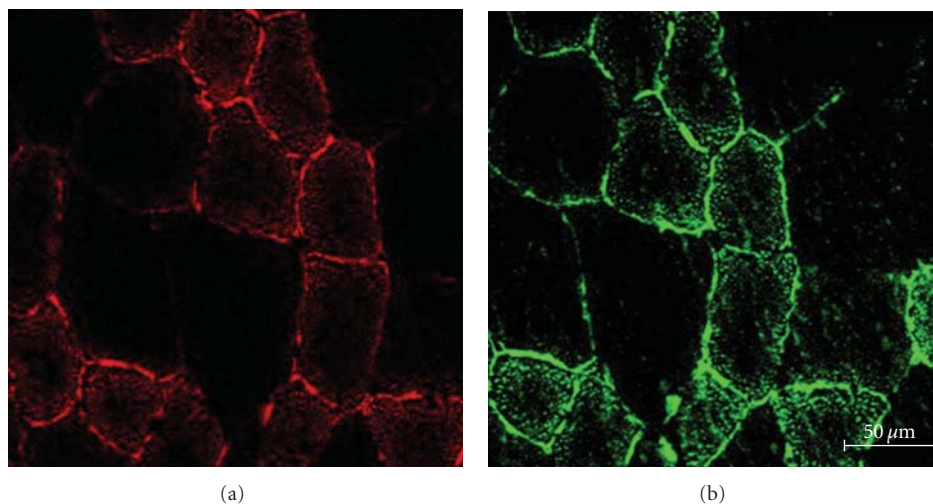


FIGURE 2: Comparison of serial cross sections from rat tibialis anterior (TA) muscle demonstrates that ORO and BODIPY staining are the strongest in the same fibers. (a) Fibers stained with ORO (red) demonstrate the appearance of spherical LDs within the muscle fibers. (b) Fibers stained with BODIPY (green) demonstrate the appearance of spherical LDs within the muscle fibers.

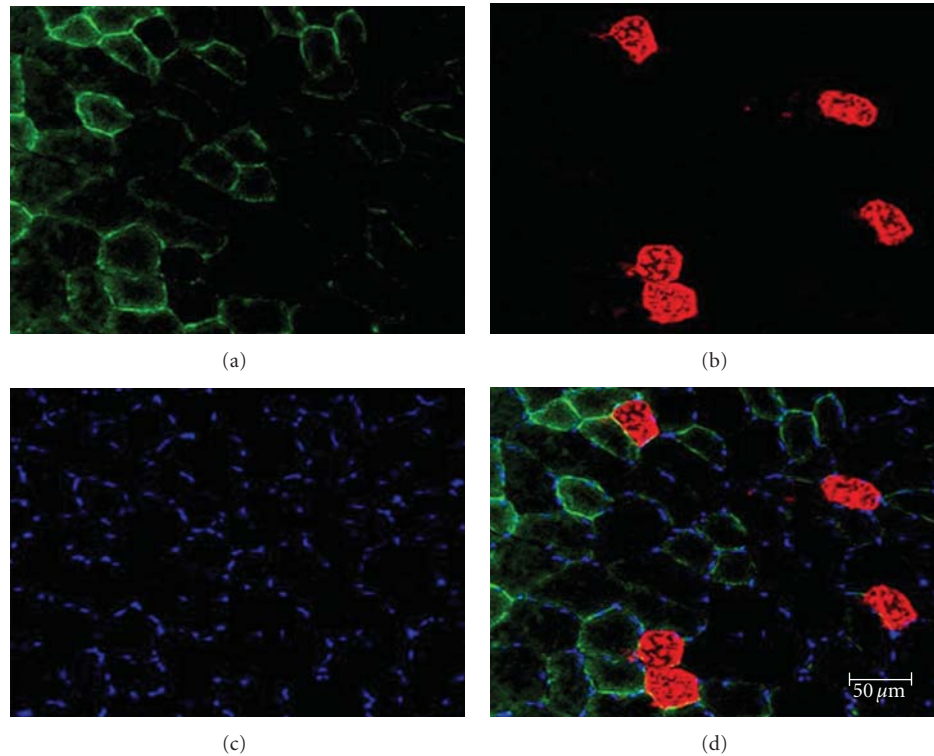


FIGURE 3: Staining of LDs with BODIPY (493/503) in cross section of rat tibialis anterior (TA) muscle demonstrates that LDs are not limited to muscle fibers expressing slow MHC. (a) Fibers stained with BODIPY (green) demonstrate the appearance of spherical LDs within the muscle fibers as previously described with Oil Red O staining procedures. (b) Slow fibers were labeled using an antibody specific for the slow form of MHC (red). (c) Nuclei were stained with DAPI (Blue). (d) Merged triple label image of the muscle section demonstrates fibers presenting with substantial BODIPY signal that do not label for slow MHC. All images were taken at 10x, and a scale bar is provided for reference.

from a rat, we found visible LDs (green, Figure 1(a)) situated within the muscle and along the sarcolemma, identified by wheat germ agglutinin staining (red). These staining patterns are very similar to our ORO images (Figures 2(a) and 2(b)) and also to previously published ORO images taken from muscle cross sections [6, 7].

Previous publications have suggested that LDs are typically more abundant in the type I MHC-positive fibers [2, 12]. Thus, we attempted to determine if LDs stained by BODIPY (493/503, green) were selectively found in only type I muscle fibers (red, Figures 3 and 4). Surprisingly, we found with regular frequency that a number of fibers that contained substantial LD stain (bright fibers in Figures 3 and 4) were not necessarily type I (Figure 3). To explore this in greater detail, we examined additional sections at increased magnification. We found that LDs are clearly not restricted to type I fibers, but are also abundant in fast fibers (presumably type IIa) (Figure 4).

To assess the use of BODIPY in live cells, we isolated and cultured single muscle fibers from the FDB of adult mice. Fibers were either placed in standard culture condition media (Figures 5(a) and 5(c)) or placed in media supplemented with equimolar concentrations of fatty acids (Figures 5(b) and 5(d)). The fibers were stained with BODIPY (493/503) and DAPI (blue). In the fibers maintained under standard culture conditions, we found a heterogeneous mix of fibers

with easily detectable LDs (Figure 5(a)) and fibers with virtually no detectable LDs (Figure 5(c)). However, when the fibers were treated overnight with the 1.0 mM FA mixture, the majority of the fibers exhibited an obvious increase in the amount of visible LDs that were found throughout the entire length of all fibers (Figures 5(b) and 5(d)). We have detected increases in LD frequency across a range of 0.5–1.0 mM FA in cultured cells (data not shown). Furthermore, using 3D confocal reconstruction of the treated fibers, it was clear that LDs were located throughout the volume of the FA-treated fibers. In agreement with previous publications, the presented Z-stack images (1 μM thick, Figure 6) allow for the appreciation of the size of the LD within the muscle fiber. The LDs in muscle are quite small (<2 μM), particularly when compared to what is found in cultured adipocytes (>10 μM) or even LDs within hepatic tissue (~10 μM).

4. Discussion

The purpose of this paper is to demonstrate the use of BODIPY (493/503) as an alternative approach to image LDs within skeletal muscle fibers. Currently, the most common approach to visualize LDs in skeletal muscle is through ORO staining, which requires tissue fixation and is a more time-consuming process. From an experimental point of view, BODIPY is a more flexible approach when compared to

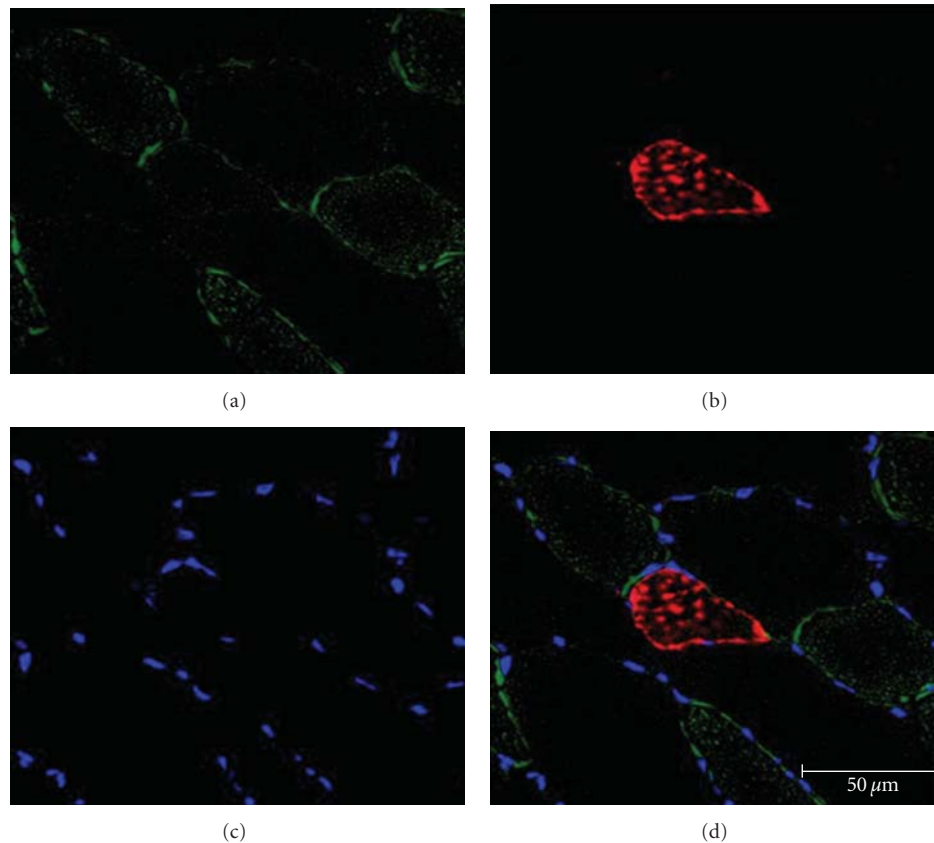


FIGURE 4: High-magnification image demonstrates the presence of LDs within nonslow muscle fibers in the cross section of the rat TA. (a) Fibers stained with BODIPY (green) demonstrate the appearance of spherical lipid droplets within the muscle fibers. (b) Slow fibers were identified using an antibody specific for the slow form of MHC (red). (c) Nuclei were stained with DAPI (Blue). (d) Merged triple label image of the muscle section demonstrates fibers presenting with substantial BODIPY signal that do not label for slow MHC. All images were taken at 63x, and a scale bar is provided for reference.

ORO. Specifically, we were able to use BODIPY on live cells and fixed cells with no appreciable differences. We also found that permeabilization did not affect staining, although others have noted that saponin treatment can reduce the number of LDs [13]. We also used BODIPY on fixed and unfixed frozen muscle sections with equal success. We found that ORO and BODIPY (493/503) resulted in comparable results between serial cross sections of the same muscle, indicating that BODIPY (493/503) is an effective alternative for LD staining in muscle. To date, only a few studies have used BODIPY as a means for visualizing LDs in muscle. Prats et al. used BODIPY (493/503) to show very clear staining of LDs in the soleus muscle [13], and, in a more recent paper, Kostominova used BODIPY to identify LDs in extraocular and peripheral muscle [14, 15]. Unfortunately, these papers have not resulted in increased utilization of this approach in skeletal muscle. Thus, for whatever reason, we believe muscle biologists may not be aware of BODIPY (493/503) as a means for examining LD presence in skeletal muscle. To the best of our knowledge, our current work represents the first use of BODIPY to identify LDs in fast-twitch skeletal muscle isolated myofibers and whole-muscle cross sections. Our images clearly demonstrate the ease with which LDs can be

visualized using the BODIPY stain in various experimental approaches in skeletal muscle.

A number of fluorescent dyes can be employed to visualize LD within skeletal muscle. ORO and Nile Red have both been successfully used in skeletal muscle [5–7]; however, each has limitations that reduce their functionality in a laboratory setting. For example, Nile Red is difficult to use in experiments that require multiple labeling, because it emits a powerful signal spanning a large wavelength [9]. ORO has been used with more regularity; however, since ORO is dependent on the use of isopropanol, it can cause the artificial fusion of LDs, making it inappropriate for analysis of LD size or number [9]. Furthermore, ORO must be filtered; tissue requires fixation and can be difficult dissolve. Scientists that study LD function in nonmuscle cells have adopted the use of BODIPY (493/503) as a means to visualize LDs within cells. BODIPY (493/503) contains a nonpolar structure that, upon binding to neutral lipid, emits a green fluorescence signal with a narrow wavelength range, making it an ideal approach for using in multi-labeling (or dye) experiments [9]. The hydrophobic nature of these dye molecules promotes rapid entry into the nonpolar environment of LDs [9]. Gocze and Freeman showed that the

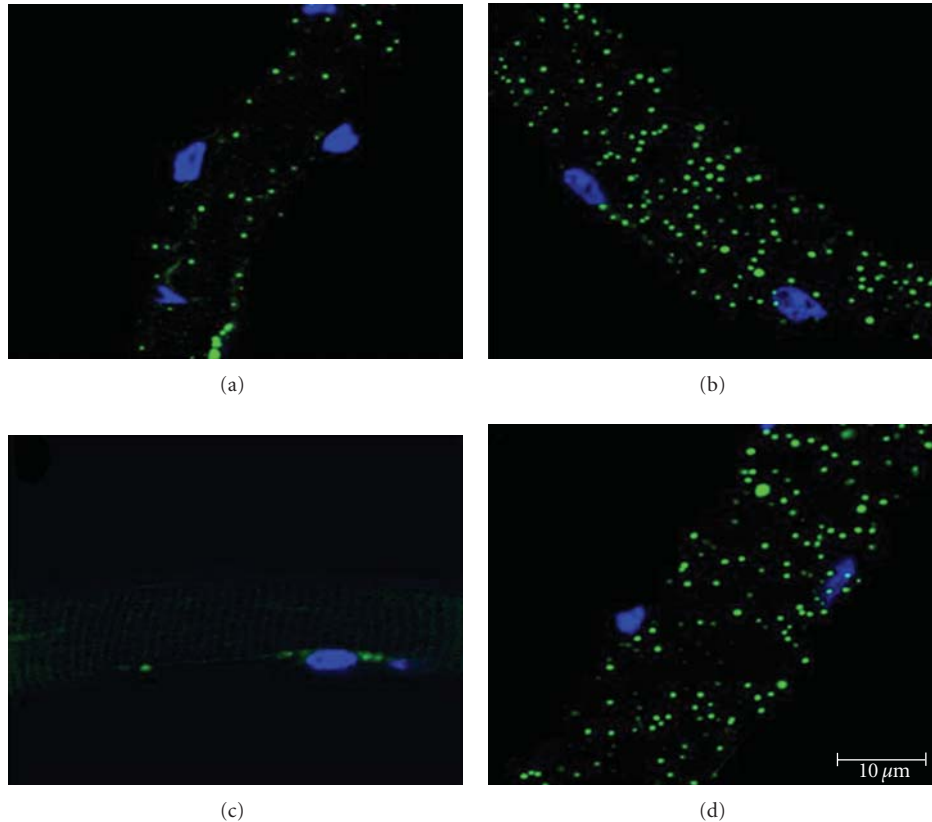


FIGURE 5: Exposure of single fibers to a palmitate-oleate mixture substantially increases the size and frequency of LDs within cultured mouse single muscle fibers. (a, c) Single muscle fibers isolated from the FDB were doubly stained with BODIPY (493/503-green) and DAPI (blue). The fibers were cultured overnight in standard media conditions. A heterogeneous mix of fibers presenting with LDs was found, in which some fibers presented with a visible number of LDs (a), while others presented with virtually no LDs (c). (b, d) Single muscle fibers isolated from the FDB were cultured overnight in standard media conditions supplemented with albumin-conjugated palmitate-oleate mixture (0.5 mM : 0.5 mM ratio). A substantially higher number and larger LDs were found consistently across all fibers that were imaged. All images were taken at 63x, and a scale bar is provided for reference.

lipid fluorescent variability is significantly lower when using BODIPY (493/503) compared to Nile Red, suggesting that it may be more specific for the LD [16].

Here, we visually detected the appearance of spherical LDs within individual skeletal muscle fibers consistent with previous descriptions [6]. In muscle cross sections, the LDs were often in close proximity to the sarcolemma, which suggests that sarcolemmal identification may be critical to determine if the LDs are located in intramuscular or intermuscular regions. This would be particularly critical if the goal is quantification of LDs within muscle fibers. LDs were found scattered throughout the individual fibers (in some, but not all) in a punctuate fashion. The punctuate pattern and the inability to find LDs in all fibers agree with previous descriptions and our findings of LD distribution based on ORO staining of muscle cross sections [6]. We also found that when staining isolated fibers in standard cell culture media, LDs were not consistently visible in all of the fibers within the culture dish. These data suggest that LDs are not found in great frequency across all fibers. However, when we treated the isolated single fibers with media containing high

concentrations of fatty acids, we found a substantial increase in the frequency of LDs and found LD present within all fibers. As expected, we found that BODIPY (493/503) works remarkably well in multiple-labeling approaches using both sectioned muscle and cultured single fibers. For example, we found that muscle fibers that contained a higher frequency of LDs were not always positive for type I MHC. Previously, van Loon et al. demonstrated a high correlation of ORO staining with human type I muscle fibers compared to lower staining in type II fibers [8]. Our data suggest at least a subpopulation of likely type II (e.g., perhaps IIa) fibers can contain a visible amount of LD in skeletal muscle taken from rodents. Overall, our data indicate that BODIPY (493/503) can be successfully used to image LDs within skeletal muscle using multiple different approaches. In addition, in much the same fashion as it is currently done for ORO staining, it would be possible to quantify LD in sections [4, 12] or as it was previously done in single fibers [13].

In summary, we found that BODIPY (493/503) works well as a means to visualize LD in skeletal muscle. This versatile dye works well in sectioned muscle and live culture under

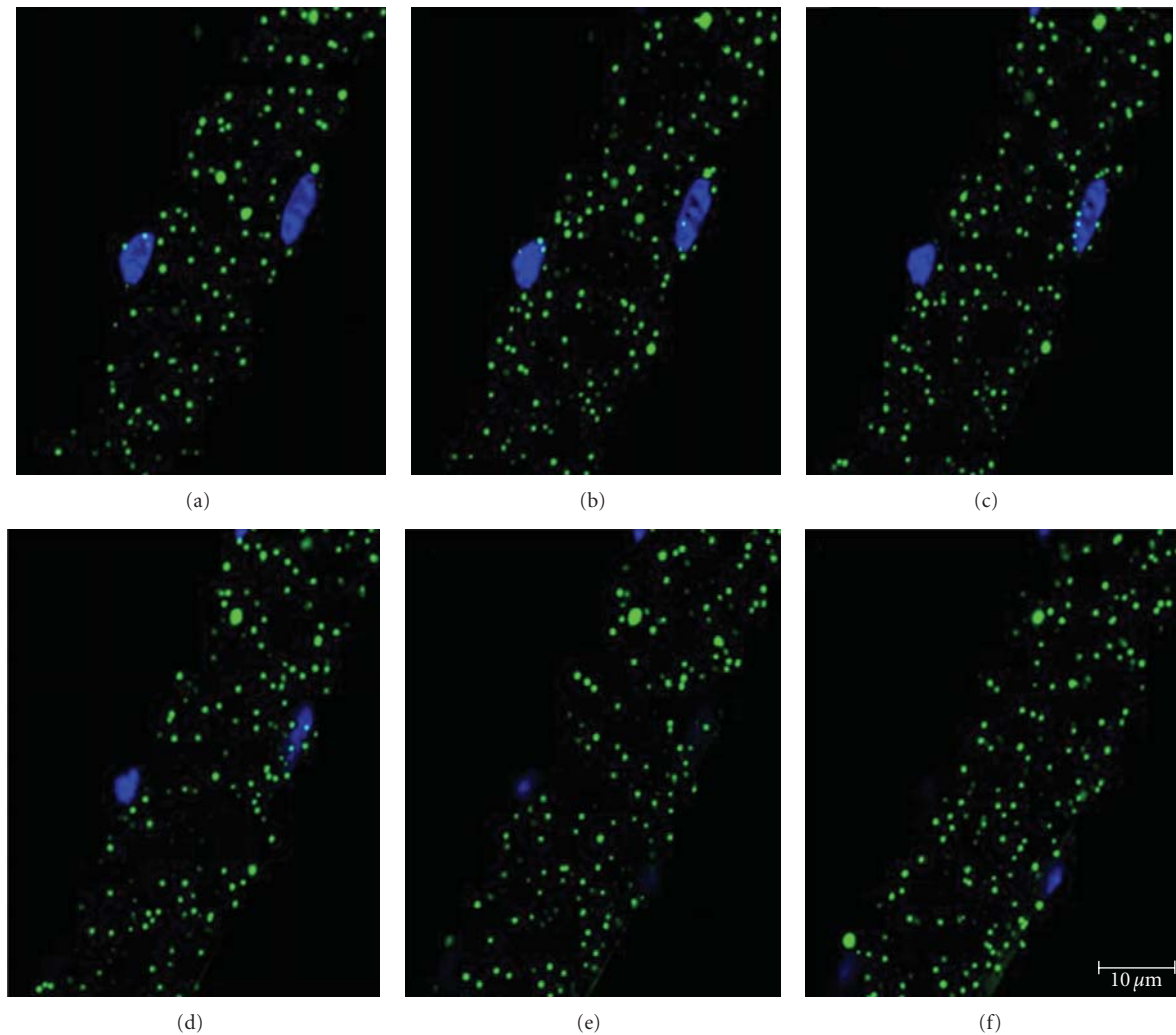


FIGURE 6: Z-stack analysis of a mouse single muscle fiber treated overnight with palmitate-oleate-supplemented media demonstrates distribution of LDs throughout the entire muscle fiber. Single muscle fibers isolated from the FDB were doubly stained with BODIPY (493/503-green) and DAPI (blue). Consecutive 1- μm -thick confocal images are shown from Z-stacks taken near the middle of the fiber (63x), and scale bar is provided for reference.

different types of conditions. BODIPY (493/503) offers a valuable and simple alternative for investigators interested in LD function in skeletal muscle.

Acknowledgment

This work was supported by grants to R. M. Lovering from the National Institutes of Health (K01AR053235 and 1R01AR059179).

References

- [1] V. B. Schrauwen-Hinderling, M. K. C. Hesselink, P. Schrauwen, and M. E. Kooi, "Intramyocellular lipid content in human skeletal muscle," *Obesity*, vol. 14, no. 3, pp. 357–367, 2006.
- [2] L. J. C. van Loon and B. H. Goodpaster, "Increased intramuscular lipid storage in the insulin-resistant and endurance-trained state," *Pflugers Archiv*, vol. 451, no. 5, pp. 606–616, 2006.
- [3] T. A. Wren, S. Bluml, L. Tseng-Ong, and V. Gilsanz, "Three-point technique of fat quantification of muscle tissue as a marker of disease progression in Duchenne muscular dystrophy: preliminary study," *American Journal of Roentgenology*, vol. 190, no. 1, pp. W8–W12, 2008.
- [4] K. De Bock, T. Dresselaers, B. Kiens, E. A. Richter, P. Van Hecke, and P. Hespel, "Evaluation of intramyocellular lipid breakdown during exercise by biochemical assay, NMR spectroscopy, and Oil Red O staining," *American Journal of Physiology*, vol. 293, no. 1, pp. E428–E434, 2007.
- [5] E. Bonilla and A. Prella, "Application of Nile blue and Nile red, two fluorescent probes, for detection of lipid droplets in human skeletal muscle," *Journal of Histochemistry and Cytochemistry*, vol. 35, no. 5, pp. 619–621, 1987.

- [6] C. S. Shaw, D. A. Jones, and A. J. M. Wagenmakers, "Network distribution of mitochondria and lipid droplets in human muscle fibres," *Histochemistry and Cell Biology*, vol. 129, no. 1, pp. 65–72, 2008.
- [7] C. S. Shaw, M. Sherlock, P. M. Stewart, and A. J. M. Wagenmakers, "Adipophilin distribution and colocalisation with lipid droplets in skeletal muscle," *Histochemistry and Cell Biology*, vol. 131, no. 5, pp. 575–581, 2009.
- [8] L. J. C. Van Loon, R. Koopman, R. Manders, W. van der Weegen, G. P. van Kranenburg, and H. A. Keizer, "Intramyocellular lipid content in type 2 diabetes patients compared with overweight sedentary men and highly trained endurance athletes," *American Journal of Physiology*, vol. 287, no. 3, pp. E558–E565, 2004.
- [9] L. L. Listenberger and D. A. Brown, "Fluorescent detection of lipid droplets and associated proteins," *Current Protocols in Cell Biology*, chapter 24, unit 24 22, 2007.
- [10] R. M. Lovering, L. Michaelson, and C. W. Ward, "Malformed mdx myofibers have normal cytoskeletal architecture yet altered EC coupling and stress-induced Ca^{2+} signaling," *American Journal of Physiology*, vol. 297, no. 3, pp. C571–C580, 2009.
- [11] S. K. Pinnamaneni, R. J. Southgate, M. A. Febbraio, and M. J. Watt, "Stearoyl CoA desaturase 1 is elevated in obesity but protects against fatty acid-induced skeletal muscle insulin resistance in vitro," *Diabetologia*, vol. 49, no. 12, pp. 3027–3037, 2006.
- [12] J. He, S. Watkins, and D. E. Kelley, "Skeletal muscle lipid content and oxidative enzyme activity in relation to muscle fiber type in type 2 diabetes and obesity," *Diabetes*, vol. 50, no. 4, pp. 817–823, 2001.
- [13] C. Prats, M. Donsmark, K. Qvortrup et al., "Decrease in intramuscular lipid droplets and translocation of HSL in response to muscle contraction and epinephrine," *Journal of Lipid Research*, vol. 47, no. 11, pp. 2392–2399, 2006.
- [14] B. A. Clark, M. Alloosh, J. W. Wenzel, M. Sturek, and T. Y. Kostrominova, "Effect of diet-induced obesity and metabolic syndrome on skeletal muscles of Ossabaw miniature swine," *American Journal of Physiology*, vol. 300, no. 5, pp. E848–E857, 2011.
- [15] T. Y. Kostrominova, "Application of WGA lectin staining for visualization of the connective tissue in skeletal muscle, bone, and ligament/tendon studies," *Microscopy Research and Technique*, vol. 74, no. 1, pp. 18–22, 2011.
- [16] P. M. Gocze and D. A. Freeman, "Factors underlying the variability of lipid droplet fluorescence in MA-10 Leydig tumor cells," *Cytometry*, vol. 17, no. 2, pp. 151–158, 1994.

Research Article

Transversal Stiffness and Beta-Actin and Alpha-Actinin-4 Content of the M. Soleus Fibers in the Conditions of a 3-Day Reloading after 14-Day Gravitational Unloading

I. V. Ogneva

State Scientific Center of Russian Federation-Institute of Biomedical Problems, Russian Academy of Sciences, 76-a, Khoroshevskoye shosse, Moscow 123 007, Russia

Correspondence should be addressed to I. V. Ogneva, iogneva@yandex.ru

Received 2 April 2011; Revised 7 July 2011; Accepted 22 July 2011

Academic Editor: J.-P. Jin

Copyright © 2011 I. V. Ogneva. This is an open access article distributed under the Creative Commons Attribution License, which permits unrestricted use, distribution, and reproduction in any medium, provided the original work is properly cited.

The aim of the work was to analyze the structural changes in different parts of the sarcolemma and contractile apparatus of muscle fibers by measuring their transversal stiffness by atomic force microscopy in a three-day reloading after a 14-day gravity disuse, which was carried out by hind-limbs suspension. The object of the study was the soleus muscle of the Wistar rat. It was shown that after 14 days of disuse, there was a reduction of transversal stiffness of all points of the sarcolemma and contractile apparatus. Readaptation for 3 days leads to complete recovery of the values of the transversal stiffness of the sarcolemma and to partial value recovery of the contractile apparatus. The changes in transversal stiffness of sarcolemma correlate with beta-actin and alpha-actinin-4 in membrane protein fractions.

1. Introduction

Results of a large number of studies in terms of real and simulated gravitational unloading suggest that in different organs and tissues negative changes are formed as a result of microgravity. Skeletal muscle is particularly exposed to weightlessness as a specialized organ that performs postural and motor functions. The subject of many studies is the soleus muscle, for which it was shown that prolonged exposure to microgravity conditions leads to a significant reduction of its mass, atrophic changes of the fibers [1–3]. Under the conditions of gravitational unloading, synthesis of myosin heavy chain of fast type is increased in the muscle fibers [3–6]. Atrophic changes and reduction of the number of slow fibers lead to a rapid transformation [7]. As a result, contraction time decreases, and soleus muscle becomes less resistant to prolonged stress [8, 9], and there is a decrease in functionality both of the whole muscle [10, 11] and single fibers [12].

But equally significant problem facing the human exploration of outer space, including missions to Mars, is the early period of readaptation to gravity. Particularly important is

to restore the functionality of the muscles, the acceleration of which is not possible without understanding the mechanism of readaptation changes.

It was shown that the readaptation to gravity of atrophied muscles leads to more pronounced negative changes than in microgravity. It became clear after SLS-2 mission (1993), during which tissues were taken in conditions of weightlessness. Serious damage to the fibers of *m. soleus* and *m. adductor longus* in these samples was absent, as well as after 3 hours of readaptation, and became prominent after 4.5 hours of stay [13]. Analyzing the results of this experiment, Riley et al. [13] concluded that the contractile activity in the early period of readaptation of atrophied muscle is perceived as an eccentric load, as sarcomere structure damages, observed after 4.5 hours of reloading, are similar to those after eccentric contractions [14–17].

After 8–11 hours in conditions of Earth's gravity after a 14-day space flight of the biosatellite "Kosmos 2044," Riley et al. [14] showed that there were extensive damages to the sarcomere of *m. adductor longus* fibers, minimal necrosis in the tissue, and a slight activation of macrophages

and satellite cells. However, a 2-day reloading after 12.5-day stay in weightless conditions on board the biosatellite “Kosmos 1887” leads to more extensive necrosis, a significant activation of macrophages and satellite cells [15].

At the same time, after 3 days of reloading after a 10-day antiorthostatic weighing of the rats, the levels of phosphorylated PKB/Akt and p70S6K were significantly increased (by 56% and 26%, resp.) in relation to control, to which they returned after 10 days of readaptation [18]. This may indicate an intensification of protein synthesis in muscle fibers during the period of 3–10 days of readaptation to gravity in 1 G. Perhaps due to the intensification of protein synthesis after 7 days of reloading after 7- and 14-day antiorthostatic weighing of the rats, an increase in cross-sectional area of soleus fibers to the level of control was observed [19].

After 14 days of readaptation after 21-day weighing of the rat, the maximum force of contraction of the soleus muscle was increased compared to that immediately after gravitational unloading [11], whereas after 9 days of stay in 1 G after a 15-day antiorthostatic weighing of the rat, it was not improved [10]. However, according to Litvinova et al. [20], the maximum force of contraction of single fibers of the soleus muscle after 3- and 7-day reloading after a 14-day gravity discharge did not differ from the level immediately after the weighing. Nonetheless, after 14 days of readaptation after a 21-day discharge, almost complete restoration of the structure of the sarcomere was observed [11].

At the same time, the muscle fiber is a three-dimensional structure in which the tension transmission occurs not only longitudinally, but also in the transverse direction [21]. Changes in the structure of muscle fibers, observed in a gravity disuse and follow-up readaptation period, naturally lead to a change in mechanical properties that depend on the integrity of the structure, such as stiffness. In turn, changes in the longitudinal and transversal stiffness are directly related to the changes in contractile properties of muscle fibers [12, 22, 23]. The results of the study of transversal stiffness of contractile apparatus suggest that gravitational unloading caused different changes in slow and fast muscles. It was shown that hindlimb suspension led to decrease of transversal stiffness of soleus fibers and increase of transversal stiffness of tibialis anterior fibers [23]. At the same time, visual observations of the structure of individual compartments of muscle fibers, such as sarcolemma, are virtually impossible, and to assess its structural changes, transversal stiffness may be useful. Structural basis of the transversal stiffness of the sarcolemma with cortical cytoskeleton is a network of filaments formed by nonmuscle actin-beta-actin. To form such a network, a host of capping proteins is needed, one of which is alpha-actinin-4, attention to which in a gravity disuse is due primarily to the fact that its binding to beta-actin depends on the content of calcium ions, the increase of which in these conditions has been shown previously [22, 24, 25].

Thus, in spite of some data on the dynamics of reloading of the various parameters characterizing the structural and functional properties of the soleus muscle, the changes at the cellular level have hardly been studied. However, the implementation of readaptation process, as a special case of

the reaction to changes in external mechanical conditions, at the cellular level is a key element in restoring the health of the muscles after a long stay in weightlessness.

Previously proposed method [26] of determination of the structure condition, based on measuring the mechanical characteristics of the different compartments of muscle fibers by atomic force microscopy, can assist in assessing the changes being implemented not only at the level of the contractile apparatus, but also at the level of the sarcolemma in readaptation to gravity after being in microgravity conditions.

2. Materials and Methods

Experiments were performed on the soleus muscle fibers (*Sol*) of a Wistar rat weighing 225–255 g. In order to simulate the conditions of gravitational unloading in rodents, antiorthostatic weighing of their hind limbs was conducted by the method of Ilyin-Novikov in the modification by Morey-Holton [27]. The duration of gravitational unloading in rats was 14 days. Reloading within 3 days was performed in the same conditions as Vivary control. The choice of this period of recovery was due, on the one hand, to the data [15] on even more significant damage to the sarcomere compared with the state immediately after unloading, and on the other hand, the data [18] on the beginning of the intensification of protein synthesis. Thus, reloading within 3 days after 14-day gravity disuse is of fundamental importance for understanding the cellular mechanisms of the acute period of readaptation. The following groups were formed: “Control,” “14-HS,” and “14-HS + 3-R” of 7 animals each.

All procedures with animals were approved by the Commission on Biomedical Ethics SSC RF Institute for Biomedical Problems, RAS.

2.1. Atomic Force Microscopy. To determine the transversal stiffness of the different compartments of muscle fibers, atomic force microscopy was used. The method of obtaining preparations for research and images of the surface of muscle fibers that allow for local measurements of the transversal stiffness we described in detail earlier [23, 26].

The muscle was excised from tendon to tendon and, in order to carry out a partial destruction of the cell membrane, it was treated according to the method of chemical skinning, which was previously described by Stevens et al. [28]. Before the time of the experiments, the samples were stored at -20°C in a buffer-containing relaxing solution in equal parts by volume of R (20 mM MOPS, 170 mM potassium propionate, and 2.5 mM magnesium acetate, 5 mM K_2EGTA , 2.5 mM ATP) and glycerol.

On the day of the experiment, the samples were transferred into solution R, in which single-permeabilized muscle fibers were isolated.

To obtain demembrated fibers, single-permeabilized muscle fibers, which were in solution R, were incubated with detergent Triton X-100, the final concentration of which was 2% by volume for 12 hours at a temperature of $+4^{\circ}\text{C}$. After

treatment with detergent, the obtained fibers were washed in the solution R.

To measure the transversal stiffness, the isolated fibers were attached to the bottom of the liquid cell of atomic force microscope, fixing their ends with a special glue Fluka shellac wax-free (Sigma, Germany). Depending on the series of experiments, a cell was filled either with a relaxing solution R or an activating solution A (20 mM MOPS, 172 mM potassium propionate, 2.38 mM magnesium acetate, 5 mM CaEGTA, and 2.5 mM ATP), or rigor solution Rg (20 mM MOPS, 170 mM potassium propionate, 2.5 mM magnesium acetate, and 5 mM K₂EGTA).

The measurements of transversal stiffness of both permeabilized and Triton-treated fibers were performed using the platform Solver-P47-Pro (NT-MDT, Russia). A preliminary scan of the surface allowed determining the length of the sarcomere as described previously [26], which was $2.48 \pm 0.03 \mu\text{m}$. The indentation depth was 150 nm. To obtain each average value, at least 35 measurements were conducted.

Processing of the results was carried out in a specially designed program in MatLab 6.5 environment.

2.2. Western Blotting. To determine protein content, the muscle was frozen at liquid nitrogen temperatures. Preparation of tissue extracts and generation membrane and cytoplasmic fraction were carried out by the method of Vitorino et al. [29]. Denaturing polyacrylamide gel electrophoresis was carried out by the method of Laemmli on Bio-Rad system (USA), as previously mentioned in [23]. Based on the measurements of concentration, each well was applied the same amount of protein. Transfer to nitrocellulose membrane was carried out by the method of Towbin et al. [30].

In order to determine each protein, the specific primary monoclonal antibodies based on mouse immunoglobulin (Sigma, Germany) were used in the dilutions recommended by the manufacturer: for beta-actin—in a dilution of 1 : 500, for alpha-actinin-4—1 : 400. As secondary antibodies, biotinylated goat antibodies were used against mice IgG (Sigma, Germany) in a dilution of 1 : 6000. Next, the membranes were treated with a solution of streptavidin conjugated with horseradish peroxidase (Sigma, Germany) in a dilution of 1 : 10000. Protein bands were detected using 3,3'-diaminobenzidine (Merck, USA).

2.3. Statistical Analysis. The results obtained in the experiments results were statistically processed using ANOVA, using for the validation of the differences between the groups post hoc *t*-test with a significance level of $P < 0.05$. The data were presented as $M \pm SE$, where *M* is the mean value of the estimated values, and *SE* is the standard error of mean value.

3. Results

3.1. Transversal Stiffness of Various Regions of the Contractile Apparatus and the Sarcolemma of *Sol* Single Fibers. In the “Control” group, the transversal stiffness of Triton-treated fibers (Figure 1(a)) in semisarcomere area, that is, between the Z-disk and M-line, significantly increases from

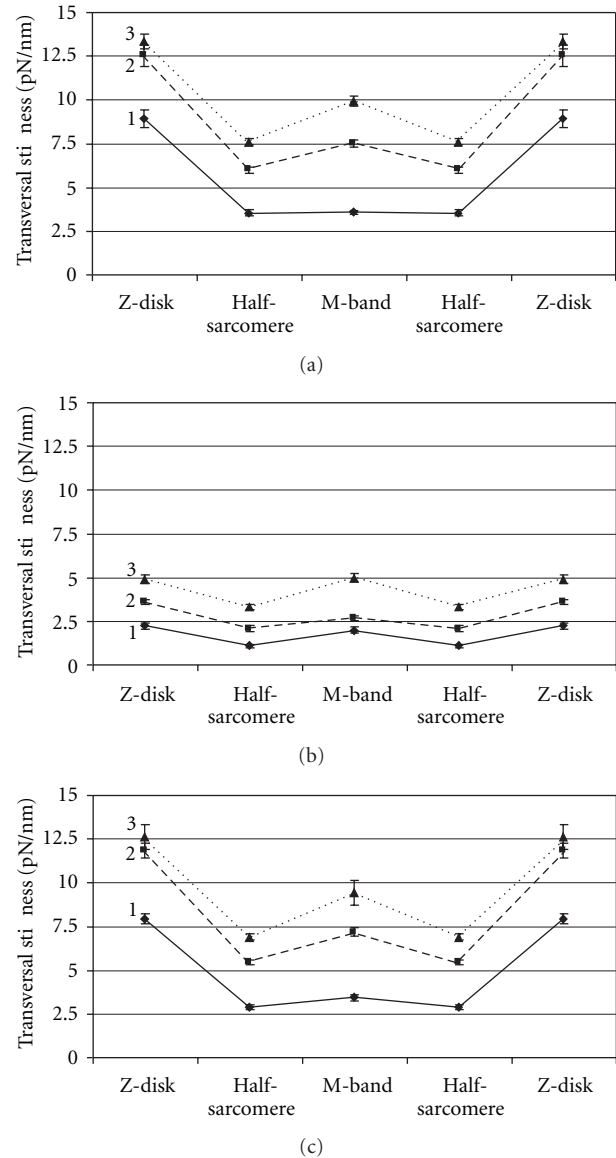


FIGURE 1: Regional distribution of the transversal stiffness along the sarcomere of isolated Triton-treated *Sol* muscle fibers in liquid relaxed (1), calcium activated (2), and rigor (3) states after 14-day gravitational unloading and 3-day reloading; A: group “Control,” B: group “14-HS,” C: group “14-HS + 3-R.”

the relaxed state to the activated and from activated to rigor. After a 14-day gravitational unloading, transversal stiffness of all Triton-treated fibers (Figure 1(b)) is significantly reduced, relative to similar measurement points in the “Control” group, especially in the Z-disk area; however, a significant increase in stiffness, typical of all sections of the fibers at contraction activation and transition to the rigor, is preserved. After a 3-day reloading (Figure 1(c)), values of the transversal stiffness of Triton-treated fibers in semisarcomere area in all the states are still significantly below the level of control, but higher than those in the “14-HS” group. In addition, the transversal stiffness of Z-disk of fibers in the

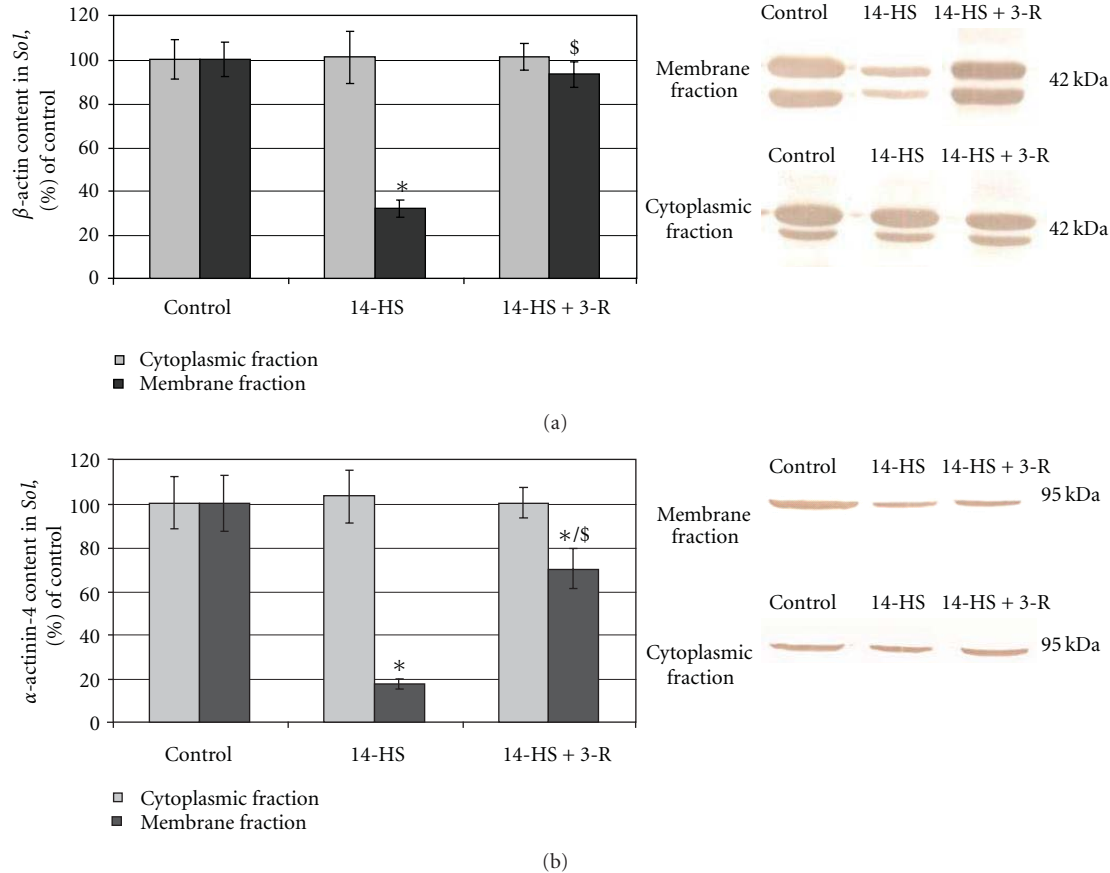


FIGURE 2: Protein content in the rat's Sol after 14-day gravitational unloading and 3-day reloading; (a) beta-actin, (b) alpha-actinin-4; * $P < 0.05$ as compared to the group "Control," $^{\S}P < 0.05$ as compared to the group "14-HS."

"14-HS + 3-R" group in the relaxed state is also reduced with respect to "Control" group.

Other trends in gravity disuse and subsequent reloading were observed in the study of permeabilized fibers (Table 1). Transversal stiffness of the sarcolemma between the projections of Z-disk and M-line in an activated state in the "Control" group did not increase compared to the relaxed state. At the same time, the stiffness in the projection of Z-disk and M-lines increased with contraction activation and transition to the rigor. After a 14-day of antiorthostatic weighing, transversal stiffness of all sections of permeabilized fibers was reduced, but the increase of this parameter in the membrane projections of Z-disk and M-line in activated and rigor state remained. After a 3-day reloading, the sarcolemma stiffness was not different from the values in similar measurement points and conditions in the "Control" group.

3.2. Protein Content. The content of beta-actin (Figure 2(a)) in cytoplasmic protein fractions did not change after the 14-day gravity disuse and subsequent three-day reloading. In the "14-HS" group, there was a reduction of beta-actin in the membrane fraction by 68% and reloading to the level of control in the "14-HS + 3-R" group.

The content of alpha-actinin-4 (Figure 2(b)), as well as beta-actin, in the cytoplasmic fraction was not changed. In the membrane fraction in the "14-HS" group, there was a decrease of alpha-actinin-4 by 82% compared with the "Control" group, and in the "14-HS + 3-R" group, its content significantly increased compared with the group "14-HS," but did not reach the level of control and was reduced by 30%.

4. Discussion

Previously, it was shown that the transversal stiffness of various sections of muscle fibers during the gravity disuse varies in different ways [23]. Thus, the transversal stiffness of various sections of the sarcolemma has been reducing through the day of gravity disuse, while changes in the contractile apparatus are observed after three days. The results, obtained in this paper, indicate that the reloading of the transversal stiffness also occurs in many ways.

After 14 days of hind-limbs suspension, the transversal stiffness of various sections of the sarcolemma and contractile apparatus is significantly reduced, apparently due to disassembly of the cortical cytoskeleton and calcium-dependent proteolysis of the contractile apparatus proteins,

TABLE 1: Transversal stiffness (pN/nm) of isolated permeabilized *Sol* muscle fibers in liquid in relaxed, calcium-activated (pCa = 4.2), and rigor states under 14-day gravitational unloading and 3-day reloading.

State group	Relaxed	Activated (pCa = 4.2)	Rigor
Transversal stiffness of sarcolemma between the M-band and Z-disk projections $k_{\perp s}$			
Control	2.94 ± 0.14	3.09 ± 0.17	3.72 ± 0.15 ^{%/#}
14-HS	1.11 ± 0.06 [*]	1.28 ± 0.09 [*]	1.42 ± 0.11 ^{*/%#}
14-HS + 3-R	2.92 ± 0.10 [§]	2.82 ± 0.19 [§]	3.13 ± 0.12 ^{§*/#}
Transversal stiffness of sarcolemma at the M-band projection $k_{\perp Ms}$			
Control	2.15 ± 0.14	2.73 ± 0.13 [%]	3.25 ± 0.19 ^{%/#}
14-HS	0.99 ± 0.11 [*]	1.36 ± 0.12 ^{*/%#}	1.81 ± 0.14 ^{*/%/#}
14-HS + 3-R	2.11 ± 0.12 [§]	2.76 ± 0.22 ^{§*/%#}	3.36 ± 0.21 ^{§*/%/#}
Transversal stiffness of sarcolemma at the Z-disk projection $k_{\perp Zds}$			
Control	3.25 ± 0.18	3.58 ± 0.16 [%]	4.15 ± 0.17 ^{%/#}
14-HS	1.32 ± 0.12 [*]	1.83 ± 0.13 ^{*/%#}	2.01 ± 0.12 ^{*/%/#}
14-HS + 3-R	3.01 ± 0.13 [§]	3.33 ± 0.11 ^{§*/%#}	3.96 ± 0.17 ^{§*/%/#}

^{*} $P < 0.05$ as compared to the analogous state of the group "Control," [§] $P < 0.05$ as compared to the analogous state of the group "14-HS," [%] $P < 0.05$ as compared to the relaxed state at the same group, [#] $P < 0.05$ as compared to the activated state at the same group.

which was discussed earlier [22, 23]. Decrease of stiffness Z-disk is especially pronounced, as shown directly by Akiyama et al. [31], may be due to the action of calpain. In addition, damages to the sarcomere, typical for type I fibers, as shown for the first time by Riley et al. [15], may also lead to a decrease in stiffness in semisarcomere area and reduced transversal stiffness. At the same time, in conditions of gravitational unloading, an increase in the proportion of type II fibers is observed [3]. It seems that gravitational unloading caused different changes in transversal stiffness of type I and type II muscle fibers. In the study of *m. soleus*, which predominantly consists of slow fibers, we observed the decrease of the transversal stiffness of contractile apparatus under conditions of hindlimb suspension, possibly due to sarcomere damage [15]. At the same time, the hindlimb suspension led to increase of the contractile apparatus's transversal stiffness of tibialis anterior fibers, among which predominate fast fibers [23]. Different responses of the transversal stiffness of the contractile apparatus of type I and type II fibers on gravity disuse could be dependent on the level of EMG activity. However, the performance of single-fiber electrophoresis, which is necessary for determination of fiber phenotype, connects with experimental problems due to insufficient dimension of fiber fragments used for stiffness measurements.

Stiffness of the contractile apparatus after 3-day reloading, though significantly increased in comparison with values immediately after the unloading, does not reach the level of control. Riley et al. [13, 17] showed that the contractile activity in the early period of readaptation (after 4.5 hours) is perceived by an atrophied muscle as eccentric load, which leads to a marked destruction of the structure of the sarcomere. At the same time after 3-day reloading after 10-day unloading of the rats, the levels of phosphorylated PKB/Akt and p70S6K significantly increased relative to control, which may be indicative of an intensification of protein synthesis [18]. Taking these data into account, we can assume that in the first few hours after unloading, there is an even greater

reduction of transversal stiffness of the contractile apparatus compared to the state immediately after unloading. Next, the intensification of protein synthesis leads to the repair of the sarcomere structure, but after 3 days of readaptation, this process is not completed, and that is reflected in the partial recovery of the values of the transversal stiffness of contractile apparatus.

At the same time, the transversal stiffness of different parts of the sarcolemma does not differ from the control level after 3 days of reloading after a 14-day antiorthostatic suspension. At the same time in the early stages of gravitational unloading, reduced transversal stiffness of the sarcolemma was seen in a day after gravity disuse, while changes in stiffness of the contractile apparatus took place just in three days [23]. Therefore, we can assume that change in the transversal stiffness of sarcolemma is more sensitive to changes in external mechanical conditions, which is of interest in connection with the ongoing search for mechanosensitive cell structures.

By analogy with the results of Costa et al. [32], obtained on human aorta cells, we can assume that changes in transversal stiffness of permeabilized fibers are associated with changes in the submembrane actin cytoskeleton, which is consistent with the data of Collinsworth et al. [33]. Reduction of the transversal stiffness of permeabilized fibers can be connected with the destruction of filaments formed by non-sarcomeric actin (beta-actin) and changes in the content of the actin-binding proteins, including alpha-actinin-4.

To test this hypothesis, we have analyzed the relative content of beta-actin in the cytoplasmic and membrane fraction of the total protein. The data indicate that the content of beta-actin in the cytoplasmic fraction did not change either as a result of a 14-day unloading, or in the subsequent three-day reloading. However, the content of beta-actin protein in the membrane fraction after disuse was reduced by more than 3 times compared to the control, but after 3 days of reloading did not differ from control, which correlated with changes in transversal stiffness of the sarcolemma.

The destruction of the cortical cytoskeleton naturally leads to a transient increase in the content of G-actin, which in its turn can trigger several signaling pathways, such as SRF dependent [34].

However, the cause of the destruction of the cortical cytoskeleton can be dissociation from the actin of actin-binding proteins, including alpha-actinin-4. Our data suggest that the content of alpha-actinin-4 in the protein cytoplasmic fraction does not change. The dynamics of change of the content of alpha-actinin-4 in the membrane fraction is similar to that for beta-actin although full reloading of its relative content after 3-day readaptation does not occur. Alpha-actinin-4 is a nonmuscle isoform of alpha-actinin, a protein belonging to the family of spectrin [35]. It functions as an antiparallel homodimer, binding the ends of actin filaments with each other [36]. In addition, alpha-actinin-4 connects the actin cytoskeleton to the membrane, and cortical cytoskeleton interacts with the cytoplasmic signaling proteins [37]. Alpha-actinin-4 can bind calcium ions at micromolar concentrations, and calcium concentration greater than 10^{-7} M completely inhibits its binding to actin [38], as well as tyrosine phosphorylation of focal adhesive kinase within actin-binding domain [39]. We have previously shown that within a one day of gravitational unloading, the basal content of calcium ions increases in the fibers of soleus muscle of a rat [22]. In addition, we know that already by the 2nd day of gravitational unloading, accumulation of calcium ions in the fibers of mouse soleus muscle occurs [24, 25].

5. Conclusion

We can assume that as a result of gravitational unloading due to changes in tension, there is deformation of the cortical cytoskeleton, which leads to the dissociation of alpha-actinin-4 from subsarcolemmal actin and, consequently, to the cortical cytoskeleton destruction and reduction of the stiffness of the membrane. However, on the other hand, changes in membrane tension can modulate ion channels work and lead to an accumulation of calcium ions. The increase of calcium ions may contribute to the binding of alpha-actinin-4, the dissociation of the latter from cortical actin, and subsequent degradation of submembrane cytoskeleton. And in fact, in both cases, the accumulation of calcium and G-actin as a result of the cortical cytoskeleton degradation will lead to the launch of a number of signaling pathways, proteolysis ones in the first place, and the formation of adaptive response to microgravity conditions.

Conflict of Interests

No conflict of interests is declared by the author.

Acknowledgments

The author expresses gratitude to V. A. Kurushin, E. V. Ponomareva, and E. G. Altaeva for their assistance in carrying out the experiments. The financial support of the Russian Foundation for Basic Research (RFBR Grant no. 10-04-00

106-a) and program of fundamental research of SSC RF-IBMP RAS is greatly acknowledged.

References

- [1] F. W. Booth and J. R. Kelso, "Effect of hind limb immobilization on contractile and histochemical properties of skeletal muscle," *Pflugers Archiv European Journal of Physiology*, vol. 342, no. 3, pp. 231–238, 1973.
- [2] D. Desplanches, M. H. Mayet, E. I. Ilyina-Kakueva, B. Sempore, and R. Flandrois, "Skeletal muscle adaptation in rats flown on Cosmos 1667," *Journal of Applied Physiology*, vol. 68, no. 1, pp. 48–52, 1990.
- [3] V. J. Caiozzo, F. Haddad, M. J. Baker, R. E. Herrick, N. Prietto, and K. M. Baldwin, "Microgravity-induced transformations of myosin isoforms and contractile properties of skeletal muscle," *Journal of Applied Physiology*, vol. 81, no. 1, pp. 123–132, 1996.
- [4] R. R. Roy, H. Zhong, S. C. Bodine et al., "Fiber size and myosin phenotypes of selected rhesus lower limb muscles after a 14-day spaceflight," *Journal of Gravitational Physiology*, vol. 7, no. 1, p. S45, 2000.
- [5] K. C. Darr and E. Schultz, "Hindlimb suspension suppresses muscle growth and satellite cell proliferation," *Journal of Applied Physiology*, vol. 67, no. 5, pp. 1827–1834, 1989.
- [6] R. J. Talmadge, R. R. Roy, and V. R. Edgerton, "Distribution of myosin heavy chain isoforms in non-weight-bearing rat soleus muscle fibers," *Journal of Applied Physiology*, vol. 81, no. 6, pp. 2540–2546, 1996.
- [7] D. Pette and R. S. Staron, "Transitions of muscle fiber phenotypic profiles," *Histochemistry and Cell Biology*, vol. 115, no. 5, pp. 359–372, 2001.
- [8] R. J. Talmadge, R. R. Roy, V. J. Caiozzo, and V. Reggie Edgerton, "Mechanical properties of rat soleus after long-term spinal cord transection," *Journal of Applied Physiology*, vol. 93, no. 4, pp. 1487–1497, 2002.
- [9] G. R. Adams, V. J. Caiozzo, and K. M. Baldwin, "Skeletal muscle unweighting: spaceflight and ground-based models," *Journal of Applied Physiology*, vol. 95, no. 6, pp. 2185–2201, 2003.
- [10] J. J. Widrick, G. F. Maddalozzo, H. Hu, J. C. Herron, U. T. Iwaniec, and R. T. Turner, "Detrimental effects of reloading recovery on force, shortening velocity, and power of soleus muscles from hindlimb-unloaded rats," *American Journal of Physiology, Regulatory Integrative and Comparative Physiology*, vol. 295, no. 5, pp. R1585–R1592, 2008.
- [11] K. Lee, Y. S. Lee, M. Lee, M. Yamashita, and I. Choi, "Mechanics and fatigability of the rat soleus muscle during early reloading," *Yonsei Medical Journal*, vol. 45, no. 4, pp. 690–702, 2004.
- [12] K. S. McDonald and R. H. Fitts, "Effect of hindlimb unloading on rat soleus fiber force, stiffness, and calcium sensitivity," *Journal of Applied Physiology*, vol. 79, no. 5, pp. 1796–1802, 1995.
- [13] D. A. Riley, S. Ellis, G. R. Slocum et al., "In-flight and postflight changes in skeletal muscles of SLS-1 and SLS-2 spaceflight rats," *Journal of Applied Physiology*, vol. 81, no. 1, pp. 133–144, 1996.
- [14] D. A. Riley, S. Ellis, C. S. Giometti et al., "Muscle sarcomere lesions and thrombosis after spaceflight and suspension unloading," *Journal of Applied Physiology*, vol. 73, pp. 335–343, 1992.
- [15] D. A. Riley, E. I. Ilyina-Kakueva, S. Ellis, J. L. W. Bain, G. R. Slocum, and F. R. Sedlak, "Skeletal muscle fiber, nerve, and

- blood vessel breakdown in space-flown rats," *FASEB Journal*, vol. 4, no. 1, pp. 84–91, 1990.
- [16] D. A. Riley, J. L. Thompson, B. B. Krippendorf, and G. R. Slocum, "Review of spaceflight and hindlimb suspension unloading induced sarcomere damage and repair," *Basic and Applied Myology*, vol. 5, no. 2, pp. 139–145, 1995.
- [17] D. A. Riley, J. L. W. Bain, J. L. Thompson et al., "Decreased thin filament density and length in human atrophic soleus muscle fibers after spaceflight," *Journal of Applied Physiology*, vol. 88, no. 2, pp. 567–572, 2000.
- [18] T. Sugiura, N. Abe, M. Nagano et al., "Changes in PKB/Akt and calcineurin signaling during recovery in atrophied soleus muscle induced by unloading," *American Journal of Physiology, Regulatory Integrative and Comparative Physiology*, vol. 288, no. 5, pp. R1273–R1278, 2005.
- [19] X. J. Musacchia, J. M. Steffen, R. D. Fell, and M. J. Dombrowski, "Skeletal muscle response to spaceflight, whole body suspension, and recovery in rats," *Journal of Applied Physiology*, vol. 69, no. 6, pp. 2248–2253, 1990.
- [20] K. S. Litvinova, P. P. Tarakin, N. M. Fokina, V. E. Istomina, I. M. Larina, and B. S. Shenkman, "Reloading of rat soleus after hindlimb unloading and serum insulin-like growth factor 1," *Russ Fiziol Zh Im I M Sechenova*, vol. 93, no. 10, pp. 1143–1155, 2007.
- [21] R. J. Bloch and H. Gonzalez-Serratos, "Lateral force transmission across costameres in skeletal muscle," *Exercise and Sport Sciences Reviews*, vol. 31, no. 2, pp. 73–78, 2003.
- [22] I. V. Ogneva, V. A. Kurushin, E. G. Altaeva, E. V. Ponomareva, and B. S. Shenkman, "Effect of short-term gravitational unloading on rat and mongolian gerbil muscles," *Journal of Muscle Research and Cell Motility*, vol. 30, no. 7-8, pp. 261–265, 2009.
- [23] I. V. Ogneva, "Transversal stiffness of fibers and desmin content in leg muscles of rats under gravitational unloading of various durations," *Journal of Applied Physiology*, vol. 109, no. 6, pp. 1702–1709, 2010.
- [24] C. P. Ingalls, G. L. Warren, and R. B. Armstrong, "Intracellular Ca²⁺ transients in mouse soleus muscle after hindlimb unloading and reloading," *Journal of Applied Physiology*, vol. 87, no. 1, pp. 386–390, 1999.
- [25] C. P. Ingalls, J. C. Wenke, and R. B. Armstrong, "Time course changes in [Ca²⁺]_i, force, and protein content in hind-limb-suspended mouse soleus muscles," *Aviation Space and Environmental Medicine*, vol. 72, no. 5, pp. 471–476, 2001.
- [26] I. V. Ogneva, D. V. Lebedev, and B. S. Shenkman, "Transversal stiffness and young's modulus of single fibers from rat soleus muscle probed by atomic force microscopy," *Biophysical Journal*, vol. 98, no. 3, pp. 418–424, 2010.
- [27] E. Morey-Holton, R. K. Globus, A. Kaplansky, and G. Durnova, "The hindlimb unloading rat model: literature overview, technique update and comparison with space flight Data," *Advances in Space Biology and Medicine*, vol. 10, pp. 7–40, 2005.
- [28] L. Stevens, Y. Mounier, and X. Holy, "Functional adaptation of different rat skeletal muscles to weightlessness," *American Journal of Physiology*, vol. 264, no. 4, pp. R770–R776, 1993.
- [29] R. Vitorino, R. Ferreira, M. Neuparth et al., "Subcellular proteomics of mice gastrocnemius and soleus muscles," *Analytical Biochemistry*, vol. 366, no. 2, pp. 156–169, 2007.
- [30] H. Towbin, T. Staehelin, and J. Gordon, "Electrophoretic transfer of proteins from polyacrylamide gels to nitrocellulose sheets: procedure and some applications," *Proceedings of the National Academy of Sciences of the United States of America*, vol. 76, no. 9, pp. 4350–4354, 1970.
- [31] N. Akiyama, Y. Ohnuki, Y. Kunioka, Y. Saeki, and T. Yamada, "Transverse stiffness of myofibrils of skeletal and cardiac muscles studied by atomic force microscopy," *Journal of Physiological Sciences*, vol. 56, no. 2, pp. 145–151, 2006.
- [32] K. D. Costa, A. J. Sim, and F. C. P. Yin, "Non-Hertzian approach to analyzing mechanical properties of endothelial cells probed by atomic force microscopy," *Journal of Biomechanical Engineering*, vol. 128, no. 2, pp. 176–184, 2006.
- [33] A. M. Collinsworth, S. Zhang, W. E. Kraus, and G. A. Truskey, "Apparent elastic modulus and hysteresis of skeletal muscle cells throughout differentiation," *American Journal of Physiology*, vol. 283, no. 4, pp. 1219–1227, 2002.
- [34] K. Kuwahara, T. Barrientos, G. C. T. Pipes, S. Li, and E. N. Olson, "Muscle-specific signaling mechanism that links actin dynamics to serum response factor," *Molecular and Cellular Biology*, vol. 25, no. 8, pp. 3173–3181, 2005.
- [35] M. J. F. Broderick and S. J. Winder, "Towards a complete atomic structure of spectrin family proteins," *Journal of Structural Biology*, vol. 137, no. 1-2, pp. 184–193, 2002.
- [36] H. Youssoufian, M. McAfee, and D. J. Kwiatkowski, "Cloning and chromosomal localization of the human cytoskeletal α -actinin gene reveals linkage to the β -spectrin gene," *American Journal of Human Genetics*, vol. 47, no. 1, pp. 62–72, 1990.
- [37] M. D. Baron, M. D. Davison, P. Jones, and D. R. Critchley, "The structure and function of alpha-actinin," *Biochemical Society Transactions*, vol. 15, no. 5, pp. 796–798, 1987.
- [38] T. Parr, G. T. Waites, B. Patel, D. B. Millake, and D. R. Critchley, "A chick skeletal-muscle α -actinin gene gives rise to two alternatively spliced isoforms which differ in the EF-hand Ca²⁺-binding domain," *European Journal of Biochemistry*, vol. 210, no. 3, pp. 801–809, 1992.
- [39] G. T. Waites, I. R. Graham, P. Jackson et al., "Mutually exclusive splicing of calcium-binding domain exons in chick α -actinin," *Journal of Biological Chemistry*, vol. 267, no. 9, pp. 6263–6271, 1992.

Review Article

On Benzofuroindole Analogues as Smooth Muscle Relaxants

Ike dela Peña and Jae Hoon Cheong

Uimyung Research Institute for Neuroscience and Department of Pharmacology, Sahmyook University, 26-21 Kongkreung-dong, Nowon-gu, 139-742 Seoul, Republic of Korea

Correspondence should be addressed to Jae Hoon Cheong, cheongjh@syu.ac.kr

Received 3 May 2011; Accepted 14 July 2011

Academic Editor: J.-P. Jin

Copyright © 2011 I. dela Peña and J. H. Cheong. This is an open access article distributed under the Creative Commons Attribution License, which permits unrestricted use, distribution, and reproduction in any medium, provided the original work is properly cited.

At least two laboratories have independently reported the synthesis of benzofuroindole compounds having potential therapeutic implications in many disease states including those that involve smooth muscle hyperactivity. Through a series of *in vitro* screenings, they demonstrated the efficacy (and selectivity) of these compounds to potentiate large conductance calcium- (Ca^{2+} -) activated K^+ (BK_{Ca}) channels, by far, the most characterized of all Ca^{2+} -dependent K^+ channels. Interestingly, promising benzofuroindole derivatives such as compound 7 (10*H*-benzo[4,5]furo[3,2-*b*]indole) and compound 22 (4-chloro-7-trifluoromethyl-10*H*-benzo[4,5]furo[3,2-*b*]indole-1-carboxylic acid) both exhibited high bladder (versus aorta) selectivity, making them attractive alternative treatments for bladder overactivity. In recent reports, compound 22 (LDD175 or TBIC) also showed inhibition of ileum and uterine contractions, indicating multiple target tissues, which is not surprising as BK_{Ca} channels are ubiquitously expressed in the animal and human tissues. In this paper, the authors discuss the value of benzofuroindole compounds and the challenges that need to be overcome if they were considered as smooth muscle relaxants.

1. Introduction

Smooth muscle contraction plays a fundamental role in regulating the functions of the hollow organs in the body such as the blood vessels, intestines, bladder, airways, and uterus. Dysfunctional contraction of the smooth muscles is a key pathological feature of many diseases including hypertension, bladder overactivity (OAB), irritable bowel syndrome, erectile dysfunction, and asthma. Abnormal uterine contractions may also lead to preterm labor, the latter being responsible for prenatal mortality, neonatal morbidity, and childhood developmental disorders [1]. By and large, smooth muscle hyperactivity disorders involve immense social cost and financial burden to the health services, thus, a considerable effort has been made to understand their etiologies and also to develop drugs with potent smooth muscle relaxant activities.

Contractions of all smooth muscles absolutely depend on the presence of Ca^{2+} which activates the contractile machineries [2, 3]. Elevating intracellular Ca^{2+} , which can be achieved by agonists (e.g., acetylcholine, oxytocin, and prostaglandin $\text{F}_2\alpha$), causes smooth muscle contractions. Acetylcholine (ACh), the main contractile transmitter in

many smooth muscle tissues (e.g., the urinary bladder and gastrointestinal tract), activates muscarinic (M_3) receptors and raises intracellular Ca^{2+} levels by activating the Gq-phospholipase C- (PLC-) inositol triphosphate (IP_3) pathway [4]. It is also believed that extracellular Ca^{2+} facilitates an increase in intracellular Ca^{2+} via opening of the voltage-gated Ca^{2+} channels [5]. M_2 receptor binding of ACh also elevates intracellular Ca^{2+} through a number of controversial mechanisms including inhibition of the production of cyclic AMP (cAMP) [6]. In the bladder smooth muscles, where muscarinic receptor is the primary efferent receptor, agonist-induced contraction is largely dependent on Ca^{2+} entry through nifedipine-sensitive channels and activation of the Rho-kinase pathway [7]. On the other hand, oxytocin and prostaglandin $\text{F}_2\alpha$ act on oxytocin and prostaglandin receptors, respectively, and release Ca^{2+} from intracellular stores through stimulation of the Gq-PLC- IP_3 system [8–10]. They may also propagate the influx of extracellular Ca^{2+} through voltage-gated L-channels [11]. In addition, oxytocin may activate nonselective cation channels and Ca^{2+} -activated Cl^- channels leading to depolarization of myometrial cells and, eventually, the opening of voltage-dependent Ca^{2+} channels [2, 11]. In light of these

observations, drugs that could block the effects of these agonists induce smooth muscle relaxation through some mechanisms that could block or interfere with Ca^{2+} entry. Antimuscarinic agents, those that oppose the effects of ACh, are effective bladder and intestinal smooth muscle relaxants and are well-known standard therapies for OAB and in some forms of gastrointestinal motility disorders. In addition, Ca^{2+} channel blockers (CCBs) are effective OAB interventions although they are more commonly used for hypertension and other cardiovascular diseases. CCBs block Ca^{2+} entry by binding to the L-type Ca^{2+} channels in the heart and smooth muscles of the peripheral vasculature, thereby generating vasodilation and eventually lowering blood pressure [12]. Oxytocin antagonists, CCBs, prostaglandin synthase inhibitors, and β -adrenergic agonists are used as tocolytics (medications to suppress premature labor) by virtue of their influence on lowering intracellular Ca^{2+} levels. β -adrenergic agonists, alike some nonsteroidal anti-inflammatory drugs, increase the level of cAMP which results in the decrease in intracellular Ca^{2+} by stimulating efflux of Ca^{2+} from the cell and also uptake by the sarcoplasmic reticulum [13].

However impressive the above-named agents are in managing abnormal smooth muscle contractions, their efficacy and application are limited due to some reported drug-induced side effects. In fact, the application of these compounds may exacerbate the diseases albeit only in extreme cases [14]. Antimuscarinic drugs, although effective in inhibiting bladder and intestinal contractility, also influence normal contractility thus affecting normal voiding and excretion functions. Moreover, muscarinic M_3 receptors are found in the salivary glands thus severe dry mouth is expected with the use of antimuscarinic agents [14]. The standard tocolytics, although efficacious in arresting preterm labor, also produce serious maternal and cardiovascular or adverse fetal side effects [15, 16]. Altogether, these findings indicate that there is a necessity to develop other smooth muscle relaxants, preferably those that act on a different mechanism.

Another way to counteract defective smooth muscle contractility is to enhance repolarizing (potassium [K^+]) currents [17]. K^+ channels are abundantly expressed in smooth muscles where they play an important role in determining and regulating the excitability of the cell by acting as an excitability “brake.” A number of K^+ channel openers have been developed, and they showed promise in preclinical and clinical studies for a variety of smooth muscle hyperactivity disorders. Among them are the openers of the ATP sensitive K^+ (K_{ATP}) channels and Ca^{2+} -activated K^+ (K_{Ca}) channels. However, as K^+ channels are ubiquitously expressed in virtually all cell types, it has been thought that K^+ channel openers may not show tissue selectivity. Indeed, the most investigated K_{ATP} channel openers pinacidil and cromakalim effectively abolished unwanted bladder contractions without affecting normal voiding [18]. However, they also exhibited limited bladder selectivity and influenced cardiovascular functions [19–23].

At least two noncollaborating laboratories have reported the synthesis of novel K^+ channel openers which they thought as effective interventions for smooth muscle hyperactivity disorders, particularly in OAB. Butera and colleagues

[24] first reported the production of *benzofuroindole* analogues in their continued effort to develop potent bladder relaxants with minimal hemodynamic effects. These benzofuroindole compounds were produced by manipulating the structure of the benzopyran-based antihypertensive and prototype K_{ATP} channel opener celikalim. Initial structural modifications of celikalim accidentally led to the production of the Fisher-indole product 10*H*-benzo[4,5]furo[3,2-*b*]indole (compound 7) (Figure 1), a derivative which displayed not only potent bladder relaxant effects in *in vitro* screenings, but also high bladder (versus aorta) selectivity. On the other hand, another group produced benzofuroindole compounds by overlaying compound 7 (see above), with BMS-204352, a prototypical opener of one type of K_{Ca} channels, the large conductance Ca^{2+} -activated K^+ (BK_{Ca}) channel [25]. One of the derivatives, compound 22, (4-chloro-7-trifluoromethyl-10*H*-benzo[4,5]furo[3,2-*b*]indole-1-carboxylic acid) (Figure 1) demonstrated *in vitro* inhibition of bladder contractions without influencing contractility of the blood vessels [26]. Multiple analyses showed that the above-mentioned benzofuroindole compounds were potent activators of the BK_{Ca} channels [24–26]. BK_{Ca} channels, relative to other K^+ channel types, have more superior biophysical, molecular, and pharmacological properties making them more appealing targets to achieve smooth muscle relaxation (see below). In the succeeding sections, the attractive features of benzofuroindole compounds as smooth muscle relaxants are described, as well as some of the concerns that need to be addressed if they were used clinically as antispasmodics or tocolytics.

2. Benzofuroindole Compounds, BK_{Ca} Channels, and Their Activators

As stated above, the first ever synthesized benzofuroindole analogue (compound 7) was derived from a K_{ATP} channel opener. Thus, it came as a surprise when the compound potently activated the BK_{Ca} channels. Accordingly, the effects of compound 7 were readily reversed by the specific BK_{Ca} channel blocker iberiotoxin, but not by glyburide (a selective K_{ATP} channel blocker). Furthermore, voltage clamp studies on isolated rat bladder myocytes showed that the compound caused an iberiotoxin-sensitive increase in hyperpolarizing current, further intensifying its BK_{Ca} channel-potentiating properties [24]. On the other hand, Gormemis et al. [25] reported another set of benzofuroindole compounds that are also potent BK_{Ca} channel openers. Compound 22, along with other novel benzofuroindole derivatives, was shown to effectively potentiate cloned BK_{Ca} channels expressed in *Xenopus laevis* oocytes. The ionic currents caused by compound 22 were blocked by the peptide BK_{Ca} channel blocker charybdotoxin indicating selective activation of the BK_{Ca} channels [25]. Further electrophysiological characterizations of one the potent derivatives, compound 8 (7-trifluoromethyl-10*H*-benzo[4,5]furo[3,2-*b*]indole-1-carboxylic acid), showed that it highly activated cloned BK_{Ca} channels from the extracellular side independent of β subunits and regardless of the presence of intracellular Ca^{2+} (for a review on BK_{Ca} channel structure, see Figure 2). In addition, it activated native BK_{Ca}

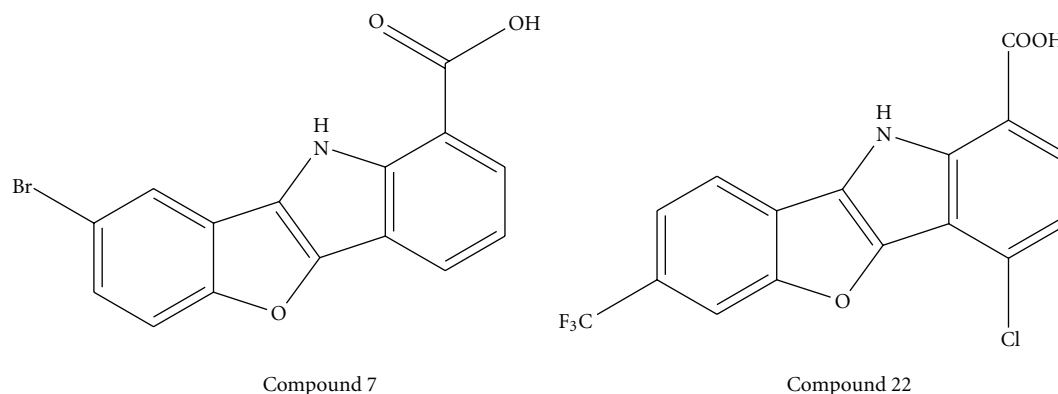


FIGURE 1: Structures of compound 7 (10H-benzo[4,5]furo[3,2-b]indole) and compound 22 (4-chloro-7-trifluoromethyl-10H-benzo[4,5]furo[3,2-b]indole-1-carboxylic acid).

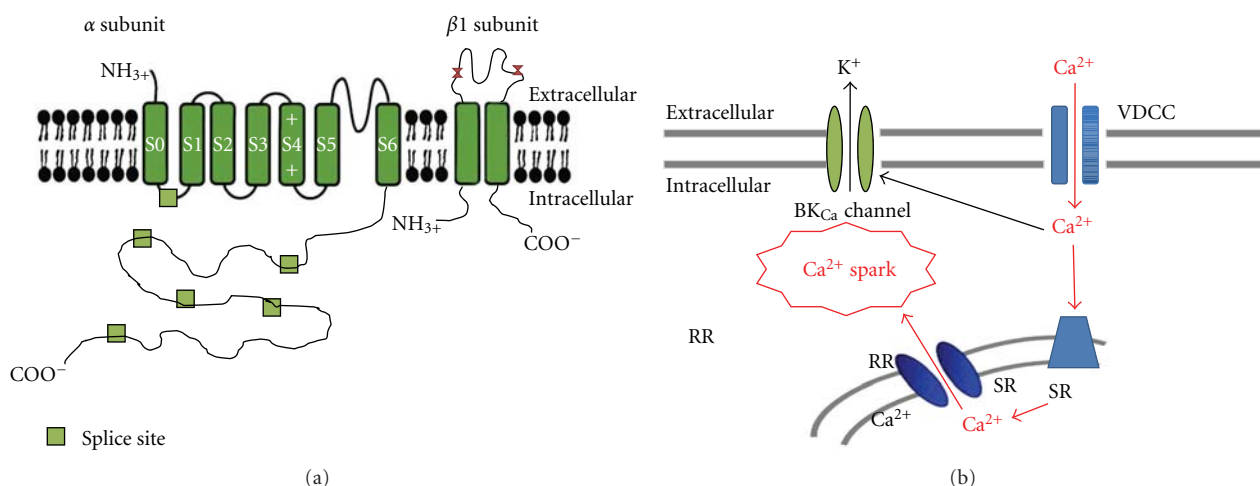


FIGURE 2: Structure and physiology of BK_{Ca} channels. (a) BK_{Ca} channels are composed of two different subunits: the pore-forming α subunit and the auxiliary β subunits. A functional channel is made up by the association of four α and four β 1 subunits. Although a single gene codes for α , splicing leads to variants that are different in biophysical properties and/or intracellular localization. (b) In smooth muscles, membrane depolarization and/or intracellular Ca^{2+} cause the influx of Ca^{2+} through voltage-dependent Ca^{2+} channels (VDCCs). This in turn causes a rise in intracellular Ca^{2+} levels and smooth muscle contraction. Increases in Ca^{2+} levels facilitate Ca^{2+} binding to ryanodine receptors (RRs) in the sarcoplasmic reticulum (SR), which produces a localized Ca^{2+} release (Ca^{2+} spark) that activates the BK_{Ca} channels. Activation of BK_{Ca} channels causes efflux of K^+ , hyperpolarization of the cell membrane, closure of VDCC, prevention of Ca^{2+} entry, and eventually smooth muscle relaxation. Adapted from Garcia et al. [27].

channels from rat hippocampus pyramidal neurons [28], a finding which might have important clinical roles. But just how remarkable is it when a compound is an opener of the BK_{Ca} channels?

Some excellent reviews on the structure, pharmacology, functions (Figure 2), and the potentiality of BK_{Ca} channels as novel therapeutic targets have been made [29, 30]. Structurally, BK_{Ca} channels are composed of two different subunits: the pore-forming α subunit and the auxiliary β subunits. Although channels formed only by four α subunits can be functional, β subunits alter the biophysical and pharmacological properties of homomeric channels, including Ca^{2+} and voltage sensitivity and gating kinetics [28, 31–34]. These characteristics of BK_{Ca} channels make them appealing targets, and their activators potent therapies

for many diseases: (1) abundant distribution like other K^+ channel types, (2) high conductance (~ 200 pS) even at low probability of opening, thus facilitating more efficient K^+ efflux and membrane hyperpolarization (relaxation), (3) high sensitivity to both intracellular Ca^{2+} concentrations and voltage, (4) Ca^{2+} independence, that is, BK_{Ca} channels can open even in the absence of Ca^{2+} and the Ca^{2+} and membrane potential dependence of the channels are independent of each other [29, 30].

A number of BK_{Ca} channel openers, derived from natural products and from synthetic chemistry, have been developed and reported (e.g., dehydrosoyasaponin-I, maxikdiol, NS1619, BMS-204352, 17 β -estradiol, ethylbromideta-moxifen, pimaric acid, and epoxyecosatrienoic acids [35–38]). These substances, however, differ in properties and

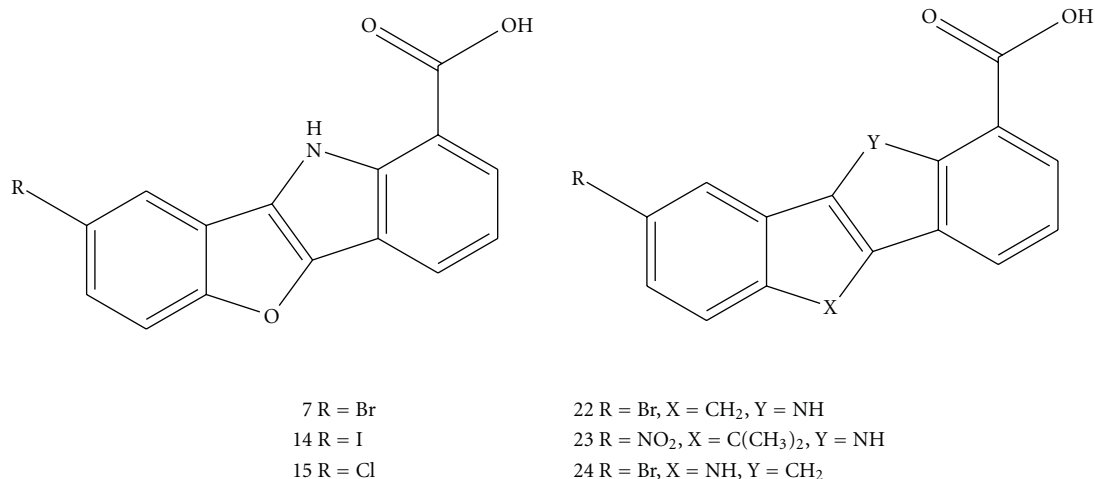


FIGURE 3: Structures of the highly bladder (versus aorta) selective benzofuroindole compounds synthesized by Butera et al. [24].

in some respects, mechanisms of action. For instance, dehydrosoyasaponin-I and 17β -estradiol may require β subunits for optimum channel potentiation [31, 39], while some compounds (e.g., dehydrosoyasaponin-I and 17β -estradiol) may act only on the intracellular side of the channel by being highly impermeable [40]. Unexpectedly, given the potentiality of BK_{Ca} channel openers as future interventions in many disease states, it is surprising that only four BK_{Ca} channel openers have entered clinical development (NS-8, TA-1702, BMS-223131, and BMS-204352) [27]. To the best of our knowledge, clinical trials for the BK_{Ca} channel openers NS8, BMS204352, and TA-1702 have been discontinued, while only one drug candidate, andolast (for the treatment of asthma), remains in the early phase of clinical development [41]. In the view of Garcia et al. [27], there is still much validation required for BK_{Ca} channel openers to progress as future smooth muscle relaxants. Novel BK_{Ca} channel openers must show appropriate potency and selectivity, efficacy in preclinical disease models, and, most of all, lesser toxicity [27].

3. Benzofuroindole Compounds, BK_{Ca} Channel Openers with Bladder (versus Aorta) Selectivity

Aside from remarkably potentiating BK_{Ca} channels from rat bladder myocytes, benzofuroindole compounds developed by Butera and colleagues were also shown to be highly bladder selective with aorta/bladder IC₅₀ ratios ranging from 8- to 46-fold. This was ascertained through organ bath studies with isolated rat bladder and aortic rings. In their studies, compound 15 showed to be the most bladder selective (IC₅₀ ratio aorta/bladder = 46). The structure-activity relationships for these compounds have been reported and reviewed [14, 24]. By looking at the structures of compounds 7, 14, 15 and those of the other highly bladder selective derivatives (compounds 22, 23, and 24), bladder specificity could be attributed to the imbedded 5,5 ring

system that is fairly tolerant of structural modifications [14] (Figure 3). Meanwhile, de la Peña et al. [26] also disclosed the bladder (versus aorta) selectivity profile of compound 22, the benzofuroindole analogue synthesized by Gormemis and colleagues. In their multiple screenings, compound 22 or LDD175 displayed 20-fold selectivity for the rat bladder compared with the aorta (when E_{max} values are compared) [26]. What is more, compound 22 did not have any significant vasorelaxant activity. *In vivo* screenings in the **Spontaneously Hypertensive rat (SHR)**, an animal model of hypertension also showed that compound 22 did not alter the **rat's** hemodynamic activities. In addition, the same group demonstrated that oral administration of compound 22 reduced voiding frequency and lengthened void intervals in SHR, a putative animal model of OAB [42]. It is noteworthy that these effects were seen only in the SHR and not in the normotensive strain, the Wistar Kyoto rats, a finding that might have significant clinical implications.

In certain disease states such as OAB, a major drawback of current pharmacotherapies as well as those drugs in development, is their ability to affect cardiovascular activities. K_{ATP} channel openers, compounds first developed for OAB, also activated K_{ATP} channels in the heart and peripheral blood vessels and brought hemodynamic side effects. For this reason, the development of K_{ATP} drugs for OAB has been abandoned in recent years [14]. The focus has been shifted to other K⁺ channel openers, such as BK_{Ca} and the recently identified KCNQ channels openers [14]. Compared with K_{ATP} channels, BK_{Ca} channels are less expressed in the heart tissue [29, 30] but are abundant in the bladder smooth muscles and also in neuronal tissues. With regard to their expression in neuronal tissues, BK_{Ca} activators could then impact OAB whether the underlying etiology is either neurogenic or myogenic in nature [14]. In fact, it is proposed that targeting the neuronal channels could minimize cardiovascular side effects, although it might also lead to the emergence of unwanted neuronal side effects [14].

TABLE 1: EC₅₀ values (concentration producing 50% of maximum inhibition of spontaneous or agonist-induced contractions) of compound 22 in the isolated bladder, ileum and uterus.

Effects of compound 22 in	EC ₅₀ values (μ M)		
	Bladder [26]	Ileum [43]	Uterus [44]
Spontaneous contractions	n.e.	1.25	4.63
Agonist-induced contractions			
ACh (1 μ M)	1.25	5.01	4.37
EFS	n.e.	3.16	n.t.
High K ⁺ (20 mM KCl)	2.51	0.79	3.04

n.e.: no effect, n.t.: not tested.

4. Compound 22 and Its Effects in Other Smooth Muscles

BK_{Ca} channels are abundantly distributed in many smooth muscle types such as gastrointestinal smooth muscles [41] and the uterus [45–47]. As not much is known about the effects of benzofuroindole compounds in other tissues, an ongoing effort has been made to investigate this matter. Compound 22 also displayed potent inhibition of both spontaneous and agonist-induced contractions of the ileum [43] and uterus [44]. EC₅₀ values of the relaxant effects of compound 22 are shown in Table 1. While compound 22 did not have any intrinsic relaxant activity in the bladder (suggesting its lack of effect on myogenic contractions), it significantly inhibited spontaneous contractions of the ileum and the uterus. However, the effect of compound 22 was more demonstrated in ACh-induced contractions of the bladder versus ileum and uterus. The detrusor was not responsive to the effects of compound 22 in electric field stimulation- (EFS-) induced contractions. Conversely, the relaxative effect of compound 22 in EFS-induced ileal contraction was comparable to that induced by ACh. In bladder and ileum strips, however, compound 22 was not as potent as atropine, an antimuscarinic drug, in inhibiting ACh-induced contractions [26, 43]. In the uterus, although compound 22 relaxed oxytocin, prostaglandin F_{2 α} , and ACh-induced contractions, its effects were not as potent as those of standard tocolytics (note, however, the similarity in the degree of potency between diclofenac and compound 22 in inhibiting PGF_{2 α} -induced contractions) [44]. Nevertheless, the effects of compound 22 were all consistent with the activation of BK_{Ca} channels, as evidenced by the counter effects of BK_{Ca} channel blockers iberiotoxin or penitrem A [26, 43, 44] on the relaxative effects of compound 22 in high K⁺- (20 mM KCl-) induced contractions (Table 1). Other ion channels or contractile machineries may also be at play considering the effects of compound 22 in high-K⁺- (60–80 mM KCl-) induced contractions [26, 43, 44, 48, 49]. Taken together, these findings indicate that in addition to bladder-relaxant activities, compound 22 also influences intestinal and uterine contractions.

5. Concluding Remarks

Although K⁺ channel openers hold promise as effective and safer alternatives to many smooth muscle relaxants that are used today, most K⁺ channel openers in development have not lived up to our expectation [14]. A majority of K_{ATP} channel openers lacked selectivity and brought unwanted side effects (e.g., cardiovascular) considered worse than those wrought by standard antispasmodics or tocolytics. Thus, the development of K_{ATP} channel openers has been discontinued, and the interest was shifted to developing other K⁺ channel openers that are as efficacious as standard smooth muscle relaxants, but with significantly better side effect profile. Recent years have seen great advances in our understanding of the structure and function of existing K⁺ channels. Due to unmet expectations with K_{ATP} channel openers, newer channels or associated channel proteins have been characterized as potential drug targets. As stated above, among those explored were the BK_{Ca} channels. While the role of BK_{Ca} channels in the CNS is complex and still an area of active academic research, there appears to be a consensus on the contribution of these channels to the regulation of smooth muscle tone [41]. In this paper, we reviewed the contribution of benzofuroindole derivatives in the field that searches for ideal compounds for OAB (or for other pathophysiologic conditions). We have stated the remarkable profiles of these compounds if considered as future OAB drug treatment. Some investigators, however, showed the potency of a certain benzofuroindole analogue (compound 22) to relax ileum and uterine contractions, indicating that like other K⁺ channel openers, selectivity is still an area of concern with benzofuroindole compounds. However, it is still too early to conclude that benzofuroindole analogues have no place in the roll of alternative or safer smooth muscle relaxants. More investigations are required to better understand their mechanics and characteristics and ultimately to address their lack of selectivity. The potency of various benzofuroindole compounds in smooth muscle types can be compared [48] and from there we may discover the drugs' most appropriate clinical application.

Finally, the worth of BK_{Ca} channel openers as “better” smooth muscle relaxants is just proven theoretically but not in clinical practice. Not much is known about the physiology of BK_{Ca} channels and their activators in the disease state, thus, whether or not a BK_{Ca} channel opener will be found to have therapeutic utility will depend on the appropriate counterbalance of BK_{Ca} channel activation versus other excitatory inputs [14]. Moreover, some reported BK_{Ca} channel openers do not satisfy some of the criteria set in clinical tests to prove their worth as effective smooth muscle relaxants (for review see [41]). This explains, in part, the slow pace in the development of BK_{Ca} channel openers as smooth muscle hyperactivity interventions. However, as molecular biology and drug development techniques are getting more and more advanced, it is plausible that, in the next few years, concerns that limit the potential use of BK_{Ca} channel openers (especially those that are recently characterized) will be resolved. Therefore, the road ahead may be tedious for

benzofuroindole compounds, but there is still optimism with regard to their potential use as effective smooth muscle relaxants.

Conflict of Interests

The authors declare no conflicts of interest.

Acknowledgment

This work was supported by funds from Sahmyook University.

References

- [1] J. J. Morrison and J. M. Rennie, "Clinical, scientific and ethical aspects of fetal and neonatal care at extremely preterm periods of gestation," *British Journal of Obstetrics and Gynaecology*, vol. 104, no. 12, pp. 1341–1350, 1997.
- [2] H. Karaki, H. Ozaki, M. Hori et al., "Calcium movements, distribution, and functions in smooth muscle," *Pharmacological Reviews*, vol. 49, no. 2, pp. 157–230, 1997.
- [3] A. Vander, J. Sherman, and D. Laciano, *Human Physiology: The Mechanism of Body Function*, McGraw-Hill, Boston, Mass, USA, 8th edition, 2001.
- [4] A. J. Pappano, "Cholinoceptor-activating and cholinesterase-inhibiting drugs," in *Basic and Clinical Pharmacology*, B. G. Katzung, Ed., pp. 93–107, McGraw-Hill, Singapore, 2007.
- [5] T. Godfraind, R. Miller, and M. Wibo, "Calcium antagonism and calcium entry blockade," *Pharmacological Reviews*, vol. 38, no. 4, pp. 321–416, 1986.
- [6] T. Uchiyama and R. Chess-Williams, "Muscarinic receptor subtypes of the bladder and gastrointestinal tract," *Journal of Smooth Muscle Research*, vol. 40, no. 6, pp. 237–247, 2004.
- [7] E. P. Frazier, S. L. Peters, A. S. Braverman, M. R. Ruggieri, and M. C. Michel, "Signal transduction underlying the control of urinary bladder smooth muscle tone by muscarinic receptors and β -adrenoreceptors," *Naunyn-Schmiedeberg's Archives of Pharmacology*, vol. 377, pp. 449–462, 2007.
- [8] H. H. Zingg and S. A. Laporte, "The oxytocin receptor," *Trends in Endocrinology and Metabolism*, vol. 14, no. 5, pp. 222–227, 2003.
- [9] L. Myatt and S. J. Lye, "Expression, localization and function of prostaglandin receptors in myometrium," *Prostaglandins Leukotrienes and Essential Fatty Acids*, vol. 70, no. 2, pp. 137–148, 2004.
- [10] A. Shmygol, J. Gullam, A. Blanks, and S. Thornton, "Multiple mechanisms involved in oxytocin-induced modulation of myometrial contractility," *Acta Pharmacologica Sinica*, vol. 27, no. 7, pp. 827–832, 2006.
- [11] A. Carl, H. K. Lee, and K. M. Sanders, "Regulation of ion channels in smooth muscles by calcium," *American Journal of Physiology*, vol. 271, no. 1, pp. C9–C34, 1996.
- [12] P. R. Conlin and G. H. Williams, "Use of calcium channel blockers in hypertension," *Advances in Internal Medicine*, vol. 43, pp. 533–562, 1998.
- [13] B. Cantabrana, J. R. Perez Vallina, L. Menéndez, and A. Hidalgo, "Spasmolytic and calmodulin inhibitory effect of non-steroidal anti-inflammatory drugs in vitro," *Life Sciences*, vol. 57, no. 14, pp. 1333–1341, 1995.
- [14] T. M. Argentieri and J. A. Butera, "An overview of potassium channel activators for the treatment of overactive bladder: a survey of new structures 2000–2005," *Expert Opinion on Therapeutic Patents*, vol. 16, no. 5, pp. 573–585, 2006.
- [15] K. Gyetvai, M. E. Hannah, E. D. Hodnett, and A. Ohlsson, "Tocolytics for preterm labor: a systematic review," *Obstetrics and Gynecology*, vol. 94, no. 5, pp. 869–877, 1999.
- [16] N. D. Berkman, J. M. Thorp Jr., K. N. Lohr et al., "Tocolytic, treatment for the management of preterm labor: a review of the evidence," *American Journal of Obstetrics and Gynecology*, vol. 188, no. 6, pp. 1648–1659, 2003.
- [17] J. H. Sheldon, N. W. Norton, and T. M. Argentieri, "Inhibition of guinea pig detrusor contraction by NS-1619 is associated with activation of BK_{Ca} and inhibition of calcium currents," *Journal of Pharmacology and Experimental Therapeutics*, vol. 283, no. 3, pp. 1193–1200, 1997.
- [18] C. D. Foster, M. J. Speakman, K. Fujii, and A. F. Brading, "The effects of cromakalim on the detrusor muscle of human and pig urinary bladder," *British Journal of Urology*, vol. 63, no. 3, pp. 284–294, 1989.
- [19] G. Edwards, M. Henshaw, M. Miller, and A. H. Weston, "Comparison of the effects of several potassium-channel openers on rat bladder and rat portal vein in vitro," *British Journal of Pharmacology*, vol. 102, no. 3, pp. 679–686, 1991.
- [20] R. Chess-Williams, S. W. Martin, C. Korstanje, and C. R. Chapple, "In vitro investigation of the bladder-vascular selectivity of levromakalim and YM934 in human tissues," *British Journal of Urology International*, vol. 83, no. 9, pp. 1050–1054, 1999.
- [21] M. E. Brune, T. A. Fey, J. D. Brioni et al., "(-)-(9S)-9-(3-bromo-4-fluorophenyl)-2,3,5,6,7,9-hexahydrothieno[3,2-b]quinolin-8(4H)-one 1-dioxide (A-278637): a novel ATP-sensitive potassium channel opener efficacious in suppressing urinary bladder contractions. II. In vivo characterization," *Journal of Pharmacology and Experimental Therapeutics*, vol. 303, no. 1, pp. 387–394, 2002.
- [22] A. C. Fabiyi, M. Gopalakrishnan, J. J. Lynch, J. D. Brioni, M. J. Coghlan, and M. E. Brune, "In vivo evaluation of the potency and bladder-vascular selectivity of the ATP-sensitive potassium channel openers (-)-cromakalim, ZD6169 and WAY-133537 in rats," *British Journal of Urology International*, vol. 91, no. 3, pp. 284–290, 2003.
- [23] K. Komersova, J. W. Rogerson, E. L. Conway et al., "The effect of levromakalim (BRL 38227) on bladder function in patients with high spinal cord lesions," *British Journal of Clinical Pharmacology*, vol. 39, no. 2, pp. 207–209, 1995.
- [24] J. A. Butera, S. A. Antane, B. Hirth et al., "Synthesis and potassium channel opening activity of substituted 10H-benzo[4,5]furo[3,2-b]indole- and 50-dihydro-indeno[1,2-b]indole-1-carboxylic acids," *Bioorganic and Medicinal Chemistry Letters*, vol. 11, no. 16, pp. 2093–2097, 2001.
- [25] A. E. Gormemis, T. S. Ha, I. Im et al., "Benzofuroindole analogues as potent BK_{Ca} channel openers," *ChemBioChem*, vol. 6, no. 10, pp. 1745–1748, 2005.
- [26] I. C. Dela Peña, S. Y. Yoon, S. M. Kim et al., "Bladder-relaxant properties of the novel benzofuroindole analogue LDD175," *Pharmacology*, vol. 83, no. 6, pp. 367–378, 2009.
- [27] M. L. Garcia, D. M. Shen, and G. J. Kaczorowski, "High-conductance calcium-activated potassium channels: validated targets for smooth muscle relaxants?" *Expert Opinion on Therapeutic Patents*, vol. 17, no. 7, pp. 831–842, 2007.

- [28] S. H. Tal, H. H. Lim, E. L. Ga, Y. C. Kim, and C. S. Park, "Electrophysiological characterization of benzofuroindole-induced potentiation of large-conductance Ca^{2+} -activated K^+ channels," *Molecular Pharmacology*, vol. 69, no. 3, pp. 1007–1014, 2006.
- [29] G. J. Kaczorowski, H. G. Knaus, R. J. Leonard, O. B. McManus, and M. L. Garcia, "High-conductance calcium-activated potassium channels: structure, pharmacology, and function," *Journal of Bioenergetics and Biomembranes*, vol. 28, no. 3, pp. 255–267, 1996.
- [30] S. Ghatta, D. Nimmagadda, X. Xu, and S. T. O'Rourke, "Large-conductance, calcium-activated potassium channels: structural and functional implications," *Pharmacology and Therapeutics*, vol. 110, no. 1, pp. 103–116, 2006.
- [31] M. A. Valverde, P. Rojas, J. Amigo et al., "Acute activation of Maxi-K channels (hSlo) by estradiol binding to the β subunit," *Science*, vol. 285, no. 5435, pp. 1929–1931, 1999.
- [32] M. Wallner, P. Meera, and L. Toro, "Molecular basis of fast inactivation in voltage and Ca^{2+} -activated K^+ channels: a transmembrane β -subunit homolog," *Proceedings of the National Academy of Sciences of the United States of America*, vol. 96, no. 7, pp. 4137–4142, 1999.
- [33] X. M. Xia, J. P. Ding, and C. J. Lingle, "Molecular basis for the inactivation of Ca^{2+} - and voltage-dependent BK channels in adrenal chromaffin cells and rat insulinoma tumor cells," *Journal of Neuroscience*, vol. 19, no. 13, pp. 5255–5264, 1999.
- [34] X. Qian, C. M. Nimigean, X. Niu, B. L. Moss, and K. L. Magleby, "Slo1 tail domains, but not the Ca^{2+} bowl, are required for the $\beta 1$ subunit to increase the apparent Ca^{2+} sensitivity of BK channels," *Journal of General Physiology*, vol. 120, no. 6, pp. 829–843, 2002.
- [35] C. Vergara, R. Latorre, N. V. Marrion, and J. P. Adelman, "Calcium-activated potassium channels," *Current Opinion in Neurobiology*, vol. 8, no. 3, pp. 321–329, 1998.
- [36] M. J. Coghlan, W. A. Carroll, and M. Gopalakrishnan, "Recent developments in the biology and medicinal chemistry of potassium channel modulators: update from a decade of progress," *Journal of Medicinal Chemistry*, vol. 44, no. 11, pp. 1627–1653, 2001.
- [37] G. M. Dick, A. C. Hunter, and K. M. Sanders, "Ethylbromide tamoxifen, a membrane-impermeant antiestrogen, activates smooth muscle calcium-activated large-conductance potassium channels from the extracellular side," *Molecular Pharmacology*, vol. 61, no. 5, pp. 1105–1113, 2002.
- [38] Y. Imaizumi, K. Sakamoto, A. Yamada et al., "Molecular basis of pimarane compounds as novel activators of large-conductance Ca^{2+} -activated K^+ channel α -subunit," *Molecular Pharmacology*, vol. 62, no. 4, pp. 836–846, 2002.
- [39] K. M. Giangiacomo, A. Kamassah, G. Harris, and O. B. Mcmanus, "Mechanism of maxi-K channel activation by dehydrosoyasaponin-I," *Journal of General Physiology*, vol. 112, no. 4, pp. 485–501, 1998.
- [40] G. J. Kaczorowski and M. L. Garcia, "Pharmacology of voltage-gated and calcium-activated potassium channels," *Current Opinion in Chemical Biology*, vol. 3, no. 4, pp. 448–458, 1999.
- [41] A. Nardi and S. P. Olesen, "BK_{Ca} channel modulators: a comprehensive overview," *Current Medicinal Chemistry*, vol. 15, no. 11, pp. 1126–1146, 2008.
- [42] G. McMurray, J. H. Casey, and A. M. Naylor, "Animal models in urological disease and sexual dysfunction," *British Journal of Pharmacology*, vol. 147, no. 2, pp. S62–S79, 2006.
- [43] I. C. Dela Peña, S. Y. Yoon, S. M. Kim et al., "Inhibition of intestinal motility by the putative BK_{Ca} channel opener LDD175," *Archives of Pharmacal Research*, vol. 32, no. 3, pp. 413–420, 2009.
- [44] H. S. Ahn, I. dela Peña, J. H. Ryu, Y. C. Kim, and J. H. Cheong, "4-chloro-7-trifluoromethyl-10H-benzo[4,5]furo[3,2-b]indole-1-carboxylic acid (TBIC), a putative BK_{Ca} channel opener with uterine-relaxant activities," *Pharmacology*, vol. 1, no. 87(5-6), pp. 331–340, 2011.
- [45] R. N. Khan, B. Matharoo-Ball, S. Arulkumaran, and M. L. J. Ashford, "Potassium channels in the human myometrium," *Experimental Physiology*, vol. 86, no. 2, pp. 255–264, 2001.
- [46] B. Chanrachakul, B. Matharoo-Ball, A. Turner et al., "Immunolocalization and protein expression of the α subunit of the large-conductance calcium-activated potassium channel in human myometrium," *Reproduction*, vol. 126, no. 1, pp. 43–48, 2003.
- [47] R. Schubert and M. T. Nelson, "Protein kinases: tuners of the BK_{Ca} channel in smooth muscle," *Trends in Pharmacological Sciences*, vol. 22, no. 10, pp. 505–512, 2001.
- [48] J. Malysz, S. A. Buckner, A. V. Daza, I. Milicic, A. Perez-Medrano, and M. Gopalakrishnan, "Functional characterization of large conductance calcium-activated K^+ channel openers in bladder and vascular smooth muscle," *Naunyn-Schmiedeberg's Archives of Pharmacology*, vol. 369, no. 5, pp. 481–489, 2004.
- [49] H. Kobayashi, S. Adachi-Akahane, and T. Nagao, "Involvement of BK_{Ca} channels in the relaxation of detrusor muscle via β -adrenoceptors," *European Journal of Pharmacology*, vol. 404, no. 1-2, pp. 231–238, 2000.

Research Article

Equal Force Recovery in Dysferlin-Deficient and Wild-Type Muscles Following Saponin Exposure

Piming Zhao, Li Xu, Younss Ait-Mou, Pieter P. de Tombe, and Renzhi Han

Department of Cell and Molecular Physiology, Stritch School of Medicine, Loyola University Medical Center, Maywood, IL 60153, USA

Correspondence should be addressed to Renzhi Han, renhan@lumc.edu

Received 28 April 2011; Revised 24 June 2011; Accepted 19 July 2011

Academic Editor: Robert J. Bloch

Copyright © 2011 Piming Zhao et al. This is an open access article distributed under the Creative Commons Attribution License, which permits unrestricted use, distribution, and reproduction in any medium, provided the original work is properly cited.

Dysferlin plays an important role in repairing membrane damage elicited by laser irradiation, and dysferlin deficiency causes muscular dystrophy and associated cardiomyopathy. Proteins such as perforin, complement component C9, and bacteria-derived cytolytins, as well as the natural detergent saponin, can form large pores on the cell membrane via complexation with cholesterol. However, it is not clear whether dysferlin plays a role in repairing membrane damage induced by pore-forming reagents. In this study, we observed that dysferlin-deficient muscles recovered the tetanic force production to the same extent as their WT counterparts following a 5-min saponin exposure (50 $\mu\text{g}/\text{mL}$). Interestingly, the slow soleus muscles recovered significantly better than the fast *extensor digitorum longus* (EDL) muscles. Our data suggest that dysferlin is unlikely involved in repairing saponin-induced membrane damage and that the slow muscle is more efficient than the fast muscle in repairing such damage.

1. Introduction

Mutations in the *dysferlin* gene lead to the development of several types of muscle wasting diseases including limb-girdle muscular dystrophy type 2B (LGMD2B) [1, 2], Miyoshi myopathy (MM) [2], and a distal anterior compartment myopathy (DACM) [3], together termed dysferlinopathy. Dysferlinopathy has also been shown to develop a late-onset cardiomyopathy [4, 5]. Dysferlin is a 230 kDa protein containing multiple-tandem C2 domains, and it is widely expressed in different tissues and cells including skeletal and cardiac muscle [6]. Previous work has established a role for dysferlin in muscle membrane repair since the dysferlin-deficient skeletal [7] and cardiac [5] muscle cells fail to efficiently reseal the membrane disruptions elicited by laser irradiation. Although the exact action of dysferlin in the membrane repair system of striated muscle remains poorly understood, it has been suggested that dysferlin may play a role in the membrane vesicle fusion step based on its primary structure properties [8, 9].

It is not very clear how laser irradiation induces membrane damage, but there is evidence showing that peroxidation of the plasma membrane lipids may be involved

in the photo-induced cell lysis [10, 11]. Such membrane damage may be similar to mechanical membrane tears as both require dysferlin and MG53 for repair at least in muscle cells [5, 7, 12]. Interestingly, in addition to oxidation-induced membrane damage, various pore-forming reagents can also cause a loss of membrane integrity and cell death *in vivo*. For example, perforin is released upon degranulation of cytotoxic T cells (CTLs) and forms transmembrane pores that promote translocation of granzymes into the cytoplasm of pathogen-infected cells, leading to their apoptotic death [13]. Previous studies have shown that cytotoxic T cells contribute to muscle pathology in dystrophin-deficient muscular dystrophy through perforin-dependent as well as perforin-independent mechanisms [14]. Cytotoxic T cells were also found in other inflammatory myopathies where they secreted perforin and invaded muscle fibers [15]. In addition, the 5th to 9th components (C5 to C9) of the complement system is involved in terminal activation of complement that leads to the formation of a large membrane lytic pore complex—the membrane attack complex (MAC) on the target cell membrane [16–18]. Interestingly, the membrane inserting part of both perforin and C9 is

mediated by the MACPF domain [19] which surprisingly shares structural similarity to the bacterial cholesterol-dependent cytolysins (CDCs) [20, 21]. Our recent study has shown that the complement activation contributes to muscle pathology in dysferlinopathy [22]. Moreover, the beta-amyloid can also form ring-shaped structures reminiscent of bacterial pore-forming toxins (PFTs) [23], which have membrane-perforating activity [24]. Interestingly, increased sarcolemmal and interstitial amyloid deposits were observed in dysferlinopathy patient muscles, and mutant dysferlin was found to be present in the amyloid deposits [25]. All the above-mentioned pore-forming proteins (PFPs) induce pore formation with diameters up to 50 nm through a very similar cholesterol-dependent mechanism [26]. Such a mechanism, through complexation with cholesterol, also applies to saponins which are natural detergents found in many plants [27, 28].

Despite the devastating consequences of membrane perforation, mammalian cells can recover the plasma membrane integrity depending on the severity and duration of the membrane damage. For example, it has been shown that striated myocytes can recover within seconds following membrane damage induced by laser irradiation and micro-electrode penetration in the presence of Ca^{2+} , dysferlin, and MG53 [5, 7, 12]. In addition, cells can restore plasma membrane integrity at the minute time scale (<1 h) following the formation of pores (30–50 nm in diameter) by CDCs or perforin [13, 29, 30]. Removal of the pores from the cell surface by calcium-dependent endocytosis and/or shedding of vesicles appears to be a critical step to repair membrane damage induced by PFPs [13, 30–32]. However, it remains unclear whether dysferlin is involved in repairing membrane damage induced by PFPs. In the present study, we designed experiments to address this question and provided evidence to show that dysferlin appears to be dispensable for membrane repair following saponin-induced membrane damage.

2. Materials and Methods

2.1. Mice. All animal studies were reviewed and approved by the Institutional Animal Care and Use Committee of Loyola University Chicago (LU no. 202288 and LU no. 202769). The wild-type C57BL/6J (stock number: 000664), A/J (stock number: 000646), and C57BL/6J-Chr6^{A/J}/NaJ (stock number: 004384) mice were obtained from the Jackson Laboratory. Mice were maintained at Loyola University Medical Center Animal Facility in accordance with animal usage guidelines. The A/J and C57BL/6J-Chr6^{A/J}/NaJ were genotyped by tail PCR using the following primers: WT-F, 5'-CAAACCATTCCTCCAGTCCCTCCT-3'; AJ-R, 5'-AAGAGAAGGCAACAGGTGACA-3'; AJ-F, 5'-CAGAGT-TCCAACGCCCTACT-3'. The WT allele will produce a 449-bp band, and the mutant allele will produce a 1-kb band. The 20 μ L PCR reaction contained 4 pmol WT-F, 4 pmol AJ-F, 8 pmol AJ-R primers, and 50 ng of DNA extracted from mice tails. PCR amplification was conducted for 40 cycles under standard conditions (denaturation at 95°C for 30 seconds, annealing at 58°C for 30 seconds, and elongation at 72°C for

1 minute). The male and female mice at 12 to 24 weeks of age were used unless otherwise specified in the text.

2.2. Antibodies. The mouse monoclonal anti-dysferlin antibody Hamlet (Novocastra) was used for the western blotting and immunofluorescence analyses. A monoclonal antibody against caveolin-3 (Transduction Laboratories) and an anti-laminin α 2-chain antibody (Alexis Biochemicals) were used for immunofluorescence analysis. DAPI was used to stain the nuclei. Peroxidase-conjugated secondary antibodies were obtained from Roche. Alexa Fluor 488- or 555-conjugated secondary antibodies were obtained from Invitrogen.

2.3. Serum Creatine Kinase Analysis. Serum samples from mice were obtained by tail bleeding, using a Sarstedt microvette CB 300, from nonanesthetized restrained mice according to institutional guidelines. Red cells were pelleted by centrifugation at 10,000 rpm for 4 minutes, and serum was separated, collected, and analyzed immediately without freezing. Serum creatine kinase assays were performed with an enzyme-coupled assay reagent kit (Stanbio Laboratory) according to the manufacturer's instructions. Absorbance at 340 nm was measured every 30 sec for 2 min at 37°C so that changes in enzyme activity could be calculated.

2.4. Western Blotting. Muscle protein samples were separated by SDS-PAGE and transferred onto PVDF membranes. Membranes were blocked with 5% nonfat dry milk in TBS-T buffer (Tris-HCl 50 mM, NaCl 150 mM, pH 7.4, Tween-20 0.1%) and incubated with primary antibodies overnight at 4°C. Blots were washed three times with TBS-T for 10 minutes each and incubated with Alexa Fluor 488- or 555-conjugated secondary antibodies (1 : 500 dilution in TBS-T; Invitrogen) for 1 hour at room temperature. After washing 3 \times 10 minutes with TBS-T buffer, the membranes were directly imaged for fluorescence using the Typhoon Trio plus imager (GE Healthcare Life Sciences, Inc.).

2.5. H&E Staining, Immunofluorescence Analysis, and Central Nucleated Fiber Counting. Histopathology studies were performed as described previously [33, 34]. Several hematoxylin and eosin stained sections (7 μ m) at the belly of the quadriceps, iliopsoas, EDL, and soleus muscles were prepared to characterize skeletal muscle pathology. Immunofluorescence staining was performed as described previously [33, 34]. Anti-dysferlin antibody Hamlet was used at 1 : 40 dilution. Anti-caveolin-3 antibody was used at 1 : 1000 dilution. Anti-laminin α 2 antibody was used at 1 : 400 dilution. All the secondary antibodies were used at 1 : 400 dilution. The numbers of central nucleated muscle fibers and the total muscle fibers were counted on muscle sections costained with caveolin-3 and DAPI or laminin α 2 and DAPI using Image Pro Plus 6.

2.6. Contractile Force Measurement. Contractile force was measured *in vitro* on *extensor digitorum longus* (EDL) and soleus muscles from C57BL/6J and dysferlin-deficient mice as described previously [35]. Mice were anesthetized by

an intraperitoneal (I.P.) injection of a mixture of ketamine (87.5 mg/kg) and xylazine (12.5 mg/kg). Intact muscles were removed from each mouse after the mice were euthanized by cervical dislocation after deep anesthesia. Muscles were immersed in an oxygenated bath (95% O₂, 5% CO₂) that contained Tyrode solution (pH 7.4) at room temperature. For each muscle, one tendon was tied securely with a 6-0 suture (Surgical Specialties Corporation) to a force transducer/servo motor (Aurora Scientific Inc., Model: 300C-LR), and the other tendon to a fixed pin. Using twitches with pulse duration of 0.2 ms, the voltage of stimulation was increased to achieve a maximum twitch. Twitches were then used to adjust the muscle length to the optimum length for force development (L_0). The muscle length was set at L_0 , and muscles were stimulated for 300 ms. Stimulation frequency was increased until the force reached a plateau at maximum isometric tetanic force (P_0).

2.7. Saponin Treatment. After three consecutive tetanic contractions with 3 minutes intervals in between, the muscle was incubated with saponin (Sigma) at 50 μ g/mL in Tyrode solution for 5 minutes. To assess the force recovery following saponin-induced membrane injury, tetanic contractions were recorded starting at 10 minutes following saponin washout, once every 10 minutes for one hour in total. The data were digitized, collected, and analyzed using the ASI Dynamic Muscle Control software (DMC V5.294).

2.8. Statistical Analysis. Data were presented as mean \pm SEM, and statistical significance ($P < 0.05$) was determined by the Student's t -test for two groups or two-way ANOVA for multiple groups using Prism 5.02 (GraphPad). When the overall F -ratio for the ANOVA was significant, the differences between individual group means were determined by a single Student's t -test.

3. Results

3.1. Characterization of C57BL/6J-Chr6^{A/J} Mice. In this study, we employed a new dysferlin-deficient mouse strain (C57BL/6J-Chr6^{A/J}/NaJ) from Jackson Laboratory. This strain is an inbred C57BL/6J strain with its chromosome 6 replaced with another inbred A/J strain, originally developed by Nadeau et al. from the Case Western Reserve University [36]. Since the mouse dysferlin gene is located on the chromosome 6, the C57BL/6J-Chr6^{A/J}/NaJ mice carry the retrotransposon insertion in the *dysferlin* gene that is present in the parental A/J strain [37]. This strain is very similar to the B6.A/J-Dysf^{prmd} strain used by Lostal et al. [38] except that the entire chromosome 6 in our strain is from A/J mice while the B6.A/J-Dysf^{prmd} strain was derived by backcrossing the A/J mice with C57BL/6J mice for 4 generations. The C57BL/6J-Chr6^{A/J}/NaJ mice were genotyped by a PCR method of the tail snips as described in Section 2. A single band of 449 bp and \sim 1.0 kb were produced in the WT and the homozygous mutant samples, respectively, while the heterozygous mice yielded two major bands (449 bp and 1.0 kb) with additional faint nonspecific bands (Figure 1(a)).

Both western blotting and immunofluorescence staining analyses confirmed that the dysferlin protein is completely absent in the skeletal muscle of the homozygous mutant mice (Figures 1(b) and 1(c)). H&E staining showed that the mice developed dystrophic features (Figure 2(a)) similar to other dysferlin-deficient mice [7, 37, 38], but the dystrophic phenotype progressed earlier and faster than the parental A/J strain. We observed that the quadriceps muscles had sparsely distributed necrotic muscle fibers and centrally nucleated muscle fibers starting from 2 months of age and that the numbers of such muscle fibers progressively increased. The quadriceps muscle from the male C57BL/6J-Chr6^{A/J} mice at 4 months of age showed a slightly increased percentage of central nucleated muscle fibers compared to age- and sex-matched A/J mice ($7.3 \pm 0.9\%$ versus $4.5 \pm 0.3\%$; $N = 14$ and 16 ; resp., $P = 0.009$). Compared to the quadriceps muscle, the iliopsoas muscle from either A/J or C57BL/6J-Chr6A/J mice had more central nucleated muscle fibers ($11.9 \pm 3.2\%$ and $27.4 \pm 4.8\%$, resp.) (Figures 2(a) and 2(b)). The serum creatine kinase level in the C57BL/6J-Chr6^{A/J} mice at 4 months of age was significantly elevated compared to that in the WT controls (157 ± 42 versus 541 ± 65 IU/L; $N = 6$ and 10 for WT and mutant; resp., $P < 0.001$) (Figure 2(c)). Thus, the C57BL/6J-Chr6^{A/J}/NaJ strain is a true dysferlin mutant mouse model in the C57BL/6J background (except the chromosome 6) and was used in the following studies (referred to as "dysferlin-deficient").

3.2. Muscle Force Recovery Following Saponin Exposure. Saponins are a diverse class of natural detergents found in many plants. Through complexation with cholesterol, saponin perforates the cell membrane. We used saponin to induce membrane pore formation in WT or dysferlin-deficient *extensor digitorum longus* (EDL) and soleus muscles and examined force recovery following saponin treatment. Both dysferlin-deficient EDL and soleus muscles displayed a limited overt pathology with a few centrally nucleated fibers (Figure 3), which allowed us to study the consequence of dysferlin deficiency on force recovery following saponin exposure without much preexisting dystrophic alterations. We performed preliminary experiments to test several doses of saponin (from 10 to 500 μ g/mL) and treated the WT EDL muscle for either 1 min or 5 min at room temperature (RT). We then selected 50 μ g/mL of saponin for 5-min incubation, as this treatment resulted in a tetanic force loss of \sim 85% in WT EDL muscle at 10 minutes after the treatment (Figures 4(a)–4(d)). We also tested a tetanic contraction at one minute after saponin washout; however, this tetanic contraction greatly decreased the final force recovery (data not shown). This data indicates that, by one minute after saponin exposure, a tetanic contraction stimulus would cause further muscle force loss. Thus, in our standard protocol, we started the tetanic force measurement 10 minutes after saponin washout unless otherwise specified.

Upon application of saponin, the baseline tension gradually increased and reached the maximum level at around 1.5 minutes after that it slowly returned to near the pre-exposure baseline (Figure 4(b)). The increase in the baseline

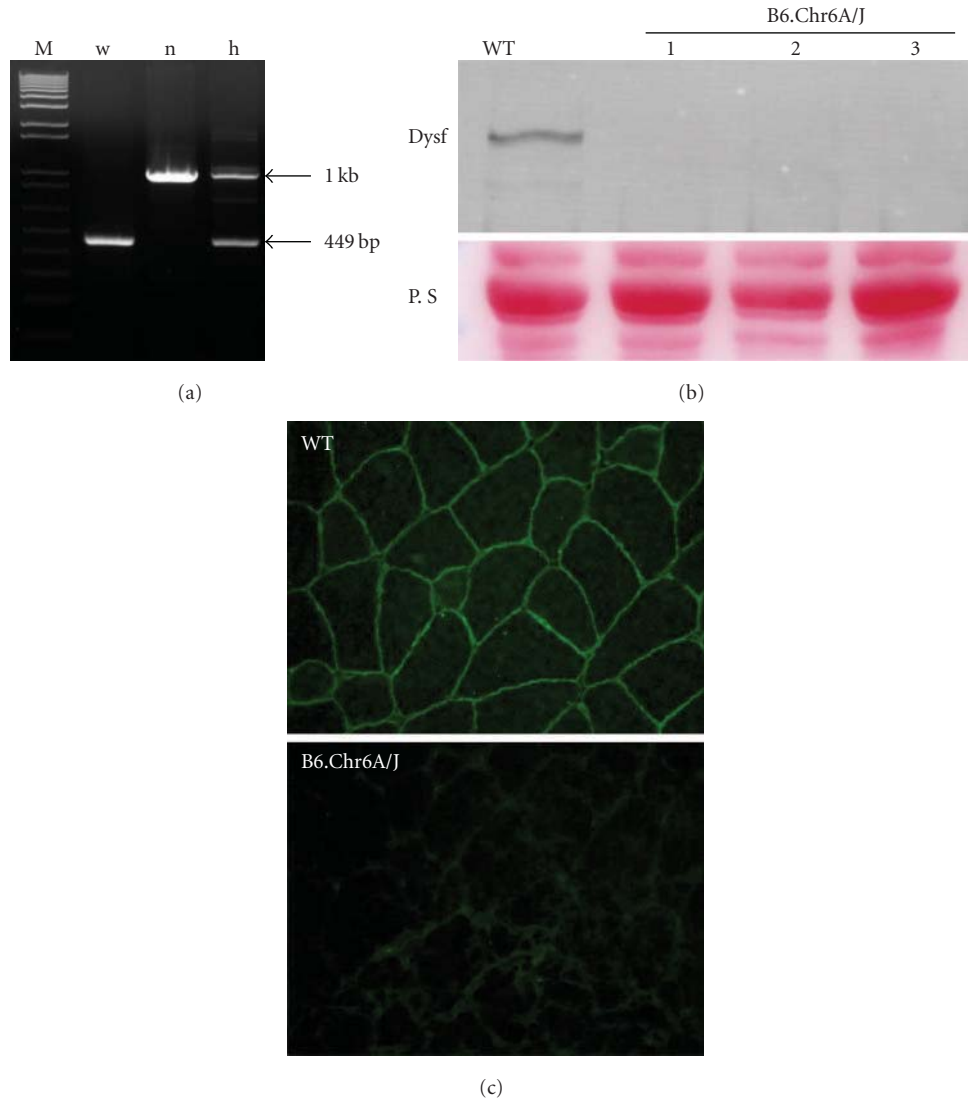


FIGURE 1: Disrupted expression of dysferlin in skeletal muscle of C57BL/6J-Chr6^{A/J}/NaJ mice. (a) PCR genotyping of WT (w), C57BL/6J-Chr6^{A/J}/NaJ (n), and heterozygous (h) mice. (b) Western blotting analysis of the quadriceps muscles from WT and C57BL/6J-Chr6^{A/J}/NaJ (B6.Chr6A/J) mice using the monoclonal anti-dysferlin antibody (Dysf). The bottom panel is the same blot stained with Ponceau-S (P.S). (c) Immunofluorescence labeling of muscle sections from WT and dysferlin-deficient mice with anti-dysferlin antibody.

tension indicates $\text{Ca}^{2+}/\text{Na}^{+}$ entry through saponin-induced membrane pores, while the subsequent decrease in the muscle tension is most likely due to secondary damage inside the muscle cell after membrane permeabilization. The tetanic force gradually recovered from $15.5 \pm 2.5\%$ at 10 minutes to $42.1 \pm 4.7\%$ at 40 minutes of the initial force prior to the treatment and did not significantly increase further after 40 minutes (Table 1 and Figures 4(c)-4(d)). These data suggest that the WT muscle can gradually repair the membrane damage induced by saponin and that this repair process may take up to 30–40 minutes. The force did not recover to 100%, indicating that some irreversible damage occurred within the muscle. Interestingly, the tetanic force also recovered to the same level within the same time frame in the dysferlin-deficient EDL muscle following the saponin treatment ($N = 5$ for either WT or mutant) (Figure 4(d) and Table 1).

These data suggest that, unlike the laser-induced membrane damage, saponin-induced membrane damage does not seem to require dysferlin for repair.

Next, we examined the effect of saponin exposure on the tetanic force recovery in the soleus muscle, which are composed of predominantly slow-fiber type. The baseline tension developed in soleus muscles during saponin exposure was similar to that in EDL muscles (data not shown). Surprisingly, the tetanic force recovered to ~80% at 10 minutes after the 5-minute saponin exposure regardless of dysferlin genotype (Figure 4(e) and Table 2). We observed only a small but significant increase in the tetanic force at 20 minutes compared to that at 10 minutes, and there was no further force recovery in the following 40 minutes (Figure 4(e) and Table 2). To further confirm that the tetanic force was indeed rapidly recovering within the first 10

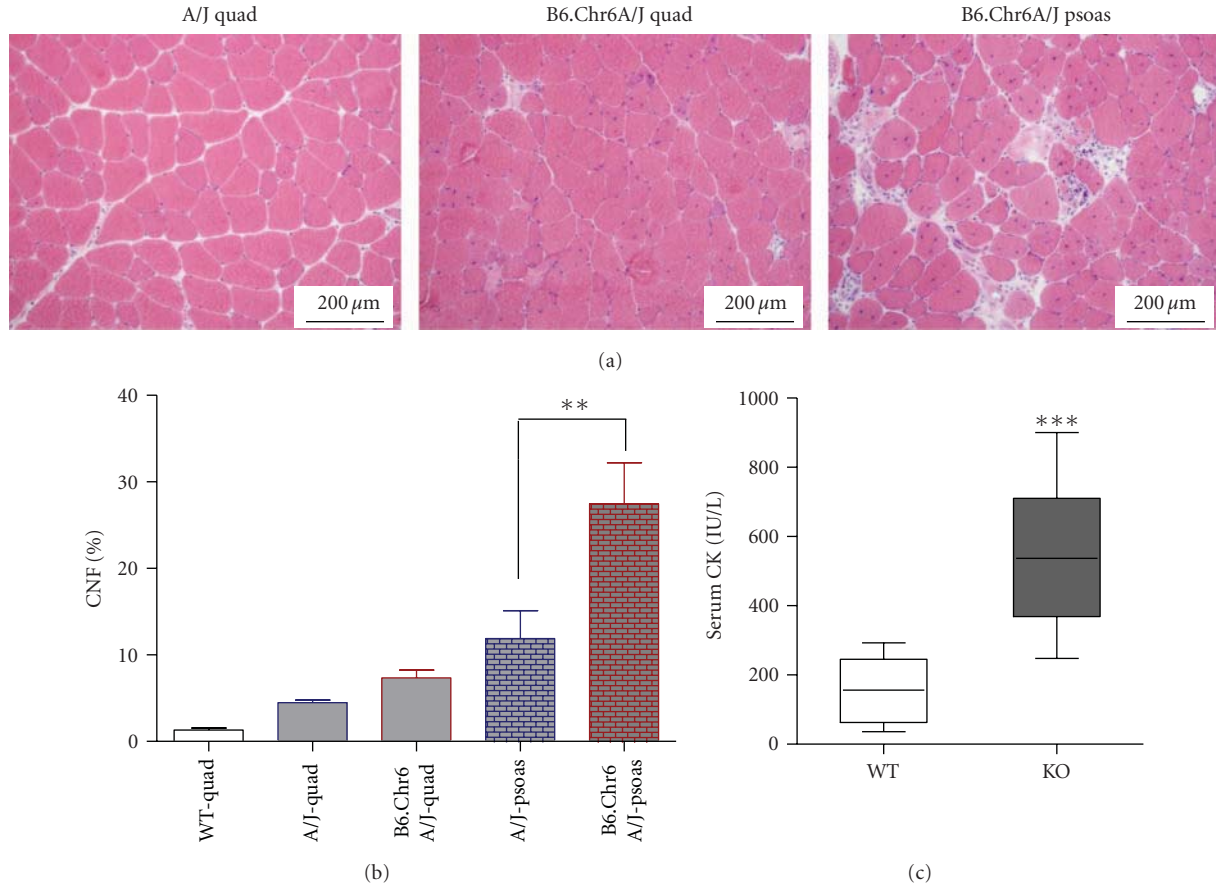


FIGURE 2: Characterization of C57BL/6J-Chr6^{A/J}/NaJ mice. (a) H&E-stained quadriceps (or iliopsoas) muscle sections of A/J, B6.Chr6A/J mice. Scale bar: 200 μm. (b) Central nucleated muscle fiber percentage (CNF) from the quadriceps or iliopsoas muscles of WT, A/J, and B6.Chr6A/J mice at 16 weeks of age. (c) Serum creatine kinase (CK) levels from WT (*N* = 6) and B6.Chr6A/J (KO) (*N* = 10) mice at 16 weeks of age. ** indicates *P* < 0.05, and *** indicates *P* < 0.001.

TABLE 1: Tetanic forces (kN/m²) of WT and dysferlin-null EDL muscles at room temperature before and after saponin exposure.

	Initial	10 min	20 min	30 min	40 min	50 min	60 min
WT, <i>N</i> = 5	273.6 ± 4.9	41.9 ± 6.1	75.7 ± 10.2 (^a) <i>P</i> = 0.002	101.7 ± 11.5 <i>P</i> = 0.0007	114.5 ± 11.8 <i>P</i> = 0.18	117.1 ± 11.8 <i>P</i> = 0.18	117.0 ± 11.1 <i>P</i> = 0.92
KO, <i>N</i> = 5	251.3 ± 13.5	47.5 ± 15.0	77.4 ± 14.8 <i>P</i> = 0.016	97.1 ± 18.3 <i>P</i> = 0.042	102.1 ± 19.0 <i>P</i> = 0.048	102.2 ± 18.7 <i>P</i> = 0.81	102.4 ± 18.6 <i>P</i> = 0.83
(^b) <i>p</i>	0.09	0.74	0.93	0.84	0.59	0.52	0.52

Note: (a) the *P* values under the force data are the paired *t*-test of the forces at the specific time point compared to that measured at the prior time point (e.g., WT force at 20 min compared to that at 10 min); (b) the *P* values in the last row are the unpaired *t*-test of forces between WT and dysferlin-null groups at each time point.

TABLE 2: Tetanic forces (kN/m²) of WT and dysferlin-null soleus muscles at room temperature before and after saponin exposure.

	Initial	10 min	20 min	30 min	40 min	50 min	60 min
WT, <i>N</i> = 5	166.5 ± 6.7	130.8 ± 4.1	139.8 ± 3.6 (^a) <i>P</i> = 0.002	137.7 ± 3.1 <i>P</i> = 0.32	135.0 ± 2.8 <i>P</i> = 0.04	133.4 ± 2.9 <i>P</i> = 0.75	132.2 ± 3.9 <i>P</i> = 0.94
KO, <i>N</i> = 7	171.0 ± 11.9	138.3 ± 8.4	145.6 ± 8.3 <i>P</i> = 0.003	142.6 ± 7.8 <i>P</i> = 0.15	139.7 ± 7.6 <i>P</i> = 0.13	138.5 ± 7.6 <i>P</i> = 0.34	136.9 ± 7.8 <i>P</i> = 0.42
(^b) <i>p</i>	0.77	0.49	0.59	0.62	0.63	0.60	0.64

Note: (a) the *P* values under the force data are the paired *t*-test of the forces at the specific time point compared to that measured at the prior time point (e.g., WT force at 20 min compared to that at 10 min); (b) the *P* values in the last row are the unpaired *t*-test of forces between WT and dysferlin-null groups at each time point.

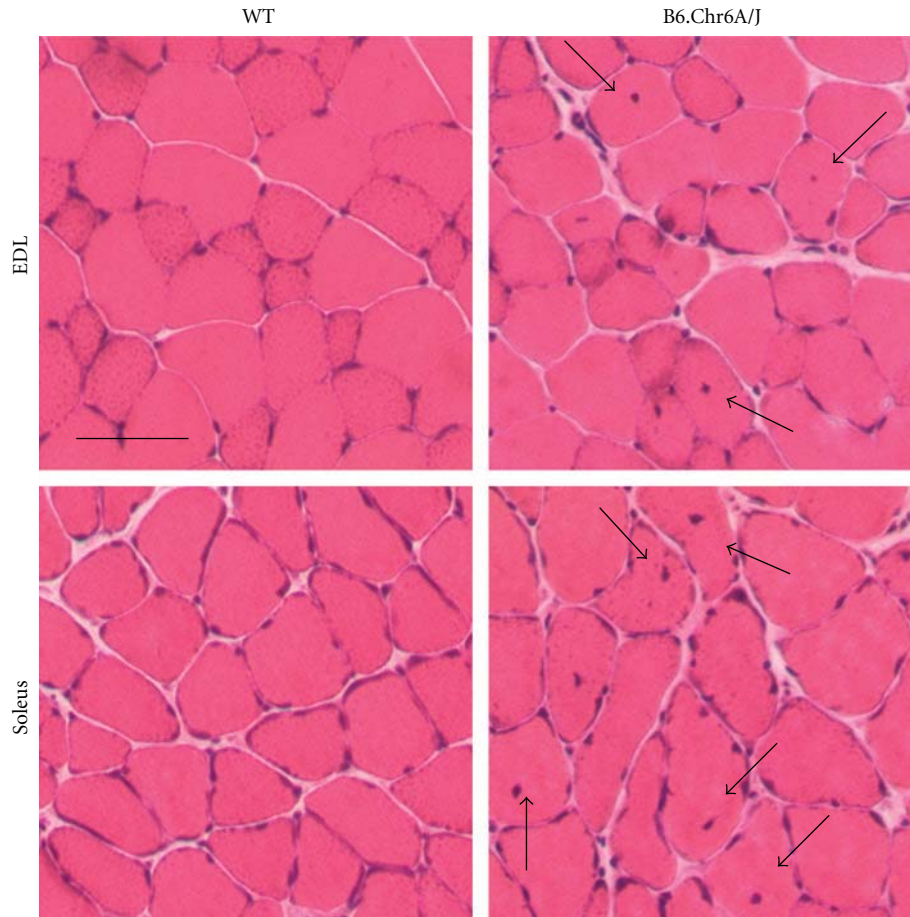


FIGURE 3: Histology examination of EDL and soleus muscles from C57BL/6J-Chr6^{A/J}/NaJ mice. H&E-stained EDL (top panel) and soleus (bottom panel) muscle sections of C57BL/6J (WT) and C57BL/6J-Chr6^{A/J}/NaJ mice. Scale bar: 100 μm .

minutes, we measured tetanic force at 5 minutes following saponin washout in four soleus muscles (two WT and two mutants). As shown in Figure 4(e), the soleus muscles developed 69% of maximum force at 5 minutes. By fitting the data with a one-phase association equation, we estimated the maximum recovery percentage to be $45.9 \pm 4.4\%$ in EDL and $84.4 \pm 1.2\%$, and the rate of recovery to be 0.057 ± 0.025 (min^{-1}) in EDL and 0.268 ± 0.097 (min^{-1}) in soleus. This data suggests that the soleus muscles recovered much faster than the EDL muscles after saponin washout.

4. Discussion

The plasma membrane defines the boundary of every single living cell, and its integrity is essential for life. However, the plasma membrane may be challenged by mechanical stress during normal physiological activities or PFPs produced by the organism itself and invading pathogens. For example, pore formation by perforin is involved in counteracting infection by microorganisms [19], while pore formation by the Bcl2 family member Bax triggers apoptosis [39]. Furthermore, it has been shown that the causative agents of Alzheimer's or Parkinson's disease are proteins capable of adopting pore-forming configurations [23, 40], and pore-forming amyloid deposits are also found in muscle diseases

[25]. Pore formation through complexation with cholesterol and subsequent oligomerization leads to permeabilization of ions and small molecules such as ATP and, in the case of CDCs, leakage of proteins [26]. Repairing the membrane damage induced by PFPs is thus a critical step for the inflicted cell to survive.

Mammalian cells have been shown to be capable of repairing breaches in their plasma membrane. Dysferlin and MG53 were two previously identified proteins that play critical roles in repairing laser irradiation- and microneedle-induced membrane damage in striated muscles [5, 7, 12, 41]. Our present study demonstrated that skeletal muscle is also capable of repairing (at least partially) saponin-induced membrane damage. In the case of EDL muscles, the maximum recovery of tetanic force was around 44.6% after a 5-min exposure to 50 $\mu\text{g}/\text{mL}$ saponin. The force deficit indicates "permanent" damage had occurred by saponin exposure. It is likely that the muscle fibers in the outer layers were more severely damaged because they were more accessible to saponin. However, there were no differences in the maximum recovery levels in the WT and dysferlin-deficient groups, suggesting that the levels of "permanent" damage in the two groups were the same. Thus, the same recovery rate in both WT and dysferlin-deficient EDL

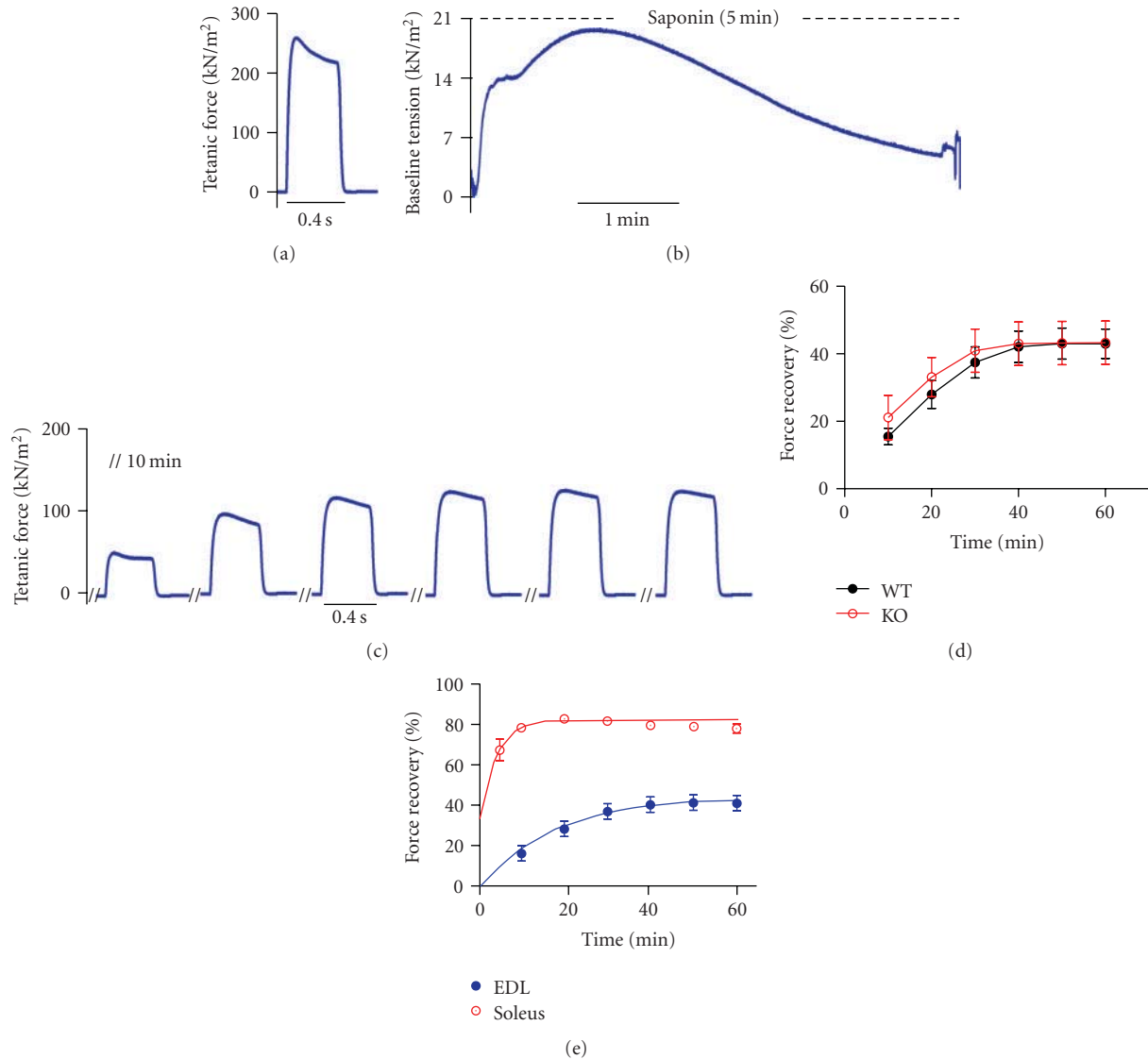


FIGURE 4: Tetanic force recovery in WT and C57BL/6J-Chr6^{A/J}/NaJ EDL and soleus muscles following saponin exposure. (a) Representative tetanic force measurement in a WT EDL muscle before saponin exposure. (b) Representative tension trace during saponin (50 μg/mL) exposure at room temperature (RT). (c) Representative tetanic force measurements within one hour after saponin washout at RT. Double slash: 10 min. (d) Quantitative analysis of the muscle force recovery in EDL muscles of WT and dysferlin-deficient mice at RT. (e) Tetanic force recovery in soleus muscles and EDL muscles ($N = 10$ and 13 for EDL and soleus, resp.) after saponin (50 μg/mL) exposure at room temperature. Note: we pooled the WT and mutant muscle data in panel (e) since there was no significant difference between the two groups (see Tables 1-2).

muscles suggests that dysferlin may not be involved in this process. We do not think this data is against previous reports showing dysferlin is required to repair laser-induced injury. Repairing laser-induced membrane damage is dysferlin-dependent, and this has been independently confirmed by several groups [12, 38, 42, 43]. Interestingly, the laser-induced membrane damage is around 5 μm in diameter at only a single spot of the muscle fiber [5, 7, 22]. However, the membrane pores induced by pore-forming reagents are up to 50 nm in diameter, but spread along the entire surface of the cells in contact with the reagents. Repairing these two different types of membrane injuries may use different

mechanisms [26]. Consistent with this notion, repairing laser-induced membrane damage takes seconds (e.g., within 1-2 minutes) [5, 7, 9], but repairing the pores induced by streptolysin O and perforin takes minutes (<1 hour) [13, 29], and it takes even longer (>6 hours) to recover from pore formation induced by toxins such as Staphylococcal α-toxin [31, 44]. In our experiments, it took up to 30-40 minutes for the EDL muscles to recover from saponin-induced membrane damage. We, thus, interpret this data to mean that skeletal muscle cells may use different mechanism to repair membrane damage induced by PFPs as compared to laser irradiation. The detailed mechanisms leading to

recovery of membrane integrity following pore formation remain to be explored. But it has been shown that this process involves a Ca^{2+} -dependent and dynamin-mediated endocytosis coupled with exocytosis which rapidly removes the PFPs from the cell membrane [13, 31, 32, 45].

Another interesting observation in our study is that the slow soleus muscle recovers significantly greater force compared to fast EDL muscle suggesting that the slow muscle has a more efficient way to recover from saponin-induced membrane injury. Compared to the fast EDL muscle, the slow soleus muscle has many different properties in addition to the difference in their contraction velocity. For example, it was shown that the soleus muscle from a glycosylation-deficient muscular dystrophy mouse model—*Large^{myd}*—exhibits no greater force deficit compared with WT soleus muscle [46] although the EDL muscle from the same mouse model is highly susceptible to contraction-induced injury [35]. This difference was attributed to the increased expression of sarcolemmal β 1-integrin in the soleus muscle than the EDL muscle [46]. The difference in the force recovery rate upon saponin-induced membrane injury between soleus and EDL muscles remains unclear and warrants further investigation.

In summary, we demonstrated that the skeletal muscle possesses the ability to repair membrane damages induced by pore-forming reagents such as saponin. This repair process takes 30–40 minutes for EDL muscles and up to 20 minutes for soleus muscles. Finally, dysferlin deficiency has little effect on the recovery.

Conflict of Interests

The authors declare that no conflict of interests exists.

Acknowledgments

The authors thank Guogen Wu for technical assistance. Research support was provided by the American Heart Association Scientist Development Award 10SDG4140138 (to R. Han), Muscular Dystrophy Association research Grant MDA171667 (to R. Han), American Heart Association postdoctoral fellowship 11POST5260038 (to Y. Ait-Mou), National Institute of Health Grants HL62426 and HL75494 (to P. de Tombe). Support for the Department of Cell and Molecular Physiology Multiphoton Imaging Facility was provided by the McCormick Foundation. The funders had no role in study design, data collection and analysis, decision to publish, or preparation of the manuscript.

References

- [1] R. Bashir, S. Britton, T. Strachan et al., “A gene related to *Caenorhabditis elegans* spermatogenesis factor *fer-1* is mutated in limb-girdle muscular dystrophy type 2B,” *Nature Genetics*, vol. 20, no. 1, pp. 37–42, 1998.
- [2] J. Liu, M. Aoki, I. Illa et al., “Dysferlin, a novel skeletal muscle gene, is mutated in Miyoshi myopathy and limb girdle muscular dystrophy,” *Nature Genetics*, vol. 20, no. 1, pp. 31–36, 1998.
- [3] I. Illa, C. Serrano-Munuera, E. Gallardo et al., “Distal anterior compartment myopathy: a dysferlin mutation causing a new muscular dystrophy phenotype,” *Annals of Neurology*, vol. 49, no. 1, pp. 130–134, 2001.
- [4] S. Kuru, F. Yasuma, T. Wakayama et al., “A patient with limb girdle muscular dystrophy type 2B (LGMD2B) manifesting cardiomyopathy,” *Clinical Neurology*, vol. 44, no. 6, pp. 375–378, 2004.
- [5] R. Han, D. Bansal, K. Miyake et al., “Dysferlin-mediated membrane repair protects the heart from stress-induced left ventricular injury,” *Journal of Clinical Investigation*, vol. 117, no. 7, pp. 1805–1813, 2007.
- [6] L. V. B. Anderson, K. Davison, J. A. Moss et al., “Dysferlin is a plasma membrane protein and is expressed early in human development,” *Human Molecular Genetics*, vol. 8, no. 5, pp. 855–861, 1999.
- [7] D. Bansal, K. Miyake, S. S. Vogel et al., “Defective membrane repair in dysferlin-deficient muscular dystrophy,” *Nature*, vol. 423, no. 6936, pp. 168–172, 2003.
- [8] D. Bansal and K. P. Campbell, “Dysferlin and the plasma membrane repair in muscular dystrophy,” *Trends in Cell Biology*, vol. 14, no. 4, pp. 206–213, 2004.
- [9] R. Han and K. P. Campbell, “Dysferlin and muscle membrane repair,” *Current Opinion in Cell Biology*, vol. 19, no. 4, pp. 409–416, 2007.
- [10] W. P. Thorpe, M. Toner, R. M. Ezzell, R. G. Tompkins, and M. L. Yarmush, “Dynamics of photoinduced cell plasma membrane injury,” *Biophysical Journal*, vol. 68, no. 5, pp. 2198–2206, 1995.
- [11] A. W. Girotti and M. R. Deziel, “Photodynamic action of protoporphyrin on resealed erythrocyte membranes: mechanisms of release of trapped markers,” *Advances in Experimental Medicine and Biology*, vol. 160, pp. 213–225, 1983.
- [12] C. Cai, H. Masumiya, N. Weisleder et al., “MG53 nucleates assembly of cell membrane repair machinery,” *Nature Cell Biology*, vol. 11, no. 1, pp. 56–64, 2009.
- [13] D. Keefe, L. Shi, S. Feske et al., “Perforin triggers a plasma membrane-repair response that facilitates CTL induction of apoptosis,” *Immunity*, vol. 23, no. 3, pp. 249–262, 2005.
- [14] M. J. Spencer, C. M. Walsh, K. A. Dorshkind, E. M. Rodriguez, and J. G. Tidball, “Myonuclear apoptosis in dystrophic mdx muscle occurs by perforin-mediated cytotoxicity,” *Journal of Clinical Investigation*, vol. 99, no. 11, pp. 2745–2751, 1997.
- [15] T. Sugihara, N. Okiyama, M. Suzuki et al., “Definitive engagement of cytotoxic CD8 T cells in C protein-induced myositis, a murine model of polymyositis,” *Arthritis and Rheumatism*, vol. 62, no. 10, pp. 3088–3092, 2010.
- [16] L. E. Ramm, M. B. Whitlow, and M. M. Mayer, “Transmembrane channel formation by complement: functional analysis of the number of C5b6, C7, C8, and C9 molecules required for a single channel,” *Proceedings of the National Academy of Sciences of the United States of America*, vol. 79, no. 15, pp. 4751–4755, 1982.
- [17] L. E. Ramm, M. B. Whitlow, and M. M. Mayer, “Size of the transmembrane channels produced by complement proteins C5b-8,” *Journal of Immunology*, vol. 129, no. 3, pp. 1143–1146, 1982.
- [18] L. E. Ramm and M. M. Mayer, “Life-span and size of the transmembrane channel formed by large doses of complement,” *Journal of Immunology*, vol. 124, no. 5, pp. 2281–2287, 1980.
- [19] M. E. Pipkin and J. Lieberman, “Delivering the kiss of death: progress on understanding how perforin works,” *Current Opinion in Immunology*, vol. 19, no. 3, pp. 301–308, 2007.

- [20] C. J. Rosado, A. M. Buckle, R. H. P. Law et al., "A common fold mediates vertebrate defense and bacterial attack," *Science*, vol. 317, no. 5844, pp. 1548–1551, 2007.
- [21] M. A. Hadders, D. X. Beringer, and P. Gros, "Structure of C8 α -MACPF reveals mechanism of membrane attack in complement immune defense," *Science*, vol. 317, no. 5844, pp. 1552–1554, 2007.
- [22] R. Han, E. M. Frett, J. R. Levy et al., "Genetic ablation of complement C3 attenuates muscle pathology in dysferlin-deficient mice," *Journal of Clinical Investigation*, vol. 120, no. 12, pp. 4366–4374, 2010.
- [23] H. A. Lashuel and P. T. Lansbury, "Are amyloid diseases caused by protein aggregates that mimic bacterial pore-forming toxins?" *Quarterly Reviews of Biophysics*, vol. 39, no. 2, pp. 167–201, 2006.
- [24] Y. Yoshiike, R. Kayed, S. C. Milton, A. Takashima, and C. G. Glabe, "Pore-forming proteins share structural and functional homology with amyloid oligomers," *NeuroMolecular Medicine*, vol. 9, no. 3, pp. 270–275, 2007.
- [25] S. Spuler, M. Carl, J. Zabojszcza et al., "Dysferlin-deficient muscular dystrophy features amyloidosis," *Annals of Neurology*, vol. 63, no. 3, pp. 323–328, 2008.
- [26] M. Bischofberger, M. R. Gonzalez, and F. G. van der Goot, "Membrane injury by pore-forming proteins," *Current Opinion in Cell Biology*, vol. 21, no. 4, pp. 589–595, 2009.
- [27] J. A. Johnson, M. O. Gray, J. S. Karliner, C. H. Chen, and D. Mochly-Rosen, "An improved permeabilization protocol for the introduction of peptides into cardiac myocytes: application to protein kinase C research," *Circulation Research*, vol. 79, no. 6, pp. 1086–1099, 1996.
- [28] S. Shany, A. W. Bernheimer, P. S. Grushoff, and K. S. Kim, "Evidence for membrane cholesterol as the common binding site for cereolysin, streptolysin O and saponin," *Molecular and Cellular Biochemistry*, vol. 3, no. 3, pp. 179–186, 1974.
- [29] I. Walev, S. C. Bhakdi, F. Hofmann et al., "Delivery of proteins into living cells by reversible membrane permeabilization with streptolysin-O," *Proceedings of the National Academy of Sciences of the United States of America*, vol. 98, no. 6, pp. 3185–3190, 2001.
- [30] O. Moskovich and Z. Fishelson, "Live cell imaging of outward and inward vesiculation induced by the complement C5b-9 complex," *Journal of Biological Chemistry*, vol. 282, no. 41, pp. 29977–29986, 2007.
- [31] M. Husmann, E. Beckmann, K. Boller et al., "Elimination of a bacterial pore-forming toxin by sequential endocytosis and exocytosis," *FEBS Letters*, vol. 583, no. 2, pp. 337–344, 2009.
- [32] V. Idone, C. Tam, J. W. Goss, D. Toomre, M. Pypaert, and N. W. Andrews, "Repair of injured plasma membrane by rapid Ca²⁺ dependent endocytosis," *Journal of Cell Biology*, vol. 180, no. 5, pp. 905–914, 2008.
- [33] R. Coral-Vazquez, R. D. Cohn, S. A. Moore et al., "Disruption of the sarcoglycan-sarcospan complex in vascular smooth muscle: a novel mechanism for cardiomyopathy and muscular dystrophy," *Cell*, vol. 98, no. 4, pp. 465–474, 1999.
- [34] M. Durbeej, R. D. Conn, R. F. Hrstka et al., "Disruption of the β -sarcoglycan gene reveals pathogenetic complexity of limb-girdle muscular dystrophy type 2E," *Molecular Cell*, vol. 5, no. 1, pp. 141–151, 2000.
- [35] R. Han, M. Kanagawa, T. Yoshida-Moriguchi et al., "Basal lamina strengthens cell membrane integrity via the laminin G domain-binding motif of α -dystroglycan," *Proceedings of the National Academy of Sciences of the United States of America*, vol. 106, no. 31, pp. 12573–12579, 2009.
- [36] J. H. Nadeau, J. B. Singer, A. Matin, and E. S. Lander, "Analysing complex genetic traits with chromosome substitution strains," *Nature Genetics*, vol. 24, no. 3, pp. 221–225, 2000.
- [37] M. Ho, C. M. Post, L. R. Donahue et al., "Disruption of muscle membrane and phenotype divergence in two novel mouse models of dysferlin deficiency," *Human Molecular Genetics*, vol. 13, no. 18, pp. 1999–2010, 2004.
- [38] W. Lostal, M. Bartoli, N. Bourg et al., "Efficient recovery of dysferlin deficiency by dual adeno-associated vector-mediated gene transfer," *Human Molecular Genetics*, vol. 19, no. 10, Article ID ddq065, pp. 1897–1907, 2010.
- [39] G. Kroemer, L. Galluzzi, and C. Brenner, "Mitochondrial membrane permeabilization in cell death," *Physiological Reviews*, vol. 87, no. 1, pp. 99–163, 2007.
- [40] M. F. M. Engel, L. Khemtémourian, C. C. Kleijer et al., "Membrane damage by human islet amyloid polypeptide through fibril growth at the membrane," *Proceedings of the National Academy of Sciences of the United States of America*, vol. 105, no. 16, pp. 6033–6038, 2008.
- [41] X. Wang, W. Xie, Y. Zhang et al., "Cardioprotection of ischemia/reperfusion injury by cholesterol-dependent MG53-mediated membrane repair," *Circulation Research*, vol. 107, no. 1, pp. 76–83, 2010.
- [42] J. Díaz-Manera, T. Touvier, A. Dellavalle et al., "Partial dysferlin reconstitution by adult murine mesoangioblasts is sufficient for full functional recovery in a murine model of dysferlinopathy," *Cell Death and Disease*, vol. 1, no. 8, article e61, 2010.
- [43] M. Krahn, N. Wein, M. Bartoli et al., "A naturally occurring human minidysferlin protein repairs sarcolemmal lesions in a mouse model of dysferlinopathy," *Science Translational Medicine*, vol. 2, no. 50, Article ID 50ra69, 2010.
- [44] M. Husmann, K. Dersch, W. Bobkiewicz, E. Beckmann, G. Veerachato, and S. Bhakdi, "Differential role of p38 mitogen activated protein kinase for cellular recovery from attack by pore-forming *S. aureus* α -toxin or streptolysin O," *Biochemical and Biophysical Research Communications*, vol. 344, no. 4, pp. 1128–1134, 2006.
- [45] L. E. Ramm, M. B. Whitlow, and C. L. Koski, "Elimination of complement channels from the plasma membranes of U937, a nucleated mammalian cell line: temperature dependence of the elimination rate," *Journal of Immunology*, vol. 131, no. 3, pp. 1411–1415, 1983.
- [46] J. D. Gumerson, Z. T. Kabaeva, C. S. Davis, J. A. Faulkner, and D. E. Michele, "Soleus muscle in glycosylation-deficient muscular dystrophy is protected from contraction-induced injury," *American Journal of Physiology*, vol. 299, no. 6, pp. C1430–C1440, 2010.

Research Article

Differential Effect of Calsequestrin Ablation on Structure and Function of Fast and Slow Skeletal Muscle Fibers

Cecilia Paolini,¹ Marco Quarta,^{2,3} Laura D'Onofrio,¹ Carlo Reggiani,^{2,4}
and Feliciano Protasi¹

¹ CeSI-Center for Research on Ageing & DNI-Department of Neuroscience and Imaging,
Università Gabriele d'Annunzio of Chieti, 66100 Chieti, Italy

² Department of Anatomy and Physiology, University of Padova, 35131 Padova, Italy

³ Department of Neurology and Neurological Sciences, Stanford University, Palo Alto, CA 94304, USA

⁴ CNR Institute of Neurosciences, 56724 Pisa, Italy

Correspondence should be addressed to Carlo Reggiani, carlo.reggiani@unipd.it

Received 30 April 2011; Accepted 12 July 2011

Academic Editor: Lars Larsson

Copyright © 2011 Cecilia Paolini et al. This is an open access article distributed under the Creative Commons Attribution License, which permits unrestricted use, distribution, and reproduction in any medium, provided the original work is properly cited.

We compared structure and function of EDL and Soleus muscles in adult (4–6 m) mice lacking both Calsequestrin (CASQ) isoforms, the main SR Ca²⁺-binding proteins. Lack of CASQ induced ultrastructural alterations in ~30% of Soleus fibers, but not in EDL. Twitch time parameters were prolonged in both muscles, although tension was not reduced. However, when stimulated for 2 sec at 100 Hz, Soleus was able to sustain contraction, while in EDL active tension declined by 70–80%. The results presented in this paper unmask a differential effect of CASQ1&2 ablation in fast versus slow fibers. CASQ is essential in EDL to provide large amount of Ca²⁺ released from the SR during tetanic stimulation. In contrast, Soleus deals much better with lack of CASQ because slow fibers require lower Ca²⁺ amounts and slower cycling to function properly. Nevertheless, Soleus suffers more severe structural damage, possibly because SR Ca²⁺ leak is more pronounced.

1. Introduction

Skeletal muscles are composed of a variety of fibers which are traditionally classified as fast and slow depending on their contractile parameters, such as time to peak in the isometric twitch or maximum shortening velocity, or as glycolytic and oxidative depending on their metabolic properties [1]. The current nomenclature, based on myosin heavy chain (MHC) isoform composition, includes 4 major fiber types, called type 1 or slow and type 2A, 2X, and 2B or fast, respectively, each of them with specific contractile properties [2].

The differences between fast and slow fibers, however, are not restricted only to myofibrillar proteins (myosin isoforms) and to metabolic enzymes (predominance of glycolytic versus oxidative activities), but also involves other subcellular systems [3]. Importantly the kinetics of Ca²⁺ mobilization are profoundly different in slow versus fast twitch fibers [4–7]. Intracellular Ca²⁺ concentrations ([Ca²⁺]_i) and Ca²⁺ release/reuptake from intracellular stores

(i.e., the sarcoplasmic reticulum, SR) are controlled by the sarcotubular system, a highly organized system of membranes formed by the association of invaginations of the sarcolemma, i.e., the transverse (T)-tubules, with the terminal cisternae of the SR [8, 9]. T-tubules contain voltage-gated L-type Ca²⁺ channel (or dihydropyridine receptors, DHPRs) which are mechanically coupled to Ca²⁺ release channels of the SR, the ryanodine receptors type-1 (RYR1) [10, 11]. Interaction between DHPR and RYR1 occurs at intracellular junctions called Ca²⁺ release units (CRUs) or triads, which mediate excitation-contraction (EC) coupling [12, 13]. CRUs contain several other proteins beside DHPRs and RYR1s: among them Calsequestrin (CASQ), the main intraluminal Ca²⁺ binding protein of the SR [14, 15], which is located in terminal cisternae of the junctional SR in close proximity to RYRs [16, 17]. In skeletal muscles, CASQ exists in two isoforms known as CASQ1 (or skeletal) and CASQ2 (or cardiac). Both isoforms can be found in slow fibers, whereas only CASQ1 is expressed in fast

fibers [18, 19]. It has been reported that the total CASQ content is greater in fast than in slow fibers [20]. A recent quantitative analysis on single fibers from rat points to a concentration of $36\ \mu\text{M}$ in fast fibers (only CASQ1) versus $10\ \mu\text{M}$ in slow fibers (CASQ1 and CASQ2) [21]. Owing to its properties (medium-low affinity, but high capacity), CASQ provides a large SR pool of releasable Ca^{2+} , while maintaining SR intraluminal concentrations of free Ca^{2+} low enough to facilitate the work of sarcoendoplasmic reticulum Ca^{2+} ATP-ase (SERCA) pumps. CASQ in skeletal muscle fibers plays an important dual role: (i) to buffer Ca^{2+} inside the SR thanks to the large number of acidic residues which allows each CASQ molecule to bind up to 60–80 Ca^{2+} ions [22]; (ii) to modulate Ca^{2+} release from the SR via a triadin/junctin-mediated interaction with RYR1 [23–25]. There is evidence that CASQ1 has different polymerization rate and Ca^{2+} buffering properties than CASQ2 [22], suggesting the possibility that RYR1 is modulated differently by CASQ1 and 2 in fast- and slow-twitch fibers [26]. Murphy and colleagues [21] recently suggested that CASQ2 is more efficient than CASQ1 in reducing SR Ca^{2+} leak, a property also shown in cardiac muscle [27].

Mice lacking CASQ1 were viable and fertile [28]. Nevertheless, lack of CASQ1 induced significant functional and structural modifications in skeletal fibers: CASQ1 ablation reduced dramatically the total SR Ca^{2+} content (of about 70%) in fast twitch from flexor digitorum brevis (FDB) muscles. However, Ca^{2+} transients evoked by a single stimulus was surprisingly not dramatically reduced so that twitch peak force was preserved [28]. This apparent minor functional impairment can be in part explained by morphological adaptations taking place in fast fibers, that is, profound remodelling of CRUs which forms multiple layers of junctional SR and T-tubules bearing an approximately doubled number of RYRs [28].

Both functional and structural changes were more evident in extensor digitorum longus (EDL) and in FDB, containing predominantly fast twitch fibers, than in Soleus muscle, a predominantly slow twitch muscle. There are reasons to believe that the impact of CASQ1 ablation is more evident in EDL and in FDB than in Soleus, because CASQ2 is expressed in CASQ1-null mice and quite abundant in slow twitch fibers. To explain the differential impact of CASQ1 ablation in fast versus slow fibers, we may also have to consider important functional differences: in fast fibers greater amounts of Ca^{2+} are released after each action potential [5], SR volume is greater, and SR is filled only to 35% of its maximal capacity [21]. In contrast SR of slow fibers is filled to its maximal capacity [21]. In view of the possible diversity in Ca^{2+} handling between slow and fast muscles and to investigate how complete ablation of CASQ will affect the different muscle types we studied EDL and Soleus muscle in mice lacking both CASQ isoforms [29, 30], generated by cross-breeding preexisting CASQ1-null and CASQ2-null mice [28, 31].

Interestingly, our results show that EDL and Soleus are differently affected by complete ablation of CASQ, as EDL, but not Soleus, becomes unable to maintain tension during

prolonged tetanic contractions, while Soleus, but not EDL, displays the early onset of a myopathic phenotype.

2. Materials and Methods

2.1. CASQ-Null Mice. CASQ1-null and CASQ2-null mice were generated as previously described [28, 31]. Double (d)CASQ-null mice lacking both CASQ isoforms were generated by cross-breeding the preexisting CASQ1-null and CASQ2-null mice. C57BL/6J mice were used as wild-type (WT) controls and obtained from Charles River Italia. Mice were housed in microisolator cages, temperature 22°C , 12 hr light/dark cycle, with free access to water and food. Mice were killed by an overdose of the anaesthetic ethyl ether, and their muscles were rapidly dissected. All experiments were conducted according to the National Institutes of Health *Guide for the Care and Use of Laboratory Animals* and were approved by the ethical committee of the University of Chieti and of the Department of Anatomy and Physiology, University of Padova.

2.2. Preparation of Homogenates, Electrophoresis, Western Blot Analysis (Figure 1). Preparation of total homogenates from WT, CASQ1-null and dCASQ-null muscles (hind limb, EDL, and Soleus), and western blot analysis were performed as previously described in 4–6 month-old mice [28]. The antibody used was a rabbit polyclonal antibody reactive with both isoforms of CASQ (Affinity Bioreagents, USA).

2.3. Spontaneous Mortality Rate (Figure 2). The rate of spontaneous mortality under standard housing conditions was assessed during the entire life span using the Kaplan-Meier method in a subpopulation of mice which were not utilized for other experiments. Age- and sex-dependent probability of survival is shown in Figure 2.

2.4. Grip Strength Test (Figure 3). Strength developed by WT, CASQ1-null, and dCASQ-null male mice of 6 months of age was measured during instinctive grasp with a grip-strength-test protocol [33]. The mouse was held by the tail in proximity to a trapeze bar connected with the shaft of a Shimpo Fgv 0.5x force transducer (Metrotec Group, San Sebastián Spain). Once the mouse had firmly grabbed the trapeze, a gentle pull was exerted on the tail. The measurement of the peak force generated by each mouse with fore and hind limbs was repeated three times with appropriate intervals to avoid fatigue, and the average of the highest peak force values was normalized to the body mass [33].

2.5. Preparation and Analysis of Samples by Light and Electron Microscopy (EM) (Figure 4 and Table 1). EDL and Soleus muscles were carefully dissected from WT, CASQ1-null, and dCASQ-null at 4–6 months of age. Muscles were fixed at RT in 3.5% glutaraldehyde in 0.1 M sodium cacodylate buffer, pH 7.2 for 2 h and kept in fixative before further use. Small bundles of fixed fibers were postfixed in 2% OsO_4 in 0.1 M sodium cacodylate buffer for 2 h and block stained

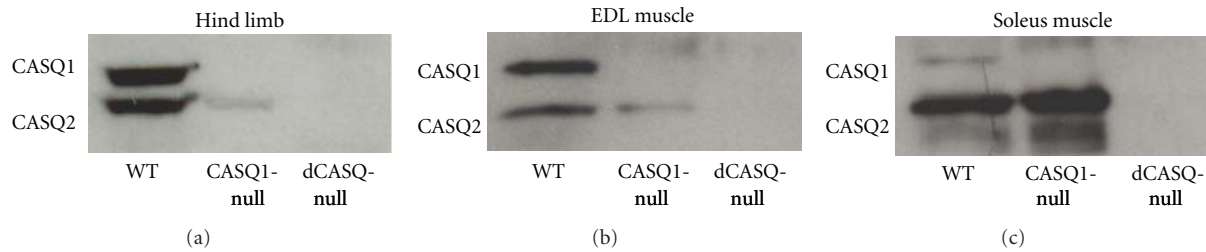


FIGURE 1: dCASQ-null mice did not express any of the two CASQ isoforms. Western blot analysis of total homogenates prepared from hind limb (a), EDL, and Soleus (b and c) muscles showed that (i) in CASQ1-null muscles CASQ1 was missing, whereas CASQ2 was still present, more in Soleus (slow twitch) and less in EDL (fast twitch); (ii) in dCASQ-null muscles both isoforms were absent.

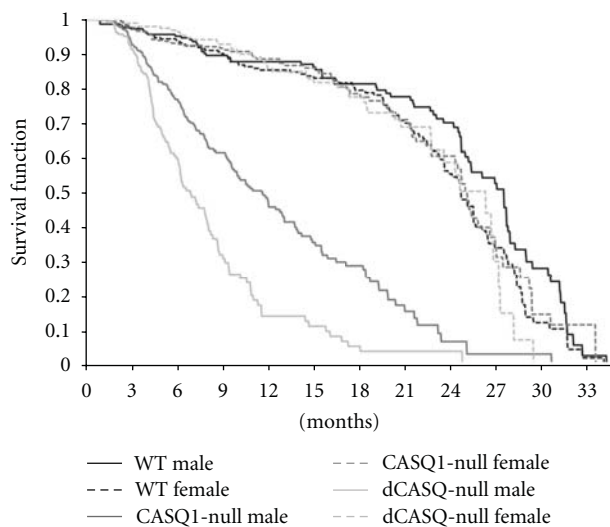


FIGURE 2: dCASQ-null male mice displayed a rate of spontaneous mortality even higher than that of CASQ1-null mice (see also [32]). Age-dependent survival analysis of male and female WT, CASQ1-null, and dCASQ-null mice housed under standard conditions evaluated using the Kaplan-Meier method. Number of animals included in the study: WT: male $n = 321$, female $n = 318$; CASQ1-null: male $n = 649$, female $n = 632$; dCASQ-null: male $n = 200$, female $n = 222$. As shown in Dainese et al. [32] male CASQ1-null mice were affected by a significantly increased rate of spontaneous mortality, particularly after 3 months of age: the additional ablation of CASQ2 worsened the phenotype.

in aqueous saturated uranyl acetate. After dehydration, specimens were embedded in an epoxy resin (Epon 812). For histological analysis, longitudinal and cross-oriented semithin sections (300 nm) were cut with a Leica Ultracut R microtome (Leica Microsystems, Vienna, Austria) using a Diatome diamond knife (DiatomeLtd. CH-2501 Biel, Switzerland). After staining with Toluidine Blue dye, the sections were viewed on a Leica DMLB fluorescence microscope (Leica Microsystems, Vienna, Austria). Quantitative analysis of damaged fibers (data in Table 1) was performed on histology images. For EM, ultrathin sections (35 nm) were cut and, after staining in 4% uranyl acetate and lead citrate, examined with a Morgagni Series 268D electron microscope (FEI Company, Brno, Czech Republic), equipped with Megaview III digital camera.

2.6. Force and Contraction Kinetics of Isolated Intact Muscles (Figures 5 and 6). EDL and Soleus muscles were dissected from the hind limbs of WT and knock-out male mice (4 months old) in warm oxygenated Krebs solution and mounted between a force transducer (SI-H Force Transducer World Precision Instruments, Inc., Sarasota, FL, USA) and a micromanipulator-controlled shaft in a small chamber where oxygenated Krebs solution was continuously circulated. The temperature was kept constant at 25°C. The stimulation conditions were optimized, and muscle length was increased until force development during tetanus was maximal. The responses to a single stimulus (twitch) or to a series of stimuli at various rates producing unfused or fused tetani were recorded. Time-to-peak tension, time-to-half relaxation, time-to-base tension, and peak-tension were measured in single twitches. Tension was measured in completely fused maximal tetani of different duration (0.5–2 s) at the peak and just after the last stimulus.

2.7. Statistical Analysis. Data were expressed as mean \pm standard errors. For analysis of force and contraction kinetics comparison between the three groups (WT, CASQ1-null, and dCASQ-null mice) was carried out using ANOVA followed by a post hoc test (Newman-keuls test), while for weight and grip test the statistical significance was assessed using the unpaired Student's t -test.

3. Results

3.1. Phenotype of dCASQ-Null Mice. The expression of the two CASQ isoforms in WT, CASQ1-null, and dCASQ-null mice was assessed by western blots of homogenates prepared from either all hind limb muscles (Figure 1(a)) or separately from EDL and Soleus (Figures 1(b) and 1(c), resp.). Analysis showed that: (a) in CASQ1-null muscles CASQ1 is missing, whereas CASQ2 is still present, more in Soleus (slow twitch) and less in EDL (fast twitch); (b) in dCASQ-null muscles both isoforms are absent. dCASQ-null mice were viable and fertile, appeared to develop and breed normally, and did not present a clear overt phenotype. However, male mice carrying the double-null mutation displayed a greatly increased mortality rate compared to WT animals, even more pronounced than that of CASQ1-null male mice (Figure 2; see also [32, 34] for more detail): more than 50% of

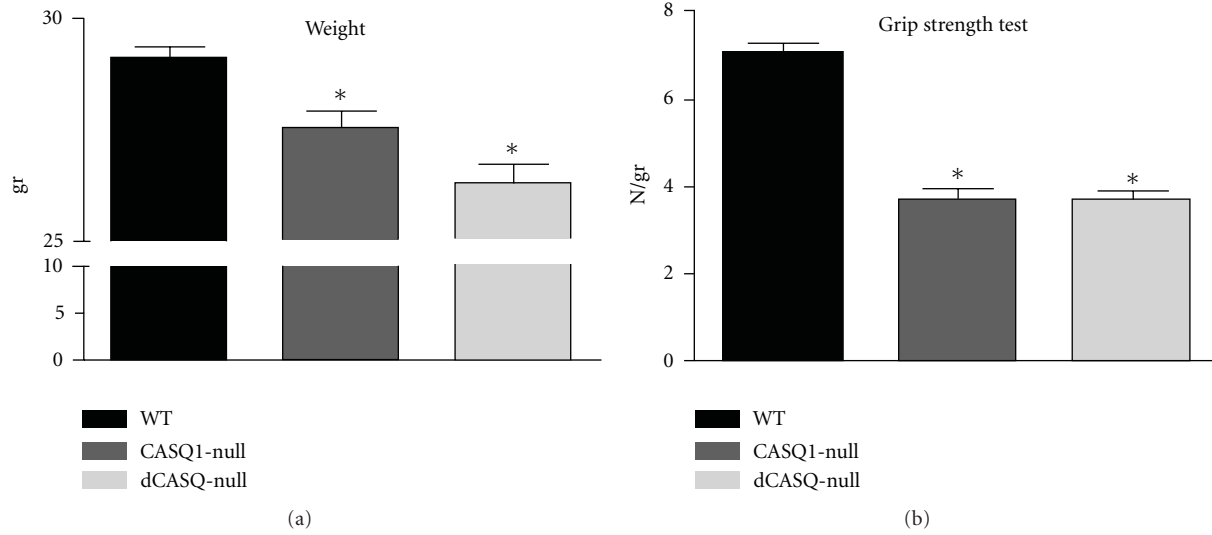


FIGURE 3: Ablation of CASQ1 and of both CASQ isoforms resulted in a significant reduction in body weight and grip strength test. (a) Ablation of CASQ1 and/or of both CASQ isoforms resulted in a significant reduction of body weight, which was more pronounced in dCASQ-null than in CASQ1-null mice ($n = 86, 65,$ and 33 animals for WT, CASQ1-null, and dCASQ-null, resp.). (b) The evaluation of the maximal force that mice produced while grasping a bar (grip strength test, [33]) showed that the force output of CASQ1-null and dCASQ-null mice was significantly lower than that of WT animals, but not different from each other ($n = 26, 39,$ and 33 animals for WT, CASQ1-null, and dCASQ-null, resp.). Both body weight and grip strength test were measured in male mice. *Significantly different from WT.

TABLE 1: Histological examination of adult Soleus fibers: fibers presenting structural damage were absent in WT, rare in CASQ1-null, but quite frequent in dCASQ-null. We classified abnormal fibers in two main classes: (a) fibers presenting large areas loosing cross striation, or *unstructured cores*, but no contractures (see Figure 4(f)); (b) fibers containing (also) *contracture cores* (see Figure 4(e), asterisk). (c) About 35% of Soleus fibers from dCASQ-null mice present severe structural alterations.

Soleus	Age (months)	Total no. of fibers analyzed	No. of fiber with alterations		(c) Total % of altered fiber
			(a) Unstructured cores	(b) Contracture cores	
WT	5	29	—	—	—
	6	15	—	—	—
CASQ1-null	5	18	1 (6%)	—	6
	6.2	27	1 (4%)	—	4
<i>Average: 5%</i>					
dCASQ-null	4.8	25	7 (28%)	5 (20%)	48
	4.2	23	3 (13%)	4 (17%)	30
	4.8	47	2 (4%)	6 (13%)	17
	4.0	32	4 (13%)	9 (28%)	41
<i>Average: 34%</i>					

male mice died before reaching the age of 6 months. Rate of spontaneous mortality of CASQ1-null and dCASQ-null females was not significantly different from that of male and female WT (Figure 2).

3.2. dCASQ-Null Mice Presented a Reduced Body Weight and Produced Less Grip-Strength Force Than WT Mice. We measured the average body weight of WT, CASQ1-null, and dCASQ-null adult male mice (4–6 months of age): dCASQ-null mice were on the average significantly smaller than WT and slightly smaller than CASQ1-null mice (Figure 3(a)). To assess basic neuromuscular function of living mice, we

used the grip strength test, which provides a simple way to test the global muscle performance during maximal isometric contraction of short duration [33]. Figure 3(b) shows that mice lacking either CASQ1 or both CASQ isoforms developed a significantly lower force output than WT. No significant difference was detectable between mice lacking only CASQ1 and both CASQ isoforms using this method.

3.3. In dCASQ-Null Soleus Muscle 30% of Soleus Fibers Displayed Severe Ultrastructural Damage. We performed structural analysis of EDL and Soleus muscles from adult

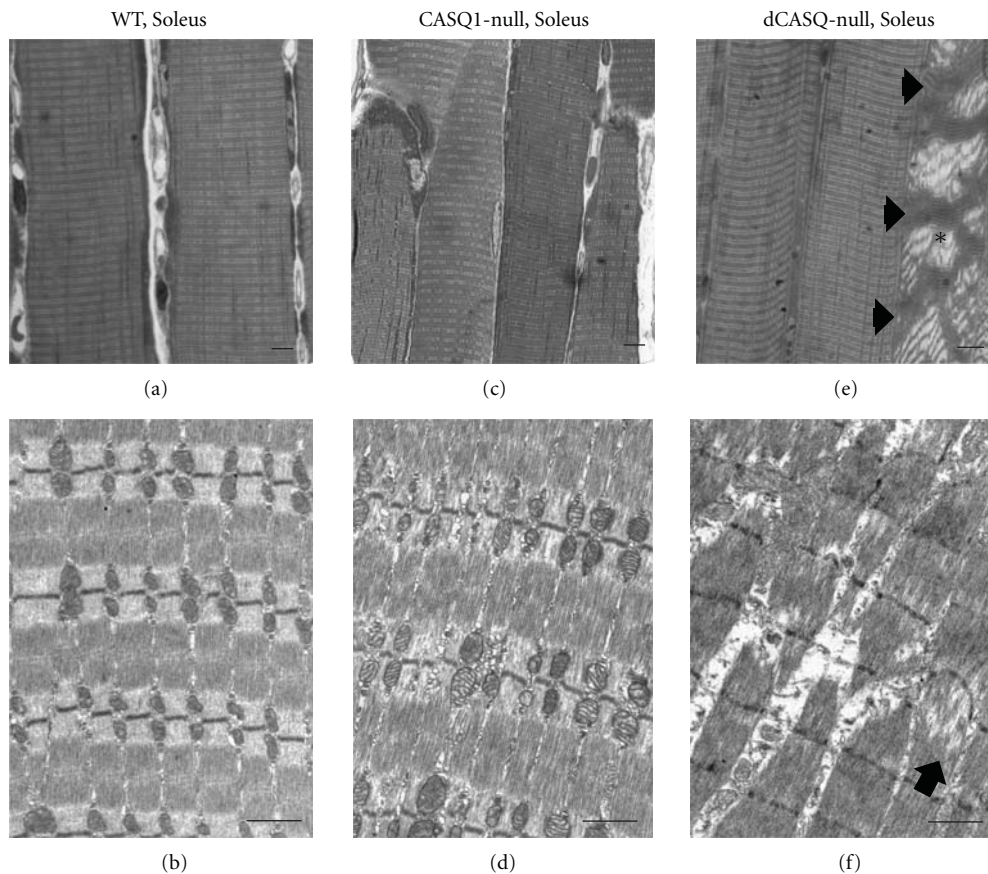


FIGURE 4: In dCASQ-null animals (4–6 months of age) ~30% of Soleus fibers presented severe structural damage. (a), (c), and (e): histology; (b), (d), and (f): EM. (a) and (b) WT Soleus fibers from adult mice (4–6 months of age) always showed a well-defined cross-striation and well-organized EC coupling (not shown) and mitochondrial apparatus. (c)–(f) At 4–6 months of age, ~30% of Soleus fibers (see Table 1) from dCASQ-null mice were affected by severe structural alterations, which were clearly visible both at the histological examination (e) and in EM (f). In (e) arrowheads point to three *contracture cores* within the same severely damaged fiber (asterisk), while in (f) is shown a small portion of a fiber presenting degeneration of the contractile elements and initial Z line streaming (arrow). Fibers with similar alterations are very rare in CASQ1-null fibers ((c) and (d)) and never seen in WT. See Table 1 for quantitative analysis.

male (4–6 months of age) WT, CASQ1-null, and dCASQ-null mice using a combination of sectioning for histology and EM (Figure 4). This examination revealed that a significant percentage of fibers in dCASQ-null Soleus exhibit severe morphological alterations (Table 1). This structural damage, which was not found in EDL at this age (4–6 months), disrupts the regular cross-striation of skeletal fibers and affects large portions of the fiber interior (Figure 4(e), asterisk). Whereas structural alterations are quite variable in appearance, we classified abnormal fibers in two main classes (Table 1): (a) those presenting large areas losing cross-striation, or *unstructured cores*, but no contractures (Figure 4(f)); (b) those containing also areas of contracture (Figure 4(e), asterisk). Fibers containing *unstructured cores* were frequent in Soleus from dCASQ-null mice, but rare in CASQ1-null Soleus and totally absent in WT (Table 1, Column (a)). Fiber presenting *contracture cores*, on the other hand, were never found in Soleus muscles from WT and CASQ1-null mice, whereas again they were quite frequent in Soleus fibers from dCASQ-null (Table 1, Column (b)). Overall, ~35% of Soleus fibers from

dCASQnull mice showed structural alterations (Table 1, Column (c)).

3.4. Ablation of Both CASQ Isoforms Results in an Alteration of Twitch Contractile Kinetics in Both EDL and Soleus. In order to assess the effects of the complete removal of CASQ on the contractile performance of fast- and slow-twitch muscles, we dissected EDL and Soleus muscles from WT, CASQ1-null, and dCASQ-null mice and studied their function *ex vivo*. The altered kinetics profile of the contractile cycle previously described in CASQ1-null muscle [28] was also evident in dCASQ-null muscles. The changes included a significant prolongation of time-to-peak tension (i.e. from the stimulus to the tension peak) in EDL compared to WT, but also to CASQ1-null (Figure 5(a)). No prolongation of time-to-peak tension was seen in Soleus (Figure 5(b)). In addition, time to base (i.e., time elapsing from stimulus to the return to base line at the end of relaxation) was significantly prolonged in both EDL and Soleus muscles of knock-out mice compared to WT. The latter effect was more pronounced in dCASQ-null than in CASQ1-null mice (Figures 5(c) and 5(d)).

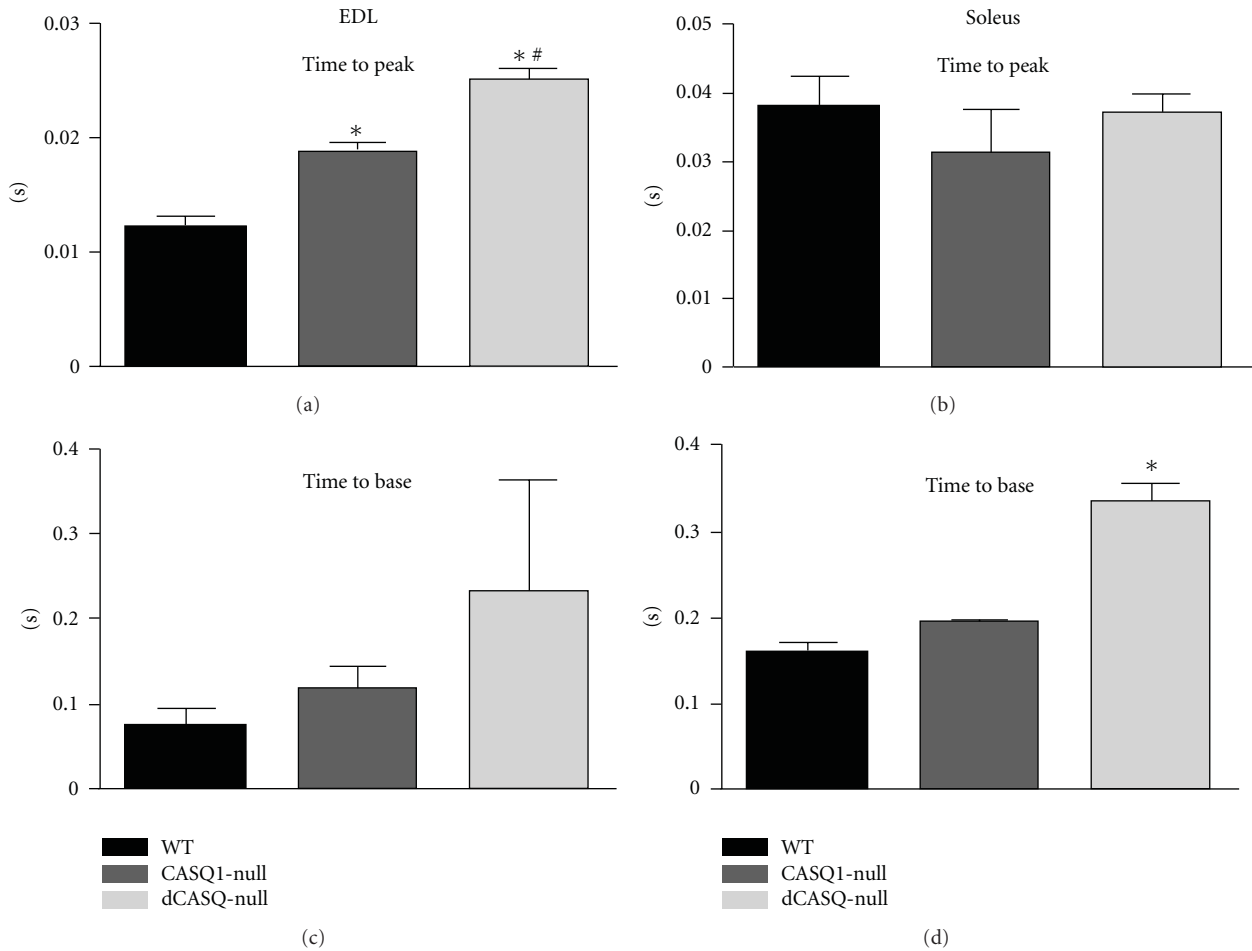


FIGURE 5: Ablation of CASQ isoforms resulted in prolongation of the twitch parameters in both EDL and Soleus. (a) and (b) Time to peak (i.e., from the stimulus to the tension peak) was prolonged in EDL from CASQ1-null, and even more in dCASQ-null, compared to WT. This effect is not seen in Soleus. (c) and (d) On the other hand, time to base (i.e., from stimulus back to base line at the end of relaxation) was prolonged compared to WT in both EDL and Soleus muscles, more in dCASQ-null than in CASQ1-null mice (EDL: WT $n = 8$, CASQ1-null $n = 10$, dCASQ null $n = 9$, Soleus: WT $n = 8$, CASQ1-null $n = 10$, dCASQ null $n = 10$). *Significantly different from WT; #significantly different from CASQ1-null.

3.5. Ablation of CASQ Impaired the Ability of EDL, But Not of Soleus, to Maintain Tension during Tetanic Contraction. Isometric tension was determined in short fused isometric tetani with a duration just sufficient to reach peak tension (500 ms in EDL and 1 s in Soleus) and found significantly reduced in EDL, but not in Soleus muscles of CASQ1-null and dCASQ-null mice (not shown). However, the most interesting result was obtained when the duration of the tetanus was prolonged up to 2 seconds (Figure 6): in both CASQ1- and dCASQ-null EDL the residual tension declined dramatically (by about 80%) (Figures 6(a) and 6(b)), while in Soleus only a minor decline of developed tension occurred in the absence of CASQ (Figures 6(c) and 6(d)). Specifically, the tension decline of Soleus during a 2 s tetanus was approximately 15% in CASQ1-null and 25% in dCASQ-null. A careful inspection of the traces showed in Figures 6(a) and 6(c) revealed that the kinetics of the rising phase of the isometric tetani were faster when CASQ is missing both in EDL and in Soleus. An increased early phase of Ca^{2+} release

has been previously reported in fibers lacking CASQ isolated from dCASQ-null mice [29]. This effect can be related to the alterations of the twitch response. In agreement with the above observations, the amplitude of the twitch (measured as peak tension, not shown) was preserved, and the duration of the twitch (measured as time-to-peak and time-to-base line, Figure 5) was prolonged, thus allowing a faster tension development during repeated high frequency stimulation.

4. Discussion

Two isoforms, CASQ1 and CASQ2, are expressed in skeletal muscle fibers [18, 19], with CASQ1 and CASQ2 being more abundant in fast- and slow-twitch fibers, respectively [21]. The impact of their removal in different fiber types has not been investigated yet. In view of the possible diversity in Ca^{2+} handling between slow and fast muscles and to investigate how complete ablation of CASQ will affect the two different muscle types, we studied EDL and

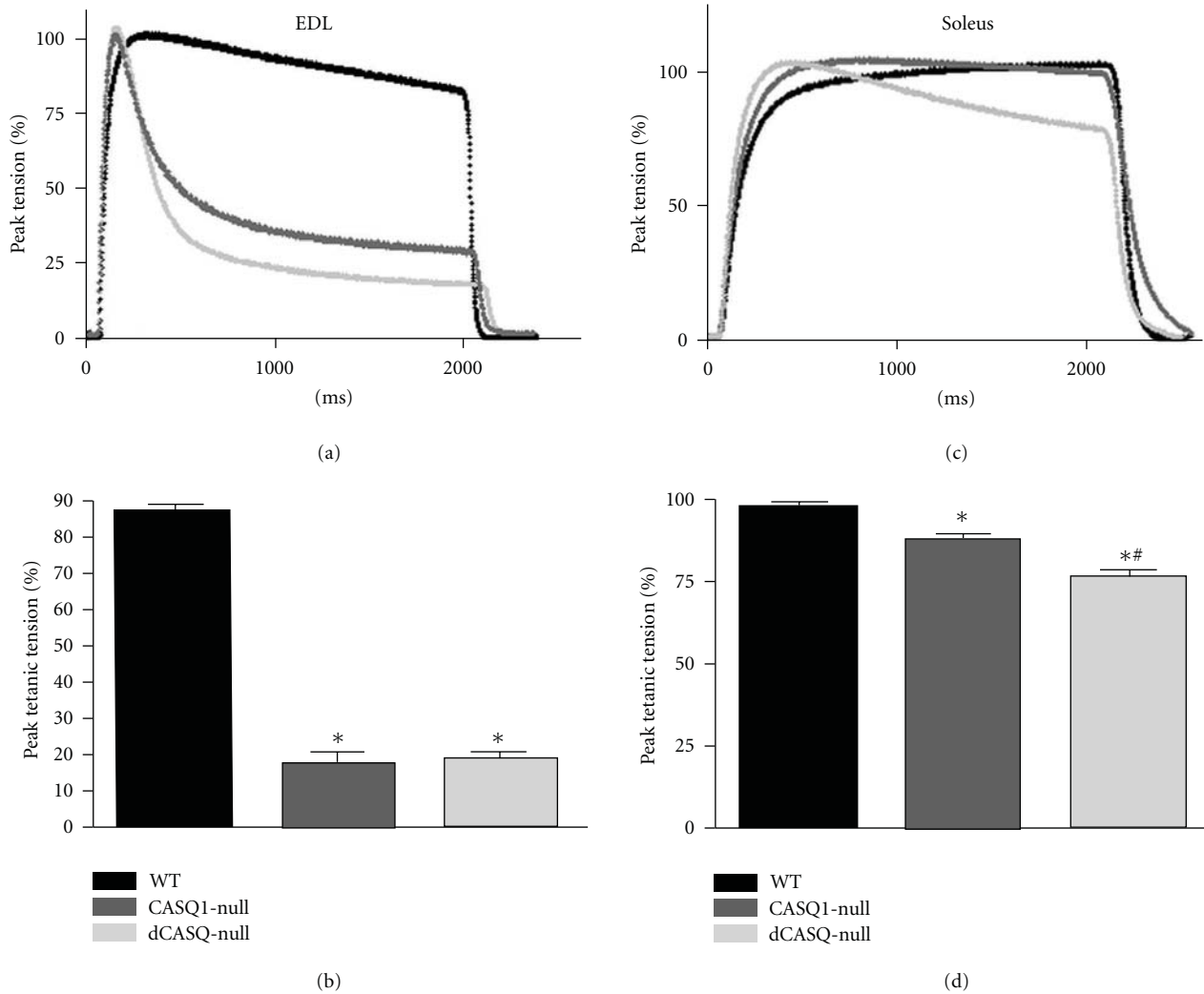


FIGURE 6: Tension decline and residual tension after 2 seconds of high-frequency stimulation in EDL and Soleus of CASQ1-null and dCASQ-null mice. (a) and (b) When stimulated at high frequency (2 s, 140 Hz) EDL muscles of both CASQ1-null and dCASQ-null displayed a strong drop in tension (by about 80%) compared to WT. (c) and (d) Conversely, in Soleus muscle (stimulated at 90 Hz for 2 s) this effect was considerably less: compared to WT, tension was decreased by ~15% in CASQ1-null and 25% in dCASQ-null (EDL: WT $n = 8$, CASQ1-null $n = 10$, dCASQ null $n = 9$, Soleus: WT $n = 8$, CASQ1-null $n = 10$, dCASQ null $n = 10$). *Significantly different from WT; #significantly different from CASQ1-null.

Soleus muscle in mice lacking both CASQ isoforms. The comparison of the structural and functional effect of the complete ablation of CASQ revealed two main distinctive features: (1) Soleus, but not EDL, shows a number of fibers with signs of structural degeneration (Figure 4); (2) EDL is unable to maintain active tension during a prolonged tetanus, while Soleus is only marginally affected (Figure 6). Both aspects require careful consideration.

4.1. Phenotype of dCASQ-Null Mice. Previous studies have shown that CASQ1-null mice are susceptible to spontaneous mortality and trigger MH-like episodes when exposed to either heat or anesthesia [32, 34]. CASQ2-null mice display frequent episodes of catecholaminergic polymorphic ventricular tachycardia (CPVT), which can be triggered by a catecholamine challenge with the β -adrenergic agonist

isoproterenol [31]. dCASQ-null mice are viable, but present high frequency of spontaneous death in male mice, even higher than that previously registered in CASQ1-null animals [32] (Figure 2). The specific reason for the increased spontaneous mortality rate of dCASQ-null mice is still under investigation, since CPVT in mice lacking CASQ2 is not lethal [31]. Grip strength test confirmed a significant impairment of the overall neuromuscular function (Figure 3(b)), similar to that of CASQ1-null mice. The lack of a significant difference in grip strength between CASQ1- and dCASQ-null mice probably reflects the fact that murine muscles show a great predominance of fast fibers expressing exclusively CASQ1 [2]. Finally, dCASQ-null mice show a reduced body weight which can be likely ascribed to a decrease in skeletal muscle mass due to a myopathic phenotype [35].

4.2. Early Onset of a Myopathy in Soleus Fibers: A Possible Explanation. We have recently reported that isolated muscles (EDL), muscle fibers (from FDBs), and myotubes lacking CASQ1 present elevated basal cytosolic Ca^{2+} at body temperature [30, 32]. This abnormally high resting cytosolic Ca^{2+} causes abnormal development of muscle tension (contracture) when body temperature is raised above physiological values (39–41°C) [32]. This reaction to heat explains why CASQ1-null mice are susceptible to trigger lethal malignant hyperthermia (MH) like episodes when exposed to either high environmental temperatures or halogenated anesthetics [34]. In the present study we show that ~30% of Soleus fibers from dCASQ-null mice present clear evidence of the early onset of a myopathic phenotype, which is not as evident in EDL fibers at the same age (4–6 months, Figure 4). These alterations, which resemble those described in other murine models of MH and central core disease (CCD) [36, 37], were not seen in Soleus fibers of CASQ1-null mice, suggesting that the abundant expression of CASQ2 in slow fibers (Figure 1) prevents the onset of the pathology. Preliminary data from our laboratory shows that also EDL of CASQ1-null mice (where a minor amount of CASQ2 is expressed) will eventually develop a similar myopathy with increasing age [38]. This considered, the difference between the two muscles is that Soleus develops a myopathy at an earlier stage. The reason can be tentatively found in the different capabilities of EDL and Soleus to deal with removal of Ca^{2+} from cytosol and with SR Ca^{2+} leak.

In support to this view, it has been recently suggested that CASQ2 in slow muscle fibers may be important to prevent Ca^{2+} leakage [21]. The SR of slow fibers is saturated with Ca^{2+} at resting myoplasmic Ca^{2+} concentration, while the SR of fast fibers is only about one-third saturated with Ca^{2+} under equivalent conditions [21, 39]. Such difference implies that the rate of SR Ca^{2+} uptake in fast fibers is predominantly controlled by myoplasmic Ca^{2+} , while in slow fibers is more likely limited by the Ca^{2+} concentration within the SR lumen [39]. The intraluminal Ca^{2+} concentration is likely increased when the buffering action of CASQ is missing in the Soleus of dCASQ-null mice, causing serious challenge to reuptake. This would in turn result in excessive SR Ca^{2+} leak and $[\text{Ca}^{2+}]_i$, which will ultimately lead to the structural decay. The dramatic prolongation of the time to base (i.e., relaxation duration) of Soleus lacking both CASQ isoforms is in agreement with the impaired Ca^{2+} reuptake.

4.3. The Capability to Sustain Tetanic Tension Is Impaired in EDL, But Not in Soleus. The complete removal of CASQ in double-null mice decreases the ability of the SR to store Ca^{2+} both in fast and in slow muscle fibers. Slow Soleus fibers, but not fast EDL fibers, are able to sustain tension during a prolonged contractions (Figure 6), due to specific feature of the Ca^{2+} kinetics as discussed here below. The RYR-mediated Ca^{2+} release from the SR is approximately two times greater in fast compared to slow fibers. The larger size of CRUs and the higher density of RYR1 and DHPR in fast fibers is instrumental to this [40, 41]. A greater Ca^{2+} release is needed in EDL fast fibers compared to Soleus slow fibers as the number of cytosolic Ca^{2+} binding sites

is greater. In the first place, the troponin-C (TnC) isoform expressed in fast-twitch fibers presents two low affinity Ca^{2+} binding sites, whereas there is only one in the slow-twitch TnC isoform and, in addition, other cytosolic Ca^{2+} binding proteins must be saturated during the contractile cycle. Among them, there are parvalbumin, present at a concentration of 400–500 $\mu\text{mol/liter}$ in fast fibers but not in slow fibers [42] and containing two Ca^{2+} binding sites, and SERCA1, with a concentration of 120 $\mu\text{mol/liter}$ and two Ca^{2+} binding sites [40]. During a twitch (or the initial phase of a tetanus) the Ca^{2+} released can efficiently saturate TnC and SERCA and other minor Ca^{2+} buffers like Calmodulin, and the amount of 300–400 μmoles is likely to be sufficient, in agreement with published evidence [40, 43]. During a tetanic train of stimuli, more Ca^{2+} enters the cytosol through repeated releases, although the amplitude of the subsequent releases progressively decreases with the fifth release being only 10% of the first release [40, 43]. In order to sustain tension for more than one second, it is necessary to saturate also parvalbumin, a process occurring with a slower kinetics related to calcium replacement for magnesium [44]: fast fibers deprived of CASQ fails to maintain a prolonged tetanic tension, probably because the Ca^{2+} released is not sufficient to saturate all cytosolic calcium-binding proteins, parvalbumin among them, with the result of reducing the Ca^{2+} available for TnC, and therefore for tension generation. Conversely, a quite different scenario takes place in a typical slow fibers of Soleus where the lower SERCA density, the single low binding site of slow TnC, and, above all, the absence of parvalbumin [42] would prevent the tension decline observed in EDL. In this contest, very likely the minor reduction (~25%) in tetanic tension recorded in dCASQ-null Soleus (Figures 6(c) and 6(d)) could be almost completely ascribed to the presence of damaged fibers, which likely have compromised contractile function, and not to an insufficient amount of Ca^{2+} to activate contraction.

4.4. Conclusion Remarks. CASQ ablation has a differential effect in fast versus slow skeletal muscle fibers. Whereas in EDL CASQ is necessary to provide the large amount of Ca^{2+} required for a maximal sustained contraction, slow-twitch fibers are only moderately affected by the absence of CASQ during prolonged tetani. However, CASQ presence in Soleus seems necessary to help Ca^{2+} reuptake, reduce Ca^{2+} leakage, and control myoplasmic Ca^{2+} , which otherwise will eventually lead to the early onset of a myopathy. In this aspect, slow fibers are reminiscent of cardiac myocytes where CASQ role is essential to control diastolic Ca^{2+} leakage [31]. These findings add novel information, which may help to better understand the differences in Ca^{2+} handling of fast and slow fibers and also offer new insights to unlock mechanisms leading to myopathies such as MH and CCD.

Abbreviations Used in the Paper

Ca^{2+} :	Calcium ions
CASQ1 and CASQ2:	Skeletal and cardiac isoform of Calsequestrin
CCD:	Central core disease

CRUs:	Calcium release units
DHPR:	Dihydropyridine receptors
EC Coupling:	Excitation-contraction coupling
EDL:	Extensor digitorum longus
EM:	Electron microscopy
MH:	Malignant hyperthermia
MHC:	Myosin heavy-chain
RYR1:	Ryanodine receptor type-1
SERCA:	Sarcoendoplasmic reticulum Ca ²⁺ ATP-ase
SR:	Sarcoplasmic reticulum
TnC:	Troponin-C
T-Tubule:	Transverse tubule
WT:	Wild type.

Acknowledgments

The authors thank Drs. P.D. Allen (Brigham & Women's Hospital, Boston, MA) and B.C. Knollmann (Vanderbilt University, Nashville, TN) for providing the doubleCASQ-null mouse colony used in the experiments. The authors also thank Dante Tatone, Cosmo Rossi, and Marco Dainese for technical assistance with equipment and mice housing. This study was supported by Research Grant no. GGP08153 from the Italian Telethon ONLUS Foundation to F. Protasi and C. Reggiani. Paolini and M. Quarta contributed equally to the work.

References

- [1] S. Schiaffino and C. Reggiani, "Molecular diversity of myofibrillar proteins: gene regulation and functional significance," *Physiological Reviews*, vol. 76, no. 2, pp. 371–423, 1996.
- [2] M. A. Pellegrino, M. Canepari, R. Rossi, G. D'Antona, C. Reggiani, and R. Bottinelli, "Orthologous myosin isoform and scaling of shortening velocity with body size in mouse, rat, rabbit and human muscles," *Journal of Physiology*, vol. 546, no. 3, pp. 677–689, 2003.
- [3] C. Reggiani and T. T. Kronnie, "RyR isoforms and fibre type-specific expression of proteins controlling intracellular calcium concentration in skeletal muscles," *Journal of Muscle Research and Cell Motility*, vol. 27, no. 5-7, pp. 327–335, 2006.
- [4] S. Carroll, P. Nicotera, and D. Pette, "Calcium transients in single fibers of low-frequency stimulated fast-twitch muscle of rat," *American Journal of Physiology*, vol. 277, no. 6, pp. C1122–C1129, 1999.
- [5] S. L. Carroll, M. G. Klein, and M. F. Schneider, "Decay of calcium transients after electrical stimulation in rat fast- and slow-twitch skeletal muscle fibres," *Journal of Physiology*, vol. 501, no. 3, pp. 573–588, 1997.
- [6] O. Delbono, K. S. O'Rourke, and W. H. Ettinger, "Excitation-calcium release uncoupling in aged single human skeletal muscle fibers," *Journal of Membrane Biology*, vol. 148, no. 3, pp. 211–222, 1995.
- [7] M. W. Fryer and I. R. Neering, "Actions of caffeine on fast- and slow-twitch muscles of the rat," *Journal of Physiology*, vol. 416, pp. 435–454, 1989.
- [8] C. Franzini-Armstrong, "Studies of the triad. 3. Structure of the junction in fast twitch fibers," *Tissue and Cell*, vol. 4, no. 3, pp. 469–478, 1972.
- [9] C. Franzini-Armstrong, L. Landmesser, and G. Pilar, "Size and shape of transverse tubule openings in frog twitch muscle fibers," *Journal of Cell Biology*, vol. 64, no. 2, pp. 493–497, 1975.
- [10] C. Paolini, J. D. Fessenden, I. N. Pessah, and C. Franzini-Armstrong, "Evidence for conformational coupling between two calcium channels," *Proceedings of the National Academy of Sciences of the United States of America*, vol. 101, no. 34, pp. 12748–12752, 2004.
- [11] F. Protasi, C. Franzini-Armstrong, and P. D. Allen, "Role of ryanodine receptors in the assembly of calcium release units in skeletal muscle," *Journal of Cell Biology*, vol. 140, no. 4, pp. 831–842, 1998.
- [12] E. Rios, J. Ma, and A. Gonzalez, "The mechanical hypothesis of excitation-contraction (EC) coupling in skeletal muscle," *Journal of Muscle Research and Cell Motility*, vol. 12, no. 2, pp. 127–135, 1991.
- [13] M. F. Schneider, "Control of calcium release in functioning skeletal muscle fibers," *Annual Review of Physiology*, vol. 56, pp. 463–484, 1994.
- [14] K. P. Campbell, D. H. MacLennan, A. O. Jorgensen, and M. C. Mintzer, "Purification and characterization of calsequestrin from canine cardiac sarcoplasmic reticulum and identification of the 53,000 dalton glycoprotein," *Journal of Biological Chemistry*, vol. 258, no. 2, pp. 1197–1204, 1983.
- [15] D. H. MacLennan, V. Shoshan, and D. S. Wood, "Studies of Ca²⁺ release from sarcoplasmic reticulum," *Annals of the New York Academy of Sciences*, vol. 402, pp. 470–477, 1982.
- [16] C. Franzini-Armstrong, L. J. Kenney, and E. Varriano-Marston, "The structure of calsequestrin in triads of vertebrate skeletal muscle: a deep-etch study," *Journal of Cell Biology*, vol. 105, no. 1, pp. 49–56, 1987.
- [17] A. O. Jorgensen, A. C. Y. Shen, K. P. Campbell, and D. H. MacLennan, "Ultrastructural localization of calsequestrin in rat skeletal muscle by immunoferritin labeling of ultrathin frozen sections," *Journal of Cell Biology*, vol. 97, no. 5 I, pp. 1573–1581, 1983.
- [18] E. Damiani, G. Tobaldin, P. Volpe, and A. Margreth, "Quantitation of ryanodine receptor of rabbit skeletal muscle, heart and brain," *Biochemical and Biophysical Research Communications*, vol. 175, no. 3, pp. 858–865, 1991.
- [19] R. Sacchetto, P. Volpe, E. Damiani, and A. Margreth, "Postnatal development of rabbit fast-twitch skeletal muscle: accumulation, isoform transition and fibre distribution of calsequestrin," *Journal of Muscle Research and Cell Motility*, vol. 14, no. 6, pp. 646–653, 1993.
- [20] E. Leberer, K. T. Hartner, and D. Pette, "Postnatal development of Ca²⁺-sequestration by the sarcoplasmic reticulum of fast and slow muscles in normal and dystrophic mice," *European Journal of Biochemistry*, vol. 174, no. 2, pp. 247–253, 1988.
- [21] R. M. Murphy, N. T. Larkins, J. P. Mollica, N. A. Beard, and G. D. Lamb, "Calsequestrin content and SERCA determine normal and maximal Ca²⁺ storage levels in sarcoplasmic reticulum of fast- and slow-twitch fibres of rat," *Journal of Physiology*, vol. 587, no. 2, pp. 443–460, 2009.
- [22] H. Park, Y. I. Park, E. Kim et al., "Comparing skeletal and cardiac calsequestrin structures and their calcium binding: a proposed mechanism for coupled calcium binding and protein polymerization," *Journal of Biological Chemistry*, vol. 279, no. 17, pp. 18026–18033, 2004.
- [23] N. A. Beard, D. R. Laver, and A. F. Dulhunty, "Calsequestrin and the calcium release channel of skeletal and cardiac muscle," *Progress in Biophysics and Molecular Biology*, vol. 85, no. 1, pp. 33–69, 2004.

- [24] N. A. Beard, M. M. Sakowska, A. F. Dulhunty, and D. R. Laver, "Calsequestrin is an inhibitor of skeletal muscle ryanodine receptor calcium release channels," *Biophysical Journal*, vol. 82, no. 1, pp. 310–320, 2002.
- [25] N. Ikemoto, M. Ronjat, L. G. Mészáros, and M. Koshita, "Postulated role of calsequestrin in the regulation of calcium release from sarcoplasmic reticulum," *Biochemistry*, vol. 28, no. 16, pp. 6764–6771, 1989.
- [26] N. A. Beard, L. Wei, and A. F. Dulhunty, "Ca²⁺ signaling in striated muscle: the elusive roles of triadin, junctin, and calsequestrin," *European Biophysics Journal*, vol. 39, no. 1, pp. 27–36, 2009.
- [27] N. Chopra, P. J. Kannankeril, T. Yang et al., "Modest reductions of cardiac calsequestrin increase sarcoplasmic reticulum Ca²⁺ leak independent of luminal Ca²⁺ and trigger ventricular arrhythmias in mice," *Circulation Research*, vol. 101, no. 6, pp. 617–626, 2007.
- [28] C. Paolini, M. Quarta, A. Nori et al., "Reorganized stores and impaired calcium handling in skeletal muscle of mice lacking calsequestrin-1," *Journal of Physiology*, vol. 583, no. 2, pp. 767–784, 2007.
- [29] L. Royer, M. Sztretzye, C. Manno et al., "Paradoxical buffering of calcium by calsequestrin demonstrated for the calcium store of skeletal muscle," *Journal of General Physiology*, vol. 136, no. 3, pp. 325–338, 2010.
- [30] M. Canato, M. Scorzeto, M. Giacomello, F. Protasi, C. Reggiani, and G. J. M. Stienen, "Massive alterations of sarcoplasmic reticulum free calcium in skeletal muscle fibers lacking calsequestrin revealed by a genetically encoded probe," *Proceedings of the National Academy of Sciences of the United States of America*, vol. 107, no. 51, pp. 22326–22331, 2010.
- [31] B. C. Knollmann, N. Chopra, T. Hlaing et al., "Casq2 deletion causes sarcoplasmic reticulum volume increase, premature Ca²⁺ release, and catecholaminergic polymorphic ventricular tachycardia," *Journal of Clinical Investigation*, vol. 116, no. 9, pp. 2510–2520, 2006.
- [32] M. Dainese, M. Quarta, A. D. Lyfenko et al., "Anesthetic and heat-induced sudden death in calsequestrin-1-knockout mice," *FASEB Journal*, vol. 23, no. 6, pp. 1710–1720, 2009.
- [33] A. M. Connolly, R. M. Keeling, S. Metha, A. Pestronk, and J. R. Sanes, "Three mouse models of muscular dystrophy: the natural history of strength and fatigue in dystrophin-dystrophin/utrophin-, and laminin alpha2-deficient mice," *Neuromuscular Disorders*, vol. 11, pp. 703–712, 2001.
- [34] F. Protasi, C. Paolini, and M. Dainese, "Calsequestrin-1: a new candidate gene for malignant hyperthermia and exertional/environmental heat stroke," *Journal of Physiology*, vol. 587, no. 13, pp. 3095–3100, 2009.
- [35] C. Paolini, M. Quarta, A. Nori et al., "Lack of Calsequestrin-1 causes impaired maturation and a progressive myopathy in skeletal fibers," *Journal of Muscle Research and Cell Motility*, vol. 30, p. A322, 2009.
- [36] S. Boncompagni, R. E. Loy, R. T. Dirksen, and C. Franzini-Armstrong, "The I4895T mutation in the type 1 ryanodine receptor induces fiber-type specific alterations in skeletal muscle that mimic premature aging," *Aging Cell*, vol. 9, no. 6, pp. 958–970, 2010.
- [37] S. Boncompagni, A. E. Rossi, M. Micaroni et al., "Characterization and temporal development of cores in a mouse model of malignant hyperthermia," *Proceedings of the National Academy of Sciences of the United States of America*, vol. 106, no. 51, pp. 21996–22001, 2009.
- [38] C. Paolini, M. Quarta, M. Dainese et al., "Initial characterization of CASQ1/CASQ2 knockout (double CASQ-null) mice," *Biophysical Journal*, vol. 98, no. 3, supplement 1, pp. 546a–547a, 2010.
- [39] M. W. Fryer and D. G. Stephenson, "Total and sarcoplasmic reticulum calcium contents of skinned fibres from rat skeletal muscle," *Journal of Physiology*, vol. 493, no. 2, pp. 357–370, 1996.
- [40] S. M. Baylor and S. Hollingworth, "Sarcoplasmic reticulum calcium release compared in slow-twitch and fast-twitch fibres of mouse muscle," *Journal of Physiology*, vol. 551, no. 1, pp. 125–138, 2003.
- [41] C. Franzini-Armstrong, F. Protasi, and V. Ramesh, "Shape, size, and distribution of Ca²⁺ release units and couplons in skeletal and cardiac muscles," *Biophysical Journal*, vol. 77, no. 3, pp. 1528–1539, 1999.
- [42] M. R. Celio and C. W. Heizmann, "Calcium-binding protein parvalbumin is associated with fast contracting muscle fibres," *Nature*, vol. 297, no. 5866, pp. 504–506, 1982.
- [43] G. S. Posterino and G. D. Lamb, "Effect of sarcoplasmic reticulum Ca²⁺ content on action potential-induced Ca²⁺ release in rat skeletal muscle fibres," *Journal of Physiology*, vol. 551, no. 1, pp. 219–237, 2003.
- [44] T. T. Hou, J. D. Johnson, and J. A. Rall, "Parvalbumin content and Ca²⁺ and Mg²⁺ dissociation rates correlated with changes in relaxation rate of frog muscle fibres," *Journal of Physiology*, vol. 441, pp. 285–304, 1991.

Research Article

Synergistic Effects between Phosphorylation of Phospholamban and Troponin I Promote Relaxation at Higher Heart Rate

Lin Zhang, Yuan Yu, Zhen Song, Yun-Ying Wang, and Zhi-Bin Yu

Department of Aerospace Physiology, Fourth Military Medical University, 169# Changlexi Road, Xi'an 710032, China

Correspondence should be addressed to Zhi-Bin Yu, yuzhib@fmmu.edu.cn

Received 13 February 2011; Accepted 17 June 2011

Academic Editor: Xupei Huang

Copyright © 2011 Lin Zhang et al. This is an open access article distributed under the Creative Commons Attribution License, which permits unrestricted use, distribution, and reproduction in any medium, provided the original work is properly cited.

We hypothesized that the extent of frequency-dependent acceleration of relaxation (FDAR) would be less than that of isoproterenol-(ISO-)dependent acceleration of relaxation (IDAR) at the same increment of heart rates, and ISO may improve FDAR. Cardiac function and phosphorylation of PLB and cTnI were compared in pacing, ISO treatment, and combined pacing and ISO treatment in isolated working heart. The increase in cardiac output and the degree of relaxation was less in pacing than in ISO treatment at the same increment of heart rates. The increasing stimulation frequency induced more significant relaxant effect in ISO perfusion than that in physiological salt perfusion. The pacing only phosphorylated PLB at Thr17, but ISO induced phosphorylation of cTnI and PLB at Ser16 and Thr17. Those results suggest that the synergistic effects of PLB and cTnI induce higher degree of relaxation which makes a sufficient diastolic filling of the ventricle at higher heart rate.

1. Introduction

Heart rate is a fundamental physiological modulator of cardiac function in all mammalian hearts. Regardless of whether the force-frequency relationship is positive or negative, an increase in heart rate is always associated with an acceleration of relaxation, named as frequency-dependent acceleration of relaxation (FDAR) [1]. This FDAR ensures the proper relaxation and diastolic filling of the ventricle at higher heart rates. Previous studies indicate that Ca^{2+} /Calmodulin-dependent kinase II (CaMKII) is a prime candidate in sensing and mediating frequency-dependent effects [2]. The CaMKII has at least four substrates involved in excitation-contraction coupling in the heart [3]. Published studies demonstrate that CaMKII can phosphorylate ryanodine receptor (RyR) [4], sarcoplasmic reticulum Ca^{2+} -ATPase (SERCA) [5], phospholamban (PLB) [6], and the L-type Ca^{2+} channels (LTCC) [7]. The phosphorylation of LTCC and RyR is related to modulation to systolic function. It has been reported that LTCC activation by CaMKII is involved in the development of early afterdepolarizations and arrhythmias in vitro and in vivo [8]. Huke and Bers found that FDAR did not rely

on phosphorylation of RyR [1]. Valverde et al. reported that SERCA phosphorylation by CaMKII was not involved in FDAR [9]. Thus, a very likely target of FDAR is PLB, an inhibitor of SERCA [10]. When PLB becomes phosphorylated at Thr-17 by CaMKII, the inhibition is relieved, and Ca^{2+} uptake of SR is accelerated [10]. However, increasing stimulation frequency still induces FDAR in PLB knock-out mouse hearts [11]. Therefore, the molecular mechanism of FDAR is still controversial.

Activation of the sympathetic nervous system leads to the secretion of catecholamines, which stimulate β -adrenergic receptors in the heart. Isoproterenol-(ISO-)dependent acceleration of relaxation (IDAR) is another important intrinsic regulator to cardiac function. Stimulation of β -adrenergic receptor (β -AR) by ISO activates Gs, which in turn activates adenylate cyclase and increases the formation of cAMP within cardiomyocytes. Elevated levels of cAMP increases the activation of protein kinase A (PKA) which phosphorylates intracellular targets such as LTCC, RyR, PLB, cardiac troponin I (cTnI), and myosin binding protein C (MyBPC). Phosphorylation of LTCCs enhances Ca^{2+} influx which increases shortening amplitude or force of contraction

[7]. Recently, MacDonnell et al. reported that adrenergic regulation of cardiac contractility did not involve phosphorylation of the cardiac RyR at serine-2808 residue [12]. Phosphorylation of MyBPC does not appear to have any effect on myofibrillar Ca^{2+} sensitivity which modulates relaxation but accelerated the kinetics of force development [13]. Phosphorylated MyBPC may link to myocardial protection in ischemia [14, 15]. The elevated intracellular Ca^{2+} concentration increases the activity of SERCA which indirectly accelerates relaxation of cardiomyocytes. The phosphorylated PLB at Ser-16 and Thr-17 by PKA also enhanced the activity of SERCA. The phosphorylation of cTnI reduced the Ca^{2+} sensitivity of myofibrils which facilitates Ca^{2+} dissociation from myofibrils [16]. Therefore, phosphorylation of PLB and cTnI may be two synergistic modulators to accelerate relaxation in ISO stimulation.

The increasing frequency of stimulation only phosphorylates one site of PLB, but not cTnI. Due to lack of the synergistic effect between PLB and cTnI, we hypothesized that the extent of FDAR would be less than that of IDAR at the same increment of heart rate, the less extent of FDAR may have a limitation on the sufficient diastolic filling of the ventricle with increasing frequency of stimulation, and ISO may improve FDAR. Therefore, the aim of the present study was to compare the cardiac function and extent of relaxation between FDAR and IDAR at the same increment of heart rate and further to observe the extent of FDAR during ISO stimulation.

2. Materials and Methods

2.1. Preparation of Isolated Working Heart. Sprague-Dawley rats weighing 220 ± 10 g were used. The animal procedure described here has been approved by the Animal Care and Use Committee at the Fourth Military Medical University.

The isolated crystalloid-perfused rat heart has previously been described [17]. Rats were heparinized (500 U i.p.) and anesthetized (sodium pentobarbital, 40 mg/kg i.p.). Hearts were excised, immediately mounted, and perfused on a Langendorff apparatus (Radnoti, USA) at a constant pressure of 60 mmHg with Krebs-Henseleit solution (in mM: 118 NaCl, 4.7 KCl, 2.25 MgSO_4 , 2.25 CaCl_2 , 23.8 NaCO_3 , 1.2 NaH_2PO_4 , 0.32 EDTA, and 11.5 D-glucose) in a nonrecirculating retrograde mode. The time from excision to perfusion was less than 60 seconds. The perfusate was oxygenated with a gas mixture of 95% O_2 -5% CO_2 , achieving pH of 7.39 to 7.41. Left atrium was cannulated through the pulmonary vein with steel cannula (inside diameter: 1.8 mm; outside diameter: 2.0 mm). In order to detect the intraventricular pressure, an ultraminiature pressure catheter transducer (model SPR-671; Millar Instruments, Houston, USA) was put into the left ventricle through the left atrium. The preload was set up at 10 mmHg. The heart was then switched from the Langendorff to a working mode. The aortic and coronary flow was recorded at the 1st, 5th, 10th, and 15th min at the working heart mode. Electrodes placed on the aortic cannula and the apex of the ventricle were connected to a square wave stimulator (Aurora Scientific Inc., Canada, 5 ms pulse duration, 20 V pulse amplitude). Hearts were paced at

300, 360, and 420 beats/min in the absence and the presence of isoproterenol (ISO, Sigma Chemical Co.). The hearts were superfused with 1.0, 10.0, and 20.0 nM of ISO for at least 5 min. The aortic flow, coronary flow, heart rate, left ventricular end-systolic (LVESP) and end-diastolic (LVEDP) pressure, and maximal rates of left ventricular pressure development ($+\text{dP}/\text{dt}_{\text{max}}$) and relaxation ($-\text{dP}/\text{dt}_{\text{max}}$) were measured to evaluate the contractile function of isolated working heart. Cardiac output is equal to aortic flow plus coronary flow. Data was acquired and analyzed using a PowerLab system and Chart software (ADInstruments Inc., Sydney, Australia).

2.2. Intracellular Ca^{2+} Measurement of the Single Cardiomyocyte. The ventricular myocyte isolation was the same as that described previously [18]. The cannulated hearts were mounted on a Langendorff perfusion apparatus and perfused with Ca^{2+} -free Joklik's modified minimum essential medium (Sigma-Aldrich, St. Louis, Mo, USA) containing 10 mM HEPES, 0.1% bovine serum albumin (BSA). After 5 min, the perfusate was switched to a circulating enzyme solution containing 0.08% collagenase I (Sigma-Aldrich) for 30 min. All the perfusion procedure was performed at 37°C in a constant flow, and the perfusion pressure was monitored. Then the ventricular tissues were chopped, and the cardiomyocytes were dispersed gently by a wide tipped pipette. The cell suspension was filtered through 200- μm nylon mesh. After 30 min, the cells were resuspended in Joklik's medium containing 1% BSA and slowly recovered Ca^{2+} concentration to 1.25 mM.

The intracellular Ca^{2+} concentration of cardiomyocytes was measured within 6 hours after isolation. Ventricular myocytes were loaded with fura-2 AM ($5 \mu\text{M}$) for 30 min in the dark at room temperature. Cells were then transferred into a 0.2 mL chamber which was on the stage of an inverted microscope (OlympusX71, Tokyo, Japan). Cells were superfused with Tyrode solution (in mM: 132 NaCl, 4.8 KCl, 1.2 MgCl_2 , 1.8 CaCl_2 , 5.0 sodium pyruvate, 10 HEPES, and 10 D-glucose, pH 7.40) at a flow rate of 0.2 mL/min at 37°C . Electric field stimulus (rectangle wave, 15 V, 5 ms, 1.0 Hz) was given by the stimulator. Then the stimulation frequency increased to 2 Hz, 5 Hz, and 10 Hz with or without ISO perfusion (1, 10, and 20 nM).

Intracellular Ca^{2+} concentration was measured by whole cell photometry (DeltaRam, Photon Technology International, USA). The emission ratio at 510 nm, during alternate excitation at 340 nm and 380 nm was used to determine intracellular Ca^{2+} concentration. Fluorescence emission was measured at 240 points/s for each of the excitation wavelengths. Background fluorescence values were determined at each excitation wavelength. These background values were subtracted from the recordings made at each wavelength during each experiment. Data were acquired and analyzed by Felix software (Version 1.4, Photon Technology International). Ca^{2+} transient amplitudes were the difference between systolic and diastolic Ca^{2+} .

2.3. Western Blotting. The expressions of cTnI, total and Ser-16-phosphorylated and Thr-17-phosphorylated PLB were

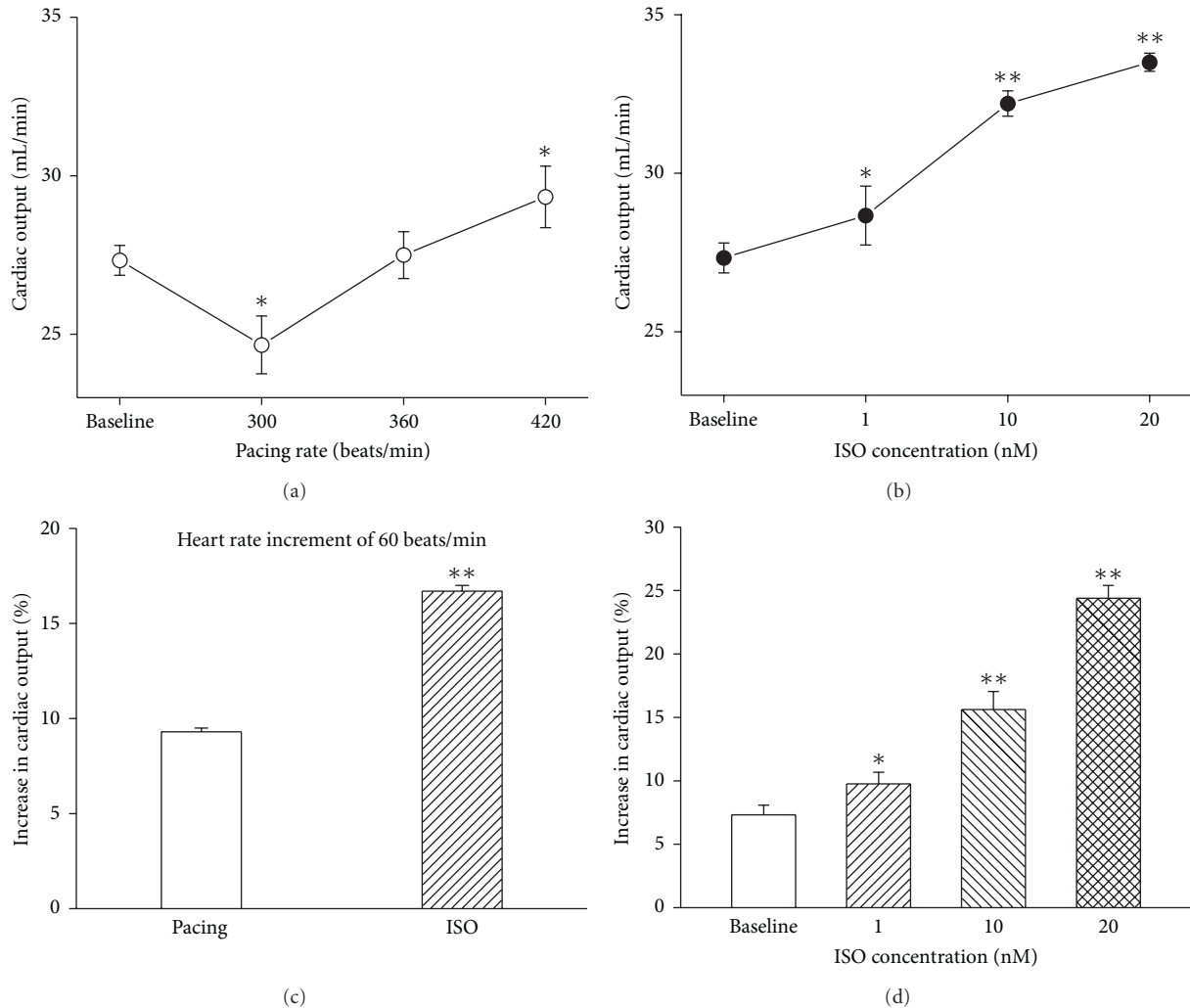


FIGURE 1: Cardiac output of isolated working hearts in the pacing and ISO treatment. All data are mean \pm SEM. (a) Cardiac output of isolated working hearts in different rates of pacing. The $n = 6$ hearts. * $P < 0.05$ versus baseline. (b) Cardiac output in different concentrations of ISO treatment. The $n = 6$ hearts in each ISO concentration. * $P < 0.05$ or ** $P < 0.01$ versus baseline. (c) The percentage increases in cardiac output in the heart rate increment of 60 beats/min. The $n = 6$ hearts for each group. * $P < 0.05$ versus the pacing group. (d) The percentage increases in cardiac output at the pacing of 420 beats/min without and with ISO treatment. The $n = 6$ hearts in each ISO concentration. * $P < 0.05$ or ** $P < 0.01$ versus baseline.

detected by Western blotting. Left ventricular myocardium was homogenized in a buffer containing 50 mM potassium phosphate buffer (pH 7.0), 0.5 mM DTT, 1 mM EDTA, 0.3 mM PMSF, and phosphatase inhibitor cocktail (1:100, Sigma-Aldrich). Samples were subjected to SDS-PAGE in polyacrylamide gels (12% or 14% depending on protein molecular weight). After electrophoresis, protein was electrically transferred to nitrocellulose membrane (0.45 μ m pore size) using a Bio-Rad semidry transfer apparatus. The blotted nitrocellulose membranes were blocked with 1% bovine serum albumin in Tris-buffered saline (150 mM NaCl, 50 mM Tris-HCl, and pH 7.5) and incubated with mouse monoclonal anti-TnI (TnI-1, 1:4,000; Courtesy of Dr. J.-P. Jin), mouse monoclonal anti-PLB (1:1000; Cell Signaling Technology, Inc. (CST), Danvers, Mass, USA), rabbit polyclonal anti-Ser-16-phosphorylated phospholamban

(Phospho16-PLB, 1:1000; CST) and rabbit polyclonal anti-Thr-17-phosphorylated phospholamban (Phospho17-PLB, 1:1000; Santa Cruz Biotechnology, Inc., Santa Cruz, Calif, USA) in TBS containing 0.1% BSA at 4°C overnight. The membranes were visualized with IRDye 680CW goat anti-mouse or IRDye 800CW goat antirabbit secondary antibodies (1:10,000, for 90 min at room temperature) using an Odyssey scanner (LI-COR Biosciences, Lincoln, Neb, USA). Quantification analysis of blots was performed with the Scion Image software.

2.4. Statistical Analysis. Data are expressed as mean \pm SEM. Differences between groups were evaluated using one-way analysis of variance (ANOVA). When ANOVA indicated significance, a *Dunnett post-hoc* test was performed. $P < 0.05$ was considered statistically significant.

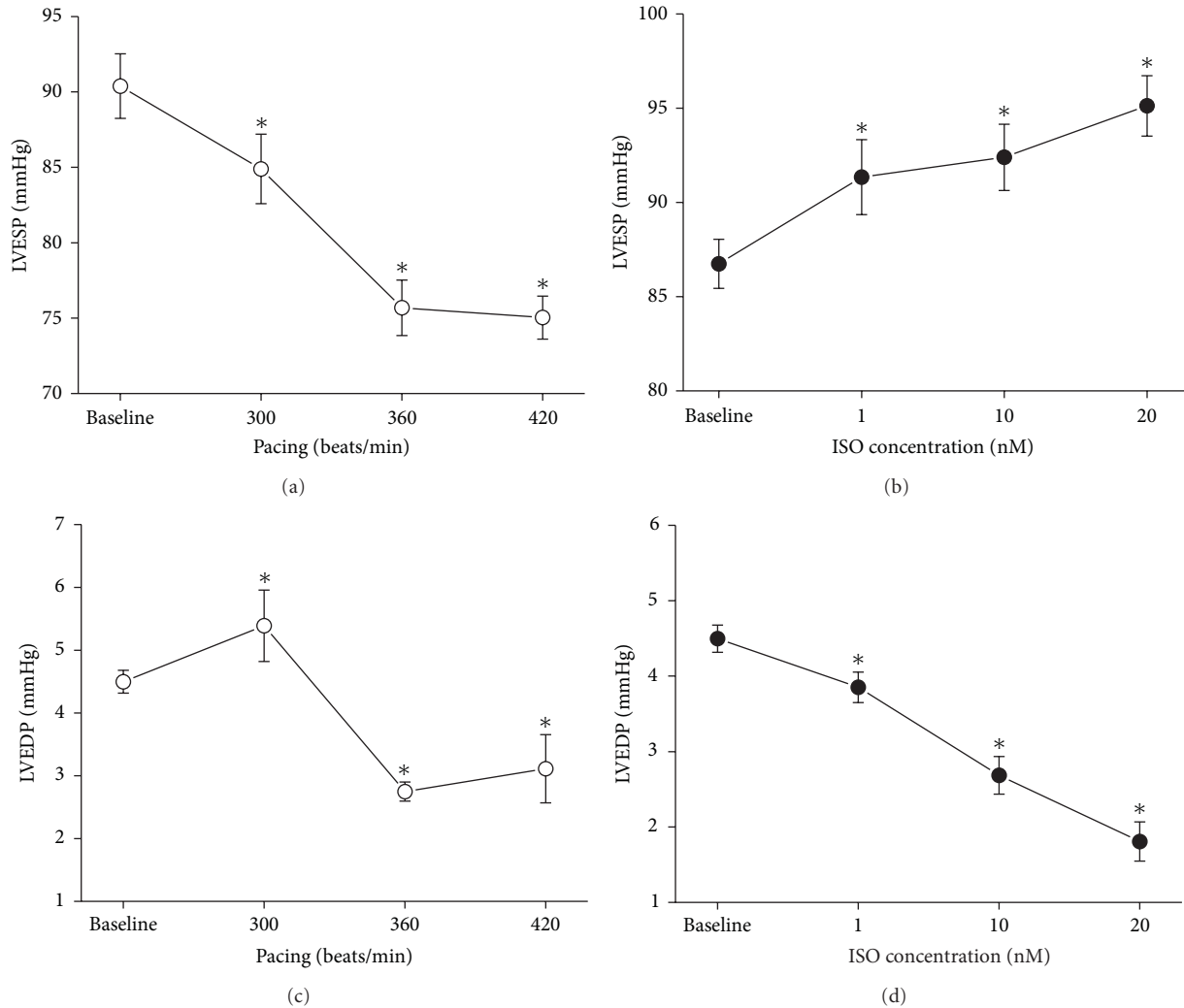


FIGURE 2: Left ventricular end-systolic pressure (LVESP) and end-diastolic pressure (LVEDP) of working hearts in the pacing and ISO treatment. (a) and (c) LVESP and LVEDP during the pacing. (b) and (d) LVESP and LVEDP in ISO treatment. Data are mean \pm SEM, $n = 6$ hearts for each ISO concentration in each group. * $P < 0.05$ versus baseline.

3. Results

3.1. Systolic and Diastolic Function of Isolated Working Hearts during the Pacing and ISO Treatment. At the preload of 10 mmHg and afterload of 60 mmHg, the intrinsic heart rate of working heart was 236.4 ± 6.4 beats/min in the baseline group. Heart rates increased to 259.9 ± 7.3 , 288.1 ± 4.1 , and 316.7 ± 6.3 beat/min in 1, 10, and 20 nM ISO stimulation, respectively. At baseline, cardiac output was 27.3 ± 0.5 mL/min. Cardiac output decreased to 24.7 ± 0.9 mL/min at the pacing of 300 beats/min, then increased to 27.5 ± 0.7 mL/min and 29.3 ± 0.9 mL/min at the pacing of 360 and 420 beats/min (Figure 1(a)). Cardiac output increased to 28.7 ± 0.9 , 32.2 ± 0.4 , and 33.5 ± 0.3 mL/min in 1, 10, and 20 nM ISO treatment, respectively, (Figure 1(b)). While the increment of heart rate was similar at 60 beats/min, the percentage increase in cardiac output was higher in ISO-treated group than in the pacing group (Figure 1(c)). Cardiac output had about 7%, 10%, 15%, and 24% increases,

respectively, at the pacing of 420 beats/min without and with 1, 10, and 20 nM ISO treatment compared to the baseline at the intrinsic heart rate (Figure 1(d)).

LVESP decreased with the increasing pacing rate (Figure 2(a)). In the opposite, LVESP increased with the increasing concentrations of ISO at the intrinsic heart rate (Figure 2(b)). LVEDP showed a significant increase at 300 beats/min but decreased progressively at 360 and 420 beats/min (Figure 2(c)). LVEDP decreased progressively with the increasing concentrations of ISO at the intrinsic heart rate (Figure 2(d)).

The $\pm dP/dt_{\max}$ decreased significantly at the pacing of 300 beats/min and increased at the pacing of 360 and 420 beats/min (Figure 3(a)). In contrast, $\pm dP/dt_{\max}$ elevated progressively with the increasing concentrations of ISO (Figure 3(b)). TR_{75} , time from peak to 75% relaxation of left ventricular pressure, is another index of cardiac diastolic function. Both the pacing and ISO stimulation reduced TR_{75} (Figures 3(c) and 3(d)).

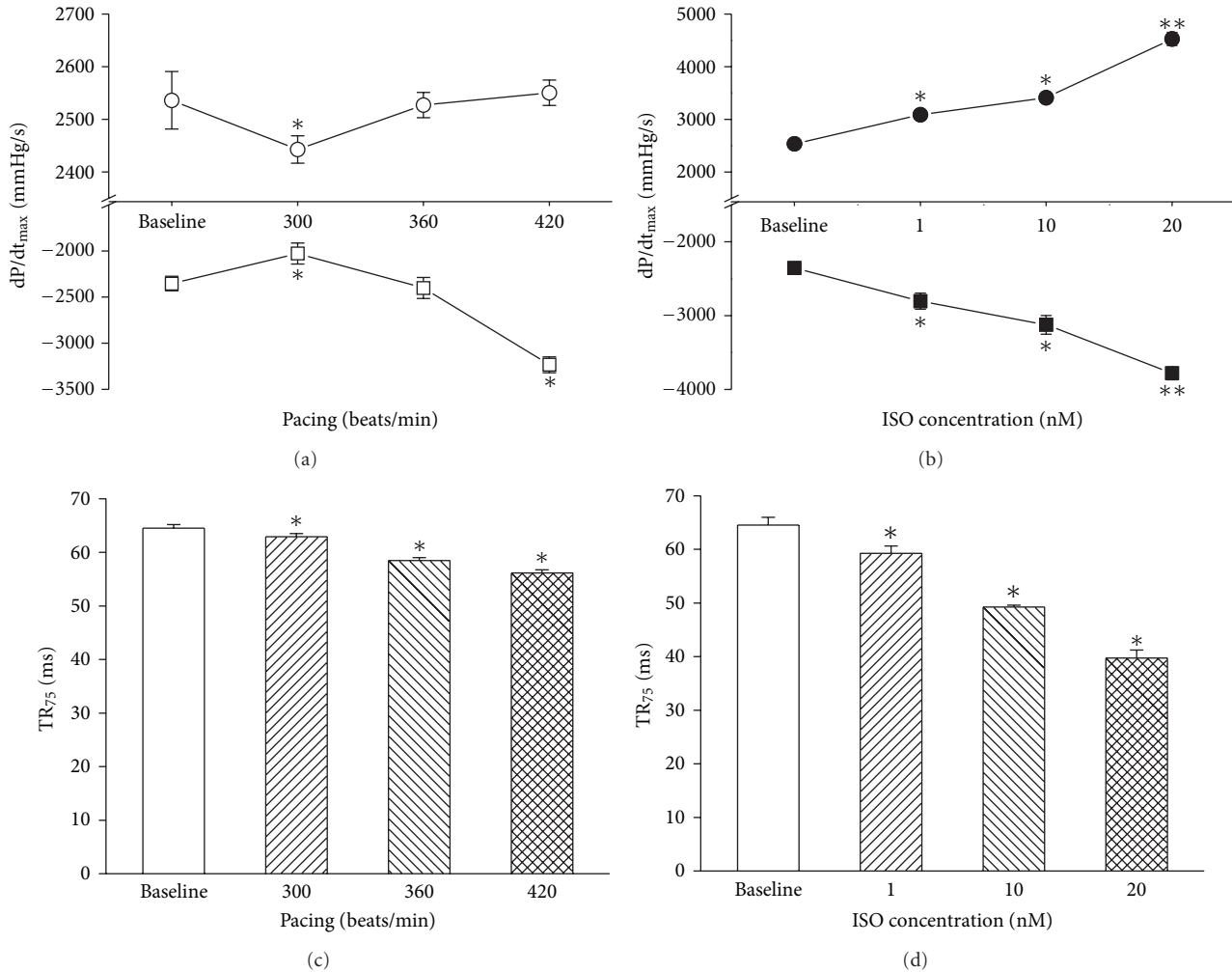


FIGURE 3: Maximal rates of left ventricular pressure development and relaxation ($\pm dP/dt_{max}$) and time from peak to 75% relaxation (TR_{75}) of left ventricular pressure. (a) and (c) $\pm dP/dt_{max}$ and TR_{75} under different rates of pacing. (b) and (d) $\pm dP/dt_{max}$ and TR_{75} in different concentrations of ISO treatment. Data are mean \pm SEM, $n = 6$ hearts for each ISO concentration in each group. * $P < 0.05$ or ** $P < 0.01$ versus baseline.

The percentage increases in $\pm dP/dt_{max}$ between the pacing of 420 beats/min and intrinsic heart rate groups without ISO stimulation were $7.1 \pm 1.0\%$ and $9.7 \pm 1.1\%$, respectively, (the baseline values in Figure 4(a)). Under ISO stimulation, the pacing of 420 beats/min induced an additional enhancement. The percentage increases in $\pm dP/dt_{max}$ between the pacing of 420 beats/min and intrinsic heart rate groups increased progressively with the increasing concentrations of ISO (Figure 4(a)). The pacing of 420 beats/min led about 13% shortening in TR_{75} without ISO stimulation. Under ISO treatment, the pacing of 420 beats/min showed stronger relaxant effects than that of the baseline group (Figure 4(b)).

3.2. Intracellular Ca^{2+} Concentrations of the Cardiomyocyte in the Pacing and ISO Treatment. The resting intracellular calcium concentration ($[Ca^{2+}]_i$) increased with the increasing frequency of stimulation; higher frequency of stimulation (i.e., >5 Hz) induced a significant elevation in resting $[Ca^{2+}]_i$

of cardiomyocytes (Figure 5(a)). The peak $[Ca^{2+}]_i$ increased to a maximal level at 5 Hz, then decreased slightly at 10 Hz. In contrast, the resting $[Ca^{2+}]_i$ decreased slightly, but the peak $[Ca^{2+}]_i$ kept elevating with the increasing concentrations of ISO (Figure 5(b)). Under ISO perfusion, the increasing degrees of resting $[Ca^{2+}]_i$ were less compared with non ISO-treated group while the frequency of stimulation increased from 300 to 420 beats/min (Figure 5(a)). The peak $[Ca^{2+}]_i$ still elevated with the increasing frequency of stimulation during different concentrations of ISO treatment. The peak $[Ca^{2+}]_i$ reached the maximal level at 10 Hz under 20 nM ISO treatment (Figure 5(a)).

TD_{75} , the time from peak to 75% decay in calcium transient, reduced both under increasing frequency of stimulation and ISO perfusion. The degrees of reduction in TD_{75} were lower in stimulation group than in ISO-treated group (Figures 5(c) and 5(d)).

3.3. The Phosphorylation of cTnI at Ser23/24 and PLB at Ser16 and Thr17 in the Pacing and ISO Treatment. Figure 6(a)

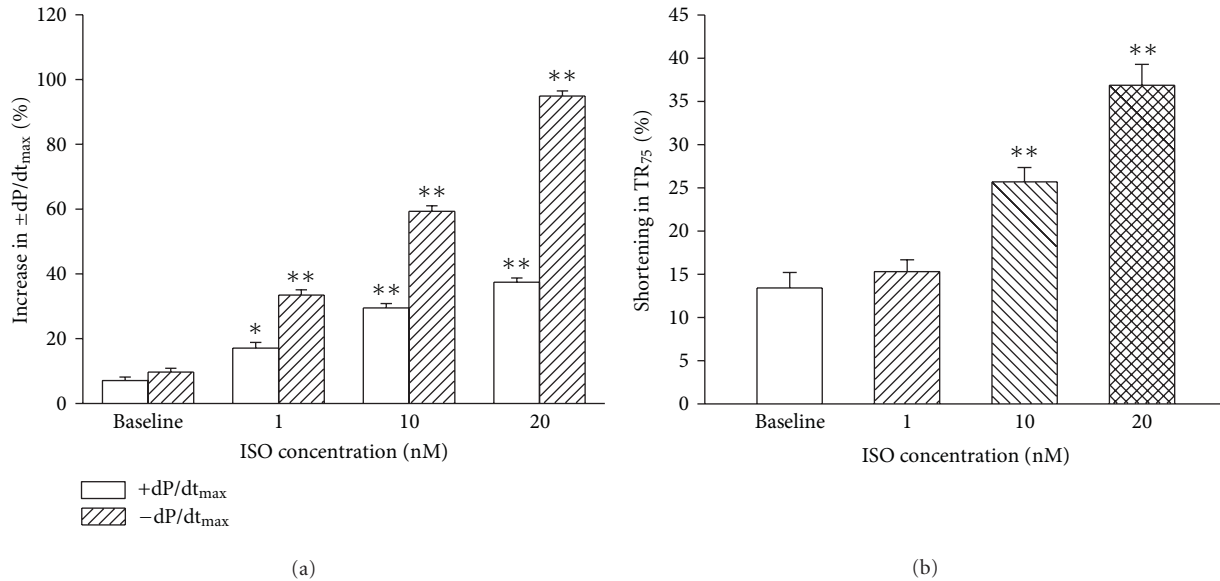


FIGURE 4: Percentage increases in $\pm dP/dt_{max}$ and TR_{75} under combined effect of the pacing and ISO. (a) The percentage increases in $\pm dP/dt_{max}$ between the pacing of 420 beats/min and intrinsic heart rate without and with ISO treatment. (b) The percentage shortenings in TR_{75} between the pacing of 420 beats/min and intrinsic heart rate without and with ISO treatment. Data are mean \pm SEM, $n = 6$ hearts for each ISO concentration in each group. * $P < 0.05$ or ** $P < 0.01$ versus baseline.

shows the representative Western blots of cTnI and phosphorylated cTnI at Ser23/24. There were no differences in expression of cTnI in the pacing, ISO treatment, and pacing plus ISO treatment groups (Figure 6(b)). Phosphorylation of cTnI at Ser23/24 showed a dose-dependent increase in ISO perfusion. But the pacing had no effect on phosphorylation of cTnI at Ser23/24 in basic and ISO-treated condition (Figure 6(c)).

Figure 7(a) shows the representative Western blots of PLB, phosphorylated PLB at Ser16, and Thr17 in isolated working hearts under the pacing and different concentrations of ISO perfusion. Total PLB, which is the sum of pentameric and monomeric PLB, did not change under the pacing and ISO perfusion (Figure 7(b)). The phosphorylation of PLB at Ser16 and Thr17 also showed a dose-dependent increase in ISO stimulation. The degrees of phosphorylated PLB at Ser16 elevated from $39.3 \pm 1.4\%$ in baseline to $50.2 \pm 1.7\%$ in 20 nM ISO treatment, and the degrees of phosphorylated PLB at Thr17 increased from $13.9 \pm 0.6\%$ in baseline to $22.5 \pm 0.6\%$ in 20 nM ISO treatments (Figures 7(c) and 7(d)). The phosphorylation of PLB at Thr17 increased with the increasing pacing rate, but the pacing did not alter the phosphorylation of PLB at Ser16. During 10 nM and 20 nM ISO perfusion, the pacing induced an additional increase in the phosphorylation of PLB at Ser16 in a frequency-dependent manner (Figure 7(d)).

4. Discussion

4.1. Coordinated Activation of Ca^{2+} Handing Proteins in Excitation-Contraction Coupling Is Important to Considerably Accelerate Relaxation in ISO Stimulation. In the present study, the increase in maximal rate of relaxation and the

shortening in TR_{75} were lower in the pacing than in ISO stimulation (Figure 4(a)). It indicates that the extent of FDAR is less than that of IDAR. FDAR is an important intrinsic regulator to cardiac function in physiological condition. However, the mechanism of FDAR is still controversial. Some studies reported that FDAR may be related to the activation of CaMKII, phosphorylation of PLB, and the increase of SERCA activity. There are evidences to indicate that inhibition of CaMKII by KN-93 [9], CaMKII and PLB knock-out [11, 19], or inhibition of SERCA also shows an acceleration of relaxation in the increasing stimulation frequency [11]. We observed that the pacing only increased the phosphorylation of PLB at Thr-17 site (Figure 7). The increase in Thr-17 phosphorylation of PLB was associated with FDAR, but the relaxation effect was weak. The Thr-17 phosphorylation of PLB can relieve the inhibition to SERCA. Since the activation of SERCA by Thr-17 phosphorylation of PLB is low, the resting intracellular Ca^{2+} concentration slightly elevated with an increasing stimulation frequency (Figure 5(a)). In contrast, ISO treatment showed not only the phosphorylation of PLB at Ser-16 and Thr-17 sites, but also the cTnI phosphorylation (Figure 7(a)). Several researches have indicated that PLB phosphorylation by ISO stimulation is a dominant mediator to the acceleration of relaxation in PLB knock-out mouse [20]. But it should not be ignored that the effect of cTnI phosphorylation was induced by ISO treatment on the acceleration of relaxation.

Early investigations indicate that phosphorylation of cTnI may not be important in the relaxant effect of ISO stimulation. Johns et al. found no effect of cTnI phosphorylation by PKA on the relaxation in skinned guinea pig ventricular trabeculae [21], and the precise experimental conditions may be important in this regard. Recently, many studies

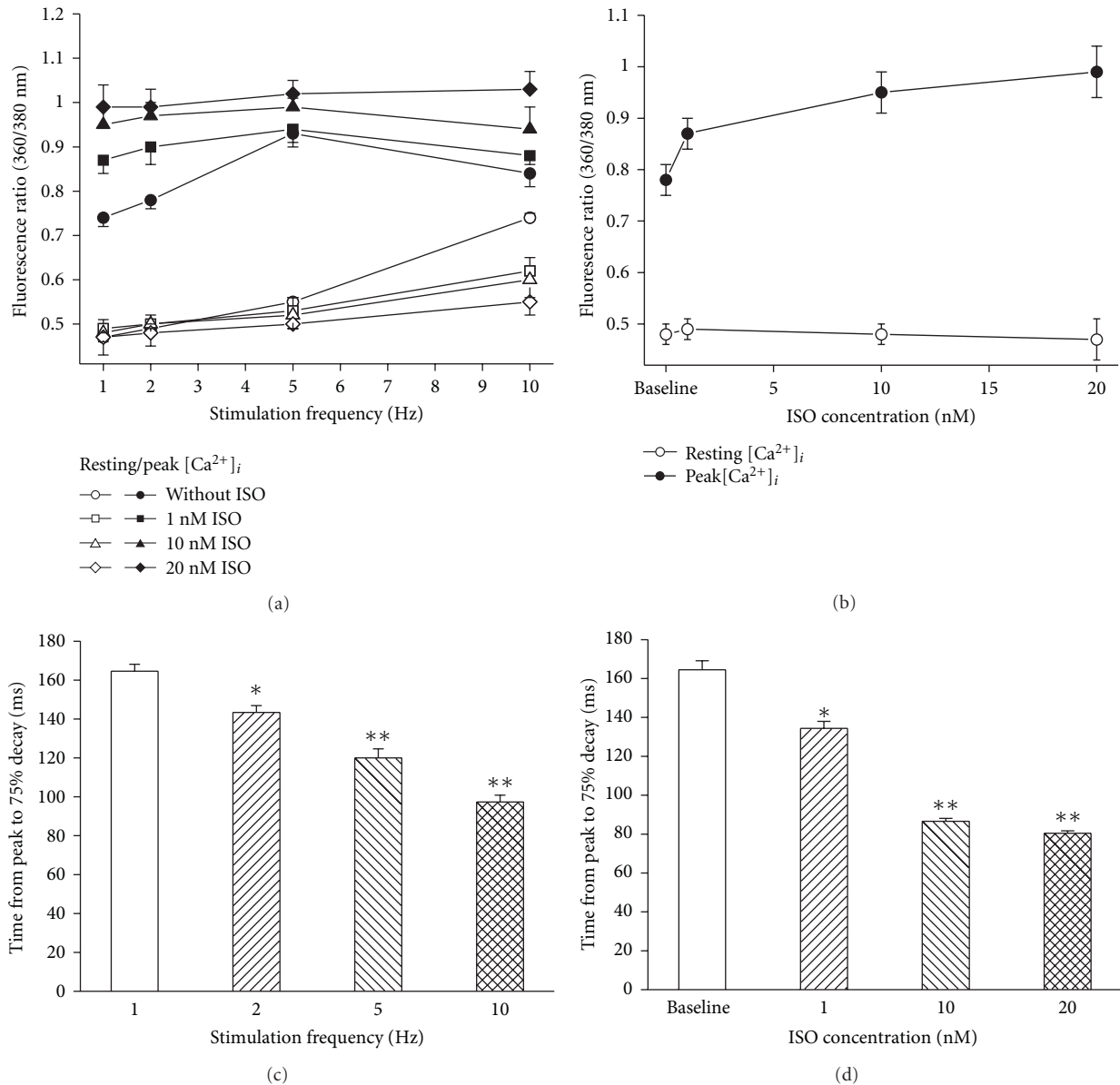


FIGURE 5: Resting and peak calcium concentrations in cardiomyocytes and time from peak to 75% decay (TD_{75}) under different frequencies of stimulations with and without ISO treatment. Data are mean \pm SEM, $n =$ at least 30 myocytes from six hearts for each concentration in each group. At least 5 myocytes were from each heart. * $P < 0.05$ or ** $P < 0.01$ versus baseline.

indicate that phosphorylation of cTnI by PKA may be particularly important in modulating diastolic function of hearts. Fentzke et al. constructed transgenic mice (TG-ssTnI); the myocardium expressed slow skeletal TnI (ssTnI) which lacks N-terminal extension containing two PKA phosphorylation sites. They reported that in situ relaxation of left ventricular pressure was significantly slowed in TG-ssTnI hearts compared with the wild-type mice [22]. Kentish et al. also studied transgenic mice with ssTnI replacing cTnI and used flash photolysis of diazo-2 to rapidly remove Ca^{2+} from skinned cardiac muscle fibers. Myocardium expressing ssTnI had no acceleration of relaxation in β -adrenergic stimulation, suggesting that cTnI phosphorylation played an important role in intrinsic relaxation [23]. Li et al. reported the first

quantitative estimates of the relative contributions of PLB and TnI phosphorylation to the ISO induced acceleration of relaxation in mouse hearts. The TnI phosphorylation may contribute up to 14–18% of the acceleration of relaxation in response to ISO during isometric contractions in mouse myocardium [20]. Wolska et al. observed four lines of mice expressed PLB/cTnI, PLB/ssTnI, PLBKO (PLB knock-out)/cTnI, and PLBKO/ssTnI in the heart, respectively. They demonstrated that expression of ssTnI in hearts of PLB knock-out mice altered the relaxant effect of β -adrenergic stimulation [24]. The underlying mechanisms of phosphorylation of cTnI by PKA regulating relaxation of hearts may be involved in myofibril Ca^{2+} sensitivity [16], an increase in crossbridge cycling [23], and increased binding of cTnI

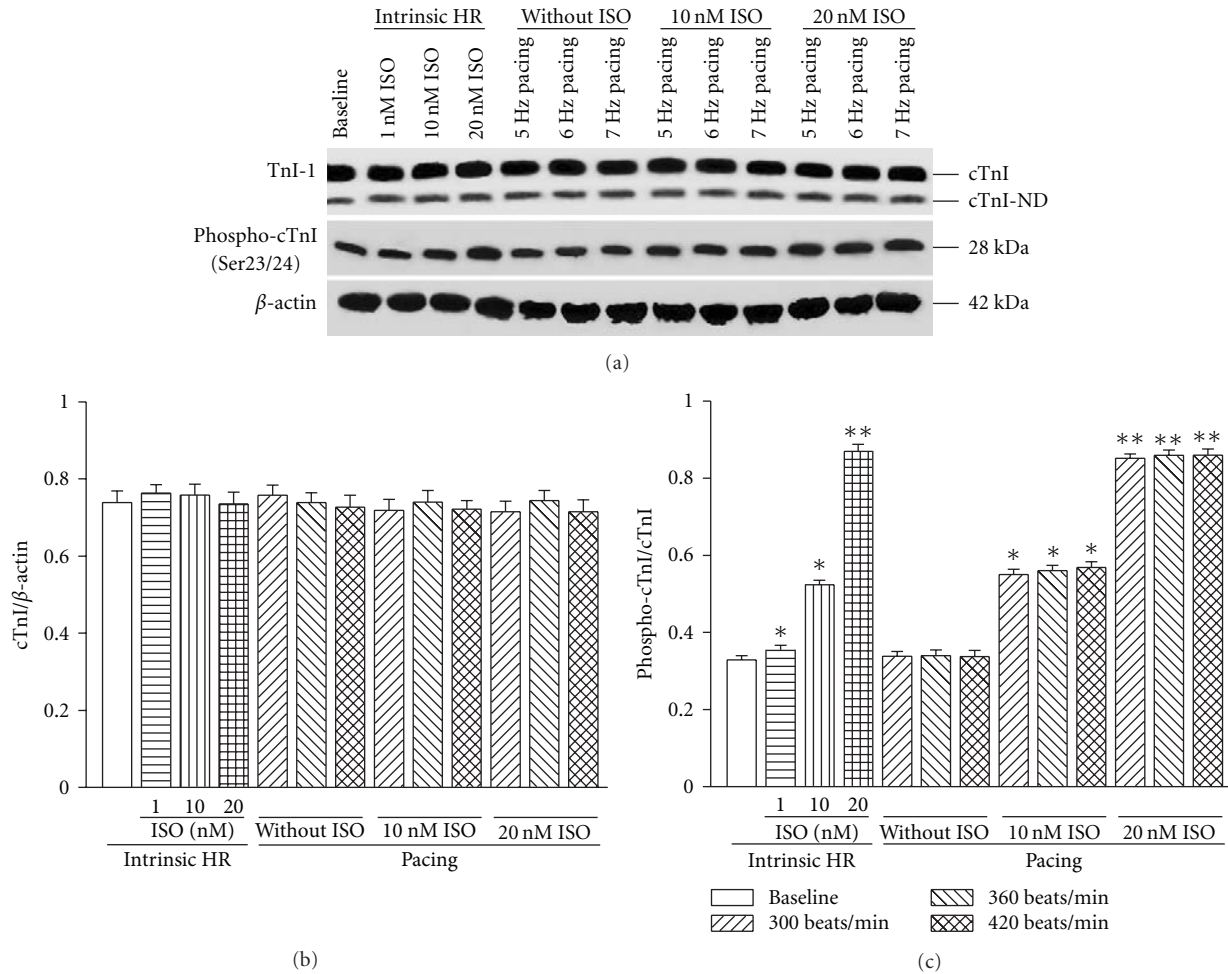


FIGURE 6: Expressions of cTnI and phosphorylated cTnI at Ser23/24 in the myocardium after the pacing and ISO treatment. (a) The representative Western blots of cTnI and phosphorylated cTnI at Ser23/24. (b) Expression of total cTnI which is the sum of cTnI and NH₂-terminal deleted fragment of cTnI (cTnI-ND). (c) The phosphorylation of cTnI. Data are mean \pm SEM, $n = 6$ hearts in each group. * $P < 0.05$ or ** $P < 0.01$ versus baseline.

to the thin filament. The phosphorylation of cTnI reduces Ca²⁺ sensitivity of myofibrils which accelerates the rate of Ca²⁺ dissociation from cardiac troponin C. Taken together, phosphorylation of PLB and cTnI induces a synergistic effect to accelerate relaxation in ISO administration. Therefore, IDAR is stronger than FDAR. The less extent of FDAR elevates LVEDP which induces an insufficient diastolic filling at higher heart rate and further may reduce cardiac output.

4.2. The Phosphorylation of cTnI Causes a Synergistic Effect between PLB and cTnI and Further Enhances the Relaxation in Increasing Frequency of Stimulation. Although PKA phosphorylates many sites in the cardiomyocyte, only phosphorylated PLB and cTnI are directly related to the acceleration of relaxation in ISO stimulation. Due to the synergistic effect of PLB and cTnI, the degree of relaxation in IDAR is higher than that in FDAR. In this study, the degrees of relaxation in increasing rate of pacing showed the additional increases during ISO perfusion. Varian and Janssen reported that FDAR involved decreased myofilament calcium sensitivity

[25]. Phosphorylation of cTnI can reduce myofilament calcium sensitivity. It suggests that phosphorylation of cTnI would be helpful to FDAR. Takimoto et al. generated transgenic mice that overexpress cTnI in which the serine residues normally targeted by PKA were mutated to aspartic acid to mimic constitutive phosphorylation (cTnI-P₂₂P₂₃). The cTnI-P₂₂P₂₃ hearts showed a frequency-dependent enhancement of systolic and diastolic in vivo and afterload sensitivity of relaxation [26]. Using similar transgenic mice, Sakthivel et al. also demonstrated that the cTnI-P₂₂P₂₃ hearts showed augmented relaxation and contraction at higher heart rates compared with the nontransgenic controls [16].

The 10 nM of ISO induced about 50% phosphorylation of cTnI, 45% phosphorylation of PLB at Ser-16 site, and 14% phosphorylation of PLB at Thr-17 site in the present study. These results are in agreement with the experiments of Kuschel and colleagues [27]. The phosphorylation of cTnI by ISO stimulation showed an enhancement in the extent of FDAR compared with that in the absence of ISO. While 90% of the cTnI was phosphorylated in

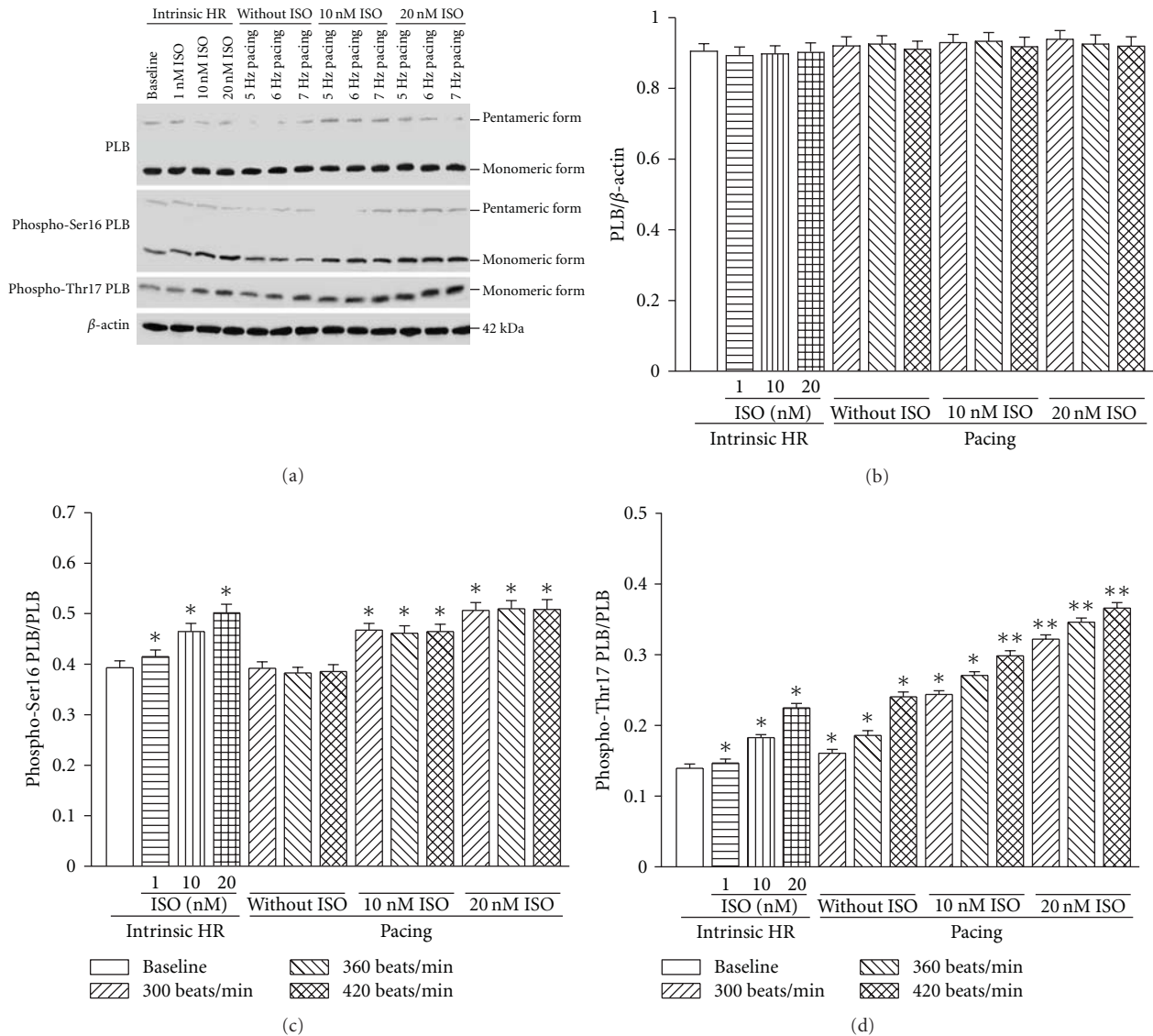


FIGURE 7: Expression of PLB, phosphorylated PLB at Ser16 (phospho Ser16-PLB) and at Thr17 (phospho Thr17-PLB) in the myocardium after the pacing and ISO treatment. (a) The representative Western blots of PLB, phosphorylated PLB at Ser16 and Thr17. (b) Expression of total PLB measured by pentameric plus monomeric forms. (c) Expression of phospho Ser16-PLB. (d), expression of phospho Thr17-PLB. Data are mean \pm SEM, $n = 6$ hearts in each group. * $P < 0.05$ or ** $P < 0.01$ versus baseline.

20 nM of ISO treatment, the PLB Ser-16 and Thr-17 had 50% and 22% phosphorylation, respectively. The extent of FDAR in the presence of 20 nM ISO further increased. The additional enhancement in phosphorylation of PLB Thr-17 may form a synergistic effect with phosphorylation of cTnI by PKA with increasing stimulation frequency, and hence, the extent of FDAR increased. Finally, cardiac output increased in the presence of ISO rather than decreased in the absence of ISO.

In summary, this study provides evidence supporting an important role for cardiac TnI phosphorylation by PKA in the enhancement of diastolic function. And the synergistic effects between the PLB and cTnI are necessary in promoting relaxation, especially at higher heart rate.

Conflicts of Interests

The authors declare that there is no conflict of interests.

Acknowledgments

This work was supported by the National Natural Science Foundation of China Grant no. 31071044 in part to Z.-B. Yu. L. Zhang and Y. Yu contributed equally to this study.

References

[1] S. Huke and D. M. Bers, "Temporal dissociation of frequency-dependent acceleration of relaxation and protein phosphorylation by CaMKII," *Journal of Molecular and Cellular Cardiology*, vol. 42, no. 3, pp. 590–599, 2007.

- [2] P. de Koninck and H. Schulman, "Sensitivity of CaM kinase II to the frequency of Ca^{2+} oscillations," *Science*, vol. 279, no. 5348, pp. 227–230, 1998.
- [3] T. Zhang, S. Miyamoto, and J. H. Brown, "Cardiomyocyte calcium and calcium/calmodulin-dependent protein kinase II: friends or foes?" *Recent Progress in Hormone Research*, vol. 59, pp. 141–168, 2004.
- [4] D. R. Witcher, R. J. Kovacs, H. Schulman, D. C. Cefali, and L. R. Jones, "Unique phosphorylation site on the cardiac ryanodine receptor regulates calcium channel activity," *Journal of Biological Chemistry*, vol. 266, no. 17, pp. 11144–11152, 1991.
- [5] A. Xu, C. Hawkins, and N. Narayanan, "Phosphorylation and activation of the $\text{Ca}(2+)$ -pumping ATPase of cardiac sarcoplasmic reticulum by Ca^{2+} /calmodulin-dependent protein kinase," *Journal of Biological Chemistry*, vol. 268, no. 12, pp. 8394–8397, 1993.
- [6] H. K. Simmerman, J. H. Collins, and J. L. Theibert, "Sequence analysis of phospholamban. Identification of phosphorylation sites and two major structural domains," *Journal of Biological Chemistry*, vol. 261, no. 28, pp. 13333–13341, 1986.
- [7] I. Dzihura, Y. Wu, R. J. Colbran, J. R. Balsler, and M. E. Anderson, "Calmodulin kinase determines calcium-dependent facilitation of L-type calcium channels," *Nature Cell Biology*, vol. 2, no. 3, pp. 173–177, 2000.
- [8] Y. Wu, J. Temple, R. Zhang et al., "Calmodulin kinase II and arrhythmias in a mouse model of cardiac hypertrophy," *Circulation*, vol. 106, no. 10, pp. 1288–1293, 2002.
- [9] C. A. Valverde, C. Mundina-Weilenmann, M. Said et al., "Frequency-dependent acceleration of relaxation in mammalian heart: a property not relying on phospholamban and SERCA2a phosphorylation," *Journal of Physiology*, vol. 562, no. 3, pp. 801–813, 2005.
- [10] D. Catalucci, M. V. Latronico, M. Ceci et al., "Akt increases sarcoplasmic reticulum Ca^{2+} cycling by direct phosphorylation of phospholamban at Thr17," *Journal of Biological Chemistry*, vol. 284, no. 41, pp. 28180–28187, 2009.
- [11] A. A. Werdich, E. A. Lima, I. Dzihura et al., "Differential effects of phospholamban and Ca^{2+} /calmodulin-dependent kinase II on $[\text{Ca}^{2+}]_i$ transients in cardiac myocytes at physiological stimulation frequencies," *American Journal of Physiology*, vol. 294, no. 5, pp. H2352–H2362, 2008.
- [12] S. M. MacDonnell, G. Garcia-Rivas, J. A. Scherman et al., "Adrenergic regulation of cardiac contractility does not involve phosphorylation of the cardiac ryanodine receptor at serine 2808," *Circulation Research*, vol. 102, no. 8, pp. E65–E72, 2008.
- [13] J. E. Stelzer, J. R. Patel, J. W. Walker, and R. L. Moss, "Differential roles of cardiac myosin-binding protein C and cardiac troponin I in the myofibrillar force responses to protein kinase A phosphorylation," *Circulation Research*, vol. 101, no. 5, pp. 503–511, 2007.
- [14] S. Sadayappan, J. Gulick, R. Klevitsky et al., "Cardiac myosin binding protein-C phosphorylation in a β -myosin heavy chain background," *Circulation*, vol. 119, no. 9, pp. 1253–1262, 2009.
- [15] S. Sadayappan, H. Osinska, R. Klevitsky et al., "Cardiac myosin binding protein c phosphorylation is cardioprotective," *Proceedings of the National Academy of Sciences of the United States of America*, vol. 103, no. 45, pp. 16918–16923, 2006.
- [16] S. Sakthivel, N. L. Finley, P. R. Rosevear et al., "In vivo and in vitro analysis of cardiac troponin I phosphorylation," *Journal of Biological Chemistry*, vol. 280, no. 1, pp. 703–714, 2005.
- [17] J. C. Barbato, Q. Q. Huang, M. M. Hossain, M. Bond, and J. P. Jin, "Proteolytic N-terminal truncation of cardiac troponin I enhances ventricular diastolic function," *Journal of Biological Chemistry*, vol. 280, no. 8, pp. 6602–6609, 2005.
- [18] Y. Y. Wang, B. Jiao, W. G. Guo, H. L. Che, and Z. B. Yu, "Excessive thyroxine enhances susceptibility to apoptosis and decreases contractility of cardiomyocytes," *Molecular and Cellular Endocrinology*, vol. 320, no. 1-2, pp. 67–75, 2010.
- [19] J. Desantiago, L. S. Maier, and D. M. Bers, "Frequency-dependent acceleration of relaxation in the heart depends on CamKII, but not phospholamban," *Journal of Molecular and Cellular Cardiology*, vol. 34, no. 8, pp. 975–984, 2002.
- [20] L. Li, J. Desantiago, G. Chu, E. G. Kranias, and D. M. Bers, "Phosphorylation of phospholamban and troponin I in β -adrenergic-induced acceleration of cardiac relaxation," *American Journal of Physiology*, vol. 278, no. 3, pp. H769–H779, 2000.
- [21] E. C. Johns, S. J. Simnett, I. P. Mulligan, and C. C. Ashley, "Troponin I phosphorylation does not increase the rate of relaxation following laser flash photolysis of diazo-2 in guinea-pig skinned trabeculae," *Pflugers Archiv*, vol. 433, no. 6, pp. 842–844, 1997.
- [22] R. C. Fentzke, S. H. Buck, J. R. Patel et al., "Impaired cardiomyocyte relaxation and diastolic function in transgenic mice expressing slow skeletal troponin I in the heart," *Journal of Physiology*, vol. 517, no. 1, pp. 143–157, 1999.
- [23] J. C. Kentish, D. T. McCloskey, J. Layland et al., "Phosphorylation of troponin I by protein kinase A accelerates relaxation and crossbridge cycle kinetics in mouse ventricular muscle," *Circulation Research*, vol. 88, no. 10, pp. 1059–1065, 2001.
- [24] B. M. Wolska, G. M. Arteaga, J. R. Pena et al., "Expression of slow skeletal troponin I in hearts of phospholamban knockout mice alters the relaxant effect of β -adrenergic stimulation," *Circulation Research*, vol. 90, no. 8, pp. 882–888, 2002.
- [25] K. D. Varian and P. M. L. Janssen, "Frequency-dependent acceleration of relaxation involves decreased myofilament calcium sensitivity," *American Journal of Physiology*, vol. 292, no. 5, pp. H2212–H2219, 2007.
- [26] E. Takimoto, D. G. Soergel, P. M. L. Janssen, L. B. Stull, D. A. Kass, and A. M. Murphy, "Frequency- and afterload-dependent cardiac modulation in vivo by troponin I with constitutively active protein kinase a phosphorylation sites," *Circulation Research*, vol. 94, no. 4, pp. 496–504, 2004.
- [27] M. Kuschel, P. Karczewski, P. Hempel, W. -P. Schlegel, E. -G. Krause, and S. Bartel, "Ser16 prevails over Thr17 phospholamban phosphorylation in the β -adrenergic regulation of cardiac relaxation," *American Journal of Physiology*, vol. 276, no. 5, pp. H1625–H1633, 1999.

Methodology Report

Adherent Primary Cultures of Mouse Intercostal Muscle Fibers for Isolated Fiber Studies

Patrick Robison, Erick O. Hernández-Ochoa, and Martin F. Schneider

Department of Biochemistry and Molecular Biology, University of Maryland School of Medicine, 108 N. Greene Street, Baltimore, MD 21201, USA

Correspondence should be addressed to Erick O. Hernández-Ochoa, ehern001@umaryland.edu

Received 26 April 2011; Accepted 24 May 2011

Academic Editor: Robert J. Bloch

Copyright © 2011 Patrick Robison et al. This is an open access article distributed under the Creative Commons Attribution License, which permits unrestricted use, distribution, and reproduction in any medium, provided the original work is properly cited.

Primary culture models of single adult skeletal muscle fibers dissociated from locomotor muscles adhered to glass coverslips are routine and allow monitoring of functional processes in living cultured fibers. To date, such isolated fiber cultures have not been established for respiratory muscles, despite the fact that dysfunction of core respiratory muscles leading to respiratory arrest is the most common cause of death in many muscular diseases. Here we present the first description of an adherent culture system for single adult intercostal muscle fibers from the adult mouse. This system allows for monitoring functional properties of these living muscle fibers in culture with or without electrical field stimulation to drive muscle fiber contraction at physiological or pathological respiratory firing patterns. We also provide initial characterization of these fibers, demonstrating several common techniques in this new model system in the context of the established Flexor Digitorum Brevis muscle primary culture model.

1. Introduction

The bodies of vertebrates include hundreds of skeletal muscles, each involved in performing different motor tasks at specific anatomical locations. This variety in skeletal muscles and their functions implies genotypic and phenotypic diversity among skeletal muscle fibers. In fact, the preferential expression of different muscular protein isoforms and therefore the existence of distinct muscle fiber phenotypes is one of the main determinants of the muscle performance [1, 2]. Not only does this diversity manifest in multiple muscle groups but also a single muscle expresses heterogeneous populations of slow and fast-type muscle fibers [1, 3]. Excitation-contraction coupling properties, the sensitivity of the contractile apparatus to Ca^{2+} , mechanical power output, shortening velocity, and rate of ATP hydrolysis are also known to vary greatly from fiber to fiber [1, 4–7]. The intercostal muscles are an exemplary case of such a heterogeneous muscle population, making them an attractive model for comparative studies.

The mechanical functions of the intercostal muscles during ventilation are highly complex. There are two major

division criteria for intercostal fibers: anatomical and functional. Anatomical divisions are based on location on the internal or external side of the ribs; functional divisions are based on participation in expiratory or inspiratory respiration [8]. The external intercostals and the parasternal intercostals function in inspiratory breathing, whereas the internal intercostals have an expiratory function [9]. Although the function of the diaphragm appears to dominate breathing at rest [10], the intercostal muscles may contribute c.a. 40% of the volume shift by movement of the thoracic wall [11]. During intensified breathing, the contribution of the intercostals becomes more prominent [12, 13]. The lateral internal intercostals are also recruited for a variety of nonventilatory functions including the cough reflex and speech as well as for postural support [10].

Previous work estimates that about 60% of the intercostal fibers are slow-type and 40% fast-type fibers [14, 15]. As a result of this diversity, the same preparation can be used to address many aspects of muscle fiber-type physiology. Also, due to their involvement in the mechanics of ventilation and the fact that respiratory pathology is common in several diseases (e.g., muscular dystrophy, chronic obstructive

pulmonary disease, amyotrophic lateral sclerosis, hereditary polyneuropathies, autoimmune conditions like myasthenia gravis, muscular paralysis, etc.), intercostal muscles represent a model of high clinical relevance.

Indeed, in cases where diagnosis and treatment for muscular dystrophy is available, respiratory arrest has become the critical factor in the majority of fatalities arising from muscular dystrophy [16, 17]. While the vast majority of studies evaluating the function of the respiratory muscles have used the diaphragm muscle as model of study, information on the intercostal muscles, in particular at cellular level, is more fragmented [8].

These muscles are also of relevance in Chronic Obstructive Pulmonary Disorder (COPD), given their critical role in manipulating the configuration of the ribs [9] and therefore the overall morphology of the thorax. In addition to the mechanical reorganization of the intercostal muscles that results from the inflated thorax common to COPD patients, clear changes in the expression of myosin heavy chain isoforms have been documented [18].

Here we describe in detail the isolation and preliminary characterization of isolated adherent intercostals muscle fibers in the common laboratory mouse based on techniques and methods previously developed by our laboratory for use on other muscles [19–25]. The loading of fluorescent Ca^{2+} indicators combined with electrophysiological approaches, including electrical field stimulation of the cultured muscle fibers using any stimulation pattern desired, and the transfection and overexpression of fluorescent fusion proteins permit the study of spatiotemporal aspects of excitation-contraction coupling and biological processes such as excitation-transcription coupling. Due to the difficulty encountered in achieving consistent adhesion of the intercostal fibers to commercial glass-bottom culture dishes, we also include detailed methods for the construction and preparation of glass-bottom dishes optimized for such muscle fiber studies. These dishes have improved the reliability and yield of attached fibers in our preparations several fold. The methods presented here can be modified to allow culture of intercostal fibers from animal at various ages or from animal models with specific genetic background. The protocol described here is intended more generally to provide a flexible new primary cell culture of the as yet poorly characterized, but clinically relevant muscular group, the intercostals.

2. Methods

2.1. Animal Use. All animals were euthanized by CO_2 exposure followed by cervical dislocation before removal of the muscles according to protocols approved by the University of Maryland Institutional Animal Care and Use Committee.

2.2. Dish Construction. Dishes are constructed from plastic Petri dishes with glass coverslips and sealed using parafilm. Wells are drilled with an 11/32" bit, cleaned with a razor, and washed with 70% ethanol (Supplemental Figures 1(a)–1(e) available online at doi:10.1155/2011/393740). Multiple wells may be cut per dish to increase plating area (Supplemental

Figure 1(f)); drilling larger holes is not recommended as we have observed that small wells improve adhesion of the fibers.

Parafilm folded to double thickness is cut using the coverslip as a template (Supplemental Figure 2). An unused pencil eraser is useful to hold the coverslip in place, but should be covered with a piece of scotch tape to minimize transfer of oils to the glass. Coverglass is then heated lightly on a hotplate with the parafilm facing up until the parafilm becomes transparent but not liquid. Dishes are pressed firmly over coverslips to seal each well and then parafilm is allowed to cool (Supplemental Figures 2(e)–2(g)). Parafilm from the center of the well is cut out with a scalpel and removed. The seal should be tested with water or media prior to use.

Prior to use, dishes are sterilized by UV irradiation and spotted with approximately $6\ \mu\text{L}$ of cold mouse laminin (1 mg/mL). Laminin is immediately covered with $100\ \mu\text{L}$ MEM and the bottom of each well is lightly scratched with the pipette tip to ensure full coverage (Supplemental Figures 2(k) and 2(l)). After at least 1 hour incubation, liquid is removed from the wells and dishes are rinsed twice with MEM and covered with 1 mL MEM plus $100\ \mu\text{L}$ MEM per well.

2.3. Dissection. Following cervical dislocation (see animal use), 70% ethanol is used to clean the mouse and dissection is carried out in a sterile laminar flow hood to prevent contamination of the culture. Hindfeet are pinned at maximal posterior extension, and forepaws are pinned at maximum lateral extension with the ventral face of the mouse up (Figure 1(b)). Skin is cut, posterior to anterior, from the lower abdomen to the throat (Figure 1(c)), and a lateral incision is made with a scalpel at the posterior end of the cut to pin back the skin (Figure 1(d)). Skin is removed by gently raking the scalpel against the interface between skin and subcutaneous tissue (Figures 1(e) and 1(f)) until the vertebral column is nearly exposed. An incision is made at the anterior end of the abdominal cavity, exposing the liver (Figure 1(g)). When the liver is pulled back, the diaphragm is exposed, although difficult to visualize. The thoracic cavity may be punctured by following the dorsal face of the sternum with a scalpel, causing the thoracic cavity to inflate (Figure 1(h)). This makes the diaphragm easier to see and remove by cutting along the posterior internal edge of the rib cage (Figure 1(i)). Once the diaphragm is free, an incision is made along the ventral face of the sternum and the superficial muscles of the thorax are removed in a similar fashion to the skin (Figures 1(j)–1(l)). This exposes the intercostal muscles which are then immediately bathed in MEM to prevent drying. One half of the rib cage is then excised by using scissors to cut along the sternum (Figure 1(m)) and thoracic vertebrae (Figure 1(n)). The half rib cage is then placed in MEM to rinse away excess debris (Figure 1(o)).

2.4. Digestion and Fiber Isolation. The media used to rinse the ribs is removed and replaced with MEM containing 2 mg/mL collagenase and 5 mg/mL dispase which has been passed through a $0.2\ \mu\text{m}$ filter. The ribs are then incubated at 37°C and 5% CO_2 for 3 hours (older mice may require

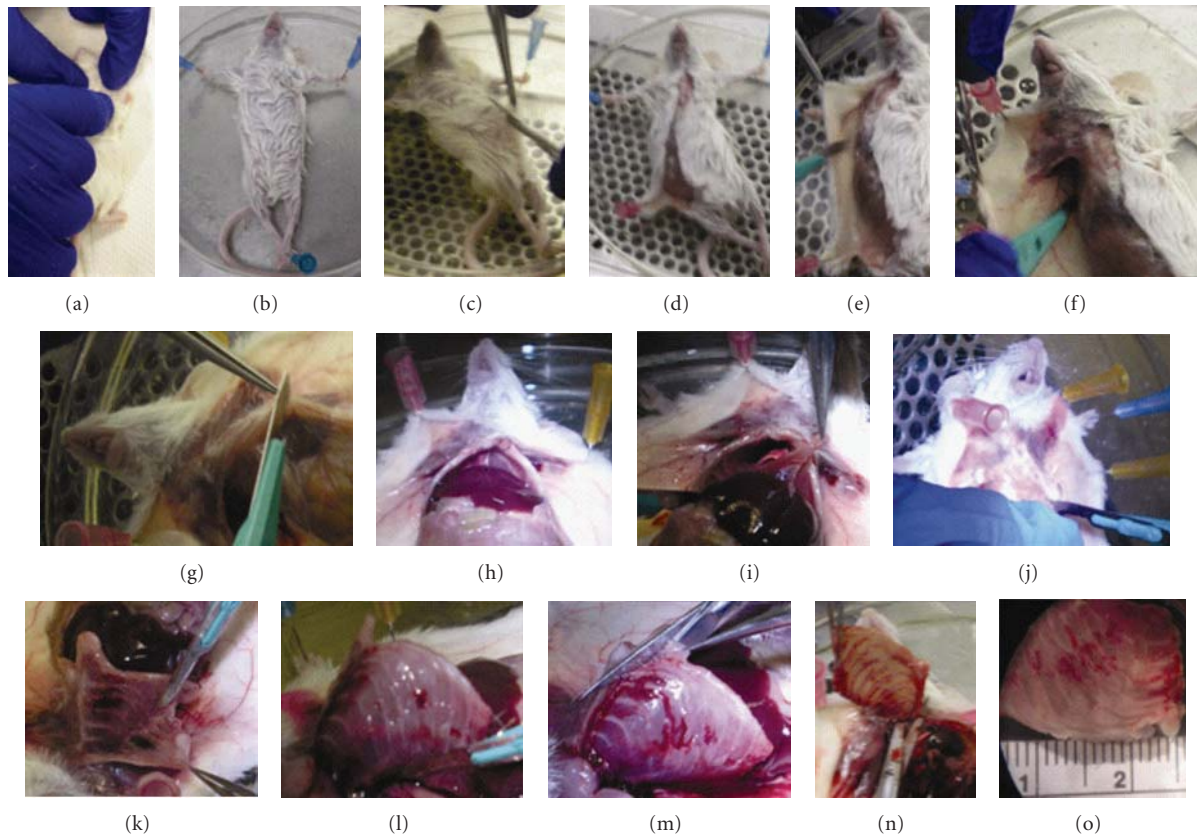


FIGURE 1: Critical Steps in Gross Dissection of Intercostal Muscles. (a) Cervical dislocation following CO₂ asphyxiation and 70% ethanol wash. (b) Pinning mouse, ventral face up. (c) First incision from posterior abdomen to throat. (d) Skinning: pinning back initial flap. (e) Skinning: cutting subcutaneous connective tissue. (f) Skinning: continue removal to vertebral column. (g) Opening incision at anterior end of abdominal cavity. (h) Exposed posterior face of thoracic cavity (after puncture). (i) Removal of diaphragm. (j) Incision along ventral face of sternum. (k) Removal of pectoral and other muscle groups. (l) Full exposure of ribs. (m) Severing ribs (ventral face). (n) Severing ribs (dorsal face). (o) Isolated ribs transferred to HBSS for imaging. Scale is centimeter ruler.

longer incubation). Following digestion, the ribs are transferred into MEM supplemented with 10% FBS and the procedure is continued under a dissection microscope. Excess vasculature and fragments of nonintercostal muscle fragments are removed with forceps. A single band of intercostal muscle is isolated with its flanking ribs (Figure 2(a), white arrows) by pulling the flanking ribs away from the next nearest (Figure 2(a), black arrows).

The isolated rib pair and the intercostal band are transferred to a clean 60 mm dish containing 7 mL of MEM supplemented with 10% FBS (Figure 2(b)). Fibers are triturated using a large bore flame polished pipette (Figure 2(c), Supplemental Figure 3) until a significant population of isolated fibers is obtained (Figure 2(d)). If muscle tissue detaches completely from ribs, a smaller bore pipette may be used. The dish is gently swirled to aggregate fibers (Figure 2(e)). If large amounts of debris are floating on the surface of the media, it may be removed. A wide bore micropipette tip is used to gather 8–12 healthy fibers per well from the periphery of the fiber cluster. Fibers are plated directly onto the glass surface in each well of the dishes prepared earlier. Fibers may be damaged or stick to the interior of the tip. These are removed and replaced; however, overplating can

cause fibers to mutually interfere with attachment and is to be avoided. Large pieces of debris or dying fibers are removed with forceps if it is possible to do so without disturbing healthy fibers. After several minutes to allow initial attachment, dishes are transferred to the incubator overnight to complete attachment. We note that fibers often attach near the periphery of the dish even when plated initially in the center.

In all cases, fibers are maintained in media without serum following dissociation. The removal of serum from the media following dissociation of the fibers mitigates gross morphological changes, proliferation of secondary cells, and some changes in calcium signaling [26, 27].

2.5. Digestion Conditions of Nonintercostal Fibers. Disperse is omitted from the digestion of both soleus and FDB muscles. FDBs (but not soleus) may be fully digested in as little as 2.5 hours, particularly if the mouse used is young. Apart from removal of bone (not required for either soleus or FDB), plating may proceed exactly as with the intercostal fibers, although a smaller bore pipette may be used for trituration if desired.

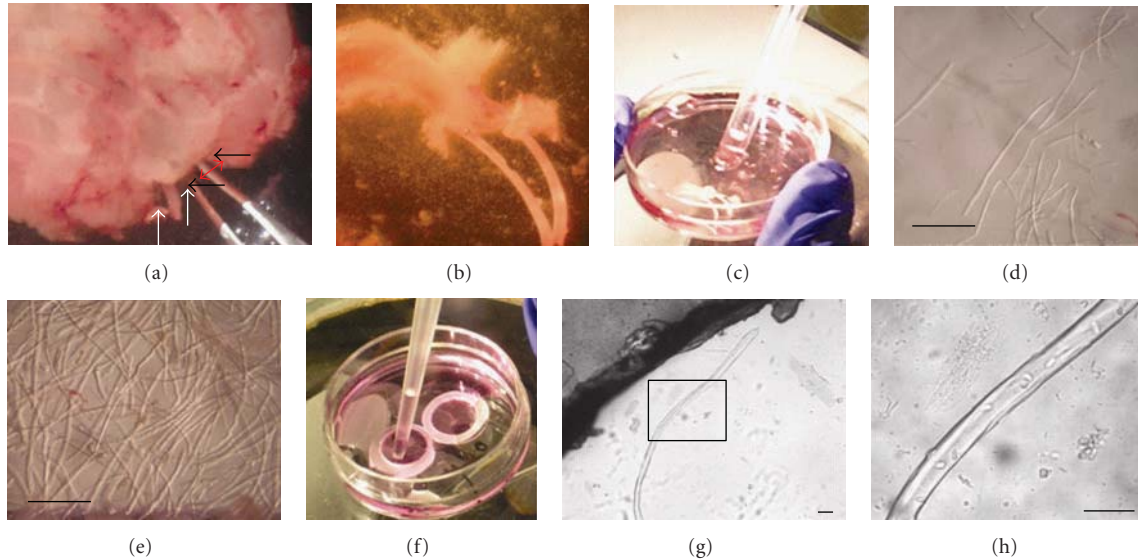


FIGURE 2: Dissociation. Following digestion, ribs are transferred into MEM containing 10% FBS and gentamycin (a). Rib pair flanking the desired muscle (white arrows) is isolated (b) and transferred into clean 60 mm Falcon Petri dish containing 7 mL MEM with 10% FBS and gentamycin. Fibers are triturated (c) until a significant population of fibers are isolated (d). Fibers may be aggregated in the center of dish (e) by shaking gently in a circular motion. FinnTip 250 Wide pipette tips are used to plate fibers (f) to prevent damage from fluidic shearing. Brightfield images of an adhered fiber at low (g) and high (h) magnification. Scale bars are approximately 1 mm (d, e) or 50 μm (g, h).

2.6. Indo1 Ratiometric Recordings. Cultured FDB or intercostal fibers were loaded with Indo-1 AM (Invitrogen, Eugene, OR) at a bath concentration of 2 μM for 30 min at 22°C. Then, the fibers were washed thoroughly with L-15 media to remove residual Indo-1 AM and incubated at 22°C for another 30 min to allow dye conversion. The culture dish was mounted on an Olympus IX71 inverted microscope and viewed with an Olympus 60x/1.20 NA water immersion objective. Fibers were illuminated at 360 nm, and the fluorescence emitted at 405 and 485 nm was detected simultaneously. The emission signals were digitized and sampled at 10 Hz using a built-in AD/DA converter of a EPC10 amplifier and the acquisition software Patchmaster (HEKA, Instruments). Field stimulation (square pulse, 14 V \times 1 ms) was produced by a custom pulse generator through a pair of platinum electrodes. The electrodes were closely spaced (0.5 mm) and positioned directly above the center of the objective lens, to achieve semilocal stimulation. Only fibers exhibiting reproducible and consistent responses to field stimulation of alternate polarity were used for the analysis.

2.7. Fluo-4 AM Ca^{2+} Recordings. Fluo-4 AM (Invitrogen, Eugene, OR) loading, high speed line scan $x-t$ imaging on a Zeiss LSM 5 Live confocal system, and image analysis were all performed as previously described [25]. Fibers were stimulated using parallel platinum field electrodes, with acquisition of the Fluo4 confocal line scan image synchronized to the field stimulus to generate a temporal profile.

2.8. Exogenous Protein Expression and Imaging. The recombinant adenovirus of Glut4-GFP was kindly provided to our laboratory by Dr. Jeffrey Pessin. The expression plasmid of

NFATc1 cDNA was a gift from Dr. Gerald R. Crabtree. The construction of recombinant adenoviruses of NFATc1-GFP as well as the procedures for infection with recombinant adenoviruses of single muscle fibers has been previously described [24]. Cultures were maintained in MEM in a 37°C, 5% CO_2 incubator until expression levels were appropriate for imaging, then transferred into Liebovitz L-15 (GIBCO) for microscope work. Images were taken using an Olympus IX70 inverted microscope equipped with an Olympus Fluoview 500 laser scanning confocal imaging system using an Olympus 60x/1.2 NA water immersion objective. A 488 nm excitation wavelength and 505 nm long-pass emission filter were used to visualize GFP.

2.9. Data Analysis. Line-scan Fluo4 images were processed using LSM examiner (Carl Zeiss, Jena). GFP and Glut4-GFP confocal images were processed using ImageJ (NIH, Bethesda, MD, USA; <http://rsb.info.nih.gov/ij/>). Indo1 and fluo4 Ca^{2+} signals and statistical analysis were conducted using Origin pro 8 (OriginLab Corporation, Northampton, MA, USA). Summary data were reported as mean \pm SEM. Statistical significance was assessed using parametric unpaired two sample t -test. Differences were considered significant when P value < 0.05.

Indo1 data was reported as the ratio of fluorescence emission at 405 nm to emission at 485 nm (indo1 ratio) which correspond to the peak values of the calcium bound and unbound forms, respectively, or the difference in indo1 ratio between peak and resting values (Δindo1 ratio). Fluo4 data was reported as the difference between fluorescence intensity and an average value of fluorescence taken when the fiber was at rest, normalized to the resting value ($\Delta F/F_0$).

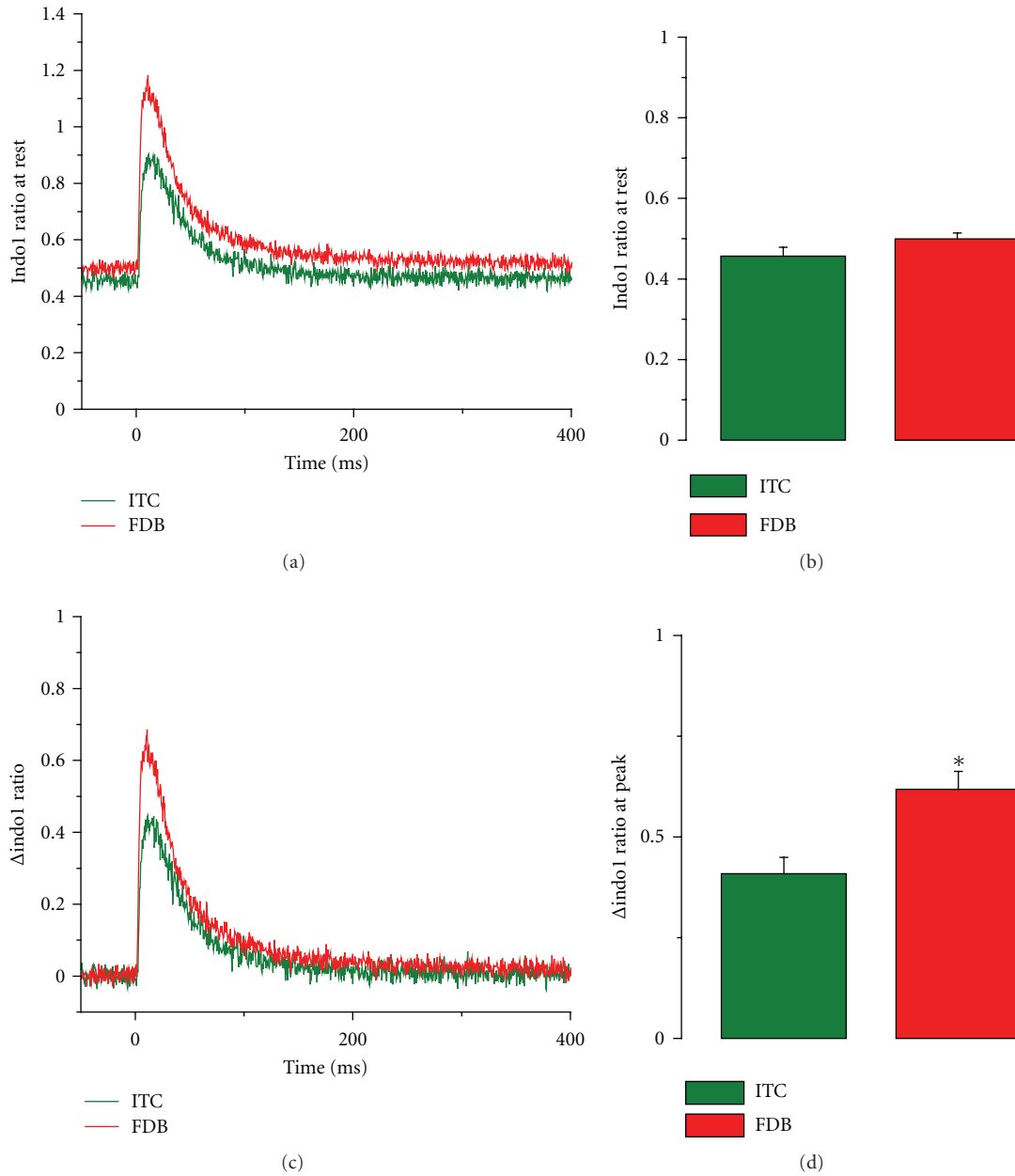


FIGURE 3: Intercostal fibers exhibit decreased peak amplitude of the Indo-1 Ca^{2+} transient following a single action potential. (a) Average Indo-1 ratio Ca^{2+} transients from FDB (red trace; $n = 9$) and Intercostal (ITC; green trace; $n = 11$) fibers. Isolated fibers were stimulated with field electrodes at time zero and emission ratio was examined. (b) Bar plot summarizing resting Indo-1 ratio averages of FDB and ITC fibers. No significant differences in resting indo1 ratio were detected between groups ($P = 0.12$). (c) Traces from panel (a), expressed as $\Delta\text{Indo-1}$ ratio (Indo1 ratio—Indo1 ratio at rest). (d) Bar plot representation of peak $\Delta\text{Indo-1}$ ratio shown in (c), FDB = 0.61 ± 0.04 , $n = 9$; ITC = 0.40 ± 0.04 , $n = 11$; $*P = 0.0015$. Error bars in (d) are the SE values. ITC fibers displayed significantly reduced Ca^{2+} transients when compared with FDB fibers.

Data from the NFATc1-GFP fusion protein was reported as the ratio of fluorescence intensity in the nucleus to the intensity in the cytoplasm (N/C) in order to correct for variations in expression level between fibers. Raw data for both Fluo4 and NFATc1 was corrected for background before analysis by subtracting the intensity measured in a region outside the muscle fiber.

3. Results

3.1. Gross Morphology. The intercostal muscles are composed of two overlapping sheets (inner and outer) of muscle fibers with roughly perpendicular orientations. Each muscle spans diagonally between two ribs from the vertebral column to the sternum. Following dissection connective tissues between

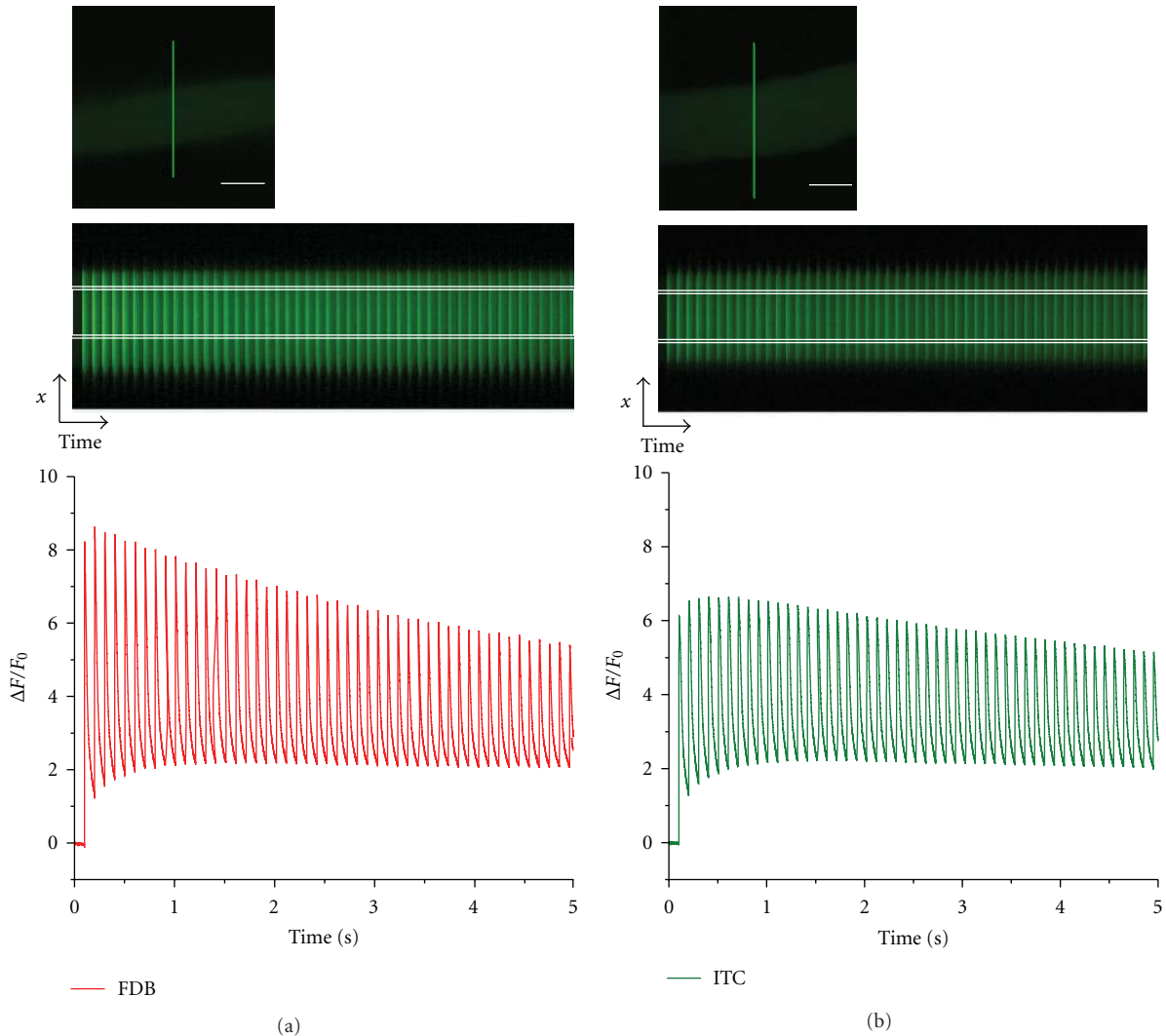


FIGURE 4: Fluo4 Ca^{2+} transients elicited by field stimulation in intercostal and FDB fibers. Representative line-scan images of Ca^{2+} transient responses in FDB (a) and intercostal (b) fibers to a 5 sec 10 Hz train of field stimulation applied at time zero, performed with nonratiometric fluo-4 AM loaded fibers and assayed with high-speed confocal line scan microscopy ($100 \mu\text{s}/\text{line}$). Images in top of panels (a) and (b) show xy images of FDB and intercostals fibers to indicate the location of the scan line, scale bar is $20 \mu\text{m}$. Note that fluo-4 signal at rest in these fibers is very low. Traces under the images are the time courses of the fluo4 Ca^{2+} transients. The white lines in the time domain images indicate the region of interest drawn at the center of the fiber and used to calculate the change in fluorescence in response to field stimulation. Data presented as $\Delta F/F_0$. Fluorescence was detected with a Zeiss LSM 5 Live ultrafast confocal system based on an Axiovert 200M inverted microscope. Fibers were imaged with a 63x/NA 1.2 water immersion objective lens. Excitation for fluo-4 was provided by the 488 nm line of a 100 mW diode laser, and emitted light was collected at $>510 \text{ nm}$.

muscle and ribs are not readily appreciable at the macroscopic scale (Figure 1).

3.2. Isolating Intercostal Fibers. The initial attempt to isolate and culture intercostal muscle fibers was based on our existing protocols for isolating and culturing mouse Flexor Digitorum Brevis (FDB) fibers [21–25], which are maintained in commercially available glass-bottomed dishes. After an initial development and optimization of dissection and enzymatic treatment methods, we achieved a high fraction of viable isolated intercostal fibers. These fibers maintained clear striations and twitch response for several days, but did not reliably form adherent cultures, even after extensive

experimentation with a variety of substrates derived from extracellular matrix. During the course of unrelated work, we noted that customized glass-bottomed dishes which we had designed with smaller diameter wells using a different glass substrate seemed to facilitate attachment in our FDB model (see Supplemental Figures 1 and 2). Plating intercostal fibers in these dishes dramatically improved the attachment rate and reliability of the culture.

After fiber isolation, our procedure yields a heterogeneous mix of internal and external intercostal fibers with a successful attachment rate around 50%. Isolated intercostal fibers (Figure 2) are similar to FDBs in width, but 4–5 times the length. This additional length makes the fibers

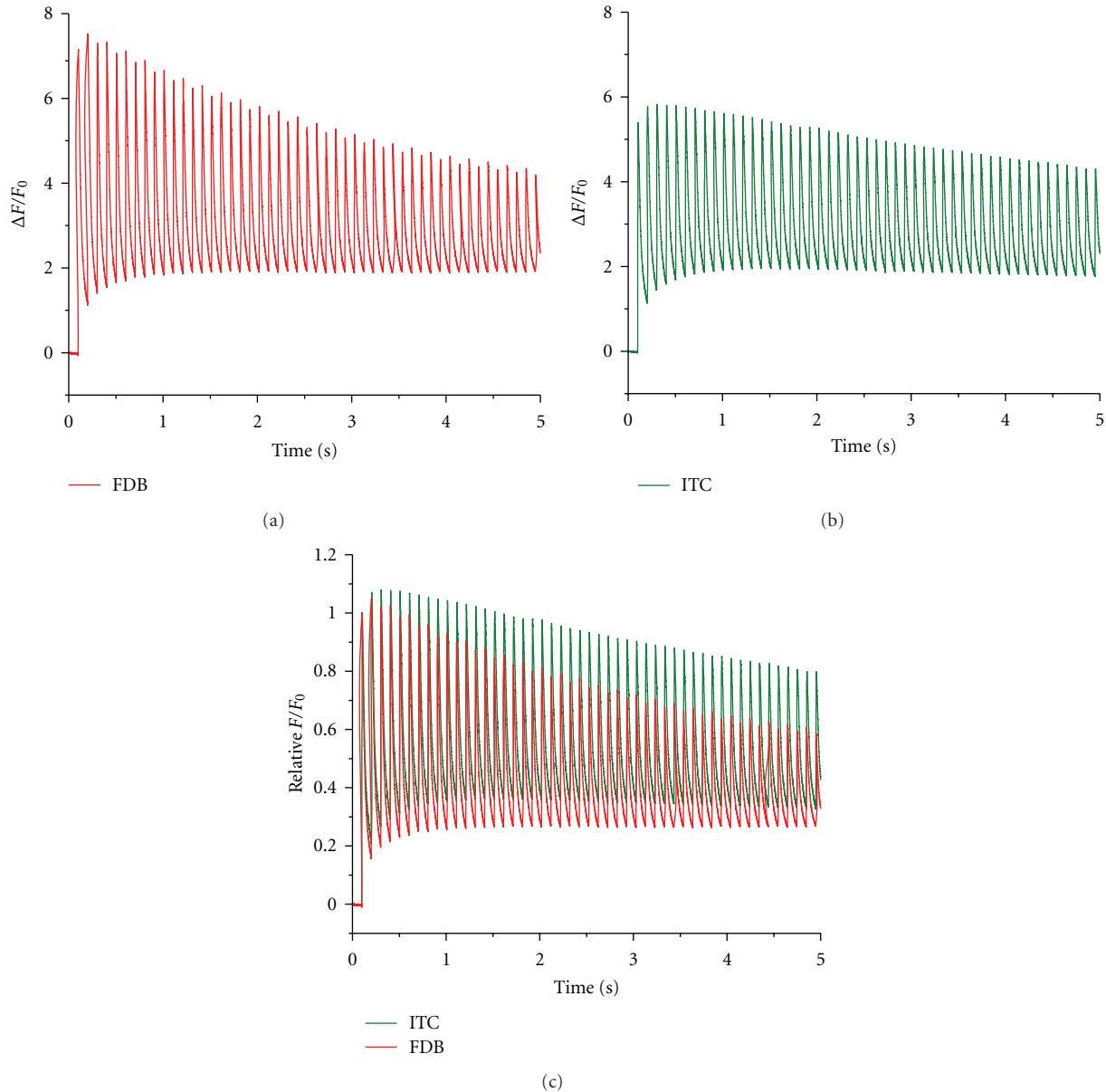


FIGURE 5: Comparison of electrically evoked Ca^{2+} transients between intercostal and FDB fibers. Average fluo-4 Ca^{2+} transient from FDB ((a), red trace; $n = 9$) or intercostals fibers ((b), ITC, green trace; $n = 9$) in response to 5 sec 10 Hz train field stimulation. Traces in (c) were normalized to the amplitude of the initial response. At the end of the 5 sec train, ITC fibers demonstrated significantly smaller relative decrease of Ca^{2+} transient amplitude compared to FDB counterparts ($P < 0.05$). ITC muscle fibers exhibit decreased peak amplitude of the fluo-4 Ca^{2+} transients in response to a single field stimulus; however, the intercostals are able to maintain consistent levels of calcium during repetitive stimulation. Fluorescence was detected as in Figure 4.

susceptible to bends when they are fully attached (see Figure 1(g)). Almost all of the whole fibers that attach to the glass display clear striations (Figure 6) and respond to external electrical field stimulation administered either as single pulses or repetitive trains with twitching similar to that of FDBs (see supplemental videos 1 and 2).

In order to examine the general applicability of these dishes, we also used them to plate fibers from the slow-type soleus muscle, which also displays poor adherence characteristics [22]. Although we used a less stringent digestion procedure, plating was carried out exactly as for intercostals.

The exceptional length of the soleus fibers causes them to interfere with each other and permits the formation of many bends and kinks which prevent complete attachment. Nonetheless, the fibers were responsive to electrical stimulation and adhered securely enough to withstand repeated twitching (see supplemental video 3) more than 24 hours after plating. Successful attachment rate was variable between the wells plated, but overall comparable to the intercostals.

3.3. Ca^{2+} Homeostasis and Electrically Evoked Ca^{2+} Transients in Intercostal Fibers. Primary cultured intercostal fibers

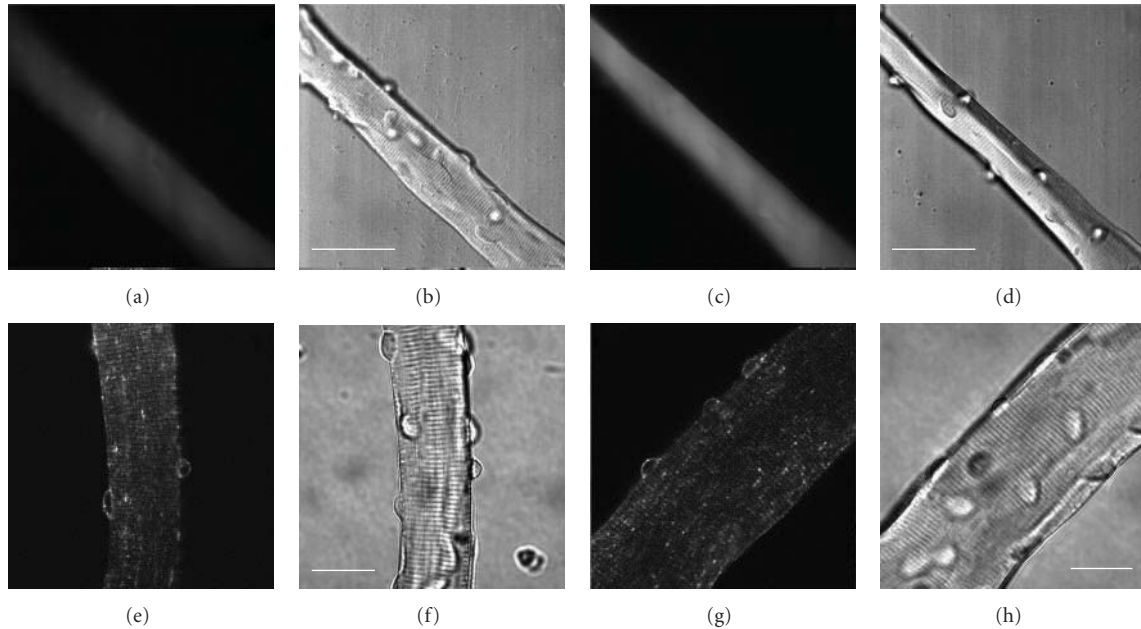


FIGURE 6: Overexpression of foreign proteins in intercostal fibers in culture. FDB (a, b, e, f) and intercostal (c, d, g, h) muscle fibers expressing either GFP (a–d) or a Glut4-GFP fusion construct (e–h). Scale bars are $50\ \mu\text{m}$ (b, d) or $25\ \mu\text{m}$ (f, h). Images were acquired as in Figure 4 for panels (a–d) or with an Olympus FluoView 500 confocal system, built on an Olympus IX71 inverted microscope for panels (e–h). Fibers were imaged viewed with a UPlan Apo 60x/NA 1.20 water-immersion objective lens using 488 nm excitation (Multiline Argon laser) for GFP with emission detected with 505 nm long-pass filter. Photobleaching and photodamage were reduced by operating the lasers at the lowest possible power that still provided images with satisfactory signal to noise ratio. Brightfield images in panels (b, d, f, h) were adjusted for improved contrast using ImageJ.

retain many properties of native fibers, including contractions and Ca^{2+} transients in response to electrical field stimuli (Figures 3, 4, and 5; see Supplemental Video 1). A brief comparative study between intercostal fibers and the established FDB isolated fiber model was also conducted (Figures 3, 4, and 5). First, we sought to evaluate Ca^{2+} handling properties in single, intact indo1-loaded intercostal ($n = 8$) and FDB ($n = 16$) muscle fibers stimulated by an action potential (AP) elicited by a 1 ms electric field stimulus (Figure 3). While resting indo1 ratio prior to stimulation was not significantly different between intercostal (0.45 ± 0.02 ; $n = 11$) and FDB fibers (0.49 ± 0.01 ; Figures 3(a) and 3(b); $n = 9$, $P = 0.12$), the peak of the indo1 Ca^{2+} transient following a single AP (Δindo1 ratio) was significantly smaller in intercostal fibers than in the FDB fibers (intercostal = 0.40 ± 0.04 , FDB = 0.61 ± 0.04 , $P = 0.0015$, Figures 3(c) and 3(d)). These results suggest that intercostal fibers exhibit a decreased AP-evoked Ca^{2+} release.

To allow better temporal resolution of the Ca^{2+} transients, we next monitored fluo-4 transients during repetitive stimulation of intercostal and FDB fibers using an ultra high-speed ($100\ \mu\text{s}/\text{line}$) confocal microscope in line scan mode. Figure 4 illustrates representative x - t confocal images and corresponding fluo4 Ca^{2+} transients, expressed as $\Delta F/F_0$, from an FDB (Figure 4(a)) and an intercostal (Figure 4(b)) fiber during a 5-second 10 Hz train. Line-scan fluorescence images were obtained along a line perpendicular to the long axis of the fiber (Figures 4(a) and 4(b), top panels). Successive vertical lines in each image reveal the time course

(left to right; middle panels) at $100\ \mu\text{s}$ resolution of the fluorescence signal along the scanned line before and during the repetitive stimulation. Bottom panels in Figures 4(a) and 4(b) show the time course of the fluo4 fluorescence. Figure 5 shows average responses from FDB (red trace; Figure 5(a)) and intercostal (green trace; Figure 5(b)) fibers stimulated by a 5-second 10 Hz train. Consistent with the Indo-1 data (Figure 3), fluo4 Ca^{2+} transients appear suppressed in intercostal fibers (Figure 5(b)) in comparison to those observed in FDB fibers (Figure 5(a)).

However, the intercostals are able to maintain a more consistent level of calcium release during repetitive stimulation (Figure 5(b)). By normalizing the traces elicited by the 10 Hz trains to the amplitude of the first fluo4 transient in their respective train, the relative differences in Ca^{2+} transient summation as well as the properties of decaying phase during the train can be appreciated (Figure 5(c)). Both intercostal and FDB fibers showed an initial increase in the peak amplitude during the 10 Hz train protocol, exceeding the peak value of the initial stimulation until 2 and 0.5 seconds, respectively (Figure 5(c)). Additionally, the relative amplitude of the Ca^{2+} transients during the 10 Hz train declines more slowly in intercostal fibers (Figure 5(c)).

Unexpectedly, subpopulations reflecting an anticipated difference between fiber types were not observed in the intercostal fibers. However, we suspect that this is not due to genuine homogeneity, but rather a limitation of the calcium ion equilibration kinetics of fluo-4 in distinguishing such sub-populations, which may be quite similar.

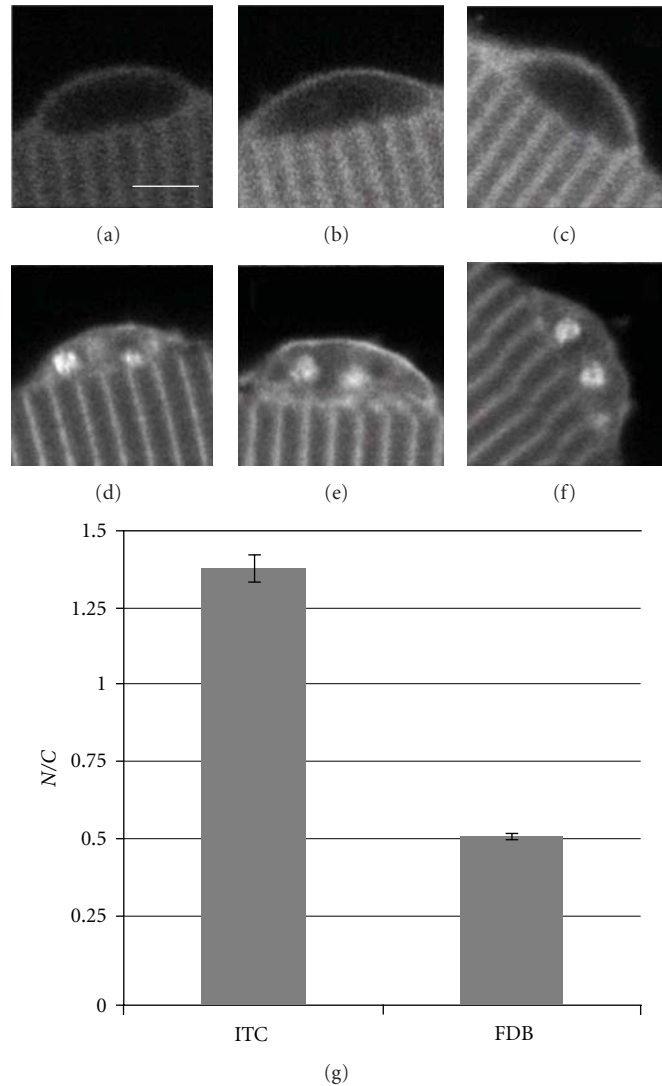


FIGURE 7: NFATc1-GFP distribution in intercostal and FDB fibers. FDB (a–c) and intercostal (d–f) fibers expressing NFATc1-GFP imaged at rest after 3 days in culture. Scale bar, 5 μm . Nuclei in intercostal fibers exhibit significantly elevated levels of NFATc1 when compared to FDBs cultured under the same conditions (g), N/C ratio of NFATc1-GFP in ITC = 1.38 ± 0.05 , $n = 102$ nuclei versus 0.51 ± 0.01 , $n = 42$ nuclei, in FDB fibers, $P < 0.05$). Fluorescence was detected as in Figure 6.

These results lead us to conclude that adherent cultures of intercostal fibers are a new and unique model for the study of Ca^{2+} -signaling pathways at the cellular and subcellular levels by using ultrafast confocal imaging combined with Ca^{2+} -sensitive fluorescent probes.

3.4. Expression of Exogenous Proteins. In order to assess the viability of the intercostal cultures for imaging studies utilizing fluorescent proteins, fibers in culture were exposed to crude lysates of recombinant adenoviral vectors expressing GFP. Exposure to virus was carried out overnight, beginning immediately after plating. Vector dosage was calibrated by expression levels in similarly treated FDB fibers. Cultures were maintained in an incubator to allow expression prior to imaging. Expression of GFP was robust after 48 hours and did not appear to damage the fibers, which maintained clear striations (Figures 6(b) and 6(d)).

We also exposed other cultures to a viral vector expressing a Glut4-GFP fusion protein. Expression continued through 96 hours (Figure 6(g)). Glut4-GFP was expressed in intercostal fibers in puncta both around the nucleus and in lines parallel to the axis of the fiber (Figures 6(e) and 6(g)). This distribution is similar to what we observe in FDB fibers infected with the native transporter characterized by immunofluorescence [28], although we observe weaker striations, presumably due to lack of exposure to insulin during the culture period reducing the Glut4 present in the transverse tubule system.

Finally, we exposed the fibers to a viral construct expressing a NFATc1-GFP fusion construct. NFATc1 is a transcription factor canonically regulated by the calcium-dependent phosphatase calcineurin [29, 30]. Typically resting FDB fibers exhibit low translocation of NFATc1 into

the nucleus (Figures 7(a), 7(b), and 7(c)) [24]. Unexpectedly, ITC fibers exhibited a higher nuclear distribution of NFATc1-GFP at rest (Figures 7(d), 7(e), and 7(f)) when compared to FDB fibers (Figures 7(a), 7(b), and 7(c)). The resting nuclear/cytosolic (N/C) ratio of NFATc1 was significantly elevated in intercostal fibers (Figure 7(g)) compared to FDB (1.38 ± 0.05 , $n = 102$ nuclei versus 0.51 ± 0.01 , $n = 42$ nuclei, resp.; $P < 0.05$).

4. Discussion

Adult skeletal muscle fiber culture currently focuses on only a handful of the myriad available muscles in the body, extrapolating from the few established culture systems like the FDB to the body as a whole. While it is generally true that various skeletal muscles resemble one another, there is significant divergence among them with respect to their physiology and the expression levels and isoforms of many muscle specific and metabolic proteins [1, 5–7]. This is dramatically illustrated by the high specificity of pathology in many skeletal muscle disease states resulting from defects in specific genes (e.g., the disproportionate targeting of facial, shoulder, and limb muscles in facioscapulohumeral muscular dystrophy or the extremities in distal muscular dystrophy [17]).

The intercostal fiber cultures introduced here themselves appear to be nearly as versatile as the more established FDB cultures. While we have not yet used intercostal cultures in applications requiring large numbers of adherent fibers, they have proven viable for a wide variety of single fiber experiments, even after several days in culture. Previous work related to the physiology of intercostal muscles comes from studies utilizing organ culture of intact muscle fiber bundles [31–35]. Whereas intercostal muscle fiber bundles offer the advantage of preserving nerve-muscle interactions, as with many organ culture systems it may not be well suited for single cell electrophysiology and high spatial resolution imaging. Furthermore, the ability to mimic stimulation patterns that may be experienced by the muscle during stressed states in vivo (such as hyperventilation or coughing) at the single muscle fiber level offers the opportunity to isolate the response of the muscle from that of the surrounding tissue in a manner not possible with organ culture methods. A variant of the single intercostal fiber isolation was described previously and was used to study satellite cell differentiation cocultured with nonadherent intercostal fibers derived from goats [36]. While these methods are valuable, the availability of adherent single fiber models for imaging and electrophysiology substantially expands our ability to study these muscle types.

The value of studying each skeletal muscle as a separate tissue is demonstrated by our unexpected observation of spontaneous accumulation of NFATc1 in the nuclei of resting fibers. It is clear that studies using only a few particular skeletal muscles risk overlooking interesting phenomena. Given the complexity of transcriptional regulation, the heterogeneous nature of the physiology and molecular biology of various skeletal muscles and the diverse tissues which surround them, we suspect that examining a wider variety

of muscles specifically relevant to individual diseases in controlled in-vitro settings will prove fruitful.

Our culturing of intercostal muscles aims to do this not only by providing a particular model system specifically relevant to the pathology of COPD and the respiratory complications of the muscular dystrophies [16, 17], but also by improving the general techniques of adherent isolated muscle fiber culture. If these techniques are optimized for poorly adhering muscle types, generating cultures from any muscle in the body may become substantially easier, and using the most relevant tissue in a given disease model may become routine.

Acknowledgment

This work was supported by NIH-NIAMS Grants R01-AR055099, R01-AR056477. P. Robison was supported by the Interdisciplinary Training Program Muscle Biology T32-AR007592.

References

- [1] R. Bottinelli and C. Reggiani, "Human skeletal muscle fibres: molecular and functional diversity," *Progress in Biophysics and Molecular Biology*, vol. 73, no. 2–4, pp. 195–262, 2000.
- [2] R. I. Close, "Dynamic properties of mammalian skeletal muscles," *Physiological Reviews*, vol. 52, no. 1, pp. 129–197, 1972.
- [3] J. C. Calderón, P. Bolaños, S. H. Torres, G. Rodríguez-Arroyo, and C. Caputo, "Different fibre populations distinguished by their calcium transient characteristics in enzymatically dissociated murine flexor digitorum brevis and soleus muscles," *Journal of Muscle Research and Cell Motility*, vol. 30, no. 3–4, pp. 125–137, 2009.
- [4] J. C. Calderón, P. Bolaños, and C. Caputo, "Myosin heavy chain isoform composition and Ca^{2+} transients in fibres from enzymatically dissociated murine soleus and extensor digitorum longus muscles," *Journal of Physiology*, vol. 588, no. 1, pp. 267–279, 2010.
- [5] R. L. Moss, G. M. Diffie, and M. L. Greaser, "Contractile properties of skeletal muscle fibers in relation to myofibrillar protein isoforms," *Reviews of Physiology, Biochemistry & Pharmacology*, vol. 126, pp. 1–63, 1995.
- [6] D. Pette and R. S. Staron, "Cellular and molecular diversities of mammalian skeletal muscle fibers," *Reviews of Physiology Biochemistry and Pharmacology*, vol. 116, pp. 1–76, 1990.
- [7] S. Schiaffino and C. Reggiani, "Molecular diversity of myofibrillar proteins: gene regulation and functional significance," *Physiological Reviews*, vol. 76, no. 2, pp. 371–423, 1996.
- [8] B. Polla, G. D'Antona, R. Bottinelli, and C. Reggiani, "Respiratory muscle fibres: specialisation and plasticity," *Thorax*, vol. 59, no. 9, pp. 808–817, 2004.
- [9] A. De Troyer, P. A. Kirkwood, and T. A. Wilson, "Respiratory action of the intercostal muscles," *Physiological Reviews*, vol. 85, no. 2, pp. 717–756, 2005.
- [10] A. Taylor, "The contribution of the intercostal muscles to the effort of respiration in man," *The Journal of Physiology*, vol. 151, pp. 390–402, 1960.
- [11] D. Faithfull, J. G. Jones, and C. Jordan, "Measurement of the relative contributions of rib cage and abdomen/diaphragm to tidal breathing in man," *British Journal of Anaesthesia*, vol. 51, no. 5, pp. 391–398, 1979.

- [12] G. H. Koepke, E. M. Smith, A. J. Murphy, and D. G. Dickinson, "Sequence of action of the diaphragm and intercostal muscles during respiration. I. Inspiration," *Archives of Physical Medicine and Rehabilitation*, vol. 39, no. 7, pp. 426–430, 1958.
- [13] A. J. Murphy, G. H. Koepke, E. M. Smith, and D. G. Dickinson, "Sequence of action of the diaphragm and intercostal muscles during respiration. II. Expiration," *Archives of Physical Medicine and Rehabilitation*, vol. 40, pp. 337–342, 1959.
- [14] M. Mizuno and N. H. Secher, "Histochemical characteristics of human expiratory and inspiratory intercostal muscles," *Journal of Applied Physiology*, vol. 67, no. 2, pp. 592–598, 1989.
- [15] M. Mizuno, N. H. Secher, and B. Saltin, "Fibre types, capillary supply and enzyme activities in human intercostal muscles," *Clinical Physiology*, vol. 5, no. 2, pp. 121–135, 1985.
- [16] L. D. Calvert, T. M. McKeever, W. J. Kinnear, and J. R. Britton, "Trends in survival from muscular dystrophy in England and Wales and impact on respiratory services," *Respiratory Medicine*, vol. 100, no. 6, pp. 1058–1063, 2006.
- [17] A. E. Emery, "The muscular dystrophies," *Lancet*, vol. 359, no. 9307, pp. 687–695, 2002.
- [18] J. G. Gea, "Myosin gene expression in the respiratory muscles," *European Respiratory Journal*, vol. 10, no. 10, pp. 2404–2410, 1997.
- [19] M. G. Klein, H. Cheng, L. F. Santana, Y. H. Jiang, W. J. Lederer, and M. F. Schneider, "Two mechanisms of quantized calcium release in skeletal muscle," *Nature*, vol. 379, no. 6564, pp. 455–458, 1996.
- [20] L. Kovacs, E. Rios, and M. F. Schneider, "Calcium transients and intramembrane charge movement in skeletal muscle fibres," *Nature*, vol. 279, no. 5712, pp. 391–396, 1979.
- [21] S. L. Carroll, M. G. Klein, and M. F. Schneider, "Calcium transients in intact rat skeletal muscle fibers in agarose gel," *American Journal of Physiology*, vol. 269, no. 1, pp. C28–C34, 1995.
- [22] S. L. Carroll, M. G. Klein, and M. F. Schneider, "Decay of calcium transients after electrical stimulation in rat fast- and slow-twitch skeletal muscle fibres," *Journal of Physiology*, vol. 501, no. 3, pp. 573–588, 1997.
- [23] Y. Liu, S. L. Carroll, M. G. Klein, and M. F. Schneider, "Calcium transients and calcium homeostasis in adult mouse fast-twitch skeletal muscle fibers in culture," *American Journal of Physiology*, vol. 272, no. 6, pp. C1919–C1927, 1997.
- [24] Y. Liu, Z. Cseresnyés, W. R. Randall, and M. F. Schneider, "Activity-dependent nuclear translocation and intranuclear distribution of NFATc in adult skeletal muscle fibers," *Journal of Cell Biology*, vol. 155, no. 1, pp. 27–39, 2001.
- [25] B. L. Prosser, N. T. Wright, E. O. Hernández-Ochoa et al., "S100A1 binds to the calmodulin-binding site of ryanodine receptor and modulates skeletal muscle excitation-contraction coupling," *Journal of Biological Chemistry*, vol. 283, no. 8, pp. 5046–5057, 2008.
- [26] L. D. Brown, G. G. Rodney, E. Hernández-Ochoa, C. W. Ward, and M. F. Schneider, "Ca²⁺ sparks and T tubule reorganization in dedifferentiating adult mouse skeletal muscle fibers," *American Journal of Physiology. Cell Physiology*, vol. 292, no. 3, pp. C1156–C1166, 2007.
- [27] L. D. Brown and M. F. Schneider, "Delayed dedifferentiation and retention of properties in dissociated adult skeletal muscle fibers in vitro," *In Vitro Cellular and Developmental Biology*, vol. 38, no. 7, pp. 411–422, 2002.
- [28] T. Ploug, B. van Deurs, H. Ai, S. W. Cushman, and E. Ralston, "Analysis of GLUT4 distribution in whole skeletal muscle fibers: identification of distinct storage compartments that are recruited by insulin and muscle contractions," *Journal of Cell Biology*, vol. 142, no. 6, pp. 1429–1446, 1998.
- [29] G. R. Crabtree and E. N. Olson, "NFAT signaling: choreographing the social lives of cells," *Cell*, vol. 109, no. 2, supplement 1, pp. S67–S79, 2002.
- [30] A. Rao, C. Luo, and P. G. Hogan, "Transcription factors of the NFAT family: regulation and function," *Annual Review of Immunology*, vol. 15, pp. 707–747, 1997.
- [31] S. M. Cardoso, P. Mutch, P. J. Scotting, and P. M. Wigmore, "Gene transfer into intact fetal skeletal muscle grown in vitro," *Muscle and Nerve*, vol. 30, no. 1, pp. 87–94, 2004.
- [32] S. G. Cull-Candy, R. Mileti, and O. D. Uchitel, "Denervation changes in normal and myasthenia gravis human muscle fibres during organ culture," *Journal of Physiology*, vol. 333, pp. 227–249, 1982.
- [33] R. L. Ruff and D. Whittlesey, "Na⁺ current densities and voltage dependence in human intercostal muscle fibres," *Journal of Physiology*, vol. 458, pp. 85–97, 1992.
- [34] L. Ziskind-Conhaim and M. J. Dennis, "Development of rat neuromuscular junctions in organ culture," *Developmental Biology*, vol. 85, no. 1, pp. 243–251, 1981.
- [35] L. Ziskind-Conhaim, I. Geffen, and Z. W. Hall, "Redistribution of acetylcholine receptors on developing rat myotubes," *Journal of Neuroscience*, vol. 4, no. 9, pp. 2346–2349, 1984.
- [36] K. Yamanouchi, T. Hosoyama, Y. Murakami, S. Nakano, and M. Nishihara, "Satellite cell differentiation in goat skeletal muscle single fiber culture," *Journal of Reproduction and Development*, vol. 55, no. 3, pp. 252–255, 2009.